

The 3rd Colloquium on Process Simulation

CONF-9606318--

Edited by
Ari Jokilaakso

Proceedings of the 3rd Colloquium on Process Simulation, 12 - 14 June 1996

**RECEIVED**

MAY 13 1997

OSTI

Helsinki University of Technology
Faculty of Process Engineering and Materials Science
Department of Materials Science and Rock Engineering
Laboratory of Materials Processing and Powder Metallurgy

Report TKK-V-B117

Espoo 1996

DISCLAIMER

**Portions of this document may be illegible
in electronic image products. Images are
produced from the best available original
document.**

TKK-V--B117

PROCEEDINGS OF THE
3rd Colloquium on
Process Simulation

Computational Fluid Dynamics coupled with
Chemical Kinetics, Combustion & Thermodynamics
Held at the Helsinki University of Technology, Espoo, Finland
12 - 14 June 1996

Edited by
Ari Jokilaakso

MASTER

DISTRIBUTION OF THIS DOCUMENT IS UNLIMITED

RB

Helsinki University of Technology
Faculty of Process Engineering and Materials Science
Department of Materials Science and Rock Engineering
Laboratory of Materials Processing and Powder Metallurgy

Report TKK-V-B117

Espoo 1996

Distribution:
Dr. Ari Jokilaakso
Helsinki University of Technology
Laboratory of Materials Processing and Powder Metallurgy
Vuorimiehentie 2 K
FIN-02150 ESPOO
Tel. +358-0-451 2775
Fax.+358-0-451 2799
E-mail: Ari.Jokilaakso@hut.fi

ISBN 951-22-3091-7
ISBN 951-22-3092-5 pbk.
ISSN 0785-5168

TKK OFFSET 1996
Espoo

ORGANISING COMMITTEE**Chairman**

Dr. Kaj R. Lilius, Professor
Helsinki University of Technology
Laboratory of Materials Processing and Powder Metallurgy
TKK-V, FIN-02150 Espoo, Finland

Dr. Philip Spencer

RWTH Aachen, Lehrstuhl für Theoretische Hüttenkunde
und Metallurgie der Kernbrennstoffe
Kopernikusstraße 16
D-5100 Aachen, Germany

Dr. D. Brian Spalding, Professor

Director, CHAM Ltd.
Bakery House, 40 High Street, Wimbledon Village,
London SW19 5AU
UK

Tony Smith, Ph.D.

Director, S&C Thermofluids Ltd.
The Old Tannery, Kelston
Bath BA1 9AN
UK

Dr. Heikki Jalkanen, Associate Professor

Helsinki University of Technology
Laboratory of Metallurgy
TKK-V, FIN-02150 Espoo, Finland

Dr. Lars Kjälman

Technical Research Centre of Finland
VTT Energy
P.O. Box 1604
FIN-02044 VTT, Finland

Dr. Ari Jokilaakso

Academy of Finland
c/o HUT, Laboratory of Materials Processing and Powder Metallurgy
TKK-V, FIN-02150 Espoo, Finland

Mr. Hannu Sippola

GEM-Systems Oy
P.O. Box 96
FIN-02210 Espoo, Finland

PREFACE

The papers collected in this volume were presented at the 3rd Colloquium on Process Simulation held at Helsinki University of Technology, Espoo, Finland, June 12 - 14, 1996.

In the more developed industrial nations, the processes for producing chemicals, energy, and materials encounter environmental concern and laws which challenge engineers to develop the processes towards more efficient, economical and safe operation. This necessitates more thorough understanding of the processes and phenomena involved. Formerly, the development of the processes was largely based on trial and error, whereas today, the development of computer performance together with the diversification of modelling software enables simulation of the processes. The increased capacity and possibilities for modelling the processes brought by the improved hardware and software, have generated a strong demand for more accurate mathematical descriptions of the processes. Especially, the coupling of computational fluid dynamics and chemical kinetics, combustion, and thermodynamics is of current interest in process oriented technology.

This colloquium attempts to give examples of modelling efforts in operation in different universities, research institutes and companies. Furthermore, the aim of this colloquium is to offer an annual opportunity to the researchers to come together and discuss their common problems and the state of their investigations.

The editor and organising committee wish to thank the invited speakers and authors who all contributed valuable modelling information presented at the colloquium and contained in this volume. We also wish to express our sincere appreciation to the staff of the Laboratory of Materials Processing and Powder Metallurgy who assisted us in organising the meeting.

Finally, thanks are due to the organising committee and session chairmen without whom such a colloquium would be impossible.

Ari Jokilaakso
Helsinki University of Technology

May 1996

TABLE OF CONTENTS

Organising Committee	iii
Preface	v
Table of Contents	vi
GENERAL COMPUTATIONAL FLUID DYNAMICS AND HEAT TRANSFER.....	1
Invited Lecture: Multi-Fluid Model of Turbulence (Abstract)	3
D. B. Spalding	
Numerical Simulation of Flow Induced by a Pitched Blade Turbine: Comparison of the Sliding Mesh Technique and an Averaged Source Term Method	7
E.O.J. Majander, M.T. Manninen	
Laminar Fluid Flow and Heat Transfer in a Fin-tube Heat Exchanger with Vortex Generators	27
J.I. Yanagihara, R.Rodrigues Jr.	
The Use of PHOENICS in the Design of Catalytic Converters.....	43
M. Luoma, A.G. Smith	
The New High-resolution Method of Godunov's Type for 3D Viscous Flow Computations	69
S.V.Yershov and Dr. A.V.Rusanov	
Nonstationary 3D Inviscid Numerical Flow Model Through Steam Turbine Exhaust Hood.....	89
V.G.Solodov	
A Method for Calculation of Turbulence with Random Numbers.....	113
J. Laine, M. Hurme	
Computer Simulation on Hydrogen Fueled Rotary Engine (Abstract).....	127
G. Fang, R.K. Green	
COMBUSTION	129
Invited Lecture: Challenges in Simulation of Combustion Processes in Furnaces.....	133
M. Hupa, P. Kilpinen	
Modelling of Local Extinction and Reignition of the Flame	151
A. Brink, P. Kilpinen, M. Hupa, L. Kjaldman, K. Jääskeläinen	
Modelling of Chalcopyrite Oxidation Reactions in the Outokumpu Flash Smelting Process	167
T. Ahokainen, A. Jokilaakso	

CHEMICAL REACTIONS	185
Keynote Lecture: Mathematical Modeling of the Flash Converting Process	189
H.Y. Sohn, M. Pérez-Tello, K.M. Riihilahti	
Simulation of Reaction Kinetics in Pyrometallurgical Reactors (not available)	221
D.G.C. Robertson	
Modelling of Nitriding and Denitriding Reactions in Liquid Ni-20 % Cr Alloy during Sieverts' Experiments	225
L. Petitnicolas, A. Jardy, D. Ablitzer	
Numerical Modeling of the Vertical Hydrofluorination Zone of the Moving Bed Furnace for the Production of UF ₄	251
J. Jourde, F. Patisson, D. Ablitzer, J.L. Houzelot	
PROCESS SIMULATION	273
Invited Lecture: Experiences of CFD Simulations at Foster Wheeler Energy Oy's Karhula R&D Center.....	277
T. Hyppänen	
Energy-dissipation-model of Metallurgical Multi-phase-systems	295
K. Mavrommatis	
Modelling of Baffled Stirred Tanks	309
H. Ahlstedt, M. Lahtinen	
Turbulent Methane Combustion in a Laboratory Scale Furnace	327
A. Oksanen, E. Mäki-Mantila	
Injection of Heavy Fuel Oil into the Blast Furnace	345
T. Paloposki, J. Hakala, P. Mannila, J. Laukkanen	
The Recovery Boiler Chemistry Advisor – Combination of Practical Experience and Advanced Thermodynamic Modelling (Abstract).....	357
R. Backman, G. Eriksson, K. Sundström	
New Applications with Time-dependent Thermochemical Simulation	361
P. Koukkari, I. Laukkanen, K. Penttilä	
Mathematical Modelling and Numerical Simulation of Czochralski Crystal Growth..	373
J. Järvinen, R. Nieminen	
Analysis of a Waste-heat Boiler by CFD Simulation	403
Y. Yang, A. Jokilaakso	
Author Index	419

SESSION 1

**General Computational
Fluid Dynamics and
Heat Transfer**

Invited Lecture

Multi-Fluid Models of Turbulence

D. Brian Spalding

.....

Multi-fluid Models of Turbulence

D. B. Spalding
Concentration, Heat and Momentum Ltd
London, UK

Abstract

Turbulence models are reviewed, distinction being made between single-fluid, multi-fluid, probabilistic and direct-numerical-simulation models. It is argued that the multi-fluid models have been too long neglected, and that, their implications being amenable to working out with the aid of widely-accessible computer programs, it is time to give them careful attention.

Examples are presented of the implications of a two-fluid model applied to an atmospheric flow, of a four-fluid model applied to transient flame propagation, of a fourteen-fluid model applied to a turbulent Bunsen-burner flame, and of a hundred-fluid model applied to a well-stirred reactor.

Helsinki University of Technology
3rd Colloquium on Process Simulation
12 - 14 June, 1996
Espoo, Finland

For Your Notes

THE UNIVERSITY OF CHICAGO PRESS

Numerical simulation of flow induced by a pitched blade turbine:
Comparison of the sliding mesh technique and an averaged source term
method

E.O.J Majander and M.T. Manninen
Technical Research Centre of Finland, VTT Energy
P.O.B 1604, FIN-02044 VTT, Finland

Abstract

The flow induced by a pitched blade turbine was simulated using the sliding mesh technique. The detailed geometry of the turbine was modelled in a computational mesh rotating with the turbine and the geometry of the reactor including baffles was modelled in a stationary co-ordinate system. Effects of grid density were investigated. Turbulence was modelled by using the standard k- ϵ model. Results were compared to experimental observations. Velocity components were found to be in good agreement with the measured values throughout the tank.

Averaged source terms were calculated from the sliding mesh simulations in order to investigate the reliability of the source term approach. The flow field in the tank was then simulated in a simple grid using these source terms. Agreement with the results of the sliding mesh simulations was good. Commercial CFD-code FLUENT was used in all simulations.

INTRODUCTION

Stirred reactors have been analysed using computational fluid mechanics since the beginning of 1980's [1-9]. In the most often used approach, the agitator has been modelled with averaged source terms for the velocity components and turbulence quantities. In this method, the geometry of the agitator is not described in the computational mesh. Turbulence has been usually computed with the standard k- ϵ model.

The basic advantage of the source term approach is the simplicity of the computational mesh and the rapidity of the numerical computation. The drawback is the need of precise experimental data for determining the source terms. In addition, the time dependent periodic nature of the flow field cannot be reproduced in the averaged flow field.

There are several ways to model the momentum source terms of the agitator. The simplest and most common method is to set the appropriate velocity components to fixed values at the boundary of the impeller. This has proved to give good results, if the velocities used as the source terms have been measured in an identical geometry [7,8].

In the second method, the lift and drag forces for the impeller are calculated using lift and drag coefficients obtained from experiments of flow over thin aerofoils and flat plates [5]. It is doubtful, however, whether the assumptions of the model are fulfilled in a highly turbulent stirred tank. Different types of agitators are also problematic, because the force coefficients are not known.

The third method is to describe the impeller by using either measured tangential and axial forces or by using the power number Ne and the pumping number Fl of the impeller type in question. The tangential force is determined by the power number. The axial force has to be adjusted to produce the volumetric flow determined by the flow number. This approach is attractive, because no experimental data is necessary for the velocities as long as Ne and Fl are known. The accuracy of this method is of course not as good as that of the first method.

An accurate computation of the periodic flow field in stirred tank requires more advanced methods. If the tank is unbaffled, the simulation can be made in a co-ordinate system rotating with the agitator. The geometry of the impeller can then be described accurately in the computational mesh. If the tank is equipped with baffles, this approach is not sufficient. This case can be simulated using a time dependent boundary condition for the impeller blades [10], or employing the sliding mesh technique [11- 15]. The latter is implemented in modern commercial CFD-codes, and is an effective tool in modelling rotating machinery with rotor stator interactions.

In this work, computation of the flow in a laboratory scale stirred tank equipped with a pitched blade turbine is reported. We employed the commercial CFD-code FLUENT

[15] in the simulations. The flow field was computed using the sliding mesh technique and standard k- ϵ model for turbulence.

The sliding mesh simulation can be used also to determine the source terms describing the agitator. If the sliding mesh modelling is accurate, precise source terms for the velocity components and turbulence quantities can be defined. An effective procedure to study the flow in stirred reactor would be to perform the sliding mesh computation once, and determine the source terms from the results. Because the flow near the impeller does not significantly change, if small modifications in the tank geometry are made, the same source terms can be applied in optimising the impeller location or geometry of the baffles, for example. In this work, averaged source terms were calculated from the sliding mesh results and a simulation was performed using these in a simple cylindrical grid. The results were compared to the flow pattern from sliding mesh simulation in other parts of the tank.

MODELLING APPROACH

Sliding mesh technique

The basic idea in the sliding mesh approach is to use two grids, one rotating with the agitator and the other being fixed to the reactor walls. The two grids slide along a defined cylindrical surface. In FLUENT, a conservative interpolation scheme is used to compute the convective and diffusive fluxes for control volumes bordering the slip surface [15]. The main restrictions of FLUENT's sliding mesh option concerning the present application are the unavailability of the higher order numerical schemes and the multigrid solver with the sliding mesh model.

Because the impeller is modelled in a rotating grid, all solid walls are at rest and a no-slip boundary condition is employed. Usual logarithmic wall functions were applied in our simulations on the tank walls and on the impeller blades. In FLUENT, the value of turbulent kinetic energy at the near-wall cell, k_p , is computed from the complete transport equation for k . Assuming that the production and dissipation of turbulence are in equilibrium the near-wall value of the dissipation can then be calculated.

The dimensionless distance from the wall, y^+ , is defined as [16]

$$y^+ = \frac{y}{\nu} \sqrt{\frac{\tau_w}{\rho}} \quad (1)$$

where y is the physical distance, ν is the kinematic viscosity, τ_w is the wall shear stress and ρ is the fluid density. The logarithmic wall function is considered to be valid if y^+ is on the range 30-300 [16]. A relationship between y^+ and k_p together with Eq. (1) and the logarithmic law for the near-wall velocity are used to compute values for the velocity at the near-wall cells.

FLUENT applies the logarithmic wall function if y^+ exceeds 11.225. When y^+ is less than this value, the near-wall node is inside the laminar sublayer and the shear stress is computed from

$$\tau_w = \mu \frac{\partial u}{\partial t} \quad (2)$$

The turbulence quantities k and ε are computed using the equilibrium boundary layer assumption as explained above.

In a stirred tank the flow is fully turbulent in the whole domain and the flow is probably separated at the blade surfaces. Consequently, the use of logarithmic wall functions may be questioned. In a more accurate simulation, the flow field should be computed in a finer grid close to the surfaces. This would, however, require the use of a low-Reynolds-number turbulence model. In FLUENT, the wall function method is used for all turbulence models.

Source term model

The solution from the sliding mesh simulation was used to determine average source terms for the simplified flow model. If the sliding mesh solution is sufficiently accurate, the source terms are well defined. Comparison of the flow pattern obtained with source term approach to that of the sliding mesh simulation is then a good validation test for the source term method.

The most common way to define the impeller source terms is to fix the appropriate velocity components and turbulence quantities at the impeller swept surface. In the case of a pitched blade turbine, the important velocity components are the axial and tangential velocities, U and W . In our simulation we chose to fix U , W , k and ε at the lower and upper impeller swept surfaces.

In practice, the periodic solution of the sliding mesh computation was averaged over the axial plane in question. A polynomial was then fitted to each variable as a function of the radius. The analytical profiles were employed to fix the source terms.

GEOMETRY AND COMPUTATIONAL GRID

The simulated tank is a cylindrical vessel, equipped with a six-bladed pitched blade turbine and four baffles on the cylindrical walls. The pitch angle of the impeller blades is 45° . LDA measurements in this tank have been made by Ranade & Joshi [17] and flow simulations using the source term approach by Ranade et al. [8]. The geometrical details of the tank are given in Table 1. The speed of rotation of the agitator was chosen to be 20 rad/s, so that the tip velocity is exactly 1 m/s. In the experiments, the flow field with several speeds of rotation were measured [17]. The measured velocity field scales quite precisely with the tip speed of the impeller.

Table 1. Details of the geometry of the simulated stirred tank [17].

Tank diameter (mm)	300
Tank height (mm)	300
Impeller diameter (mm)	100
Impeller blade width (mm)	30
Clearance from bottom to the center of impeller (mm)	100
Width of baffles (mm)	30
Shaft diameter (mm)	16
Hub diameter (mm)	25
Hub height (mm)	28

Sliding mesh simulation was first performed in a grid covering the whole volume of the tank. The computational mesh had about 105 000 cells ($66 \times 27 \times 59$ in the ϕ -, r - and z -directions) and is illustrated in Fig. 1. The sliding surfaces were located at $r = 0.09$ m and $z = -0.05$ m. The width of the near wall cell at the impeller blade was 5.8 mm, corresponding to $y^+ = 10$ -90 according to the computed results.

Because the computation is time consuming, further studies were made in a smaller volume, comprising a 60° sector of the tank. One impeller blade is then inside the domain. The geometry does not, however, fully correspond the original one because now the number of blades is increased from four to six. At the same time we decided to decrease the tank height to 200 mm in order to further reduce the number of computational cells. The results of flow simulations showed that these modifications did not significantly alter the flow pattern near the impeller.

Two different grids were studied in the reduced geometry. The coarser grid had about 16 000 cells ($12 \times 31 \times 44$). The cells nearest to the impeller had a width of 5.2 mm and the value of y^+ varied between 20 and 110. The denser grid had about 91 000 cells ($30 \times 54 \times 56$) and the width of the cell at the impeller blade was 0.15 mm, corresponding to $y^+ = 3$ -10. In this case the logarithmic profile for the velocity is not used. The shear stress is computed from Eq. (2). Fig. 2 shows the denser grid and illustrates the tight spacing of gridlines on the impeller blades.

The time step in the sliding mesh simulations was large at the beginning, so that the general flow fields was developed. The final computation was made using a time step which corresponds to a rotation of approximately one computational cell.

A cylindrical grid was used in the simulation made with the source term approach. The number of cells was about 15600 in the 60° sector, with a distribution of 12 cells in the ϕ -direction, 31 cells in the r -direction and 42 cells in the z -direction.

RESULTS

Sliding mesh simulations

The results of the sliding mesh simulations in the original grid for the whole tank and in the two grids for the 60° sector are shown in Figs. 3-5 together with the measured values [17]. The velocity components and kinetic energy of turbulence 30 mm below the impeller centerline are shown in Fig. 3. The axial velocity agrees exactly with the experimental values. The simulated results with the three different grids also give almost identical result.

A clear disagreement between simulations and measurements is in the radial velocity. The measured values are close to zero, whereas the simulation gives a positive radial component of about 0.08 m/s, at maximum. The result indicates that the flow in the simulation bends to the radial direction nearer to the impeller than in the measurements. Because the values are small just below the impeller, the radial velocity is more susceptible to errors than the other velocity components.

The tangential component is in fair agreement with experimental values. Small differences are also observed between the full tank simulation and the results obtained in the 60° sector. The location of the maximum tangential velocity is in the simulation slightly displaced when compared to the measurement.

The largest discrepancy is found in the kinetic energy of turbulence. The simulation in the 60° sector gives maximum values of k which are only about 30% of the measured values. In the full tank simulation, the values are even smaller. We believe that this result can be attributed to the use of wall functions on the impeller surfaces. It is remarkable, that the velocity components are in good agreement with measurements, even though the turbulence quantities are not.

Because the flow in the tank is highly turbulent, all stirring power is dissipated in the turbulent eddies. Consequently, the turbulent dissipation integrated over the volume of the tank should equal the stirring power. The latter can be calculated from the Newton number, which has a value of 2.3 for the simulated impeller [17], corresponding to a power of 0.74 W. From the modelling we obtain 0.14 W in the whole tank simulation, 0.25 W in the coarse grid (60° sector) and 0.44 W in the dense grid (60° sector).

The results at a lower axial position (55 mm from the impeller centerline) are shown in Fig. 4. Here the simulated axial and radial components follow closely the measured ones. In the tangential component, the agreement is not as good. Fairly accurate results are obtained also with the reduced geometry. Increasing the number of computational cells does not change the simulated results significantly. The simulated values of the kinetic energy of turbulence are small also at this z -plane.

Results for the axial and radial velocities 55 mm above the impeller are shown in Fig. 5. Experimental values of tangential velocity are not available above the impeller. Again,

the axial velocity is well reproduced by the simulation. The radial velocity is somewhat lower than in the experiment. The simulated turbulent kinetic energy has approximately the correct value in the simulations made in the 60° sector, whereas the full tank simulation gives much smaller values near the shaft. At this location, the results obtained in the reduced geometry differ more from the full tank results, as expected due to the reduction in the tank height.

Simulation using the source term approach

The source terms were determined from the simulations in the 60° sector with the dense grid. The polynomials fitted to U , W , k and ε at the upper impeller surface are (all quantities in SI-units)

$$\begin{aligned} U_u &= 15863r^3 - 1966.6r^2 + 69.266r - 0.3816 \\ W_u &= 2.682 \cdot 10^6 r^4 - 3.062 \cdot 10^5 r^3 + 1.218 \cdot 10^4 r^2 - 209r + 1.242 \\ k_u &= -10461r^3 + 27.002r^2 + 2.5274r - 0.0247 \\ \varepsilon_u &= -3.938 \cdot 10^5 r^3 + 2.817 \cdot 10^4 r^2 - 407.96r + 1.9682 \end{aligned} \quad (3)$$

The corresponding fitted polynomials at the lower impeller swept surface are

$$\begin{aligned} U_l &= -12907r^3 + 430.69r^2 + 20.01r - 0.2023 \\ W_l &= 1.477 \cdot 10^6 r^4 - 1.572 \cdot 10^5 r^3 + 5.573 \cdot 10^3 r^2 - 84.79r + 0.3380 \\ k_l &= 1648.5r^3 - 175.68r^2 + 6.2346r - 0.052 \\ \varepsilon_l &= 2.306 \cdot 10^4 r^3 - 3.333 \cdot 10^3 r^2 + 162.3r - 1.4768 \end{aligned} \quad (4)$$

Results of the source term simulations are shown in Figs. 6 and 7 corresponding to axial planes 55 mm below and 55 mm above the impeller centerline. The sliding mesh results of both the coarse and dense grid are also plotted in the figures.

Axial and radial velocities are predicted quite accurately with the source term approach on both axial planes. The largest discrepancy is in the tangential velocity above the impeller. Note that the direction of the tangential velocity at $z = 0.055$ (above the impeller) is opposite to that of the impeller. No empirical values exist for the tangential velocity in this region for verifying this prediction. In a baffled tank, a flow pattern of this type is possible, however.

The turbulent kinetic energy is not very accurately reproduced in the source term simulation. Above the impeller, the sliding mesh solutions also deviate from each other, indicating a clear grid dependence. Thus, a denser grid might improve also the source term result. The integrated dissipation gives a stirring power of 0.49 W.

DISCUSSION

Encouraging results were obtained from the sliding mesh simulation of the turbulent flow caused by a pitched-blade turbine in a stirred tank. The velocity components were predicted quite accurately throughout the tank. The predicted turbulence level, however, was much smaller than observed in measurements.

The comparison of results computed with the two grids in the reduced geometry indicate that reasonably accurate results can be obtained with a relatively coarse grid. It is also noteworthy that the increase of the number of baffles from four to six did not change the flow pattern significantly. A clear discrepancy was observed between the computed turbulence level in the whole tank and in the 60° sector. The cause of this result is not fully understood at the moment. One possible reason could be that the turbulence quantities have not reached their final values in the whole tank simulation, although the averaged velocity components do not change.

The comparison of simulation with the source term approach and the sliding mesh technique implies that the source term approach is a good way to quickly simulate the overall flow pattern in a stirred tank. In this work we did not try to optimise the procedure of fixing the source terms. Nevertheless, the results were in good agreement with the sliding mesh computation. We believe that a more thorough study of the various ways to define the source terms would produce even more accurate results.

In turbulence modelling, we employed the standard (high-Reynolds-number) k - ϵ model. Boundary conditions were described with wall functions on all solid walls, including the impeller blades. This approach may not be justified because flow separation is likely to occur at the blade surface. Moreover, the flow is highly turbulent already when it comes to the turbine region. Under these circumstances, the grid density at the impeller region should be high and a low-Reynolds-number turbulence model should be used.

The use of the standard k - ϵ model in the swirling flow of a stirred tank is also questionable, because it assumes isotropic turbulence. Models that take into account the anisotropic nature, e.g. the RNG k - ϵ model with a swirl correction or the Reynolds stress model, should possibly be used. Although the standard k - ϵ model has produced reasonably good results in baffled stirred tanks, the model may be inaccurate in the near-impeller region.

The fact that the velocity field is simulated correctly, despite of the poor turbulence modelling, deserves special notice. The main effect of the impeller blades is to force the flow along the blade surfaces, i.e., the most important boundary condition is that the normal velocity component is zero. Consequently, the velocity field near the impeller region is may be computed correctly, although the turbulence is modelled inaccurately.

Important conclusions may be drawn from the results. With the sliding mesh technique, the flow field can be simulated with an accuracy comparable to that of measurements. At least in sufficiently simple geometries, the experiments can therefore be replaced with computational fluid dynamic simulations. Moreover, the simple source term simulation gives the flow field with sufficient accuracy, if the source terms are correctly determined. Only the periodic nature of the flow pattern near the agitator is lost in the averaged computation.

REFERENCES

1. Harvey, P.S. & Greaves, M., Turbulent flow in an agitated vessel. Part I: A predictive model. *Trans. IChemE*. Vol. 60, pp. 195-200 (1982).
2. Harvey, P.S. & Greaves, M., Turbulent flow in an agitated vessel. Part I: Numerical solution and model predictions. *Trans. IChemE*. Vol. 60, pp. 201-210 (1982).
3. Middleton, J.C., Pierce, F. & Lynch, P.M., Computations of flow fields and complex reaction yield in turbulent stirred reactors, and comparison with experimental data. *Chem. Eng. Res. Des.* Vol. 64, pp.18-22 (1986)
4. Placek, J. & Tavlarides, L.L., Turbulent flow in stirred tanks. Part I: Turbulent flow in the turbine impeller region. *AIChE Journal*, Vol. 31, no. 7, pp. 1113-1119 (1985).
5. Pericleous, K.A. & Patel, M.K., The modelling of tangential and axial agitators in chemical reactors. *Physicochemical Hydrodynamics*, Vol. 8, no. 2, pp.105-123 (1986).
6. Ju, S.Y., Mulvahill, T.M. & Pike, R.W., Three-dimensional turbulent flow in agitated vessels with a nonisotropic viscosity turbulence model. *Can. J. Chem. Eng.*, Vol. 68, pp. 3-16 (1990).
7. Ranade, V.V. & Joshi, J. B., Flow generated by a disc turbine: Part II Mathematical modelling and comparison with experimental data. *Trans. IChemE*, Vol. 68, Part A, pp.34-50 (1990).
8. Ranade, V.V., Joshi, J.B., and Marathe, A.G. (1989). Flow generated by pitched blade turbines II: Simulation using k- ϵ model. *Chem. Eng. Commun.*, Vol 81, pp. 225-248.
9. Suresson, C., Rasmuson, A., and Fort, I. (1993), Numerical simulation of turbulent flow of agitated liquid with pitched blade impeller. The 11th International Congress of Chemical Engineering, Chemical Equipment Design and Automation, 29 August - 3 September 1993, Praha, Czech Republic.

10. Röberg, K.-E., Time-dependent numerical simulation of the turbulent flow around a Rushton-type impeller. Åbo Akademi, Department of Chemical Engineering, Heat Engineering Laboratory, Report 93-5 (1993).
11. Luo, A.D. Gosman, R.I. Issa, J.C. Middleton, and M.K. Fitzgerald, Full flow field computation of mixing in baffled stirred vessels, Trans. IChemE, Vol. 71, Part A, pp.342-344 (1993).
12. Brucato, M. Ciofalo, F. Grisafi, and G. Micale, Complete numerical simulation of flow fields in baffled stirred vessels: the inner-outer approach. IChemE Symposium Series No. 136, pp.155-162 (1994)
13. Murthy, S.R. Mathur, and D. Choudry, CFD simulation of flows in stirred tank reactors using a sliding mesh technique, IChemE Symposium Series No 136, pp. 341-348 (1994).
14. Luo, R.I. Issa, and A.D. Gosman, Prediction of impeller induced flows in mixing vessels using multiple frames of reference, IChemE Symposium Series No. 136, pp. 549-556 (1994).
15. FLUENT User 's guide, Fluent Inc., Lebanon (1995).
16. Wilcox, D.C, Turbulence modeling for CFD. DCW Industries Inc., La Cañada (1994).
17. Ranade, V.V., Joshi, J.B. (1989). Flow generated by pitched blade turbines I: Measurement using laser Doppler anemometry. Chem. Eng. Commun., Vol 81, pp. 225-248.

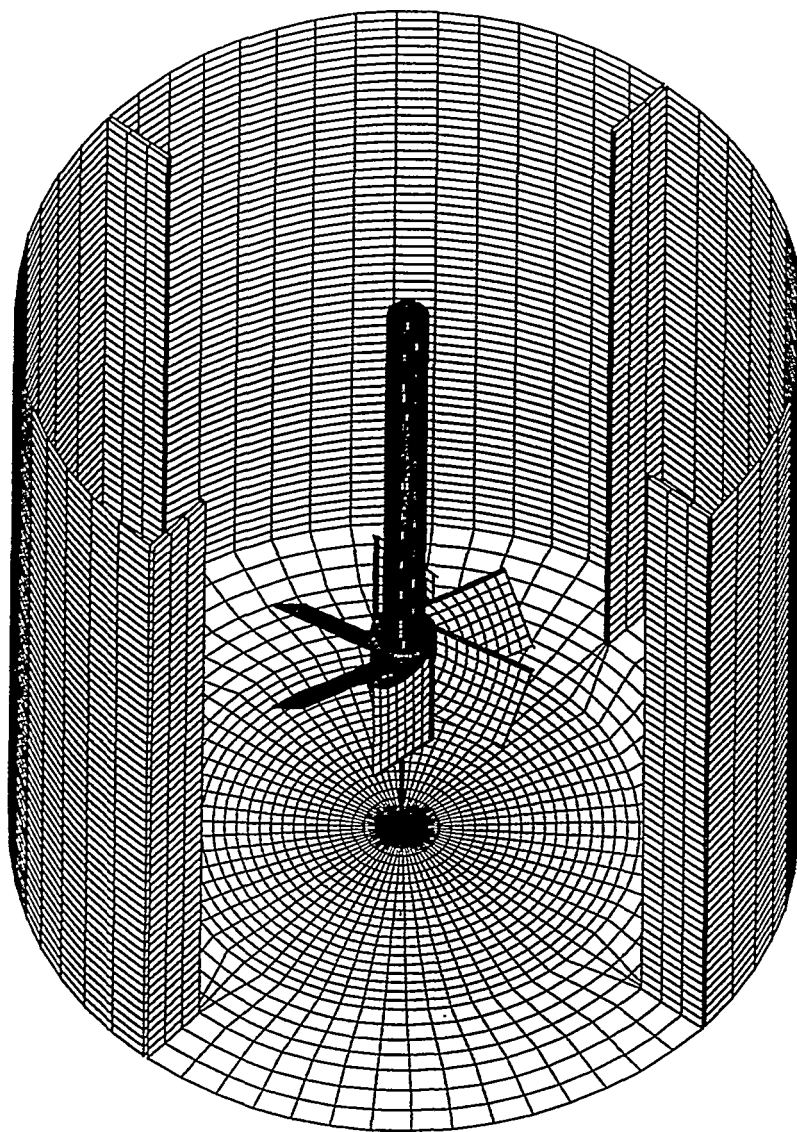


Fig. 1. Computational grid used in the simulations of the whole volume of the stirred tank.

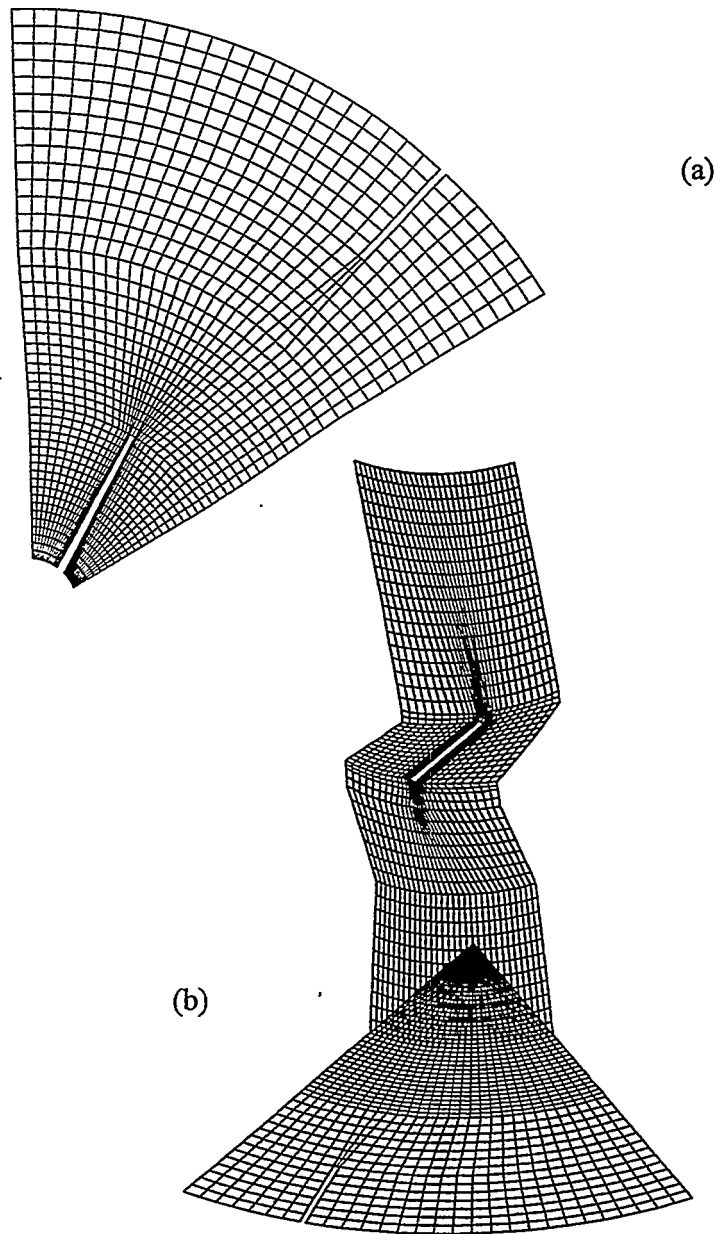


Fig. 2. The denser computational grid used in the simulations of the 60° sector. (a) z-plane at the impeller region. (b) Constant-J plane and z-plane at the bottom.

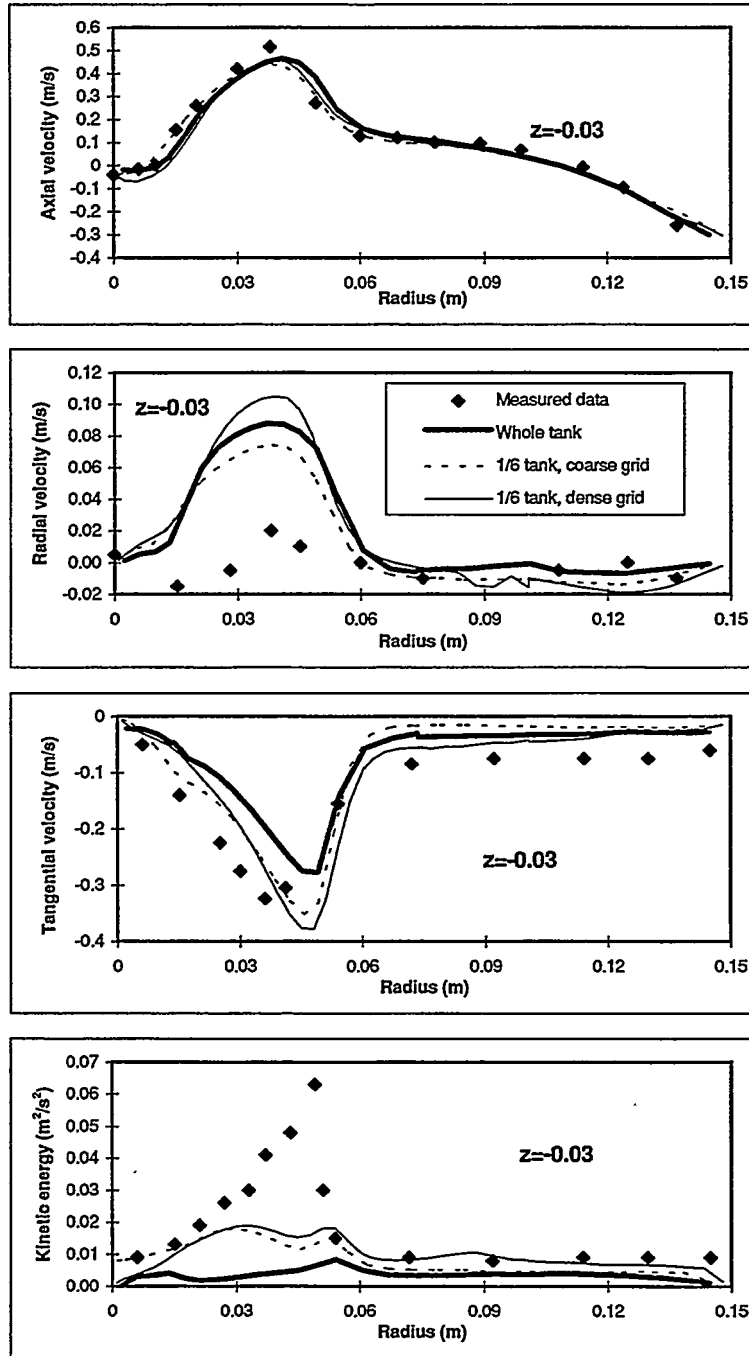


Fig 3. Velocity components and kinetic energy of turbulence 30 mm below the impeller centerline.

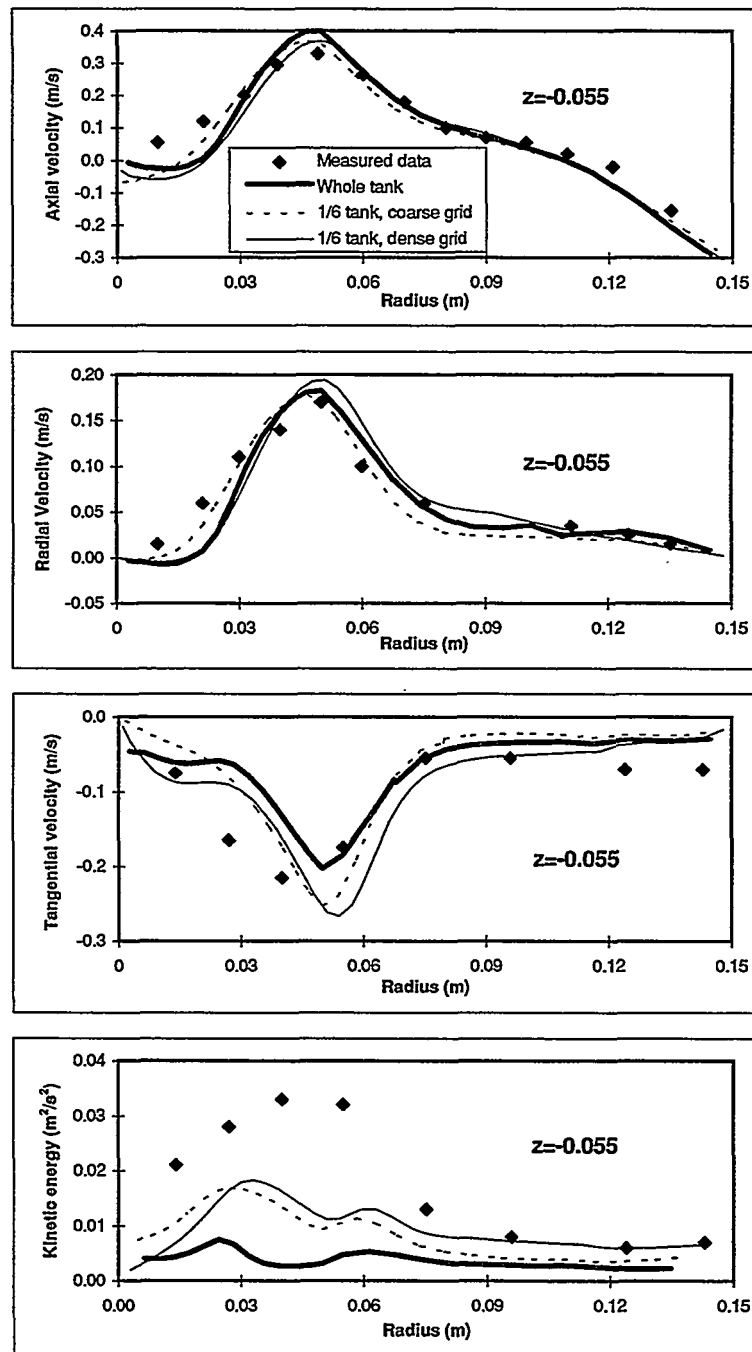


Fig 4. Velocity components and kinetic energy of turbulence 55 mm below the impeller centerline.

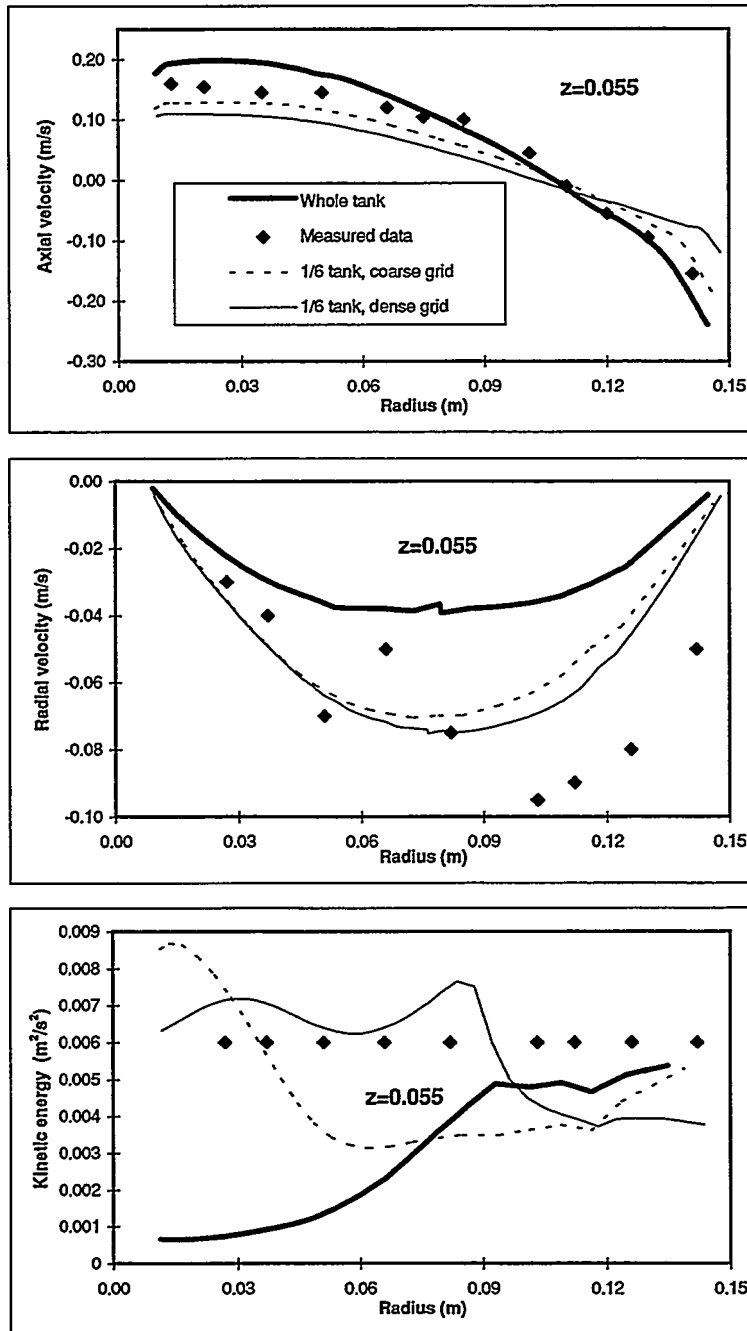


Fig 5. Velocity components and kinetic energy of turbulence 55 mm above the impeller centerline.

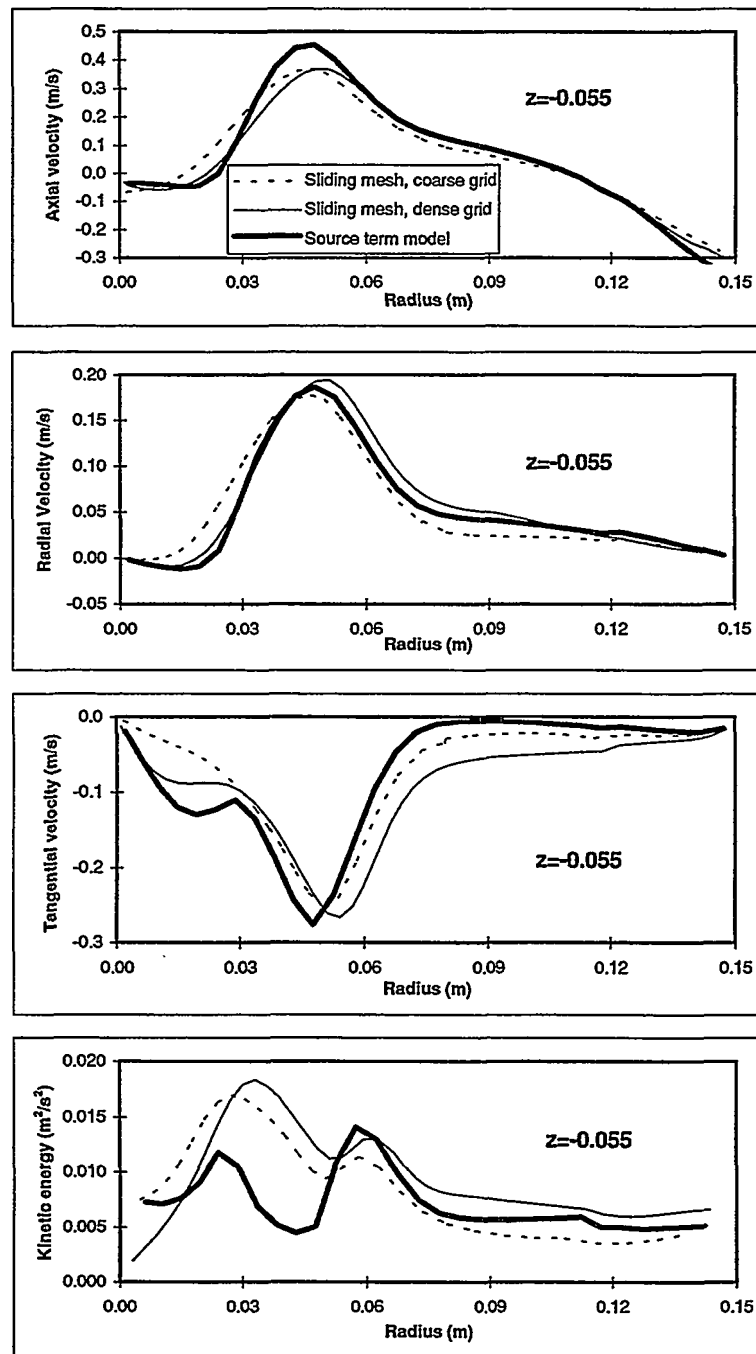


Fig 6. Velocity components and kinetic energy of turbulence 55 mm below the impeller centerline.

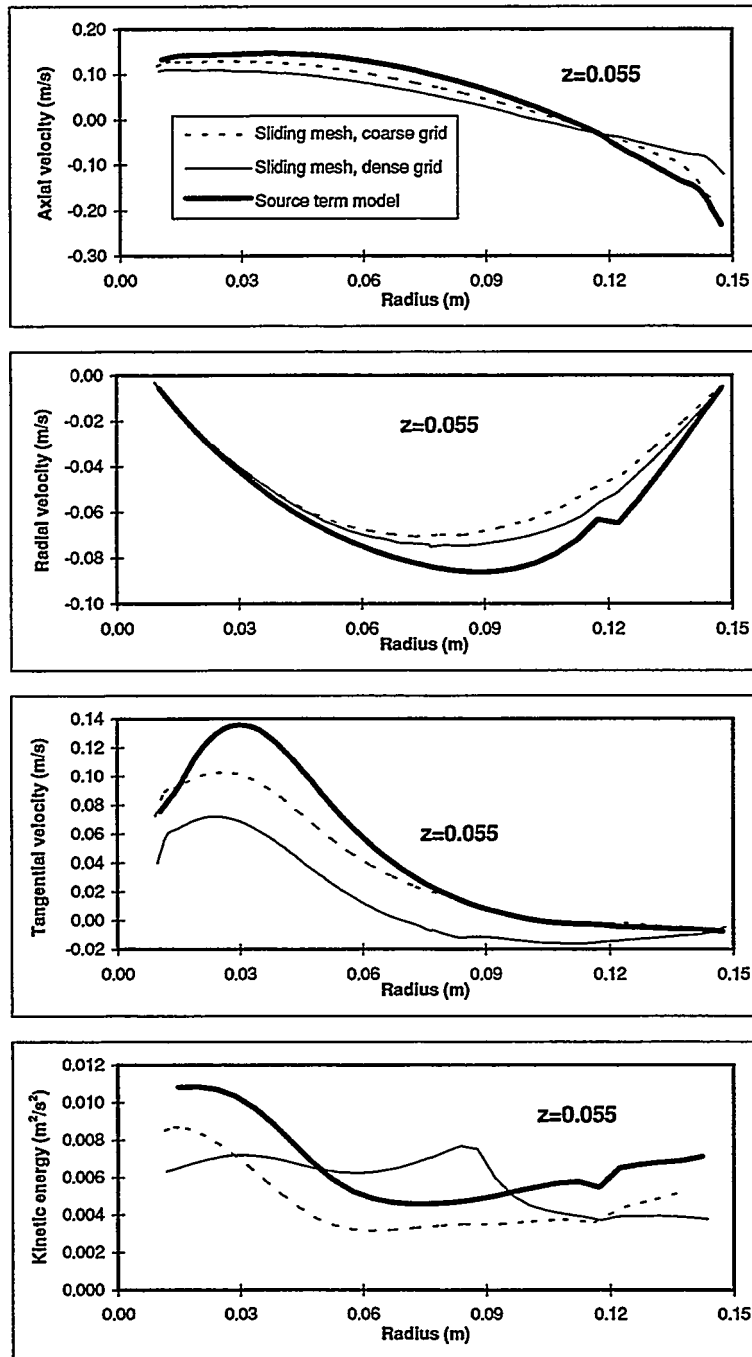


Fig 7. Velocity components and kinetic energy of turbulence 55 mm above the impeller centerline.

For Your Notes

1. The first part of the document discusses the importance of maintaining accurate records of all transactions and activities. It emphasizes the need for transparency and accountability in financial reporting.

2. The second part of the document outlines the various methods and techniques used to collect and analyze data. It highlights the importance of using reliable sources and ensuring the accuracy of the information gathered.

3. The third part of the document focuses on the interpretation and analysis of the collected data. It discusses the various statistical methods and models used to identify trends and patterns in the data.

4. The fourth part of the document provides a detailed overview of the results and findings of the study. It includes a comprehensive analysis of the data and a discussion of the implications of the findings.

5. The final part of the document concludes with a summary of the key findings and a discussion of the limitations of the study. It also provides recommendations for future research and practical applications of the findings.

.....

**Laminar Fluid Flow and Heat Transfer in a Fin-Tube Heat Exchanger with
Vortex Generators**

J. I. Yanagihara and R. Rodrigues Jr.
Polytechnic School of University of São Paulo
Department of Mechanical Engineering
São Paulo 05508-900
Brazil

Abstract

Development of heat transfer enhancement techniques for fin-tube heat exchangers has great importance in industry. In recent years, heat transfer augmentation by vortex generators has been considered for use in plate fin-tube heat exchangers. The present work describes a numerical investigation about the influence of delta winglet pairs of vortex generators on the flow structure and heat transfer of a plate fin-tube channel. The Navier-Stokes and Energy equations are solved by the finite volume method using a boundary-fitted coordinate system. The influence of vortex generators parameters such as position, angle of attack and aspect ratio were investigated. Local and global influences of vortex generators in heat transfer and flow losses were analyzed by comparison with a model using smooth fin. The results indicate great advantages of this type of geometry for application in plate fin-tube heat exchangers, in terms of large heat transfer enhancement and small pressure loss penalty.

Helsinki University of Technology
3rd Colloquium on Process Simulation
12 - 14 June, 1996
Espoo, Finland

LAMINAR FLUID FLOW AND HEAT TRANSFER IN A FIN-TUBE HEAT EXCHANGER WITH VORTEX GENERATORS

J. I. Yanagihara and R. Rodrigues Jr.
 Polytechnic School of University of São Paulo
 Department of Mechanical Engineering
 São Paulo 05508-900
 Brazil

ABSTRACT - Development of heat transfer enhancement techniques for fin-tube heat exchangers has great importance in industry. In recent years, heat transfer augmentation by vortex generators has been considered for use in plate fin-tube heat exchangers. The present work describes a numerical investigation about the influence of delta winglet pairs of vortex generators on the flow structure and heat transfer of a plate fin-tube channel. The Navier-Stokes and Energy equations are solved by the finite volume method using a boundary-fitted coordinate system. The influence of vortex generators parameters such as position, angle of attack and aspect ratio were investigated. Local and global influences of vortex generators in heat transfer and flow losses were analyzed by comparison with a model using smooth fin. The results indicate great advantages of this type of geometry for application in plate fin-tube heat exchangers, in terms of large heat transfer enhancement and small pressure loss penalty.

NOMENCLATURE

A_c	minimum free-flow area	[mm ²]
A_r	heat transfer area	[mm ²]
B	channel width	[mm]
b	vortex generator chord length	[mm]
c_p	specific heat	[J / kg °C]
D_h	hydraulic diameter	[mm]
D	tube diameter	[mm]
E	distance between fins	[mm]
h	enthalpy	[J / kg]
h_c	local heat transfer coefficient	[W / m ² °C]
\bar{h}	mean heat transfer coefficient	[W / m ² °C]
H^f	vortex generator height	[mm]
k	thermal conductivity	[W / m °C]
L	channel length	[mm]
p	pressure	[Pa]
r	radial position of the vortex generator	[mm]
T	temperature	[°C ou K]
t	time	[s]
u, v, w	components of velocity in Cartesian space	[m/s]
x, y, z	coordinates in Cartesian space	[m]

S source term in the Navier-Stokes equations [kg / m².s²]

Greeks

β vortex generator angle of attack [deg]
 ν cinematic viscosity [m² / s]
 μ dynamic viscosity [kg / m.s]
 ρ density [kg / m³]
 θ angular position of the vortex generator [deg]

Dimensionless numbers

C_f friction coefficient
 Nu local Nusselt number
 \overline{Nu} global Nusselt number
 Re Reynolds number
 Λ aspect ratio of the vortex generator

Subscripts

D diameter
 E height
 in inlet
 o surface not enhanced
 $wall$ wall
 out outlet

1.INTRODUCTION

Since compact fin-tube heat exchangers are widely used in industrial applications, development of techniques to improve its performance is very important. The industry has concentrated effort to develop techniques for reduction of operation costs, construction costs and size. The flow structure in these devices is complex and highly dependent of geometrical parameters such as distance between tubes, tube arrangement and fin geometry. The use of computational fluid dynamics to analyze this kind of problem has many advantages over other approaches because allow flow visualization and easy variation of geometrical parameters with lower costs.

Fin-tube compact heat exchangers used in industry already bring in their conception heat transfer enhancement techniques such as louver-fins, corrugated fins, perforated fins, etc. However, there is a constant search for new methods that yield performance improvement. Many heat transfer enhancement techniques have been proposed for use in fin-tube compact heat exchangers. In recent years, application of longitudinal vortex generators to this geometry was considered by some authors.

Heat transfer augmentation by longitudinal vortex generators consist in the generation of a complex secondary flow by wings (vortex generators) positioned with an attack angle to the main flow direction (Fig. 1). The dominant mechanism of enhancement, for laminar flows with a low angle of attack, is the downwash flow of streamwise vortices generated.

This fact has been related by Yanagihara & Torii [7,8].

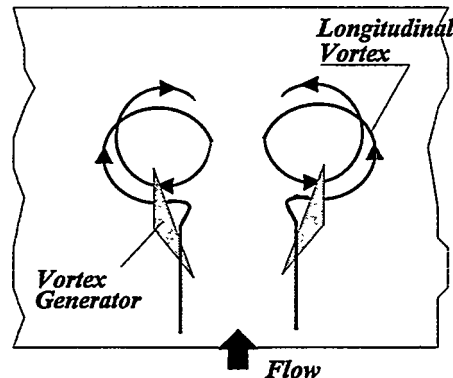


Fig. 1 - Longitudinal Vortex Generator.

Fiebig et al [2] conducted an experimental investigation ($2000 \leq Re_E \leq 5000$) about the influence of delta winglet longitudinal vortex generators on flow losses and heat transfer in a fin-tube channel. Angle of attack and position of vortex generators were investigated. Results indicate $\beta=45^\circ$ as the best attack angle in terms of heat transfer augmentation. Local heat transfer enhancements of 100% and global heat transfer enhancement of 20% were achieved. However, the most important result was the reduction of flow losses in a channel with vortex generators. The authors have observed the existence of a position, behind the tube, which allows simultaneously flow losses reduction and heat transfer enhancement. It was observed a reduction of 8% in the flow losses, at $Re_E=2000$, with larger reduction for increasing Reynolds number.

Valencia et al [6] carried out experimental studies about the influence of delta winglet longitudinal vortex generators on a compact fin-tube heat exchanger with three rows of staggered and in-line tubes. Vortex generators parameters such as attack angle and position were fixed according to the best results of Fiebig et al [2]. Results show that for the chosen geometry the longitudinal vortices increase the heat transfer by 55% to 65% for the in-line and by 9% for the staggered arrangement. Flow losses increase by 20% to 44% for the in-line and by 3% for the staggered arrangement. The in-line arrangement with vortex generators, compared to the staggered one, gives the same heat transfer and lower flow loss at $Re < 1000$ and higher heat transfer and flow losses at $Re > 1000$. The authors observed a small advantage of in-line over the staggered arrangement when using vortex generators in a compact fin-tube heat exchanger.

Biswas et al [1] conducted a numerical investigation ($Re_E=500$ and $Re_E=1000$) about the flow structure and heat transfer augmentation in a fin-tube channel with delta winglet vortex generators. Vortex generators parameters as attack angle and position were fixed according to best results of Fiebig et al [2]. Local heat transfer enhancement of about 240% was obtained. The influence of vortex generators on flow losses was not presented by the authors.

The present study consists of a numerical investigation about the influence of delta winglet pairs of vortex generators on a simplified model of fin-tube compact heat exchanger. The

influence of parameters such as position, attack angle and aspect ratio of vortex generators was investigated. The local and global influence of vortex generators in heat transfer and flow losses are analyzed by comparison with a smooth fin. The computational analysis was carried out by using the computational fluid dynamics (CFD) package PHOENICS (version 2.0).

2. PHYSICAL MODEL AND PARAMETERS

The choice of the geometrical parameters was made considering the basic dimensions of a typical channel of evaporator for domestic air-conditioning system. However, the physical model has only one row of tubes and the fins present some simplifications when compared with the original fin model. Heat transfer augmentation techniques used in that fin, as corrugations and louvers, were eliminated. The vortex generators influence was evaluated by comparison between smooth fins with and without vortex generators. Fig. 2 presents the physical model. The geometric parameters of the fin-tube channel are:

$$\begin{aligned} B &= 2.89 D \\ L &= 2.17 D \\ E &= 0.2 D \quad (\text{distance between fins}) \end{aligned}$$

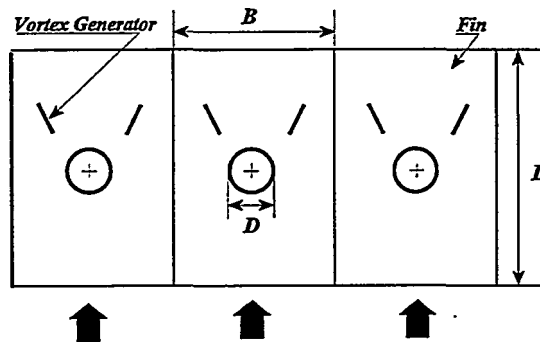


Fig. 2 - Physical Model

There are many geometrical forms for the vortex generators. Comparison between the influence of the generators geometries in a fin-tube channel would be very interesting, and never has been accomplished before. Nevertheless, only built-in delta winglet vortex generators have been considered in this study. Possible effects caused by the stamping holes of vortex generators were not considered in the present study.

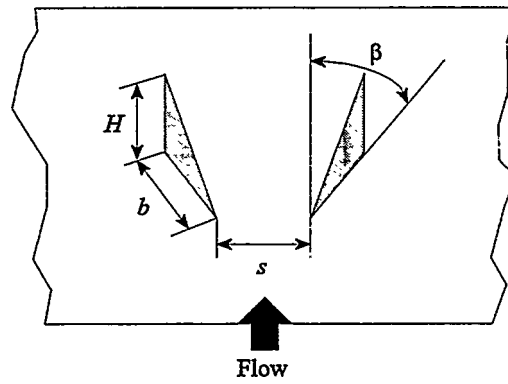


Fig. 3 - Delta Winglet Vortex Generator.

The investigation was divided in two parts. At first, all vortex generators parameters, except the position, were fixed according to the best results encountered in literature (see Table I), and only the position was varied.

Table I - Vortex Generators Parameters

Height	(H)	0.2 D
Chord	(b)	0.2 D
Aspect Ratio	(Λ)	2
Angle of Attack	(β)	45°

The position of vortex generators was changed in the following interval (See Fig. 4):

$$70^\circ < \theta < 150^\circ$$

$$0.6D < r < 0.9D$$

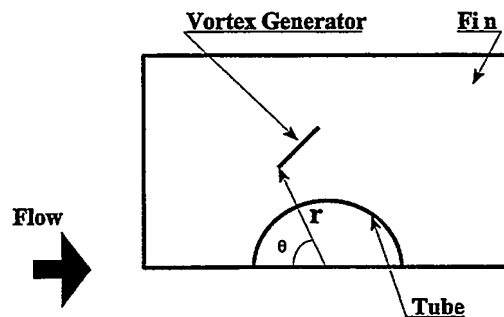


Fig. 4 - Region of Investigation

Secondly, the influences of aspect ratio (Λ) and angle of attack (β) were investigated. The vortex generators position was fixed according to the best value obtained in the first step. The ranges used were the following:

$$\begin{aligned} 1.0 < \Lambda < 2.0 \\ 15^\circ < \beta < 60^\circ \end{aligned}$$

3. NUMERICAL MODEL

Governing equations

The fluid flow and heat transfer processes were modelled by partial differential equations describing the conservation of mass, momentum and thermal energy in three dimensional boundary-fitted coordinate system, since the geometry of the problem is very complex.

Conservation of mass:

$$\frac{\partial \rho}{\partial t} + \frac{\partial}{\partial x_i}(\rho u_i) = 0 \quad (1)$$

Conservation of momentum:

$$\frac{\partial}{\partial t}(\rho u_i) + \text{div}(\rho u_j u_i) = \text{div}(\mu \nabla u_i) - \frac{\partial p}{\partial x} + S \quad (2)$$

Conservation of energy:

$$\frac{\partial}{\partial t}(\rho h) + \text{div}(\rho u_j h) = \text{div}(\mu \nabla h) \quad (3)$$

The numerical model used a control finite-volume formulation. The above equations are integrated over each control volume of the domain, and solved by the widely used CFD package PHOENICS (version 2.0). The package use a staggered grid arrangement for discretization of the momentum equations. The hybrid scheme is employed for the discretization of the convective transport.

Boundary conditions

The computational model is presented in Fig.5. The symmetry of the problem was considered to reduce data storage and computational efforts necessary to obtain the solution. The flow was assumed in steady-state with constant properties and absence of

gravitational effects.

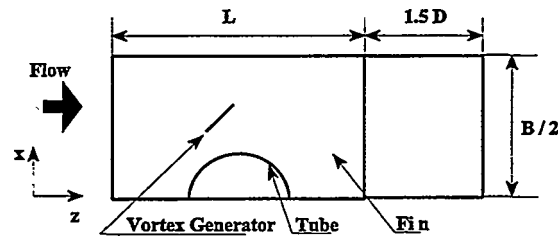


Fig. 5 - Computational Model

The boundary conditions used were the following:

- Inlet : $w = W_{in}$ and $T = T_{in}$
- Outlet : $p = p_o$ and null diffusive fluxes in streamwise direction
- Walls (fins, tube, vortex generators) : $T = T_{wall}$ and no-slip condition
- Symmetry planes : null mass and heat flux across surface

Comparing the physical model with the computational model it can be observed a difference in channel length. Such alteration was used to reduce the influence of boundary condition applied on the channel exit in the region of recirculation formed behind the tube, since in this region the diffusive fluxes have great importance.

The numerical model assumed a flow symmetry along the two sides of the tube. This hypothesis includes the assumption of a stable wake behind the tube, which is reasonable due to the wall effects caused by the small E/D ratio.

Convergence criteria

The convergence was assumed when the sum of the residual errors for each of equations sets took a negligible value. The reference residual errors used in this work are 10^{-6} for variables p, u, v, w and 10^{-5} for variable T .

Grid Refinement Influence

The influence of grid refinement was investigated. An arbitrary configuration was simulated with three degrees of refinement and the results were compared in terms of flow losses and global heat transfer coefficient. It was concluded that a grid with $36 \times 20 \times 67$ volumes would give reasonable results for these calculations.

4. RESULTS

The results of the calculations performed with PHOENICS are presented in terms of Reynolds number (Re) and Nusselt number (Nu), defined according to Kays & London [4],

$$Nu = \frac{D_h h_c}{k} \quad (4)$$

$$Re = \frac{w_{max} \cdot D_h}{\nu} \quad (5)$$

where w_{max} is mean velocity on the minimum free-flow area and h_c is the convection heat transfer coefficient. The hydraulic diameter is defined as:

$$D_h = \frac{4 \cdot A_t}{A_c} L \quad (6)$$

where A_t = total heat transfer area
 A_c = minimum free-flow area
 L = flow length of heat exchanger

The evaluation of Nusselt number was based on the classical Logarithmic Mean Temperature Difference (LMTD). Flow Losses has been evaluated by using the Friction Coefficient (C_f), which was defined as follows:

$$C_f = \frac{\Delta p}{\frac{1}{2} \rho W_{in}^2} \frac{E}{2L} \quad (7)$$

The simulations were performed to $Re=284$, which was obtained from operation condition of a real compact heat exchanger. Fig. 6 presents some streamlines in a fin-tube channel with built-in vortex generators ($r=0.9D$; $\theta=80^\circ$; $\Lambda=2.0$; $\beta=45^\circ$). The strong tri-dimensional flow caused by the delta winglets to enhance the heat transfer as the fresh fluid is carried toward the wall, reducing the boundary layer thickness.

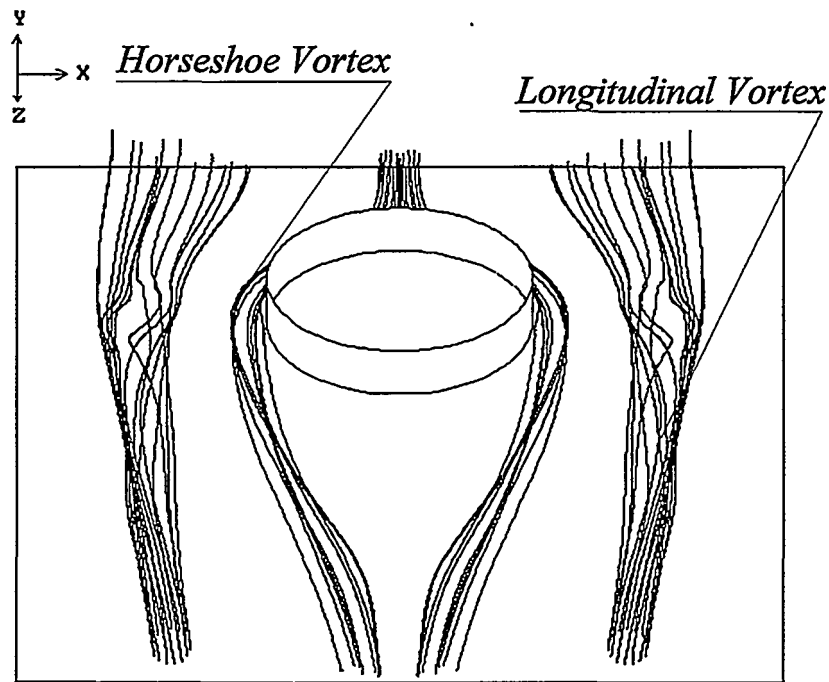


Fig. 6 - Streamlines in a Fin-Tube Channel with Built-In Vortex Generators.

At first, only the vortex generators position was varied. The angle of attack and the aspect ratio of delta winglets were fixed. The results indicate that the best position, in terms of flow losses, was $r=0.9D$ and $\theta=80^\circ$. In such position the channel with vortex generators presents flow losses 12% lower than the channel without vortex generators. This flow losses reduction is consequence of a reduction of the form drag due to the tube, since the presence of a delta winglet pair disturbs the pressure distribution along the tube surface. The global heat transfer enhancement was about 3% for the same position.

The best positions, in terms of heat transfer, were $r=0.9D$ and $\theta=130^\circ$, $r=0.7D$ and $\theta=130^\circ$, and $r=0.8D$ and $\theta=90^\circ$, where a global heat transfer enhancement of about 7% was obtained. This result can be explained by the fact that the local velocity at these positions is high. As the vortex strength increases with velocity, the heat transfer enhancement

becomes larger for these positions. However, the comparison among the three positions shows a lower flow loss to $r=0.8D$ and $\theta=90^\circ$.

In a second step, the influence of aspect ratio and angle of attack was investigated. The vortex generator position was fixed in agreement with the best position in terms of flow losses ($r=0.9D$ and $\theta=80^\circ$). Figure 7 presents the influence of aspect ratio in flow losses and global heat transfer. The results show that the reduction of aspect ratio caused an increase of flow losses. This result is the consequence of the increase of the vortex generator frontal area with the decrease of aspect ratio. Therefore, as a large vortex generator (lower aspect ratio) has a higher form drag, the reducing of flow losses is smaller for these configurations.

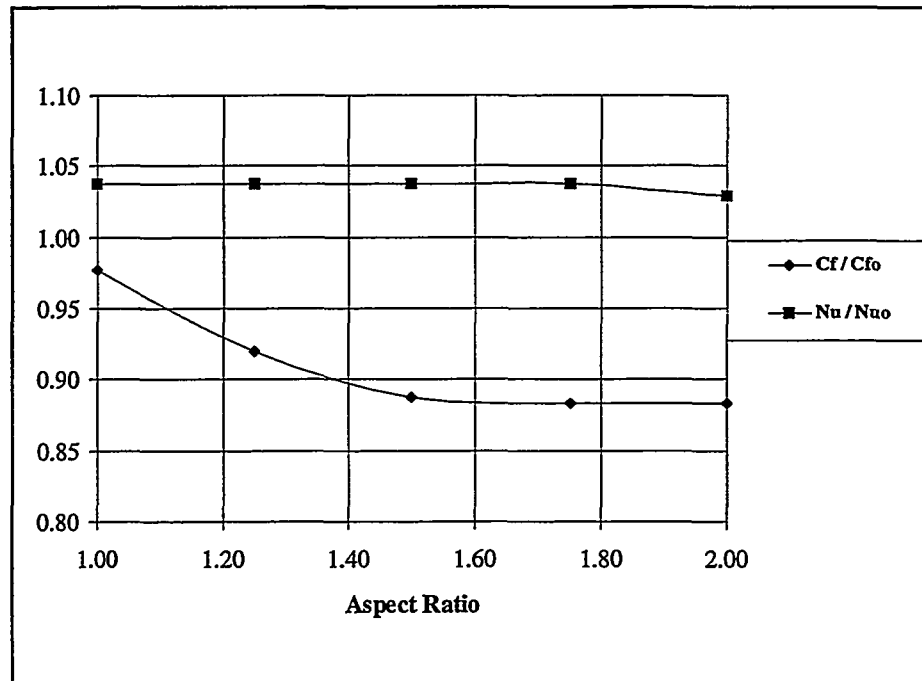


Fig. 7 - Influence of Aspect Ratio on Heat Transfer and Flow Losses ($r=0.9D$; $\theta=80^\circ$).

The Fig. 7 presents the influence of aspect ratio on global heat transfer. It can be seen that, for the range studied, this influence is small. The influence of aspect ratio on heat transfer is much smaller than that on the flow losses because of the relatively small heat transfer area that is perturbed by the presence of the vortex generator. This fact shows the need for a careful investigation involving channel and vortex generators parameters with the objective of obtaining best performances in terms of heat transfer.

The influence of attack angle in flow losses and global heat transfer is presented in Fig. 8. These curves indicate $\beta=45^\circ$ as the better angle of attack, which is in accordance with the experimental results of Fiebig [2]. However, this result is highly dependent on the vortex generator position because of flow complexity in a fin-tube channel. Therefore a

generalization of this result is difficult.

In Fig. 8 it can be observed that $\beta=60^\circ$ presents lower global heat transfer enhancement than $\beta=45^\circ$. This result can be explained by the fact that the vortex intensity increases with the increase of angle of attack until a critical value is reached. Beyond that value, the vortex generator performance decreases. Such behaviour was detected by previous works, but the critical angle was not the same.

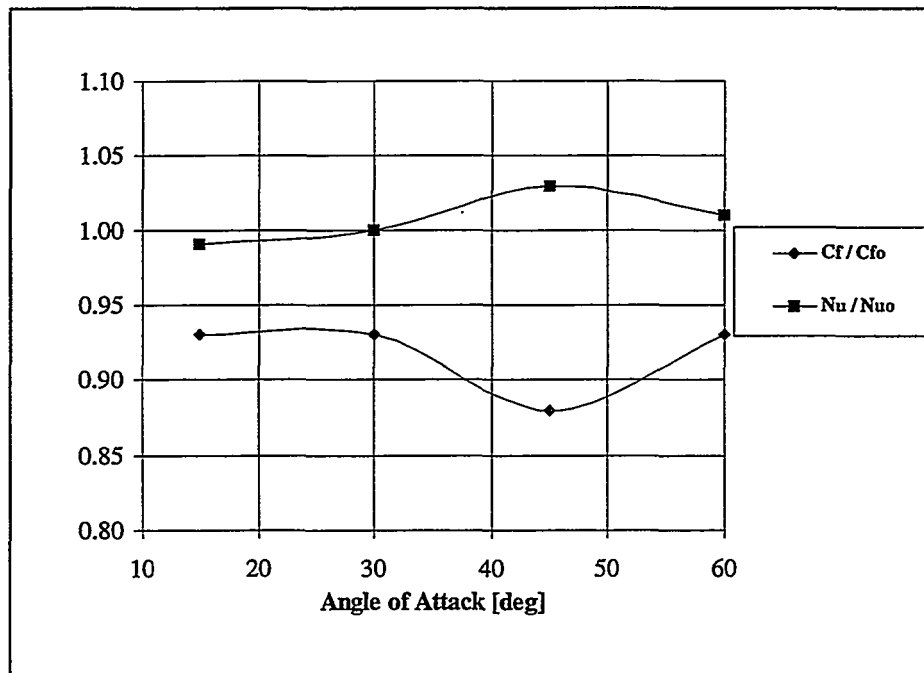


Fig. 8 - Influence of Angle of Attack on Heat Transfer and Flow Losses ($r=0.9D$; $\theta=80^\circ$).

Results in terms of local heat transfer enhancement showed promising tendencies. Fig. 9 and 10 presents local heat transfer enhancement for the best configuration ($r=0.9$ and $\theta=80^\circ$), where it is observed local enhancements of about 350%. In these figures it is evident that greatest local enhancements occur near the vortex generator.

Fig. 9 (lower fin) presents two peaks of enhancement. The first, positioned just before the delta winglet is a evidence of a corner vortex in this region. This type of structure has been related by Yanagihara & Torii [7,8], and it is formed in the corner between the front side of the vortex generator and the fin.

The second peak, positioned near the trailing edge of vortex generator is caused by the main vortex. This vortex is generated as the result of the flow separating in the tip of the delta winglet and rolling up due to the lower pressure in the rear side of the generator. The peak of heat transfer enhancement observed in Fig. 10 (higher fin) is caused by strong flow toward the wall at that position.

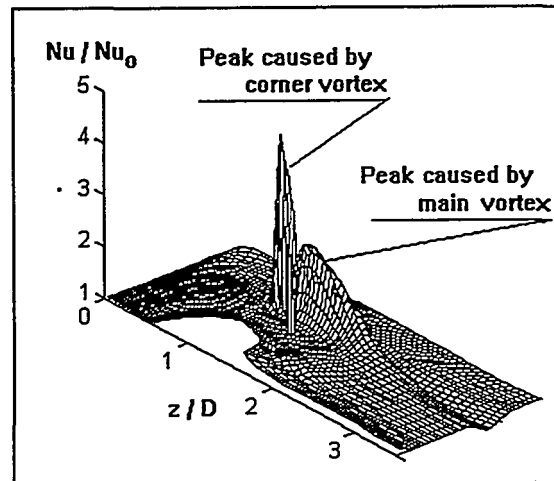


Fig. 9 - Local Heat Transfer Enhancement ($r=0.9D$; $\theta=80^\circ$; $\Lambda=2.0$; $\beta=45^\circ$)- Lower Fin

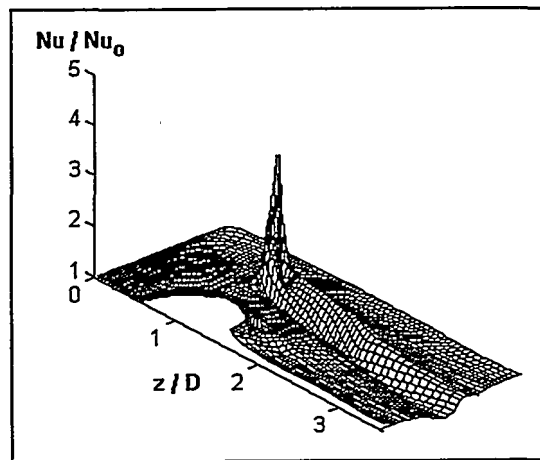


Fig. 10 - Local Heat Transfer Enhancement ($r=0.9D$; $\theta=80^\circ$; $\Lambda=2.0$; $\beta=45^\circ$)- Higher Fin

5.CONCLUSIONS

This work presents a numerical investigation about the influence of longitudinal vortex generators on heat transfer and flow losses in a fin-tube channel. Delta winglet vortex generators were used, and the influence of parameters such as position, aspect ratio and

angle of attack was investigated. A steady-state analysis was carried out using PHOENICS 2.0 CFD package for $Re=284$.

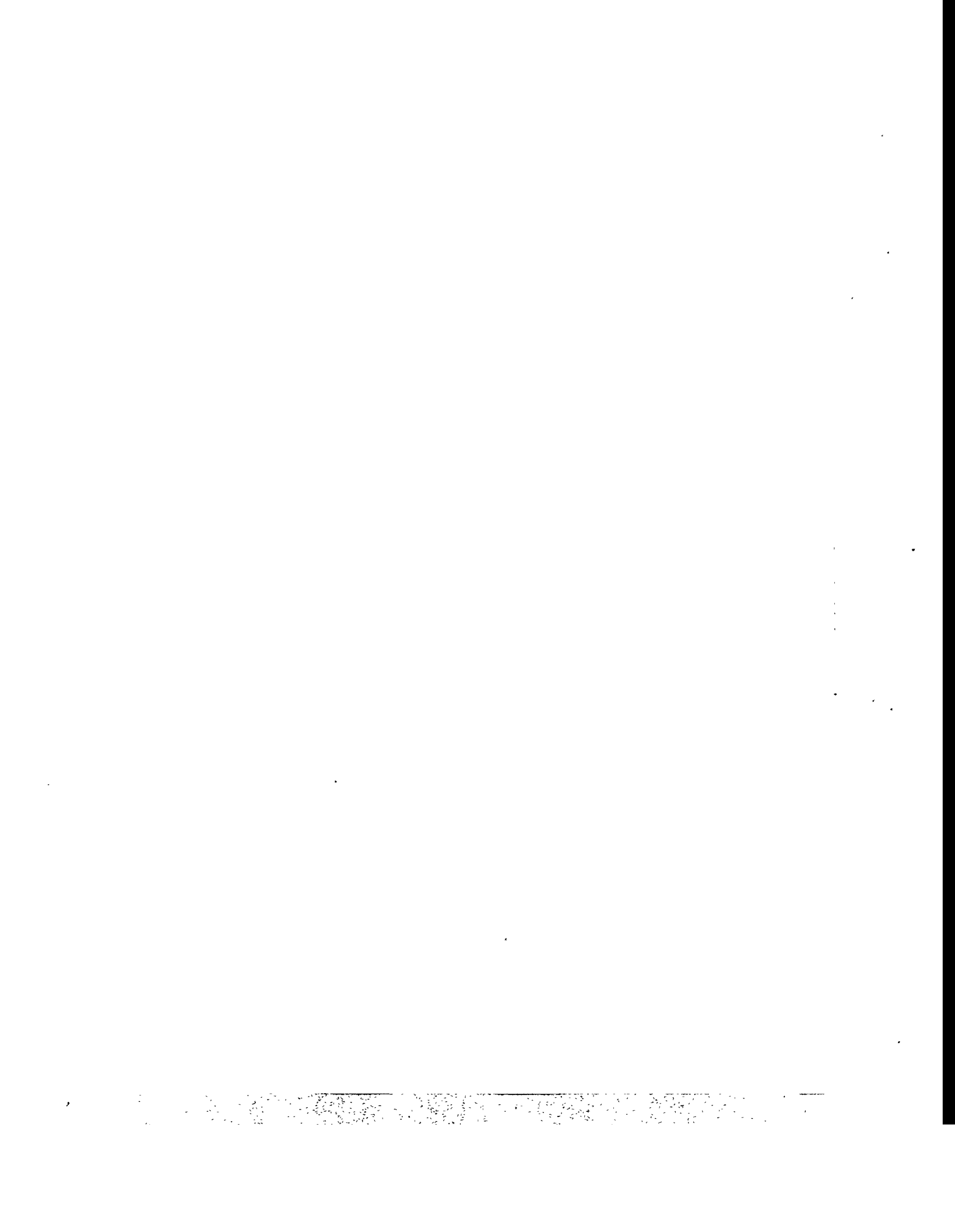
Reduction of flow losses of about 12% was obtained with vortex generators positioned at $r=0.9D$ and $\theta=80^\circ$. For the same configuration, global heat transfer enhancement of about 3% and local heat transfer enhancement of about 350% was achieved.

The influence of vortex generators parameters such as aspect ratio and angle of attack was investigated. Results indicated that $\beta=45^\circ$ is the best angle, in agreement with the experimental results of Fiebig [2]. However, this result is influenced by the vortex generator position since the direction of the local velocity vary remarkably with the position in the channel. Therefore a generalization of this result can be precipitated unless a more detailed investigation is carried out.

The influence of aspect ratio was investigated for the range $1.0 < \Lambda < 2.0$. Results indicate $\Lambda=2.0$ as the best aspect ratio. The aspect ratio has a great influence in flow losses, but a small influence on global heat transfer. With the vortex generators in the best position ($r=0.9D$ and $\theta=80^\circ$) and angle of attack $\beta=45^\circ$, the increasing of aspect ratio increases the flow losses and heat transfer.

REFERENCES

1. Biswas, G., Mitra, N. K., Fiebig, M., Heat Transfer Enhancement in Fin-Tube Heat Exchangers by Winglet Type Vortex Generators. *Int. J. Heat Mass Transfer*, vol. 37, n.2, p. 283-291, 1994.
2. Fiebig, M. et al, Simultaneous Heat Transfer Enhancement and Flow Loss Reduction of Fin-Tube. *Heat Transfer - 1990*, Hemisphere, 1990.
3. Kakaç, S. et al, *Handbook of Single-Phase Convective Heat Transfer*, (1989).
4. Kays, W. M., London, A. L., *Compact Heat Exchangers*. McGraw-Hill Book Co., 3rd Ed., New York, 1984.
5. Patankar, S. V., *Numerical Heat and Fluid Flow*. Hemisphere, 1980.
6. Valencia, A., Fiebig, M., Mitra, N. K., Experimental Investigation of Heat Transfer and Flow Loss in a Fin-Tube Heat Exchanger Element with Longitudinal Vortex Generators. *Proc. of EURO THERM - 93*, Bochum, 1993.
7. Yanagihara, J. I., Torii, K., Heat Transfer Characteristics of Laminar Boundary Layers in the Presence of Vortex Generators. *Proc. of 9th Int. Heat Transfer Conference*, Jerusalem, vol. 6, p. 323-328, 1990.
8. Yanagihara, J. I., Torii, K., Enhancement of Laminar Boundary Layer Heat Transfer by Longitudinal Vortices. *Proc. of 4th Int. Symposium of Transport Phenomena in Heat and Mass Transfer*, Sydney, 1991.



**The use of PHOENICS in the
design of catalytic converters**

M.Luoma^{*)} and A.G.Smith^{**)}

^{*)} Kemira Metalkat OY, P.O. BOX 171, FIN-90101 Oulu, FINLAND

^{**)} S & C Thermofluids Ltd, The Old Tannery, BATH, BA1 9AN, U.K.

Abstract

Manufacturers of automotive catalytic converters are constrained to design a system which is mechanically reliable, puts low back pressure on the engine, has adequate conversion performance, is low cost and of minimum size. In recent years, computational fluid dynamics (CFD) has been widely examined as a means of predicting the performance of catalytic converters to aid with the design process. Kemira Metalkat and S & C Thermofluids have put together and developed a number of existing CFD techniques in order to create a tool which is integrated within the design process. PHOENICS is used in the heart of the system in order to produce predictions of transient (light-off) and steady state catalyst performance. Grid generation tools have been provided to allow simplified and rapid geometry definition with suitable integration (via FEMGEN) within other parts of the catalyst design process. Simplified input techniques have been provided along with associated translators to create specification of the model for PHOENICS. Post-processing software has been provided through FEMVIEW to allow visualisation of catalyst monolith variables and transient performance animation. The whole system is controlled via a menu. The system has been used to study the effects of the catalyst design parameters on the converter performance. The results obtained using the system have so far been more qualitative than quantitative. However, validation studies have been carried out to check pressure drop prediction. A new model for the pressure drop over a metallic monolith has been developed.

Helsinki University of Technology
3rd Colloquium on Process Simulation
12 - 14 June, 1996
Espoo, Finland

INTRODUCTION

Catalytic converters have been successfully used to control automobile emissions for nearly two decades. A catalytic converter usually contains exhaust pipes, front and rear cones and one or two catalytic monolith reactors (Fig. 1). To make the chemical reactions possible, the catalytic monolith is designed to have as much surface area as possible. Therefore, it consists of thousands of parallel ceramic or metallic channels. A thin washcoat layer of alumina is applied to the surface of the substrate to provide a high surface area support onto which catalytically active noble metals are impregnated. In a so called three way catalytic converter (TWC) a mixture of the precious metals - platinum (Pt), palladium (Pd), and rhodium (Rh) - is used. Pt and Pd are the most active for the oxidation of hydrocarbons (THC) and carbon monoxide (CO) to carbon dioxide (CO_2) and water (H_2O). Rh is supplied mainly to reduce selectively nitrogen oxides (NO_x) to nitrogen (N_2).

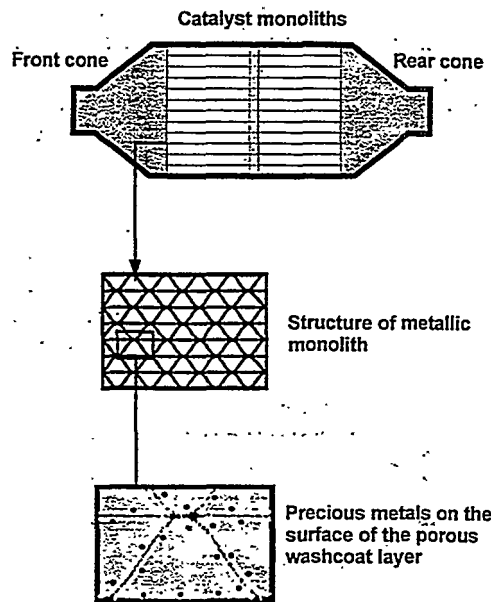


Fig.1 - A metallic exhaust gas catalytic converter.

Manufacturers of automotive catalytic converters are constrained to design more effective systems to meet the more stringent emission limits (LEV, ULEV) anticipated for the end of the decade /1/. Catalytic converters have to be also mechanically reliable and to put low back pressure on the engine. They should be low cost and of minimum size. Since converter performance is a complex function of operating conditions, converter geometries, and catalyst properties, an empirical approach to the problem can be very costly and time consuming. Reactor models and computer simulations can play an important role in meeting the new challenges in the area of the optimal catalytic converter design.

In most monolith modelling studies reported in literature /2-5/ the catalytic monoliths were assumed to be adiabatic, and exhaust gas flow distribution uniform. The entire monolith could therefore be represented by one single monolith channel. These 1-dimensional (1D) models were used primarily to analyze the steady state operation of catalytic converters, but also the transient light-off performance of the converter have been modelled /6/. Besides, the high temperature mass transfer limited performance of converters has been modelled separately /7,8/. In more recent studies the catalytic converters have been modelled as a whole /9-13/ and computational fluid dynamics (CFD) has been widely examined as a means to simulate the performance of catalytic converters /14-18/.

The aim of this study is to present a general design tool for catalytic converters having simplified input techniques, grid generation and post-processing tools. One commercial available CFD code - PHOENICS - is used in the heart of the system in order to produce predictions of transient and steady state catalyst performance.

MODEL REQUIREMENTS

The modelling of the catalyst performance contributes to a more exact understanding of the chemical and physical phenomena occurring inside the catalytic converter. In Figure 2 and in the following paragraphs are indicated the aspects that a full catalyst design model must provide.

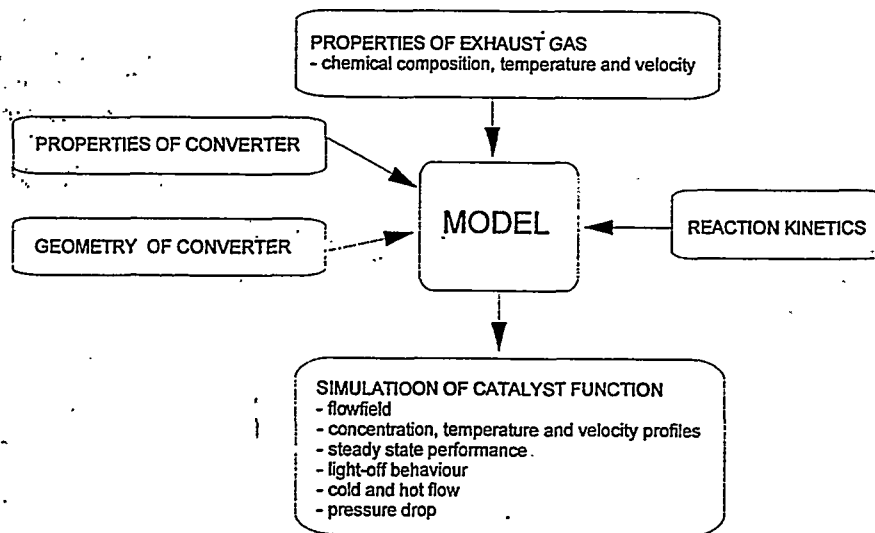


Fig. 2 - Catalytic converter model requirements.

Geometry definition

The geometry of the can and the monolith must be reproduced in terms of the model. This must be in 2D or 3D and make use of symmetry as appropriate. The monolith shape can typically be of round, elliptic or race-track cross-section. The geometry may already be defined in a CAD system. The model must then be capable of using this data efficiently. Where CAD data is not available, the method of geometry specification must be simple and allow an easy study of changes in the geometry.

Cold and hot flows

For initial design evaluation of catalytic converters, pressure drop and velocity profiles are measured using cold exhaust flow conditions. For this reason the model must allow simulation of cold flows. Ultimately, of course, the catalyst runs with hot exhaust flow. The catalyst prediction technique must include this.

Pressure drop

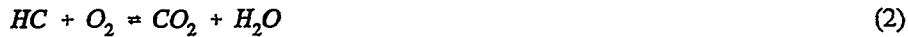
The catalytic converter is a resistive component in the engine exhaust system. As such, it puts a back-pressure on the engine and affects performance adversely. There is a requirement to minimise back-pressure and to indicate likely levels to engine manufacturers at the design stage. The pressure drop results mainly from the flow through the channels of the monolith. As the flow heats up from light-off, the density of the gas falls and the velocity increases in order to maintain continuity. This, coupled with some geometrical changes from expansion, can result in the back pressure increasing with light-off. These back pressure changes must be represented in the model.

Flow distribution

Experimental studies /19-21/ have shown that the flow across the monolith face is often non-uniformly distributed and this maldistribution can adversely affect the converter performance and durability. By creating a uniform flow distribution, the lifetime of the converter would be increased and/or a smaller converter could be used. The model must therefore be capable of predicting the flow field through the catalytic converter geometry. This entails solving the Navier-Stokes equations in such a way that all aspects of the flowfield will be considered. The catalyst flowfield is compressible, with heat transfer and is turbulent. The solution must therefore allow for varying density, temperature, direction and some form of turbulence model must be used.

Chemical reactions

Exhaust gas catalytic converters are used to oxidize CO and THC and to simultaneously reduce NO_x. For an effective converter high CO, THC and NO_x conversions are required in the stoichiometric exhaust gas conditions. The following total reactions take place within the catalyst /6/



The model must allow these reactions and the resultant change in gas temperature to be predicted. The model must be flexible enough to allow other reactions to be included.

Heat transfer

The model must allow heat released as a result of chemical reactions to be transferred through the catalyst and through and along the can. It is important that the model should enable "hot spots" within the solid surfaces of the catalytic converter to be identified so that the mechanical integrity of the converter can be assessed.

Transient phenomena

The light-off performance is often critical to the overall performance of a catalytic converter. For many seconds after a cold start, the reactor temperature is too low for the catalytic reactions to take place. As a result, significant amounts of pollutants pass unconverted through the reactor before it can reach catalytic light-off temperatures. This means that in the cold phases of the engine test cycles, ECE 15 and FTP 75, 80 % of all the emissions of these tests can be formed /6/. The design model must therefore predict the transient aspects of the catalyst performance.

Overall utility of the system

The model must be easy to use (i.e through a suitable menu system) and manageable in terms of run time and platform requirement (i.e to run on a PC).

APPROACH TO MODELLING

The above requirements for a catalytic converter design model have been met by bringing together and enhancing a number of existing techniques and enveloping them within an outer menu system. PHOENICS is a general purpose transport equation solver which is well suited to this application for two main reasons:

- 1) The code handles 1D, 2D and 3D flow phenomena involving compressibility and heat transfer and has a range of turbulence modelling techniques available. Transient and steady state flowfields can be predicted. Thus it immediately addresses the flow prediction requirements indicated above.
- 2) The ability to describe chemical reactions within PHOENICS has already been successfully applied to the catalyst problem, first by Fueyo /14/ in 1D and subsequently by Clarkson et al. /17/.

From the view of the modelling, the chemical and physical phenomena occurring inside a catalytic converter are really complicated and depend on each other. That is why a comprehensive 3D transient model, which can reliably predict the catalyst behaviour is extremely large and difficult to handle. Our way to model this complicated problem was to divide it up into smaller, more easily verified submodels and combine these to a total model as is described in Figure 3.

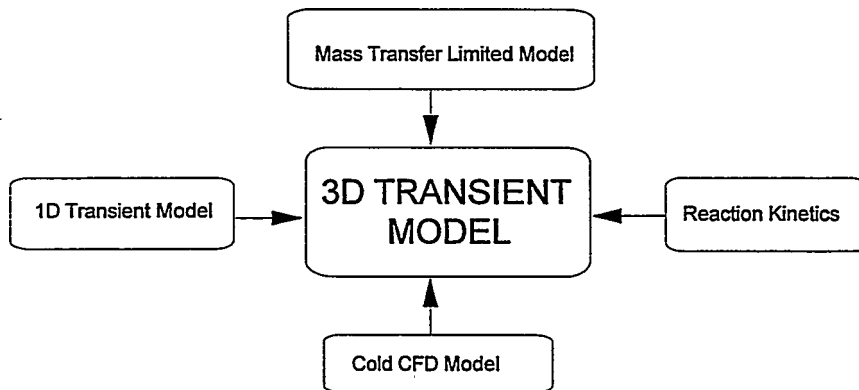


Fig. 3 - The phases of modelling.

As a function of temperature two different kinds of behaviour areas can be found in the catalyst. At low temperatures, the catalytic reaction kinetics are controlling the catalyst function, whereas at high temperatures, the mass transfer from the gas to the solid catalyst is limiting the reactions. The catalyst behaviour in the mass transfer limiting conditions has been predicted with the model, in which the complicated reaction kinetics were not necessary to be taken into account. The model has been used for example to compare reliably catalysts with different cell densities /8/.

The 1D transient model which is based on the work of Fueyo /14/ aims at describing at least in a satisfactory way the most important phenomena within the catalyst monolith. The monolith was assumed to be adiabatic and the exhaust gas flow distribution at the catalyst face uniform. The entire monolith could, therefore, be represented by one single monolith channel. The physical properties of the exhaust gas were assumed to be constant. The CO oxidation has been assumed to take place only on the surface of the catalytic washcoat. The reaction kinetics of the Kemira Pt/Rh-catalyst have been widely studied and modelled, both under steady state and transient conditions based on the reaction mechanisms and experimental data /22,23/. So far, however, the literature kinetics for CO oxidation /6,24/ has been used in the model.

In the cold CFD model the converter geometry is reproduced to describe the flow phenomena inside the converter in the most realistic and best way as possible. The catalyst monolith is assumed to be a porous flow obstacle, through which the laminar exhaust gas is flowing in the axial direction and creating a pressure drop. All the channels of the substrate is assumed to be round. The cold CFD model enables one to study how the mechanical structures of the front and rear cones, the exhaust pipes and the catalyst substrate affect the flow distribution and pressure drop.

The 3D model is developed based on the 1D transient and the cold CFD models. The equations for the radial heat transfer in the monolith and for heat transfer to the environment have been added. The physical properties of the exhaust gas have now to depend on gas temperature. The equivalent continuum approach is used in which flow through the substrate is not considered in terms of each individual channel being modelled but rather the averaged effect of a number of channels within each computational cell. This approach, which Clarkson et al. /17/ have successfully used, reduces the problem down to a manageable size.

MODEL SPECIFICATION

Geometry specification

The geometrical aspects are handled by using the PHOENICS Body Fitted Coordinates (BFC) gridding approach to match the geometry being considered. To obtain an efficient method of grid generation, two techniques have been incorporated into the system. One technique uses a specially written grid generator to read certain catalytic converter geometric parameters and then produce appropriate PHOENICS GSET commands within a Q1 file. The catalyst model, allows for the modelling of circular and elliptic catalyst geometries with concentric inlet and outlet locations. The grid generation capability handles the following inputs as indicated in Figure 4:

- Inlet pipe radius
- Inlet diffuser cone length
- Pre-monolith length
- Monolith length
- Monolith radius
- Monolith exit length
- Exit cone length

- Exit pipe radius
- Aspect ratio of ellipse.

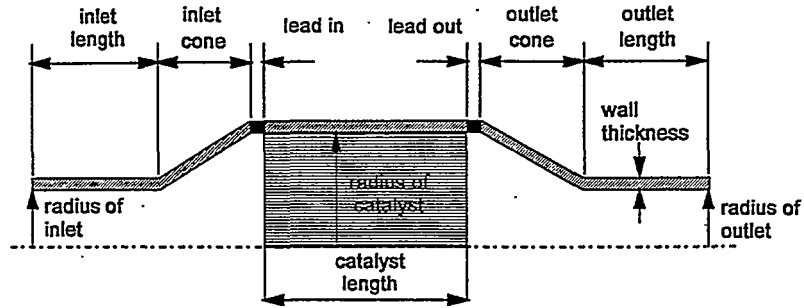


Fig. 4 - Using the menu system for the geometry input.

If the aspect ratio of the catalyst is set as 1, a 2D axisymmetric grid is created. The grid refinement levels in each direction can be factored by the user.

The second technique uses the FEMGEN grid generator by Femsys Limited to read and display IGES or DXF format CAD files, as shown in Figure 5. FEMGEN is then used to produce a mesh which can be translated into a GRID file for use by PHOENICS.

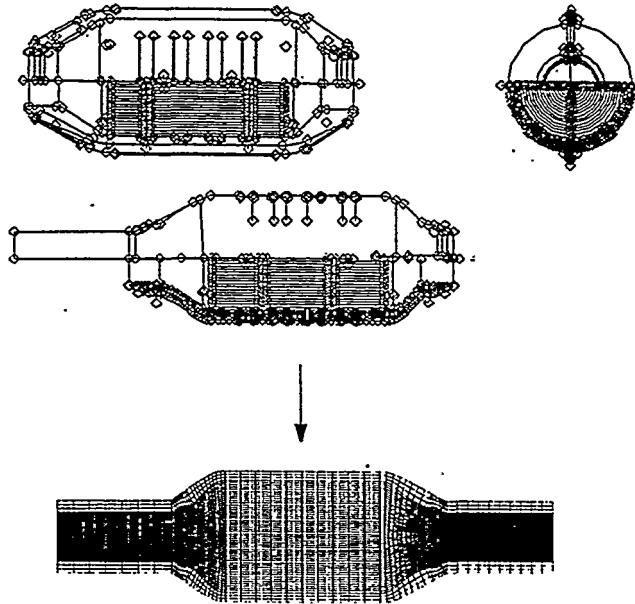


Fig. 5 - Using of FEMGEN for the grid generation.

Boundary conditions

The user interface was designed to handle the inputs for the exhaust gas and the catalytic converter shown in Table 1.

Table 1 - The inputs for the exhaust gas and the catalytic converter.

	Input
Exhaust gas	Mass flow
	Temperature
	Concentration of species
Catalytic converter	Void fraction
	Geometric surface area per unit reactor volume
	Substrate density, conductivity and heat capacity
	Catalytic surface per unit reactor volume
	Transport properties (Nusselt and Sherwood number)
	Hydraulic diameter of a single channel

Governing equations

The 3D transient model is developed based on the equations reported earlier in the papers of Fueyo /14/ and Clarkson et al. /17/. The flow in the exhaust pipes, front and rear cones of the catalytic converter is assumed to be turbulent. The Reynolds averaged Navier-Stokes equations are solved and the $k-\epsilon$ turbulence model is used for these regions. Pressure drop through the monolith is calculated assuming laminar flow through out the channels. As the entrance effects were neglected, the Hagen-Poiseuille equation

$$\frac{\partial p}{\partial z} = -\frac{32\nu\rho_g w}{D_h^2} \quad (5)$$

could be used for the pressure gradient in the monolith. p is the pressure, z the axial distance, ν the kinematic viscosity, ρ_g the gas density, w the axial velocity and D_h the hydraulic diameter of a catalyst channel. The axial areas in the region of the monolith are reduced in order to allow for the blockage of the catalyst (void fraction). The interaction between the channels is neglected by presuming the radial velocity inside the monolith to be zero.

A number of reactions are considered in the model - i.e those of CO; C₃H₈, CH₄, H₂ and O₂. The reaction kinetics used are those given by Oh and Cavendish /6,24/. They can all be presented as a form of Arrhenius rate expressions

$$R_i = k_i c_i c_j e^{(k_2/T_s)} \quad (6)$$

R_i is the reaction rate of species i, c_i and c_j are the concentrations of species i and j involved in the reaction, k₁ is the reaction rate coefficient, k₂ the activation energy and T_s the temperature of the substrate.

As with Fueyo /14/, although coding has been provided with reaction rate coefficients k₁, and activation energies, k₂ for a number of reactions, only the CO oxidation reaction with O₂ is implemented at this stage. The heat energy released as a result of the CO reaction is factored to take account of the likely effects of the hydrocarbon reactions.

The reactions occur only for concentrations of species on the catalyst surface as opposed to in the gas. Two variables are thus solved for the CO level in the system - 1CG (the concentration of pollutant in the gas) and 2CS (the concentration of pollutant on the catalyst surface). Only 1CG enters the domain with the exhaust gas. Source terms are thus provided for both of these concentrations to indicate the effect of catalytic material on promoting reaction on the surface.

For the concentration in the gas, the source term, S₁, is given by

$$S_1 = \rho_g k_{mi} S (C_{si} - C_{gi}) \quad (7)$$

Thus the difference between the concentration on the surface and in the gas leads to a large sink of c_{gi} towards the surface. In the equation (7) the coefficients affecting the mass transfer rate are a special mass transfer coefficient

$$k_{mi} = \frac{Sh_{lim} D_i}{D_h} \quad (8)$$

and the ratio of surface area to reactor volume, S. This is a function of the catalyst cell density. In the model the cross section of the catalyst channels are assumed to be round. Therefore, the effects of the cross section shape on heat and mass transfer efficiencies have been taken into account by using limiting Nusselt, Nu_{lim}, and Sherwood number, Sh_{lim}, for the calculation of the heat and mass transfer coefficients /25,26/. D_i is the diffusivity of the species i.

For the concentration at the surface, the source term is given by,

$$\frac{M}{10^3 \rho_g} a(x) R_i = k_{mi} S (c_{gi} - c_{si}) \quad (9)$$

Thus, concentration at the wall is a function of the transfer of the gas concentration and the rate of reaction at the wall. Ideally at full conversion, all of the gas concentration coming to the surface can be converted at the temperature. The constant a(x) is the

catalytic material loading and indicates the influence of the catalyst precious metal content on the reaction rate. M is the relative molecular mass of the exhaust gas.

The temperature of the exhaust gas and the catalyst monolith are also considered as separate variables. They take into account heat transfer between the gas and the solid, as well as heat released as a result of reaction.

The gas temperature, $T_g = h_g / C_{pg}$, is given by the equation,

$$\frac{C_{pg} \partial \rho_g T_g}{\partial t} + C_{pg} \nabla(\rho_g U T_g) - \nabla(\lambda_g T_g) = S2 \quad (10)$$

The left hand side of the equation deals with the transient, convection and diffusion of the gas enthalpy, h_g , and the gas temperature. C_{pg} and λ_g are the specific heat capacity and the thermal conductivity of the gas.

The source term of the right hand side of the equation comes purely from heat transfer from the solid, i.e.

$$S2 = hS(T_s - T_g) \quad (11)$$

where h is the heat transfer coefficient and calculated analytically to the mass transfer coefficient (eq. (8)) with the equation

$$h = \frac{N_{lim} \lambda_s}{D_h} \quad (12)$$

As shown in equations (8) and (12), both the mass and heat transfer coefficients are assumed constant throughout the monolith.

The solid temperature, T_s , is governed by the equation

$$\rho_s \frac{\partial T_s}{\partial t} - \frac{\lambda_s}{C_{ps}} \left(\frac{\partial^2 T_s}{\partial z^2} + \frac{G}{(1-\epsilon)} \left(\frac{\partial^2 T_s}{\partial x^2} + \frac{\partial^2 T_s}{\partial y^2} \right) \right) = S3 + S4 \quad (13)$$

In the first term of this equation, the solid density, ρ_s , is constant. The second term describes the conduction through the solid. λ_s and C_{ps} are the thermal conductivity and the specific heat capacity of the solid. The z -direction is along the monolith. The factor G indicates that the conductivity along the monolith is different to that across it. The void fraction, ϵ , indicates effectively the amount of solid (porosity) within a given cell.

The two source terms S3 and S4 are given by the equations

$$S_3 = \frac{hS}{(1 - e)C_{ps}}(T_g - T_s) \quad (14)$$

$$S_4 = \frac{a(x)R_i\Delta H_i}{(1 - e)C_{ps}} \quad (15)$$

The first is a result of heat transfer from the gas to the solid, the second is a result of heat release, ΔH_i from the reaction considered R_i . Thus as heat is transferred to the solid from the gas, the solid temperature builds up, resulting in reaction which raises the solid temperature which then raises the temperature of the gas.

In the model, the gas density is allowed to vary according to the ideal gas equation,

$$\rho_g = \frac{p}{RT_g} \quad (16)$$

The value of the gas constant, R, could be varied according to the species concentrations although this is not currently implemented. The compressibility correction is also implemented.

Having allowed the gas density to vary, a problem arises with the transient term in the solid temperature (STS) equation. This problem, which is mainly due to studying the case as if it were one phase instead of two phases, is discussed extensively by Clarkson et al. /17/. The use of the built-in transient term for STS in the model by Fueyo /14/ is justified by the assumption that the gas density is fixed to the value of 1. This concept can be extended to the idea that the gas density has a value other than 1, provided that the other terms in the STS equation are multiplied by the ratio of the gas density to the solid density. The use of ground coding for the STS coefficient in the Q1 file allows for the value of density to vary.

However, this still assumes that the density is a constant, which it is not. To overcome the problem, Clarkson et al. /17/ describe switching of the transient term altogether and constructing a source term which corresponds to the true transient term for the solid. A special volumetric source term has been provided to facilitate this. The Q1 file contains the PATCH location and calls ground coding for the coefficient and value for STS. The PHOENICS formulation for STS is then

$$Source = C_{sts}(V_{sts} - STS) \quad (17)$$

$$= -C_{sts}(STS - V_{sts}) \quad (18)$$

In the ground coding, the coefficient is set to

$$C_{sts} = \frac{\rho_s}{\Delta t} \quad (19)$$

where ρ_s is the solid density and Δt the time step size. The value V_{sts} is set to the value of STS at the previous time steps.

Obtaining a value of STS at the previous time step is made difficult by the fact that PHOENICS does not store this information when the transient term is switched off - which it is in the Q1 file. A new variable TSOL is therefore stored for. At the end of each iz slab, the value of TSOL is set equal to STS. As no further calculations on STS are carried out at that slab on that time step, TSOL can then be used in the formulation described above.

The value of laminar viscosity is a function of temperature using the formulation suggested by Clarkson et al. /17/. The laminar viscosity is calculated according to the equation

$$\nu = (6.542 \cdot 10^{-11} T_g^2) + (6.108 \cdot 10^{-8} T_g) - 0.89 \cdot 10^{-5} \quad (20)$$

Post-processing

The system is arranged such that the user can obtain immediate visualisation of the more important results of the analysis. For example, the user can request to see the pressure drop through the catalyst as shown in Fig. 6. This request runs AUTO PLOT with a "use" file which displays the centreline axial pressure distribution.

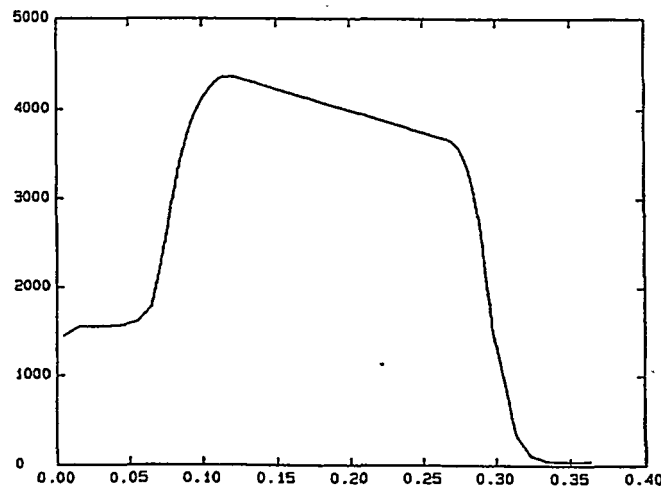


Fig. 6 - An example of results: using AUTO PLOT to see the pressure drop through the converter.

PHOTON can be used to show normal flowfield distributions as indicated in Fig. 7.

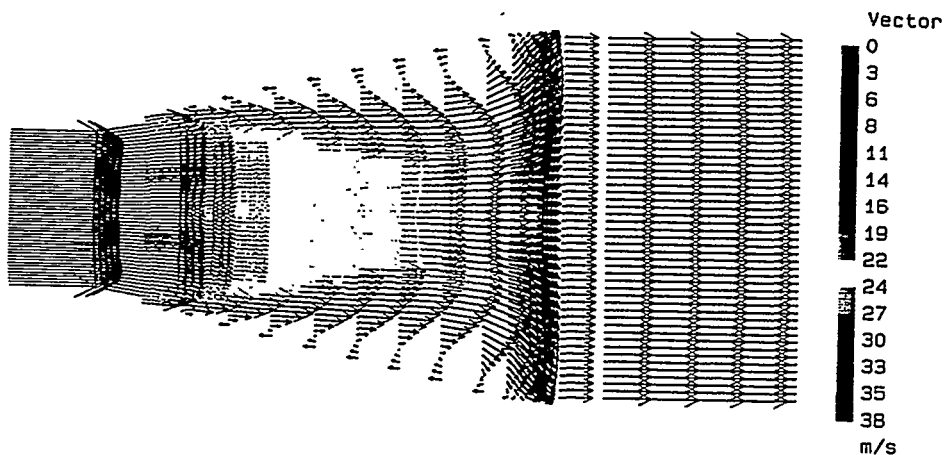


Fig. 7 - An example of results: using PHOTON to see flowfield distributions inside the converter.

The user can ask to see the catalytic converter wall (can) or monolith temperatures. Using FEMVIEW, the cells relevant to these components are copied to a separate set. This set along with temperature results can then be displayed using a hidden line view. When the catalyst has been modelled as 2D using an axisymmetric grid, an assembly can be created within FEMVIEW to allow a full 3D model to be examined. By making the assembly incomplete, a cut-away view is obtained. Figure 8 shows a typical result.

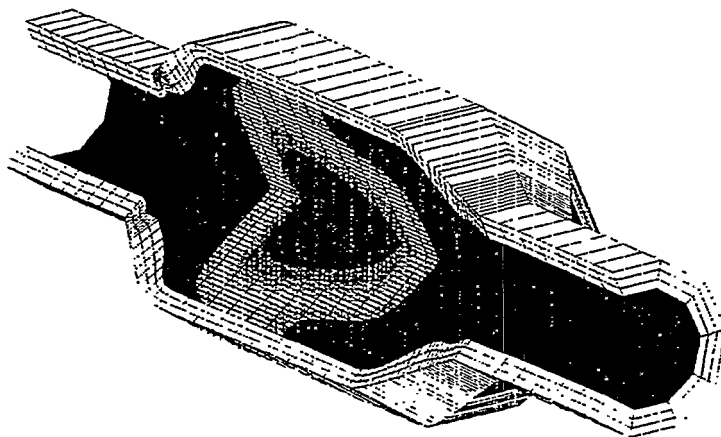


Fig. 8 - An example of results: using FEMVIEW to see the solid temperatures of the can and the monolith.

Results from several time steps can be appended to a single FEMVIEW model. These results can then be animated to show for example the light-off performance of a catalytic converter.

Menu control

The overall system is provided controlled via a menu. Figure 9 shows the layout of the system. Pop-down menus allow settings to be made for the parameters described above. The various PHOENICS and FEMVIEW modules can be executed from the menu.

The system can be run on 486 or Pentium PC. A typical 2D grid uses 30x50 cells. Transient light-off calculations typically may use 30 time steps to cover a 60 second period. Within each time step 30 sweeps are required for convergence resulting in run times of around half and hour on a 60 MHz Pentium machine.

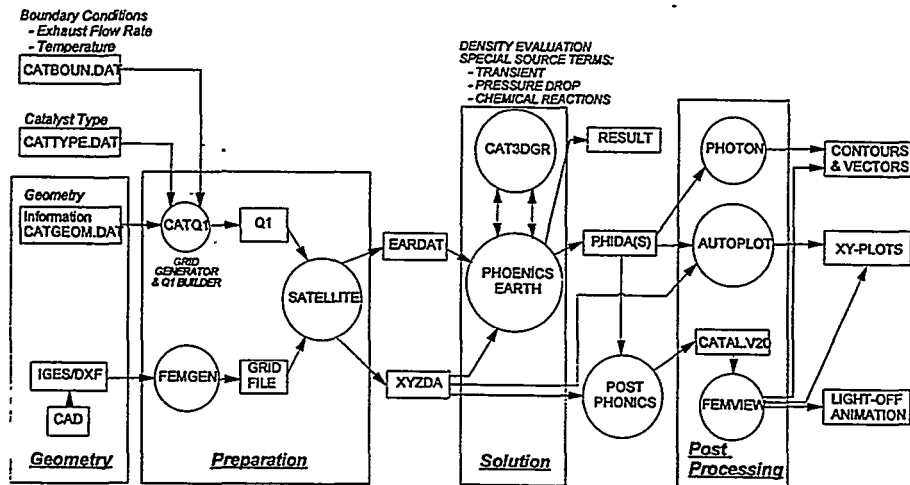


Fig. 9 - Catalytic prediction system.

RESULTS AND VALIDATION OF THE MODELS

The validation of the total 3D transient model has been started up by checking the accuracy of the results of the submodels. As long as the literature reaction kinetics are used in the model, the comparison of the results with experimental data is really difficult. That is why the validation of the 1D transient model, too, concentrates only on explaining the effects of different parameters on the catalyst function. The validation of the cold CFD model was performed concerning the pressure drop prediction. Naturally, the velocity profile prediction must also be validated.

1D transient model

With the 1D transient model the effects of exhaust gas properties and different catalyst design parameters on the warm-up characteristics, light-off and steady-state CO conversion efficiencies were studied by making a step change in the feedstream temperature. The results /27/ indicated that a fast light-off can be achieved by increasing the exhaust gas temperature or decreasing its CO concentration. The end conversion efficiencies could be affected by decreasing the exhaust gas flow rate. The precious metal loading, the thermal inertia (mass) and the heat conductivity of the substrate material (ceramic or metallic) were the most important catalyst design factors affecting the light off. The geometric total area (length and cell density) and the diffusion distance (cell density) had the main effect on the steady state conversion efficiency. The results responded well to the experimental results reported in literature /28,29/.

The 1D model was also used to optimise the performance of the metallic catalyst. The optimisation led inevitably to the use of high cell density to obtain the best steady-state behaviour. The optimised 1200 cpsi metallic catalyst having half the length and the same amount of precious metals, lighted off earlier and its CO end conversion was much higher than that of the traditional ones (see Fig. 10). The real differences between the behaviour of the catalysts were seen when the cumulative CO-emissions were drawn in Figure 11. The better mass and heat transfer characteristics of the optimised 1200 cpsi metallic catalyst enabled almost one third of the total cumulative CO emissions of the traditional ceramic one.

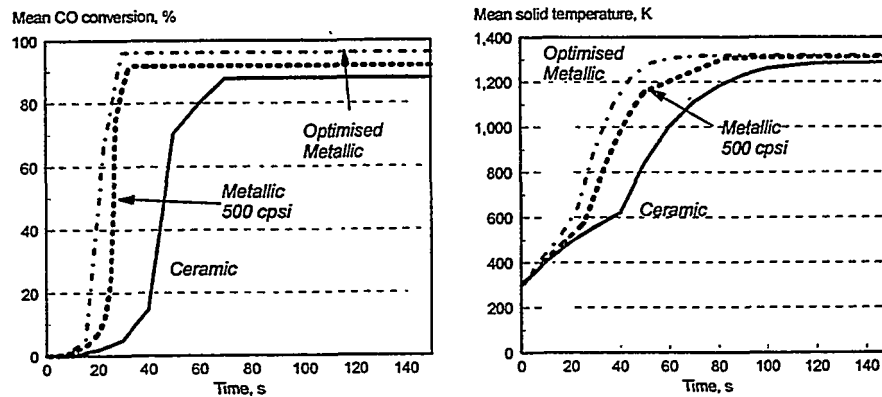


Fig. 10 - The average CO conversion efficiencies and solid temperatures as a function of time, when an exhaust gas flow at 600 K at time $t = 0$ s were led to the catalytic converters at 300 K.

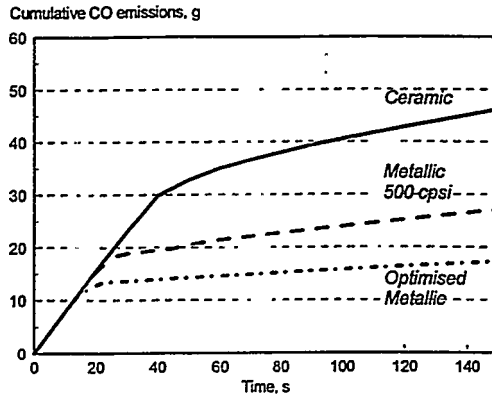


Fig. 11 - Cumulative CO-emissions.

Cold CFD model

The aim of the experimental measurements was to study the effect of the catalyst monolith on the pressure drop. Therefore, the catalyst monolith was placed in a straight tube which had the same dimension as the catalyst monolith (75 mm diameter). As the catalyst cell density has a great effect on the pressure drop, monoliths with cell densities of 200, 300, 400, 500 and 600 cpsi were studied. The length of the monoliths were 75 mm. The pressure drop in the monoliths were measured as a function of the volumetric flow rate. In the measurements, air at ambient temperature was used. Experimental results are shown in Figure 12.

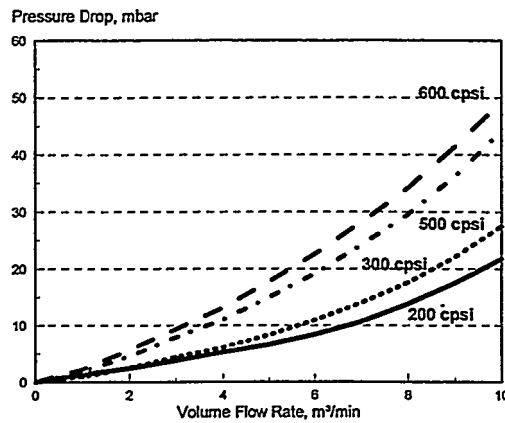


Fig. 12 - Experimental pressure drops.

As similar cases to those of experiments were calculated using the cold CFD model (see results in Fig. 13 for 500 cpsi catalyst) it was noticed that the Hagen-Poiseuille equation used for the pressure drop prediction did not give satisfactory results especially for high volume flows. Therefore, a new pressure drop model was developed based both on the physical phenomena and experimental data.

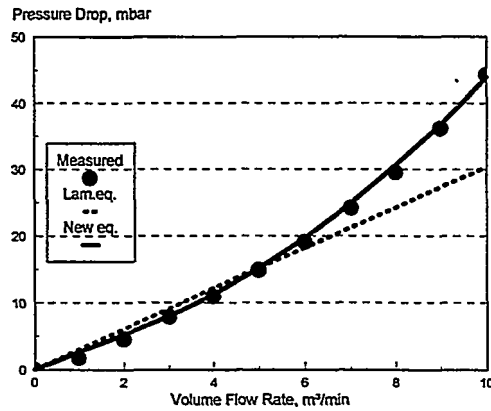


Fig. 13 - Pressure drop in 500 cpsi monolith as a function of the exhaust gas flow.

The formulation used to reproduce the pressure drop within the model takes into account the developing laminar flow area, the length of which can be calculated using the following equation

$$L_e = 0.0288ReD_h \quad (21)$$

where the Reynolds number is

$$Re = \frac{D_h w}{\nu} \quad (22)$$

w is the average velocity in the channel.

The pressure drop caused in the developing flow area is calculated using the turbulent pressure drop equation

$$\Delta p_{urb} = \frac{4}{D_h} \frac{1}{2} \rho_g (w)^2 f L_e \quad (23)$$

in which the friction factor /30/ is

$$f = 0.0791 Re^{1/4} \quad (24)$$

In the laminar flow area ($L - L_e$), the pressure drop is calculated using the laminar pressure drop equation

$$\Delta p_{lam} = - \frac{32 \nu \rho_g w}{D_h^2} (L - L_e) \quad (25)$$

where L is the monolith length.

The total pressure drop caused in a one channel of the catalytic monolith is then calculated

$$\Delta p_{tot} = C_1 \Delta p_{urb} + C_2 \Delta p_{lam} \quad (26)$$

where C_1 and C_2 are correction factors estimated from the experimental results. For the metallic catalysts having the cell density under 600 cpsi, only the turbulent equation needs to be corrected. C_1 can be calculated from the equation

$$C_1 = 1 - A e^{-\frac{|Re-Ro|}{q_o}}^F \quad (27)$$

where the estimated parameters are $A = 0.2787$, $Ro = 3177.3$, $q_o = 1382.1$ and $F = 1.263$. The correction factor for the laminar equation is $C_2 = 1$.

For comparison the model was run with a number of the experimental test cases described above. Figure 14 shows a plot of pressure drop against flowrate for a 500 cpsi case. The plot compares experimental and calculated pressure drops. It can be seen that the predicted pressure drop, which has been calculated using the new equation, shows excellent agreement with experiment. The calculated laminar values show a discrepancy which increases with flowrate. The new model which uses the turbulent and laminar pressure drop equations is therefore clearly necessary to obtain good prediction of pressure drop against a range of flowrates.

3D transient model

Because the comparison of results of the 3D transient model with the experimental data was not yet possible, the initial assessment of the model's performance was made by comparing the results with published results from the model of Chen et al. /12,13/ Clarkson et al. have also simulated the same case /17/. Our results showed general agreement with these previously reported values.

CONCLUSIONS

A system has been created for the analysis of catalytic converter performance within the design context. The system uses PHOENICS in its heart to provide predictions of the transient and steady state mass and heat transfer within 2D and 3D catalytic converter geometries. The whole system is controlled via a menu which allows simple specification of catalyst geometrical and performance parameters. Geometrical specification via CAD data is achieved through the use of the FEMGEN software. The input data is translated by the system to create a Q1 file. Special ground coding is used to provide source terms describing the chemical kinetics and pressure drop. FEMVIEW is used to display the temperature results for certain components of the system and to provide animations of the light-off performance.

The results obtained using the system have so far been more qualitative than quantitative, except for those of the pressure drop. Further validation work is still required. In addition, future work with the system aims to cover the following areas:

1. Use of multi-block capability
2. Use of other turbulence models
3. Use of conjugate heat transfer (i.e. single temperature variable)
4. Nusselt and Sherwood number dependence upon temperature and position
5. The temperature dependence of the diffusion coefficients
6. Two phases instead of one phase
7. Heat transfer to the environment
8. Transport of other chemical species
9. Use of all existing reaction kinetics
10. Use of new kinetic equations for steady state and transient performance.
11. Effect of catalyst deactivation
12. Use of pulsating flow boundary conditions.

ACKNOWLEDGEMENTS

The authors wish to thank the staff members of Kemira's engine laboratory, especially Mr. J. Heikkinen, for performing the pressure drop measurements and Mr. H. Haario, ProfMath Oy, for the pressure drop correlations and their parameter estimation.

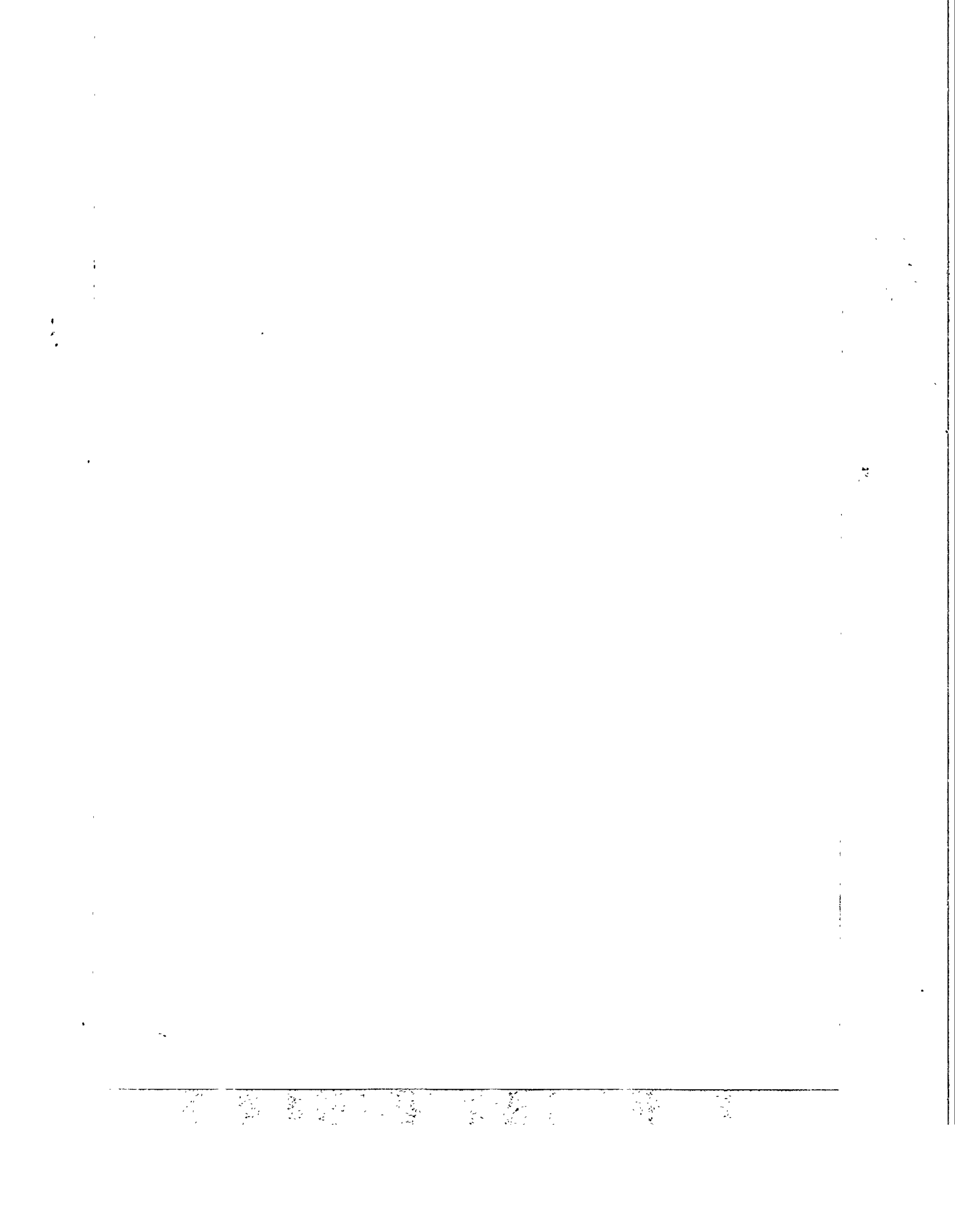
REFERENCES

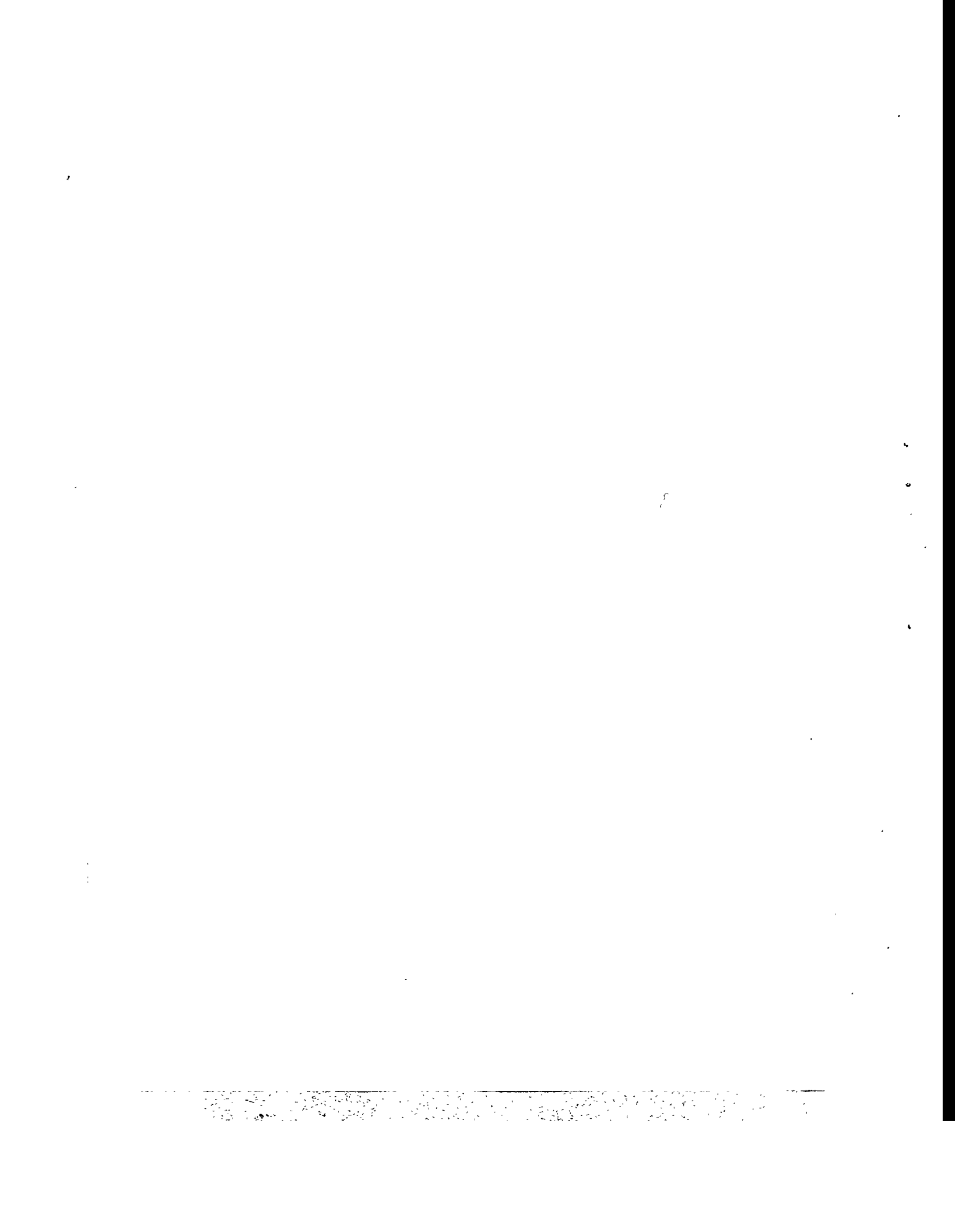
1. Heck, R.M., Hu, Z. et al. Close coupled catalyst systems design and ULEV performance after 1050 °C aging. Warrendale 1995, SAE International, SAE Technical Paper Series SP-1120 952415. p. 107-112.
2. Kuo, J.C.W., Morgan, C.R. & Larsen, H.G. Mathematical modelling of CO and HC catalytic converter systems. Warrendale 1971, SAE International, SAE Technical Paper Series 710289. p. 1089-1125.
3. Young, L.C. & Finlayson, B.A. Mathematical models of the monolith catalytic converters: Part I. Development of model and application of orthogonal collocation. *AIChE Journal* 22(1976), p. 331 - 343.
4. Carberry, B.P. & Douglas, R. A simple but effective catalyst model for two-stroke engines. Warrendale 1992, SAE International, SAE Technical Paper Series 921693. 11 p.
5. Payri, F., Benajes, J. & Galindo, J. One-dimensional fluid-dynamic model for catalytic converters in automotive engines. Warrendale 1995, SAE International, SAE Technical Paper Series 950785. p. 159-168.
6. Oh, S.H. & Cavendish, J.C. Transients of monolithic catalytic converters. Response to step changes in freestream temperature as related to controlling automobile emissions. *Ind.Eng.Chem.Prod.Res.Dev.* 21(1982)1, p. 29 - 37.
7. Hegedus, L.L. Effects of channel geometry on the performance of catalytic monoliths. ACS symposium on catalytic approaches to environmental control. Chicago Aug. 1973, p. 487 - 502.
8. Luoma, M., Lappi, P. & Lylykangas, R. Evaluation of high cell density Z-flow catalyst. Warrendale 1993, SAE International, SAE Technical Paper Series 930940. p. 187-198.
9. Flytzani-Stephanopoulos, M., Voecks, G.E. and Chang, T. Modelling of heat transfer in non-adiabatic monolith reactors and experimental comparisons of metal monoliths with packed beds. *Chem.Eng.Sci.* 41(1988), p. 1203 - 1212.
10. Becker, E.R. & Zygourakis, K. Monolith catalyst design options for rapid light-off. The annual meeting of AIChE. Miami Beach. Nov. 2-7 1986. 47 p.
11. Ryan, M.J., Becker, E.R. & Zygourakis, K. Light-off performance of catalytic converters: the effect of heat/mass transfer characteristics. Warrendale 1991, SAE International, SAE Technical Paper Series 910610. 12 p.

12. Chen, D.K.S., Oh, S.H. et al. A three-dimensional model for the analysis of transient thermal and conversion characteristics of monolithic catalytic converters. Warrendale 1988, SAE International, SAE Technical Paper Series 880282. p. 29-37.
13. Chen, D.K.S. & Cole, C.E., Numerical simulation and experimental verification of conversion and thermal responses for a Pt/Rh metal monolith converter. Warrendale 1989, SAE International, SAE Technical Paper Series 890798. 13 p.
14. Fueyo, N. 1-D simulation of a catalytic converter for car. Phoenix Demonstration Report PDR/CFDU/IC/35, CHAM Ltd. London 1987. 30 p.
15. Lai, M.-C., Kim, J.-Y. et al. Three-dimensional simulations of automotive catalytic converter internal flow. Warrendale 1991, SAE International, SAE Technical Paper Series 910200. 11 p.
16. Will, N.S. & Bennett, C.J. Flow maldistributions in automotive converter canister and their effect on emission control. Warrendale 1992, SAE International, SAE Technical Paper Series 922339. p. 183-210.
17. Clarkson, R.J., Benjamin, S.F. et al. An integrated computational model for the optimisation of monolith catalytic converters. Warrendale 1993, SAE International, SAE Technical Paper Series 931071. p. 11-24.
18. Baxendale, A.J. The role of computational fluid dynamics in exhaust system design and development. Warrendale 1993, SAE International, SAE Technical Paper Series 931072. p. 25-37.
19. Wendland, D.W. & Matthes, W.R. Visualization of automotive catalytic converter internal flows. Warrendale 1986, SAE International, SAE Technical Paper Series 861554. 14 p.
20. Hwang, K., Lee, K. et al. Dynamic flow study in a catalytic converter using laser doppler velocimetry and high speed flow visualization. Warrendale 1995. SAE International, SAE Technical Paper Series 950786. p. 169-186.
21. Brück, R., Diewald, R. et al. Design criteria for metallic substrate for catalytic converters. Warrendale 1995. SAE International, SAE Technical Paper Series 950789. 11 p.
22. Mannila, P. Modelling of the kinetics of automobile exhaust catalyst. Oulu 1993. University of Oulu, Dep. of Process Engineering, Master's thesis. 92 p. (in Finnish)
23. Ahola, J. Transient kinetics of automobile exhaust catalyst. Oulu 1993. University of Oulu, Dep. of Process Engineering, Master's thesis. 83 p. (in Finnish)

24. Voltz, S., Morgan, C.R., et al. Kinetic study of carbon monoxide and propylene oxidation on platinum catalysts. *Ind.Eng.Chem.Prod.Res.Dev.* 12(1973)4, p. 294 - 301.
25. Kays, W.M. *Convective Heat and Mass Transfer*. New Delhi 1979, Tata McGraw-Hill Publishing Company Ltd. 387 p.
26. Shah, R.K. & London, A.L. Laminar flow forced convection in ducts. In: Irvine, T.F. & Harnett, J.P (ed.). *Advances in heat transfer. Supplement I*. New York 1978, Academic Press. 476 p.
27. Luoma, M. *Modelling of exhaust gas catalytic converters*. Oulu 1996. University of Oulu, Dep. of Process Engineering, Lisenciate thesis. 94 p. (in Finnish)
28. Socha, L.S.Jr., Day, J.P. & Barnett, E.H. Impact of catalyst support design parametres on FTP emissions. Warrendale 1989, SAE International, SAE Technical Paper Series 892041. 9 p.
29. Day, J. P. & Socha, L.S.Jr. The design of automotive catalyst supports for improved pressure drop and conversion efficiency. Warrendale 1991, SAE International, SAE Technical Paper Series 910371. 10 p.
30. Coulson, J.M. Richardson, J.F. et al. *Chemical Engineering. Volume 1. Fluid Flow, Heat Transfer and Mass Transfer*. Oxford 1990, Pergamon Press. 708 p.

For Your Notes





The New High Resolution Method of Godunov's Type for 3D Viscous Flow Calculations

Sergey V. Yershov and Andrey V. Rusanov
Institute for Problems in Machinery of the Ukrainian
National Academy of Sciences
2/10 Pozharsky St.
310046, Kharkov, Ukraine

Abstract

The numerical method is suggested for the calculations of the 3D viscous compressible flows described by the thin-layer Reynolds-averaged Navier-Stokes equations. The method is based on the Godunov's finite-difference scheme and it uses the ENO reconstruction suggested by Harten to achieve the uniformly high-order accuracy. The computational efficiency is provided with the simplified multi grid approach and the implicit step written in δ - form. The turbulent effects are simulated with the Baldwin - Lomax turbulence model. The application package *FlowER* is developed to calculate the 3D turbulent flows within complex-shape channels. The numerical results for the 3D flow around a cylinder and through the complex-shaped channels show the accuracy and the reliability of the suggested method.

INTRODUCTION

In the recent time the computational fluid dynamics develops impetuously. We witness the increase of a role of computational methods in the modern theoretical and applied studies. On the one hand these methods are the basic tools of the gasdynamic device designing and on the other hand they may be irreplaceable even today for the investigations of the complex 3D flow phenomena. Thereby the requirements demanded from methods for a solution of the fluid dynamics equations become more and more exacting.

At present two main approaches of the construction of numerical methods are widespread. Most methods applied today is based on the central-difference schemes [1,2,3 and others]. Such methods are non-monotonous and non-linear unstable. Therefore they cannot calculate reliably the flows with the shock waves if the artificial viscosity, which distorts the solution, does not be used. Recent years the non-linear-stable total variation diminishing (TVD) schemes are widely applied [4,5,6]. These schemes ensure the monotonicity preserving at the discontinuities but the main drawback of them is the degeneration into the first-order accuracy at the local extremes. Thus both the central-difference schemes and TVD ones do not provide the high accuracy for the non-linear problems of the fluid dynamics. Therefore it is necessary to develop more accurate numerical methods for the solution of the fluid dynamics equations in order to achieve on the one hand the high-order accuracy everywhere for smooth solution and on the other hand the weak smearing of discontinuities.

Harten [7] has suggested the theoretical ideas needed to construct high resolution methods named as essentially non-oscillatory (ENO) schemes. The Godunov's type ENO scheme has been proposed by Yershov [8].

In the present paper the basic peculiarities of the suggested implicit monotonicity-preserving ENO scheme of the Godunov's type are described. The problem framework is considered for the Reynolds-averaged thin-layer Navier-Stokes equations. The new boundary conditions to provide the well-posedness of an initial boundary value problem are suggested. The numerical results compared with the experimental data are presented.

NUMERICAL TECHNIQUES

Governing equations and turbulence model

The flow is described by the thin-layer Reynolds-averaged unsteady Navier-Stokes equations that are written for local curvilinear coordinate system (ξ, η, ζ) rotated with the angular speed Ω :

$$\frac{\partial QJ}{\partial t} + \frac{\partial E}{\partial \xi} + \frac{\partial F}{\partial \eta} + \frac{\partial G}{\partial \zeta} = JH + \frac{\partial E_v}{\partial \xi} + \frac{\partial F_v}{\partial \eta}, \quad (1)$$

where

$$Q = \begin{pmatrix} \rho \\ \rho u \\ \rho v \\ \rho w \\ h \end{pmatrix}; \quad E = J \begin{pmatrix} \rho U \\ \rho uU + p\xi_x \\ \rho vU + p\xi_y \\ \rho wU + p\xi_z \\ (h+p)U \end{pmatrix}; \quad F = J \begin{pmatrix} \rho V \\ \rho uV + p\eta_x \\ \rho vV + p\eta_y \\ \rho wV + p\eta_z \\ (h+p)V \end{pmatrix};$$

$$G = J \begin{pmatrix} \rho W \\ \rho uW + p\zeta_x \\ \rho vW + p\zeta_y \\ \rho wW + p\zeta_z \\ (h+p)W \end{pmatrix}; \quad H = \begin{pmatrix} 0 \\ 2\rho v \Omega + \rho \Omega^2 r_x \\ -2\rho u \Omega + \rho \Omega^2 r_y \\ 0 \\ 0 \end{pmatrix};$$

$$E_v = \mu J \begin{pmatrix} 0 \\ \frac{1}{3}\sigma_\xi \xi_x + \xi_0^2 \frac{\partial u}{\partial \xi} \\ \frac{1}{3}\sigma_\xi \xi_y + \xi_0^2 \frac{\partial v}{\partial \xi} \\ \frac{1}{3}\sigma_\xi \xi_z + \xi_0^2 \frac{\partial w}{\partial \xi} \\ \frac{1}{3}\sigma_\xi U + \xi_0^2 \left(u \frac{\partial u}{\partial \xi} + v \frac{\partial v}{\partial \xi} + w \frac{\partial w}{\partial \xi} + \frac{1}{\text{Pr}} \frac{\partial i}{\partial \xi} \right) \end{pmatrix};$$

$$F_v = \mu J \begin{pmatrix} 0 \\ \frac{1}{3}\sigma_\eta \eta_x + \eta_0^2 \frac{\partial u}{\partial \eta} \\ \frac{1}{3}\sigma_\eta \eta_y + \eta_0^2 \frac{\partial v}{\partial \eta} \\ \frac{1}{3}\sigma_\eta \eta_z + \eta_0^2 \frac{\partial w}{\partial \eta} \\ \frac{1}{3}\sigma_\eta V + \eta_0^2 \left(u \frac{\partial u}{\partial \eta} + v \frac{\partial v}{\partial \eta} + w \frac{\partial w}{\partial \eta} + \frac{1}{\text{Pr}} \frac{\partial i}{\partial \eta} \right) \end{pmatrix};$$

$$\xi_0 = \sqrt{\xi_x^2 + \xi_y^2 + \xi_z^2}; \quad \eta_0 = \sqrt{\eta_x^2 + \eta_y^2 + \eta_z^2};$$

$$\sigma_\xi = \xi_x \frac{\partial u}{\partial \xi} + \xi_y \frac{\partial v}{\partial \xi} + \xi_z \frac{\partial w}{\partial \xi}; \quad \sigma_\eta = \eta_x \frac{\partial u}{\partial \eta} + \eta_y \frac{\partial v}{\partial \eta} + \eta_z \frac{\partial w}{\partial \eta};$$

p is the pressure; ρ is the density; u, v and w are the Cartesian velocity components; $U = u\xi_x + v\xi_y + w\xi_z$, $V = u\eta_x + v\eta_y + w\eta_z$ and $W = u\zeta_x + v\zeta_y + w\zeta_z$ are the contravariant velocity components; r is the distance from the rotation axis; $\xi_x, \xi_y, \xi_z, \eta_x, \eta_y, \eta_z, \zeta_x, \zeta_y, \zeta_z$ and J are the metric coefficients and the Jacobian of the coordinate transformation; Q is the conservative variables vector; E, F and G are the flux vectors; H is the source term vector caused by rotation; E_v and F_v are the viscous terms vector; $h = \frac{p}{\gamma-1} + \rho \frac{u^2 + v^2 + w^2 - \Omega^2 r^2}{2}$ is the rothalpy; $i = \frac{\gamma}{\gamma-1} \frac{p}{\rho}$ is the enthalpy; γ is the ratio of specific heats; Pr is the Prandtl number; μ is the viscosity coefficient which is equal to zero for the Euler equations. The simulation of turbulent effects is carried out with the modified algebraic turbulence model developed by Baldwin and Lomax [9].

Boundary conditions

At the permeable inlet boundary of a computational domain the total pressure, total temperature and flow direction distributions are specified. At the exit permeable boundary the static pressure distribution is imposed. Such boundary conditions are accepted for the Euler and Navier-Stokes equations but they are not always well-posed. So the pressure exit condition is not correct for the low flow-rate compressor throughflows. That is why in this case the mass flow-rate M through a compressor is imposed. Numerically this exit condition is provided with the prescription of the time-variant left Riemann invariant:

$$I_-^{n+1} = I_-^n + \frac{\sigma}{\rho S} (M - M^n); \quad I_- = w - \frac{2}{\gamma-1} \sqrt{\frac{\gamma p}{\rho}}, \quad (2)$$

where σ is the constant, S is the exit cross-section area, M^n is the current flow-rate calculated at the exit.

The non-slip condition as well as the temperature or the heat flux is imposed on the solid walls. The relations derived from the governing equations are used to calculate the wall pressure. So on the solid wall $\eta = \text{const}$ the following relation is valid:

$$\begin{aligned} \frac{\partial p}{\partial \eta} = \frac{1}{J} \left\{ \left(\frac{1}{3} + \eta_0^2 \right) \mu \frac{\partial}{\partial \eta} \left[\frac{\partial (JV)}{\partial \eta} \right] + (x_\xi x_\eta + y_\xi y_\eta + z_\xi z_\eta) \right. \\ \left. \times \frac{\partial}{\partial \eta} \left[\eta_0^2 \mu \frac{\partial (JU)}{\partial \eta} \right] + (x_\eta x_\zeta + y_\eta y_\zeta + z_\eta z_\zeta) \frac{\partial}{\partial \eta} \left[\eta_0^2 \mu \frac{\partial (JW)}{\partial \eta} \right] \right\}, \quad (3) \end{aligned}$$

where $x_\xi, x_\eta, x_\zeta, y_\xi, y_\eta, y_\zeta, z_\xi, z_\eta$ and z_ζ are the inverse metric coefficients. The equation (3) may be approximated by the three-point one-side differences to ensure the

second-order accuracy. As shown by Yershov [10] the numerical boundary condition (3) is compatible with the Navier-Stokes equations but the reflecting condition [1] and the zero normal pressure gradient one [11] are not.

Numerical scheme

The governing equations (1) are solved numerically with the new finite-difference scheme developed by Yershov [8,10]. The main peculiarities of this scheme are the following:

- implicit factored algorithm with the opening explicit finite-volume step;
- simplified multi grid;
- upwind differencing due to the Riemann problem solver (explicit step) and flux-difference splitting (implicit step);
- limitation of the slopes and curvatures of the solution with ENO reconstruction;
- second and third order accuracy at the smooth regions;
- weak smearing of discontinuities (shock capturing);
- entropy preserving;
- monotonicity;
- high stable;
- computational efficiency.

Explicit step

The explicit step of the scheme is written in the finite-volume form:

$$\begin{aligned}
 \delta Q_{i,j,k}^n &= Q_{i,j,k}^{n+1} - Q_{i,j,k}^n = \\
 &= -\frac{\tau}{(\Delta\xi \Delta\eta \Delta\zeta J)_{i,j,k}} \left\{ (E - E_v)^n \Delta\eta \Delta\zeta \right\}_{i+1/2,j,k} \\
 &\quad - \left[(E - E_v)^n \Delta\eta \Delta\zeta \right]_{i-1/2,j,k} + \left[(F - F_v)^n \Delta\xi \Delta\zeta \right]_{i,j+1/2,k} \\
 &\quad - \left[(F - F_v)^n \Delta\xi \Delta\zeta \right]_{i,j-1/2,k} + \left(G^n \Delta\xi \Delta\eta \right)_{i,j,k+1/2} \\
 &\quad - \left(G^n \Delta\xi \Delta\eta \right)_{i,j,k-1/2} \left. \right\} + \tau H_{i,j,k}^n, \quad (4)
 \end{aligned}$$

where $\Delta\xi$, $\Delta\eta$, $\Delta\zeta$ and τ are the spatial and time increments respectively. The integer subscripts correspond to the cell centers and fractional ones correspond to the cell sides. The superscripts mean the time level.

To increase the scheme accuracy to the second and third order the ENO reconstruction suggested by Harten [7] is used:

$$q(\xi, \eta, \zeta, t) = q_m^n + \left(\frac{\partial q}{\partial \xi} \right)_m^n (\xi - \xi_m) + \left(\frac{\partial q}{\partial \eta} \right)_m^n (\eta - \eta_m) \\ + \left(\frac{\partial q}{\partial \zeta} \right)_m^n (\zeta - \zeta_m) + \left(\frac{\partial q}{\partial t} \right)_m^n (t - t^n);$$

$$\Delta_m \phi = L_\psi \Delta_m q;$$

$$\left(\frac{\partial \phi}{\partial \psi} \right)_m^n = \frac{1}{\Delta \psi} \text{minmod}[\Delta_m \phi, \\ + \alpha \text{minmod}(\Delta_m \phi - \Delta_{m-1} \phi, \Delta_{m+1} \phi - \Delta_m \phi), \\ \Delta_{m+1} \phi - \beta \text{minmod}(\Delta_{m+1} \phi - \Delta_m \phi, \Delta_{m+2} \phi - \Delta_{m+1} \phi)];$$

$$\left(\frac{\partial q}{\partial \psi} \right)_m^n = L_\psi^{-1} \left(\frac{\partial \phi}{\partial \psi} \right)_m^n, \quad (5)$$

where $q = [\rho, u, v, w, p]^T$ is the vector of the primitive variables; ϕ is the vector of characteristic variables; $\Delta_m q = q_m - q_{m-1}$; ψ is a grid line direction ξ, η or ζ ; L_ψ is the matrix of eigenvectors; α and β are constants. The scheme is second-order accurate ENO for $\alpha + \beta = 1$ (in particular for $\alpha = \beta = 1/2$) and it is locally third-order accurate for $\alpha = 2\beta = 2/3$. The upwind differencing is achieved with the Riemann problem solver.

Implicit step

The implicit step is written in the accepted Beam-Warming-Steger δ -form [11]:

$$\delta \tilde{q}^n = \frac{1}{1+\chi} T \delta Q^n + \frac{\chi}{1+\chi} \delta q^n;$$

$$L_\xi^{-1} \left[I + \frac{\tau \theta}{(1+\chi) J} \frac{\partial}{\partial \xi} (\Lambda_\xi^+ + \Lambda_\xi^-) \right] L_\xi \delta q^{n+1/3} = \delta \tilde{q}^n;$$

$$\begin{aligned}
L_\eta^{-1} \left[I + \frac{\tau \vartheta}{(1+\chi)J} \frac{\partial}{\partial \eta} (\Lambda_\eta^+ + \Lambda_\eta^-) \right] L_\eta \delta q^{n+2/3} &= \delta q^{n+1/3}; \\
L_\zeta^{-1} \left[I + \frac{\tau \vartheta}{(1+\chi)J} \frac{\partial}{\partial \zeta} (\Lambda_\zeta^+ + \Lambda_\zeta^-) \right] L_\zeta \delta q^{n+1} &= \delta q^{n+2/3}; \\
q^{n+1} &= q^n + \delta q^{n+1}, \tag{6}
\end{aligned}$$

where ϑ and χ are constants, $\Lambda_\psi^\pm = (\Lambda_\psi + |\Lambda_\psi|)/2$; $|\Lambda_\psi| = \text{diag}(|\lambda_\psi^i|)$; λ_ψ^i are the eigenvalues of the Jacobian matrices, T is the matrix that transforms the conservative variables into primitive ones.

The use of the implicit monotonous high resolution ENO scheme provides the weak smearing of the discontinuities, the high accuracy for smooth solutions and comparatively small computational time. For this scheme unlike other known schemes such as central-difference or TVD the approximation error (scheme viscosity) does not suppress the real viscosity. Therefore the use of ENO scheme ensures the impossibility of the excessive error accumulation on the flow calculations for the complex-shape channels. The additional efficiency improvement for the implicit algorithm is achieved with the spatially variant time increment. Besides the steady state solution convergence can be accelerated with the simplified multi grid algorithm that consists in the following. The solution on the coarse grid transfers to the fine grid as the initial conditions with the aid of a linear interpolation. Usually three levels of a mesh refinement are enough. In this case the convergence rate does not depend practically from the initial conditions for the coarse grid. The implicit operators, the spatially variant time increment and the simplified multi grid algorithm provide a reduction of the computational time more over one hundred times.

Viscous term approximation

To calculate the viscous terms the slopes $(\partial \tilde{q} / \partial \psi)$ obtained accordingly to the equations (5) are used. So the quantity $\mu(\partial u / \partial \eta)$ at the cell side $j+1/2$ is determined with a linear interpolation:

$$\left(\mu \frac{\partial u}{\partial \eta} \right)_{j+1/2} = \frac{(\eta_{j+1/2} - \eta_j)}{(\eta_{j+1} - \eta_j)} \left(\mu \frac{\partial u}{\partial \eta} \right)_{j+1} + \frac{(\eta_{j+1} - \eta_{j+1/2})}{(\eta_{j+1} - \eta_j)} \left(\mu \frac{\partial u}{\partial \eta} \right)_j. \tag{7}$$

Such approach ensures the second-order accuracy and it is simpler and more natural than traditional central-difference approximations. Moreover since the magnitudes of the slopes are limited by minmod function of the equations (5), the magnitudes of

$\mu(\partial u/\partial \eta)$ are limited too and therefore the viscosity effects cannot be overpredicted in the regions where the flow gradients change significantly.

Computational grid

The computational grid of H-type consisting of the arbitrary hexahedrons is used. Such grid is generated by the algebraic method. To increase the accuracy in the regions of the high gradients the cell sizes near the walls is reduced exponentially in the cross-flow directions. The example of computational grid is shown in Figure 1. Here only the first (coarse) grid level is presented for a clarity of the drawing. In the finest grid each 3D coarse cell is split into 64 fine cells. Usually the fine grid contains more over 300,000 cells.

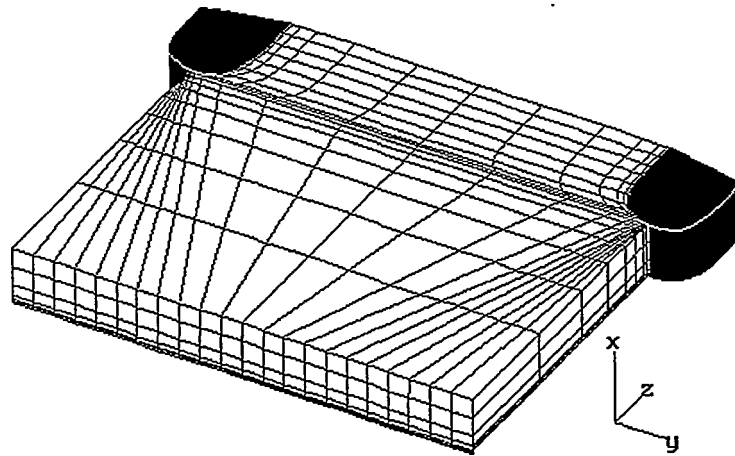


Fig. 1 - Computational grid of H-type for the flow around a cylinder.

NUMERICAL RESULTS

The numerical method described above has been incorporated in a computer code named as *FlowER* [12]. This code permits to calculate the 2D and 3D viscous and inviscid flows through complex-shape channels.

The code *FlowER* has been subjected to the detailed testing. It includes:

- the checking for under different operation systems;
- the solution of 1D, 2D and 3D model problems and comparison with the exact and numerical solutions as well as experimental data of other authors;
- the calculations of the flow through turbomachine cascades.

Flow around a cylinder

The turbulent flow around a cylinder centered between the sidewalls of wind tunnel [13] has been considered. The inlet Mach number is $M_{in}=0.2$ and Reynolds number is

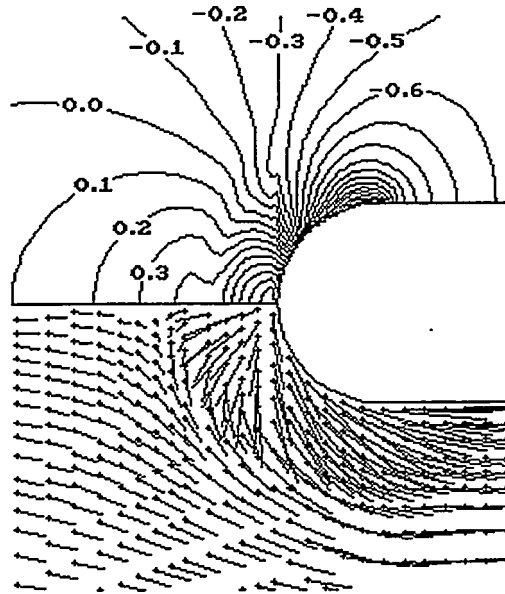


Fig. 2 - Pressure coefficient contours (top) and velocity vectors (bottom) on the endwall (present method).

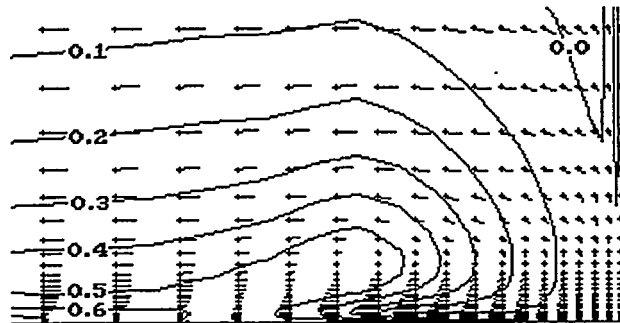


Fig. 3 - Velocity vectors and pressure loss coefficient contours at the flow symmetry plane (present method).

$Re_D=550000$ in this calculation. The upstream boundary layer thickness is equal $0.1 D$ where D is the cylinder diameter. Shown in Figure 2 are the contours of the pressure coefficient C_p (top) and the velocity vectors (bottom) on the endwall. Here and below the point is the cell center where a velocity vector begins. The endwall flow occurred is caused by the horseshoe vortex. This vortex is evidently seen in Figure 3 that displays the velocity profiles at the flow symmetry plane. Here the contours of the total pressure loss coefficient C_{pt} are represented too. These results are in a good qualitative and quantitative agreement with the numerical and experimental data represented in [13].

Flow through the Langston cascade

The test calculation of the viscous flow with the prescribed method has been performed for the 3D straight cascade investigated by Langston [14]. The calculated velocity vectors at the endwalls are displayed in Figure 4. It is seen that one of the horseshoe branches propagates to the blade suction side and the other spreads to the blade pressure side. Besides the surface streamline, that divides the passage and corner vortices, is observed evidently near the suction side of the blade. The corresponding experimental endwall flow obtained by Langston [14] is given in Figure 5.

The calculated and experimental pressure contours on the endwall are given in Figures 6 and 7 respectively.

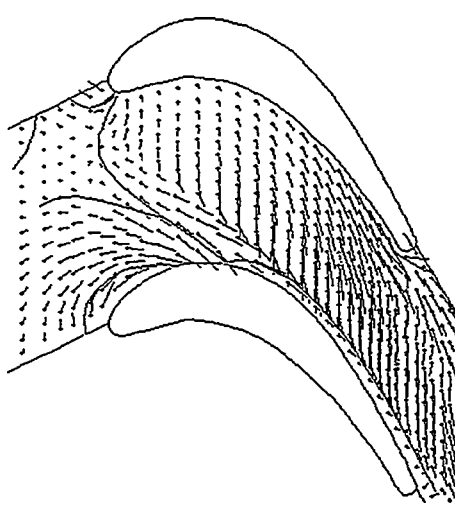


Fig. 4 - Velocity vectors on the endwall of Langston cascade (present method).

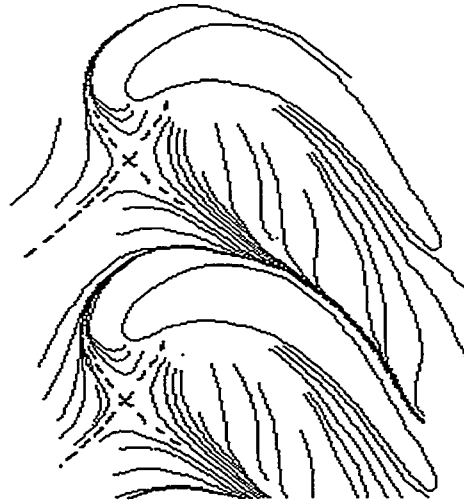


Fig. 5 - The endwall flow for the Langston cascade (experiment [14]).

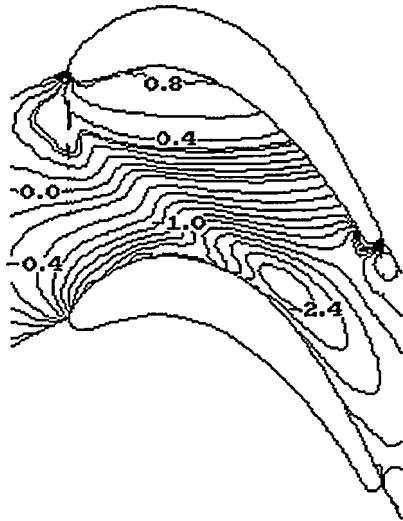


Fig. 6 - Endwall pressure contours for the Langston cascade (present method).

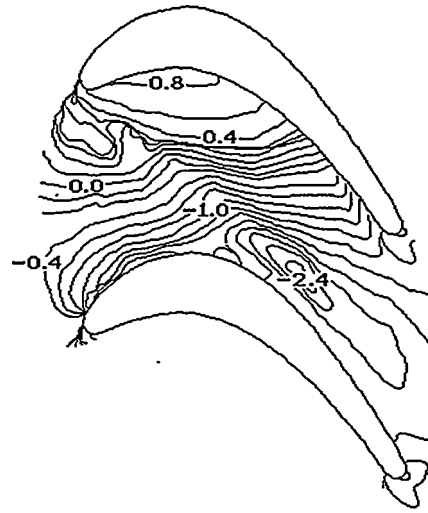


Fig. 7 - Endwall pressure contours for the Langston cascade (experiment [14]).

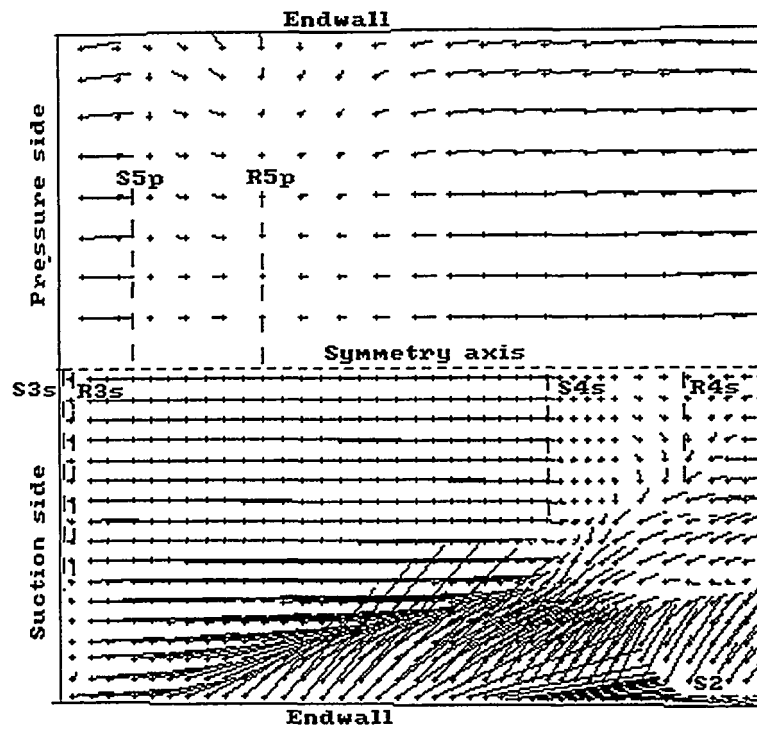


Fig. 8 - Flow on the blade surfaces for the Hodson cascade (present method).

Flow through the Hodson cascade

The test calculation of the viscous flow with the prescribed method has been performed for the 3D straight cascade that has been investigated by Hodson and Dominy [15]. Velocity vectors on blade surfaces of the cascade are given in Figure 8. The positions of separations and reattachments are shown schematically by dashed-lines S and R respectively. The exit distribution of the total pressure loss coefficient along the blade span is given in Figure 9. Shown in the Figure 10 are the calculated secondary flow velocity vectors (left) and the total pressure loss contours (right) at the cascade

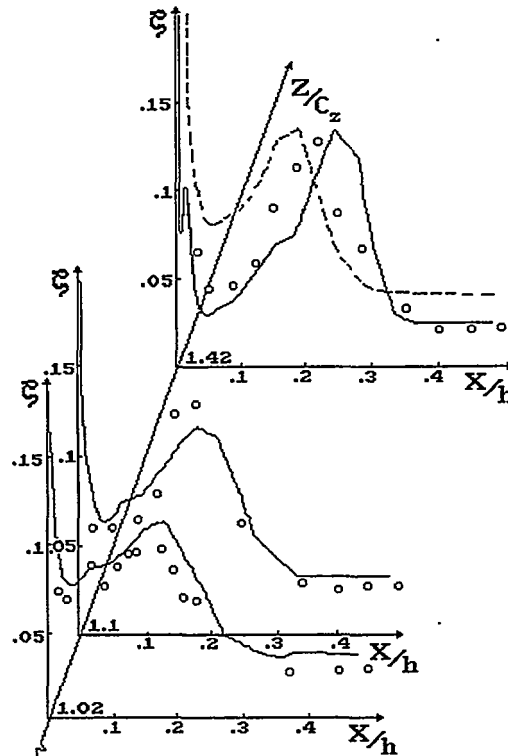


Fig. 9 - The distribution of the total pressure loss coefficient along the blade span for various distances from the cascade trailing edge.

— present method
 - - - TVD method [6]
 ○ experiment [15]

exit. The symbols A, B and C mark respectively the corner, passage and discrete wake vortices. The corresponding experimental data, obtained by Hodson and Dominy [15], are presented in Figure 11. Thus the aforesaid results correspond to the physical ideas of the 3D viscous cascade flows, and are in good quantitative and qualitative agreement with the experimental data.

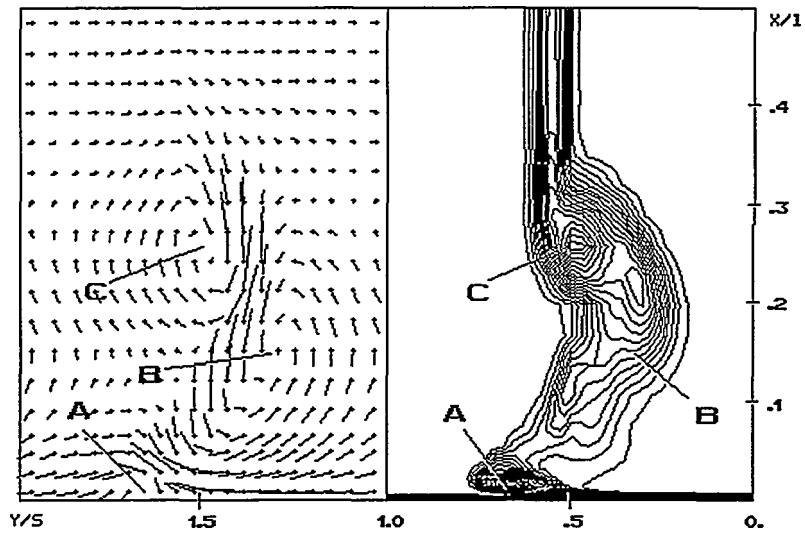


Fig. 10 - Pressure loss coefficient contours (right) and velocity vectors (left) at the exit cross-section of the Hodson cascade (present method).

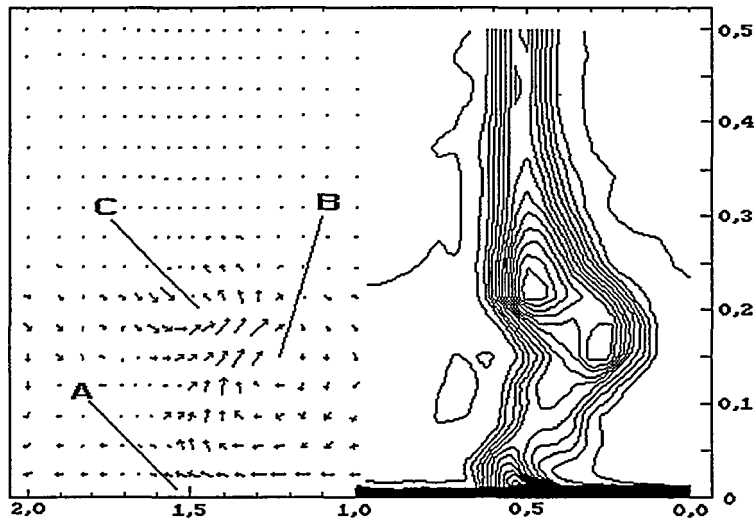


Fig. 11 - Pressure loss coefficient contours (right) and velocity vectors (left) at the exit cross-section of the Hodson cascade (experiment [15]).

Flow through the turbine stage

The Navier-Stokes solver developed by authors permits to calculate the 3D viscous flows through the multi stage turbomachines. The above-mentioned algorithm is applied to obtain the solution for each blade row separately. The exchange of the flow parameters averaged over a circumferential direction is used on the mixing plane at axial spaces for the ensuring of the reciprocal influence of rows. To reduce the undesirable effects evoked by the use of the averaging procedure too close to blade edges this exchange is realized in terms of non-reflecting conditions.

The computation of the 3D viscous flow through a turbine stage has been carried out. The blade midspan Mach number contours are shown in Figure 12.

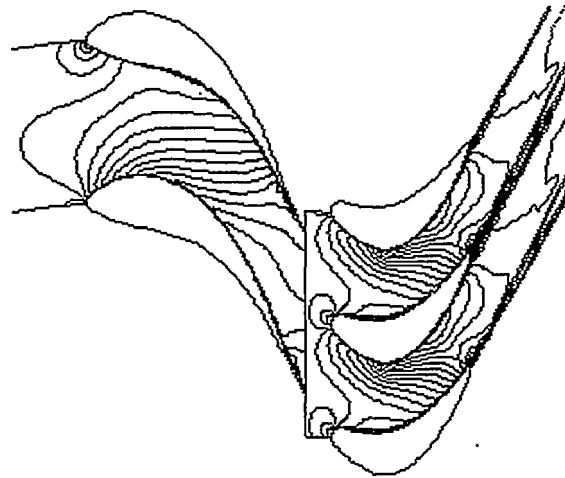


Fig. 12 - Mach number contours at the mid span of the turbine stage (present method).

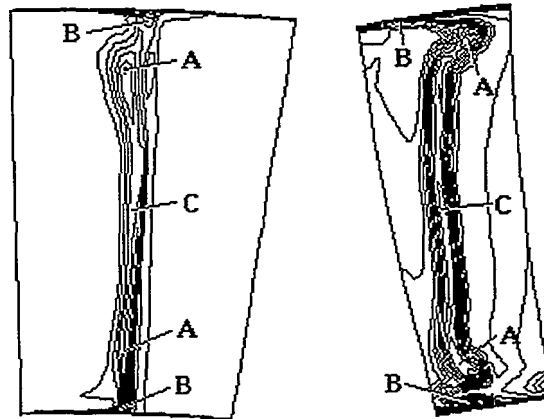


Fig. 13 - Total pressure contours at the stage exit (present method).

Figure 13 displays the total pressure contours at the exit of the stator (left) and the rotor (right). The positions of the passage and corner vortices as well as the wakes are marked schematically by symbols A, B and C respectively. It is noted that the rotor blade wake smearing near the hub and tip surfaces is more considerable than that for the stator blade. This effect is evoked by the wake rotation regarding endwalls.

Flow through multi row compressors

The 3D flow through the five-row supersonic fan of an aeroengine has been investigated. The Mach number contours near the root are shown in Figure 14.

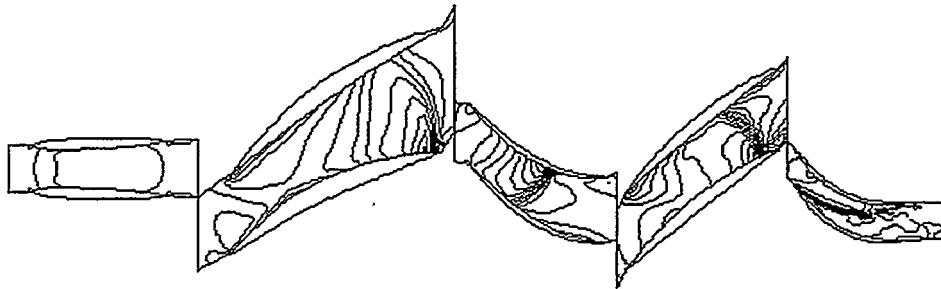


Fig. 14 - Mach number contours at the root section of the supersonic five-row fan (present method).

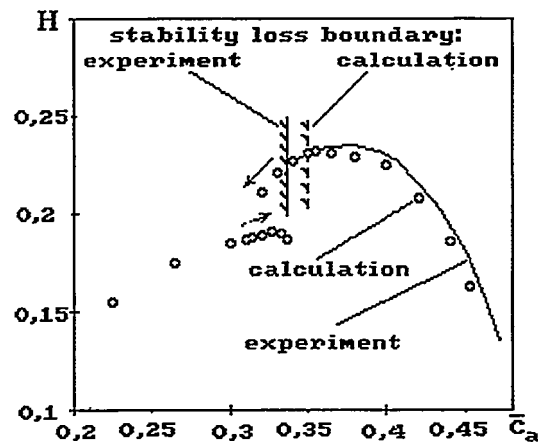


Fig. 15 - The characteristic of the subsonic four-row compressor.

The numerical simulation of the stability loss of the 3D flow through multi row compressors has been performed. The characteristics of four-row compressor are presented in Figure 15 by points (present calculations) and the solid line (experiment [16]). The characteristics are represented as the dependences of the adiabatic work coefficient H on the flow-rate \bar{C}_a . The calculated stability boundary compared with the experimental one is predicted with the error about 5%.

The study of the compressor flow stability with the inlet total pressure disturbances has been carried out. Shown in Figure 16 is the stability diagram in coordinates of the disturbance amplitude versus the disturbance time. In most cases the stability loss occurs owing to the oscillating return flow formation at the tip of a rotor. This return flow extends to the compressor inlet at the small flow-rates and at the prolonged or intensive inlet pressure disturbances.

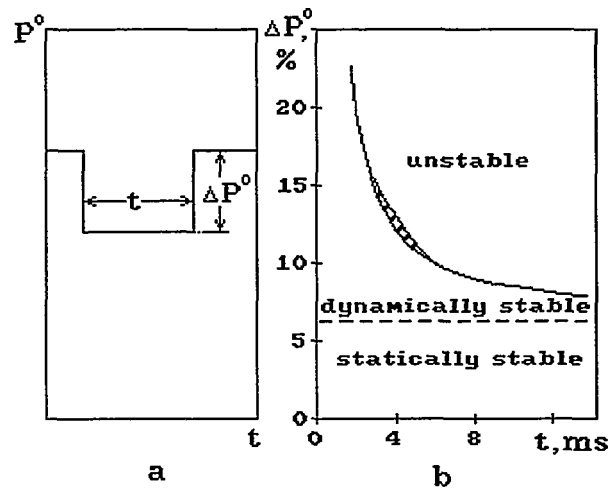


Fig. 16 - The flow stability diagram of the subsonic four-row compressor.

a - the inlet pressure disturbance
b - the stability diagram

Conclusions

The numerical method for the 3D turbulent separated flow simulation has been developed. The results obtained are in a good qualitative and quantitative agreement with the numerical and experimental data of other investigators [13-16].

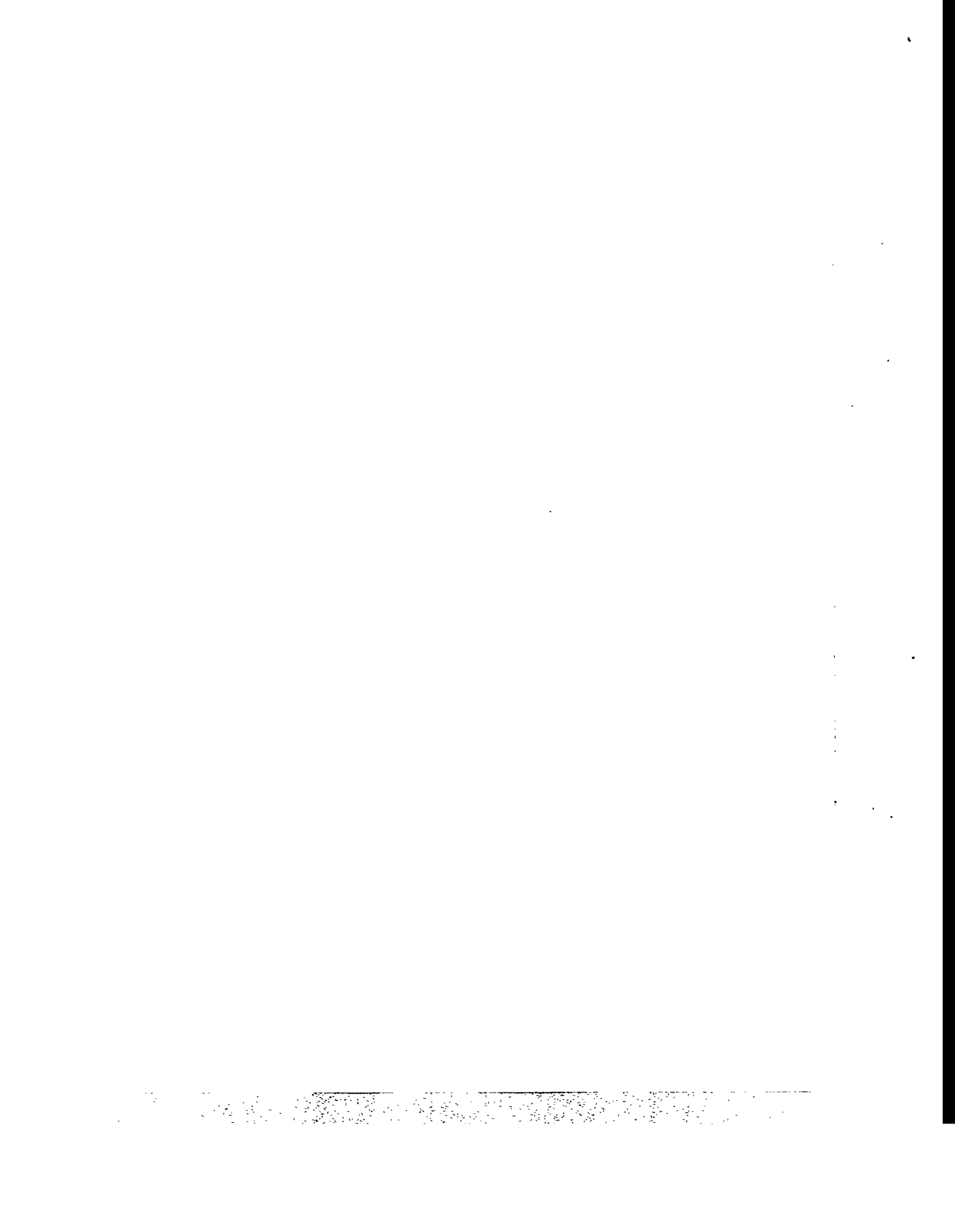
Reference

1. MacCormack, R.W., The effect of viscosity in hypervelocity impact cratering. AIAA Pap. 1969, N 354, p. 1-12.
2. Beam, R.M. and Warming, R.F., An implicit factored scheme for the compressible Navier-Stokes equations. AIAA J. 16(1978) April, p. 393-402.
3. Denton, J.D., Solution of the Euler equations for turbomachinery flows. Thermodynamics and Fluid Mechanics of Turbomachines. 1985, p. 283-345.

4. Harten, A., High resolution schemes for hyperbolic conservation laws. *J. Comput. Phys.* 49(1983) March, p. 357-393.
5. Chakravarthy, S.R., Szema, K.Y., Goldberg, V.C. and Gorski, J.J., Application of a new class of high accuracy TVD schemes to the Navier-Stokes equations. *AIAA Pap.* 1985, N 165, p. 1-12.
6. Ivanov, M.Y. and Krupa, V.G., Computation of 3D viscous cascade flow. *News of RAS. Fluid and Gas Mechanics*, 1993, April, p. 58-64 (in Russian).
7. Harten, A. and Osher, S., Uniformly high-order accurate nonoscillatory schemes. *SIAM J. Num. Analysis.* 24(1987) N 2, p. 279 - 309.
8. Yershov, S.V., The quasi-monotone ENO scheme of increased accuracy for the integrating Euler and Navier-Stokes equations. *Mat. Model.* 6(1994) November, p. 63 - 75 (in Russian).
9. Baldwin, B.S. and Lomax, H., Thin layer approximation and algebraic model for separated turbulent flows. *AIAA Pap.* 1978, N 257, p. 1 - 8.
10. Yershov, S.V., Simulation of separated viscous flows using implicit monotonicity-preserving high-resolution Godunov's scheme. In: Kharitonov, S.M. (ed.). *ICMAR/92. Proc. Int. Conf. Meth. Aerophys. Researches*, Novosibirsk, Russia, 1992, ITAM SD RAS, p. 152 - 155.
11. Steger, J.L. and Warming, R.F., Flux vector splitting of the inviscid gasdynamic equations with application to the finite difference methods. *J. Comput. Phys.* 40(1981), N 2, p. 263 - 293.
12. Yershov, S.V. and Rusanov, A.V., 3D separated viscous flow calculation using Godunov's high resolution scheme. In: Kharitonov, S.M. (ed.). *ICMAR/94. Proc. Int. Conf. Meth. Aerophys. Researches*, Novosibirsk, Russia, 1994, ITAM SD RAS, p. 209-214.
13. Chima, R.V. and Yokota, J.W., Numerical analysis of three-dimensional viscous internal flows. *AIAA J.* 28(1990) May, p. 798-806.
14. Langston, L.S., Nice, M.L. and Hopper, R.M., Three-dimensional flow within a turbine blade cascade. *Trans. ASME. J. Eng. Power.* 99(1977) January, p. 21-29.
15. Hodson, H.P. and Dominy, R.G., Three-dimensional flow in a low-pressure turbine cascade at its design condition. *J. of Turbomachinery.* 109(1987) February, p. 116 - 128.
16. Baryshev, I.V., Borisenko, A.I., Yershov, V.N., Pavlenko, G.V. and Gerasimenko, V.P., Aerodynamic investigations of model compressor stage with small relative hub diameter. *KhAI Scientific Report N 561/25.* 1977, p. 1 - 29 (in Russian).

For Your Notes

3 4 5 6 7 8 9 10 11 12 13 14 15 16 17 18 19 20 21 22 23 24 25 26 27 28 29 30 31 32 33 34 35 36 37 38 39 40 41 42 43 44 45 46 47 48 49 50 51 52 53 54 55 56 57 58 59 60 61 62 63 64 65 66 67 68 69 70 71 72 73 74 75 76 77 78 79 80 81 82 83 84 85 86 87 88 89 90 91 92 93 94 95 96 97 98 99 100



**Nonstationary 3D Inviscid Numerical Flow Model
Through Steam Turbine Exhaust Hood**

V.G.Solodov
Kharkov State Automobile and Highway Technical University,
Department of Theoretical Mechanics and Hydraulics,
310078, Kharkov, Ukraine

Abstract

This paper represents nonstationary 3D inviscid numerical flow models through exhaust hood and exhaust compartment of power steam turbine and some results of 3D flow simulation.

INTRODUCTION

The most loaded elements of flow path of large steam turbines are last compartments of low pressure cylinders, which consist of last stage and exhaust hood. Owing to technological restrictions this elements of last compartments have maximal reserves of efficiency, so the problem of their improvement is actual [1,2]. Taking into account the high costs of experimental investigations and recent progress in CFD the numerical models of flow in exhaust hoods and in last compartments with modelling of last hood-exhaust hood aerodynamical interaction in 3D nonstationary formulation are represented in this paper.

FORMULATION OF PROBLEM

The inviscid and non-heat-conductive gas flow through the last compartment is considered in the domain which consist of full set of channels of stator and rotor, interrow and interstage spacings, flow path of axisymmetrical diffuser and space under the casing of exhaust hood (fig.1).

The flow is described by nonstationary 3D Euler's equations, represented in the integral conservation law form:

$$\begin{aligned} \frac{\partial}{\partial t} \int_{\Omega} \rho d\Omega + \oint_{\sigma} \rho \bar{v} \cdot d\bar{\sigma} &= 0, \\ \frac{\partial}{\partial t} \int_{\Omega} \rho \bar{v} d\Omega + \oint_{\sigma} \hat{T} \cdot d\bar{\sigma} + \int_{\Omega} \bar{H} d\Omega &= 0, \\ \frac{\partial}{\partial t} \int_{\Omega} E d\Omega + \oint_{\sigma} (E + p) \bar{v} \cdot d\bar{\sigma} &= 0, \end{aligned} \quad (1)$$

where t - time, ρ , p - density, pressure: $\hat{T} = \{T^{ik}\} = \{\rho v^i v^k + g^{ik} p\}$ - density tensor of impulse flux; g^{ik} - metrics tensor; $H^i = \{\rho a_e^i + 2e^{jk} \omega_j v_k\}$, $\bar{a}_e, \bar{v}_e, \bar{v}$ - acceleration and velocities of translation and relative movement; $\bar{\omega}$ - rotor angular velocity; e^{jk} - Levi - Chivita tensor. System is completed by ideal gas equation $p = p(\rho, \varepsilon)$.

Finite-difference scheme

The integration of Euler's equations is carried out by numerical method with use of explicit finite difference Godunov's scheme of 2nd time and space order accuracy. The difference scheme uses the Rieman's problem for calculation of fluxes through the surfaces of finite-difference division of computational region.

To obtain the finite-difference approximation of Euler's equations the computational region Ω is divided on the elementary hexahedral volumes. Structure of finite-difference scheme does not depend on choice of local curvilinear coordinate basis. The finite-difference analogues of conservation laws can be obtained by integration procedure of every equation applied to the elementary volume of finite-difference division of computational region:

$$\begin{aligned}
 \rho_{m_1+\frac{1}{2}}^{n+1} &= \rho_{m_1+\frac{1}{2}}^n - \frac{\Delta t}{\Omega_{m_1+\frac{1}{2}}} \sum_{k=0,1} \{(\rho \vec{v} \cdot \vec{\sigma})_{m_1+k, m_2+\frac{1}{2}, m_3+\frac{1}{2}} + \\
 &+ (\rho \cdot \vec{v} \cdot \vec{\sigma})_{m_1+\frac{1}{2}, m_2+k, m_3+\frac{1}{2}} + (\rho \cdot \vec{v} \cdot \vec{\sigma})_{m_1+\frac{1}{2}, m_2+\frac{1}{2}, m_3+k}\}, \\
 (\rho v)_{m_1+\frac{1}{2}}^{n+1} &= (\rho v)_{m_1+\frac{1}{2}}^n - \frac{\Delta t}{\Omega_{m_1+\frac{1}{2}}} \sum_{k=0,1} \{(\hat{T} \cdot \vec{\sigma})_{m_1+k, m_2+\frac{1}{2}, m_3+\frac{1}{2}} + \\
 &+ (\hat{T} \cdot \vec{\sigma})_{m_1+\frac{1}{2}, m_2+k, m_3+\frac{1}{2}} + (\hat{T} \cdot \vec{\sigma})_{m_1+\frac{1}{2}, m_2+\frac{1}{2}, m_3+k}\} - \Delta t \cdot H_{m_1+\frac{1}{2}}^n, \\
 E_{m_1+\frac{1}{2}}^{n+1} &= E_{m_1+\frac{1}{2}}^n - \frac{\Delta t}{\Omega_{m_1+\frac{1}{2}}} \sum_{k=0,1} \{([E+p] \cdot \vec{v} \cdot \vec{\sigma})_{m_1+k, m_2+\frac{1}{2}, m_3+\frac{1}{2}} + \\
 &+ ([E+p] \cdot \vec{v} \cdot \vec{\sigma})_{m_1+\frac{1}{2}, m_2+k, m_3+\frac{1}{2}} + ([E+p] \cdot \vec{v} \cdot \vec{\sigma})_{m_1+\frac{1}{2}, m_2+\frac{1}{2}, m_3+k}\}.
 \end{aligned} \tag{2}$$

Upper indices represent the number of time step, lower half-integer indices are related to center of cell. The gasdynamical parameters fields in limits of cell boundaries are approximated on the base of linear interpolation procedure using the values of parameters in centers of neighboring cells under the basis of Kolgan's principle[5] of minimal derivatives.

The gradient components of field φ are determined from linear equations, joining the increments of parameter φ between centers of cells:

$$\varphi_{m_j-1/2} - \varphi_{m_j+3/2} = \left\{ \frac{\partial \varphi}{\partial q^k} \right\}_{m_j-1/2} \cdot (q^k_{m_j-1/2} - q^k_{m_j+3/2}), \quad j=1,2,3.$$

The use of local curvilinear basis gives the diagonal matrix of equations system and the components of gradient φ are calculated explicitly.

The second set of gradient component values is found from the same relation on the symmetrical template. The choice of gradient components for cell may be done from the pairwise comparison of the derivatives with use of Kolgan's minimum principle:

$$\frac{\partial \varphi}{\partial q^k} = \begin{cases} \text{sign}\left(\frac{\partial \varphi}{\partial q^k}\right)^I \cdot \min\left[\text{abs}\left(\frac{\partial \varphi}{\partial q^k}\right)^I, \text{abs}\left(\frac{\partial \varphi}{\partial q^k}\right)^{II}\right], & \text{if } \left(\frac{\partial \varphi}{\partial q^k}\right)^I \cdot \left(\frac{\partial \varphi}{\partial q^k}\right)^{II} > 0, \\ 0, & \text{if } \left(\frac{\partial \varphi}{\partial q^k}\right)^I \cdot \left(\frac{\partial \varphi}{\partial q^k}\right)^{II} < 0, \end{cases}$$

The substance of Kolgan's modification for Godunov's scheme consists in determination of gasdynamical parameters in central points of cell surfaces both of sides using their values from relations for derivatives. For these parameters values the Riemann's problem is solved on development of the arbitrary discontinuity and the values of fluxes of conservative variables are determined.

The spatial linear interpolation procedure according to Kolgan ensures the 2nd order of accuracy in spatial directions for the domains of monotonicity of solution. The 2nd order accuracy for time variable is reached due to use of extrapolation procedure along the time coordinate [5] and may be applied for solution of nonstationary problems. Namely, for the Euler's equations in symbolic vector form:

$$\partial U^k / \partial t + \nabla_i T^{ik} + H^k = 0, \quad k = 1, \dots, 5 \quad (3)$$

The interpolation of parameter to the face of cell with number

$$(m_1, m_2+1/2, m_3+1/2)$$

in the q^l - coordinate direction is done in accordance to formula [5]

$$U = U_{m_i+1/2} + \left\{ \frac{\partial U}{\partial q^1} \right\}_{m_i+1/2}^n + \frac{\tau}{2} \cdot \left\{ \frac{\partial U}{\partial t} \right\}_{m_i+1/2}^n$$

The time-derivative $\partial U / \partial t$ is calculated from right parts of system of equations for previous time point.

Boundary conditions. Initial data.

The given problem is a problem with initial and boundary data. The hypothesis about existence of stationary or periodical solution admits to choose the initial approximation accordingly to one-dimensional methods. The problem is solved under stationary boundary conditions. At the rigid boundaries of calculation region the condition of non-leakage $(\vec{v} \cdot \vec{\sigma}) = 0$ is formulated, which means the exclusion of mass, impulse, energy fluxes in normal direction of boundary.

For the permeable boundaries of region in places of gas inlet or outlet the number and choice of boundary conditions follow from the analysis of disturbances propagation along the characteristic directions. In paper the quasi-one-dimensional characteristic relations are used in normal direction relatively the surface of gas inlet, outlet because of complexity of full 3D theory.

The application of quasi-one-dimensional relations is justified under suggestion of flow local parameter uniformity in plane of free boundary.

Quasi-one-dimensional relations are obtained under consideration of Euler's equations (3) supposing the independence of gasdynamical variables from x^1, x^2 :

$$\frac{\partial \bar{U}}{\partial t} + \hat{A} \frac{\partial \bar{U}}{\partial x^3} = \bar{Q}, \quad (4)$$

where

$$\bar{U} = \begin{bmatrix} \rho \\ v^1 \\ v^2 \\ v^3 \\ p \end{bmatrix}, \quad \hat{A} = \begin{bmatrix} v^3 & 0 & 0 & \rho & 0 \\ 0 & v^3 & 0 & 0 & 0 \\ 0 & 0 & v^3 & 0 & 0 \\ 0 & 0 & 0 & v^3 & \frac{1}{\rho} \\ 0 & 0 & 0 & \rho a^2 & v^3 \end{bmatrix}, \quad \bar{Q} = \begin{bmatrix} \rho v^1 \\ \frac{v^2 v^2}{h_2} \frac{\partial h_2}{\partial x^1} - a_e^1 + 2\omega v^2 \\ -\frac{v^1 v^2}{h_2} \frac{\partial h_2}{\partial x^1} + 2\omega v^1 \\ 0 \\ -\rho a^2 v^1 \frac{\partial h_2}{\partial x^1} \end{bmatrix},$$

$a^2 = \gamma p / \rho$, h_2 - Lamé coefficient (τ - for cylindrical and 1 for Cartesian coordinate system).

The eigenvalues of matrix \hat{A} $\lambda_{1,2,3} = v^3$, $\lambda_4 = v^3 - a$, $\lambda_5 = v^3 + a$ are the angular coefficients of characteristics of system (4). Introducing in plane t, x^3 the new coordinate system φ, x^3 in which the coordinate line $\varphi = \text{const}$ is the characteristic $\varphi(t, x^3)$ the equation (4) can be reduced to form

$$\left(\hat{I} \frac{\partial \varphi}{\partial t} + \hat{A} \frac{\partial \varphi}{\partial x^3} \right) \cdot \frac{\partial_{x^3} \bar{U}}{\partial \varphi} = \bar{Q}_1,$$

where $\bar{Q}_1 = \bar{Q} - \hat{A} \cdot \frac{\partial_{x^3} \bar{U}}{\partial x^3}$, \hat{I} - unit matrix, $\frac{\partial_{\varphi} \bar{U}}{\partial x^3}$, $\frac{\partial_{x^3} \bar{U}}{\partial \varphi}$ - derivatives

under φ and $x^3 = \text{const}$.

The differential relations along the characteristics follow from the conditions of consistency of system (4) for the characteristic directions λ_i :

$$\begin{aligned}
d_{\lambda_1} p - a^2 d_{\lambda_1} \rho &= 0, \\
d_{\lambda_1} v^v - \frac{1}{\lambda_2} \left\{ \frac{v^2 v^2}{h_2} \cdot \frac{\partial h_2}{\partial x^1} \right\} dx^2, \\
d_{\lambda_1} v^v - \frac{1}{\lambda_3} \left\{ \frac{v^1 v^2}{h_2} \cdot \frac{\partial h_2}{\partial x^1} \right\} dx^3, \\
d_{\lambda_4} \left(v^3 - \frac{2a}{\gamma - 1} \right) - \frac{1}{\lambda_4} \left\{ \frac{v^1 a}{h_2} \cdot \frac{\partial h_2}{\partial x^1} \right\} dx^3, \\
d_{\lambda_5} \left(v^3 + \frac{2a}{\gamma - 1} \right) - \frac{1}{\lambda_5} \left\{ \frac{v^1 a}{h_2} \cdot \frac{\partial h_2}{\partial x^1} \right\} dx^3
\end{aligned} \tag{5}$$

The analysis of characteristic relations shows, that under $v^3 < a$ at the inlet boundary of region four gasdynamical parameters locally must be determined; at the outlet boundary - one parameter. Missing parameters at these boundaries are ensured from characteristic relations. The flow modelling through exhaust hood requires the formulation of physical boundary conditions at the inlet section and backpressure distribution in the condenser. At the inlet section the distributions of angles of velocity vector, total flow parameters are formulated, coordinated along the radius on the base of radial projection of impulse equation.

Description of computational region

Flow model is oriented to axial-radial diffusers. The meridional section of diffuser contains not less 4 angular points a, b, c, d and is mapped onto square one-to-one. The geometrical model of the diffuser is not a rotational body in general and permits to consider elliptic and circular axial-radial diffusers of variable meridional section.

Finite-difference division of diffuser \mathfrak{R} is described in cylindrical coordinate system (r, φ, z) , where r - radial direction, z - axial direction). Every diffuser section of $r-\varphi$ plane topologically corresponds to unit square, and its division is obtained by mapping of square divided by coordinate lines being parallel to their sides. This mapping of meridional section $abcd$ onto unit square is realized in polar coordinate system for every meridional section. New variables ξ, η on the unit square may be defined as:

$$\xi = \frac{\theta - \theta_{ac}(\rho)}{\theta_{ba}(\rho) - \theta_{ac}(\rho)}, \quad \eta = \frac{\rho - \rho_{cd}(\theta)}{\rho_{ab}(\theta) - \rho_{cd}(\theta)}, \quad 0 < \theta < \pi/2.$$

For the construction of finite-difference approximation of gasdynamical equations in ξ, η plane it is possible to use the uniform mesh or construct curvilinear division on the base of some appropriate mesh generation algorithm.

The internal elements modelling

Such special elements of flow guidance as deflectors, circular blades, special profile of outer diffuser shell need to their detail describing. Deflectors and circular blades are described by ξ – set of mesh lines and their effect to flow is expressed as non-leakage condition for the corresponding part of mesh line. Special profiling of outer diffuser contour may contain back-face steps, discontinuities of wall for gas rejection or injection of high energetic jet. The geometric realization of such procedures consists in organization of series circular blades near the outer wall as it is shown in fig. 1.

The rejection through the perforation is realized by the formulation of boundary conditions with back pressure behind the faces of cells with perforation. The injection modelling is realized as a jet with high total energy and low entropy function.

The finite-difference division of exhaust chamber space

The variety of constructions of exhaust hoods requires sufficiently universal description of their geometry. The flow path of exhaust hood is usually divided on two parts: the flow region in diffuser and exhaust chamber one. The exhaust surface of diffuser is same as the circular fragment of cylindrical inlet surface of exhaust chamber. Spatial division of exhaust chamber may be done by two ways depending on geometrical characteristics of casing.

The $\mathcal{R}1$ (fig. 1) division is provided by the partition of the section bd , that separates the exhaust on two parts. Such flow regions are one-to-one mapped onto cube with angular points being immovable. This type of finite-difference division of exhaust chamber does not permit to describe accurately the geometry of guide blading and cavity for bearing.

The division $\mathcal{R}2$ (fig. 1) supposes the partition of exhaust chamber space by the surface ef . This surface geometrically simulates the upper vertical wall and cavity for bearing access. A set of sections, done under consideration of meridional geometry, guide blades, forms the space of exhaust chamber and line ef may contain various number of nodes depending on section position. This type of division admits the simple extension for case of exhaust hood with doubled side exhaust. But sometimes the bevel of cells near ae boundary can be noticeable, so it may cause computational difficulties.

The mesh division in the meridional surfaces is determined by geometry of front and back walls of chamber and is not rectilinear. So the sections $abef$ are not plane: the generation of mesh for curvilinear meridional boundaries may be done by method [11].

Flow in the diffuser and its geometry are described in cylindrical coordinate system. Flow in the chamber may be represented using Cartesian or curvilinear coordinate system. The calculation procedure of joining of subregions - diffuser and exhaust chamber is realized basing on averaged fluxes of conservative variables.

Nonstationary 3D model of last turbine-exhaust hood compartment

The solution of problem is based on the isolated stage model[3] and exhaust hood model. The calculation region of stage consists of 2 interacting channels of stator and rotor, inlet, outlet interstage spacings (fig. 2). The periodical solution in the calculation region is ensured by integration procedure of Euler's equations in interval of stage periodicity using above described Godunov's type scheme. For formulation of inlet, exit boundary conditions the usual channel approach is used, which consists in assigning of distributions of Riemann's invariants (5)(far-field formulation) in the inlet, outlet sections of stage domain. For interrow axial spacing the generalized conditions of spacing and periodicity(GSP-conditions) are assigned[3], which take into account the flow pulsation phase shift in the row adjacent channels.

The most general approach to numerical simulation of exhaust compartment operation supposes the common computational region, being built in the exhaust hood and all the channels of stage. But the realization of such approach meets the technical difficulties. Namely, in consequence of difference in scales of volumes of exhaust hood and stage channel the spatial division of exhaust hood has to be sufficiently fine for the joining of exhaust hood and rotor domains. The time which is needed for getting the periodical flow regime through all channels of stator and rotor may be equal to time of several rotor revolutions. The described procedure directly simulates the interaction process of stage and exhaust hood, but is not acceptable for most of power computers. Moreover, the efficiency of such approach does not increase proportionally to reducing of difference division of computational region, but is limited in principle by pithiness of ideal gas model.

The experiments for estimation of circular nonuniformity in stage diffuser axial spacing of exhaust compartment [1] point out to sufficiently smooth character of circular distributions of gasdynamical parameters. This fact leads to use of quasi-static approach in simulation of stage - exhaust hood interaction, which consists in exclusion of transfer processes in the rotor channels, caused by their movement in field of large-scale nonuniformity from exhaust hood. In this case the nonuniformity of fields of gasdynamical parameters in stage-diffuser spacing is approximated by piecewise-constant function, as it has been firstly proposed in [6]. This hypothesis is based on fact, that the ratio of time interval of particle translation through rotor channel to time interval of revolution essentially less than 1. Actually, comparing the Strouhal number for the nonstationarity in the interrow spacing due to pitch nonuniformity $Sh_1 = n \cdot z_1 \cdot b_2 / w_2$ and its analogue in consequence of large-scale circular nonuniformity from exhaust hood $Sh_2 = n \cdot b_2 / w_2$, one can see, that they are distinguished in z_1 times. Therefore, the flow nonstationarity in rotor due to nonuniformity behind them in z_1 times less than high frequency nonstationarity due to interaction with stator blades.

According to the quasi-static approach every piecewise-constant interval Ω_i is correlated to the corresponding flow in stage fragment "STAGE-i" (fig.1), being calculated on the base of constant boundary conditions from Ω_i and

with use of GSP-conditions. The general solution for fixed time point in the stator and rotor domains is given by the superposition of solutions in all stage fragments on the intervals Ω_j .

The parameters values in the interstage spacing are the inlet boundary conditions for flow calculation through the exhaust hood. The joining model, i.e. the data transmission from exhaust hood to stage and in the reverse direction may be various. In paper all conservative gasdynamical parameters transmission up and down the stream was used. The general interaction problem is solved by the global iterations in a common time scale with a parameters transmission for every time iteration. The receipt of a periodical flow in stage and stable one in the exhaust hood is based on the time-marching procedure.

One of criteria of solution stabilization is the stabilization in time of integral flow rate in the inlet and exit of exhaust hood. The supplementary condition is the stabilization of flow rates through all stage fragments and sectors of diffuser. The final conclusion about reaching the stable state in compartment is done, when the stabilization or periodical regime of flow in the axial spacings has been reached. The dimensions of typical computational region are: 3000 cells in single stator(rotor) channel, 20 stage fragments, near 15000 cells in diffuser and 20000 cells in exhaust chamber.

As it has been pointed, the relatively low circular gradients of parameters in the interstage spacing were the characteristic peculiarity of stage - exhaust hood interaction. Its exclusion leads to full stationary model of interaction in exhaust compartment, which is rigorous for case of "stage-axisymmetrical diffuser" interaction and is representative to characterize the radial parameter distributions in the interstage spacing. In this case the flow is calculated only in a single diffuser sector with parameters from Ω_j under hypothesis of flow axial symmetry. The solution of such problem is bounded by 3D computational region of a single stage fragment and corresponding diffuser sector Ω_j . Calculation is carried out by global time iterations "stage-diffuser" until full stabilization of integral characteristics in the diffuser and periodical regime in the axial spacings of stage.

In the developed approach the ideal gas model is used. The analysis, done in [4,9], points out on the possibility of qualitative description of real flow structure under the great Reynolds numbers with use of the Eulerian finite-difference model. Methodical study shows that the structure and nonstationary characteristics of flows in different devices of flow path with sudden expansion described by the Eulerian model correspond to the experimental data [6,9,10] relatively Strouhal numbers and integral characteristics.

NUMERICAL RESULTS AND DISCUSSION

Some results of flow simulation in the isolated exhaust hood under uniform flow conditions, compartment "stage-diffuser" under constant pressure p_{cond}

and examples of calculation of exhaust compartment are represented below. All gasdynamical data are reduced to dimensionless form using the critical values of velocity and density being calculated from total inlet flow parameters.

The exhaust hood chosen as a study subject is a model one of Kharkov Turbine Plant (XTZ)[13], has the diffuser areas ratio $F_{out}/F_{in}=2.2$, casing is characterized by relative width $B/D=2.0$, length $L/D=0.54$, height $H/D=1.55$. The exhaust compartment chosen as a study subject consists of last stage of LP cylinder of "Skoda", Pizen turbine 500Mw and exhaust hood (Stastny, [7,8]). The diffuser has areas ratio $F_{out}/F_{in}=1.9$. Exhaust hood is characterized by relative width $B/D=2.6$, length $L/D=0.9$, height $H/D=1.96$.

The verification of method is based on the evaluation of their parts: stage model and diffuser model with exhaust chamber being done in [3,4]. The comparison with experimental data (Stastny, [8]) for isolated diffuser under $M_\infty=0.07-0.15$ is given in fig. 3. The main discrepancies take place in sections 2,3 on a convex contour because of boundary-layer separation which is absent in the model for these regimes. For Garkusha's experiment being made on the compartment "stage-diffuser" for partial regime [1] one can see a good agreement in section before flow separation. The comparison with Maier's experiment [12] shows a good agreement for high loaded operational regime of last compartment using the semi-empirical clearance flow model that is based on the jet with high energy and low entropy modelling.

Flow through the isolated exhaust hood

The flow calculations were made for wide range of inlet Mach numbers. Projections of velocity vector in two section of exhaust chamber are represented in fig. 5. Isolines of Mach number in some sections for regime $M_\infty=0.37$ are shown in fig. 4. Represented data are demonstrated all qualitative peculiarities of swirled flow in the diffuser and chamber known from experiments. The Rossby numbers $Ro=u_c/u_p$ are given for all calculated regimes show the rise of vorticity depending on the increase of inlet Mach number. The existence of swirled flow may transport water drops from condenser to diffuser inlet. The flow velocity in the kernel of swirl corresponds to its analogue for rotated rigid body (fig. 5,6) as this has been verified by experiments [13].

Flow through the compartment "stage - diffuser"

The range of operational regimes of last stage with diffuser in form of plots of mass and volumetric flow rate is represented in fig. 6. When pressure ratio drops below 0.3, axial component of velocity exceeds the speed of sound and it limits the rise of rate. On fig. 6 the structure of flow in the diffuser for different operational regimes of compartment is given: *A(0.56GV)*, *B(0.33GV)*, *C(0.15GV)*.

Fig. 10 represents the radial distributions of main flow parameters in spacings; all values are averaged in time and along the circular coordinate. Re-

gime *A* is near the design point for stage, regime *B* gets into design interval, but is characterized by low volumetric flow rate; regime *C* is partial. For regime *A* one can see the region of low velocities in the outlet part near the outer diffuser shell, which reveals the flow separation. The similar phenomenon in a weak form takes place for regime *B*. The flow in the stage and diffuser for regime *C* has the developed diagonal character with small retardation zone in the outer shell and developed recirculation zone near the inner shell. The analysis of radial distributions of static pressure for these regimes shows, that for regular regimes the flow in this stage may be predicted on the base of isolated model under the constant along the radius static pressure.

Flow through the compartment "stage - exhaust hood"

Some data about flow through the compartment for a regular *A* (0.5GV) and partial *B* (0.2GV) regimes are given in fig. 7-9, 11, 12. The flow in the exhaust chamber is determined by tangential supply of steam from the diffuser and represents the swirl flow with expansion into condenser. Non-axial flow exit from stage creates the swirl at the diffuser inlet and shifts the division surface of exhaust streams in a chamber in anti-swirl direction (similar phenomenon was observed in the extraction circuits [1,6]).

The maximum of vorticity for a regular regime of studied model is observed in the vicinity of horizontal joint. For regime *B* the flow in the diffuser has the diagonal structure due to exit stage swirl. In the inner diffuser wall the wide separation zone arises with recirculation flow which is able to transport water drops from condenser to trailing blade edges (see flow structure in fig. 8, 9).

Exhaust hood with one-sided exhaust causes essential circular nonuniformity of flow parameters in the section placed behind the rotor. Inlet circular coefficient of static pressure $K_p = (P_\varphi - P_{cond}) / (0.5\rho_2 C_{z2}^2)$ for regular regime in the peripheral layer is greater than for hub. For the partial regimes one can see the inverse tendency due to decrease of $0.5\rho_2 C_{z2}^2$ value in the hub.

The Fourier analysis of full aerodynamic blade force is done on full blade revolution. High frequency (HF) component of full aerodynamic force (on a stage period) due to "stator-rotor" interaction (with nz_1 main frequency) and low frequency (LF) component due to rotor rotation (with n main frequency) are represented on fig. 11. Calculations show, that the absolute values of amplitudes of initial harmonics of blade force rise when the volumetric rate diminishes, but at the same time the average blade force (A_ρ) diminishes. The behavior along the blade length of relative amplitude of first harmonic of LF and HF force components for hub and tip layers depending on the regime are represented in fig. 12. For regular regime the amplitudes of initial harmonics of high frequency pulsation of full aerodynamic force (FAF) on a stage period are comparable to ones of low frequency pulsation of FAF on rotor revolution (fig. 10-12).

The increase of volumetric flow rate through the compartment leads to increase of velocity level in the exit of stage and the supersonic zone locked by shock arises in outer diffuser shell. For such high loaded regimes the flow in the bevel cut becomes supersonic and the disturbances up to flow are getting weaker. These regimes are accompanied by rise of the vorticity near the horizontal joint and M_{c2} , but at the same time the diminishing of circular nonuniformity in the axial spacing occurs.

In the last compartment of LP cylinder the primary formation of nonuniformity occurs due to the effect of casing. Last stage mainly diminishes the nonuniformity of parameters in the inlet of exhaust hood. Namely, the flow in the exhaust hood under uniform inlet conditions and without inlet swirl has the nonuniformity till 1.5 times greater than for compartment case.

Conclusions

The developed models permit to evaluate 3D flow structure in stage and exhaust hood, to study the operation of rotor channel on full rotor revolution, to obtain the blade force characteristics and phenomena caused by relative and absolute LF, HF flow nonstationarity.

The methodical study shows that applications of method and proposed models are more preferable for high loaded regimes due to better correspondence of scheme viscosity to physical one.

Further development of proposed approach consists in application of non-stationary viscous gas model. Other way of investigations one can see in modelling of two-phase steam flow with process of spontaneous condensation.

Acknowledgments

This work was supported by the Ukrainian Government Committee of Science and Technology under Grant No 5.51.01/023-93.

Nomenclature

b	blade chord	c	absolute velocity
n	rotational frequency	α, β	tangential angles
L	blade length	γ	meridional angle
z_1, z_2	numbers of stator, rotor blades		
u	rotational velocity		
F	distributed full blade force,		
F_u	circular blade force		
G	flow rate		
GV	volumetric flow rate		
			Subscripts:
		$cond$	condenser
		tot	total
		z	turbine axis
		φ	circular coordinate
		w	relative velocity
		$1,2$	stage spacings

References

1. Garkusha, A.V. Aerodynamics of Flow Path of Steam Turbines. *Machinostroenie*, Moscow, 1983, p.184. (In Russian)
2. Migai, V.K., Gudkov, E.I. The Design and Calculations of Turbines Exhaust Diffusers. *Machinostroenie*, Leningrad, 1981, p.278. (In Russian)
3. Gnesin, V.I. The Calculation of 3D Transonic Flow Through an Axial Turbine Stage. *Izvestia AN SSSR. Mechanika Zhidkosti i Gaza*, No.6, 1982, p.138-146. (In Russian)
4. Solodov, V.G. Numerical Simulation of 3D Nonstationary Ideal Gas Flow Through the Turbine Exhaust Hood. *Problemi Machinostroenia*, No.40, 1994, p.41-45. (In Russian)
5. Eidelman S., Colella P., Shreeve R. Application of the Godunovs Method and its 2nd Order Extension to Cascade Flow Modeling. *AIAA Journal*, 1984, v.22, No 11, p.1609-1615.
6. Gnesin, V.I., Solodov, V.G. Turbine Stage Aerodynamical Interaction with Supplying and Rejecting Devices of Flow Path. *Proc. of Int. Symp. on Exp. and Comput. Aerothermodynamics of Internal Flows*, Prague, Czech Rep., 1993, p.243-248.
7. Stastny, M. Untersuchung Eines Dampfturbinen-Austritts gehauses in einem breiten Betriebsbereich. *Maschinenbautechnik*, Vol.38, No.1, 1989, p.27-29.
8. Stastny, M. Untersuchung Eines Typendiffusors und Eines Ausstrittsgehause für Dampfturbinen. *Maschinenbautechnik*, Vol.31, No.4, 1982, p.154-160.
9. Belotserkovsky O.M. Numerical Simulation in Continuum Mechanics. Moscow, Nauka, 1984, 520p. (In Russian)
10. Gnesin, V.I., Solodov, V.G. The Influence of Flow Nonuniformity in Extraction Chamber and Exhaust Hood on Nonstationary Characteristics of Turbine Stage. *Teploenergetika*, No.4, pp.22-26, 1988. (In Russian)
11. Fletcher, C.A.J. Computational Techniques for Fluid Dynamics. Fundamental and general techniques. Springer-Verlag, Berlin, 1988, 504 p.
12. Maier, R. Experimentelle Unterzuchung Selbsterregter Stoss-Grenzschicht. Pulsationen in Abdampfdiffusoren. Dissertation Universitat Stuttgart, 1989, s. 66-73.
13. Galatsan, V.N., et al. Study of exhaust hood of LP cylinder of steam turbine. *Teploenergetika*, 1990, No.5, p.35-39. (In Russian)

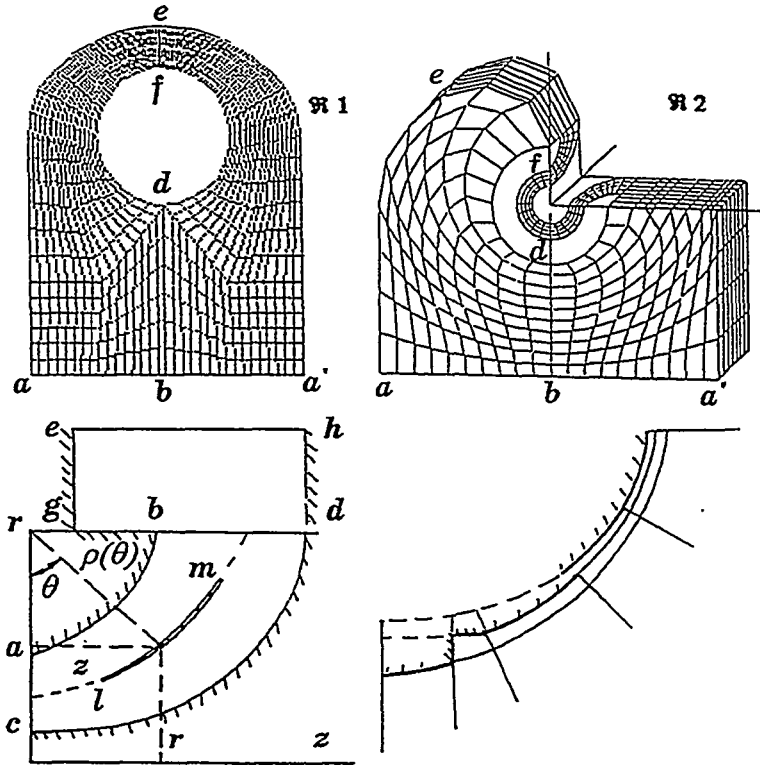


Fig. 1-Variants of computational mesh for exhaust hood region.

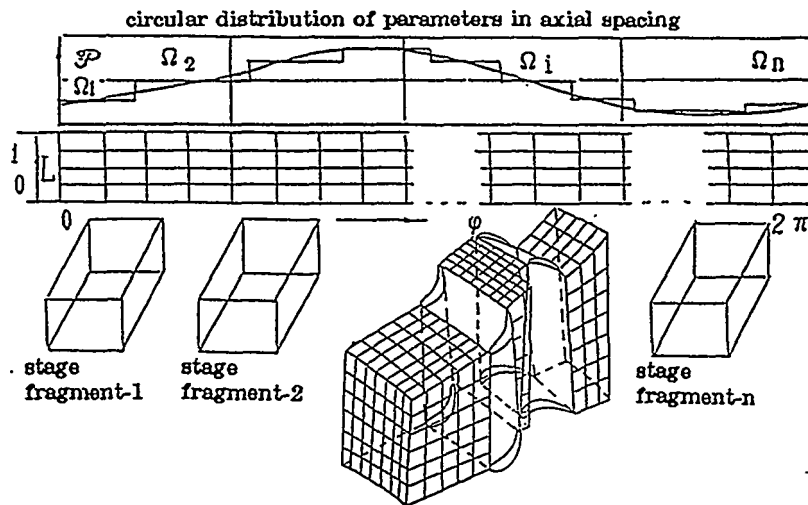


Fig. 2-Conception of "stage-exhaust" hood joint.

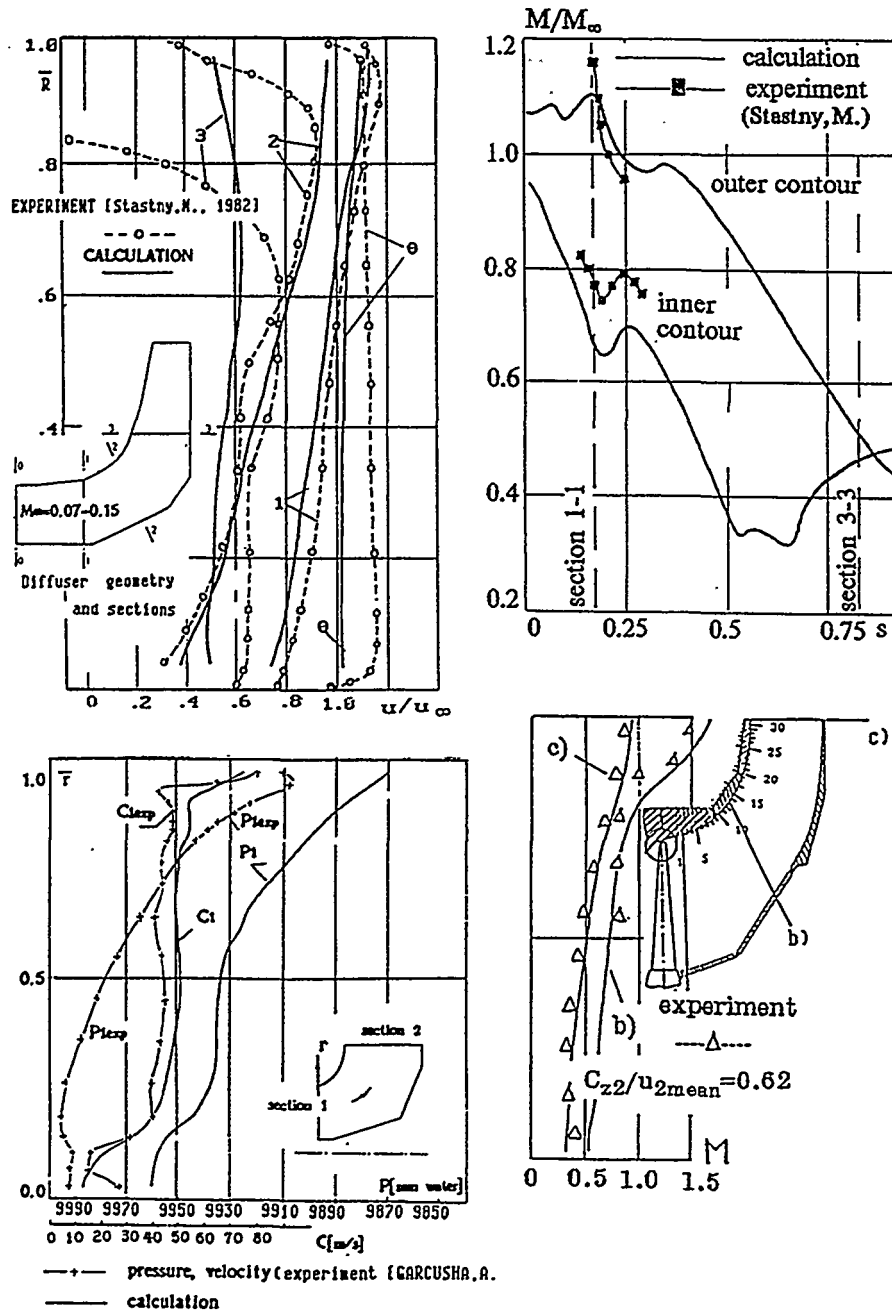


Fig. 3-Experimental (Stastny, M., Garcusha, A.) and predicted distributions of pressure and velocity in diffusers; clearance flow model - comparison with Maier's experiment for stable regime.

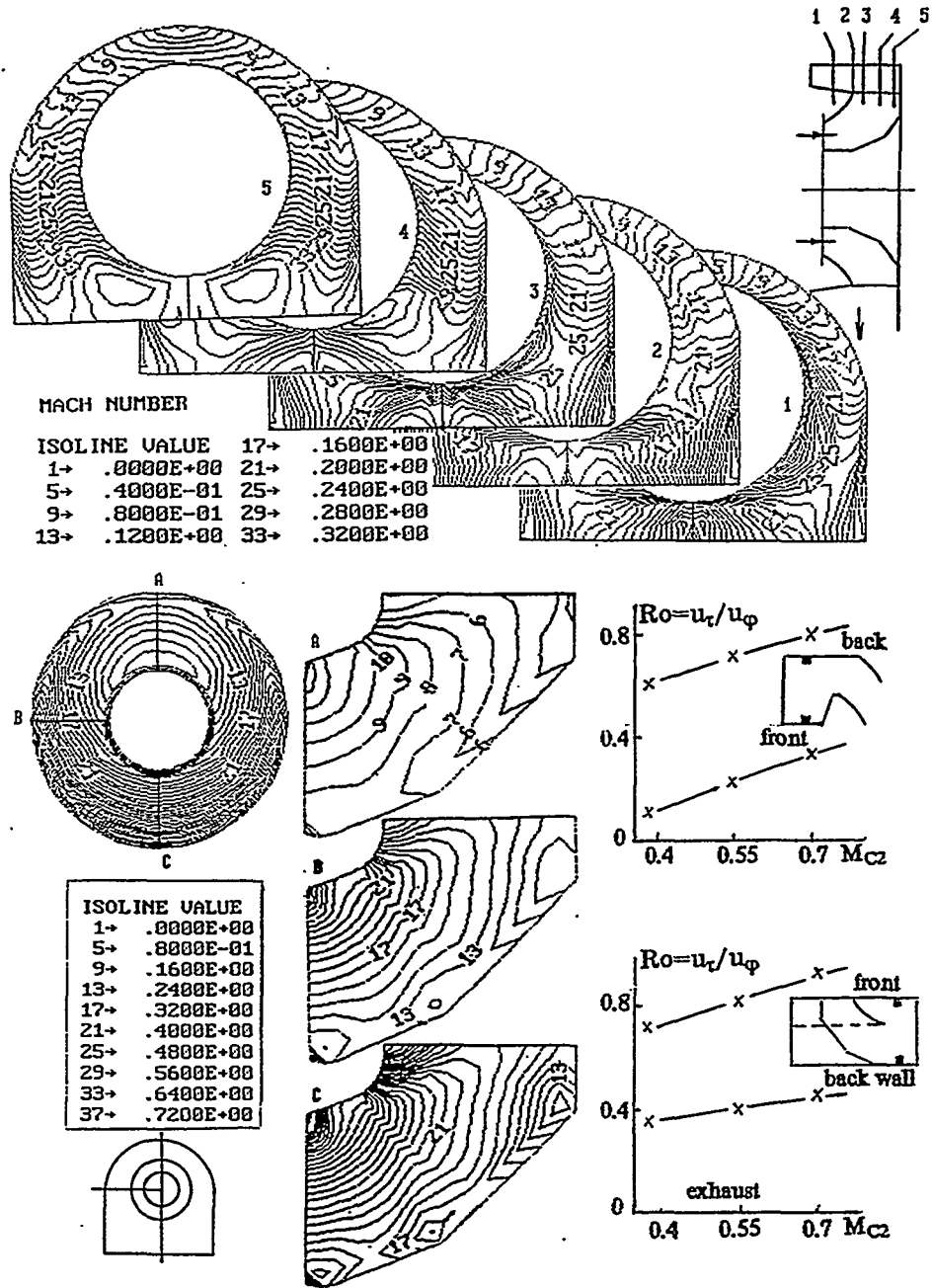


Fig. 4-Isolines of Mach numbers in sections of isolated model exhaust hood for $M_\infty=0.37$ and Rossby number depending on Mach number.

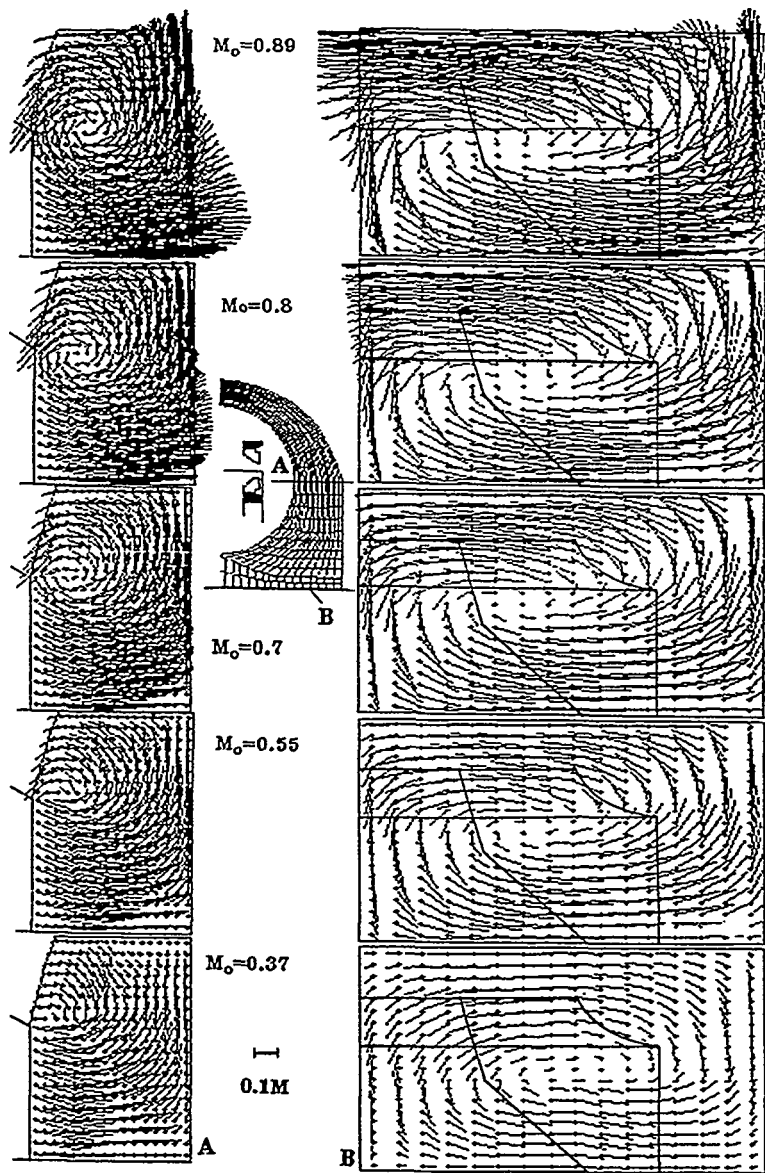


Fig. 5-Flow structure in model XTZ exhaust hood depending on M_o under $\alpha_\infty=0$, $\gamma_\infty=0$.

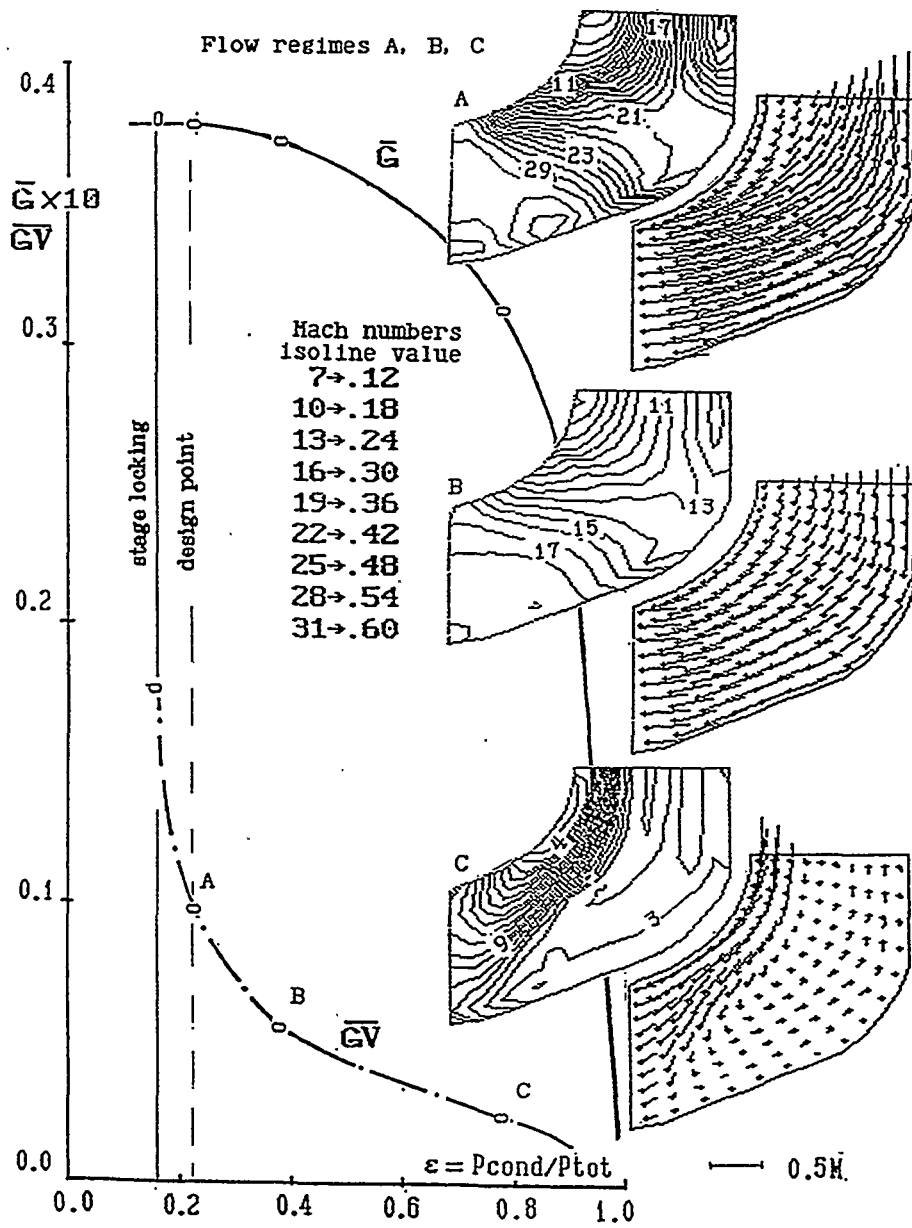


Fig. 6-Operational range of exhaust compartment and flow regimes in "Skoda" diffuser.

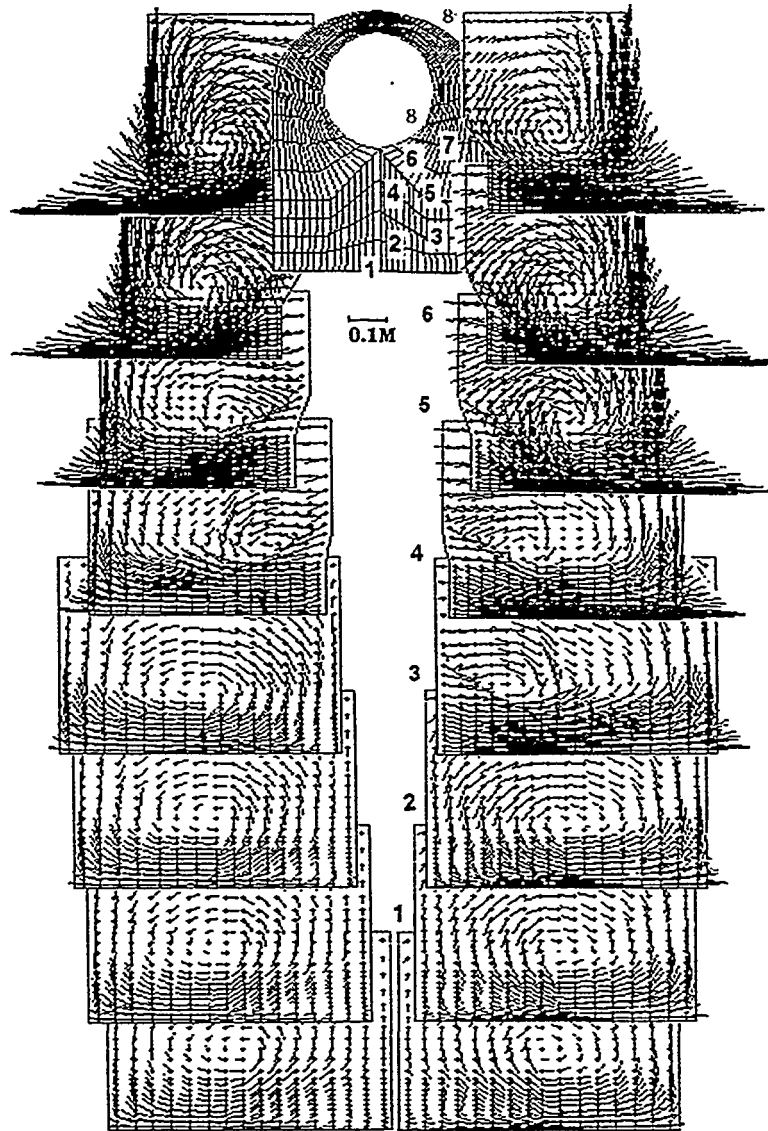


Fig. 7- Flow structure in "Skoda" exhaust hood for designed (A) operational regime of compartment.

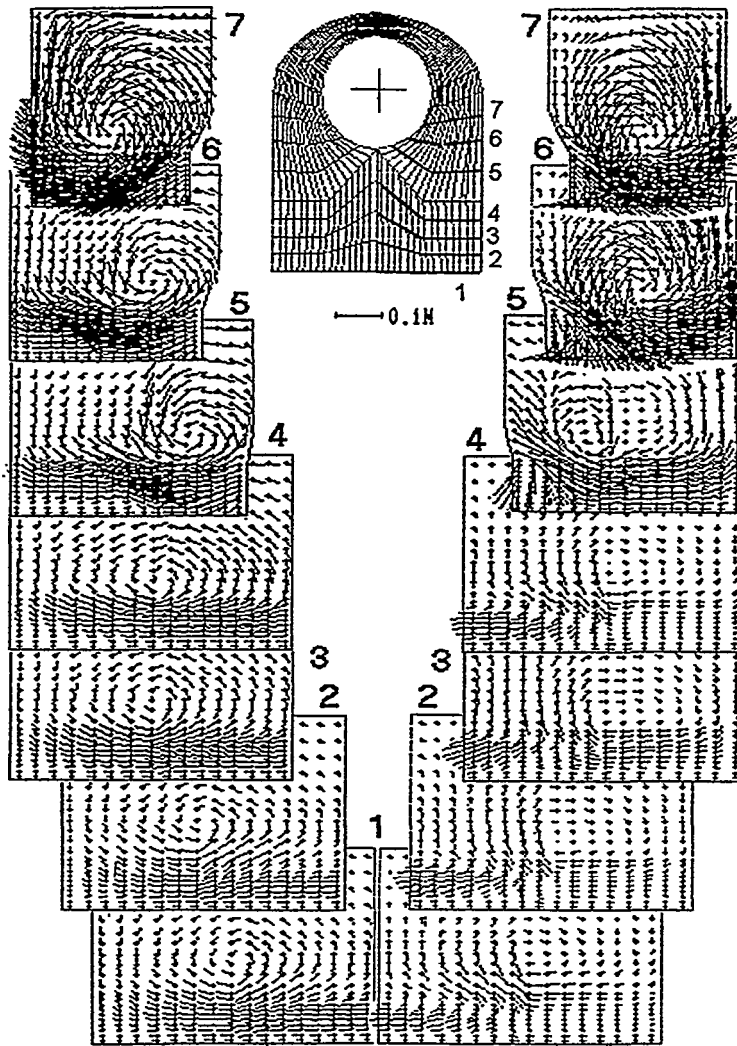


Fig. 8- Flow structure in "Skoda" exhaust hood for partial (B) operational regime of compartment.

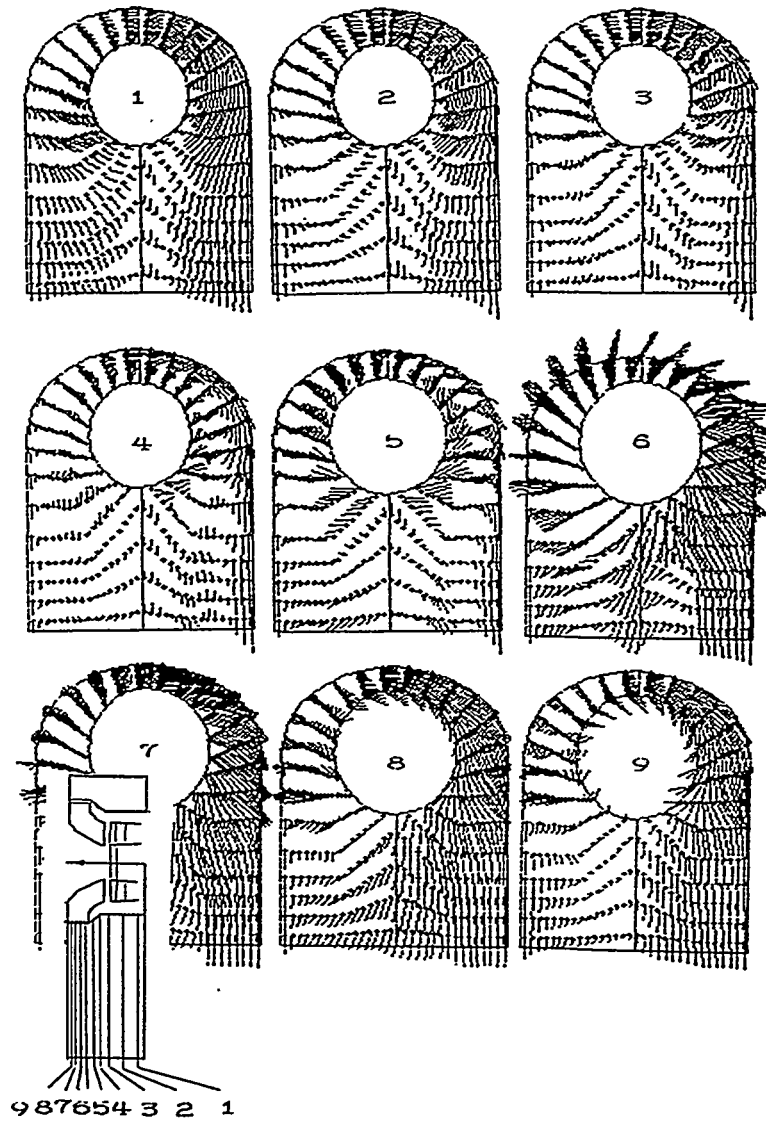
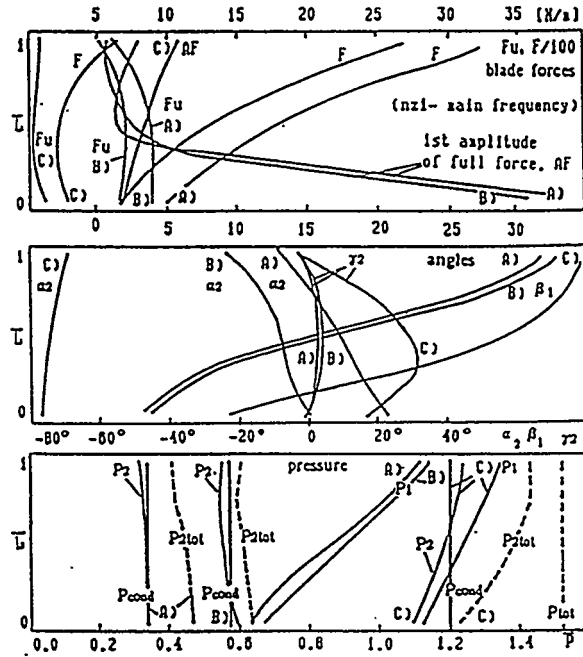


Fig. 9- Flow structure in "Skoda" exhaust hood for partial (B) operational regime of compartment.



A(0.56GVmax)
B(0.33GVmax)
C(0.15GVmax)

Fig. 10-Pitch- and time-averaged distributions of flow parameters in 1st and 2nd spacings of "stage-diffuser" compartment for regimes A, B, C.

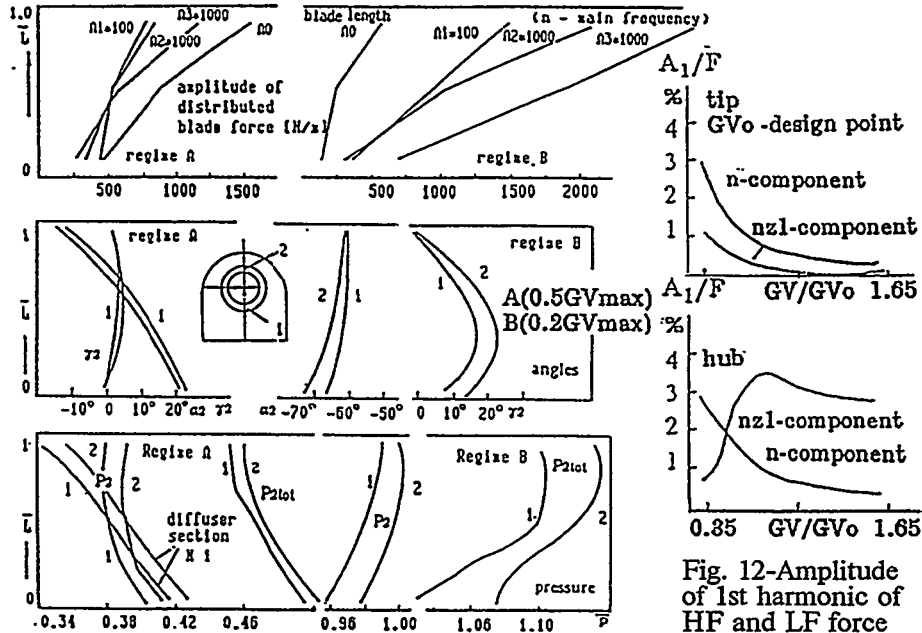


Fig. 11-Gasdynamical and force characteristics for case "stage-exhaust hood" interaction.

Fig. 12-Amplitude of 1st harmonic of HF and LF force components on blading of "Skoda" compartment.

For Your Notes

A Method for Calculation of Flow Turbulence with Random Numbers

Jouko Laine and Markku Hurme
Helsinki University of Technology
Department of Chemical Engineering
Kemistintie 1 M, FIN - 02150 ESPOO, Finland

Abstract

In this paper a new method has been presented and preliminarily tested for calculation of fluid flow with random numbers and basic mathematical operations. In the calculation the volume of fluid is divided into a great number of elements. The simulation is done in a continuous loop by calculation only in a single randomly selected element (a core) at a time. The flow vector of an element is calculated from the flow vectors of the neighbouring elements. The result is varied by using a random disturbance to make the result time variant corresponding to reality. Because of the nature of the simulation algorithm, it is possible to change the values of element during the calculation. The calculation converges quickly to the result corresponding the new input values. Preliminary two-dimensional tests have given promising results. They have shown that it is seemingly possible to solve fluid flow problems rather quickly and accurately by the presented method.

Introduction

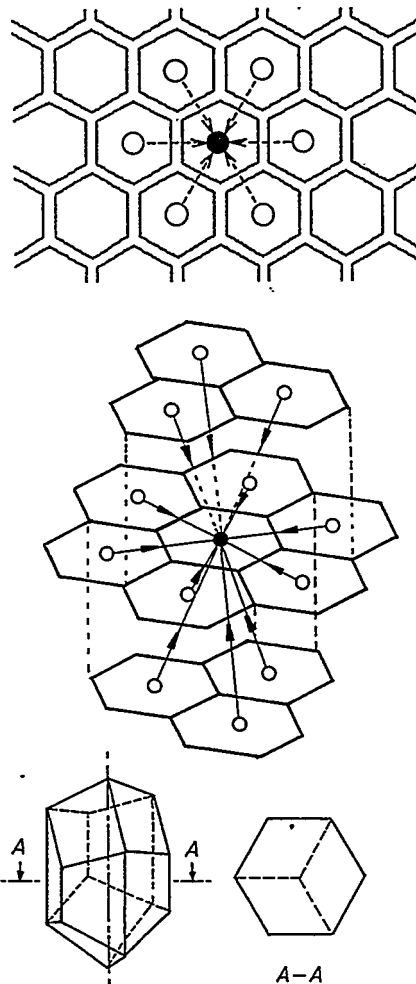
A turbulence is a stochastic and time variant phenomenon, which is dependent on the geometry of the system, phase boundaries, properties of fluids, forced flows and energy dissipation. The calculation of fluid flows can be done by different computational fluid dynamics (CFD) methods implemented as computer programs (e.g. *Phoenix*) which are intended for various purposes. The principle of a conventional program is either $k-\epsilon$ model or Reynolds stress model. This paper presents a new preliminarily tested approach for calculating turbulence in non-steady-state by using random numbers and basic mathematical operations without differential calculations.

Basic principle

Fluid space is divided into a large number of elements. A two-dimensional system is represented by a layer of honeycomb shaped elements. A three-dimensional system is composed of a large number of honeycomb layers (Fig. 1).

In a two-dimensional system an element is encircled with six neighbouring elements and in a three-dimensional system with twelve elements. This is called the information circle. Every single element is considered to be independent. It can receive information only from the neighbouring elements (i.e. the information circle) and it can transmit information only to the elements of information circle. This implies that single elements can be evaluated in an arbitrary order in the simulation. Different types of information can be transmitted from the information circle by free movement of the neighbouring element, vessel wall, fluid surface, constant energy input, etc. (i.e. system geometry, process variables, physical properties, ...)

Fig. 1. The calculation elements, core and information circle in 2- and 3-dimensional systems. Also one 3-D element is in figure.



The elements are either free or constrained. In a free element the fluid flow is determined freely, whereas in a constrained element the flow is determined partly or fully by preconditions: For example a constant power input determines the velocity and direction of flow in a constrained element. The direction of flow of an element at vessel wall is partly constrained.

In a hermetic system the flow velocities of the free elements are very slow in the beginning and their direction is chaotic (i.e. diffusion). This is managed in simulation by giving random initial values to the flow vectors of free elements.

The flow vector of a randomly selected element is determined by the resultant of the flow vectors of the neighbouring elements (i.e. by the information circle). Because the flow phenomena are not exact in a real situation, but have a certain tolerance of velocity and direction, the stochastic variation is taken into account in simulation by using a randomly generated revision in the velocity and direction of the flow vector at the core. Therefore the exact prediction of the simulation result is not possible - which applies also to the reality.

Calculation method

Types and number of basic elements

The simulation proceeds in the following way: The flow volume is divided into the previously described elements, the number of which depends on the required accuracy of the calculation and the computation CPU-time available. Experience has shown that for a rough calculation of a two-dimensional system it is enough to have from 500 to 2000 elements and the number of loops about from 15 to 20 times the number of elements.

There are several types of elements: e.g. free element, wall, element next to wall, air space above the liquid surface, interphase between two phases, the element next to interphase, element with a forced flow (liquid inlet or outlet, power input: e.g. impeller).

Initial values

Before simulation certain initial values of elements are required. To correspond diffusion very small values are randomly given to the direction and velocity of the flow vectors of the free elements. Forbidden flow directions and the wall friction are determined by the direction and elasticity of the wall or surface. If the direction or velocity of the flow is forced (impeller, flow inlet etc.), constant flow velocities and directions are given to the elements, which are being kept unchanged during the simulation. If required, it is possible to give also information on reaction rates, concentration disturbances, viscosity of fluid, changes in liquid level etc. Initial values are possible to feed to the program in different ways e.g. by using a graphical user interphase. Examples of initial values and different element types are given in Fig. 2. It is possible to modify the values of elements

at any time during the simulation before the next element is randomly chosen for calculation. This is made possible by the new simulation methodology presented.

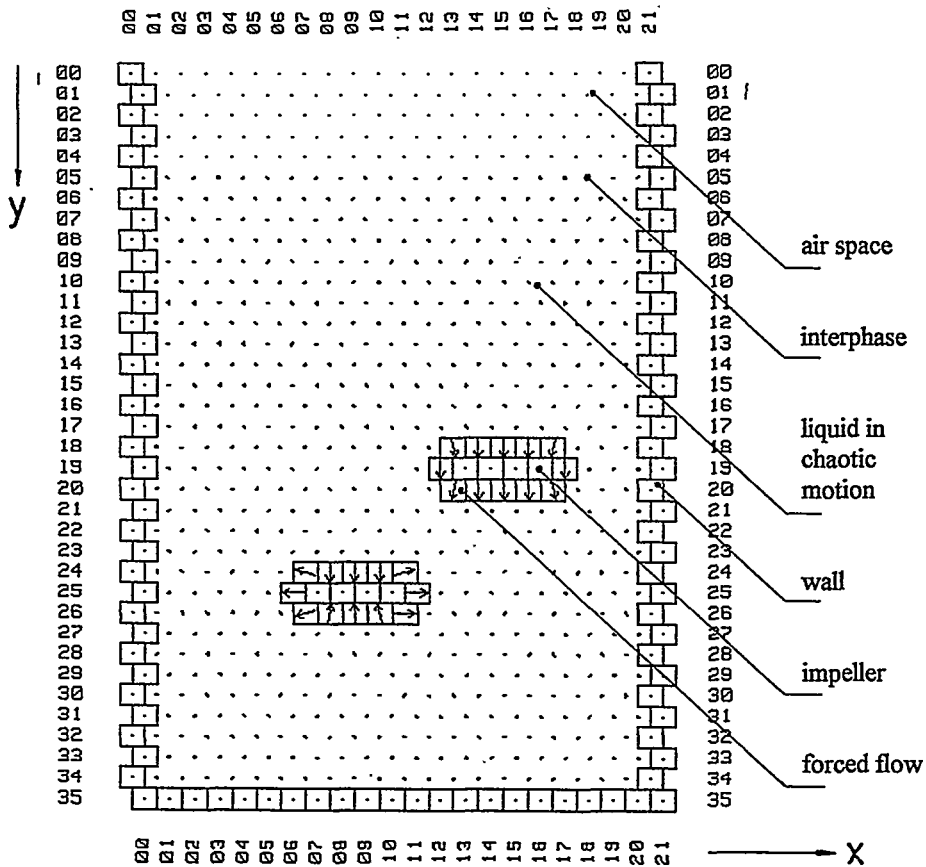


Fig. 2. An initial state of simulation. Examples of different initial values and types of elements. The elements forms are hexagons in reality.

Calculation

After the definition of initial data, the core to be calculated is chosen by randomly selecting the x, y, z co-ordinates in a continuous loop. Data, such as the flow velocities and directions, are gathered from the elements of information circle surrounding the core. The value of the flow velocity and direction of the core element is calculated as a resultant of the flow vectors of the information circle elements by using only basic mathematic operations. If the calculated element is not a free element (e.g. the wall of a tank) and the

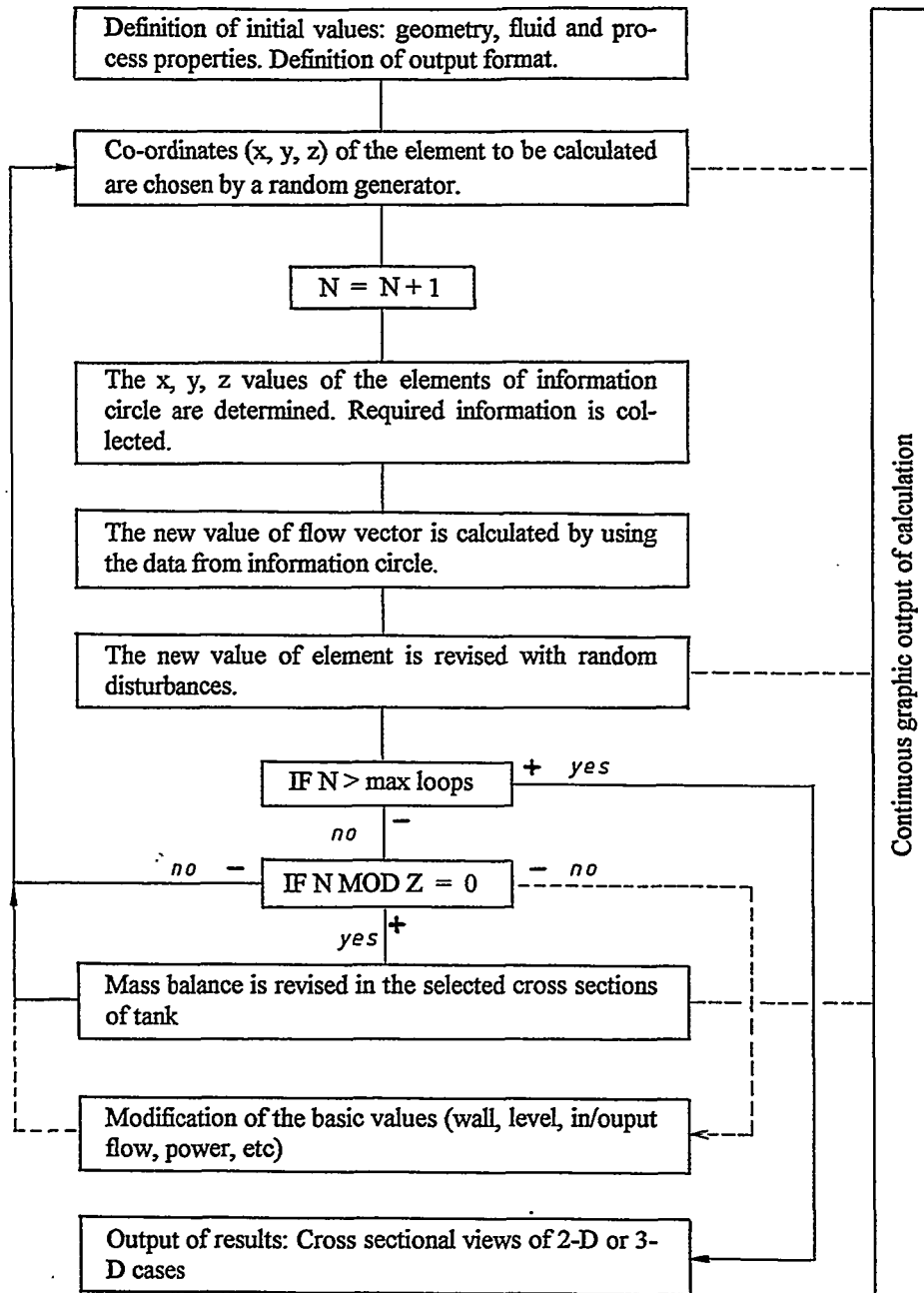
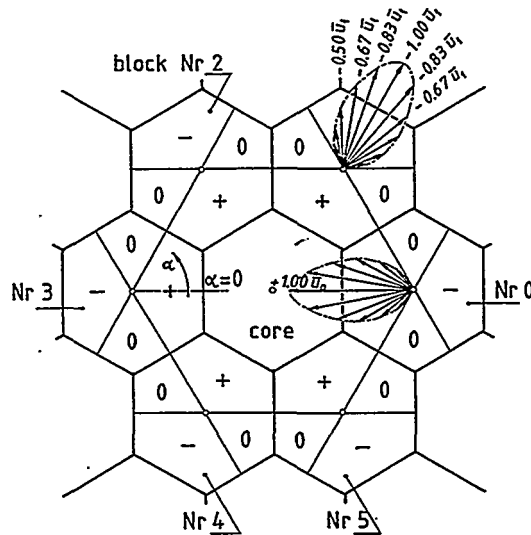


Fig. 3. The scheme of calculation algorithm. The value of Z is about from 500 to 1000.

calculation would give a flow direction into a forbidden area (e.g. towards the wall), a correction of the direction is being made by a special function. When the calculation and the correction of the flow vector of the core element has been done, a new element is being chosen by the random generator and the calculation is started again. This procedure is being continued until the results are satisfactory (see Fig. 3).

The calculation of the flow resultant is being done by using the data of the information circle in the following way: The direction of flow of a information circle element is considered to be from the circle element to core if the flow is to that direction and deviates less than ± 60 degree from the line drawn between the centers of circle element and core. The flow direction is from the core to circle element, if the deviation is the same but the flow direction is opposite i.e. from core to circle (see Fig. 4).

Fig. 4. Core element and the surrounding information circle (elements or block numbers from 0 to 5). The relative effect of a flow vector of information circle element has been shown as an example (+) flow into the core, (-) flow from the core and (0 and dotted area) dead angle; i.e. no effect. Relative effect of flows as a function of angle is shown in blocks number 0 and 1.



The flow velocity is considered to be linearly dependent on the angle between the flow direction and the line drawn between the centers of the two elements. If the flow direction of the circle element is in dead angle (i.e. absolute value deviates from 60 to 120 degree from the line) the flow is not considered to affect on the new flow value of the core. Consequently in a two-dimensional system the flow of an element can effect only two neighbouring elements in a positive way and only two in a negative way and there is no effect on two elements (Fig. 4). When all the vectors of the information circle elements (with direction into or out from the core) have been calculated, the new value of the flow vector of the core element can be calculated as a function of the vector sum.

When the new direction of core is into a forbidden direction (e.g. towards a wall), a correction of the direction is being made by a special function. The more the original direction is towards the wall the more the flow direction will change.

Stochastic nature of flow

The direction and velocity of the new static flow vector, which was calculated for the element in the previously described way, will be revised with a stochastic oscillator (Fig. 5). Consequently the dynamic character of the flow will be simulated and the result becomes time variant. The instability of the result depends on which kind of variation is allowed to the static vector values ($\pm\Delta\alpha$, $\pm\Delta u$). When the calculation is repeated many times enough, the result will converge to resemble the real state. If the simulation will be run fast and the results displayed as graphics, the flow image will be in motion corresponding the real turbulence.

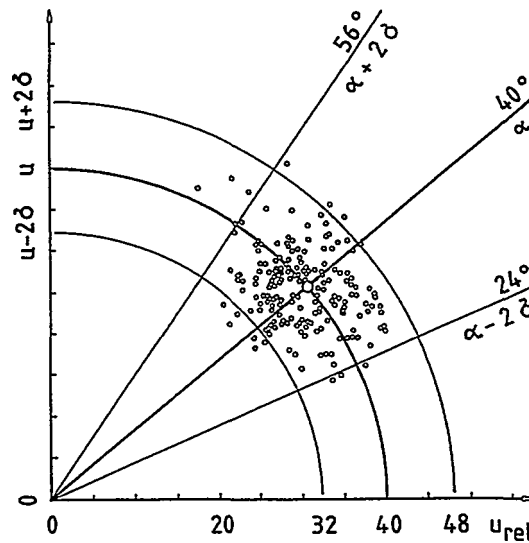


Fig. 5. The revision of the flow vector directing out from the origin by a random generator. There are many end points (o) of the revised vectors in the figure. For the original vector $u = 40$ [cm/s] and $\alpha = 40$ degree. Tolerances are $u = 40 \pm 8$ (probability, $P = 95$ per cent) and $\alpha = 40 \pm 16$ degree ($P = 95$ per cent).

The disturbance term has been formed so that the variation of flow velocity ($\pm\Delta u$) is normally distributed and the average is the original flow velocity given by the static calculation. The standard deviation is defined as an input value. The variation of flow direction ($\Delta\alpha$) is calculated in a similar way.

Revision of balances

It has been noticed that the calculation will slightly distort the material balance when the simulation continues for a long time. For example the sum of upward and downward flows will not exactly stay equal to the total mass balance when the simulation run is very long. For this reason it has been necessary to revise the material balance in a certain interval during the run. In a two-dimensional simulation a line of balance correction is chosen. The sum of flows going over the line to both directions is calculated. If the sum deviates from the value given by the total material balance, the flow velocities of the elements at the correction line are revised by an algorithm to satisfy the material balance.

Properties of the method

In the preliminary test the main properties of the method, the advantages and disadvantages appear to be the following:

Advantages:

- Initial values are possible to input in a graphics mode with a mouse.
- Calculation can be done and results seen continuously in real time.
- The result corresponds to the real flow pattern.
- The graphic output is dynamic because of the stochastic nature of system.
- The eddies are in motion depending on the magnitude of disturbance terms.
- Without a disturbance term the result will converge quickly to a steady-state.
- The magnitude of disturbance term can be selected.
- The input values can be changed during the simulation (form of the tank, etc.).
- In a symmetrical tank the result is not symmetrical (which corresponds to reality).
- The method is mathematically simple (no differential, matrix or nabla operations).
- CPU time is reasonable.
- The method is very fast when the element values are calculated in a parallel way.

Disadvantages:

- The method has not been exactly verified.
- Program is in a prototype state and need much further development.
- The results are not absolute.
- Tendency to distort the material balance, which has to be revised.
- Scientific basis of method is not exactly derived.
- A too large disturbance leads to a chaotic solution.
- Suitability to multiphase systems is fully open.

The following things can likely be considered in calculation (untested possibilities): effects of physical properties of liquid (viscosity, density), calculation of the form of surface (vortex), effect of reaction kinetics (local concentration of reactants and products), surface friction at the wall, concentration as a function of time at tracer tests, calculation of flow pressure and various outputs of views of three-dimensional systems.

Examples

Some examples of test results are shown in Figs. from 6 to 8. Fig. 6 represents a typical basic situation, where a standard flat blade turbine (FBT) in a stirred tank is simulated. It can be clearly seen from the figure that simulation result is unsymmetrical in spite of the symmetrical geometry. Fig. 7 is also a symmetrical configuration, but there are two impellers on the same shaft in a stirred tank. The unsymmetry of the results can be seen clearly. Also the passive fluid layer (no flow between upper and lower part of the tank) between the impellers can be seen. This layer is formed also in a real situation. The dy-

namics of the simulation can be seen in the Figs 8 a and 8 b. When the calculation starts, both impellers start pumping and fluid flows to the expected direction. When the simulation goes on the flow from axial pumping impeller (upper right) takes over and the eddy from radial pumping impeller becomes smaller. This is a typical example of the situation, in which the calculated result is somewhat surprising but corresponds well to the result which can be concluded.

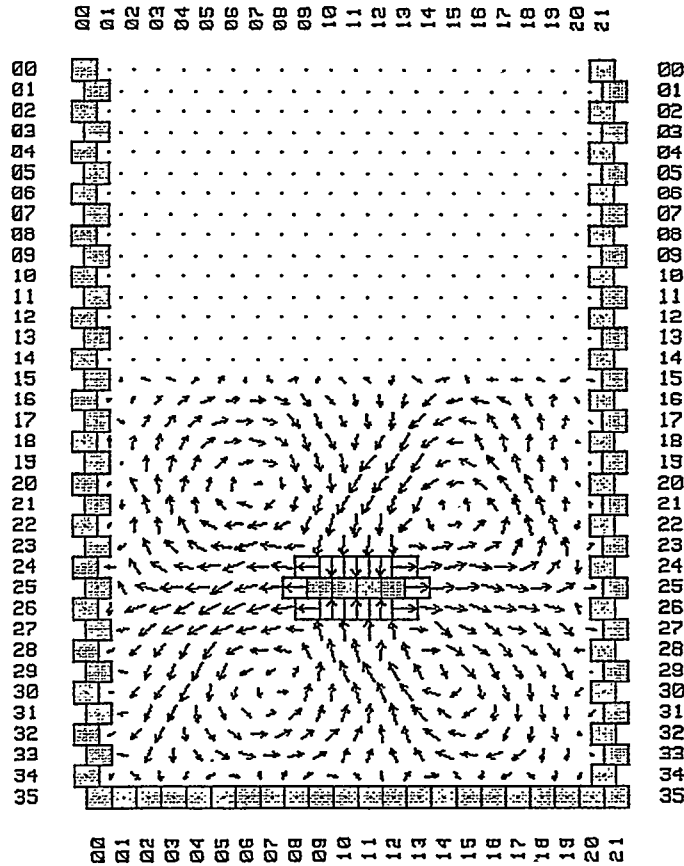


Fig. 6. A symmetrical mixing tank. The results of calculation after 15 000 loops. Pay attention that the scheme is not symmetrical. The dead points (the centres of fluid circulations) move slowly when the calculation goes on. The square elements (in calculation hexagon elements) represent the elements with forced flows.

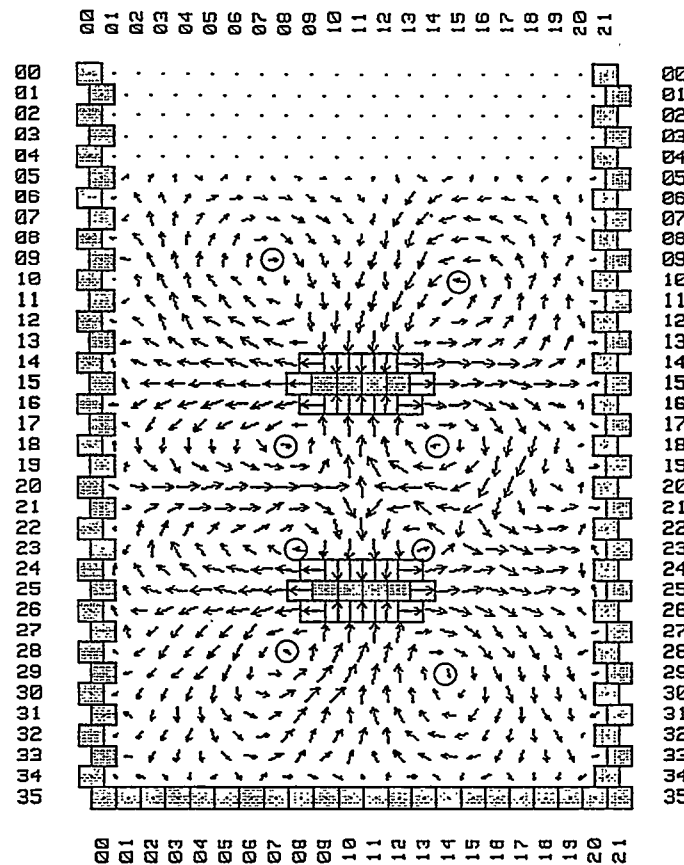
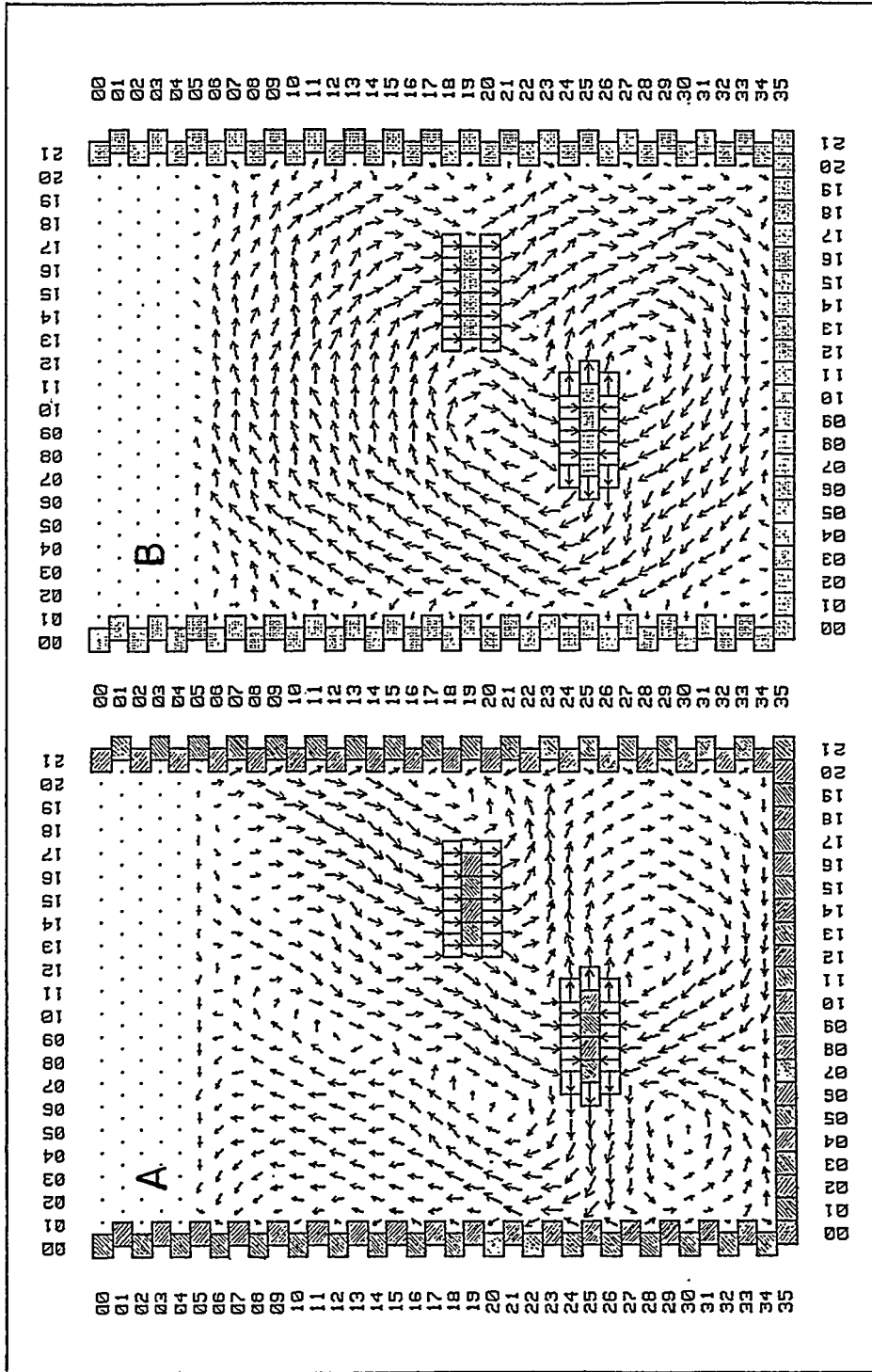


Fig. 7. As Fig. 6 but there are two impellers in the tank. The passive layer between the impellers can be seen clearly especially on the left. On the right the passive level is less clear (calculation is not fully developed). Also in the reality a similar phenomenon can be met. The centres of circulation are marked in figure.

Figs 8a and 8b (on the following page). A good example of a view of the dynamic simulation. A mixing tank with a radial (flat blade turbine - on down left) and axial (propeller - upper right) impeller. Fig. 8a depicts the result after 10 000 loops. It can be seen clearly that the radial impeller is dominant as in reality. Fig. 8b depicts the result after 50 000 loops. The axial impeller is dominating and causing a massive circular flow pattern corresponding to the reality.



Applicability

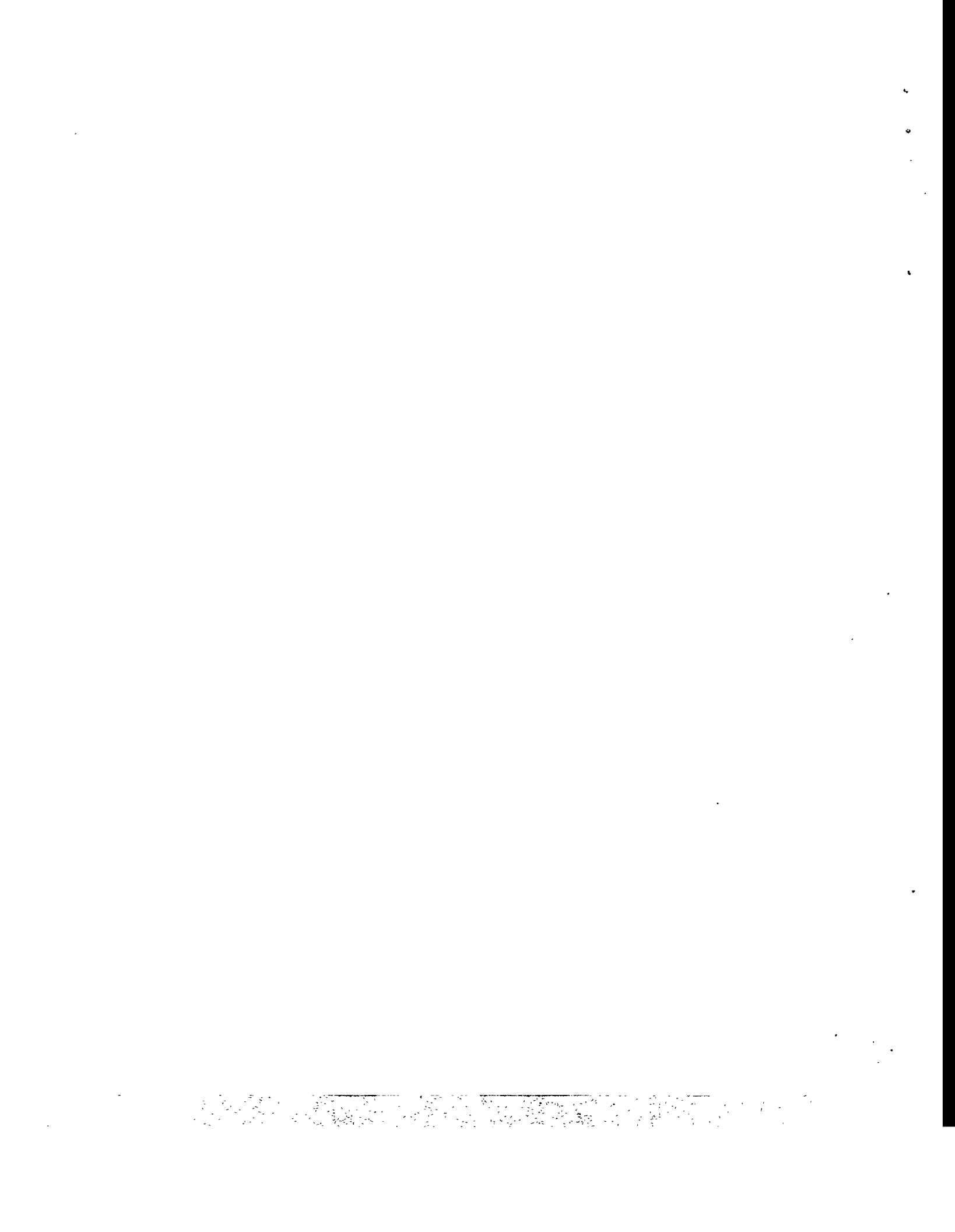
Important areas of application are expected to be the fluid dynamic calculations made when preparing tenders of equipment, rough analysis of operating processes, etc. Especially the cases where quick and reasonably accurate (but not exact) results are important starting points for design (e.g. selection of geometry). Also when it is necessary to estimate the dynamic behaviour of the flow patterns (e.g. selection of the stirrer type for a reactor). This is specially advantageous when the equipment geometry is different from conventional (e.g. special form of vessel or several different impellers in a same reactor) or when it is difficult to conclude the flow pattern.

Conclusion and future

The principle of the presented simulation method seems clearly promising. The approach is especially interesting due to the real time output of results, stochasticity and the possibility to change input data during the run. The method gives results which can be expected from experience. The simulated flow pattern is in motion corresponding to the real turbulence when the calculation goes on for a long time. The testing of the method has been done only with two-dimensional models.

The key questions in the further development of the method are the verification of feasibility of the method and the allocation of development resources. The development of the method into a practical tool requires considerable effort, since the promising results received are preliminary.

For Your Notes



Computer Simulation on a Hydrogen Fueled Rotary Engine

G. Fang and R.K. Green
Department of Mechanical Engineering
University of Canterbury
Christchurch, New Zealand

Abstract

When compared with other primary energy resources, hydrogen has many advantages. It is a clean, affordable and long-lasting fuel resource, which does not produce CO, CO₂ and hydrocarbons after combustion.

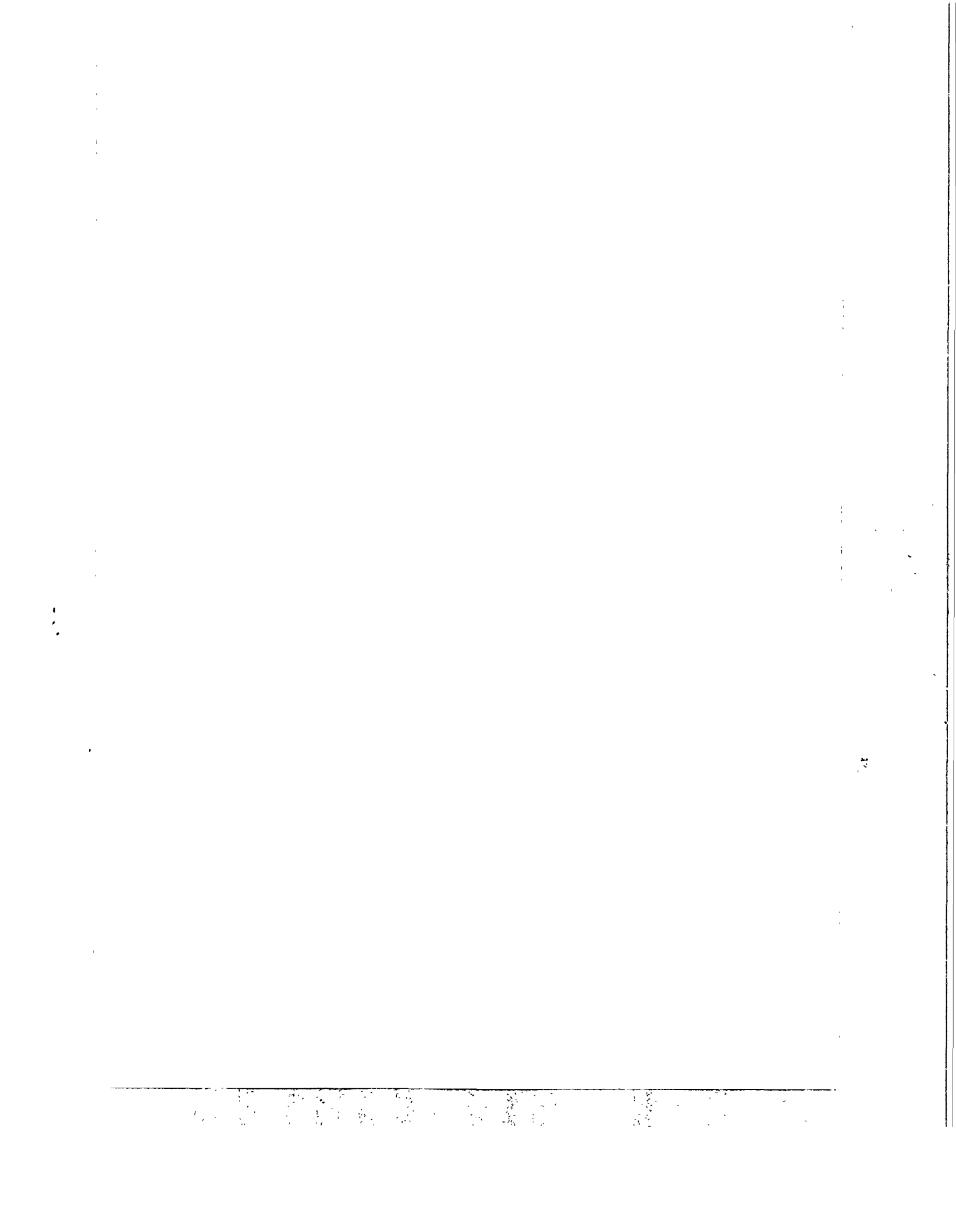
A computer simulation code is produced to predict the performance of a hydrogen fueled rotary engine. A multi-zone combustion model is developed for studying the combustion behaviors. The predicted pressures fit experimental pressures very well over a wide range of settings.

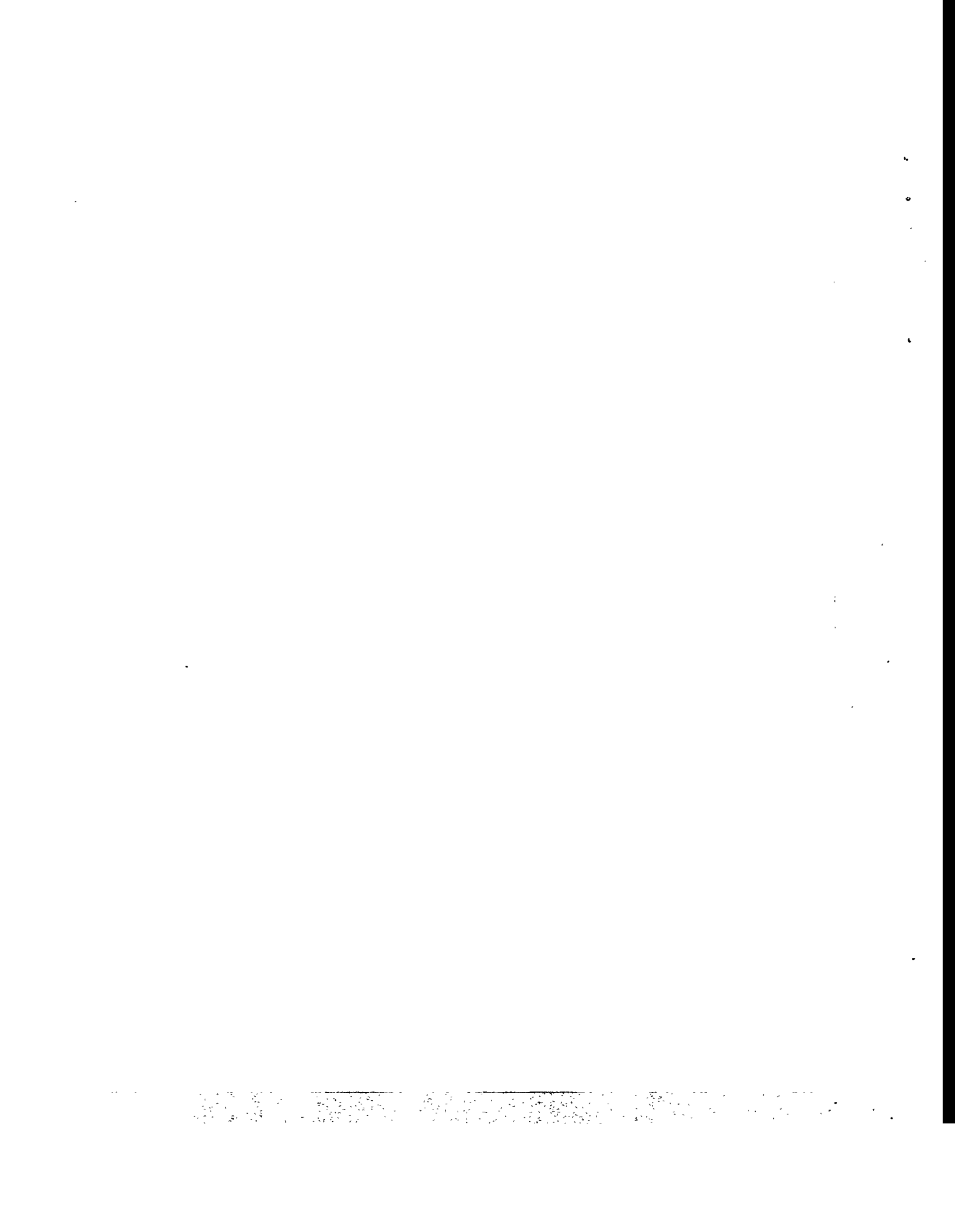
The flame propagation speed calculation is based on the data of fiber probe measurement; because of the high flame speed of hydrogen, the flame generated turbulence is included in the turbulence speed calculation. The results of different kinds of laminar speed formulas are compared with the experimental results.

The boundary layer of hydrogen fuel is much less than that of conventional hydrocarbon fuels, so the effects of heat transfer to the engine's performance is studied.

It is concluded that with the comparison of the predicted and experimental results the empirical factors can be chosen, and the model is a good tool to optimize the engine.

For Your Notes





SESSION 2
Combustion

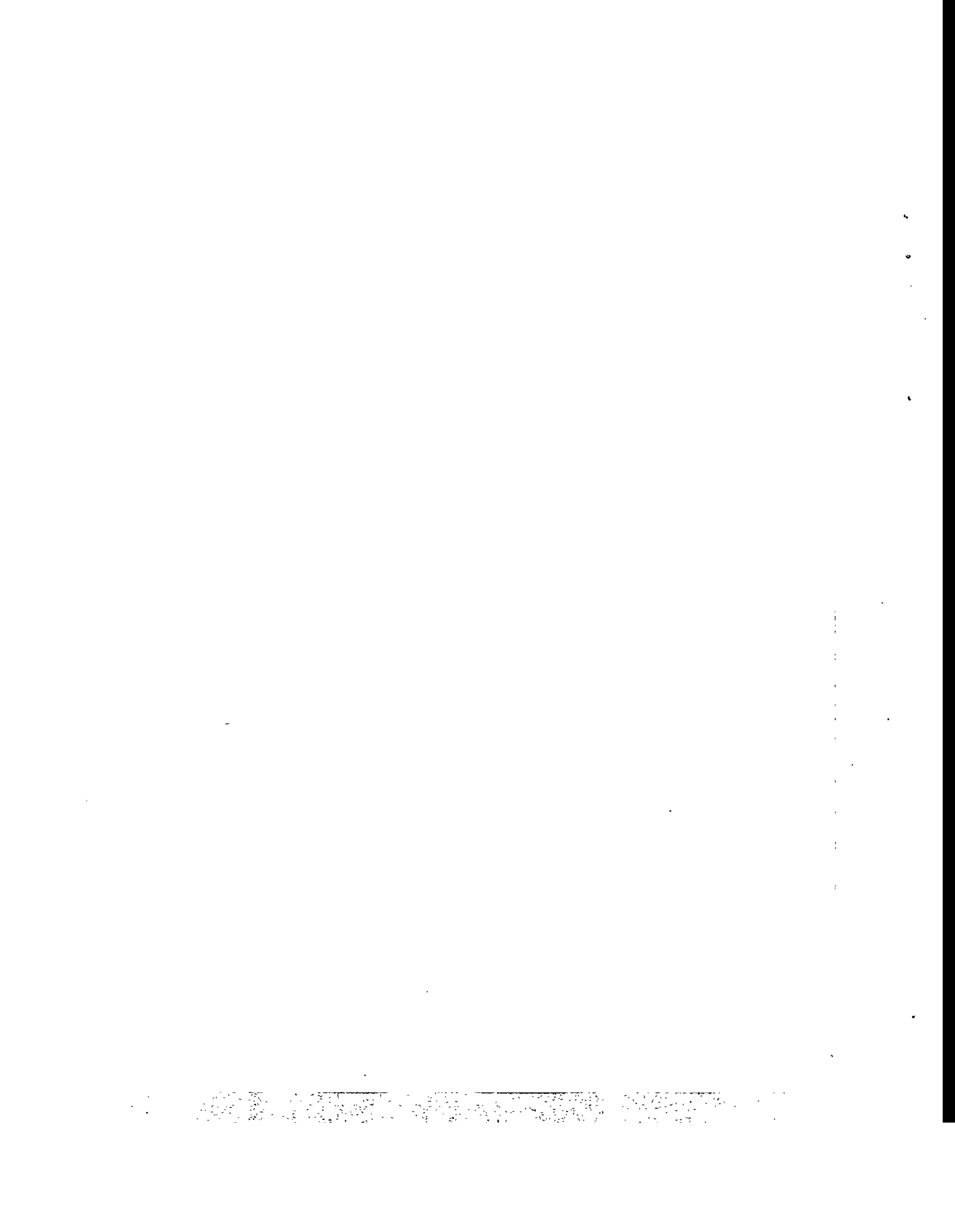


Invited Lecture

Challenges in Simulation of Combustion

Processes in Furnaces

M. Hupa, P. Kilpinen



Challenges in Simulation of Chemical Processes in Combustion Furnaces

Mikko Hupa and Pia Kilpinen
Åbo Akademi University
Department of Chemical Engineering
FIN-20520 Turku/Åbo, Finland

Abstract

The paper gives an introduction to some of the present issues and problems in treating the complex chemical processes in combustion. The focus is in the coupling of the hydrocarbon combustion process with nitrogen oxide formation and destruction chemistry in practical furnaces or flames. Detailed kinetic modelling based on schemes of elementary reactions are shown to be a useful novel tool for identifying and studying the key reaction paths for nitrogen oxide formation and destruction in various systems. The great importance of the interaction between turbulent mixing and combustion chemistry is demonstrated by the sensitivity of both methane oxidation chemistry and fuel nitrogen conversion chemistry to the reactor and mixing pattern chosen for the kinetic calculations. The fluidized bed combustion (FBC) nitrogen chemistry involves several important heterogeneous reactions. Particularly the char in the bed plays an essential role. Recent research has advanced rapidly and the paper proposes an overall picture of the fuel nitrogen reaction routes in circulating FBC conditions.

Helsinki University of Technology
3rd Colloquium on Process Simulation
12 - 14 June, 1996
Espoo, Finland

particle devolatilization stage and partly remain in the char residue (Boxes 1 and 2 in Fig. 1). The volatile nitrogen compounds will finally be converted to simple nitrogen species, typically ammonia, NH_3 , and hydrogen cyanide HCN. These two are the key "fixed nitrogen" compounds, which are readily oxidized to nitrogen oxides if suitable oxidation agents are present (Box 5, Fig. 1). In the case of staged combustion, some of these volatile fixed nitrogen species may be converted to molecular nitrogen (Box 4). The fuel nitrogen remaining in the char residue of the fuel particle may also form nitrogen oxide (Box 7) or molecular nitrogen (Box 6), depending on the conditions at which the char burning takes place.

In spite of the fact that many of the key processes governing the NO chemistry in combustion of solid fuels are well understood, lots of open questions and undone work still remain. Quantitative modeling of the nitrogen oxide processes in combustion is still very immature. Additional information is needed concerning details of the release of the fuel nitrogen, the rate of the conversion processes involved and, in particular, concerning the interaction between chemical processes and the turbulent mixing.

Fluidized bed combustion (FBC) systems have many special features as compared with, for instance, pulverized fuel (PF) firing, such as the relatively low temperature and intensive contact between gas and particles (bed material, char, limestone, etc.). These features make the nitrogen chemistry in FBC systems very different from the PF firing. Also, the fairly recent recognition of nitrous oxide, N_2O , as an important potential FBC emission and a "third" nitrogen oxide, has required - and will still require for some years to come - significant research work before all the details are well enough understood for an effective control of N_2O .

An additional challenge for in-furnace emission control is caused by the strong coupling between the various emission compounds. This is a general problem in all combustion systems but particularly sensitive in FBC. Tight control of one emission (e.g. NO) will very easily lead to an increase of another emission (e.g. CO, SO_2 , or N_2O), and, consequently, emission control in practical systems has become a fairly complicated optimization problem.

Potential new fuel conversion techniques based on pressurized combustion or pressurized gasification followed by combustion have raised increased interest in research concerning the influence of pressure on the fuel nitrogen chemistry in combustion.

The purpose of this paper is to give a short introduction to some of the present issues and problems of the nitrogen chemistry in combustion, by examples of the recent research. First, some central gas phase nitrogen reactions and schemes are shortly reviewed. Then, the interaction between gas mixing and chemistry is discussed taking the methane oxidation and fuel nitrogen oxidation chemistries as two examples. Finally, some recent results of the intense research on nitrogen oxide chemistry in FBC are presented and commented.

GAS PHASE REACTIONS

Our understanding of the gas phase nitrogen chemistry in combustion has advanced very rapidly during the past ten years. Extensive databases of the key elementary reactions are available, and for many of the reactions also the kinetic constants have been determined with some accuracy. These reaction schemes typically consist of several hundreds of elementary reactions.

The destruction and oxidation reactions of (simple) hydrocarbon compounds form the bases of these schemes. The schemes further contain reactions which describe:

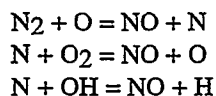
- oxidation of molecular nitrogen, N₂ ("thermal NO", etc.)
- nitrogen/hydrocarbon interactions ("prompt NO", reburning, etc.)
- oxidation of HCN and NH₃ ("fuel volatile NO", SNR, N₂O)

These reaction schemes and powerful computing software (CHEMKIN, etc.) have made it possible to start with detailed kinetic modeling of the nitrogen chemistry in hydrocarbon combustion. In spite of the fact that the identified reactions and the kinetic data are far from being complete, detailed kinetic modeling has already been quite successful in helping to solve some technically interesting nitrogen oxide chemistry problems.

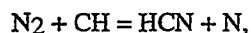
In this chapter we discuss some gas phase nitrogen chemistry issues using detailed kinetic modeling as a tool.

Fixation of the molecular nitrogen

Traditionally, fixation of molecular nitrogen has been described as a result of either "thermal NO":

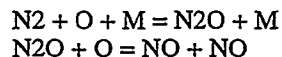


or "prompt NO":



where the HCN and N are further oxidized to NO.

Kinetic model calculations of NO formation from N₂ during oxidation of methane with air show clearly that thermal NO dominates, as expected, but it is interesting that the third mechanism "N₂O-NO" makes a significant contribution, too. The N₂O-NO is a mechanism where N₂ reacts with atomic oxygen and an energy absorbing third molecule, "M", forming N₂O. It is then this N₂O that will be converted to NO:



This N₂O-NO is usually not taken into account in the simple N₂ oxidation models, which only consider the thermal NO reactions. However, the lower the temperature, the

more significant the N_2O -NO is as compared with the thermal NO. In more accurate models for typical PF furnace conditions, the N_2O -NO should be included. (On the other hand, the description of the turbulent mixing and temperature fluctuations in the furnace or burner models has still been far too inaccurate to make the omission of the N_2O -NO a significant error so far.)

The thermal NO and the N_2O -NO are - for the sake of simplicity - described by one common reaction box Box 8 in Figure 1. The prompt NO route is described by the Box 3 combined with the HCN oxidation in Box 5.

Oxidation of the volatile nitrogen species

Oxidation of the volatile nitrogen species HCN and NH_3 has been subject to great research interest in the previous years. Figure 2 shows the most important reaction paths which convert the various nitrogen containing species into each other. The picture is quite complicated indicating that the fixed nitrogen species have many possible reaction routes. This implies, at least in principle, that there are good opportunities to control these reactions in practice by choosing suitable conditions in the furnace.

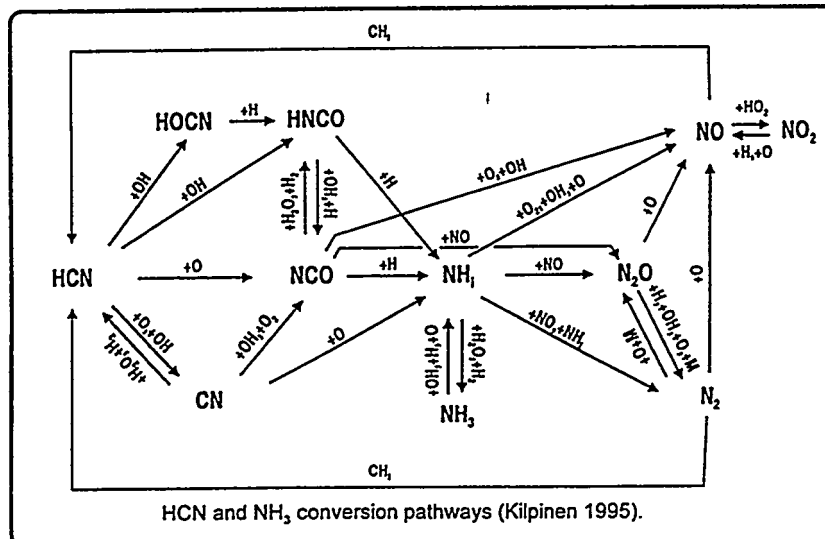


Figure 2 - Simplified scheme of the most important gas phase reactions of NO in combustion (Kilpinen 1995).

Figure 3A shows results of a kinetic calculation where a fuel gas containing HCN is burned at $850^\circ C$ (thus simulating combustion of the volatilized gases in the freeboard of a coal fired stationary FBC). At these conditions the HCN is rapidly (milliseconds) and quantitatively converted to NO. The figure also shows the sharp rise of the reactive radicals H, OH, and O during the first tenths of a millisecond.

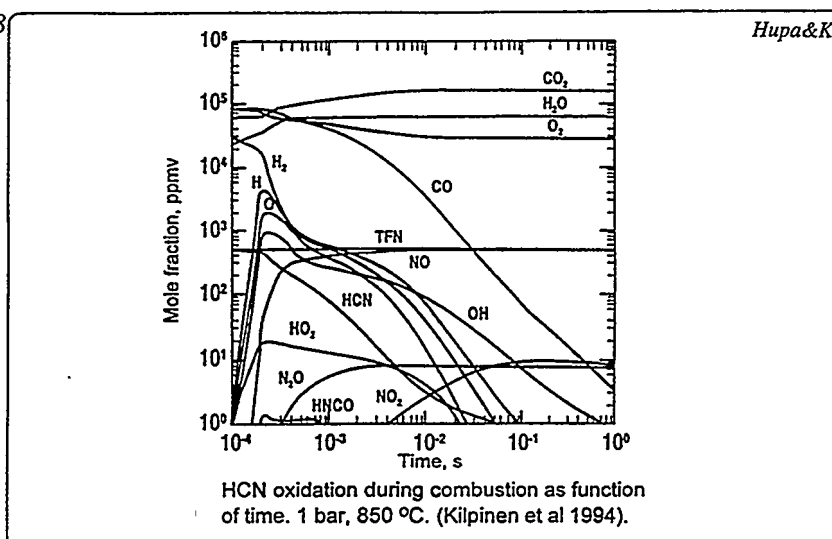


Figure 3 A - Predicted concentrations for gaseous species as a function of time in combustion of typical coal pyrolysis gas (Kilpinen et al., 1994). Calculation conditions: PFR, temperature 850°C. Gas concentrations at inlet (vol-%): 8 CO, 6 CO₂, 3 H₂, 2 H₂O, 0,05 HCN, 8 O₂, 73 N₂. Pressure 1 bar.

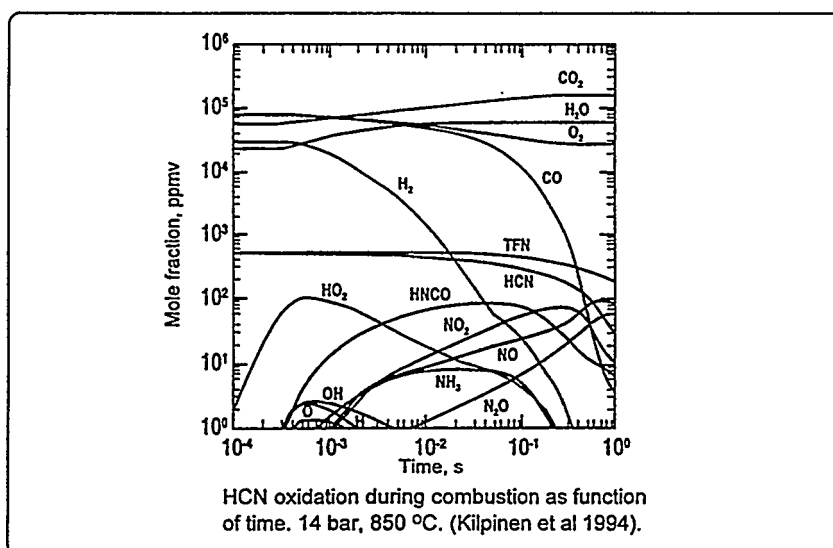
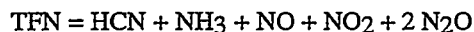


Figure 3 B - Predicted concentrations for gaseous species as a function of time in combustion of typical coal pyrolysis gas (Kilpinen et al., 1994). Calculation conditions: PFR, temperature 850°C. Gas concentrations at inlet (vol-%): 8 CO, 6 CO₂, 3 H₂, 2 H₂O, 0,05 HCN, 8 O₂, 73 N₂. Pressure 14 bar.

The "total fixed nitrogen" TFN is the total of all other nitrogen compounds except the molecular nitrogen. In practice:



TFN is a useful parameter when various nitrogen oxide minimization concepts ("low-NO_x" schemes) are studied. By staging the feed of air or/and fuel in the furnace, the TFN in the various zones can be lowered and this way the final NO_x level decreased.

In the case of Figure 3A, the TFN remains unchanged. The HCN is quantitatively converted to NO, and no N₂ is formed.

Figure 4 shows results of similar calculations presented as flow schemes. These schemes give a better picture of the chemical steps behind the HCN oxidation. At high temperatures (Figure 4A), HCN is converted via the radical NCO and several additional steps finally to NO. At lower temperatures (Figure 4B), this oxidation yields, besides NO, also significant amounts of N₂O and N₂. Ammonia is also very readily oxidized to NO. However, at lower temperatures the behavior of ammonia differs from that of the HCN. Ammonia oxidation even at low temperatures practically quantitatively leads to NO and N₂, and only negligible conversion of NH₃ into N₂O is found.

These results were originally presented as kinetic modeling data only. However, they have been later confirmed by laboratory measurements, and at present the oxidation of the volatile fuel nitrogen intermediate HCN at low temperatures is believed to be one major source of N₂O in FBC combustion (see below).

These results clearly show the complexity of the gas phase nitrogen reactions. But they also show the power of the detailed kinetic modeling. The main use of the detailed kinetic modeling is not that much in quantitative predictions of concentrations but in finding out the key reaction routes and in determining the influence of various parameters on these key reactions.

Pressure

The gas phase chemistry is influenced by the total pressure of the system. The elevated pressure implies higher molar concentrations of all the species present in the mixture, which naturally influences the rate of the overall process. However, total pressure may also change kinetic parameters for some of the reactions involving "third bodies", M . Also, some completely new elementary reactions, which are not taken into account in the present schemes for atmospheric pressure, may become significant when system pressure is increased.

In spite of these uncertainties, some first attempts have been made to apply detailed kinetic modeling also to combustion cases at high pressures. Figure 3B shows how the HCN oxidation chemistry may change from the atmospheric pressure case (Fig. 3A) when the total pressure is increased to 14 bar. Typically, in this particular case (850°C), radical levels are considerably lower at high pressures, which leads to slower overall oxidation rate of all the species, including the HCN. These interesting observations may have significance for example to the freeboard phenomena in pressurized fluidized bed combustion (PFBC), but they need still to be verified by laboratory measurements.

MIXING AND CHEMISTRY

One of the most difficult areas in combustion chemistry is associated with the concept of the chemical reactor. To be able to model the chemical processes in combustion, one needs - besides the chemical kinetic information as discussed in the previous chapter - detailed information on the reactor in which the reactions take place. In the model calculations presented above, the reactor in which the reactions were assumed to take place was either an ideal plug flow reactor PFR or a perfectly stirred tank reactor CSTR. In these ideal reactors the mixing pattern between the reactant and products is completely defined.

In a burner, furnace, or combustion chamber, the mixing pattern is usually not well defined, and no simple reactor can be directly applied as a basis for model calculations. This is not true only of whole furnaces but also of any calculation volumes in modern three dimensional furnace modeling. In the grid volumes, even in those with the highest turbulence, the mixing is far from perfect. The simple assumption of every grid volume forming, for example, a CSTR does not give good results when nitrogen chemistry is modeled.

The various proposed solutions to this "reactor problem", such as the eddy dissipation concept by Magnussen (Byggstøl et al. 1987, Magnussen 1989), are not discussed in this paper. However, it is worth stressing that, at the present stage of furnace modeling the understanding of the nitrogen chemistry mechanisms and kinetics is far ahead from the understanding of the mixing in the turbulent furnace flows.

To illustrate the importance of mixing on the nitrogen chemistry, we present some results of model calculations on the reduction of NO by secondary fuel injection with reference to the "reburning" technique. Figure 5 illustrates the principle of the reburning technique. The NO formed in the primary burning zone reacts in the reburn zone with the

hydrocarbon radicals produced by the added reburn fuel. This reaction produces HCN and NH_3 . Part of these fixed nitrogen intermediates then continue reacting with the remaining NO, thus yielding N_2 . This way the TFN can be decreased and, consequently, the final NO after the burn-out zone will be lower than the NO produced in the primary zone.

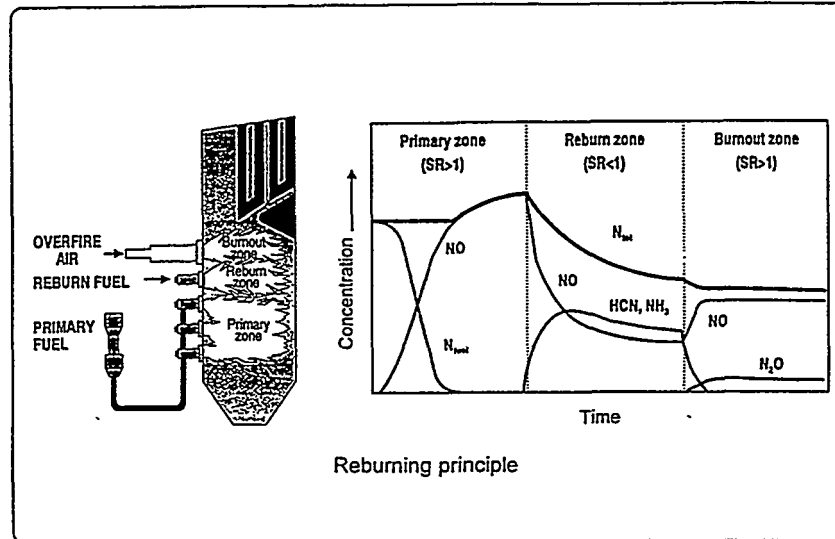


Figure 5 - Reburning principle.

The importance of the mixing mode with respect to the reburn chemistry is illustrated in Figure 6. In these model calculations, the reburn zone nitrogen chemistry is studied assuming a mixing pattern consisting of combined CSTR and PFR. Figure gives the reduction of the TFN as a function of the reburn zone stoichiometry (being proportional to the amount of reburn fuel) for various combinations of residence time splits between the two reactors. The total residence time is 400 ms in all three cases studied:

$$t(\text{CSTR}) + t(\text{PFR}) = 400 \text{ ms}$$

One case for the PFR reactor alone, i.e., $t(\text{CSTR}) = 0$, $t(\text{PFR}) = 400$ ms. Two cases with $t(\text{CSTR}) = 10$ ms, and $t(\text{CSTR}) = 100$ ms, respectively. The introduction of a CSTR before the PFR clearly improves the efficiency of the reburn process. Also, the optimum reburn stoichiometry is shifted to a higher number, implying that less reburn fuel would be required when the CSTR is introduced.

These few examples show how intimately the gas phase nitrogen chemistry in combustion is coupled with the mode of mixing, and how important it is to be able to describe the turbulent mixing processes in a reasonable way before any modeling of the nitrogen oxide formation in any practical systems is realistic.

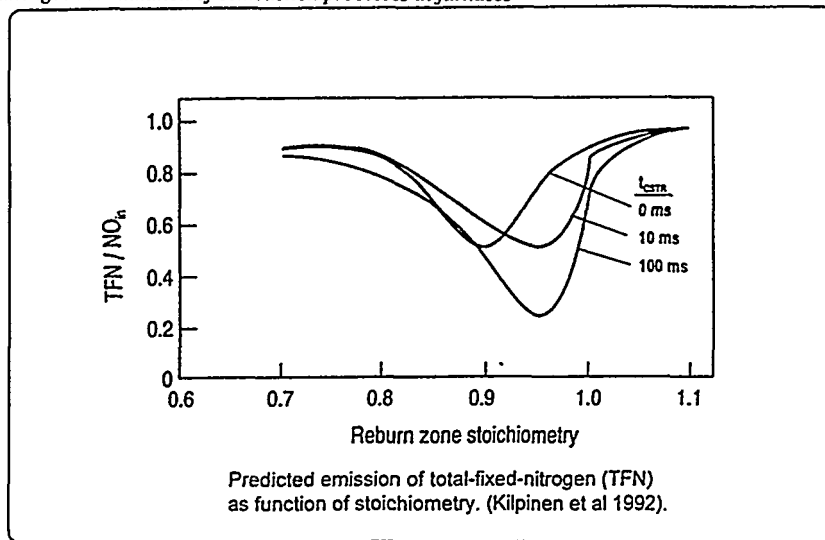


Figure 6 - Predicted change of total-fixed-nitrogen, TFN, in the reburn zone as a function of stoichiometry for CSTR+PFR approach (Kilpinen et al., 1990). Calculation conditions: $SR_1=1.1$, $[NO]_{1,out}=660$ ppm, $T_2=1700$ K, total residence time 400 ms. CSTR residence time 0 ms (solid line), 10 ms (dash-dot line) or 100 ms (dashed line).

FLUIDIZED BED COMBUSTION

Fluidized bed combustion chemistry is strongly influenced by the high concentration of solid particles present. Besides homogeneous gas phase reactions, a great number of heterogeneous gas-solid reactions play an important role in FBC. Our understanding of the nitrogen chemistry in the FBC has improved very significantly during the last five years only. One of the factors speeding up the recent research activities has been the nitrous oxide N_2O , which has been shown to be an important nitrogen intermediate and potential emission component in FBC.

Significant fundamental findings concerning the FBC nitrogen oxides have been made by detailed measurements in the 12 MW circulating FBC at the Chalmers University of Technology, Gothenburgh, Sweden. Vertical concentration profiles for nitrogen compounds along the centerline of the Chalmers furnace show many of the characteristic features of the FBC (Figure 7). Nitric oxide NO formation is very rapid and takes place immediately in the lower part of the furnace but then starts to decrease steeply towards the upper parts of the furnace. The ammonia NH_3 and hydrogen cyanide HCN both decrease to a fairly low level already at the low elevations in the furnace. The nitrous oxide N_2O is also primarily formed at the bottom of the furnace, but there is an ongoing increase of the N_2O when moving upwards. The trend for isocyanic acid HNCO is opposite to the one for the N_2O .

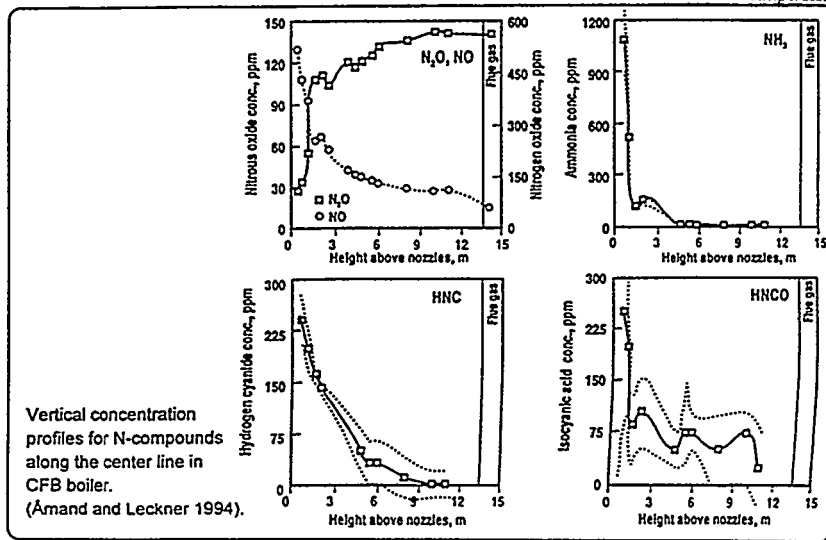
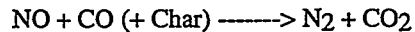


Figure 7 - Vertical concentration profiles for N-compounds along the centerline in CFB boiler. Fuel: bituminous coal (Åmand and Leckner 1994).

We have tried to summarize the most important fuel nitrogen reaction routes in FBC. Figure 8 shows a typical case for coal firing, Figure 9 for wood firing. Both diagrams contain the same principle reaction "boxes", but their significance is very different for the two different fuels. For coal, the volatile-N (Box 2, Figures 15 and 16) and char-N (Box 1) are roughly equally important; for wood, the volatile-N route is far more important.

For coal, the HCN oxidation route dominates the volatile-N conversion, and a significant fraction of the volatile-N will be converted to N_2O (Boxes 4 and 7 in Fig. 8). For wood, the NH_3 oxidation route dominates leading to NO with very little N_2O formed (Boxes 3 and 10 in Fig. 9).

For wood, the role of the char-N or char in general is very small. For coal, the char-N and the larger amounts of char in general, influence significantly the nitrogen chemistry. The char in the bed functions as an efficient catalyst for the reduction of NO to N_2 by reducing gases, mainly CO (Box 16 in Fig. 9):



This reaction explains the relatively sharp decrease in the vertical NO profile in Figure 7.

CONCLUSIONS

Understanding of the homogeneous gas phase combustion chemistry has advanced rapidly during the past several years and detailed kinetic modeling based on elementary reaction schemes has become a useful tool for identifying and studying the key reaction paths for nitrogen oxides formation or destruction in various systems.

The influence of the total pressure on these gas phase reactions is not fully clear, and more laboratory work is required to establish the kinetic parameters for the key reactions at high pressures.

The interaction between turbulent mixing and nitrogen chemistry remains the key problem in mathematical modeling of furnace processes. Many of the relevant nitrogen reactions are very sensitive to the reactor type and the mode of mixing. Today the bottleneck of the emission prediction from full scale furnaces is not that much lack of information concerning the details of the emission formation/destruction chemistry as lack of detailed understanding of the mixing in a turbulent furnace gas mixture.

Nitrogen chemistry in FBC involves several important heterogeneous reactions. Particularly the char in the bed plays an essential role. Recent research has made it possible to construct an overall picture of the many fuel nitrogen reaction routes at FBC conditions.

ACKNOWLEDGEMENTS

This paper was prepared as part of the activities in the Combustion and Gasification Research Program LIEKKI in Finland. Support from Ahlstrom Corporation, Tampella Power, Wärtsilä Diesel, the Ministry of Trade and Industry and the Academy of Finland is acknowledged. The authors also express their sincere thanks to the "SO_xNO_x" collaboration group within the Nordic Energy Research Program. Especially the many discussions with Prof. Bo Leckner and Dr. Lars-Erik Åmand at Chalmers University of Technology in Gothenburg and Dr. Peter Glarborg and Prof. Kim Dam-Johansen at the Technical University of Denmark have been essential inspirations for the thoughts presented in this paper.

References

- Byggstøyl, S., Lilleheie, N. I., Magnussen, B. F., "Strategy for Inclusion of Chemical Kinetics into the Eddy Dissipation Concept". *IX Task Leaders Meeting - Energy Conservation in Combustion*, IEA, 1987.
- Kilpinen, P., Hupa, M., Glarborg, P., Hadvig, S.: "Parametric Study of Natural Gas Reburn Chemistry Using Kinetic Modeling", *Report 90-7, Åbo Akademi University, Combustion Chemistry Research Group*, 1990.

Kilpinen, P. and Hupa, M.: "Homogeneous N_2O Chemistry at Fluidized Bed Combustion Conditions - A Kinetic Modeling Study", *Combustion and Flame*, 85 (1991), pp. 94-104.

Kilpinen, P., Glarborg, P., Hupa, M.: "Reburning Chemistry - A Kinetic Modeling Study", *Ind. Eng. Chem. Res.*, 31 (1992), pp. 1477-1490.

Kilpinen, P., Aho, M., Seetula, J., Hupa, M.: "Gas Phase Chemistry of NO_x and N_2O at Pressurized Combustion Conditions between Temperatures 700 and 1000°C", *Proc. 6th Int. Workshop on Nitrous Oxide Emissions*, Turku, 7-9 June, 1994.

Kilpinen, P.: "Typen oksidien muodostuminen ja hajoaminen", *Poltto ja palaminen - polttoteknikkakäsikirja*, Suomen IFRF osasto ("Formation and Destruction of Nitrogen Oxides", *Handbook on combustion, Finnish IFRF*, in Finnish), in press, 1995.

Magnussen, B. F., "The Eddy Dissipation Concept". *XI Task Leaders Meeting - Energy Conservation in Combustion*, IEA, 1989.

Åmand, L-E. and Leckner, B.: "Formation of N_2O in a Circulating Fluidized Bed Combustor", *Energy and Fuels*, 7, 6 (1993), pp. 1097-1107.

Åmand, L-E. and Leckner, B.: "Homogeneous and Heterogeneous Reactions for Formation and Destruction of N_2O - Results from the 12 MW CFB Boiler at Chalmers", *Proc. 6th Int. Workshop on Nitrous Oxide Emissions*, Turku, 7-9 June, 1994.

For Your Notes

.....

Modelling of local extinction and reignition of the flame

A. Brink, P. Kilpinen, M. Hupa
Åbo Akademi University
Combustion Chemistry Research Group
FIN-20520 Turku, Finland

L. Kjälman
Technical Research Centre of Finland
VTT Energy
P.O.Box 1604
FIN-02044 VTT, Finland

K. Jääskeläinen
Imatran Voima Oy
FIN-01019 IVO, Finland

Abstract .

The influence of the relations between the chemical time scale and the turbulent time scale on local extinction in turbulent flames has been studied. The results from the numerical investigation of a non-swirling flame in a sudden-expansion combustor was compared with measurements and computations reported in the literature. The turbulence-chemistry interaction was modelled using the Eddy-Dissipation Concept (EDC). In the study, different turbulent time scales were used; the Kolmogorov related time scale proposed in the EDC model and two turbulent time scales related to k/ϵ . The chemical time scale has been obtained from a model based on calculations with a comprehensive chemical reaction scheme. The results indicate that the Kolmogorov related time scale of the EDC model is too short to be used as an extinction criterium. The two k/ϵ related time scales both resulted in a closer agreement between the numerically obtained and the measured results. The result indicates that the time scale used in the EDC model should be further investigated before confident results from modelling of flows with extinction effects can be obtained.

Helsinki University of Technology
3rd Colloquium on Process Simulation
12 - 14 June, 1996
Espoo, Finland

INTRODUCTION

Flows, where extinction occurs, are of practical and theoretical interest. The practical aspect may deal with fuel consumption, stability and security. From the theoretical point of view, such flows, show a strong interaction between turbulence and chemistry and are an excellent environment for testing of turbulence-chemistry interaction models. Hence, several studies deal with the problem of calculating the lift off or the blow off velocity of flames¹⁻⁵.

For the flamelet approach⁶, local extinction is of special importance since this phenomenon restricts the use of the flamelet model. Here, local extinction is modelled comparing a critical stretch rate with the local stretch rate. The local stretch rate can be taken proportional to the scalar dissipation rate or to the strain rate of the eddies.

Together with the Eddy-Dissipation Concept⁷ (EDC) an approach has been used where the Kolmogorov related time scale of the EDC model is compared to a chemical one^{1,8}.

In the probability density function (PDF) approach⁹, the extinction modelling is related to the mixing model. Especially outside the flamelet region the mixing rate is often assumed to be proportional to k/ϵ , where k is the kinetic energy of turbulence per unit mass and ϵ its dissipation rate.

More recently, direct numerical simulation (DNS) of turbulent reacting flows has been used to study extinction^{10,11}. The results from the DNS show that extinction or quenching of the flame is an extremely complex process. The result indicates that the vortices of the Kolmogorov size have, in general, a life time too short to effect the flame, although they are associated with the highest strain rates¹⁰.

EDC is a model for turbulence-chemistry interaction and with a relatively small computational effort, it makes the incorporation of multi-step chemistry possible. The characteristic time scale describing the residence time in the fine structure in the model is closely related to the Kolmogorov time scale. Results obtained with other models indicate that the extinction effect is overpredicted if not a longer time scale is used^{2,10}. However, earlier work with the EDC model has shown good agreement between the measurements and the computationally obtained result^{1,4}.

The purpose of this study was to investigate which turbulent time scale should be compared with the chemical time scale when predicting local extinction. The chemical time scale has been obtained with a model based on calculations with a comprehensive reaction mechanism. The effect of the reaction scheme is also briefly discussed. The work presented here is a part of the development of the computational environment Ardemus¹² of VTT Energy and Imatran Voima Oy.

THEORY

Combustion model

In the present work, the turbulence-chemistry interaction was modelled using the EDC method⁷. EDC is based on the assumption that the reactions occur in regions where the dissipation of turbulent energy occurs. It is also assumed that these regions are concentrated to isolated regions occupying only a fraction of the fluid. Further, the size of these fine structure regions is assumed to be of the Kolmogorov length scale in one or two directions.

Using these assumptions, expressions can be set up giving the fraction of the fluid consisting of fine structures. E.g., the fluid can be divided into two parts; a reacting one having a certain composition and temperature and a non-reacting one, referred to as the surrounding, having another composition and temperature. Using similar arguments as when deriving the fraction of the fluid consisting of fine-structures, a time scale for these fine-structures can be derived. This characteristic time of the fine structures is closely related to the Kolmogorov time scale and has the value $0.41(\nu/\epsilon)^{1/2}$, where ν is the kinematic viscosity. In the EDC model, the reactions are assumed to occur at perfectly stirred reactor conditions in the fine structure.

Fuel chemistry

To keep the computational demand at an acceptable level, a simplified description of the reaction kinetics was used. Earlier studies¹³ has shown that a two-step formulation correctly describes the overall reaction rate in a satisfactory way. However, at fuel rich conditions, the omission of H_2 as an intermediate gives rise to an overprediction of the CO level. At the same time, the CO_2 concentration is underpredicted whereas the H_2O concentration is overpredicted. In order to improve

the description, a reaction scheme including CO and H₂ where the final water-shift equilibrium is taken into account has been used¹³. The computational effort is in this way still kept at its minimum.

Although the simplified description of the reaction kinetics works, short residence times possess a problem. To obtain a description as accurate as possible of the chemistry at the extinction point, a separate model was used. The model consists of a simple expression and is based on calculations using a comprehensive mechanism. A closer description of this model can be found in Appendix.

Extinction model

In the flow simulations the chemical time scale obtained using the model described in Appendix was compared with a local turbulent time scale. If the turbulent time scale was shorter than the chemical one, the flow was assumed to be extinguished. Otherwise the reaction rate given by the chemical mechanism described above was used.

Apart from the residence time of the fine structure reactors in the EDC model, two more turbulent time scales were used. Both these time scales are related to the bulk mixing time and are proportional to k/ϵ . They are $0.09k/\epsilon$ and $4k/\epsilon$. The turbulent quantities needed when calculating the turbulent time scales were obtained using a two-time scale turbulence mode¹⁴.

Radiative heat transfer

Radiative heat transfer within the chamber was computed with the built-in four flux model of Phoenix. The local absorption coefficient was determined from the composition of the gas and from modelled soot concentration¹². In the simulations it was assumed that no loss of heat through radiative heat transfer took place.

SUDDEN-EXPANSION COMBUSTOR

A gaseous jet flame in a cylindrical sudden expansion combustion chamber measured by Lewis and Smoot¹⁵ was used to examine the extinction model. The combustor is shown schematically in Fig. 1. The walls of the combustion chamber are insulated. Fuel and air enter the chamber through coaxial straight pipes. The fuel and air

streams are non-swirling. In the experiment the fuel was mixed with a small amount of argon. The mixture consisted of methane (84.31 vol-%), ethane (7.09 vol-%), hydrogen (0.09 vol-%), and inert components. The measured velocities at the inlets were 21.3 m/s for the fuel and 34.3 m/s for the air. The corresponding temperatures were 300 K for the fuel and 589 K for the air, respectively.

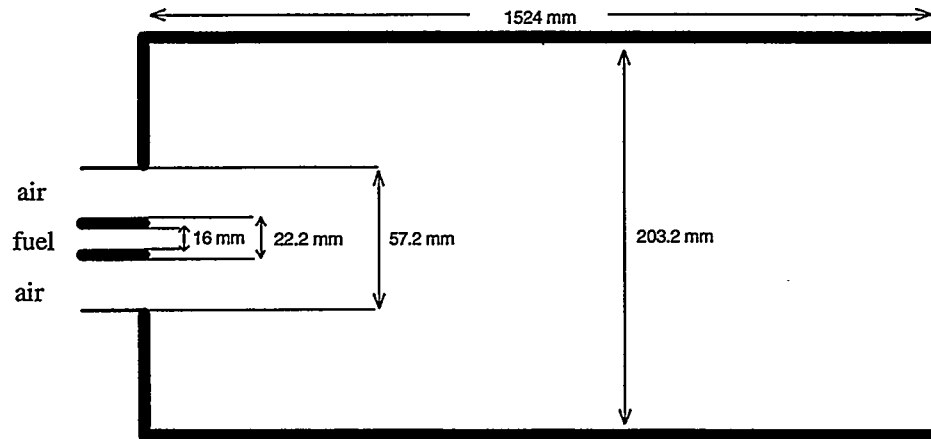


Fig. 1. The cylindrical sudden expansion combustor chamber. The chamber ends in a contraction and an exit pipe of diameter 104 mm (not shown).

The case defined above was analysed numerically with the computational environment Ardemus¹² which uses the commercial Phoenics program to solve the flow equations. A 2D representation was used. The computational grid consists of unevenly spaced cells. Altogether 47 cells in the radial direction times 223 cells in the axial direction were used. Within the first 600 mm of the chamber, 150 of the 223 cells in the axial direction were located.

RESULTS

The air and fuel jets enter the combustion chamber and mix and burn in a mixing-layer. The flow is dominated by axial velocities but an external recirculation zone is formed in the front corner region of the chamber.

Fig. 2 shows the computed temperature field in a case without extinction and in a case where local extinction was computed comparing a turbulent mixing time related to the break-up time of the eddies, i.e. $4 k/\epsilon$. The chemical time was obtained using the model described in Appendix. It can be noted that the flame is lifted off when extinction is taken into account. This can also be seen in Fig. 3, which compares the measured results of Lewis and Smooth¹⁵ with the numerically obtained ones. The temperature profiles are taken at a axial distance of 95 mm from the front wall of the chamber. In the case with no extinction the combustion starts close to the inlet pipe and causes a peak in the radial temperature profile. The result obtained with the Kolmogorov scale, i.e. $0.41(\nu/\epsilon)^{1/2}$, as the turbulent time in the extinction condition is also shown in Fig. 3.

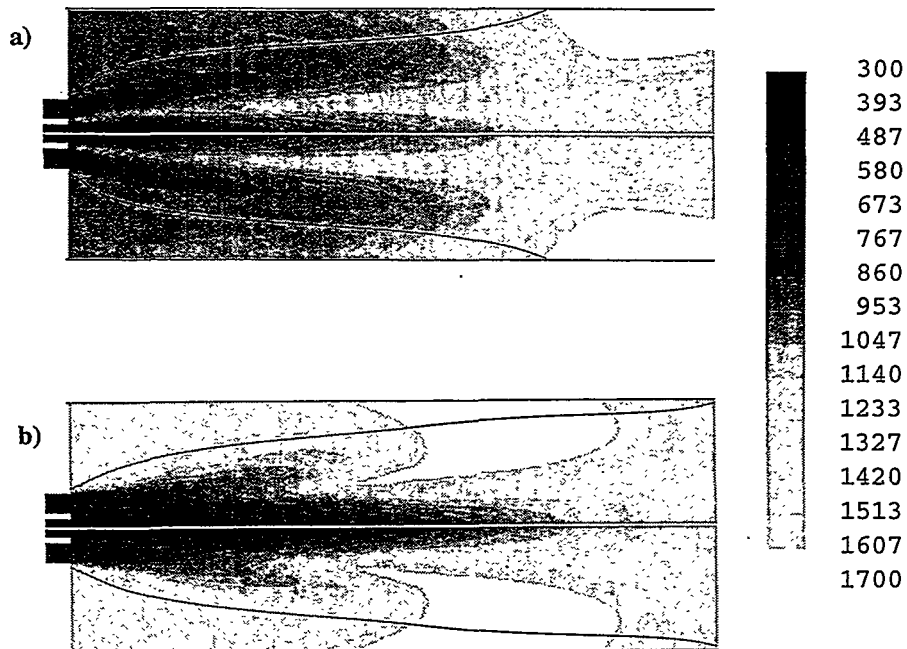


Fig. 2. Computed temperature (K) field and boundary of external recirculation zone for a gaseous jet flame in the sudden expansion combustion chamber. Only the front part of the chamber is shown. a) Result without an extinction condition. b) Result with local extinction computed with the mixing time $4 k/\epsilon$ as the turbulent time scale.

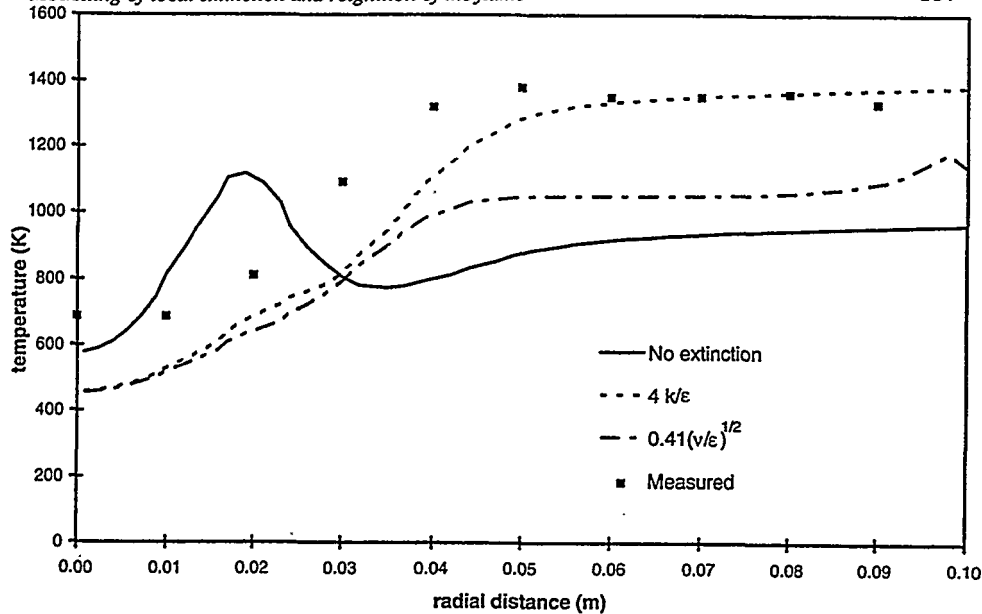


Fig. 3. Computed and measured radial temperature profiles at the axial distance of 95 mm from the front wall of the combustion chamber.

DISCUSSION

The flow in the combustion chamber is dominated by the axial flow. However, correct predictions of the exact positions of the recirculation zone formed in the corners in the front of the burner are of great importance and may be sensitive to disturbance. The coaxial fuel and air pipe are straight for 600 mm before entering the reactor. This justifies the assumption of fully developed pipe flow as boundary condition. Gran⁵ has studied this case in some details and points out some uncertainties in the measurements. He concludes that there exist some inconsistency and that the temperature measurements should be more reliable than the measurements of the composition at the measurement points.

The high temperature level closer to the outer wall of the chamber is due to the recirculation of the hot combustion products. In the case with no extinction, the length of the external recirculation zone is too short to bring enough hot combustion products towards the front area of the chamber. However, when extinction described with a mixing based turbulent time is included in the computation, the radial temperature profile at a axial distance of 95 mm has a shape similar to that obtained

in the experiments. Also the values closer to the outer wall correspond to the measurements. The computed lower temperature values closer to the centerline are according to Gran⁵ probably due to different air and fuel temperatures at inflow compared with those used in the computations due to heat conduction through the wall of the fuel inlet pipe.

The results obtained in the present work indicate that the turbulent time used in the extinction criterium should be of the order of eddy break-up time rather than based on the Kolmogorov time scale. Profiles of temperature and concentrations of the main species at other cross sections also support this finding. This is also supported by results obtained from the DNS of the interaction of a vortex pair with the flame¹⁰. The DNS indicates that vortices of the Kolmogorov scale have a life time too short to quench the flame. Only for weakly turbulent flames, the Kolmogorov scale should affect the extinction.

Gran et al.^{4,5} have simulated the same case earlier. They have used both a single irreversible reaction as well as a detailed chemical scheme for combustion together within the EDC model. For the case where no extinction is taken into account, our computations also show a peak in the radial temperature profile.

In a study, where a single step irreversible reaction chemical scheme was used, Gran et al.⁴ determined the chemical time from a separate modelling study of methane in air⁸. When we used a turbulent time scale related to the break-up rate of eddies, we obtained a similar result as they for the radial temperature profile at a axial distance of 95 mm from the front wall. However, in their analysis, the Kolmogorov related residence time of the EDC was used in the extinction criterium. The use of a single step chemical scheme for combustion leads to a locally higher heat release and higher temperature than the use of a chemical scheme with CO and H₂ as intermediate species. A higher temperature makes the chemical time shorter and the Kolmogorov time longer and, consequently, the extinction condition is satisfied in a smaller region. Such a behaviour of the flame could be found also in our work if a single step chemical scheme was used.

In a study⁵ where a comprehensive reaction mechanism was used, Gran obtained reasonable agreement between the measured and the calculated temperatures. Here, no separate model giving the chemical time is needed. Our results, obtained using the Kolmogorov related time scale resulted in an overprediction of the extinction effect,

and are not in agreement with those of Gran. However, qualitatively, our results when an eddy break-up related time scale was used were similar to those of Gran. The reason for this discrepancy is unclear.

The present study indicates that the turbulent time scale, related to the Kolmogorov time scale, used in the EDC model results in an overprediction of the lift off of the flame entering a sudden-expansion combustor. Better agreement between measured and numerically obtained results are obtained when a time scale proportional to k/ϵ is used. This finding is also supported by results from DNS¹⁰. In this study both the turbulent time $4k/\epsilon$ as well as $0.09k/\epsilon$ resulted in comparable agreement. However, in the studies referred to above^{4,5} a the Kolmogorov related time scale have been used with success. Conceptually, the use of a mixing time related to the break-up of eddies is not fully in agreement with the present basis of the EDC model. The conclusion is that further investigation of the turbulent mixing time in the EDC model is needed before highly turbulent flames can be modelled confidently. An example of such a study is that of Karlsson and Chomiak¹⁶ who used the geometrical mean of the eddy break-up time and the Kolmogorov time.

SUMMARY

A simple extinction condition of the flame based on the comparison of a chemical time and a characteristic turbulent time was applied to a jet flame. The results indicate that the turbulent time used in the extinction criterium should be of the order of eddy break up time, i.e., proportional to k/ϵ , rather than based on the Kolmogorov scale. The proper turbulent time seems, however, to depend on the chemical scheme used in the computation. Conceptually, the use of a mixing time related to the break-up rate of eddies is not fully in agreement with the present basis of the EDC model. Further investigation of the time scales of the reacting part of the fluid in the EDC model is needed.

ACKNOWLEDGEMENT

Additional funding from the Finnish National Combustion and Gasification Research Program LIEKKI 2, the Finnish National CFD-Technology Programme, and the Academy of Finland is acknowledged.

REFERENCES

1. Byggstøyl, S., and Magnussen, B. F., A Model for Flame Extinction in Turbulent Flow, Fourth Symposium on Turbulent Shear Flows, 7 p., 1983.
2. Sanders, J. P. H., and Lamers, A. P. G. G., Modelling and Calculation of Turbulent Lifted Diffusion Flames, *Combust. Flame* 96, pp. 22-33, 1994.
3. Norris, A. T. and Pope, S. B., Modeling of Extinction in Turbulent Diffusion Flames by the Velocity-Dissipation-Composition PDF method., *Combust. Flame* 100, pp. 211-220, 1995.
4. Gran, I. R., Melaan, M. C., and Magnussen, B. F., Numerical Simulation of Local Extinction Effects in Turbulent Combustor Flows of Methane and Air, Twenty-Fifth Symposium (Int.) on Combustion, The Combustion Institute, pp. 1283-1291, 1994.
5. Gran, I. R., Mathematical Modeling and Numerical Simulation of Chemical Kinetics in Turbulent Combustion, *NTH* 1994:49, 229 p., 1994.
6. Peters, N., Laminar Diffusion Flamelet Models in Non-Premixed Turbulent Combustion, *Prog. Energ. Combust. Sci.* 10, pp. 319-339, 1984.
7. Magnussen, B. F., Modeling of NO_x and Soot Formation by the Eddy Dissipation Concept, 1st Topic Oriented Technical Meeting of IFRF. Amsterdam, The Netherlands, 20 p., 1989.
8. Lilleheie, N. I., Byggstøyl, S., Magnussen, B. F., Kilpinen, P., and Hupa, M., Modeling and Chemical reactions. Development and Test of Reduced Chemical Kinetic Mechanism for Combustion of Methane, NGC-report, Nordic Gas Technology Centre, Hørsholm, Denmark, 1991.
9. Pope, S.B., PDF Methods for Turbulent Reactive Flows, *Prog. Energy Combust. Sci.* 11, 119-192, 1985.

10. Meneveau, C., and Poinso, T., Stretching and Quenching of Flames in Premixed Turbulent Combustion, *Combust. Flame* 86, pp. 311-322, 1991.
11. Lee., Y. Y., and Pope, S. B., Nonpremixed Turbulent Reacting Flow near Extinction, *Combust. Flame* 101, pp. 501-528, 1995.
12. Kjaldman, L., Numerical simulation of combustion and nitrogen pollutants in furnaces. Espoo, Finland, Technical Research Centre of Finland, VTT publications 159, 132 p., 1993.
13. Brink, A., Kilpinen, P., Hupa, M., Kjaldman, L., and Jääskeläinen, K., Fuel Chemistry for Computational Fluid Dynamics, 2nd Colloquium on Process Simulation, Helsinki University of Technology Report TKK-V-B102, 19 p., 1995.
14. Kim, S-W., and Chen, C-P., A multiple-time-scale turbulence model based on variable partitioning of the turbulent kinetic energy spectrum. *Numerical Heat Transfer, Part B*. Vol 16, No. 2, pp. 193-211., 1989.
15. Karlsson J. A. J. and Chomiak, J., Physical and Chemical Effects in Diesel Spray Ignition, 21st Congress of CIMAC, 21 p., 1995.

APPENDIX

Close to extinction, global or simplified reaction schemes may not provide an adequate description of the chemistry. To properly describe the chemistry at conditions close to extinction, radical reactions need to be taken into account. Unfortunately the use of a comprehensive reaction scheme is not practical in CFD modelling. To solve this problem, it has been suggested that a constant chemical time at which extinction occurs could be used¹. A more complex description has also been proposed where the extinction time has been calculated as a function of stoichiometry and inlet temperature for a mixture of methane and air². However, if extinction occurs, partly burned fuel, which behave differently from the pure hydrocarbon fuel, will be present. Direct numerical simulations of turbulent reacting flows have shown that dilution of the fuel mixture is important to take into account³.

To investigate the extinction behaviour at a broader variety of conditions, a study was made where the fuel composition as well as the dilution with product gases were taken into account. Two base mixtures were considered. The first one consisted mainly of methane whereas the other one consisted mainly of carbon monoxide. The mixtures were diluted with a product gas consisting of CO₂ (18 vol-%), H₂O (12 vol-%) and N₂ (70 vol-%). Ten different degrees of dilution were considered, the extremes being pure fuel and a fuel-product gas mixture consisting of 90% product gas. The extent of dilution is given by

$$D = 1 - \frac{(X_{\text{CO}_2} + X_{\text{H}_2\text{O}} + X_{\text{N}_2} - 3.762X_{\text{O}_2})}{\left(1 + 4.762 \frac{(1-\lambda)}{\lambda} X_{\text{O}_2}\right)}$$

where X is the mole fraction.

The air ratio, λ , was also taken into account. Here too, ten different air ratios were considered ranging from 0.1 to 10.0. All in all, 200 different mixtures were considered. To account for the strong temperature dependence on the chemistry, four different inlet temperatures to the perfectly stirred reactor were used; 300K, 500K, 700K and 900K.

Each case was calculated as a function of residence time in the perfectly stirred reactor. Then the critical residence times at which extinction occurred were fitted to a mathematical expression. To obtain a model as simple as possible, the parameters were expressed as a function of inlet temperature. The resulting expression is

$$\log_{10}(\tau) = - \left(\max \left(0, b^2 \left(\frac{D}{c} - d - \frac{1}{(a_0 + k_a \log_{10} \lambda)^2} (\log_{10} \lambda)^2 \right) \right) \right)^{1/2}$$

The suggested expressions for the temperature dependent parameters are given below:

$$a_0 = a_{00} + a_{01}T$$

$$k_a = k_{a0} + k_{a1}T$$

$$b = b_0 + b_1T$$

$$c = c_0 + c_1T$$

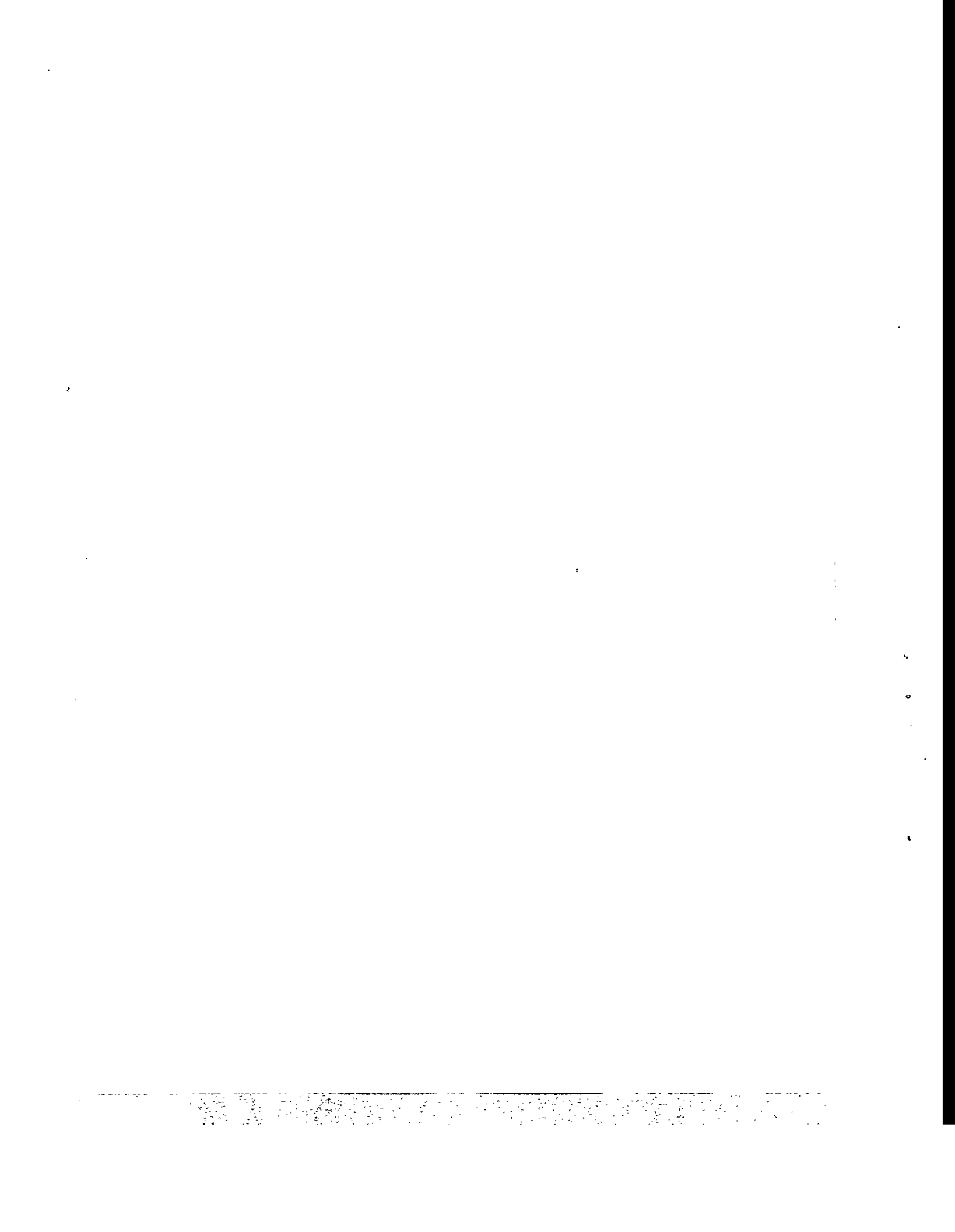
$$d = d_0 + d_1T + d_2T^2$$

The parameters were fitted using Marquardt's method. The procedure was done separately for the two base mixtures. During the modelling, the proper extinction time is obtained by means of interpolation using a parameter F that describes the composition of the fuel through its CO-content.

References

1. Byggstøyl, S., and Magnussen, B. F., A Model for Flame Extinction in Turbulent Flow, Fourth Symposium on Turbulent Shear Flows, 7 p., 1983.
2. Lilleheie, N. I., Byggstøyl, S., Magnussen, B. F., Kilpinen, P., and Hupa, M., Modeling and Chemical reactions. Development and Test of Reduced Chemical Kinetic Mechanism for Combustion of Methane, NGC-report, Nordic Gas Technology Centre, Hørsholm, Denmark, 1991.
3. Meneveau, C., and Poinso, T., Stretching and Quenching of Flames in Premixed Turbulent Combustion, *Combust. Flame* 86, pp. 311-322, 1991.

For Your Notes



**Modelling of chalcopyrite oxidation
reactions in the Outokumpu flash smelting process**

Tapio Ahokainen, Ari Jokilaakso
Laboratory of Materials Processing and Powder Metallurgy
Helsinki University of Technology
FIN-02150 Espoo, Finland

Abstract

A mathematical model for simulating oxidation reactions of chalcopyrite particles together with momentum, heat and mass transfer between particle and gas phase in a flash smelting furnace reaction shaft is presented. In simulation, the equations governing the gas flow are solved numerically with a commercial fluid flow package, Phoenix. The particle phase is introduced into the gas flow by a Particle Source In Cell (PSIC) - technique, where a number of discrete particles is tracked in a gas flow and the relevant source terms for momentum, mass, and heat transfer are added to the gas phase equations.

The gas phase equations used are elliptic in nature and the fluid turbulence is described by the (k - ϵ)-model. Thermal gas phase radiation is simulated with a six-flux radiation model. The chemical reactions of concentrate particles are assumed to happen at two sharp interfaces, and a shrinking core model is applied to describe the mass transfer of chemical species through the reaction product layer. In a molten state, the oxygen consumption is controlled by a film penetration concept. The reacting concentrate particles are a mixture of chalcopyrite and silica. Also a certain amount of pure inert silica is fed to the process as flux.

In the simulations the calculation domain includes the concentrate burner and a cylindrical reaction shaft of an industrial scale flash smelting furnace. Some examples about the simulations carried out by the combustion model are presented.

INTRODUCTION

The flash smelting process /1/, developed by Outokumpu company of Finland, is widely used throughout the world for copper production, accounting more than 40% of global capacity for primary copper production. It is based on the utilisation of the heat of oxidation reactions of sulfidic concentrates. These reactions take place in a downwards flowing turbulent gas-solid suspension and they are very fast and efficient due to the high surface-to-volume ratio of the fine concentrate particles. The feed mixture in the flash smelting process (concentrates, flux, reverts, and the process gas) is fed through the concentrate burner into the reaction shaft. Then, the concentrate particles react with gas phase to a predetermined oxidation degree. After the reaction shaft, the particle-gas suspension flows to the settler, where the particles/drops separate from the gas and form slag and matte layers on the bottom of the settler. The gases continue to the uptake, through which they flow to a waste-heat boiler.

One of the few pioneers of mathematical modeling of metallurgical processes was S. Ruottu who simulated the Outokumpu flash smelting process already in the mid-1970s /2,3/. That study was not continued, however, perhaps because the time had not yet come for modeling. During the 1980s Themelis et al. /4,5/ and Sohn and his group /6-10/ made valuable modeling efforts in this field. At that time the models of the flash smelting furnace were one- or two-dimensional and the geometry of the concentrate burner was greatly simplified. On the other hand, the chemical reactions and heat transfer were already fairly comprehensively included. Both groups used their own codes for fluid flow, heat transfer, and turbulence, which is most probably a result of the early stage of commercially available packages at that time.

More recently, two research groups have adopted a commercial package for simulation of the flash smelting process in a more detailed way: Jorgensen and co-workers /11-17/ are concentrating on modeling the nickel flash smelting operations in the Kalgoorlie smelter of Western Mining Corporation, Australia; Jokilaakso and his group /18-23/ are dealing with the copper flash smelting process of Outokumpu, Finland.

In this paper, a mathematical model for chalcopyrite particle combustion is presented. The model includes the oxidation scheme proposed by Kim /5/ for simulating gas-particle reactions in flash smelting furnace. The kinetics and thermodynamics of the oxidation reactions are written as a separate module and then connected to the calculation of the flow field which, together with particle trajectories in the flow field, is solved by a commercial fluid flow package, Phoenix. The kinetic module and its connection to fluid flow and heat transfer calculation is still under development, and further testing and validation of the program is continuing. Anyway, a huge amount of preliminary results about the concentrate combustion in a two dimensional calculation grid of an industrial scale flash smelting furnace are obtained. Some of these results is presented in this paper.

SIMULATION AND BOUNDARY CONDITIONS

General

The numerical simulation of the flash smelting process was carried out with Phoenix. Phoenix is a general-purpose solver for fluid-flow, heat-transfer and combustion processes. It was created in 1979-80 and first released in 1981 [25]. In Phoenix, the governing equations for dependent flow variables are presented by the general form of a differential equation. Differential equations together with mass conservation (continuity) equation are discretized by control volume method and the resulting nonlinear set of algebraic equations are solved line-by-line with Tri-Diagonal Matrix Algorithm using the well-known pressure correction technique in a staggered calculation grid.

In the present work, a cylindrical co-ordinate system in radial and axial directions was used, and the simulation was steady-state. Then, a general form of the solved differential equation for variable ϕ is written

$$\frac{\partial}{\partial x}(\rho U \phi) + \frac{1}{r} \frac{\partial}{\partial r} r(\rho V \phi) = \frac{\partial}{\partial x} \left(\Gamma_{\phi} \frac{\partial \phi}{\partial x} \right) + \frac{1}{r} \frac{\partial}{\partial r} \left(r \Gamma_{\phi} \frac{\partial \phi}{\partial r} \right) + S_{\phi} \quad (1)$$

where ρ is the density of the fluid, and Γ_{ϕ} is the exchange coefficient for variable ϕ . x and r are the spatial co-ordinates in axial and radial directions, respectively, and U and V are the axial and radial velocity components. The source term S depends on the solved variable. When turbulent problems are solved, the variable ϕ is the time-averaged value, and the fluctuations terms (Reynolds stresses, turbulent heat flux and diffusion) are expressed in a terms of a mean properties of the flow with the turbulence model. In the present simulation, 10 differential equations of the form (1) were solved ($\phi = U, V, k, \epsilon, h, Y_{O_2}, Y_{N_2}, Y_{SO_2}, R_x, R_r$).

The simulation was performed with cylindrical grid of 62×64 radial and axial cells, respectively, in a geometry representing a hypothetical industrial scale flash smelting furnace. The boundary conditions are presented in Table I.

Table I Simulated operation conditions.

Inlet name	Flow rate, Nm ³ /h	Oxygen enrich., at-%	Temperature, K (°C)
Process gas	35000	57	493 (220)
Distribution air	2500	21	298 (25)
Central oxygen	1300	95	298 (25)
Solids feed			
- concentrate	125 t/h	wt-% CuFeS ₂ = 79	298 (25)
- flux	35 t/h		298 (25)

The simulations were carried out by the Eulerian-Lagrangian method, where a size distribution can be given for particles, and it is based on solving the equation of motion of the particles. The particles exchange heat and momentum with the continuous (gas) phase. To represent these interphase phenomena, source terms are added to the gas phase equations. This is done by first solving the continuous phase equations to a more or less converged level, and subsequently tracking the individual particles in the flow field, which leads to the relevant source terms.

In the model, the solid feed is presented with two different types of particles. A concentrate particle is a mixture of chalcopyrite and an inert material, whereas the inert particle is pure silica. The particle diameters used were 31, 56, 87, and 125 μm for concentrate particles, and 31, 60, 152, 490, 1125, and 1500 μm for inert particles. The solid feed was described with 15 computational particles per 0.02 rad of distance in angular direction. Nine of these 15 particles were reacting ones. It should be noted that a larger number of computational particles should be used to obtain the statistical reliability. Because the model is under development, the number of computational particles were restricted to 15. In principle, there is no upper limit for particles, but to remain practical calculations times, about 1000 particles in three-dimensional calculation should be enough.

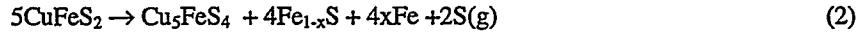
The feed mixture of the flash smelting furnace consists of different sizes and types of particles. Temperature history and flow dynamics of a single reactive (concentrate) particle depends much on the particle size, and larger particles behave differently as compared to smaller ones, especially beyond their melting point. Anyway, chemical behavior of all reactive particles in the model are similar for all sizes of particles. After the particles are fed through the burner, they are heated up by convection and radiation. Soon after the particle temperature exceeds 500 K (227°C), thermal decomposition of the chalcopyrite starts. Due to the exothermic oxidation reaction of dissociated gaseous sulfur, that is released by thermal decomposition, particle temperature is further increased and oxidation reactions of the decomposed chalcopyrite products can proceed rapidly.

Due to the heat releasing oxidation reactions, particle temperature rises rapidly and reaches the melting point of the sulfide. Because the melting point of the sulfide is lower than that of the oxide phase produced in the oxidation, further oxidation (and dissociation) is assumed to take place in a molten sulfide core surrounded by an oxide crust /5/.

Chemical reactions of a single particle

In the mathematical model for sulfide combustion, the reactions are supposed to proceed in a way proposed by Kim /5/. The particles to be oxidized are assumed to be initially dense and homogeneous mixture of chalcopyrite (CuFeS_2) and silica (SiO_2). The reaction is confined to a sharp interface between the unreacted core and the product layer. Therefore, a shrinking core model can be applied. In the case of chalcopyrite oxidation, the overall reaction occurring can be roughly divided into three phases /5/:

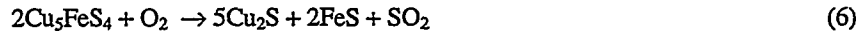
Thermal decomposition of the chalcopyrite particle and dissociation of the labile sulfur:



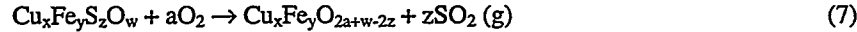
Subsequent oxidation of the diffused sulfur inside a particle and in the gas phase:



Oxidation of the decomposed sulfide by the gas-solid reactions



or by gas-liquid reaction.



The oxidation of the dissociated gaseous sulfur (3) is highly exothermic and raises the particle temperature. Oxidation of the decomposed sulfide products (4-6) start with gas-solid reactions and complete with gas-liquid reactions (7). Sulfides have lower melting temperature than oxides, and a molten sulfide core, enclosed in the solid oxides crust is first formed during the reactions.

Rate controlling mechanism

The rate controlling mechanism of oxygen consumption depends on the temperature of the particle. Below the melting point of the sulfide, gas-solid reactions prevail, and the oxygen consumption (gO_2/s) related to the thermal decomposition reaction (2) is calculated with the aid of the sulfur removal rate /5/

$$\left. \frac{dm_{\text{O}_2}}{dt} \right|_{\text{dis}} \equiv \frac{M_{\text{O}_2}}{M_{\text{S}}} \frac{dm_{\text{S}}}{dt} = \frac{M_{\text{O}_2}}{M_{\text{S}}} \alpha \pi d_p^2 \rho_p k_{\text{dis,ov}} \quad (8)$$

where M is the molecular weight (g/mol), d_p is the particle diameter (m), ρ_p is the original density of the particle (kg/m^3) and α is weight of labil sulfur per gram of sulfide. The rate coefficient for dissociation $k_{\text{dis,ov}}$ (m/s) is calculated from the equation

$$\frac{1}{k_{\text{dis,ov}}} = \frac{1}{k_d} + \frac{d_p(d_p - d_{cl})}{2d_{cl}D_{\text{S,eff}}} + \frac{d_p^2}{d_{cl}^2 k_{\text{dis}}} \quad (9)$$

Here, subscript d_{c1} is a diameter on an unreacted chalcopyrite core (m), see Figure 1, k_d is the mass transfer coefficient (m/s), D is diffusivity (m^2/s), and k_{dis} is the reaction rate coefficient (m/s) of reaction (2). Oxygen consumption of the particle oxidation reactions (4)-(6) is controlled by the same mechanisms as in the dissociation reaction

$$\left. \frac{dm_{O_2}}{dt} \right|_{ox} = \pi d_p^2 \rho_g Y_{O_2} k_{ox,ov} \quad (10)$$

where ρ_g is the density of the gas mixture (kg/m^3), and Y_{O_2} is the mass fraction of oxygen in gas. The rate coefficient for oxidation, $k_{ox,ov}$ is expressed by the equation

$$\frac{1}{k_{ox,ov}} = \frac{1}{k_d} + \frac{d_p(d_p - d_{c2})}{2d_{c2}D_{O_2,eff}} + \frac{d_p^2}{d_{c2}^2 k_{ox}} \quad (11)$$

where d_{c2} is a diameter on thermally decomposed core (m), and k_{ox} is the combined rate coefficient (m/s) of reactions (4)-(6).

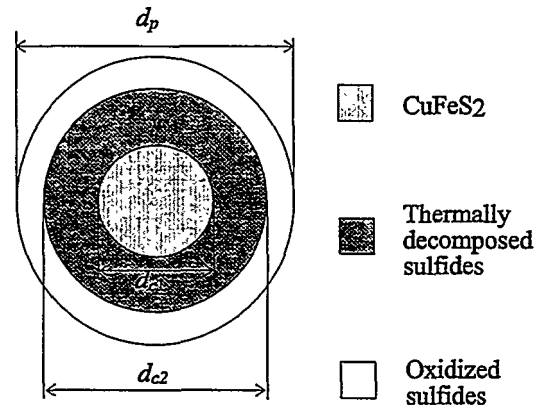


Figure 1 – The shrinking core model for chalcopyrite combustion.

Once the particle becomes molten the gas-liquid reaction (7) become dominant. Beyond that point, the oxygen consumption rate is determined by similar kind of expression as in the oxidation reactions, equation (11), but the effect of oxygen mass transfer through the surface film of the molten sulfide is included in the model using the film penetration concept proposed by Huang & Kuo [29]. The mathematical expression of the rate coefficient $k_{ox,l}$ (m/s) at the liquid state is written

$$k_{ox,l} = \sqrt{k_r D_{O_2,l} (1 + \beta)} \coth \sqrt{\frac{1 + \beta}{\alpha}} \quad (12)$$

where D is the diffusivity of oxygen in liquid (m^2/s) and k_r is the reaction velocity constant ($1/\text{s}$). The dimensionless groups α and β are defined as

$$\alpha = D_{\text{O}_2, l} / k_r L^2 \quad (13)$$

and

$$\beta = s / k_r \quad (14)$$

where L is the average thickness of the surface element (m), and s is the surface renewal rate ($1/\text{s}$).

Heat balance of the particle

In order to determine the temperature history of the particles, it is necessary to describe the heat balance between one particle and its surroundings. When the particles are introduced in the reaction shaft, they are first heated up by the heat transfer from the surroundings. This includes the heat transfer by convection and radiation from the refractory walls. After the ignition, the heat generated by the oxidation reactions raises the particle temperature and also "flows" to the surroundings. The mathematical expression of these phenomena is given by the heat balance of a particle as

$$\rho_p C_{p,p} \frac{dT_p}{dt} = h_{pg} (T_g - T_p) A_p + Q_{\text{rad}} - \Delta H_{\text{dis}} \left. \frac{dm_{\text{O}_2}}{dt} \right|_{\text{dis}} - \Delta H_{\text{ox}} \left. \frac{dm_{\text{O}_2}}{dt} \right|_{\text{ox}} \quad (15)$$

where $C_{p,p}$ is the heat capacity of the particle (J/kgK), h_{pg} is the convective heat transfer coefficient ($\text{W/m}^2\text{K}$), T is temperature (K), A_p is the particle surface area (m^2), Q_{rad} is the rate of heat released/consumed by radiation (J/s) and ΔH is the heat of chemical reaction (J/kg). Subscripts g and p denote the gas and particle phase, respectively. The term on the left-hand side of equation (15) accounts for the accumulation of heat in the particle. The right-hand side represents convection between the particle and the gas, radiation between a particle cloud and gas, and the rate of heat generation by chemical reactions (dissociation and oxidation). Equation (15) can be integrated to yield an equation for new particle temperature after a small time step Δt (s)

$$T_p = T_g - (T_g - T_p^0) e^{-\Delta t / \tau'} + \left(Q_{\text{rad}} - \Delta H_{\text{dis}} \left. \frac{dm_{\text{O}_2}}{dt} \right|_{\text{dis}} - \Delta H_{\text{ox}} \left. \frac{dm_{\text{O}_2}}{dt} \right|_{\text{ox}} \right) (1 - e^{-\Delta t / \tau'}) / \pi \text{Nu} \lambda_g d_p \quad (16)$$

where τ' is a relaxation time for enthalpy and is defined as

$$\tau' = \rho_p d_p^2 C_{p,p} / 6 \text{Nu} \lambda_g \quad (17)$$

where Nu is the particle Nusselt number, and λ_g is the thermal conductivity of the gas phase (W/mK).

Calculation procedure

The equation of motion for the particle is written

$$m_p \frac{d\mathbf{u}_p}{dt} = \frac{1}{2} \rho A_p C_D |\mathbf{u} - \mathbf{u}_p| (\mathbf{u} - \mathbf{u}_p) + V_p \nabla p + \mathbf{F}_e \quad (18)$$

where m_p is the mass of the particle (kg), \mathbf{u} is the velocity vector (m/s) of the continuous phase, C_D is the drag coefficient, p is pressure of the continuous phase (N/m²). When the pressure gradient is negligible and gravity is the only external force (\mathbf{F}_e) acting on the particle, and there is no buoyancy effects included, equation (18) can be integrated to give

$$\mathbf{u}_p = \mathbf{u}_g - (\mathbf{u}_g - \mathbf{u}_p^0) e^{-\Delta t/\tau} + \mathbf{g}\tau(1 - e^{-\Delta t/\tau}) \quad (19)$$

Here Δt is the time step (s). Superscript 0 indicates the value at the old particle position. τ is the relaxation time for momentum (s) and it is calculated from

$$\tau = \frac{4\rho_p d_p^2}{3\mu C_D Re_p} \quad (20)$$

where μ is the dynamic viscosity of the continuous phase (kg/ms), and Re_p is the particle Reynolds number ($= d_p |\mathbf{u} - \mathbf{u}_p| \rho / \mu$). Correlation of Clift & al. /32/ for spherical particles is used for calculating drag coefficient C_D . Equation (19) is used to calculate the new particle velocity after a time step. The new particle position can be calculated by integrating the particle velocity with respect to time. Equation (15) is solved together with the particle momentum equation (18) with the Gentra (General particle-tracking facility)-module of Phoenix. The approach is based on the Particle-Source-In-Cell (PSIC)-method by Crowe et al. /30/.

The source terms to the gas phase enthalpy and momentum equations are determined by calculating the new particle temperature and velocity, Eq.'s (16) and (19), and by summing the enthalpy and momentum changes of particles crossing one computational cell. The momentum source term for gas phase velocities is given by equation /31/

$$\bar{S}_{u,p} = \pi \sum_{n=1}^{N_p} \frac{\rho_{p,n,in} \eta_n \mathbf{u}_{p,in} d_{n,in}^3}{6} - \pi \sum_{n=1}^{N_p} \frac{\rho_{p,n,out} \eta_n \mathbf{u}_{p,out} d_{n,out}^3}{6} \quad (21)$$

where the summation is over all of the Lagrangian time steps required for the particle to traverse the cell, and for all particles (N_p). η_n is the number flow rate of the particles (1/s) represented by one computational particle, or mass flow rate of particles divided by

the mass of the single computational particle ($=\dot{m}_p/m_{p,i}$). The enthalpy and mass sources can be calculated by similar kind of a procedure.

The calculation proceeds with alternating iteration of the gas flow field and of solving the momentum and enthalpy equation of the particle. The calculation begins by solving the gas flow field assuming no particles are present. Using this flow field, particle trajectories together with temperature histories along the trajectories are calculated. The momentum and energy source terms together with chemical species consumption/production for each computational cell throughout the flow field are then determined. The gas flow field is solved again, incorporating these source terms. The new gas flow field is used to establish new particle trajectories and temperature histories, which constitute the effect of the gas phase on the particles. Calculating new source terms and incorporating them into the gas flow field equations constitutes the effect of particle cloud on the gas phase, thereby completing the cycle of mutual interaction (two-way coupling).

Verification of the kinetic model

A separate program was written with Fortran 77 for checking the kinetic module of the chalcopyrite combustion. This program simulates the concentrate oxidation reactions in the laminar flow furnace, and it is possible to calculate the individual particle temperatures and mineral composition of the particle as it flows in a laminar, preheated gas stream. Figure 2 shows some calculated particle temperatures for different sizes (45, 63.5 and 89.5 μm) of chalcopyrite concentrate burning in air at 973 K (700 °C).

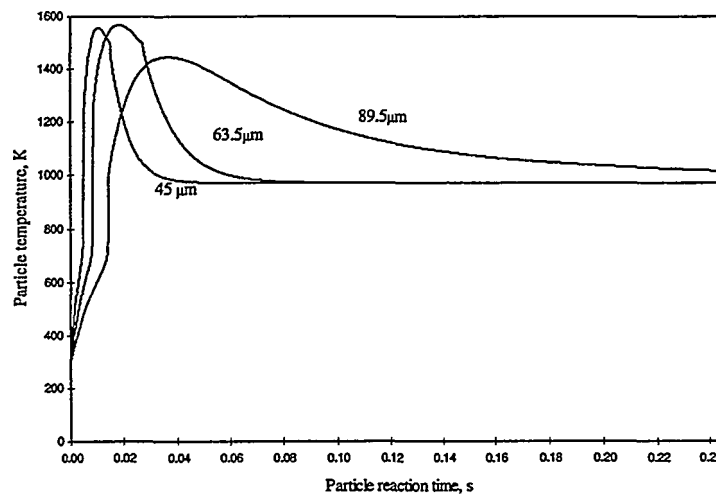


Figure 2 – Calculated temperature of chalcopyrite particles in laminar flow furnace.

Jorgensen /27/ has measured the temperatures of chalcopyrite particle in laminar flow furnace. In Table II, a comparison is made between calculated and measured maximum

particle temperatures, and a very good agreement is obvious, although the combustion times of particles in Jorgensens work are much longer than indicated by the current work.

Table II Comparison of the measured and calculated maximum particle temperatures of chalcopyrite particle in laminar flow furnace.

Maximum temperature	37-53 μm	53-74 μm	74-105 μm
Measured [27], K ($^{\circ}\text{C}$)	1568 (1295)	1568 (1295)	1503 (1230)
Calculated, K ($^{\circ}\text{C}$)	1558 (1285)	1568 (1295)	1447 (1174)

RESULTS AND DISCUSSION

Some preliminary calculations have been carried out with chemically reacting particles, and the results obtained so far suggest that the particle heat-up period in the reaction shaft is concentrated to a very narrow region of space and time. This causes serious problems for the calculation of gas phase because of large source terms and extra care had to be taken to be able to calculate the flow field.

Simulated temperature distribution in the reaction shaft is presented in Figure 3. Temperature in the lower part of the shaft and near the vertical wall is more or less uniform. In the upper part, however, large gradients exist. Almost all particles seem to ignite in a very narrow region. This is more obviously seen from the O_2 - and SO_2 -concentration profiles, shown in Figure 4. It is also noteworthy to mention that in Figure 4, the high SO_2 concentration area is mainly due to the oxidation reactions of the small particles. The reaction rates (=oxygen consumption) at that position of the larger particles are much slower than those of the small ones.

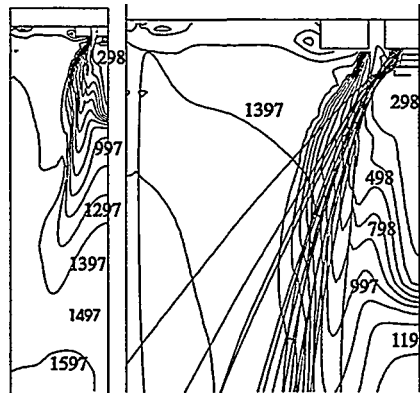


Figure 3 – Temperature distribution (K) in the symmetric half of the reaction shaft.
Right: A magnification of the near burner region with particle tracks.

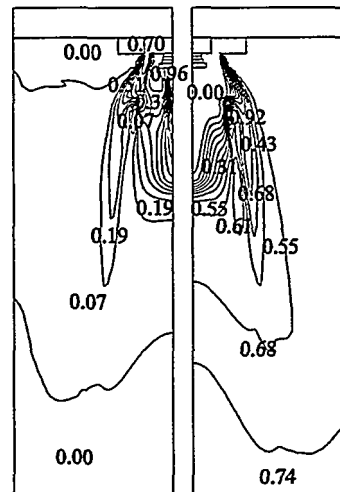


Figure 4 – Calculated oxygen and sulfur dioxide mass fractions in the reaction shaft.
Left: O₂, Right: SO₂.

Figure 5 shows temperatures of selected individual particles and their position in the shaft. The larger particles flow more towards the wall region of the shaft than the small ones. The maximum temperatures of the particles vary significantly as a function of the particle diameter. The reaction rate of small particles is so high, that the particle melts instantly soon after the temperature reaches the ignition temperature of the particle. Larger particles undergo a slower heating period after ignition because of the resistance of the oxide layer to the mass transfer of oxygen.

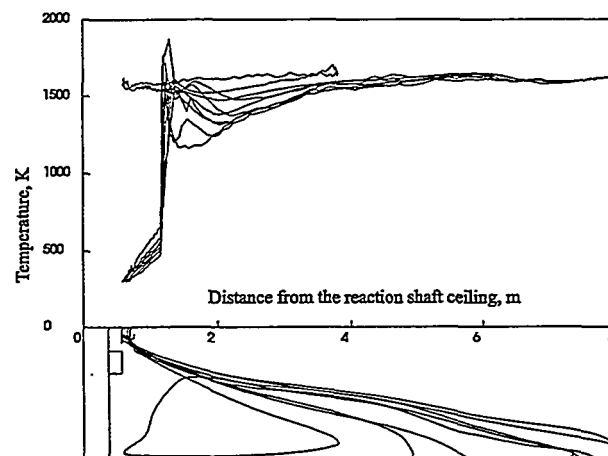


Figure 5 – Temperature histories of the reacting particles and their position in the reaction shaft.

In Figure 6, temperatures of the inert particles are shown. The temperature of the smaller particles follow the gas temperature. Some of the inert particles are much larger than the concentrate particles and their path in the reaction shaft differs significantly from that of the reacting particles. As the particle diameter increases, the maximum particle temperature decreases and the largest particles do not notably heat up before they hit the wall of the shaft.

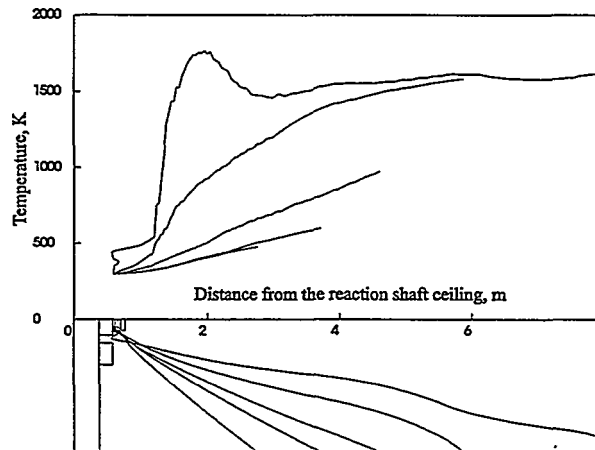


Figure 6 – Temperature histories of the inert particles and their position in the reaction shaft.

Present status of the work

The chemical reactions of the particle are coded into the Phoenix. The particle equation of motion is calculated using the standard-equation of Gentra. The effect of gas phase turbulence on the particle motion is also calculated with the standard stochastic treatment of Gentra. However, the particle effects on turbulence is not included. These effects have to be modeled and added to the calculation. The enthalpy equation for a single particle was, rewritten in order to take into account the proper rate controlling mechanisms of the particle heat-up period. The main reason for this is the incapability of the standard-enthalpy-equations of Gentra to handle complicated phenomena, such as the sulfide particle oxidation. Due to this limitation in the software, the modeling work was concentrated on the proper presentation of the particle enthalpy equation and the source terms for enthalpy, mass and gas species. The heat transfer equations for convection, radiation, and reactions for particle temperature calculation are coded. However, the model still needs some fine-tuning, especially at the ignition-stage of the particles, and later in liquid state when the particles may fragment. The connection between the gas and particle phase calculations also needs some further verification. The particle-gas and particle-wall radiation is already included in the present model, but for gas-wall radiation a proper set of transfer equations have to be implemented to the model, because the current radiation model of Phoenix (six-flux-method) is not physically meaningful in a three dimensional cylindrical-polar co-ordinate-system.

CONCLUDING REMARKS

The Outokumpu flash smelting furnace is a challenging object for computer simulation due to the difference between the smallest dimensions of the distribution cone in the burner and largest dimensions of the shaft diameter and height (e.g. four and eight meters, respectively). Therefore, in the present modeling work, several simplifications were found necessary. However, with different models of varying grid density, the reaction shaft together with the concentrate burner was possible to simulate, and a lot of preliminary results were obtained concerning the chalcopyrite combustion. The temperature profiles of individual particles shows a similar kind of trend as was calculated by Kim /5/ in his one-dimensional model. Also the maximum temperatures attained by particles are very close to values measured by Jorgensen /27/.

The highly exothermic oxidation reactions and their kinetics have been coded as a separate module in the program. The model still needs a lot further development, testing, and validation. The difficulties are due to the huge amounts of heat released during the extremely fast reactions (milliseconds) after the concentrate particles ignite. The particle temperature also rise to very high values and this causes difficulties in coupling the heat transfer and other interactions between the particles and the gas phase.

In spite of the problems mentioned above, it was possible to simulate the oxidation of sulfide particles in the symmetric calculation domain of the reaction shaft of an industrial size flash smelting furnace. From the results, the following topics were analysed in typical cases:

- oxygen and sulfur dioxide concentrations in the reaction shaft,
- temperature distribution in the reaction shaft,
- tracks and temperature histories of different types of particles,

Further on, it is possible to evaluate oxygen utilisation efficiency, potential hot spots in case of an uneven temperature distribution, and the optimal size of the reaction shaft. According to the present results, combined kinetic and CFD-modeling can produce vast amounts of new information for engineering and development purposes about high temperature processes, such as the flash smelting process.

ACKNOWLEDGEMENTS

The authors wish to thank the Ministry of Trade and Industry, and the Technology Development Center (Tekes), Finland, and the national SULA 2 programme for financing the research and Outokumpu Research Oy for permission to publish this paper. The authors are also indebted to Mr. Markku Kytö, Vice President of Outokumpu Engineering Oy, and Docent Pekka Taskinen, Pyrometallurgy Research Director of Outokumpu Research Oy, for their interest in this work and for their valuable advice.

REFERENCES

1. Bryk, P. et al., *Journal of Metals*, Vol.10, June, 1958, 395-400.
2. Ruottu, S., "Aineen, impulssin ja energian siirtyminen turbulentissa hiukkaskaasususpensiossa", Ph.D. thesis (in Finnish), Lappeenranta University of Technology, 1976.
3. Ruottu, S., *Combustion and Flame*, Vol.34, 1979, 1-11.
4. Jiao, Q., Wu, L. and Themelis, N.J., "Mathematical modeling of flash converting of copper matte", J.Szekely et al., Eds., *Mathematical Modelling of Materials Processing Operations*, The Metallurgical Society, Warrendale, PA, USA, 1986, 835-858.
5. Kim, Y. "Studies of the rate phenomena in particulate flash reaction systems: oxidation of metal sulfides", Doctoral dissertation. Columbia University, 1986.
6. Hahn, Y.B. and Sohn, H.Y., "Prediction of the behavior of a particle-laden gas jet as related to the flash smelting process", *The Reinhardt Schuhmann Int. Symp. on Innovative Technology and Reactor Design in Extraction Metallurgy*, D.R. Gaskell et al., Eds., The Metallurgical Society, Warrendale, PA, USA, 1986, 469-499.
7. Hahn, Y.B. and Sohn, H.Y., "Mathematical modeling of the combined turbulent transport phenomena, chemical reactions, and thermal radiation in a flash furnace shaft", *Mathematical Modeling of Materials Processing Operations*, J. Szekely, H. Henein and N. Jarret, Eds., The Metallurgical Society, Warrendale, PA, USA, 1987, 799-834.
8. Hahn, Y.B. and Sohn, H.Y., "Mathematical modeling of sulfide flash smelting process: Part I. Model development and verification with laboratory and pilot plant measurements for chalcopyrite concentrate smelting", *Met. Trans. B*, Vol 21B, 1990, 945-958.
9. Hahn, Y.B. and Sohn, H.Y., "Mathematical modeling of sulfide flash smelting process: Part II. Quantitative analysis of radiative heat transfer", *Met. Trans. B*, Vol 21B, 1990, 959-966.
10. Seo, K.W. and Sohn, H.Y., "Mathematical modeling of sulfide flash smelting process: Part III. Volatilization of minor elements", *Met. Trans. B*, Vol. 22B, 1991, 791-799.
11. Smith, T.N., "Model study of gas flow in Kalgoorlie nickel smelter", *Extractive Metallurgy Conference*, 1991, 245-250.
12. Jorgensen, F.R.A. and Elliot, B.J., "Flash Furnace Reaction Shaft Evaluation Through Simulation", Paper presented at the AusIMM Int. Conf. on Extractive

- Met. of Gold and Base Metals, Kalgoorlie, Australia, 26-28 October 1992, 387-394.
13. Nguyen, T.V. et al., "Numerical Modelling of Fluid Flow, Heat Transfer and Combustion in the Kalgoorlie Nickel Smelter", Paper presented at the AusIMM Int. Conf. on Extractive Met. of Gold and Base Metals, Kalgoorlie, Australia, 26-28 October 1992, 413-419.
 14. Koh, P.T. and Taylor, R.N., "Mathematical Modelling of Heat Transfer in Flash-Smelting Burners", Paper presented at the AusIMM Int. Conf. on Extractive Met. of Gold and Base Metals, Kalgoorlie, Australia, 26-28 October 1992, 407-411.
 15. Koh, P.T., "Numerical Simulation of Two-Phase Flow in Flash-Smelting Burners", Paper presented at the Australian Chem. Eng. Conf., Chemeca '92, Canberra, Australia, 1992, 487-494.
 16. Jorgensen, F.R.A. et al., "Modelling the burners and reaction shaft of a flash smelting furnace", Flash reaction processes, Davies, T.W., Ed., Kluwer Academic Publishers, Netherlands, 1995, 201-238.
 17. Elliot, B.J., Jorgensen, F.R.A. and Kemori, N., "Aspects of burner design for flash smelting" Metallurgical Processes for the Early Twenty-First Century, Vol. II: Technology and Practice, Sohn, H.Y., Ed., Proceedings of the second Symposium on Metallurgical Processes for the year 2000 and Beyond, San Diego, September 21-23, 1994, 943-962.
 18. Jokilaakso, A., Teppo, O., Ahokainen, T. and Yang, Y., "Computer simulation of the Outokumpu flash smelting process". Proceedings of the Helsinki University of Technology Colloquium on Process Simulation, A. Jokilaakso, Ed., Report TKK-V-B99, 1994, 157-167.
 19. Jokilaakso, A., Ahokainen, T., Yang, Y., Teppo, O., Riihilahti, K., Tuominen, J., "Computer simulation of fluid flow in an Outokumpu type flash smelting furnace", Metallurgical Processes for the Early Twenty-First Century, Vol. I: Basic Principles, Sohn, H.Y., Ed., Proceedings of the second Symposium on Metallurgical Processes for the year 2000 and Beyond, San Diego, September 21-23, 1994, 841-858.
 20. Yang, Y., Jokilaakso, A., Ahokainen, T. and Teppo, O., "Gas flow and heat transfer in a waste-heat boiler". Proceedings of the 1994 European Phoenix User Conference, 16.-18. November 1994, Warwick, England. Paper 16.
 21. Yang, Y., Jokilaakso, A., Ahokainen, T. and Teppo, O., "Numerical simulation of fluid flow and heat transfer in a waste-heat boiler of the Outokumpu flash smelting process". EPD Congress 1995, Warren, G.W., Ed., TMS, 1995, 3-18.
 22. Ahokainen, T., Jokilaakso, A., "Modelling of gas-particle reactions in the copper flash smelting", Paper presented at The Int. Conf. on Modelling and Simulation

- in Metallurgical Engineering and Materials Science. 11 - 13 June, 1996. Beijing, China.
23. Jokilaakso and O. Teppo, "Numerical Simulation of Concentrate Burners of the Flash Smelting Process", Paper presented at The Int. Conf. on Modelling and Simulation in Metallurgical Engineering and Materials Science. 11 - 13 June, 1996. Beijing, China.
 24. Jorgensen, F.R.A., et al., "Sampling and taking measurements in the shaft of the Kalgoorlie Nickel Smelter". The Paul E. Queneau Int. Symp. — Extr. Met. of Copper, Nickel and Cobalt — Vol. I: Fundamental Aspects, Reddy, R.G. and Weizenbach, R., Eds., TMS 1993, 639-651.
 25. Rosten, D.B. Spalding, and D.G. Tatchell, "PHOENICS: a General Purpose Program for Fluid-Flow, Heat-Transfer and Chemical-Reaction Processes", Paper presented at the 3rd International Conference on Engineering Software, Imperial College, London, 1983, 639-655.
 26. Kim, Y.H. and Themelis, N.J., "Effect of phase transformation and particle fragmentation on the flash reaction of complex metal sulfides", The Reinhardt Schuhmann int. symp. on innovative technology and reactor design in extraction metallurgy, Gaskell, D.R., Hager, J.P., Hoffmann, J.E. and Mackey, P.J., Eds., Warrendale, 1986, TMS-AIME, 349-369.
 27. Jorgensen, F.R.A., "Single-particle combustion of chalcopyrite", Proc. Australas. Inst. Min. Metall., No. 288, December 1983, 37-46.
 28. Jokilaakso, A.T., Suominen, R.O., Taskinen, P.A. and Lilius, K.R., "Oxidation of chalcopyrite in simulated suspension smelting", Trans. Instn. Min. Metall. (Sect. C: Mineral Process. Extr. Metall.), Vol. 100, May-August, 1991, C79-C90.
 29. Huang, C-J., Kuo, C-H. "General mathematical model for mass transfer accompanied by chemical reaction". AIChE Journal, Vol. 9, No. 2., 1963, 161-167.
 30. Crowe, C.T., Sharma, M.P., Stock, D.E., "The Particle-Source-In Cell (PSI-CELL) model for gas-droplet flows", J. Fluids Eng., June, 1977, 325-332.
 31. Kjaldman, L. "Numerical Simulation of combustion and nitrogen pollutants in furnaces". Doctoral dissertation, VTT-Publications 159. VTT-OFFSETPAINO, Espoo, Finland 1993.
 32. Clift, R., Grace, J.R., Weber, M.E., Bubbles, Drops and Particles, Academic press, New York, 1978.

For Your Notes

1. The first part of the document discusses the importance of maintaining accurate records of all transactions. This is essential for ensuring the integrity of the financial statements and for providing a clear audit trail. The second part of the document outlines the various methods used to collect and analyze data, including interviews, surveys, and focus groups. The third part of the document describes the process of identifying and defining the research objectives, which is a critical step in the research process. The fourth part of the document discusses the importance of selecting a representative sample of the population, and the fifth part of the document describes the various methods used to collect and analyze data, including interviews, surveys, and focus groups. The sixth part of the document discusses the importance of maintaining accurate records of all transactions, and the seventh part of the document outlines the various methods used to collect and analyze data, including interviews, surveys, and focus groups. The eighth part of the document describes the process of identifying and defining the research objectives, and the ninth part of the document discusses the importance of selecting a representative sample of the population. The tenth part of the document describes the various methods used to collect and analyze data, including interviews, surveys, and focus groups.

[Illegible text]

SESSION 3
Chemical Reactions

Keynote Lecture

***Mathematical Modeling of the
Flash Converting Process***

H.Y. Sohn, M. Pérez-Tello, K. Riihilahti

Mathematical Modeling of the Flash Converting Process

H. Y. Sohn, M. Pérez-Tello, and K.M. Riihilahti
Departments of Metallurgical Engineering and of Chemical and Fuels Engineering,
University of Utah, Salt Lake City, UT 84112, U.S.A.

Abstract

An axisymmetric mathematical model for the Kennecott-Outokumpu flash converting process for converting solid copper matte to copper is presented. The model is an adaptation of the comprehensive mathematical model formerly developed at the University of Utah for the flash smelting of copper concentrates. The model incorporates the transport of momentum, heat, mass, and reaction kinetics between gas and particles in a particle-laden turbulent gas jet. The standard k- ϵ model is used to describe gas-phase turbulence in an Eulerian framework. The particle-phase is treated from a Lagrangian viewpoint which is coupled to the gas-phase via the source terms in the Eulerian gas-phase governing equations. Matte particles were represented as $\text{Cu}_2\text{S}\cdot\gamma\text{FeS}$, and assumed to undergo homogeneous oxidation to Cu_2O , Fe_3O_4 , and SO_2 . A reaction kinetics mechanism involving both external mass transfer of oxygen gas to the particle surface and diffusion of oxygen through the porous oxide layer is proposed to estimate the particle oxidation rate. Predictions of the mathematical model were compared with the experimental data collected in a bench-scale flash converting facility. Good agreement between the model predictions and the measurements was obtained. The model was used to study the effect of different gas-injection configurations on the overall fluid dynamics in a commercial size flash converting shaft.

Helsinki University of Technology
3rd Colloquium on Process Simulation
12 - 14 June, 1996
Espoo, Finland

INTRODUCTION

The Kennecott-Outokumpu flash converting process (FCP) is a new technology that incorporates the principles of the Outokumpu flash smelting process in the converting step of solid matte particles to produce copper [1]. The process is aimed at replacing the converting of molten copper matte in the Peirce-Smith converters, a century old technology still in use. The first industrial FCP plant was started up at Kennecott's Utah Smelter. Relevant technical aspects of this process have been documented in the literature [1,2].

In the FCP, the molten matte produced in a smelting furnace is granulated and ground before being fed to the flash converter. In the converter shaft, matte particles are oxidized in an industrial-strength oxygen stream. Turbulent conditions prevail in the furnace, and gas temperatures of the order of 1400 K and above are typical. A slightly negative pressure is maintained to minimize the possibility of fugitive SO₂ emissions.

The many advantages of the FCP as a copper-converting technology create the need for fundamental understanding towards its future optimization. Although some theoretical studies [3,4] and experimental data [5-8] on the FCP have been reported in the literature, the overall process involving all the subprocesses occurring in a flash converter shaft, namely, turbulence, heat, mass, and momentum transport coupled with particle-gas reactions has not been analyzed.

The present study is part of a comprehensive investigation currently undergoing at the University of Utah, the major objective of which is to describe the FCP from a fundamental standpoint. Experimental work and mathematical modeling are being conducted to that end. The present paper describes the current status towards the development of a mathematical model of a flash converting operation based on basic principles.

PREVIOUS WORK

Although the FCP has been under development since the early-eighties, experimental data have been rather scarce until recently. Asteljoki et al. [1] and Asteljoki and Kytö [2] reported experimental data from a flash converting pilot-scale facility. They focused on the copper content in the slag and the distribution of minor elements between the blister copper

and slag in the settler. Suominen et al. [5] reported on oxidation tests of industrial copper matte particles in a laminar-flow furnace. They studied the reactivity of copper matte particles as a function of particle size, matte grade, and oxygen concentration in the reacting gas. In a subsequent paper [6], they discussed the morphology and mineralogy of the reacted particles obtained in their first study. In this laboratory, both kinetic studies [7,8] and actual flash converting experiments [9,10] have been conducted recently. The experimental data on flash converting and those on the smelting of sulfide minerals [11-14] indicate the complexity of the reaction path of a sulfide particle in the interior of a flash furnace. Physical models of the particle transformations along its flight have been proposed in the literature [6,13]. However, the physical and chemical phenomena involved are still uncertain, which complicates the task of modeling the system on a fundamental basis.

Jiao et al. [3] applied a two-dimensional turbulent flow model similar to that used in this work to the flash converting process. In the calculations describing the gas and particle phases, two distinct methods, Eulerian and Lagrangian, respectively, were employed. Turbulence was accounted for by means of the $k-\epsilon$ model [15]. They assumed Cu_2O , Fe_3O_4 , and SO_2 as the oxidation products throughout the shaft. PbO and ZnO were also assumed to be produced as a result of the impurities in the matte. Although the authors reported the behavior of both particle and gas phases along the reactor shaft, no experimental work was included and no assessment regarding the validity of the model was made. A simplified mathematical model was also reported by Chaubal et al. [4]. Their study focused on the volatilization of minor elements and their distribution patterns in blister copper and slag phases.

MODEL FORMULATION

The major goal of this work is to develop a comprehensive mathematical model that includes the transport of momentum, mass, and energy, coupled with particle-gas reaction kinetics in a flash converting shaft. No attempt was made to model the settler bath.

Figure 1 shows the schematic representation of the flash converting shaft to be modeled. An axisymmetric, two-dimensional geometry is considered.

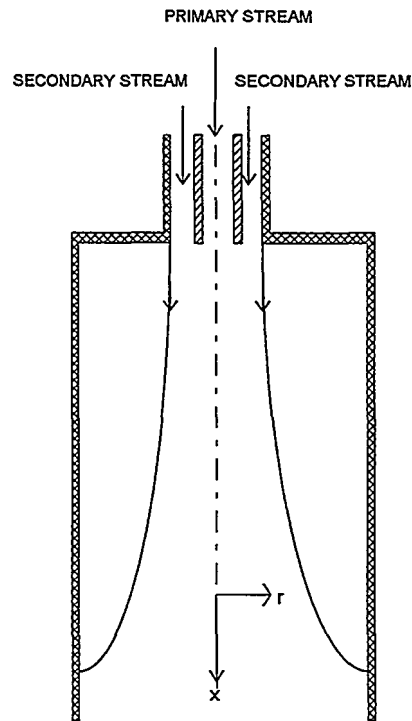


Fig. 1 - Schematic representation of an axisymmetric flash furnace shaft.

The mathematical model originally developed by Hahn and Sohn [16] for the flash smelting of copper concentrates was adopted in this work. In this formulation, gas-phase turbulence is treated by the standard $k-\varepsilon$ model [15]; particle-phase turbulent dispersion is treated by a particle-diffusivity property based on Kolmogorov's scaling relationships [18]. The governing equations for both the gas phase (Eulerian framework) and the particle phase (Lagrangian framework) in cylindrical coordinates are given as follows:

Gas-phase equations (Eulerian framework):

$$\frac{\partial}{\partial x}(\overline{\rho u \phi}) + \frac{1}{r} \frac{\partial}{\partial r}(r \overline{\rho v \phi}) - \frac{\partial}{\partial x}(\Gamma_e \frac{\partial \phi}{\partial x}) - \frac{1}{r} \frac{\partial}{\partial r}(r \Gamma_e \frac{\partial \phi}{\partial r}) = S_\phi \quad (1)$$

Particle-phase equations (Lagrangian framework):

$$m_p \frac{dV_p}{dt} = \frac{1}{2} C_D \rho_g A_p |\mathbf{V}_g - \mathbf{V}_p| (\mathbf{V}_g - \mathbf{V}_p) + m_p \mathbf{g} \quad (2)$$

$$\frac{\partial}{\partial x} (\overline{un_k}) + \frac{1}{r} \frac{\partial}{\partial r} (r \overline{vn_k}) - \frac{\partial}{\partial x} (D_p' \frac{\partial \overline{n_k}}{\partial x}) - \frac{1}{r} \frac{\partial}{\partial r} (r D_p' \frac{\partial \overline{n_k}}{\partial r}) = 0 \quad (3)$$

$$\mathbf{V}_{pd} \overline{n_k} = D_p' \nabla \overline{n_k} \quad (4)$$

$$\frac{d}{dt} (m_p h_p) = \dot{H}_r + q_{rp} - Q_p - \dot{H}_v - \dot{H}_m \quad (5)$$

$$\frac{dn_i}{dt} = \sum_{j=1}^{j=q} v_{ij} R_{r,j} + R_{v,i} \quad (6)$$

where ϕ is the general gas-phase dependent variable. A total of seven equations of the form of equation (1) are written to describe the mass balance for O_2 and SO_2 , the overall continuity equation, the axial and radial transport of momentum, enthalpy, and the governing equations for the turbulent quantities k and ε . Equations (2) through (5) describe the velocity field, the particle number density continuity equation, the turbulent particle dispersion model, and the energy balance, respectively. Equation (6) represents the mass balance equations for the condensed species in the particle as a result of the oxidation reactions and vaporization.

Equation (1) was cast into finite-difference equations and solved using a tridiagonal matrix algorithm. Gosman and Punn's TEACH code [19] was used to solve the gas-phase equations. The pressure field was calculated by means of the SIMPLER algorithm developed by Patankar [20].

The particle-phase equations were solved by the particle-source-in-cell (PSI-CELL) technique developed by Crowe et al. [21]. The algorithm couples the Lagrangian particle-phase equations to the Eulerian gas-phase equations through the source terms, S_ϕ . The reader is referred to Hahn and Sohn's original articles [16,17] for the explicit form of the gas-phase governing equations, the estimation of the turbulent properties, the boundary conditions, and the radiation field model.

Particle representation

Outokumpu-produced copper matte particles were used in the present experimental work. The elemental analysis of this matte was 72 % Cu, 20.7 % S, and 4.4 % Fe with $\pm 0.01\%$ variation. The balance was assumed to be an inert constituent such as SiO_2 . In this study, matte particles were represented as $\text{Cu}_2\text{S}\cdot y\text{FeS}$, where y is the $\text{FeS}/\text{Cu}_2\text{S}$ molar ratio calculated from the original matte chemical analysis; in the present case, $y = 0.14$.

Particle oxidation kinetics

In the furnace shaft the following chemical reactions were assumed to occur:



Reactions (7) and (8) were assumed to be ignited at 800 K; this temperature is an approximate average of the incipient reaction temperatures of high-grade copper matte particles measured in this laboratory in a previous study [7,8]. Before the particle ignites, the rate of oxidation is slow and thus it was ignored in this study. Upon ignition, solid particles were assumed to react topochemically forming a porous crust of Cu_2O and Fe_3O_4 surrounding the unreacted core of $\text{Cu}_2\text{S}\cdot y\text{FeS}$. The matte core was assumed to melt at 1470 K [22], and the oxide crust was assumed to melt at 1870K.

The total rate of oxygen consumption by a single particle was computed from the following expression:

$$R_{\text{O}_2} = k_{\text{ov}} A_p (C_{\text{O}_2,b} - C_{\text{O}_2,e}) \quad (9)$$

where k_{ov} is the overall reaction rate constant given by:

$$\frac{1}{k_{\text{ov}}} = \frac{1}{k_{\text{O}_2,b}} + \frac{r_p - r_c}{\left(\frac{r_c}{r_p}\right) D_{\text{O}_2,e}} \quad (10)$$

Equation (10) assumes a mass-transfer control mechanism. The first term on the right-hand side accounts for the external mass transfer of oxygen from the bulk to the particle surface; the second term involves the diffusion of oxygen through the solid oxide layer. The intrinsic kinetics of the oxidation reactions is assumed to be very fast compared with these mass transfer processes.

The equilibrium oxygen concentration at the reaction interface $C_{O_2,e}$ in equation (9) is negligible compared with the bulk oxygen concentration $C_{O_2,b}$, and thus was assumed to be zero. The oxygen bulk-phase mass transfer coefficient $k_{O_2,b}$ required in equation (9) was computed from the Sherwood number correlation [23]:

$$Sh = 2 + 0.6 Re_p^{1/2} Sc^{1/3} \quad (11)$$

where Sc is the Schmidt number for gas species and Re_p is the particle Reynolds number, as defined in the nomenclature. The oxygen effective diffusivity through the porous oxide layer $D_{O_2,e}$ was estimated from:

$$D_{O_2,e} = D_{O_2,b} \psi^2 \quad (12)$$

where $D_{O_2,b}$ is the oxygen molecular diffusivity in a mixture with SO_2 and N_2 , estimated from the Chapman-Enskog equation [23], and ψ is the porosity of the oxide shell. Based on calculations of the particle volume before and after oxidation, a constant value of 0.16 was used for the oxide shell porosity. The unreacted core radius r_c also required to evaluate the right-hand side of equation (9) was computed from:

$$r_c = \left(\frac{V_c}{V_p}\right)^{1/3} r_p \quad (13)$$

where V_c is the volume of the unreacted matte core, V_p is the particle volume, and r_p is the particle radius. Although the computer code allows for particle volume changes as the reactions proceed, in the present study constant-size particles were assumed for simplicity.

Equation (10) was assumed to be valid up to the melting point of the oxide shell and while the oxide phase is being melted; if the particle becomes totally molten, an external mass-

transfer control mechanism was assumed; i.e., the second term in the right hand side of equation (10) was set equal to zero.

The particle heat capacity was calculated at every time step along the particle trajectory as a weighted average of the heat capacities of the individual phases present. The heats of fusion for both the sulfide and oxide phases were computed based on Richard's law [24]. No copper volatilization was considered.

Reactions (7) and (8) and equations (9)-(13) complete the kinetic model proposed. These equations were coupled with equations (5) and (6) and solved using an Adam's predictor-corrector algorithm. The solution provides the particle compositions and particle temperature along a set of representative trajectories in the shaft. If the particle reaches the melting point of either the sulfide core or the oxide shell, the temperature is held constant, and the rate of melting is computed from the right-hand side of equation (5).

RESULTS AND DISCUSSION

This section describes the results of numerical simulations performed with the present model. The simulation strategy involved two stages: the model verification with laboratory-scale flash converting measurements and the simulation of its general performance, and the prediction of an industrial flash converting shaft.

Model verification and analysis of a bench-scale furnace

An experimental program is currently being conducted in a large bench-scale flash furnace shaft at the University of Utah. Different operating conditions are being tested to evaluate their influence on the behavior of a flash converting operation. Details of the experimental setup can be found in reference [10] and are similar to those of the apparatus described elsewhere [25]. A complete report of the experimental data so far collected in this furnace is currently under preparation [9].

Table I shows the furnace dimensions as well as the general operating conditions during the experiments reported here. Table II shows the input variables tested in the experiments.

Table I. Experimental parameters for the bench-scale flash furnace shaft

<u>Inlet and reactor geometry:</u>	
Primary stream diameter, m	0.0195
Secondary stream diameter, m	0.065
Reactor diameter, m	0.24
Reactor length, m	1.52
<u>Wall temperature (K):</u>	
Top wall:	1373
Side walls:	1373
Bottom surface:	1373
<u>Primary stream (particles):</u>	
Matte feed rate, kg/s	8.33×10^{-4}
Temperature, K	303
Axial particle velocity, m/s	3.3
<u>Secondary stream (process gas):</u>	
Temperature, K	303
Feed rate, ton O ₂ /ton matte	0.33

Table II. Input variables tested in the experiments

	Test No.			
	1	2	3	4
Particle size fraction, μm	74-105	74-105	105-149	105-149
Oxygen concentration, vol. %	70	100	70	100
Gas feed rate, kg/s	3.75×10^{-4}	2.72×10^{-4}	3.75×10^{-4}	2.72×10^{-4}

In Table II, the first two rows represent the independent variables actually specified prior to conducting the experiments. Row 3 can be calculated from the gas feed rate in ton O₂/ton matte given in Table I and the oxygen concentration values given in Table II.

A convergent gas-flow burner was used in the experiments. The gas flow was equally distributed through six inlet ports symmetrically located on top of the burner. The gas was injected through these ports and entered the furnace through six 2-mm diameter nozzles at the burner tip. The gas streams at the tip of the nozzles are aimed to converge at the centerline of the shaft at 17° angle with respect to the centerline. Because the actual

boundary conditions for this type of flow cannot be accommodated in an axisymmetric formulation, the gas-injection configuration was represented as the annulus for the secondary stream shown in Figure 1. A negative radial velocity component was assigned to the secondary stream to represent the convergent flow. The area of the annulus was selected so that the magnitude of the inlet gas velocity computed by the discretized model was as close as possible to the actual gas velocity at the burner's nozzles; the latter was calculated by dividing the volumetric flow rate through each nozzle by the area of the nozzle.

Fractional Conversion

For a flash converting process, the following definition of fractional conversion (F_c) has been recently introduced by Sohn et al. [9]:

$$F_c = 1 - \frac{(OR)_{sample}}{(OR)_{feed}} \quad (14)$$

where $(OR)_{sample}$ and $(OR)_{feed}$ represent the amount of oxygen requirement to oxidize all sulfur and iron in sample and feed particles, respectively, to SO_2 and Fe_3O_4 . These quantities are computed as the difference between the stoichiometric amount of oxygen to oxidize all sulfur and iron in the particles to SO_2 and Fe_3O_4 and the amount of oxygen already in the particle. When the fractional conversion is unity, either all iron and sulfur have been oxidized to magnetite and sulfur dioxide or, if the sample contains sulfur, it also contains excess of oxygen just enough to form SO_2 when it reaches the molten bath. Fractional conversion as defined by equation (14) may take on values higher than unity if the sample is overoxidized. Since the goal of a flash converting operation is to form elemental copper and not copper oxides, the fractional conversion is a better indicator of the degree of oxidation of matte particles than the fraction of sulfur remaining, which is generally used to study the oxidation behavior of sulfide particles [5,12,16].

Figure 2 shows the comparison between the experimental and computed values of fractional conversion for the conditions summarized in Table II. Some scatter in the experimental data is observed, which accounts among other things for the difficulties in the sampling techniques in a flash converting reactor as well as the uncertainties in chemical analysis.

Overall, a good agreement with the experimental data was obtained. This suggests that the estimation of the rate of oxygen consumption from equation (9) is reliable.

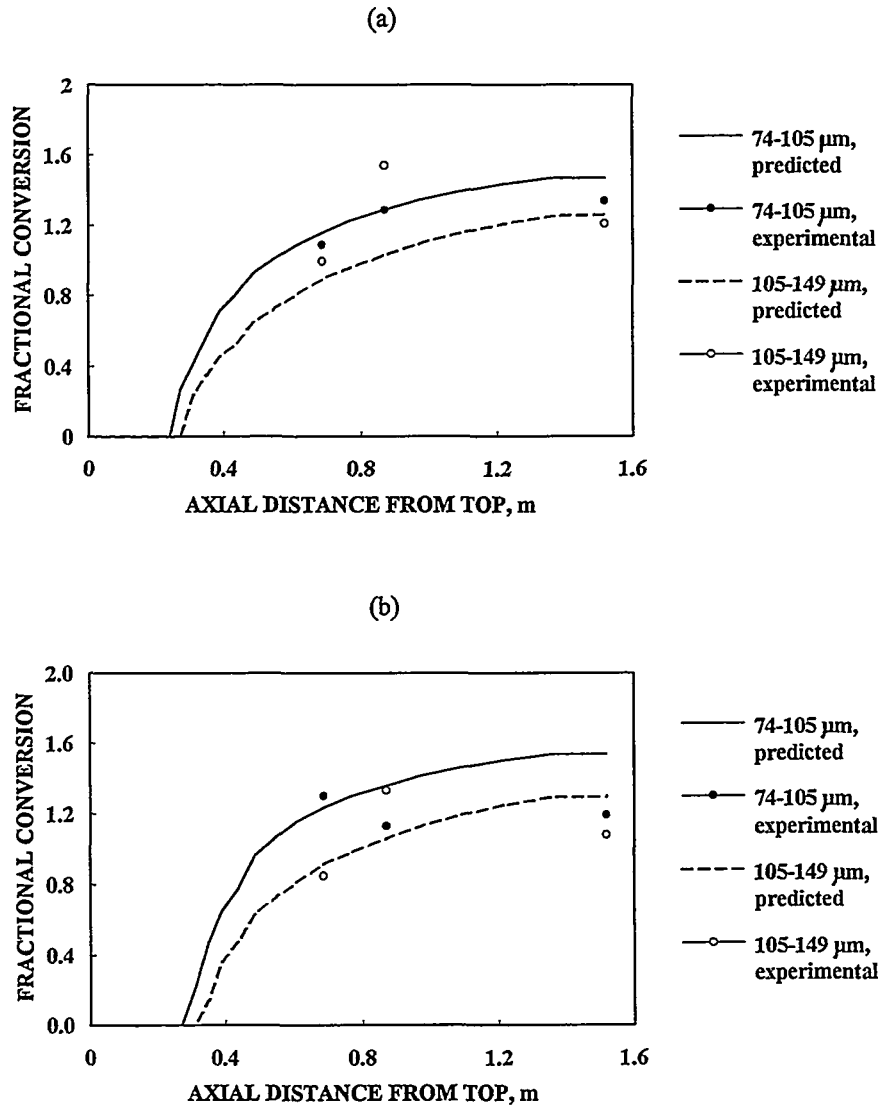


Fig. 2 - Predicted and experimental values of fractional conversion of matte particles along the centerline.
 (a) 70% O_2 ; (b) 100% O_2 in feed.

It is of interest that between 70 and 100%, the effect of oxygen concentration on the conversion along the centerline is relatively small. Unlike in a plug flow situation, the fractional conversion is a more complicated function of many factors in this type of a system, including the recirculating flow and gas injection configuration.

It would normally be expected that the ignition and reaction would take place further away from the burner tip with a lower oxygen concentration for two reasons: (1) The reaction rate is slower and (2) the gas flowrate is larger for the same solid feed rate. Apparently, these factors do not make a sufficient difference compared with the complex flow conditions when the oxygen concentration in the process gas is varied from 70 to 100%.

The effect of a much lower oxygen concentration was tested using 10% O₂ in the process gas as shown in Figure 3 along with the replotted results for 70 and 100% O₂ from Figure 2. A substantial effect can be seen, as perhaps expected.

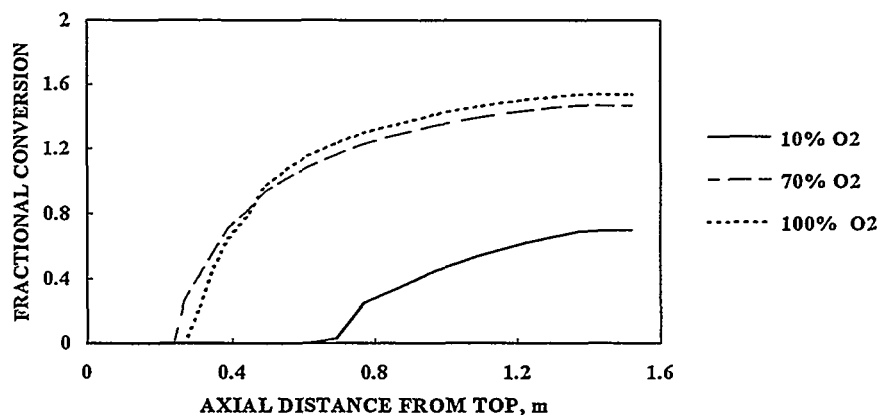


Fig. 3 - Predicted values of fractional conversion along the centerline for different oxygen concentration in the gas feed, particle size 74-105 μm and conditions given in Table I.

The major differences shown in Figure 3 are due to the variation in the gas flow rate. The volumetric flow rate increases in the ratio 1:1.4:11.7 as the oxygen concentration in the feed is decreased from 100 to 70 to 10%. Thus, in the last case, ignition takes place much further away and once ignited the reaction proceeds more slowly.

Sulfur remaining in the particles

The amount of sulfur left in the particle is another indicator of the progress of the oxidation reactions. Experimentally, the fraction of initial sulfur left in the particle was calculated from the particle's chemical analysis as follows [5]:

$$S_{rem} = \frac{(wt\%S)_{sample} (wt\%Fe)_{feed}}{(wt\%S)_{feed} (wt\%Fe)_{sample}} \quad (15)$$

Equation (15) is a normalized measurement against the iron concentration, and it is based on the assumption that iron does not volatilize. Computationally, the fraction of sulfur remaining was calculated from the ratio between the total sulfur in the particle as $Cu_2S \cdot yFeS$ at a given time and the total sulfur in the original particle.

In Figure 4 the corresponding values of S_{rem} predicted by this model are presented. The model consistently represents the trend observed in the experiments. Quantitatively, however, the model underpredicts the S_{rem} values by a difference of nearly 0.2. This suggests that the assumption of a constant FeS/Cu_2S molar ratio may have to be more closely examined. The agreement between predicted and experimental values is slightly better for the large particles (105-149 μm) than for the small particles (74-105 μm).

Copper content in particle

Figure 5 shows the weight fraction of total copper in the matte particles obtained experimentally and those predicted by the present model. Overall, a good agreement is observed. The experimental data show that some copper might be lost by volatilization, since copper weight fraction values tend to decrease slightly along the furnace. Reactions (7) and (8) are weight-loss reactions. Therefore, the predicted values show that copper weight fraction increases slightly as a result of the oxidation. Since no copper volatilization was considered in the present model, predicted values tend to an asymptotic value as reactions (7) and (8) tend to completion.

Bench-scale furnace analysis

Since the present model has been largely verified with experimental data, it can be used to study the main features of the bench-scale furnace.

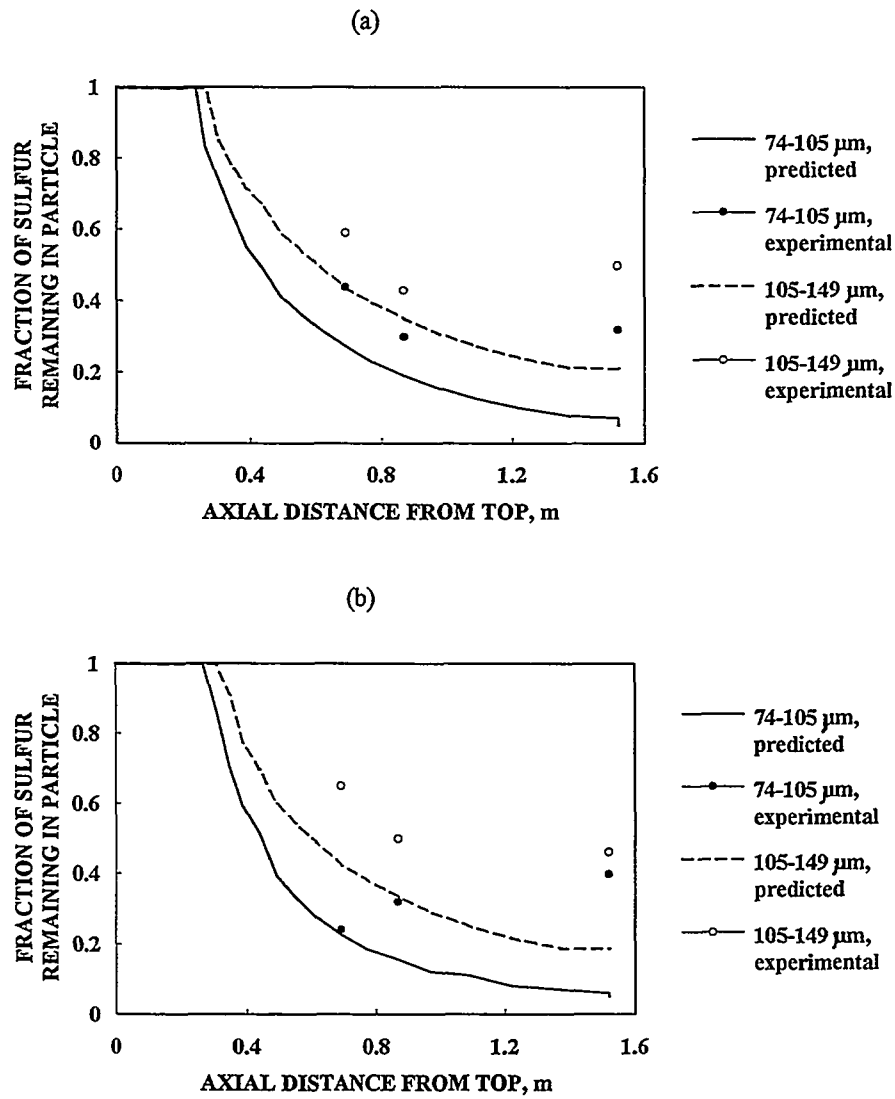


Fig. 4 - Predicted and experimental values of fraction of sulfur remaining in copper matte particles along the centerline. (a) 70% O_2 ; (b) 100% O_2 in feed.

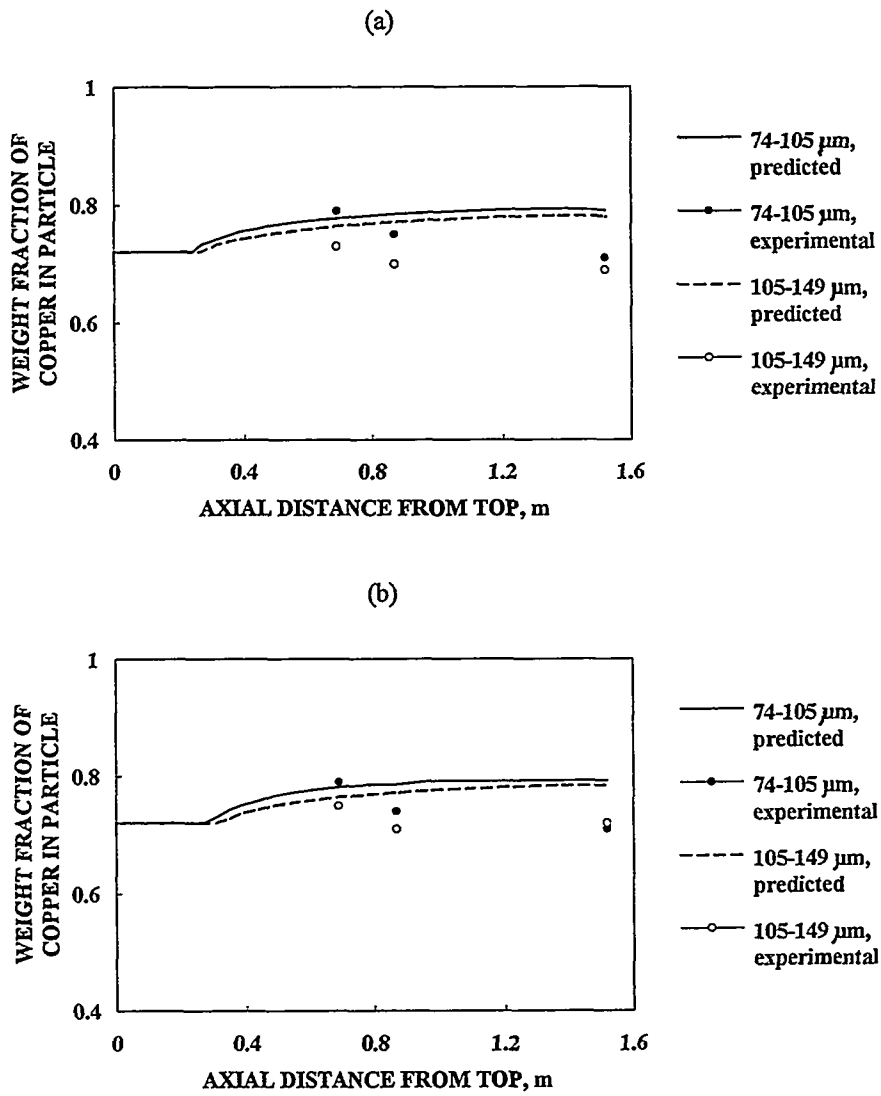


Fig. 5 - Predicted and experimental values of weight fraction of total copper in matte particles along the centerline; a) 70 % O_2 ; b) 100 % O_2 in feed.

A summary of predicted particle temperatures along the centerline for all tests reported in Table II is shown in Figure 6. The results are consistent with the furnace behavior so far discussed. Depending on the operating conditions, ignition is predicted within the first 20-40 cm from the burner tip. The reactions proceed fast after this point, heating the particles up to the melting point of the sulfide core, 1470 K. The net heat gained by the particles is thereafter used to partly melt the sulfide core. The presence of partially melted particles was confirmed experimentally [10].

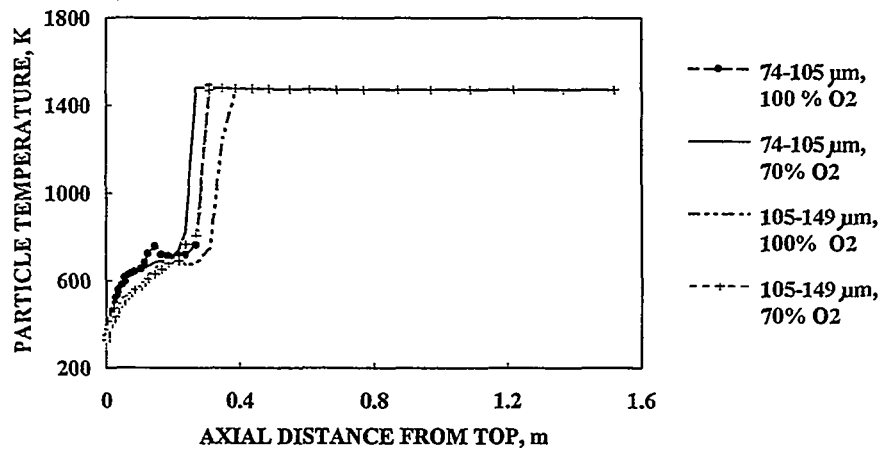


Fig. 6 - Computed particle temperature along the centerline for all experimental conditions of Table II.

Figure 7(a) shows the computed gas-velocity vectors in the furnace shaft for a typical run. Test No. 3 was used for the purpose of illustration. Turbulent-flow conditions are predicted in the vicinity of the burner tip; a large recirculation zone extending close to the shaft end is also predicted. The bulk gas-flow seems to be concentrated within a short distance from the centerline. Figure 7 also shows that stagnant-flow conditions are expected at the shaft end.

A magnification of the gas flow in the vicinity of the burner tip is shown in Figure 7(b). Radial flow is significant only close to the inlet port of the secondary stream (dimensionless radial distance 0.2-0.25). Since no gas is fed with matte particles through the primary stream, the axial velocity at the centerline increases until the secondary stream hits the centerline; this occurs within a 20 cm away from the burner tip.

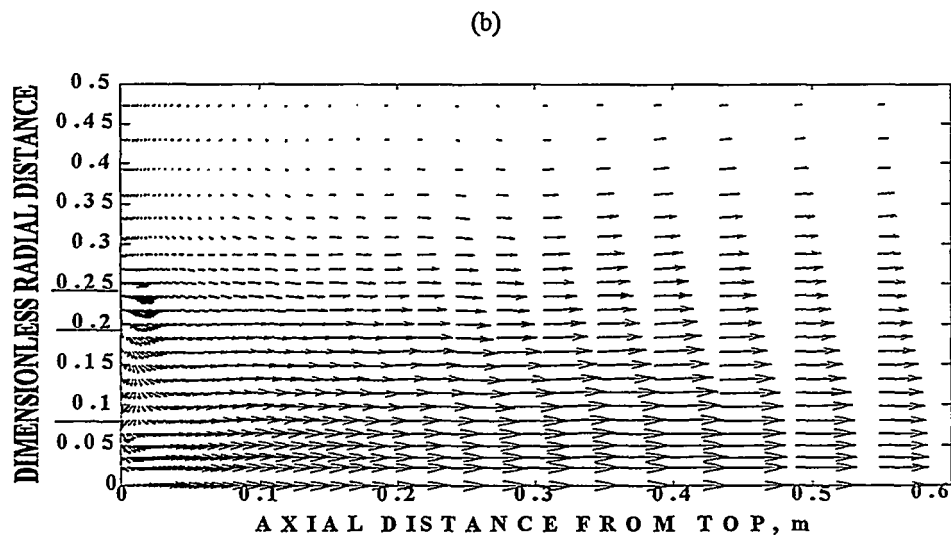
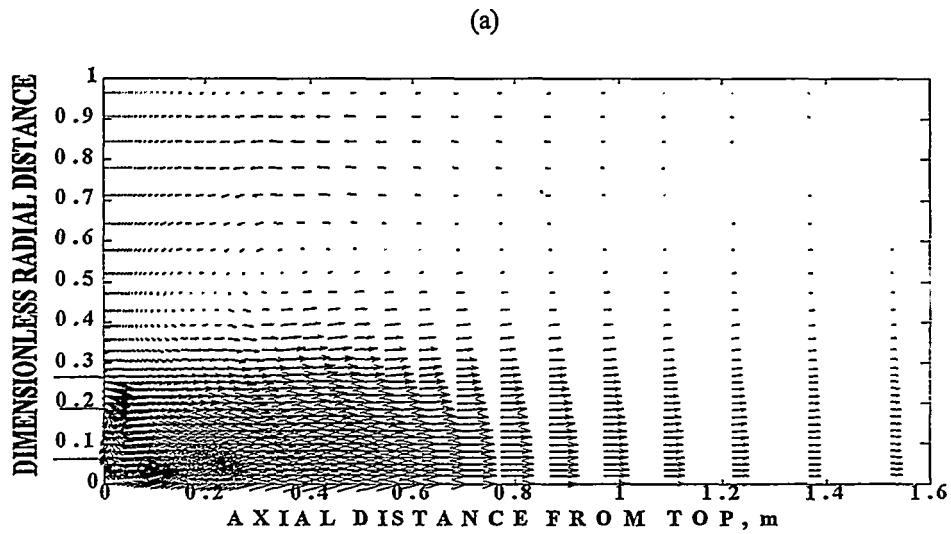


Fig. 7 - Computed gas-velocity vectors in the bench-scale flash furnace for Test 3 in Table II. a) whole furnace; b) magnification in the vicinity of the burner tip.

Gas-composition contours for oxygen and sulfur dioxide are shown in Figures 8(a) and 8(b). Unlike temperature contours (Figure 9), composition contours still change beyond the burner's vicinity. This can be explained from Figure 6. Whereas most of the energy exchange between particles and gas occurs close to the burner, beyond that point reactions are still taking place at a constant particle temperature (1470 K).

Figure 9 shows the corresponding gas temperature contours in the vicinity of the burner tip. No further temperature changes occur beyond about 0.5 m from the burner.

Particle trajectories are shown in Figure 10. Again, because of the flow pattern observed, particles are concentrated within a short distance from the centerline.

Simulation of an industrial flash converting furnace

Table III shows the parameters used to simulate the performance of an industrial flash converting furnace. The furnace dimensions are approximately those of an industrial unit. Two different gas-injection configurations listed in Table IV were tested. In Case 1 the primary stream does not have a radial velocity component. In Case 2 the primary stream is given an outward (positive) radial velocity component, simulating the Outokumpu burner with a distributor cone. In both cases, the same feed rate is used for the secondary stream, which has axial velocity only. Matte particles are fed through the secondary stream in this test case. In other axisymmetric simplification of the burner configuration, the particles can be considered to be fed with the primary gas. A more realistic description of the burner and injection configuration would require a three-dimensional model.

Figure 11 shows the velocity vectors computed for Cases 1 and 2 in the whole furnace. In both cases the highest velocities are concentrated within a short distance from the burner tip. It is also seen that the gas jet is spread more widely in Case 2 where the primary stream is given an outward radial velocity component.

Figure 12 shows the magnification of the flow patterns computed in the vicinity of the burner tip. Much larger recirculation zones with a greater variation of flow velocities are seen for Case 1 compared with Case 2. Consequently, the gas flow is distributed more evenly in Case 2 in the region near the burner where matte particle reaction takes place.

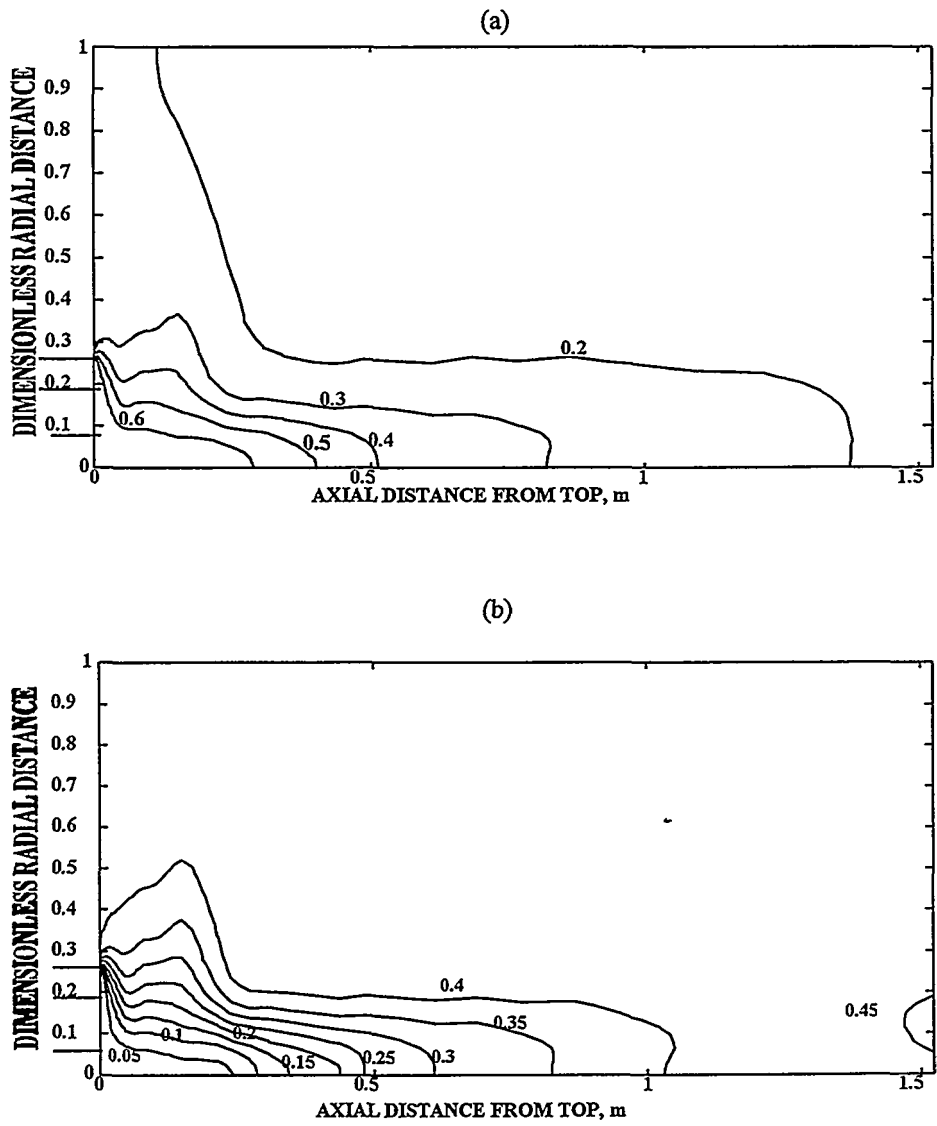


Fig. 8 - Gas-phase concentration contours for Test No. 3. a) oxygen; b) sulfur dioxide. Values indicate concentration in mole fraction.

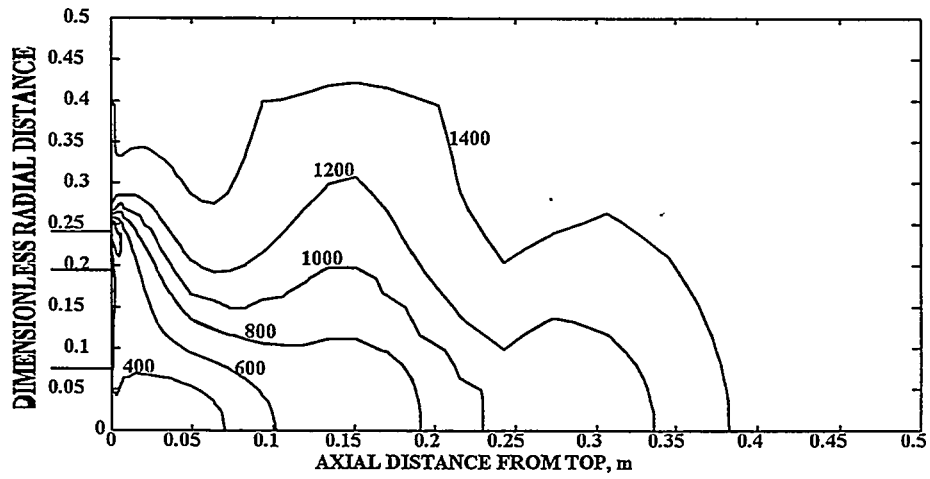


Fig. 9 - Gas temperature contours for Test No. 3. Values indicate temperature in Kelvins.

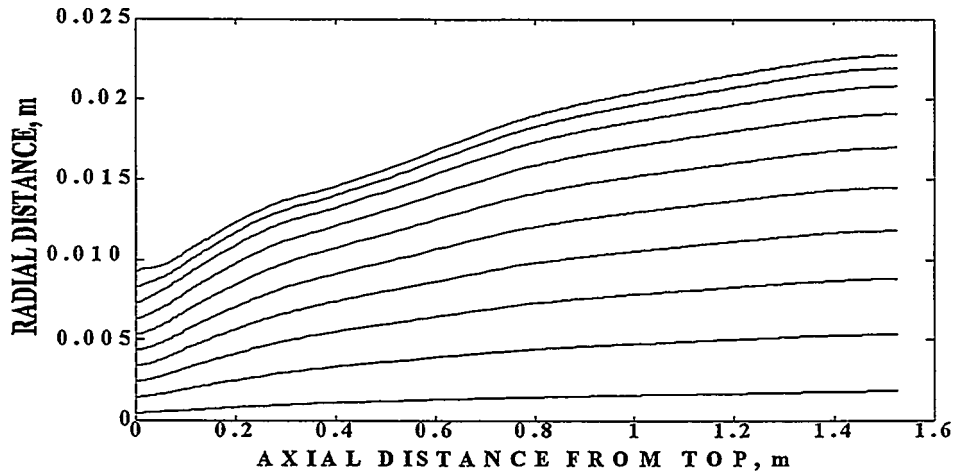


Fig. 10 - Computed particle trajectories for Test No. 3.

Table III. Parameters for the simulation of an industrial flash converting furnace

<u>Inlet and reactor geometry:</u>	
Primary stream diameter, m	0.36
Secondary stream diameter, m	1.0
Reactor diameter, m	4.4
Reactor length, m	8.4
<u>Wall temperature (K):</u>	
Top wall:	1543
Side walls:	1543
Bottom surface:	1543
<u>Primary/secondary streams:</u>	
Temperature, K	303
Total feed rate, ton O ₂ /ton matte	0.3*
O ₂ concentration, mol fraction	0.7
<u>Matte feed (secondary stream):</u>	
Matte feed rate, kg/s	12.6
Particle size, μm	120

*1.2 times oxygen requirement.

Table IV. Gas-injection configurations tested

	Case No.	
	1	2
<u>Primary stream:</u>		
Flow rate, kg/s	1.4	1.4
Axial velocity, m/s	12.6	12.6
Radial velocity, m/s	0	28
<u>Secondary stream:</u>		
Flow rate, kg/s	5.6	5.6
Axial velocity, m/s	8.6	8.6
Radial velocity, m/s	0	0

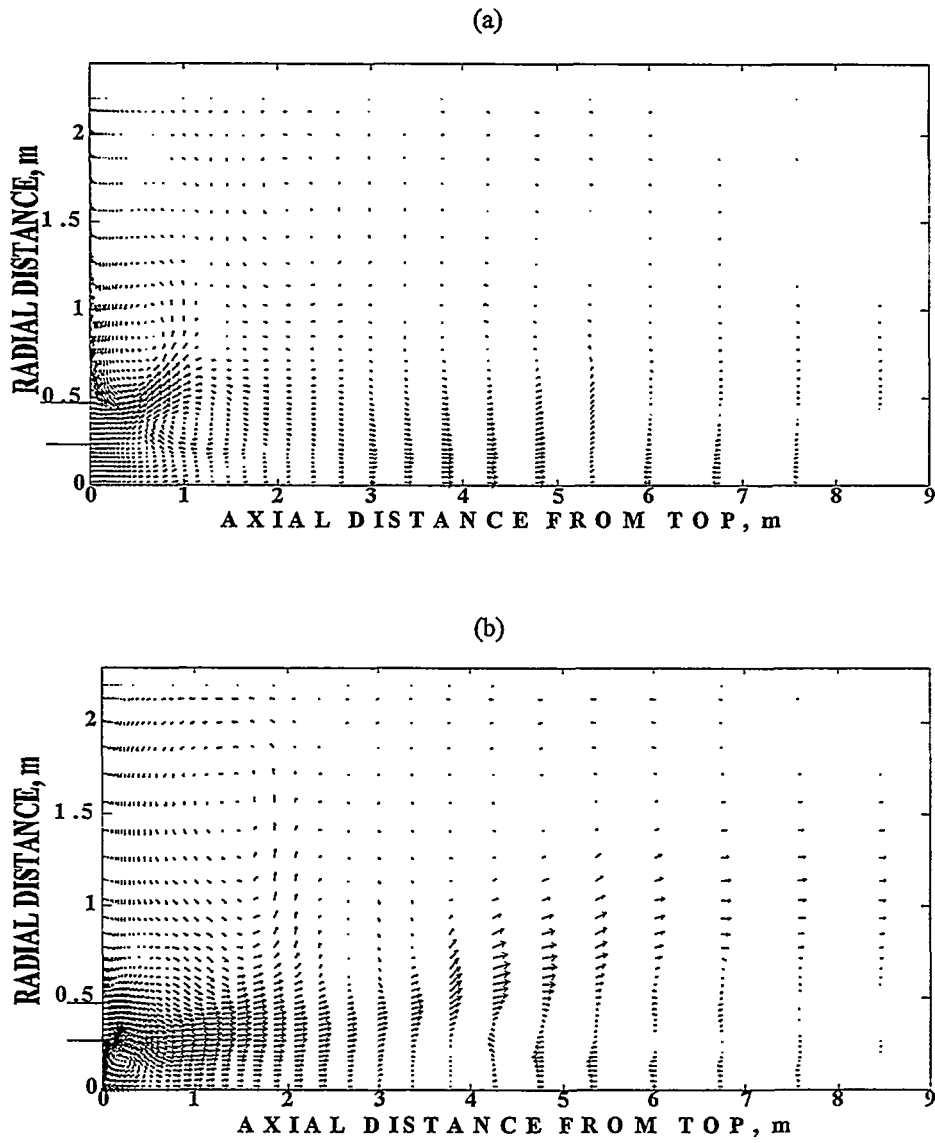


Fig. 11 - Computed velocity vectors in an industrial flash converting furnace. (a) Case 1; (b) Case 2.

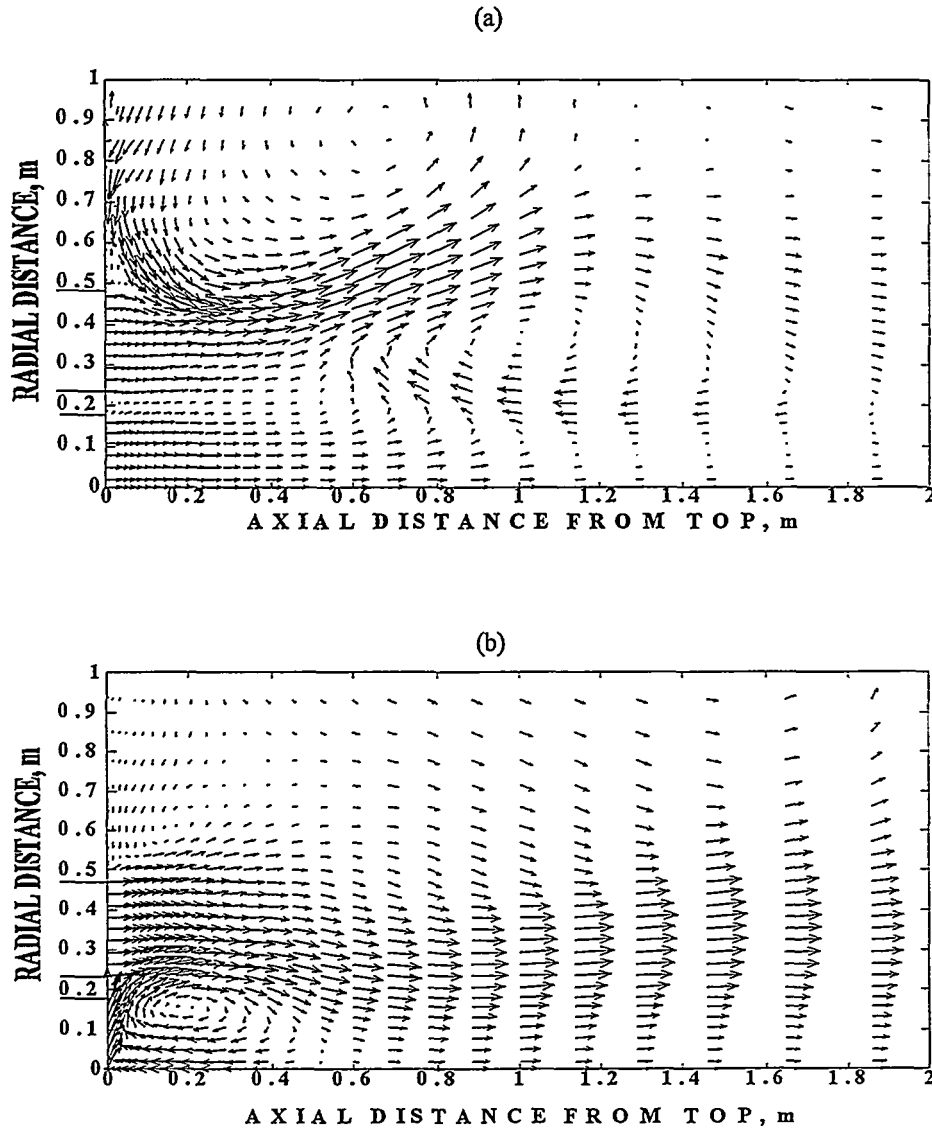


Fig. 12 - Computed velocity vectors in an industrial flash converting furnace. Magnification in the vicinity of the burner tip.
(a) Case 1; (b) Case 2.

As a result of the turbulent transport of particles (equation 4) and the velocity fields shown in Figure 11, it is expected that close to the shaft end the particles will be concentrated closer to the centerline in Case 1, whereas in Case 2 the particles will be dispersed more evenly along the furnace diameter.

The greater variation in the gas velocity in Case 1 is expected to cause much less even reaction of particles, i.e. some of the particles will be overoxidized and some underoxidized out of the fixed amount of oxygen. Thus, more of the overall converting reaction to produce elemental copper would need to take place in the settler. In addition to the more even distribution of particles, which would allow the reaction to be completed within a shorter shaft length, the more even reaction of the particles in Case 2 would allow more rapid completion of reaction and equilibration of the molten phases in the settler.

The results discussed throughout this paper for both the bench-scale and the industrial flash converting furnaces show that the present model can be used to perform further studies on the basic principles of the flash converting process. Work is continuing to improve the mathematical model based on the contributions of other researchers in the field, as well as new experimental data from the bench-scale facility at the University of Utah.

CONCLUSIONS

A mathematical model for the Kennecott-Outokumpu flash converting process for converting solid copper matte to copper was developed. The model solves the governing equations for the transport of momentum, heat, mass, and particle-gas reaction kinetics in a turbulent particle-laden gas jet.

The verification of the present model with experimental data collected in a bench-scale flash converting furnace showed a good agreement between the predicted and experimental values for the fractional conversion of matte particles and the weight fraction of total copper in the particles. The fraction of sulfur remaining in the particle was underpredicted by the model. The results suggest that the estimation of the rate of oxygen consumption by the present model is reliable, whereas the assumption of a constant FeS/Cu₂S molar ratio may have to be more closely examined.

Simulations of the bench-scale facility showed that turbulence is concentrated within 0.2-0.4 m from the burner tip. Within this distance most of the mass exchange and thus chemical reactions between gas and particles takes place. Partially molten particles are predicted at the end of the reaction shaft. Oxygen and sulfur dioxide gas-phase concentrations were predicted to decrease gradually along the reaction shaft.

Two gas-injection configurations were tested in the simulation of an industrial flash converting furnace. The simulations showed that the inclusion of a radial gas velocity component in the primary stream increases the particle and gas dispersion along the furnace diameter.

Acknowledgments

The authors wish to express their gratitude to Outokumpu Oy for the financial support of this work, providing the raw materials and for performing the sample analysis; in particular to Dr. Pekka Taskinen, Mr. Asko Parviainen, and Dr. Juho Mäkinen of Outokumpu for their continuing technical input and support; to Mr. David George of Kennecott for his interest and technical support; to our colleague Daniel Swartling for his indefatigable work during the experimental runs as well as for providing new ideas and first-hand data analyses; to our colleague Byung-su Kim who helped in the early stages of the experimental work. MPT expresses his gratitude to CONACYT, Universidad de Sonora (Mexico), and IIE-Fulbright (USA) for providing the scholarship grants for his graduate program. KMR thanks the Outokumpu Foundation and the Finish Academy for providing the funding for her graduate program.

Nomenclature

A_p	External surface area of particle
C	Molar concentration
C_D	Drag coefficient
d_p	Particle diameter
D_{O_2b}, D_{O_2p}	Oxygen molecular/effective diffusivity
D_p^t	Turbulent particle diffusivity
F_c	Fractional conversion

g	Gravity acceleration vector
$\Delta H_1, \Delta H_2$	Reaction enthalpies
\dot{H}_m	Rate of heat loss due to melting
\dot{H}_r	Rate of heat production by reaction
\dot{H}_v	Rate of heat loss due to volatilization
h_p	Particle enthalpy
k	Turbulent kinetic energy
k_{O_2b}	Bulk-gas oxygen mass transfer coefficient
k_{ov}	Overall reaction rate constant
m_p	Particle mass
\bar{n}_k	Particle number density of k-th particle size
n_i	Moles of condensed species i in the particle
$(OR)_{feed}, (OR)_{sample}$	Oxygen requirement of feed/sample
q	Total number of chemical reactions
q_{rp}	Radiative heat transfer rate for the particle phase
\dot{Q}_p	Rate of heat loss due to gas-phase convection
r	Radial distance from the axis of symmetry
r_c	Unreacted core radius
r_p	Particle radius
R_{O_2}	Total rate of oxygen consumption
$R_{r,j}$	Reaction rate of species i in reaction j
$R_{v,i}$	Vaporization rate of species i
Re_p	Reynolds number = $\rho_g \mathbf{V}_g - \mathbf{V}_p d_p / \mu_g$
S_{rem}	Fraction of sulfur remaining in particle
S_ϕ	Source term in gas-phase governing equations
Sc	Schmidt number = $\mu_g / \rho_g D_{O_2b}$
Sh	Sherwood number = $k_{O_2b} d_p / D_{O_2b}$
t	Time
u	Axial velocity
v	Radial velocity
\mathbf{V}	Velocity vector
\mathbf{V}_{pd}	Particle diffusion velocity vector
V_p, V_c	Volume of particle, volume of the unreacted core
x	Axial distance from burner tip
y	FeS/Cu ₂ S molar ratio

Greek symbols

Γ_e	Effective transport exchange coefficient
ε	Dissipation rate of turbulent kinetic energy
μ	Laminar viscosity
ν_{ij}	Moles of species i per mole of oxygen consumed in reaction j
ρ	Density
ψ	Porosity

Subscripts

b	bulk
g	gas
e	equilibrium
p	particle

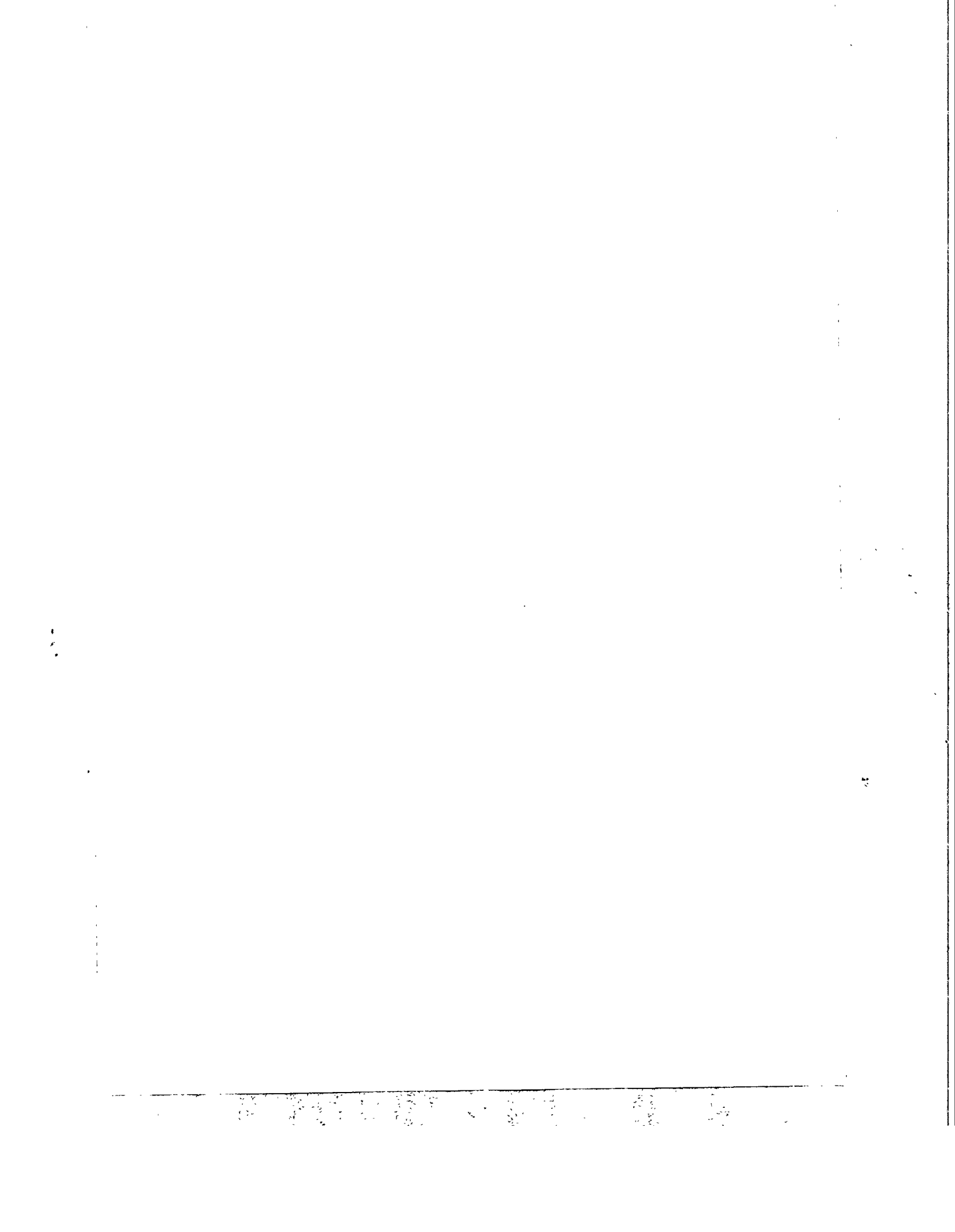
References

1. Asteljoki, J.A., Bailey, L.K., George, D.B., and Rodolff, D.W., "Flash Converting Continuous Converting of Copper Mattes". Journal of Metals, Vol. 20, 1985, 245-250.
2. Asteljoki, J.A., and Kytö, S.M., "Minor Element Behavior in Flash Converting". TMS Technical Paper A86-57. TMS Annual Meeting, New Orleans, 1986.
3. Jiao, Q., Wu, L., and Themelis, N.J. "Mathematical Modeling of Flash Converting of Copper Matte". Mathematical Modeling of Materials Processing Operations, Szekely, J., Hales, H.B., Henein, H., Jarret, N., Rajamani, K., and Samarsekera, I., Eds., TMS, Warrendale, Pennsylvania, 1987, 835-858.
4. Chaubal, P.C., Sohn, H.Y., George, D., and Bailey, L. "Mathematical Modeling of Minor-Element Behavior in Flash Smelting of Copper Concentrates and Flash Converting of Copper Mattes", Metallurgical Transactions, Vol. 20B, 1989, 39-51.
5. Suominen, R., Jokilaakso, A., Taskinen, P., and Lilius, K. "Behavior of Copper Mattes in Simulated Flash Converting Conditions", Scandinavian Journal of Metallurgy, Vol. 20, 1990, 245-250.
6. Suominen, R., Jokilaakso, A., Taskinen, P., and Lilius, K. "Morphology and Mineralogy of Copper Matte Particles Reacted in Simulated Flash Converting Conditions", Scandinavian Journal of Metallurgy, Vol. 23, 1994, 30-36.

7. Pérez-Tello, M., Sohn, H.Y., and Löttiger, J. "Oxidation Characteristics of Solid Copper Matte Particles", Proceedings of Copper 95, Vol. IV, Pyrometallurgy of Copper, Chen, W.J., Díaz, C., Luraschi, A., and Mackey, P.J., Eds., CIM, Montreal, Quebec, Canada, 1995, 499-514.
8. Löttiger, J. "Oxidation Characteristics of Solid Copper Matte Particles", M.Sc. Thesis, Royal Institute of Technology, 1995, Stockholm, Sweden.
9. Sohn, H.Y., Riihilahti, K., and Pérez-Tello, M. "Oxidation of Copper Matte Particles in a Simulated Flash Converting Furnace Shaft", report in preparation, University of Utah, Salt Lake City, Utah.
10. Swartling, D. "Study of Particle Fragmentation in a Laboratory-Scale Simulation of the Flash Converting of a Copper Matte", M.Sc. Thesis, Royal Institute of Technology, 1996, Stockholm, Sweden.
11. Jorgensen, F., and Segnit, E.R. "Copper Flash Smelting Simulation Experiments", Australas. Inst. Min. Metall., Vol. 261, 1977, 39-46.
12. Jorgensen, F., "Single-Particle Combustion of Chalcopyrite", Australas. Inst. Min. Metall., Vol. 288, 1983, 37-46.
13. Kim, Y.H., and Themelis, N., "Effect of Phase Transformation and Particle Fragmentation on the Flash Reaction of Complex Metal Sulfides", The Reinhardt Schuhman Intl. Symp. on Innovative Technology and Reactor Design in Extractive Metallurgy, Gaskell, D., Hager, J.P., Hoffman, J.E., Mackey, P., Eds., TMS, Warrendale, Pennsylvania, 1986, 349-369.
14. Warczok, A., Utigard, T.A., Mroz, W., and Kowalczyk, J., "Oxidation of Copper Sulphide Minerals in Suspended State", EPD Congress 1992, Hager, J.P., Ed., TMS, Warrendale, Pennsylvania, 1991, 729-744.
15. Launder, B.E., and Spalding, D.B. Mathematical Models for Turbulence, Academic Press, London, 1972.
16. Hahn, Y.B., and Sohn, H.Y. "Mathematical Model of Sulfide Flash Smelting Process. Part I." Metallurgical Transactions, Vol. 21B, 1990, 945-958.
17. Hahn, Y.B., and Sohn, H.Y., "Mathematical Model of Sulfide Flash Smelting Process. Part II." Metallurgical Transactions, Vol. 21B, 1990, 959-966.

18. Tennekes, H., and Lumley, J.L. A First Course in Turbulence, MIT Press, Cambridge, MA, 1972, 2-26.
19. Gosman, A.D., and Punm, W.M., "Lecture Notes for Course Entitled 'Calculation of Recirculating Flows'", Imperial College, London, 1973.
20. Patankar, S.V. Numerical Heat Transfer and Fluid Flow, McGraw-Hill, New York, NY, 1980, 79-135.
21. Crowe, C.T., Sharma, M.P., and Stock, D.E., "The Particle-Source-in Cell Model for Gas-Droplets Flows", Journal of Fluids Engineering, June, 1977, 325-332.
22. Biswas, A.K., and Davenport, W.G. Extractive Metallurgy of Copper, Pergamon Press, New York, NY, 1976.
23. Bird, R.B., Stewart, W.S., and Lightfoot, E.N. Transport Phenomena, John Wiley & Sons, New York, NY, 1960, 647.
24. Darken, L.S., and Gurry, R.W., Physical Chemistry of Metals, McGraw-Hill, New York, NY, 1953, 125.
25. Sohn, H.Y. "The Coming-of-Age of Process Engineering in Extractive Metallurgy" Metallurgical Transactions, Vol. 22B, 1991, 737-754.

For Your Notes



1998

Simulation of Reaction Kinetics in Pyrometallurgical Reactors

David G.C. Robertson
Center for Pyrometallurgy
University of Missouri-Rolla
Rolla, MO, 65409-1460, USA

Abstract

Not available

Helsinki University of Technology
3rd Colloquium on Process Simulation
12 - 14 June, 1996
Espoo, Finland

For Your Notes

1948

Modeling of Nitriding and Denitriding Reactions in Liquid Ni-20% Cr Alloy during Sieverts' Experiments

L. Petitcolas, A. Jardy, D. Ablitzer
Laboratoire de Science et Génie des Matériaux Métalliques, U.R.A. 159,
Ecole des Mines, Parc de Saurupt, 54042 NANCY Cedex

Abstract

In order to give a detailed description of the kinetic laws governing the exchanges at the liquid metal/gas interface, a mathematic model has been developed for the hydrodynamic behavior of the liquid metal and solute transport in an induction furnace. With the aid of this model, it has been shown that, during Sieverts' experiments, the nitriding and denitriding reactions in a liquid Ni-20% Cr alloy at 1873 K both follow a chemical regime. In the case of nitriding, nitrogen transfer is controlled by the rate of dissolution of the adsorbed atoms ($N_{ad} \rightarrow N_i$). For denitriding, the rate-limiting step is the chemical reaction at the interface at the adsorption sites ($2N_{ad} \rightarrow N_{2ad}$) and/or the desorption of gaseous nitrogen ($N_{2ad} \rightarrow N_{2i}$).

Vectors

\vec{A}	potential vector (T.m)
\vec{B}	magnetic induction (T)
\vec{F}	Lorentz forces (N.m ⁻³)
\vec{J}	current density in the metal charge (A.m ⁻²)
\vec{J}_{ex}	excitation current density (A.m ⁻²)
\vec{V}	velocity (m.s ⁻¹)

Notations

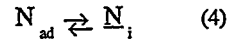
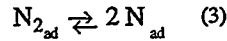
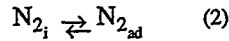
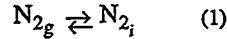
D	atomic diffusivity (m ² .s ⁻¹)
D _t	turbulent diffusivity (m ² .s ⁻¹)
h _m	mass transfer coefficient in the liquid boundary layer (m.s ⁻¹)
k	turbulent kinetic energy per unit mass (J.kg ⁻¹)
k ₁	overall reaction rate constant for first order kinetics (m.s ⁻¹)
k ₂	overall reaction rate constant for second order kinetics (m.s ⁻¹)
kr ₁	chemical reaction rate constant for first order kinetics (m.s ⁻¹)
kr ₂	chemical reaction rate constant for second order kinetics (m.s ⁻¹)
K _S	Sieverts' constant (ppm.Pa ^{-1/2})
P	pressure (Pa)
S	interface area (m ²)
Sc _t	Schmidt number for turbulent flow
t	time (s)
V	bath volume (m ³)

Greek symbols

ε	rate of dissipation of the turbulent kinetic energy (W.kg ⁻¹)
μ	dynamic viscosity of the alloy (kg.m ⁻¹ .s ⁻¹)
μ _t	turbulent viscosity (kg.m ⁻¹ .s ⁻¹)
μ ₀	magnetic permeability of vacuum (H.m ⁻¹)
σ	electrical conductivity of the metal (Ω.m) ⁻¹
ρ	density of the liquid metal (kg.m ⁻³)
ω _N	weight concentration of dissolved nitrogen
ω _{Ne}	weight concentration of dissolved nitrogen at equilibrium
ω _{Ni}	weight concentration of dissolved nitrogen at the interface

INTRODUCTION

The overall mechanism of nitriding or denitriding from a liquid alloy can be broken down into five steps, only four of which (steps 2 to 5) are potentially rate-controlling [1, 2]:



(g : gas, i : interface, ad : adsorbed)

A rigorous determination of the rate-controlling step requires a knowledge of the rate of each step. However, the experimental measurements provide information on the rate of the **overall** nitrogen dissolution reaction, $N_{2g} \rightarrow 2\underline{N}_{bath}$. It has been shown elsewhere [1, 3] that this reaction can obey:

- either overall kinetics of first order with respect to the dissolved nitrogen concentration, in which case:

$$\varphi_{\underline{N}} = k_1 \rho (\omega_{\underline{N}_e} - \omega_{\underline{N}}) \quad (1)$$

where k_1 ($m.s^{-1}$) is the rate constant for an **overall** reaction of first order. Nitrogen dissolution is then controlled either by transport in the liquid (step 5), or by chemical reaction at the interface (step 4), or by both (mixed regime);

- or overall kinetics of second order with respect to the dissolved nitrogen concentration, in which case:

$$\varphi_{\underline{N}} = k_2 \rho (\omega_{\underline{N}_e}^2 - \omega_{\underline{N}}^2) \quad (2)$$

where k_2 ($m.s^{-1}$) is the rate constant for an **overall** reaction of second order. The rate controlling step is then either step 2 or step 3, or both.

A previous experimental study [1] revealed that, during a Sieverts' experiment (see below), the overall kinetics of the nitriding reaction in liquid Ni-20% Cr alloy at 1873 K are of first order, whereas those for the corresponding denitriding reaction are of second order. In order to study the mechanisms involved in these reactions in more detail, a mathematical model has been developed for the hydrodynamic behavior of the liquid metal and for solute transport. The aim of the model is to simulate nitriding and denitriding in a liquid alloy either in the VIM (vacuum induction melting) process or in an experimental installation where melting is produced by induction heating (e.g. in the Sieverts'

technique). The reaction chamber in the Sieverts' installation is composed of an alumina crucible containing the liquid metal, surrounded by an induction coil. The concentration of nitrogen dissolved in the alloy is determined by measuring the temperature and pressure during the stages of absorption or desorption.

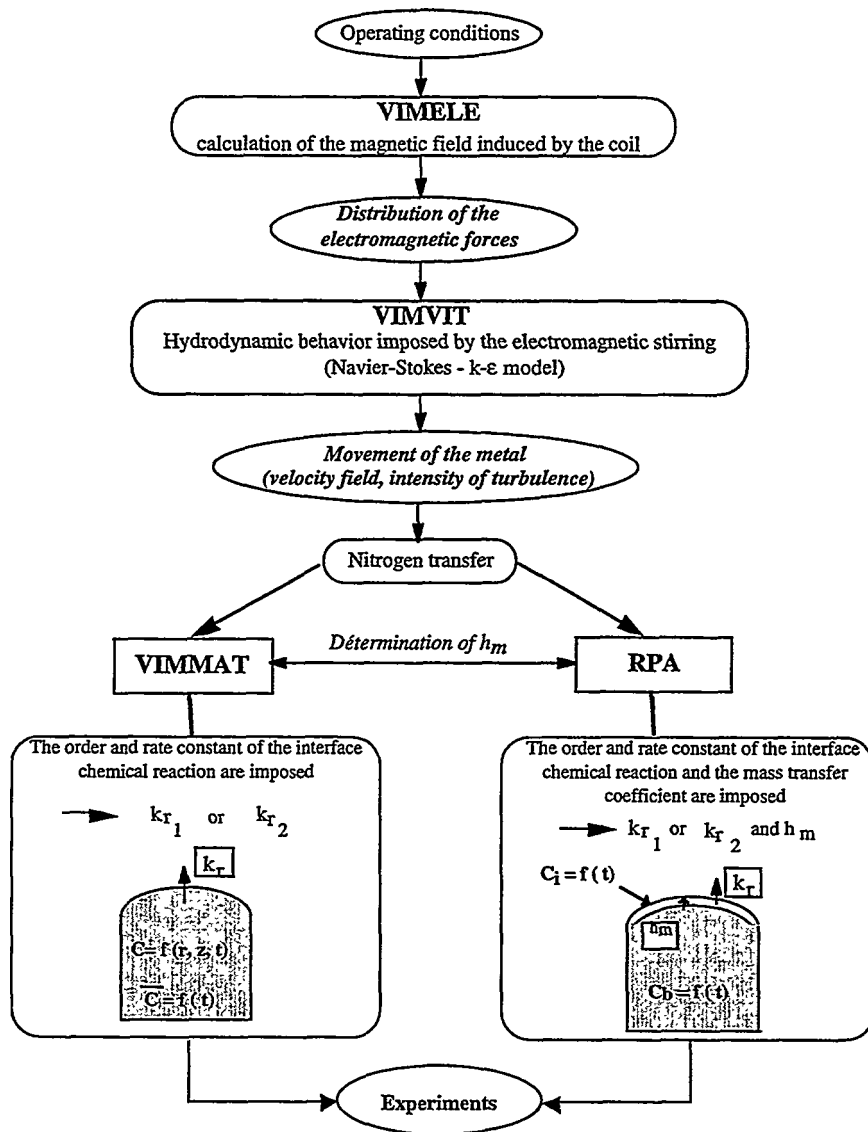


Fig. 1 - Principle of the model employed.

The aim of this procedure is to determine the rate controlling step in the transfer of nitrogen between the gas and the liquid metal. The general modeling approach employed is shown schematically in Figure 1, and will be described below. During induction melting, because of the electromagnetic forces, the free surface of the liquid can become dome-shaped [4-6]. This has been observed experimentally in Sieverts' tests, as demonstrated by the photograph of a sample after testing (Fig. 2). In order to simulate these real conditions as closely as possible, this deformation of the free surface has been taken into account in the model, requiring the use of a curved mesh.

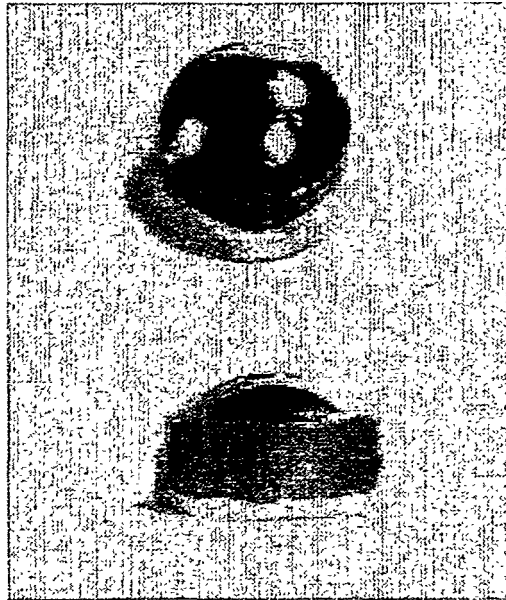


Fig. 2 - Sample after experiment (top and front views) : radius 13 mm, center height 17 mm, dome height 4 mm.

DESCRIPTION OF THE HYDRODYNAMIC BEHAVIOR OF THE BATH

The calculation of the variation in solute content is based on a nitrogen balance in the liquid bath, taking into account mass transport by convection, diffusion and turbulence. The description of flow in the liquid metal requires solution of the Navier-Stokes equations associated with a turbulence model, necessitating prior determination of the three-dimensional electromagnetic force field acting on the metal.

Calculation of electromagnetic forces ("VIMELE")

The stirring forces are created by interaction between the alternating electromagnetic field generated by the copper coil and the currents induced in the metal by the electromotive force resulting from the fluctuations in magnetic induction. The flow of electric current in the inductor creates a magnetic field given by the Maxwell equations :

$$\frac{1}{\mu_0} \nabla \times (\nabla \times \vec{A}) = -\sigma \frac{\partial \vec{A}}{\partial t} + \vec{J}_{\text{ex}} \quad (3)$$

where \vec{J}_{ex} represents the density of the current in the induction coil. This term is therefore zero everywhere except inside the coil. The first term on the right hand side is also zero at all points in the field covered by the calculation other than in the metal charge. Using the (r, θ, z) coordinates imposed by the system geometry, together with the complex exponential representation, the model solves equation (3), associated with appropriate boundary conditions, by separating the real part of the complex potential vector A_r from the imaginary part A_i . Knowledge of the potential vector A at all points in the system studied (Fig. 3) enables determination of :

- the resulting magnetic induction $\vec{B} : \vec{B} = \nabla \times \vec{A}$
- the current density \vec{J} in the metal charge : $\vec{J} = \frac{1}{\mu_0} \nabla \times \vec{B}$
- the Lorentz forces at all points in the metal bath : $\vec{F} = \vec{J} \times \vec{B}$

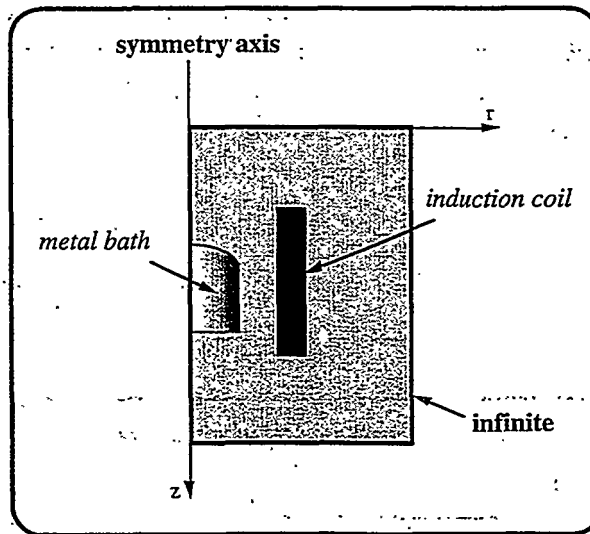


Fig. 3 - Schematic representation of the region described by the model (VIMELE).

Calculation of the liquid metal flow ("VIMVIT")

Calculation of the velocity field in the liquid bath requires solution of the total mass conservation and momentum transport equations in the steady state regime, taking into account the turbulent nature of the flow. For an incompressible fluid, the momentum transport equation is :

$$\rho (\vec{V} \cdot \vec{\nabla}) \vec{V} = -\vec{\nabla} P + \vec{\nabla} \cdot ((\mu + \mu_t) \vec{\nabla} \vec{V}) + \vec{F} \quad (4)$$

The left hand side term in this equation corresponds to the convective transport, and the second term on the right to transport by diffusion and turbulence. The other terms represent the creation of momentum due to pressure and electromagnetic forces. In order to solve this equation, the model uses a formulation in terms of the secondary variables, vorticity (ω) and current function (ψ), as proposed by Gosman et al. [7].

The turbulent nature of the flow is taken into account by using the concept of turbulent viscosity, defined in terms of the classical k- ϵ turbulence model originally developed by Launder and Spalding [8]. The k- ϵ model is based on the solution of two additional transport equations, one for k, the turbulent kinetic energy per unit mass, and the other for ϵ , the rate at which this energy is dissipated. The turbulent viscosity at all points is calculated via the relation :

$$\mu_t = C_\mu \rho \frac{k^2}{\epsilon} \quad (5)$$

where C_μ is an empirical constant, equal to 0.09 [8].

Boundary conditions

The boundary conditions must be specified at the symmetry axis, the free surface, and the liquid metal/refractory interface (Fig. 4). In particular, these conditions specify the axial symmetry, the conditions of zero velocity and turbulence at the crucible walls, and the nature of the turbulence at the free surface. From a theoretical standpoint, very few studies have been made on the conditions to be applied to the turbulence variables at the free surface. Indeed, the physical nature of the turbulence phenomenon at the gas/liquid metal interface (attenuation, anisotropy, etc.) is not fully established. Nevertheless, some authors [9, 10] have proposed that the free surface can be stabilized, for example by the surface tension. As regards the turbulence, this effect could be compared to that of a solid wall and could lead to zero turbulence at the surface [11]. As a first approximation, it is this latter boundary condition which has been chosen.

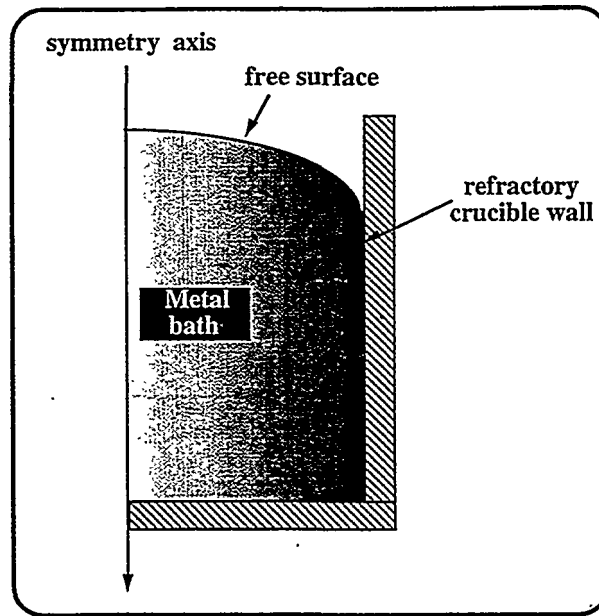


Fig. 4 - Boundaries of the region covered by the hydrodynamics calculation (VIMVIT).

Results obtained with the model

Numerical solution of the partial differential equations is performed using the finite volume method [12]. The physical and electrical parameters involved in the calculation are summarized in Table I. The complete modeling procedure is applied here to the experimental Sieverts' installation.

Table I Physical and electrical parameters used in the model

Number of winds in the coil	8
Frequency	8×10^3 Hz
Coil current	150 A
Electrical conductivity of the alloy	10^6 ($\Omega \text{ m}$) ⁻¹
Density of the alloy	7.74×10^3 kg.m ⁻³
Dynamic viscosity of the liquid alloy	5×10^{-3} kg.m ⁻¹ .s ⁻¹
Atomic diffusion coefficient for nitrogen in the liquid alloy	5×10^{-9} m ² .s ⁻¹

Electromagnetic forces

The force calculation takes into account the geometrical characteristics of the metal-induction coil assembly in the experimental rig, together with the electrical adjustments used during the experiments (Table I). The force field created in the metal bath is illustrated in Figure 5. It can be seen that the intensity of the stirring forces increases near the side walls of the crucible. The maximum values attained are of the order of $3 \cdot 10^4 \text{ N.m}^{-3}$.

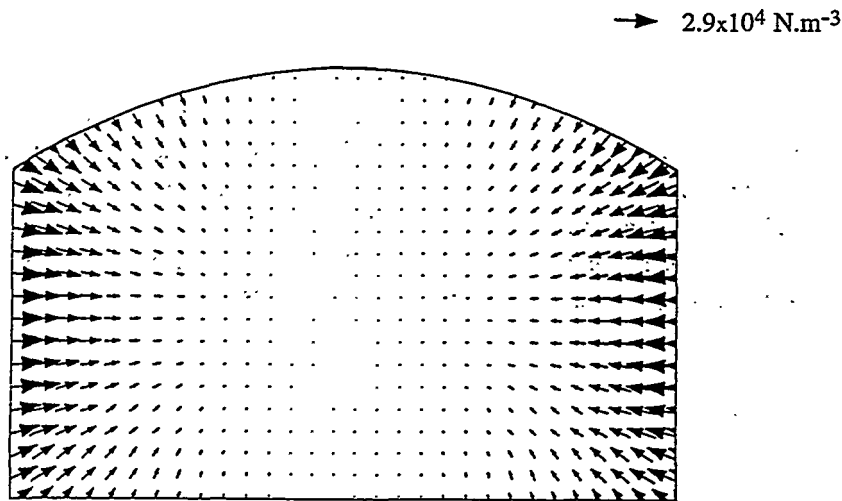


Fig. 5 - Electromagnetic force field induced in the metal.

Mean flow velocity and turbulence

The velocity field obtained enables the movement of the metal to be visualized (Fig. 6). The presence of two oppositely directed recirculation loops can be seen around the symmetry axis. The lowest velocities occur in the bottom part of the bath. At the free surface, the movement is directed towards the crucible walls. The maximum velocities reached are 0.114 m.s^{-1} and are situated at the bath surface.

As regards the turbulence, its intensity can be characterized by the ratio between the turbulent viscosity and the dynamic viscosity. Figure 7 shows an isovalue map of this ratio $\frac{\mu_t}{\mu}$. The lowest values occur near the crucible walls. The ratio is of the order of 20 at the point where the symmetry axis intersects the free surface.

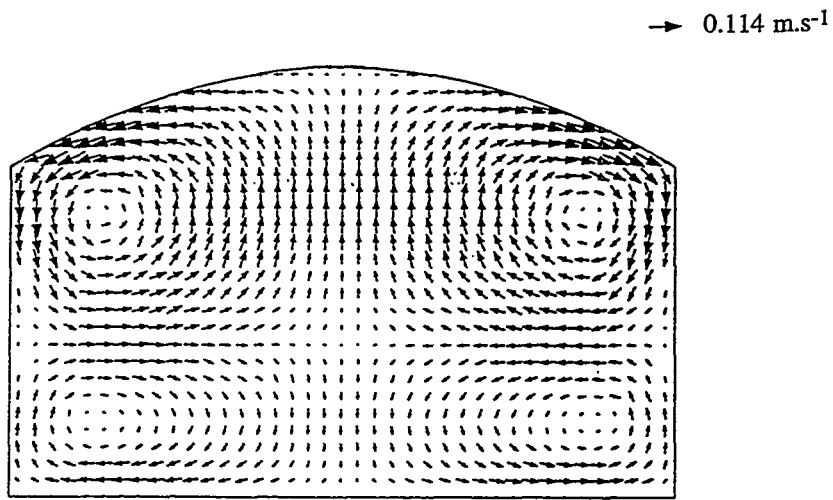
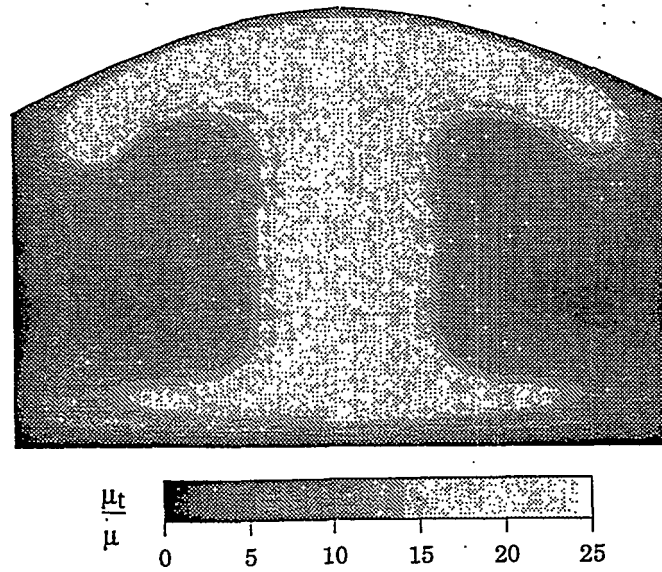


Fig 6 - Velocity field.

Fig. 7 - Intensity of turbulence (ratio μ_t/μ).

MODELING MATTER TRANSPORT

Solute transport model ("VIMMAT")

In the transient regime, the transport of nitrogen dissolved in the liquid metal can be represented by the following partial differential equation, which expresses the conservation of solute in an infinitely small volume element :

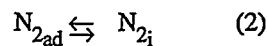
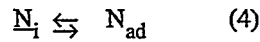
$$\frac{\partial \omega_N}{\partial t} = - \vec{\nabla} \cdot (\omega_N \vec{V} - (D + D_t) \vec{\nabla} \omega_N) \quad (6)$$

The turbulent diffusivity D_t is calculated from the Schmidt number for turbulent flow Sc_t , assumed to be equal to unity [13] and defined by the expression :

$$Sc_t = \frac{\mu_t}{\rho D_t} \quad (7)$$

It can be seen that solution of the transport equation (6) requires the knowledge of the velocity \vec{V} and turbulent viscosity μ_t at all points. These two quantities have been calculated previously, using the "VIMVIT" hydrodynamic model.

The boundary conditions express the symmetry of the problem and the requirement of zero mass flow at the crucible walls. At the free surface, it is necessary to take into account either the supply of nitrogen in the case of nitriding, or the loss of nitrogen during denitriding. The representation of nitrogen transfer across the liquid metal/gas interface during denitriding takes into account the chemical reaction of formation of gaseous nitrogen from the nitrogen dissolved in the liquid metal, or the reverse reaction in the case of nitriding :



If the rate of the chemical reaction at the interface is limited by steps (2) or (3), the kinetics are of second order with respect to the dissolved nitrogen concentration at the interface. The nitrogen flux density entering the liquid metal at any point on the surface is then expressed in the form :

$$\phi_N = k_{r2} \rho (\omega_{N_e}^2 - \omega_N^2) \quad (8)$$

where k_{r2} (m.s^{-1}) is the second order rate constant of the **chemical reaction**, and ω_{N_e} and ω_N are the weight concentrations of dissolved nitrogen, at equilibrium and at the point considered respectively.

On the contrary, if the rate of the chemical reaction at the interface is limited by step (4), its kinetics are of first order with respect to the dissolved nitrogen concentration, and :

$$\varphi_N = k_{r1} \rho (\omega_{N_e} - \omega_N) \quad (9)$$

where k_{r1} (m.s^{-1}) is the first order rate constant of the **chemical reaction**.

The concentration of dissolved nitrogen at equilibrium, ω_{N_e} is obtained from Sieverts' law, which expresses the dissolved nitrogen content in equilibrium with the gas phase as a function of the square root of the nitrogen partial pressure :

$$\omega_{N_e} = K_S \cdot \sqrt{P_{N_2}} \quad (10)$$

where the Sieverts' constant K_S represents the solubility of nitrogen in the Ni-Cr alloy under a nitrogen partial pressure of 1.013×10^5 Pa [1].

The two expressions (8) and (9) represent the boundary conditions at the liquid metal/gas interface. In the model, one or other of these conditions is used, with an appropriate adjustment of the value of the chemical reaction rate constant in order to obtain the best fit with the experimental results. By improving the agreement between the experimental and simulated results in this way, a more reliable conclusion can be drawn concerning the order of the chemical reaction at the interface.

The nitrogen transfer equation (6), associated with the boundary conditions, is solved by the finite volume method, using the same curvilinear mesh as that employed in the "VIMVIT" model.

Results obtained with the "VIMMAT" model

Nitriding and denitriding experiments based on the Sieverts' technique have been simulated. The results of the numerical simulations are maps of the instantaneous concentration of nitrogen, together with the curve representing the variation with time of the mean dissolved nitrogen content of the bath.

Nitriding experiments

The experiment C2n1, for which the experimentally determined overall rate constant k_1 is equal to $4.4 \times 10^{-4} \text{ m.s}^{-1}$ was simulated by imposing boundary conditions corresponding to an interface reaction of first order (Fig. 8a). By fitting the experimental measurements and the simulated results, a value of $5.5 \times 10^{-4} \text{ m.s}^{-1}$ is found for the interface reaction rate constant k_{r1} .

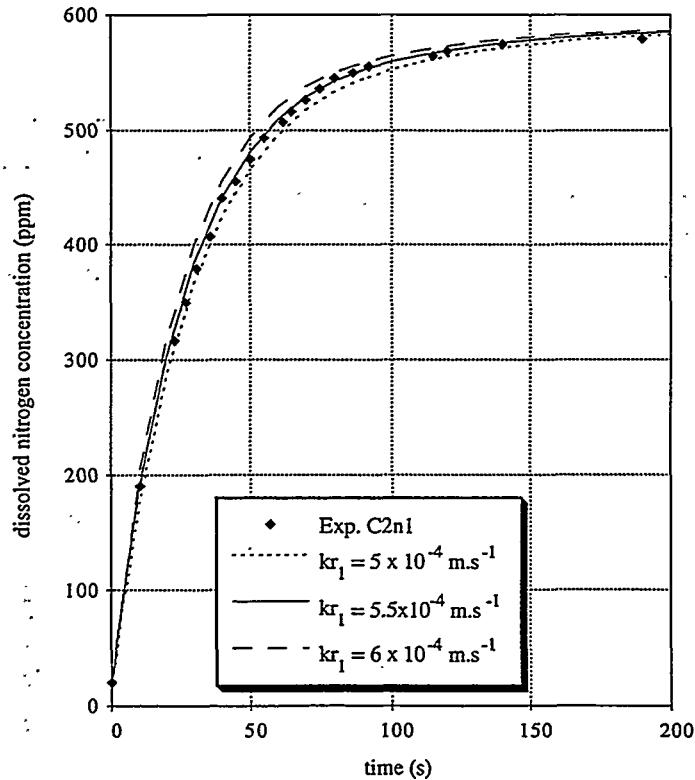


Fig. 8a - Simulation of experiment C2n1, imposing a first order interface reaction.

This same experiment was also simulated with the imposition of second order kinetics for the interface reaction. Figure 8b shows that the best fit with the experimental results is obtained for a value k_{r2} of 0.70 m.s^{-1} . Even in this best-fit case, it can be seen that the simulation does not describe the experiment accurately throughout its duration. The interface reaction cannot therefore be considered to follow second order kinetics.

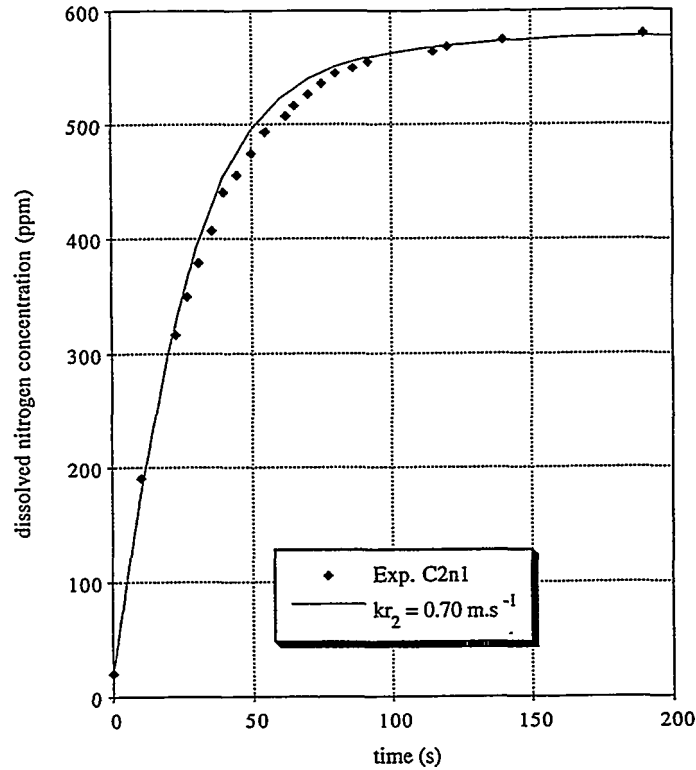


Fig. 8b - Simulation of experiment C2n1, imposing a second order interface reaction.

Consideration of all the simulated Sieverts' nitriding experiments shows that the interface reaction follows first order kinetics. For each simulated experiment, the value of the rate constant k_{r1} is close to that of the overall rate constant k_1 (Table II), but the two values are not exactly equal. This could indicate that transport in the liquid phase has a slight influence on the overall nitriding kinetics, corresponding to a mixed regime dominated by the chemical reaction at the interface.

Table II Simulation results for several nitriding experiments in Ni-20% Cr alloy at 1873 K

Experiment n°.	Overall kinetics	Overall rate constant k_1 (m.s^{-1})	Kinetics of the interface reaction	Interface reaction rate constant k_{r1} (m.s^{-1})
C1n1	1st order	4.3×10^{-4}	1st order	5.2×10^{-4}
C2n1	1st order	4.4×10^{-4}	1st order	5.5×10^{-4}
C2n2	1st order	4.4×10^{-4}	1st order	5.5×10^{-4}

Denitriding experiments

Figure 9a shows the results of the simulation of a denitriding experiment (Exp. C5d, for which the overall rate constant k_2 is equal to 0.81 m.s^{-1}), imposing an interface chemical reaction with second order kinetics. The best fit with the experimental results is obtained for a value of k_{r2} equal to 1.05 m.s^{-1} . This experiment was also simulated with an imposed interface reaction of first order. It can be seen in Figure 9b that, in this case, the model does not correctly describe the results over the whole length of the experiment.

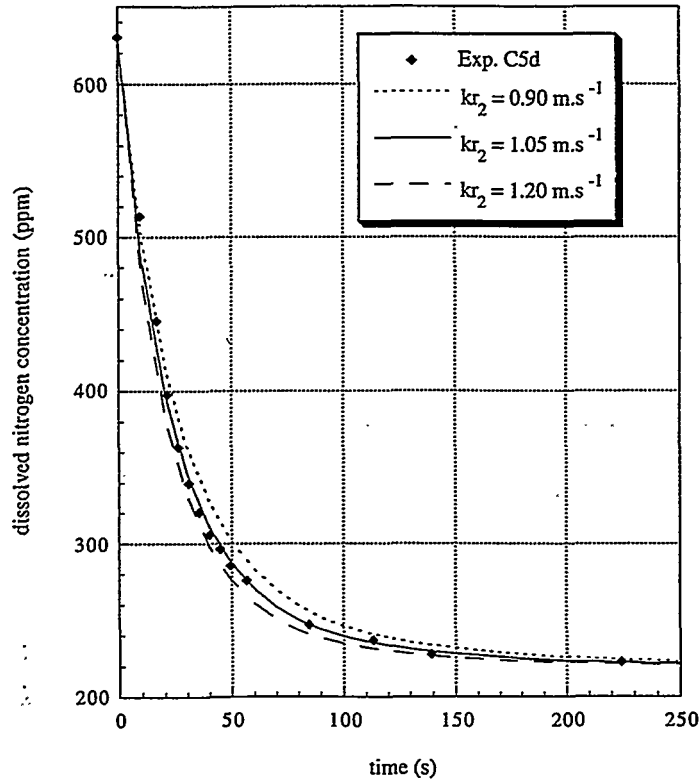


Fig. 9a - Simulation of experiment C5d, imposing a second order interface reaction.

For all the simulated denitriding experiments, the rate constant k_{r2} for the chemical reaction at the interface is found to have a value close to that of the overall rate constant k_2 (Table III). However, as in the case of the nitriding reaction, the two constants are not exactly equal, probably for the same reasons. It can therefore be concluded that the rate of denitriding in the Ni-Cr alloy is controlled principally by the second order chemical reaction at the interface.

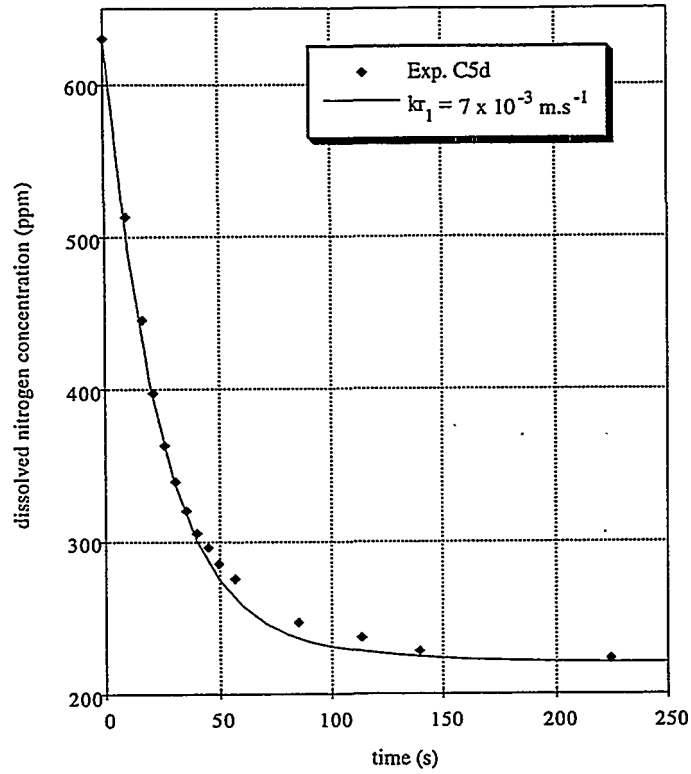


Fig. 9b - Simulation of experiment C5d, imposing a first order interface reaction.

Table III Simulation results for several denitrating experiments in Ni-20% Cr alloy at 1873 K

Experiment n°.	Overall kinetics	Overall rate constant k_2 (m.s^{-1})	Kinetics of the interface reaction	Interface reaction rate constant k_{r2} (m.s^{-1})
C2d1	2nd order	0.79	2nd order	0.95
C4d1	2nd order	0.39	2nd order	0.50
C5d	2nd order	0.81	2nd order	1.05

The batch reactor model ("RPA")

At this stage, it is of interest to point out that, in the Sieverts' experiments, electromagnetic stirring is sufficiently strong to prevent matter transport in the liquid from being the rate controlling step in the nitriding and denitriding processes. Examination of a nitrogen concentration map for any given instant during denitriding (Fig. 10) shows that stirring produces excellent homogeneity at virtually all points in the bath. It is for this reason that a simplified matter transfer model was also developed.

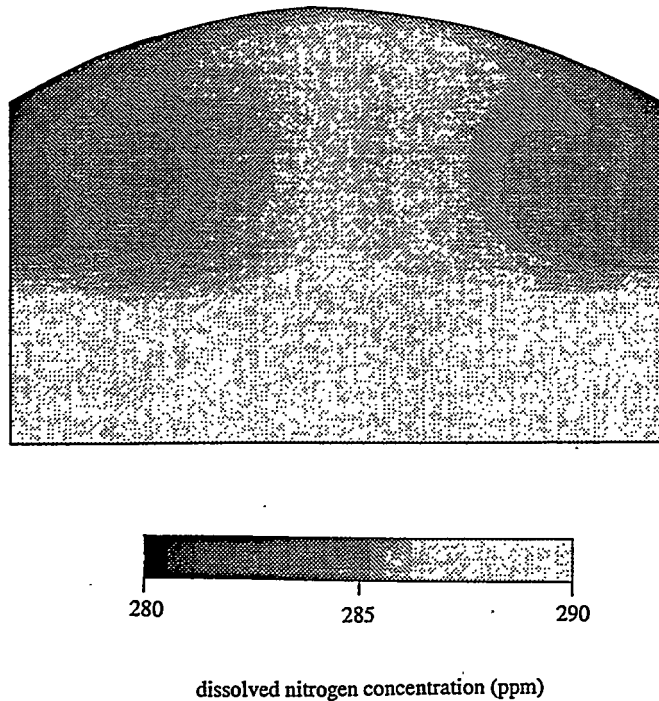


Fig. 10 - Typical nitrogen concentration map during a denitriding reaction
(Exp. C5d, $t = 50$ s).

Principle

The model assumes the existence of two regions in the liquid bath (Fig. 11), corresponding respectively to a boundary layer of negligible thickness adjacent to the gas/liquid metal interface, and the remainder of the bath.

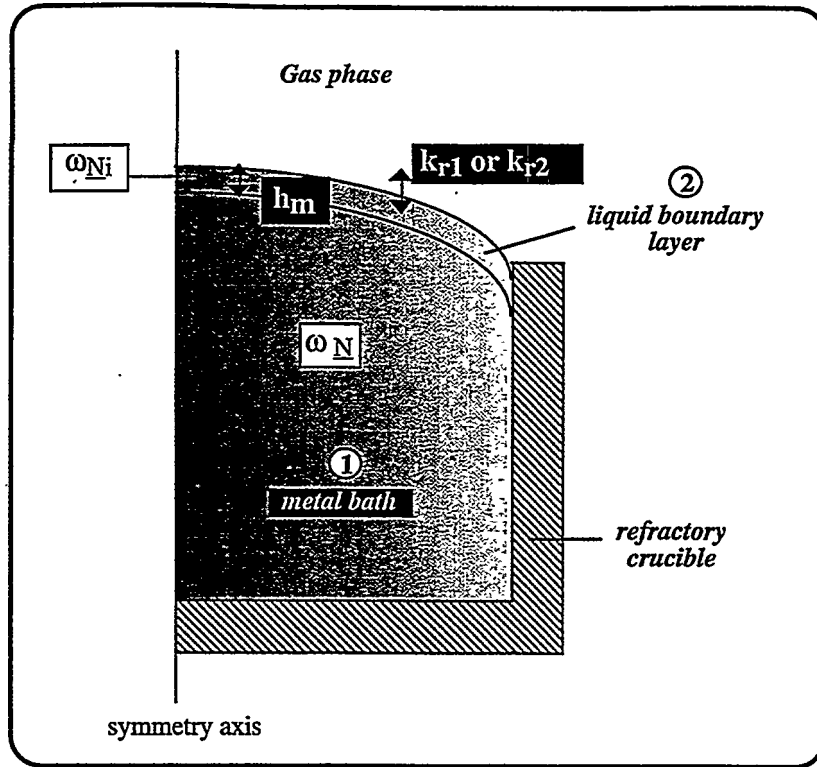


Fig. 11 - Schematic representation of the regions used in the RPA model.

As in the "VIMMAT" model, the nitrogen flux across the interface depends on the order of the chemical reaction at the interface (equations 8 or 9). The model is based on a global solute balance in each of the two regions. The variation of the nitrogen concentration in the liquid metal is related to the transport of nitrogen in the liquid boundary layer :

$$V \frac{\partial \omega_N}{\partial t} = S h_m (\omega_{N_i} - \omega_N) \quad (11)$$

Solution of equation 11 is performed directly using an explicit Euler representation. The model neglects the accumulation of nitrogen in the very thin boundary layer. In these conditions, a nitrogen balance leads to the following equality of flux densities :

$$\varphi_N = h_m \rho (\omega_{N_i} - \omega_N) \quad (12)$$

where $\varphi_N = k_{r1} \rho (\omega_{N_e} - \omega_{N_i})$ if the chemical reaction is of first order,
 $\varphi_N = k_{r2} \rho (\omega_{N_e}^2 - \omega_{N_i}^2)$ if the chemical reaction is of second order.

By fixing the values of the mass transfer coefficient h_m and the chemical reaction rate constant k_{r1} or k_{r2} , the model calculates the concentration of nitrogen in the bath at the liquid metal/gas interface at each instant.

Determination of the mass transfer coefficient h_m

It should be noted that in the "VIMMAT" model, nitrogen transfer within the liquid boundary layer is represented by the prior determination of the hydrodynamic behavior of the bath, so that the use of a mass transfer coefficient h_m is not necessary. In the "RPA" model, the use of a transport coefficient enables all of the results obtained in the global "VIMELE-VIMVIT" approach to be summarized. It is theoretically possible to determine the value of h_m , which depends on the operating conditions, by comparing the results of the "RPA" and "VIMMAT" models, and to deliberately choose imaginary conditions which maximize the influence of this coefficient on the variation of the dissolved nitrogen concentration in the bath, i.e. conditions which impose a transport regime for the overall reaction (corresponding to an extremely rapid chemical reaction at the interface).

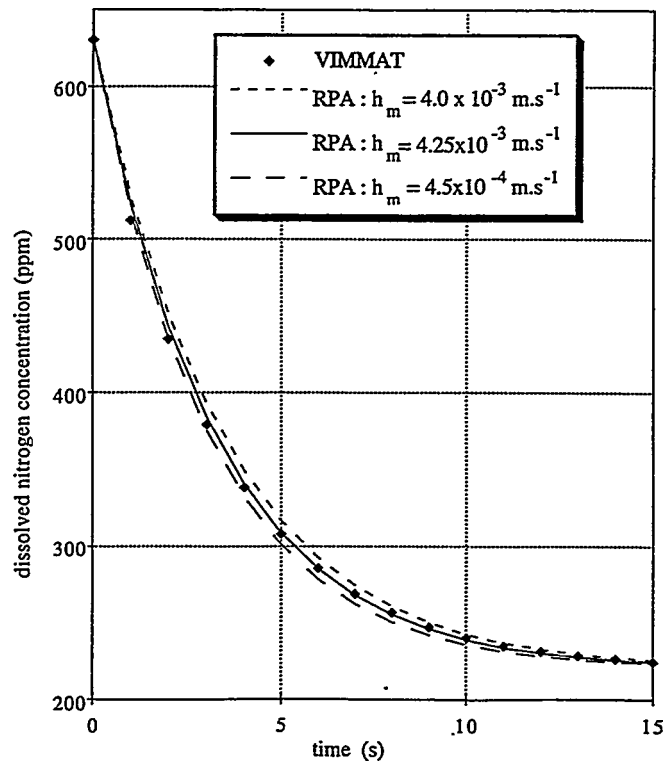


Fig. 12 - Determination of h_m by comparison of "VIMMAT" and "RPA" simulations of an imaginary denitriding experiment controlled by the transport regime.

Based on the knowledge of the hydrodynamic behavior (the results of "VIMELE" and "VIMVIT"), an imaginary denitrifying or nitrifying experiment is simulated with the "VIMMAT" model, deliberately choosing a transport regime (typically, k_{r1} or k_{r2} is taken equal to 10^8 m.s^{-1}). A certain variation of the mean nitrogen content in the bath with time is obtained. The same experiment is then simulated using the batch reactor "RPA" model, with the same kinetic conditions (transport regime). The value of the mass transport coefficient h_m is adjusted to obtain the same variation of mean nitrogen content with time as that given by the "VIMMAT" model (Fig. 12). The best agreement between the curves predicted by the two models is obtained for a value of h_m of $4.25 \times 10^{-3} \text{ m.s}^{-1}$ for both nitrifying and denitrifying experiments.

Simulation of experiments using the "RPA" model

By imposing the h_m value determined as indicated above in the "RPA" model, a number of Sieverts' experiments have been simulated in order to determine the order and the rate constants for the interface reactions which best describe the experimental results (Figs. 13 and 14). The simulations using the "VIMMAT" model had already enabled the values of k_{r1} and k_{r2} to be determined, for the nitrifying and denitrifying reactions respectively. It can be seen that the "RPA" model enables the experiments to be simulated with these same values for the chemical reaction rate constants.

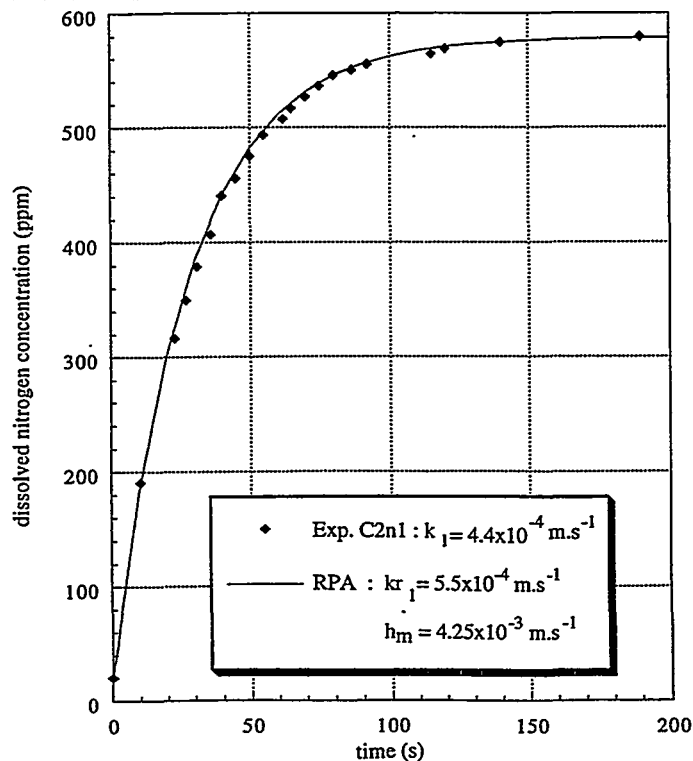


Fig. 13 - Simulation of the experiment C2n1 using the "RPA" model, imposing a first order interface reaction.

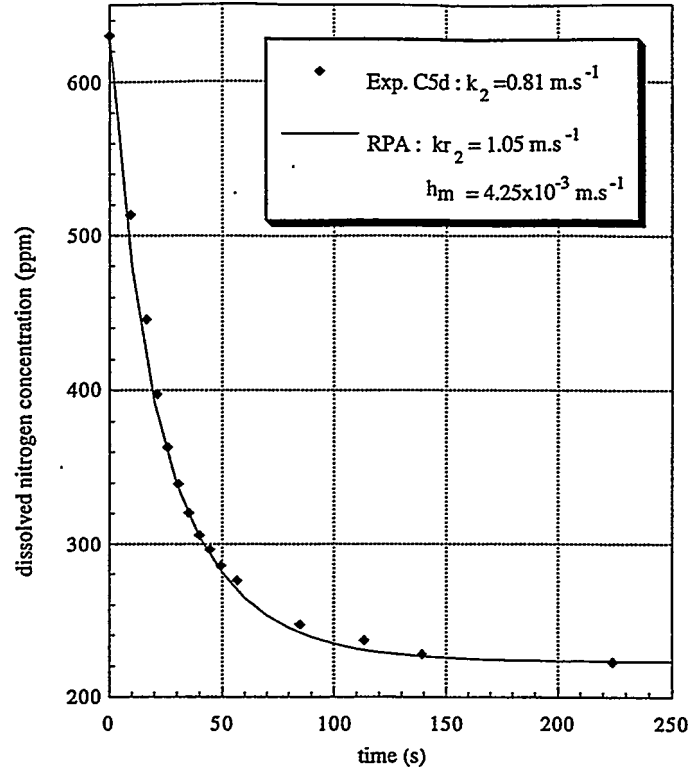


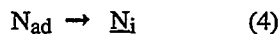
Fig. 14 - Simulation of the experiment C5d using the "RPA" model, imposing a second order interface reaction.

The use of this model proves to be extremely fruitful, since it enables nitriding and denitriding experiments to be simulated almost instantaneously with good accuracy. The results are identical to those obtained with the "VIMMAT" model, but the flexibility of use and rapidity of execution represent major advantages.

CONCLUSIONS

Comparison of the results of simulations using the "VIMMAT" and "RPA" models with experimental measurements has enabled values to be determined for the rate constants of the chemical reaction at the interface and for the mass transfer coefficient, indicating the relative importance of these two types of transport. It can be concluded that, in Sieverts' experiments, the overall reaction takes place in a predominantly chemical regime.

Nitriding experiments on a Ni-20% Cr alloy had shown that the overall reaction follows first order kinetics [1]. At this point, it could simply be concluded that the potential rate-controlling steps are :



The use of mathematical models shows that it is the desorption of nitrogen at the interface (step 4) which controls the transfer rate. Published experimental data indicates that the nitriding reaction follows first order kinetics with respect to the dissolved nitrogen concentration. However, all the authors [14-16] interpret this observation as proof that nitrogen transport in the liquid phase is the rate-controlling process. In fact, none of them breaks the chemical reaction down into the three steps (2, 3 and 4), and while they consider that the interface reaction is potentially rate-controlling, they take into account only the global interface reaction ($N_{2g} \rightarrow 2N_{bath}$) expressing its kinetics by a second order rate law with respect to the dissolved nitrogen concentration. The present approach, based on the numerical simulation of experiments, would tend to throw doubt on their conclusions.

The experimental results had also shown that the denitriding reaction in liquid Ni-20% Cr alloy follows overall kinetics of second order [1], apparently indicating that nitrogen transfer is controlled by the chemical regime. The modeling results confirm that the nitrogen transfer is governed by a second order chemical reaction at the interface. It can therefore be concluded that the rate-controlling step in the nitrogen transfer is the chemical reaction itself at the interface at the adsorption sites ($2N_{ad} \rightarrow N_{2ad}$) and/or the desorption of gaseous nitrogen ($N_{2ad} \rightarrow N_{2i}$).

Acknowledgements

This work was carried out within the framework of the Contract Research Program "Liquid Metal Quality". The authors wish to express their sincere thanks to the members of this C.R.P. for many fruitful discussions during the course of the study.

References

1. PETITNICOLAS L., JARDY A., ABLITZER D. - Etude thermodynamique et cinétique de la nitruration et de la dénitruration des alliages Ni-Cr par la technique de Sieverts - La revue de Métallurgie, CIT/SGM, n°2 (1996), p. 225-235.
2. MORI K., SANO M., SUZUKI K. - A Kinetic Study of Gas-Metal Reactions by Mixed Control Model - Trans. ISIJ, 13 (1973), p. 63-70.
3. INOUE M., CHOH T. - Rate of Absorption of Nitrogen in Liquid Iron and Iron Alloys - Trans. ISIJ, 8 (1968), p. 134-145.

4. FAUTRELLE Y.R.- Deux aspects de la magnétohydrodynamique, la dynamo convective, le brassage dans les fours à induction - Thèse de Doctorat-ès-Sciences, Grenoble (1982).
5. BARBIER J.N., FAUTRELLE Y.R. , EWANS J.W., CREMER P.- Simulation numérique des fours chauffés par induction - Journal de Mécanique Théorique et Appliquée, 1 (1982), n°3, p. 533-556.
6. DRIOLE J., LAVIALLE I., REVET F., DURAND F. - Elaboration d'alliages de niobium en creuset froid inductif - Revue de Métallurgie CIT/SGM, 91 (1994), n°12, p. 1759-1766.
7. GOSMAN A.D. , PUN W.M. , RUNCHAL A.K., SPALDING D.B. , WOLFSTEIN M., - Heat and mass transfer in recirculating flows - Academic Press, London and New-York (1969).
8. LAUNDER B.E., SPALDING D.B. - The numerical computation of turbulent flows - Comput. Meths. Appl. Mech. Eng., 3 (1974), p. 269-289.
9. LEVICH V.G. - Physicochemical hydrodynamics - Prentice -Hall Inc.(1962).
10. DAVIES J.T. - Turbulence phenomena - Academic Press (1972).
11. EL KADDAH N. , SZEKELY J. - The electromagnetic force field, fluid flow field and temperature profile in levitated metal droplets - Met. Trans., 14B (1983), p. 401-410.
12. PATANKAR S.V.- Numerical heat transfer and fluid flow - Hemisphere Publishing Corporation (1980).
13. SCHLICHTING H. - Boundary layer theory - Mc Graw - Hill, New York (1960).
14. PEHLKE R.D. , ELLIOTT J.F. - Solubility of nitrogen in liquid iron alloys II. Kinetics -Trans. Met. Soc. AIME, 227 (1963), p.844-855.
15. INOUE M., CHOH T. - Some considerations on the nitrogen transfer across gas-liquid iron interface - Trans. ISIJ, 12 (1972), p. 189-196.
16. FRUEHAN R.J., MARTONIK L.J. - The rate of absorption of nitrogen into liquid iron containing oxygen and sulfur - Met. Trans., 11B (1980), p. 615-621.

For Your Notes

1 2 3 4 5 6 7 8 9 10 11 12

.....

INIS

Numerical modeling of the vertical hydrofluorination zone in the moving bed furnace for the production of UF_4

J. Jourde[°], F. Patisson^{*}, D. Ablitzer^{*} and J-L. Houzelot[°]

^{*}Laboratoire de Science et Génie des Matériaux Métalliques (URA CNRS 159),
Ecole des Mines, Parc de Saurupt, 54042 Nancy Cedex, France.

[°]Laboratoire des Sciences du Génie Chimique (UPR CNRS 6811),
ENSIC, 1 rue Grandville, 54000 Nancy, France.

Abstract

Uranium tetrafluoride UF_4 is produced in the moving bed furnace, a reactor in which solid and gas counterflow. Due to the highly exothermic nature of the chemical reactions involved, the reactor operation requires a careful temperature control. To provide operators with an appropriate tool for the predictive simulation, optimization and control of the process, we have developed an overall numerical model of the furnace. The present paper describes the part of the model concerning the vertical hydrofluorination zone.

The differential equations representing the mass, energy and momentum balances are solved using the finite volume method. The physicochemical parameters necessary for the calculation are detailed. The rate of the main reaction, the hydrofluorination of UO_2 , has been determined with the aid of a specific kinetic model. The computed parameters, namely the temperature and solid and gas compositions, are visualized in the form of isovalue maps.

The initial results reveal the influence of a thermodynamic limitation of the reaction at temperatures higher than 650 K.

Introduction

Uranium-bearing ores are processed in a number of stages to obtain the uranium hexafluoride UF_6 employed in isotope enrichment plants. One of the stages used in the french process successively transforms uranium trioxide UO_3 to the dioxide UO_2 , then to the tetrafluoride UF_4 , under the action of reactive ammonia NH_3 and hydrogen fluoride HF gases. All these transformations take place in a single reactor, known as a moving bed furnace, in which the solid descends under the effect of gravity and comes in contact with a counterflow of reactive gases (Fig. -1-).

The conversion of UO_2 to UF_4 occurs in the vertical hydrofluorination zone (VHZ), and is completed in the horizontal hydrofluorination zone (HHZ) from which the solid is removed. The hydrofluorination reaction is highly exothermic and the heat of reaction is removed partly by cooling the outer furnace walls, and partly by a cylindrical coaxial packed heat exchanger situated within the solid bed and called a *depolymerizer*. The principal physicochemical phenomena involved in the VHZ are the following:

- (i) flow of the solid particles (UO_2/UF_4 pellets);
- (ii) counterflow of gas through the porous pellet bed;
- (iii) heat transfer between the gas and the pellets and between the gas and the vessel walls;
- (iv) the heterogeneous gas-solid hydrofluorination reaction;
- (v) the liquid→gas transformation of HF in the depolymerizer.

The industrial moving bed furnace proves delicate to control. In particular, in order to maximize the yield of UF_4 , the temperature of the solid must be carefully controlled to avoid accidental overheating. Moreover, to optimize the process, it is necessary to quantitatively evaluate the influence of certain operating conditions and kinetic parameters.

The mathematical modeling approach provides a means of meeting these requirements. It was therefore decided, in collaboration with the company COMURHEX, to develop an overall numerical model of the moving bed furnace. The first stage of this work, the results of which are described in the present paper, was to model the vertical hydrofluorination zone, which represents the core of the process.

The model calculates the temperature and the solid and gas compositions at each point in the VHZ in the steady state regime. The results of the various simulations are presented in the form of isovalue maps.

Description of the mathematical model

The principle of the model is to use local balance equations to describe the thermal and physicochemical phenomena involved. In an axial cross-section of the VHZ, eight zones can be described distinctly in terms of mass and heat transfer (Fig. -2-):

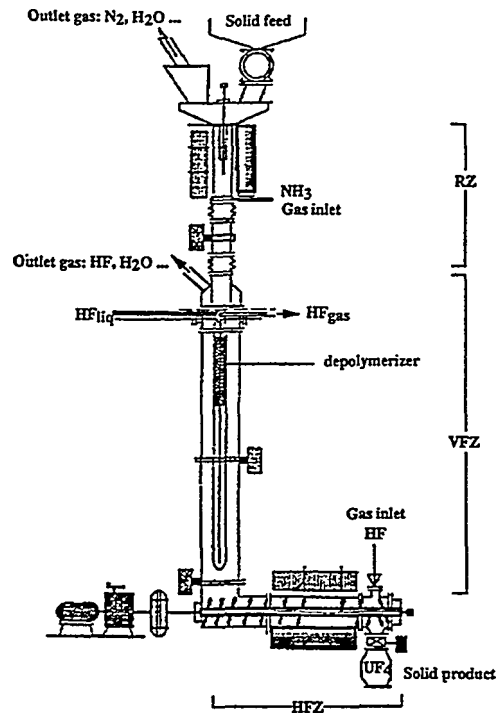


Figure -1- The moving bed reactor

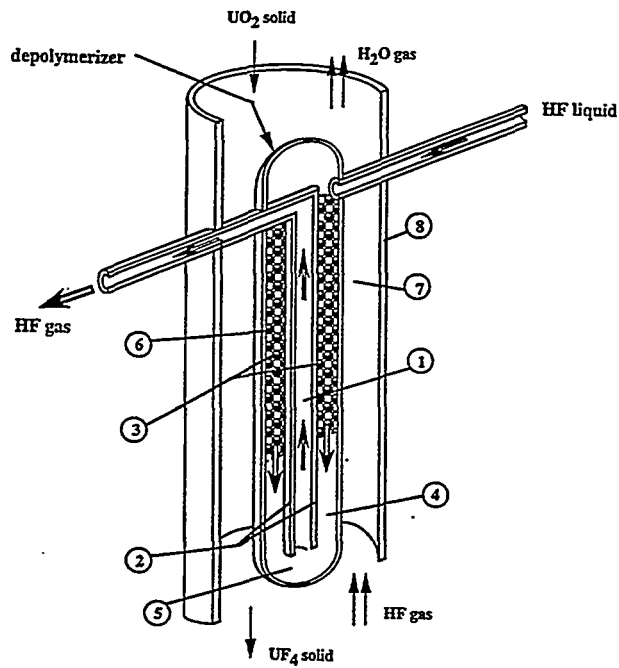


Figure -2- Section of the vertical hydrofluorination zone

1. the central tubular zone in which the hot HF gas rises in the depolymerizer;
2. the wall of this HF riser tube;
3. the packed zone of the depolymerizer, where liquid HF transforms to gaseous HF;
4. the non-packed zone, in which the HF descends;
5. the bottom of the depolymerizer, where the HF flow changes direction;
6. the wall of the depolymerizer in contact with the moving bed;
7. the moving bed, in which the hydrofluorination reaction occurs;
8. the outer furnace wall, in contact with the ambient air.

Assumptions

The model developed is two-dimensional and concerns the steady state regime. The coordinates adopted are for a cylindrical system, in which r is the distance from the symmetry axis and z is the height.

The flow of solid in the moving bed is considered to be of the piston type, without dispersion. Observation of the flow in a cold transparent 1/10 scale model of the furnace justifies this assumption [1]. The counterflow of gas is also of the piston type, but with both axial and radial dispersion.

The pressure drop in the gas through the solid bed is calculated using a differential form of Ergun's law [2], which represents a simplified form of the momentum balance. The moving bed is thus considered as a stack of spherical pellets of mean diameter d_p , forming a porous medium of mean porosity ϵ . Local variations in both the bed porosity and in the mean pellet diameter can be taken into account.

In the depolymerizer, because of the high velocities of the HF fluid, the flow is considered to be of the piston type. Since the pressure drop in this zone is small, the local pressure in the depolymerizer is considered to be uniform and equal to 1.5 bar.

The heat transfers considered are of the conductive type in the walls, and conductive, convective and radiative in the moving bed and depolymerizer. In the packed region of the depolymerizer and in the moving bed, the gas-solid heat transfer is sufficiently large [3] to justify the assumption of a pseudo-homogeneous medium, in which at all points:

$$T_{solid} = T_{gas} \quad (1)$$

In both these zones, the model uses an effective axial and radial thermal conductivity, which combines the contributions of radiation, solid and gaseous conduction, and the influence of gaseous convection [4].

The only chemical reaction considered in the VHZ is the equilibrium hydrofluorination reaction, corresponding to the conversion of uranium dioxide to uranium tetrafluoride by hydrogen fluoride:



The rate of this reaction is calculated from the Grainy Pellet Model [5], the parameters of which have been determined from independent measurements [6]. A strong coupling between the heat transfer and mass transfer results from the exothermic nature of the hydrofluorination reaction.

The function of the depolymerizer is to cool the moving bed and at the same time to convert the liquid HF to gaseous HF, which is then fed to the bottom of the moving bed. Between 30.5 °C (the boiling point at 1.5 bar) and about 80 °C, the HF gas is polymerized and becomes a monomer only above 80 °C. The changes of state of HF, vaporization and depolymerization, are simply described by the equivalent-*c_p* method.

The solid species considered are UO₂ and UF₄, respectively reactant and product of the conversion reaction, and UO₂F₂, formed in the upper part of the moving bed furnace and inert in the VHZ. The gaseous species are HF and H₂O, reactant and product of the reaction, and N₂, an inert gas, introduced via the UF₄ removal lock in the HHZ. The fraction of nitrogen is never more than a few percent.

Equations

The principal equations used in the model are the local matter balances in the moving bed (for each solid or gaseous species), the local heat balances in each of the eight zones described, and the momentum balance for the gas phase passing through the moving bed. All the notations employed are given at the end of the paper.

In the moving bed

Matter balance for solid UO₂

$$\frac{\partial(u_s \rho_s w_{UO_2})}{\partial z} = -M_{UO_2} r_f \quad (3)$$

Matter balance for solid UO₂F₂ (inert) .

$$\frac{\partial(u_s \rho_s w_{UO_2F_2})}{\partial z} = 0 \quad (4)$$

Total matter balance for the solid phase

$$\frac{\partial(u_s \rho_s)}{\partial z} = (M_{UF_4} - M_{UO_2}) r_f \quad (5)$$

Matter balance for gaseous HF

$$\frac{\partial (u_g C_i x_{HF})}{\partial z} = -4r_f + \frac{1}{r} \frac{\partial}{\partial r} \left[r D_r C_i \frac{\partial x_{HF}}{\partial r} \right] + \frac{\partial}{\partial z} \left[D_a C_i \frac{\partial x_{HF}}{\partial z} \right] \quad (6)$$

Matter balance for N₂ gas (inert)

$$\frac{\partial (u_g C_i x_{N_2})}{\partial z} = \frac{1}{r} \frac{\partial}{\partial r} \left[r D_r C_i \frac{\partial x_{N_2}}{\partial r} \right] + \frac{\partial}{\partial z} \left[D_a C_i \frac{\partial x_{N_2}}{\partial z} \right] \quad (7)$$

Total matter balance for the gas phase

$$\frac{\partial (u_g C_i)}{\partial z} = -2r_f \quad (8)$$

Heat balance

$$(u_s \rho_s c_{p_s} + u_g C_i c_{p_g}) \frac{\partial T}{\partial z} = r_f (-\Delta H_r) + \frac{1}{r} \frac{\partial}{\partial r} \left[r \lambda_r \frac{\partial T}{\partial r} \right] + \frac{\partial}{\partial z} \left[\lambda_a \frac{\partial T}{\partial z} \right] \quad (9)$$

Differential form of the Ergun equation

$$-\frac{\partial P}{\partial z} = 150 \frac{(1-\varepsilon)^2}{\varepsilon^3 d_p^2} \mu u_g + 1.75 \frac{(1-\varepsilon)}{\varepsilon^3 d_p} \rho_g u_g^2 \quad (10)$$

These equations have the same form at all points within the bed, the physical (ε , D_r , D_a , etc.), thermal (λ_r , λ_a , etc.) and kinetic (r_f) parameters depending on the point considered. In addition to these equations, the concentrations and apparent densities of each gaseous and solid species are calculated, together with the equation of state for perfect gases.

In the depolymerizer

The assumption of a uniform velocity field avoids the need for a momentum balance, so that only the energy balance is necessary:

$$q_{HF} c_{pHF} \frac{\partial T}{\partial z} = \frac{1}{r} \frac{\partial}{\partial r} \left[r \lambda_r \frac{\partial T}{\partial r} \right] + \frac{\partial}{\partial z} \left[\lambda_a \frac{\partial T}{\partial z} \right] \quad (11)$$

In the walls

For each wall, the classical heat conduction equation is applied:

$$\frac{1}{r} \frac{\partial}{\partial r} \left[r \lambda_w \frac{\partial T}{\partial r} \right] + \frac{\partial}{\partial z} \left[\lambda_w \frac{\partial T}{\partial z} \right] = 0 \quad (12)$$

Boundary conditions

In terms of matter, the boundary conditions correspond to the input flowrates. The thermal boundary conditions at each wall represent the continuity of heat flow by conduction, convection and radiation:

$$\lambda_w \left(\frac{\partial T}{\partial r} \right)_w = h(T - T_w) + \sigma E (T^4 - T_w^4) \quad (13)$$

Depending on the case, E is either the emissivity of the solid wall, or an emissivity coefficient dependent on the emissivities of both the solid and the wall.

Method of numerical solution

Each partial differential equation is rendered discrete using the finite volume technique [7]. In order to accurately take into account the various boundary conditions, particularly those with the largest intensity gradients, a variable size mesh was employed, with a larger number of nodes near the walls. The non-linear terms in the equations (source terms of the chemical reaction, radiation terms) must be carefully linearized to ensure convergence of the model. Otherwise, the variation of the reaction rate with temperature, according to the Arrhenius law, could cause instabilities in the reaction zone.

The system of equations (3) to (13) is solved for each volume over the whole of the VHZ by successive iterations. The explicit iteration procedure employed is of the Gauss-Seidel type. The calculation algorithm is shown in Figure -3-.

Data employed

In order to calculate the variables in equations (3) to (13), the model requires both input data and the appropriate physicochemical and thermal parameters.

Input data

The input data necessary are the imposed boundary conditions. They are known for each simulation of an industrial furnace operation, and concern the characteristics of the solid charge and the gases entering the VHZ, together with those of the HF entering the depolymerizer. All these data are contained in an input file.

Parameters required by the model

The physicochemical and thermal parameters in equations (3) to (13) must be determined as precisely as possible. Data from the literature are used to calculate the viscosity of the gases, together with the specific heats and true thermal conductivities of the gases and solids, as functions of temperature and composition. The other parameters are determined as follows:

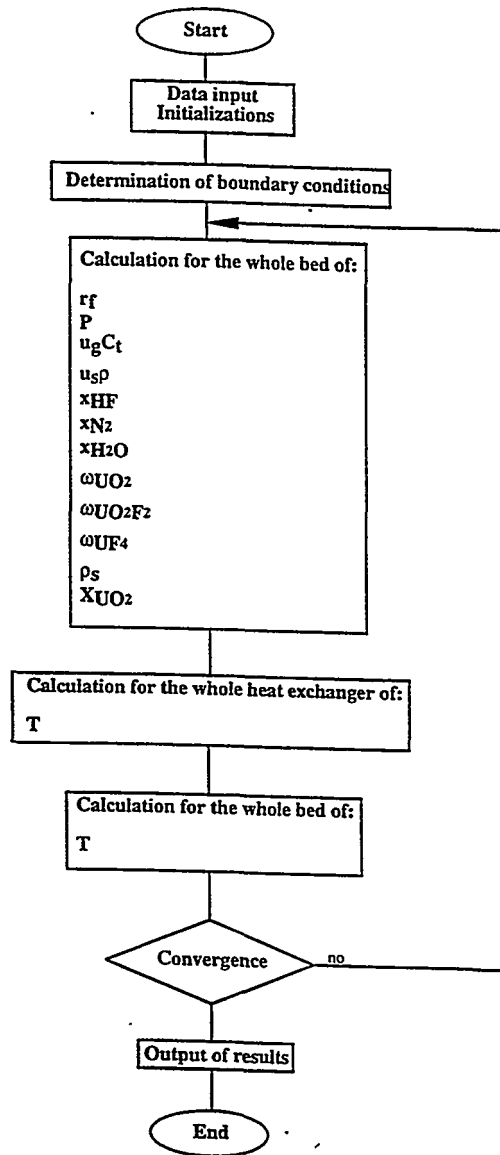


Figure -3- Calculation flow diagram

ϵ mean porosity of the moving bed

The porosity of the solid bed is a poorly known parameter and is difficult to measure in an industrial reactor. So far, a value of $\epsilon = 0.5$ has been used. Subsequently, it will be possible to introduce an axial or radial gradient of mean porosity to represent the existence of preferred gas flow paths.

d_p mean pellet diameter

From particle size measurements made in the plant, d_p has been estimated to be about 6 mm. However, the model enables allowance to be made for radial and axial variations in d_p . This parameter particularly affects the reaction rate r_f , and is also involved in the calculation of the effective thermal conductivities.

ΔH_r enthalpy of the hydrofluorination reaction

Data taken from the recent thermodynamic literature are used to calculate ΔH_r . In the temperature range 273-1273 K, the following approximate polynomial expression is obtained:

$$\Delta H_r = -227274 + 6.4091T - 1.05849 \times 10^{-3}T^2 + 1.01278 \times 10^{-5}T^3 - 1.15347 \times 10^{-9}T^4 \quad (14)$$

r_f rate of the hydrofluorination reaction

The kinetics of the hydrofluorination reaction have been studied using thermogravimetric experiments [6]. The results are well described by the Grainy Pellet Model [5], which considers each solid pellet to be composed of a cluster of grains of initial diameter d_g which individually react according to the Shrinking Core Model. Three resistances to the transfer of HF occur in series: external transfer, intergranular diffusion, and the UO₂/UF₄ interface reaction in the grains. In the present model of the moving bed, use is made of the approximate relation proposed by Sohn [8], giving the time t_r necessary to obtain a given degree of conversion X_{UO_2} :

$$t_r \approx \underbrace{\tau_{chem} \left(1 - (1 - X_{UO_2})^{1/3} \right)}_{\text{chemical reaction}} + \underbrace{\tau_{diff} \left(1 - 3(1 - X_{UO_2})^{2/3} + 2(1 - X_{UO_2}) \right)}_{\text{intergranular diffusional transport}} + \underbrace{\tau_{diff} \frac{2X_{UO_2}}{S_h^*}}_{\text{external transfer}} \quad (15)$$

where X_{UO_2} is the degree of conversion of UO₂ defined by:

$$X_{UO_2} = 1 - \frac{\rho_{UO_2}}{\rho_{UO_2}^0} \quad (16)$$

The parameters τ_{diff} and τ_{chem} represent the characteristic times for diffusion and chemical reaction respectively. According to Nicole [9], they can be calculated from the following expressions:

$$\tau_{diff} = \frac{\left(\frac{d_p}{2}\right)^2 \rho_{mUO_2}^0 \left(\frac{z_{HF} - z_{HF_{eq}}}{2}\right)}{6bD_{HF_{eff}} (C_{HF} - C_{HF_{eq}}) \ln\left(\frac{2 - z_{HF_{eq}}}{2 - z_{HF}}\right)} \quad (17)$$

and

$$\tau_{chem} = \frac{\frac{d_p}{2} \rho_{mUO_2}^0}{(1 - \varepsilon_p) bk \left(C_{HF} - \frac{\sqrt{C_{H_2O}}}{K_e}\right)} \quad (18)$$

S_h^* is a modified Sherwood number, defined by:

$$S_h^* = 2 \frac{T_p}{\varepsilon_p} S_h \quad (19)$$

where

$$S_h = 2 + 0.6Re^{1/2} Sc^{1/3} \quad (20)$$

The following expression is then derived for the rate of hydrofluorination τ_f in the moving bed (in moles of $UO_2/s/m^3$ of bed):

$$\tau_f = \frac{\rho_{UO_2}^0}{M_{UO_2}} \left[\frac{\tau_{chem}}{3} (1 - X_{UO_2})^{-2/3} + 2\tau_{diff} \left((1 - X_{UO_2})^{-1/3} + \frac{1}{S_h^*} - 1 \right) \right]^{-1} \quad (21)$$

K_p and K_e thermodynamic equilibrium constants

Analysis of the thermodynamic data gives the following approximate expression for the free enthalpy of the hydrofluorination reaction, valid between 273 and 1273 K:

$$\Delta G_r^0 = -RT \ln(K_p) = -224988 + 239.709T \quad (22)$$

The equilibrium constant K_e in equation (18) is expressed by:

$$K_e(T) = \frac{\sqrt{C_{H_2O_{eq}}}}{C_{HF_{eq}}} = K_p^{1/4} \left(\frac{RT}{P_0}\right)^{1/2} \quad (23)$$

where P_0 is the reference pressure equal to 1 bar.

D_a , D_r axial and radial gaseous dispersion coefficients

The dispersion coefficients for the gases in the axial and radial directions are calculated from the axial and radial Péclet criteria (P_{e_a} and P_{e_r}), for which numerous correlations are available. We use the results of Wen and Fan [10], which give the axial Péclet criterion for gas flow in a fixed bed in the form $P_{e_a} = f(R_e S_c)$:

$$\frac{1}{Pe_a} = \frac{0.3}{ReSc} + \frac{0.5}{1 + 3.8/ReSc} \quad (24)$$

and DeWash and Froment's relation was used [11] to calculate Pe_r :

$$Pe_r = \frac{1}{0.14} \left[1 + 46 \left(\frac{d_p}{d_t} \right)^2 \right] \quad (25)$$

λ_r, λ_a effective radial and axial thermal conductivities

In each direction, λ is considered to be the sum of a static contribution λ_{stat} and a dynamic contribution λ_{dyn} :

$$\begin{aligned} \lambda_a &= \lambda_{stat} + \lambda_{dyn,a} \\ \lambda_r &= \lambda_{stat} + \lambda_{dyn,r} \end{aligned} \quad (26)$$

λ_{stat} accounts for the effects of radiation, interparticle conduction and gaseous conduction, while λ_{dyn} represents the influence of gaseous convection on the effective conduction. The semi-empirical relation proposed by Zehner and Schlünder [4] is used:

$$\lambda_{stat} = \lambda_g \left[(1 - \sqrt{1 - \varepsilon})(1 - \varepsilon C) + A \frac{2\sqrt{1 - \varepsilon}}{1 + (C - B)\Lambda} \right] \quad (27)$$

where A, B, C and Λ are defined by:

$$\begin{aligned} A &= \frac{1 + (C - B)\Lambda}{(1 + (C - B)\Lambda)^2} B \ln \left(\frac{1 + C\Lambda}{B\Lambda} \right) - \frac{B - 1}{1 + (C - B)\Lambda} + \frac{B + 1}{2B} (C - B) \\ B &= 1.25 \left(\frac{1 - \varepsilon}{\varepsilon} \right)^{10/9} \\ C &= \frac{\alpha_{rs} d_p}{\lambda_g} \\ \Lambda &= \frac{\lambda_g}{\lambda_s} \\ \alpha_{rs} &= 0.227 \frac{E}{2 - E} \left(\frac{T}{100} \right)^3 \end{aligned} \quad (28)$$

Because of dispersion phenomena, the axial and radial dynamic contributions are distinct, and by analogy with matter transport, can be written:

$$\lambda_{dyn,a} = \frac{q_g c_{p_g} d_p}{Pe_a} \quad (29)$$

$$\lambda_{dyn,r} = \frac{q_g c_{p_g} d_p}{Pe_r} \quad (30)$$

where Pe_a and Pe_r are the axial and radial Péclet mass numbers, and q_g is the mass flow density of the gas. These relations are used to describe heat transfer within the moving bed and also in the packed zone of the depolymerizer, considered as a porous medium of mean porosity $\varepsilon_{rask} = 0.905$.

h convective heat transfer coefficient

The coefficient h must be determined for each face of the wall, in contact with either the process gas or the ambient air.

- For the external surface in contact with the air, natural convection occurs and h is given by:

$$h = 0.13 \lambda_{air} (P_r G_r)^{1/3} \quad (31)$$

where $P_r G_r$ is evaluated at the temperature $T_f = \frac{1}{2}(T_w + T_{air})$.

- The coefficient h representing the convective heat transfer between the wall and a porous medium (moving bed, packed zone of the depolymerizer) is calculated using Leva's correlation [12]:

$$h = 0.813 \frac{\lambda_g}{2R} R_e^{0.9} e^{-\frac{6d_p}{3R}} \quad (32)$$

- The hemispherical wall at the bottom of the depolymerizer, in contact with the moving bed, is assimilated to a flat plate of equivalent surface area. However, in order to calculate the gas-wall convection terms, the relation given by Pasternak and Gauvin for a hemispherical shell [13] is used:

$$N_u = 2 + (N_{u_t}^2 + N_{u_s}^2)^{1/2} \quad (33)$$

where the laminar flow term is given by:

$$N_{u_t} = 0.664 R_{e_t}^{1/2} P_r^{1/3} \quad (34)$$

and the turbulent flow term by:

$$N_{u_s} = \frac{0.0366 R_{e_t}^{0.8} P_r}{1 + 2.443 R_{e_t}^{-0.1} (P_r^{2/3} - 1)} \quad (35)$$

- The calculation of h in the non-packed tubular zones of the depolymerizer are based on the classical correlations available in the literature, such as that proposed by Kays [14], used for the riser tube:

$$N_u = 0.22 P_r^{0.6} R_e^{0.8} \quad (36)$$

and that of Lundberg, Reynolds and Kays [15] for flow in an annular space.

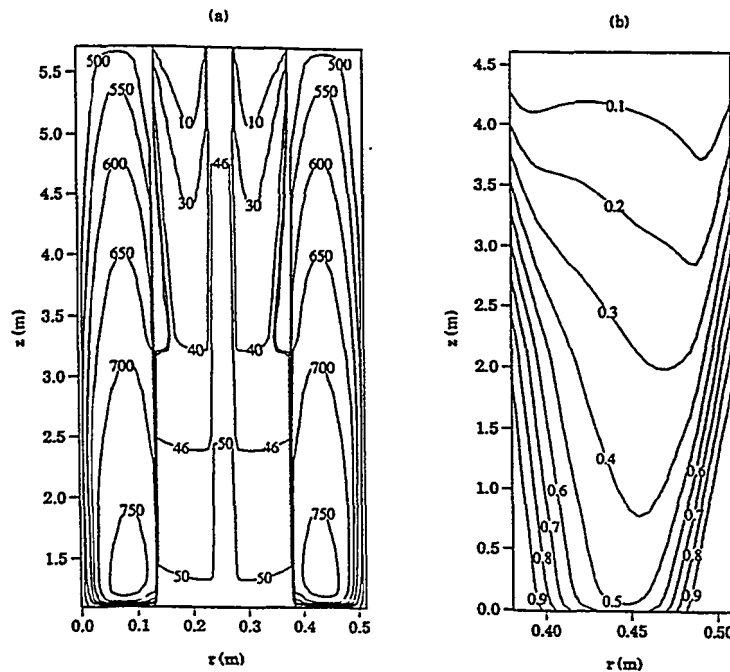


Figure -4- Reference simulation - a) Temperature map for the whole VFZ (symmetry axis at center), b) X_{UO_2} map for the moving bed only

Results

Presentation

All the variables calculated by the model can be visualized in the form of isovalue maps. Examples will be shown below for the temperature and the degree of conversion, for three simulations: a reference one and two others, showing the influence of pellet diameter and the influence of VHZ input gas flowrate. The calculations were performed on a Hewlett-Packard 9000/735 workstation.

Reference simulation

The gas flowrates entering the VHZ and the depolymerizer are set at their nominal values. The composition of the gas entering the VHZ is not known exactly, since the HHF is not described in the model as it stands today. This composition must therefore be fixed. Thus, x_{HF} is taken equal to 0.85. The mean pellet diameter d_p is taken as 6 mm. Figure -4- shows the isovalue maps obtained for the temperature and the degree of conversion of UO_2 . The temperature map reveals the existence of a hot point ($\approx 750^\circ C$) at the bottom of the reaction zone. However, it can be seen that this hot point does not correspond to the region of the bed where the degree of conversion is highest, as might have been expected for a thermally activated process. This observation suggests the existence of a thermodynamic limitation on the hydrofluorination reaction. Indeed, the fraction of HF at equilibrium increases

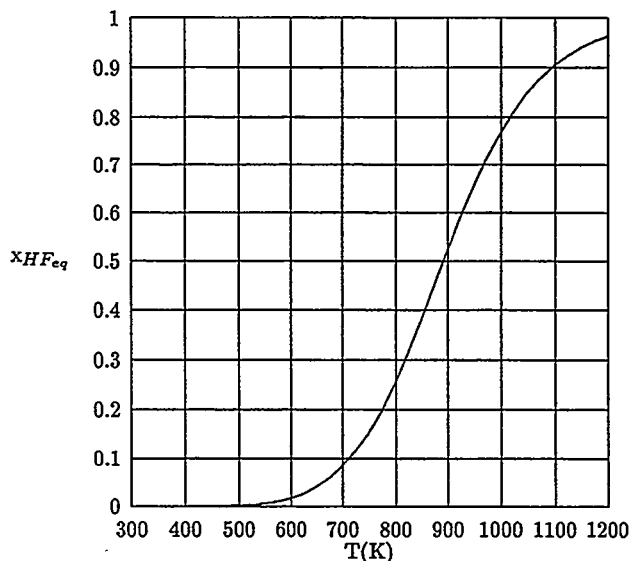


Figure -5- Fraction of HF at equilibrium

strongly with temperature above 650 K (Fig. -5-), so that the driving force in the rate law ($x_{HF} - x_{HF_{eq}}$) decreases with temperature.

Figure -6- shows that this driving force is very low throughout the central zone of the moving bed. In contrast, in the vicinity of the cooled walls, the chemical reaction is thermodynamically enhanced, explaining the higher degrees of conversion in the wall regions. The mean degree of conversion is 78%, but with marked radial deviations.

As regards the gas flowing in the depolymerizer, it can be seen that, after being heated in the descent zone, it is cooled in the riser zone, due to convective heat exchange with the wall in contact with the cold fluid.

Influence of mean pellet diameter d_p

The mean pellet diameter d_p principally affects the reaction rate r_f via τ_{diff} , but also influences the effective thermal conductivity in the bed (equations (26)-(30)). When d_p increases, the fall in reaction rate and the rise in λ lead to a drop in the hot point temperature in the reaction zone (Fig. -7-). The mean extent of conversion (79%) is close to that obtained in the reference conditions, but the radial variations are smaller. Conversion is greater in the central zone due to more favorable thermodynamic circumstances, whereas conversion in the wall zones is not as complete, because of slower kinetics (increase in diffusional resistance).

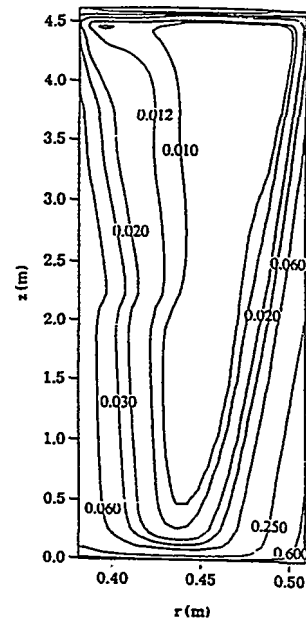


Figure -6- Reference simulation -Deviation from equilibrium $(x_{HF} - x_{HF,e})$ for the moving bed only

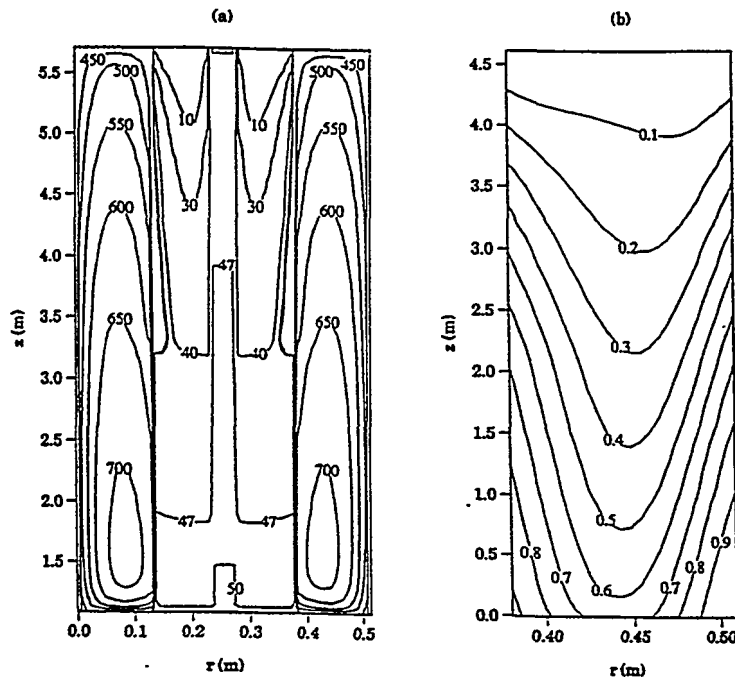


Figure -7- $d_p = 1.2$ cm - a) Temperature map for the whole VFZ (symmetry axis at center), b) X_{UO_2} map for the moving bed only

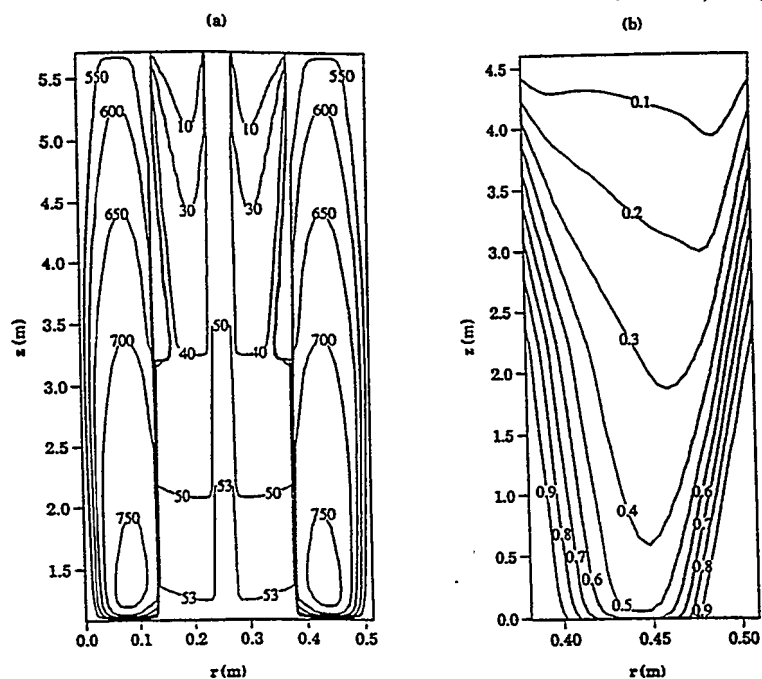


Figure -8- Increase of input gas flowrate - a) Temperature map for the whole VFZ (symmetry axis at center), b) X_{UO_2} map for the moving bed only

Influence of VHZ input gas flowrate

It can be seen that an increase of 11% in the reactive gas input flowrate extends the hot zone towards the upper part of the VHZ (Fig. -8-). The mean UO_2 conversion yield increases slightly to 82%.

Conclusions

A numerical model of a moving bed furnace for the production of uranium tetrafluoride has been developed, based on the description of the principal physicochemical and thermal phenomena. In its present version, the model calculates the temperature and solid and gas compositions at all points in the vertical hydrofluorination zone, in the steady state regime.

Initial results demonstrate the ability of the approach employed to provide accurate indications concerning the effect of process variables on the operation of an industrial reactor. In particular, they have revealed the existence of a thermodynamic limitation on the hydrofluorination reaction in the high temperature zone. The influence of operating conditions and physical parameters can be simply studied by numerical experimentations.

The model must now be validated, based on independent measurements of certain parameters, such as the effective axial and radial thermal conductivities, together

with comparisons between calculated values and those that can be measured in industrial plant.

Aknowledgements

This work is a part of a joint project associating the company COMURHEX in Malvési, PECHINEY's Voreppe Research Centre, the Laboratoire des Sciences du Génie Chimique and the Laboratoire de Science et Génie des Matériaux Métalliques, both in Nancy. The authors express their sincere thanks to Drs P.Bernasconi, S.Davied and R.Faron (COMURHEX) for their technical and financial support and Dr G.Baluais (PECHINEY) for his close collaboration.

Notations

b	stoichiometric coefficient = 0.25	[-]
c_{p_s}	specific heat of the solid	[J/kg/K]
c_{p_g}	molar specific heat of the gas	[J/mol/K]
$c_{p_{HF}}$	specific heat of HF	[J/kg/K]
C	molar concentration	[mol/m ³]
C_t	total gas concentration	[mol/m ³]
d_g	mean initial grain diameter of the UO ₂	[m]
d_p	mean diameter of the solid pellets	[m]
d_t	equivalent tube diameter	[m]
D	molecular diffusivity	[m ² /s]
$D_{a,r}$	axial and radial gaseous dispersion	[m ² /s]
$D_{HF,eff}$	effective diffusivity of HF in the pellets	[m ² /s]
E	emissivity	[-]
h	convective heat transfer coefficient	[W/m ² /K]
k	rate constant of the hydrofluorination reaction	[m/s]
K_e	thermodynamic equilibrium constant	[m ^{3/2} /mol ^{1/2}]
K_p	thermodynamic equilibrium constant	[-]
M	molecular weight	[kg/mol]
P	total gas pressure	[Pa]
q	mass flow density	[kg/m ² /s]
r	radial coordinate	[m]
r_f	rate of the hydrofluorination reaction	[mol/m ³ /s]
R	perfect gas constant	[J/K/mol]
R	characteristic radius	[m]
t_r	reaction time to obtain a conversion yield X_{UO_2}	[s]
T	temperature	[K]
u_g	superficial gas velocity	[m/s]
u_s	solid flow velocity	[m/s]
x	molar fraction	[-]
X_{UO_2}	degree of conversion of UO ₂	[-]
z	axial coordinate	[m]

Dimensionless parameters

G_r	$= \frac{l^3 \rho^2 g \beta \Delta T}{\mu^2}$	Grashof number
N_u	$= \frac{hl}{\lambda}$	Nusselt number
P_e	$= \frac{u_g l}{D}$	Péclet number
P_r	$= \frac{c_p \mu}{\lambda}$	Prandtl number
Re	$= \frac{u_g l}{\nu}$	Reynolds number
Sc	$= \frac{\mu}{\rho_g D}$	Schmidt number
S_h	$= \frac{k_d l}{D}$	Sherwood number
S_h^*	$= 2 \frac{D}{\epsilon_p} S_h$	modified Sherwood number

Greek symbols

ΔH_r	enthalpy of reaction (2)	[J/mol]
ΔG_r	free enthalpy of reaction (2)	[J/mol]
ε	porosity of the bed	[-]
ε_p	porosity of the solid pellets	[-]
λ	true thermal conductivity	[W/m/K]
$\lambda_{a,r}$	effective axial and radial thermal conductivities	[W/m/K]
μ	dynamic viscosity	[Pa.s]
ρ_{UO_2}	apparent weight concentration of UO_2	[kg/m ³ of bed]
$\rho_{UO_2}^0$	= ρ_{UO_2} at the bed inlet	[kg/m ³ of bed]
$\rho_{mUO_2}^0$	initial molar concentration of UO_2 in the pellets	[mol/m ³ of pellet]
ρ_s	apparent density of the solid	[kg/m ³ of bed]
σ	Stefan-Boltzmann constant	[W/m ² /K ⁴]
τ_p	tortuosity of the pores in the solid pellets	[-]
τ_{chem}	characteristic time for chemical reaction	[s]
τ_{diff}	characteristic time for intergranular diffusion	[s]
ω	mass fraction	[-]

Subscripts

a	axial
eq	at thermodynamic equilibrium
g	gas
l	laminar
w	wall
p	pellet
r	reaction
r	radial
s	solid
t	turbulent
0	initial

Superscripts

0	in the reference state
-----	------------------------

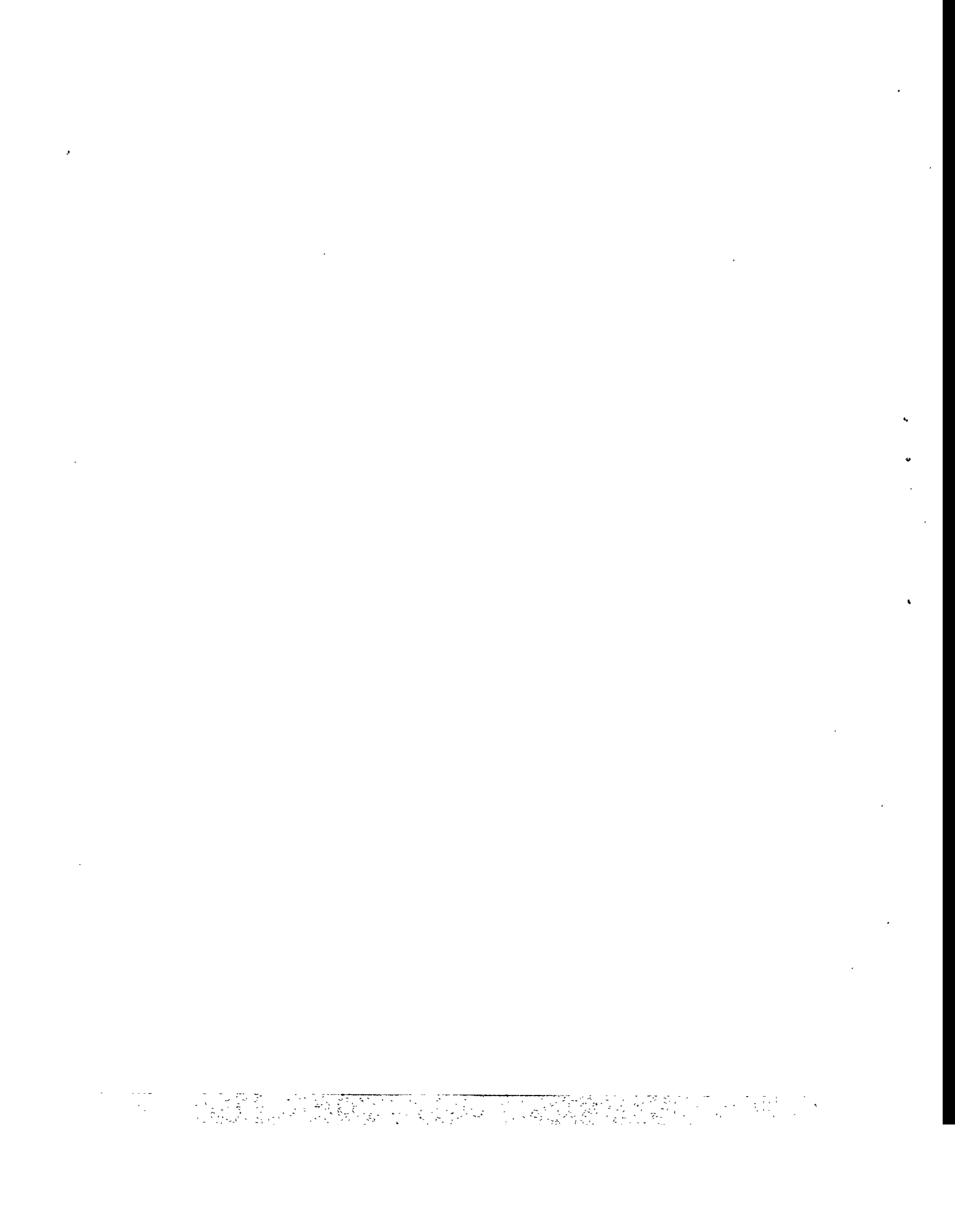
Bibliography

- [1] Félis, V., Hydrodynamique du four à lit coulant pour la production de tétrafluorure d'uranium. DEA Dissertation, ENSIC, Nancy (1993)
- [2] Kunii, D. and Levenspiel, O., Fluidization engineering. Wiley, New York (1969)
- [3] Sabatier, L., Le four à lit coulant réalisant la transformation du trioxyde d'uranium en tétrafluorure d'uranium. Étude et modélisation cinétique. Doctorate Thesis, INPL, Nancy (1994)
- [4] Zehner, P. and et Schlünder, E.U., Chem. Eng. Technol., 42, 333 (1970); 44, 1303 (1972)
- [5] Szekeley, J., Evans, J.W., and Sohn, H.Y. Gas-solid reactions. Academic Press (1976), 125-160
- [6] Nicole, C., Patisson, F., Ablitzer, D. and Houzelot, J.L., A thermogravimetric study of the kinetics of hydrofluorination of uranium dioxide. Chem. Eng. Sci. (1996), accepted
- [7] Patankar, S.U., Numerical heat transfer and fluid flow. Hemisphere, New York (1980)
- [8] Sohn, H.Y., The law of additive reaction times in fluid-solid reactions. Metall. Trans., 9B (1978), 89-96
- [9] Nicole, C., Etude et modélisation de l'hydrofluorination du dioxyde d'uranium en four tournant. Doctorate Thesis, INPL, Nancy (1996), 25-32
- [10] Wen, C.Y. et Fan, L.T., Model for flow systems and chemical reactors. Dekker (1975)
- [11] Froment, G.F., et Bischoff, K.B., Chemical reactor analysis and design. 2nd ed., Wiley (1990)
- [12] Leva, M., Heat transfer to gases through packed tubes. Ind. Eng. Chem. 39, 7 (1947)
- [13] Pasternak, I.S., et Gauvin, W.H., Can. J. Chem. Eng., 35, 38, (1960); AIChE J. 254, 7 (1961)
- [14] Kays, W.M., Convective heat and mass transfer. McGraw-Hill New York (1966)
- [15] Lundberg, R.E., Reynolds, W.C., et Kays, W.M., NASA TN D, Washington (1963)

For Your Notes

1998

SESSION 4
Process Simulation



Invited Lecture

***Experiences of CFD Simulations at
Foster Wheeler Corporation's
Karhula R&D Center***

T. Hyppänen

**Experiences of CFD simulations at Foster Wheeler
Energia Oy's Karhula R&D Center**

Timo Hyppänen
Foster Wheeler Energia Oy
Karhula R&D Center
P.O.Box 66, FIN-48601 Karhula, Finland

Abstract

Karhula R&D Center is specialized in the research of solid fuel combustion based on Circulating Fluidized Bed technology. Since the 1970's, numerical models have been utilized in process development to enhance fundamental understanding of the technology. Both own and commercial computer models have been used. Until now, a special problem in Circulating Fluidized Beds has been the modeling of dense phase multiphase flow, especially for industrial solid-fuel boilers. This has prevented the Karhula R&D Center from using commercial codes, and as a consequence, own modeling approaches have been necessary. This paper describes some main points of the modeling activities in Circulating Fluidized Bed boilers.

Helsinki University of Technology
3rd Colloquium on Process Simulation
12 - 14 June, 1996
Espoo, Finland

INTRODUCTION

Foster Wheeler Energy International, Inc. supplies steam generation technology and related customer services to the utility and industrial customers. The company is headquartered in Clinton, USA and has about 3000 employees. In 1995, Ahlstrom Pyropower joined Foster Wheeler to strengthen and complement each other's steam generation technology, especially Circulating Fluidized Bed (CFB) technology, in which area Foster Wheeler is the world market leader. The Karhula R&D Center with its 60 employees is one of two R&D centers in the company. It is specialized in the research and development of Foster Wheeler PYROFLOW CFB boilers, including pressurized CFB combustion and gasification which are necessary in advanced combined steam and gas power cycle systems.

The CFB process

The CFB process utilizes a water-cooled combustion chamber and a refractory-lined, or a steam or water-cooled hot separator to recirculate hot bed material consisting largely of inert ash constituents (Figure 1). Primary combustion air fluidizes and suspends the circulating bed which is augmented by fuel and limestone fed into the lower part of the combustor. Combustion takes place in the combustor at a temperature range optimum for this reaction, i.e. of approximately 850 - 900 °C. Heat is transferred to the water-cooled membrane-wall combustor and the larger fraction of the bed material is recirculated from the hot separator through a non-mechanical seal back to the combustor. From the outlet of the hot separator, the gas enters the convective heat transfer surfaces in the backpass.

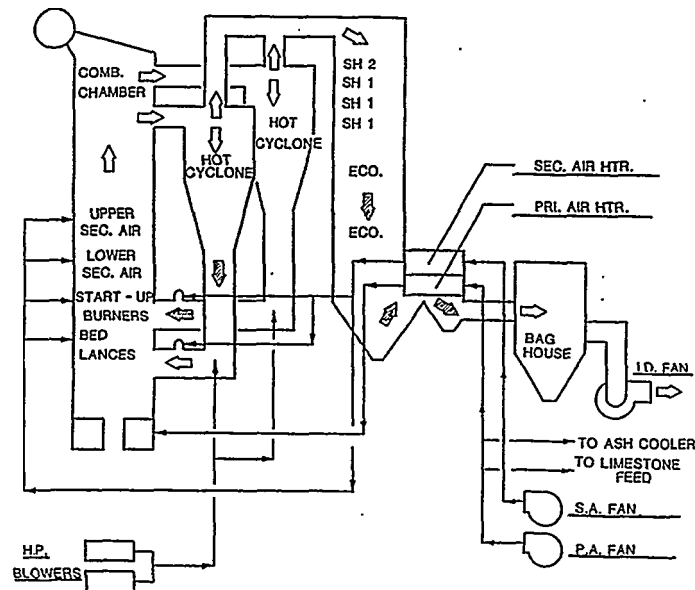


Fig. 1 PYROFLOW circulating fluidized bed combustion system

In the development of CFB boilers the main goals are as follows

- to make solid fuel combustion more economic
- to achieve higher combustion and plant efficiencies
- to increase the flexibility in burning various types and grades of fuels
- to meet all current and anticipated near-term and future emission standards

Achieving of these goals depends on a comprehensive understanding of the combustion process and a capability to develop a new concept from an initial idea to a product ready for demonstration and commercialization. To serve this purpose, the Karhula R&D center provides several experimental facilities including chemical laboratory services, bench scale testing equipment and several specialized pilot plants.

In addition to the experimental research carried out at the Karhula R&D, computer modeling has been used since the mid 1970's in various research projects to support R&D efforts. Several internal computer models have been developed and also commercial softwares have been used.

In the mid 1970's, the first CFD code was developed for modeling turbulent gas-solid suspension flow including heat transfer into the surrounding walls. Based on promising experiences of modeling capabilities, a more general multiphase code was developed at the beginning of the 80's when a special interest was to analyze the behaviour of centrifugal separators. The code was applied during the first half of the 80's into various analyzes and it proved to provide a useful, qualitative aid in the industrial development practise. However, towards the end of the decade, commercial CFD codes were developed onto such a level that they started to emerge into the market with more efficient calculation routines and pre- and postprocessing capabilities. Since that time, a commercial code has also been used at the Karhula R&D Center for analyzing single phase, or lean multiphase calculations.

However, the circulating fluidized bed, which is the most important process for the Karhula R&D, is based on a dense multiphase flow which has not been possible to be calculated for industrial boilers by any commercial codes. For that reason, internal comprehensive models were developed in the end of the 80's to be able to analyze flow, heat transfer and combustion in boilers. After that, models have been developed to include the calculation of mechanisms of sulfur and nitrogen oxides.

Only recently, first attempts to include dense multiphase calculation capabilities into commercial codes have been made. These capabilities have been tentatively tested also at the Karhula R&D Center. However, the current codes do not yet seem to provide a solution for calculating flow in industrial boilers.

A HISTORY AND DEVELOPMENT OF A CFD CODE IN 1980

At the end of the 1970's, a strong interest of the Karhula R&D was to develop and analyze centrifugal separators intended to be used in CFB boilers. At that time, there were not too many alternatives to utilize CFD in flow analysis, especially for high swirling flows. Actually, it was during the 80's when the code was found and agreed that the widely used k-e turbulence model did not give a right description of velocity profiles in high swirling flows - it dampened considerably the swirling flow near the axis region.

Due to the lack of a tool available for the swirling flow cases, a development of an own CFD code was started. Very limited computer capacity restricted the objectives of the code only to 2-dimensional cases. However, it allowed calculations of axisymmetric 3-dimensional cases which is quite realistic assumption for centrifugal separators.

The main features and objectives for the code were as follows:

- General geometry, rectangular and triangular grid
- General Eulerian multiphase calculation
- Time-dependent semi-implicit calculation
- 1-equation turbulence model (kinetic energy)
- Symmetric or upwind difference schemes
- Staggered grid

Calculation example

The first calculations were made for a conventional cyclone separator. Due to the status of computer capacities at that time, the calculation grids were very limited. The axi-symmetric case was analyzed by using 66 cells including 5 solid phases with different solid particle sizes. Without any graphical pre-processing tools, a typical calculation case required manual numbering of cell volumes (Figure 2) and surfaces, and boundary conditions were fed directly into a file. However, due to a small grid, it was possible to program and calculate a new case within one day.

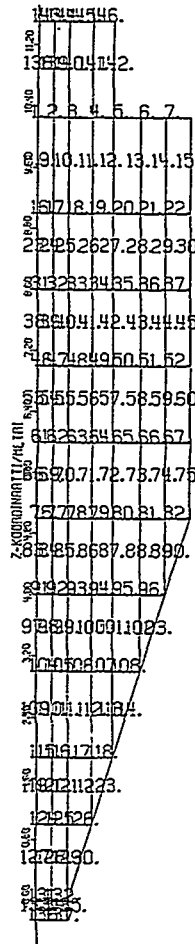


Fig.2 Calculation grid

Results, features

The most important results of the capabilities of the code were:

With 1-equation turbulence model it was possible to calculate the tangential velocity profile with right attenuation of angular momentum, which is the most important feature when analyzing the separation efficiencies of cyclones. Later, when measurements were possible in real, hot separators of the CFBs, it was confirmed that the calculated results were complied with the ones obtained in real unit, as shown in Figure 3.

An example of gas and particle flow profiles for a case are shown in Figure 4. When zero derivative of axial velocity was used as a boundary condition in the outlet, the axial flow velocity in the axis was negative. The similar result was obtained later with a commercial CFD code as well.

Eulerian multiphase flow equations seemed to provide reasonable results for solid density profiles, and for the separation of solid particles. Also, falling of particles due to gravity was seen near the walls when particles were not allowed to escape from the calculation volume as a boundary condition.

The code was applied at the beginning of the 80's to approximately 20-30 different applications with about 200 calculations altogether, until most of the normal flow calculations were started to be analyzed with a commercial CFD code.

The code was also tested with calculations of multiphase flow in dense fluidized bed, but a restriction to two dimensions and inadequate model equations, e.g. particle stresses and gas-particle friction,

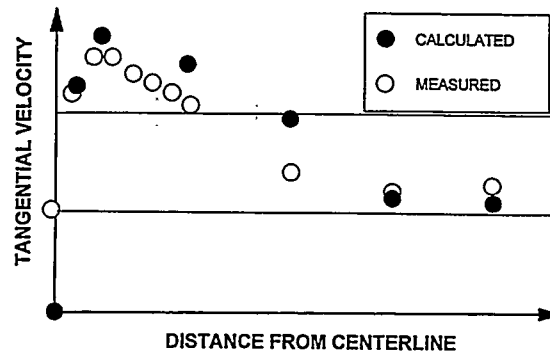


Fig.3 Measured and calculated tangential velocity profiles

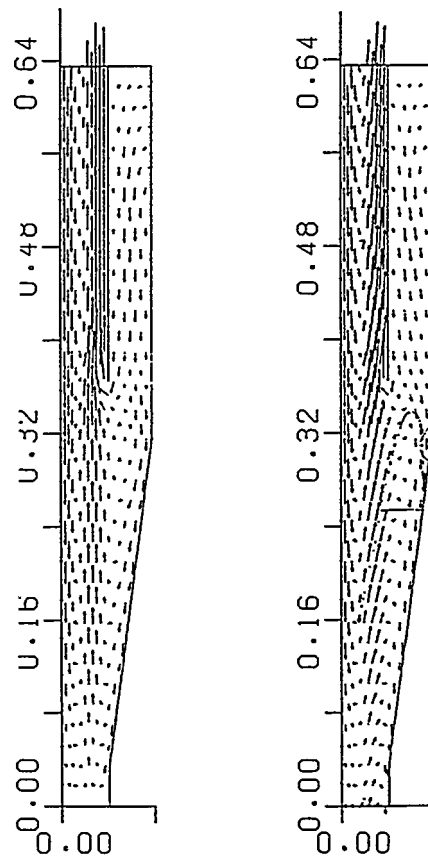


Fig.4 Calculated gas and particle velocities

prevented reliable quantitative analyses.

Subconclusion

At that time, with a quite simple computational program and open-minded approach it was possible to attain more reasonable results for a high swirling flow case than with more sophisticated programs.

FLOW CALCULATIONS WITH A COMMERCIAL CFD CODE

General

During the 1980's and 90's, the use of commercial CFD codes has grown and become common in industrial companies. Various applications calculated in industry have been presented in numerous papers. The activities of the Karhula R&D in normal, single and lean phase CFD do not provide any special added value to the existing general knowledge and therefore, examples of applications have only been listed in the following without going into the same CFD details which are presented in the context of papers describing other similar types of calculation cases.

Examples of flow calculations for single or lean solid phases:

- maximising of heat transfer in a waste heat boiler
 - + optimal flow profile with inserted obstacles
- optimizing mass transfer between gas and a surface
 - + to find right locations for flow inlets
- analyze droplet trajectories and evaporation
 - + to design the right geometry and velocities
- prevention of erosion, availability of a component
 - + inserting obstacles, modifications in channel geometries
- uniform flow requirements by a process
 - + necessary baffles to e.g. increase the ratio of friction to inertia
- separation of solids from gas
 - + identification of reasons for malfunctions
 - + improvements of designs
 - + avoid solids accumulation
 - + develop, evaluate new ideas
- back pulse cleaning of filters
 - + to design right cleaning devices
- prevention of thermal shocks in equipment
 - + unsteady operation - optimising the barrier heat capacity
- optimize mixing

- + feed locations of gaseous additives
- + number of necessary gas streams
- fouling of equipment
 - + redirection of flow by inserts
- analysis of pressure losses in a channel
 - + lower power consumption by modifications
- cooling of critical hot structures
 - + locations and rates for cooling fluid
- visualization of process behavior
 - + to illustrate the operation of a process
 - + animation of dynamics
 - + 3-d steady state profiles

Subconclusion

Quantitatively, without any experimental verification CFD codes do not have enough credibility to be used as design tools. However, in most cases, a qualitative result is enough in order to select one of the alternative designs for further experimental research or for installation into an industrial unit. It can also be used to support important decisions of new designs or design modifications.

In general, the experiences about the flow calculations at the Karhula R&D Center have shown that in many cases important decisions in industrial activities can strongly be supported by the results of CFD analyses and it has become a valuable research tool especially when used together with experimental methods.

MODELING OF CIRCULATING FLUIDIZED BED COMBUSTION

CFB Modeling, background

CFB combustion modeling aims at better understanding and ability to estimate combustion efficiency, emissions and heat transfer in the CFB combustion process. In the development of the comprehensive CFB model, flow model forms the basis for the balance equations. Flow models based on momentum conservation have been formulated during the years for 1-dimensional (Arastoopour and others 1982) and also for 2 or 3-dimensional FB or CFB flow (Pritchett and others 1978, Schneyer and others 1981, Militzer 1985, Gidaspow 1986, 1994). However, there is no consensus on the form of the equations, which describe gas-solid flow in CFB. If an agreement for the equations for microscopic models is reached, there is still a problem of extremely large computation times needed for numerical calculations. Faster calculation can be reached by using coarser grid systems, but then the aggregate nature of flow must be taken into consideration in the equations for macroscopic scale models. It can be accomplished by macroscopic averaging procedure (Hughes and others 1976, Bachmat and Bear 1986, Hyppänen 1989, Kallio and others 1996), which

however introduces some new model parameters to be evaluated by experiments.

In CFB systems, in addition to the hydrodynamics of the combustor fluid flow in hot separator and bottom ash discharge equipment must be considered. Thus, practical models are required to take into consideration the design of industrial components.

In order to study combustion chemistry and heat transfer phenomena in CFB systems, submodels describing char particle combustion, devolatilization, heat transfer, attrition and fragmentation, SO_x and NO_x emissions have to be included. In the model, an overall reaction approach is used to formulate a simplified kinetic model for N₂O/NO_x formation and destruction. The details of the NO_x/N₂O kinetic model, which is partially based on the kinetic studies of Johnsson (1991) and Goel et al. (1994), are discussed in previous papers (Tsuo et al., 1993 and 1995). In summary, NO forms through direct char-N oxidation and oxidation reactions of NH₃ with O₂ and NO over the catalysts of char, ash and CaO. NO reduces through a series of heterogeneous reactions with CO and H₂ over the char, ash and CaO. N₂O forms through direct char-N oxidation and oxidation reactions of HCN. N₂O reduced through thermal decomposition and heterogeneous reactions with CaO and char.

Both calcination and sulfation reactions are considered in the SO₂ model. Calcination reaction is assumed as a very fast reaction. A constant reaction rate is used for the calcination reaction. Sulfation reaction is a first order reaction as a function of SO₂ concentration, CaO concentration, and bed temperature. The influence of oxygen on the sulfation reaction is not considered in the model. The effect of bed temperature on the sulfation rate is monotonous as that sulfation rate increases with increasing bed temperature. The pore plugging effect due to higher reaction temperature on the surface of calcined limestone is not simulated by the model. As a result, the current SO₂ model is only suitable for simulating the cases with lower combustion temperature, which is below the optimum sulfation temperature. An enhanced model is under development.

Model description

In this model, solution of three dimensional balance equations is based on the finite volume method, in which the geometry is divided into different control volumes. The volumes are formed applying rectangular cartesian coordinate system as presented in Fig. 5. Balance equations are integrated over each of these control volumes. Each equation is based on the principle; $\text{CHANGE} = \text{FLOW IN} - \text{FLOW OUT} + \text{SOURCE}$. In this model, only steady-state equations were used. For any property, the number of equations equals the number of volumes and the discrete values for a property for each volume can be calculated.

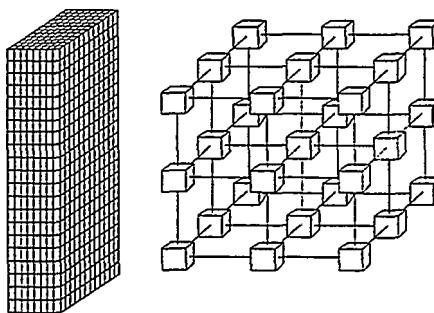


Fig. 5 Calculation grid and the structure of the corresponding process model

Due to limiting computer capacities, the grid size is usually in practice so large that flow cannot be considered homogeneous within one grid size and thus microscopic time/volume averaged equations are not valid without averaging over a larger scale. Averaging produces new correlation terms, which must be modelled and require experimental parameters. The most challenging terms are the averaged gas-solid drag term and fluctuation term of particle momentum.

Solid Flow Profile

In this comprehensive model, solid momentum balance can be applied in a hybrid method by calculating it separately, so that interaction between the comprehensive model is not tightly binded. When a final solution is obtained, all the equations are converged. In this way, the computation of the comprehensive code is speeded up by avoiding frequent time-consuming calculation of solid flow. In addition, solid flow profile can be given as an input with the assumption that solid flow profile is not affected by combustion process. Thus, solid flow profile can be calculated separately or an experimental flow profile can be given whichever is more reliable. In the calculations of this study, experimental solid profiles were used. Calculated solid flow profile values will be used when the computational requirement and reliability of 3-dimensional solid flow models have been tested to be appropriate.

Gas And Energy Balance

Balance equations for the gas phase are momentum, mass and species conservation equations. Only one energy balance is calculated in this version of the model. So both gas and solid phases are considered in the same balance and thus locally, gas and solid phases are assumed to remain at the same temperature. Temperature of fuel particle can, if required, be calculated separately and is dependent on particle reactivity model.

Mixing of different gas species is calculated by applying dispersion type mixing terms in species' equation. Mixing parameters are based on the results obtained from the tracer tests performed in pilot and commercial units. The results of the tracer tests are analyzed applying a 3-dimensional finite volume convection /dispersion model. Fig. 6 shows an example of a test in a commercial unit. In this case, radioactive gas tracer is fed into the bottom of the reactor (feed point F7) and experimental and calculated detector signals are presented for the highest detector level. It is shown that signal intensity is at its

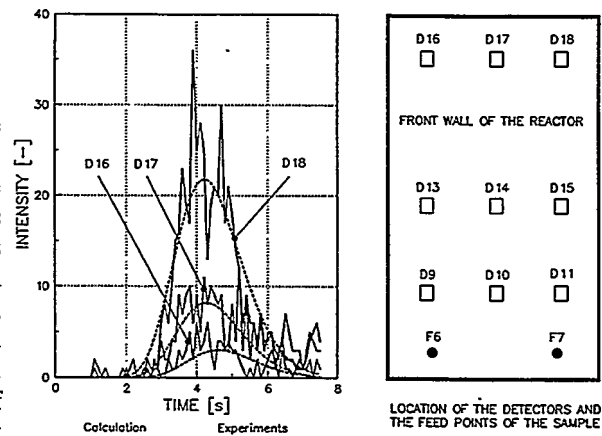


Fig. 6 Mixing experiments. Results showing location of the signal detectors and comparison of the calculated and measured signals

maximum straight above the feed point (detector D18). The intensity profile is affected by the relative magnitude of convection and dispersion. Since the same mixing models have been applied in analyzing experimental mixing data and in calculation of comprehensive models, it provides a direct way to transfer the mixing parameters from experiments into comprehensive model.

The conservation equations mentioned above allow the calculation of velocities and concentrations for gas and solid, pressure and temperature profiles. In balance equations source terms are required, which contain all the rate coefficients and heat production/sink correlations. Also, devolatilization and penetration of secondary air feed are given as a source term in gas balance. The parameters for these submodels are obtained experimentally by laboratory tests or from performance data of pilot or commercial units. Furthermore, separate theoretical analyses can be utilized when determining the parameters for a submodel.

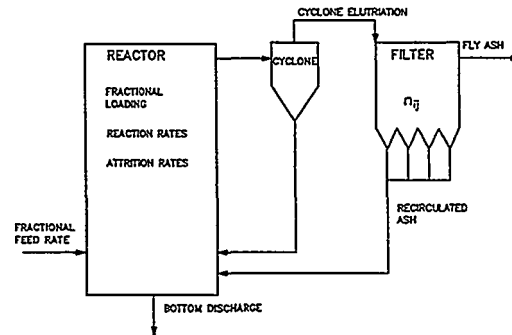


Fig. 7 Elements of the solid material balance

Solid Species' Balance

In this model, solid is divided into different materials such as char, ash, CaO, CaCO₃, CaSO₄ and make-up sand, which each are divided into different size fractions. A balance equation is written for all of these fractions as presented in Fig. 7. In the balance equations, fractional feed, reactions, bottom discharge, elutriation through the cyclone, ash recirculation and attrition/fragmentation are included (Lee and Hyppänen 1989).

In this equation system, the coefficients are linearized and they can be easily written in matrix form and the solution is found by Gaussian elimination. Fractional values are usually known only for feed, but the models for fractional flow out of the cyclone and from the bottom discharge system must also be included. Total bottom discharge rate is usually controlled by bed inventory, but fractional classification ability is dependent of the

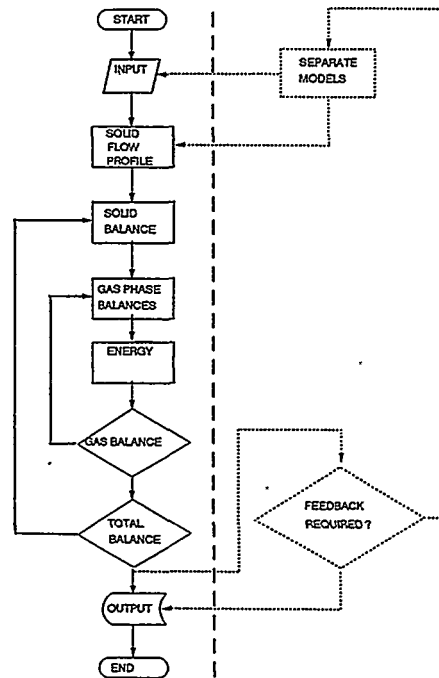


Fig. 8 Flowchart of the code

design of the device and thus it must be an input for the code.

Program structure

The flow diagram of the computer code is presented in Fig. 8. After the initial data have been read, the solid flow profile is obtained either by experimental values or separate models. Then, the first iteration values are calculated for solid balance equations, which give fractional solid flow rates and concentrations. These values can be used for calculation of local heterogeneous reactions thus giving source terms for gas mass balance, which is calculated next together with gas momentum balance. Average gas velocities can be used then in gas species equations, in which relative mixing is calculated according to dispersion model. The energy equation is calculated last to correct the temperature field. After that convergence of gas and total energy balances is evaluated, iteration is continued until criteria is satisfied. When all the iteration criteria are satisfied, the program writes the output and then stops. In this stage the feedback to the hybrid models can be considered and the criteria for a new calculation introduced.

In obtaining the solution for the gas phase mass and momentum equations, they are combined to give pressure equation, which is solved by relaxation method. Then, velocities are calculated from the momentum balance. Staggered grid and upwind differencing scheme is used in calculation procedure. Non-linear terms in species' equations are linearized and solution is obtained iteratively.

Results

The model calculations discussed in this paper have been done to study the performance of the industrial size PYROFLOW CFB boiler in Pori, Finland (Fig. 5). Its thermal capacity is 85 MW and the main fuel is Colombian coal. The boiler has two cyclones and fuel is fed to the loop seals. The secondary air is usually fed from all 4 walls.

Each material was divided in this calculation into 5 different fractions: 0-50 μm , 50-100 μm , 100-500 μm , 500-2000 μm and over 2000 μm . The computation grid was 8 elements deep 12 elements wide and 20 elements high as shown in Fig. 9.

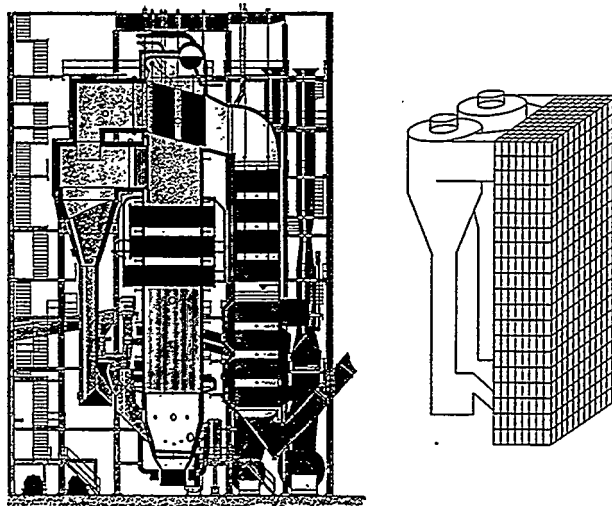


Fig. 9 Commercial CFB boiler and respective calculation grid

During these calculations, the model was still in the parameter evaluation stage and the accuracy of the results especially for three dimensional profiles is not known mainly because no experimental profiles were measured from this boiler. However, the boiler performance data was available and comparison between the model and the boiler was possible.

In order to illustrate the capability of the model, two examples of model calculations are presented below. The first one utilized the results from solid balances to study the effect of fly ash recirculation on combustion efficiency. The second example utilized the results from gas balances to study the effect of secondary air feed ports modification on gas flow and concentration profile.

Effect Of Flyash Recirculation

Fly ash recirculation, which is the recycling of flyash from baghouse to the combustor, can be used to improve combustion efficiency and limestone utilization. It increases especially the amount of ash fines in the reactor as presented in Fig. 10.

The bottom ash to total ash percentage was increased from 12.9 % to 16.4 % due to fly ash recirculation. In both experiments and calculations solid inventory in the furnace was constant.

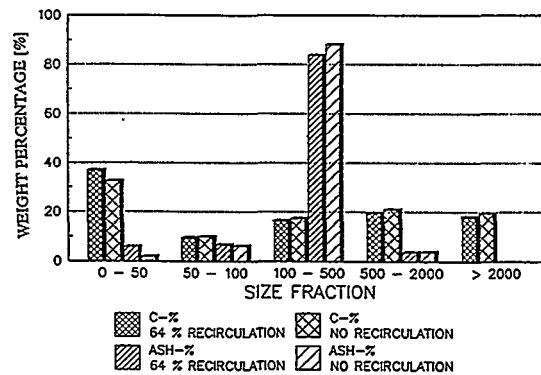


Fig. 10 Calculated size distribution of char and ash in the reactor

In the model calculations, total carbon loss was decreased by 49 % when compared with the calculations without fly ash recirculation. This result as well as combustion efficiency were in agreement with experimental data.

Effect Of Secondary Air Feed Points

Model calculations are performed for a case where the secondary air ports on the side walls are closed. However, there are two secondary air ports in both the front and the back wall. In this calculation the penetration of secondary air is based on experimental tests using radioactive tracers in secondary air ports of large industrial CFB units. The 3-dimensional profiles of gas velocity, oxygen and volatile concentration are presented in Fig. 11.

Although gas is uniformly distributed through the grid, the gas finds its way through the least resistance path. Therefore, it is shown that gas velocity is higher in the middle of the reactor, where solid concentration is lower. Because of wall effect, solid concentration is higher in the wall region, where some solids are falling down and dragging some gas with

it causing additional macroscopic mixing of gas. Due to the gas flow profile, higher oxygen concentrations can be seen in the middle at the first level. In the wall region, oxygen concentration is lower due to lower velocities and also to higher combustion. A lot of combustion occurs close to the grid due to high char concentration. Thus, oxygen concentration is decreased fast below the secondary air feed points. After the secondary air ports, there is first large local oxygen increase near the feed points as shown in the oxygen concentration profile in the second level in the Fig. 11. Then, above the secondary air feed points the difference decreases due to gas mixing. In the upper levels, oxygen concentration is higher in the middle and lower near the narrow walls, which is due to elimination of the secondary air ports from the side wall in this calculation.

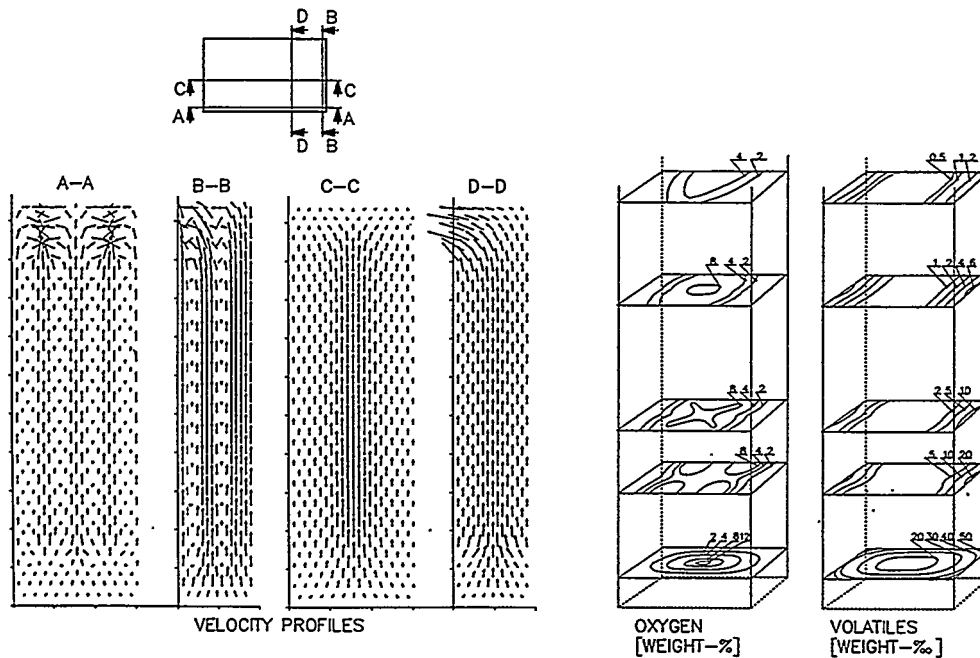


Fig. 11 Three-dimensional profiles for gas velocity, oxygen and volatile concentration.

In this calculation, volatiles are assumed to be released uniformly in the bottom region, where the coal is fed. The main part of the volatiles are burned in the system, but a small portion is escaping from the reactor near the wall region, where oxygen concentration and temperature are low.

CONCLUSIONS

In 1980, a quite simple own computational program gave more reasonable results for a special case than the more sophisticated programs of the time. Today, the development of own programs for normal flow calculations seems not to be reasonable due to all features which are already available in commercial flow codes. However, there are practical industrial processes with special features which are not adequately modeled with the CFD softwares available. In such cases, an open-minded approach and an emphasis on modeling right magnitudes of phenomena may be more preferable than using more rigorous codes on cases which they have not been meant for or verified to.

Important decisions in industrial activities can strongly be supported by the results of commercial CFD code analyses and CFD has become a valuable research tool especially when used together with experimental methods.

A comprehensive model has been developed for the analysis of CFB combustion. Additional experimental and theoretical data is required for phenomenological models, which are used in balance equations and through which the accuracy of the model can be increased. Thus, further research and development is required especially for improving understanding of each phenomenon separately. Also, gas-solid flow equations must be developed to allow practical flow calculations in the CFB boilers. Nevertheless, together with the existing knowledge of different phenomena, the comprehensive models can be used effectively to analyze the detailed CFB performance.

REFERENCES

- Arastoopour, H., Lin, S.-C. & Weil, S.A., 1982. Analysis of vertical pneumatic conveying of solids using multiphase flow models. *AIChE J.* **28**, 3, pp. 467-473.
- Bachmat, Y. & Bear, J., 1986a. Macroscopic modelling of transport phenomena in porous media. 1: The continuum approach. *Transport in Porous Media*, **1**, pp. 213-240.
- Bachmat, Y. & Bear, J., 1986b. Macroscopic modelling of transport phenomena in porous media. 2: Applications to mass, momentum and energy transport. *Transport in Porous Media*, **1**, pp. 213-240.
- Basu, P., & al., 1987. A simplified model for combustion of carbon in a circulating fluidized bed combustor. *International Conference on Fluidized Bed Combustion*. Boston, Massachusetts, May 3-7, 1987. The American Society of Mechanical Engineers, 1987. Vol. 2, pp. 738-742.
- Breault, R., 1986. Hydrodynamic characteristics and coal combustion modeling of a high

velocity fluidized bed. Dissertation. University of New Hampshire. Michigan.

Fett, F.N. & Werther, J., 1989. Modellierung der Wirbelschichtfeuerung an ausgewählten Fallbeispielen. *BWK*, 41, Nr.5, pp. 213-221.

Gidaspow, D., 1986. Hydrodynamics of fluidization and heat transfer: Supercomputer modeling. *Appl. Mech. Rev.* 39, 1, pp. 1-23.

Gidaspow, D., 1994. *Multiphase Flow and Fluidization Continuum and Kinetic Theory Descriptions*, Academic Press, Boston.

Goel, S.K., A. Morihara, C. Tullin, and A. Sarofim, "Effect of NO and O₂ Concentration on N₂O Formation During Coal Combustion in a Fluidized Bed Combustor: Modeling Results", Presented in the 25th International Symposium on Combustion, 1994.

Hughes, E.D., Lyczkowski, R.W., McFadden, J.H. & Niederauer, G.F., 1976. An evaluation of state-of-the-art two-velocity two-phase flow models and their applicability to nuclear reactor transient analysis. EPRI-Report NP-143, Volume 2, Technical services agreement SOA 75-317, 254 p.

Hyppänen, T., 1989. An experimental and theoretical study of a multiphase flow in a circulating fluidized bed. Ph.D. thesis, Lappeenranta University of Technology.

Johnsson, J.E., 1991. Nitrous Oxide Formation and Destruction in Fluidized Bed Combustion - A Literature Review of Kinetics, Presented at the 23rd IEA-FBC Meeting, Nov. 6-9, 1991.

Kallio, S., Poikolainen, V. & Hyppänen, T., 1996. *Mathematical Modeling of Multiphase Flow in a Circulating Fluidized Bed*. Report to be published by Åbo Akademi, Institutionen för Värmeteknik, Finland.

Lee, Y. & Hyppänen, T., 1989. A coal combustion model for circulating fluidized bed boilers. International Conference on Fluidized Bed Combustion. San Francisco, California, April 30-May 3, 1989. Vol. 2, pp. 753-764.

Miltzer, J., 1985. Numerical solution of the fully developed two-phase (air-solids) flow in a pipe. in Proc. 1st Int. Conf. on Circulating Fluidized Beds, Halifax, Nova Scotia, ed. Basu, P., Pergamon Press, 1985, pp. 173-183.

Pritchett, J.W., Blake, T.R. & Garg, S.K., 1978. A numerical model of gas fluidized beds. *AIChE Progress Symposium Series* 176, 74, pp. 134-148.

Schneyer, G.P., 1981. Computer modeling of coal-gasification reactors. DOE-Report DOE/ET/10242-T1, Vol.2.

Tsuo, Y., A. Basak, Y. Lee, A. Rainio, and T. Hyppänen, "Simulation of NO_x Emission from Circulating Fluidized Bed Boilers, Proceedings of the 4th CFB Conference, 1993.

Tsuo, Y., Y. Lee, A. Rainio, and T. Hyppänen, "Three-Dimensional Modeling of N_2O and NO_x Emissions from Circulating Fluidized Bed Boilers", Proc. 13th International Conference on Fluidized Bed Combustion, Vol 2, pp. 1059-1069, 1995.

Weiss, V., 1987. Mathematische modellierung zirkulierender wirbelschichten für die kohleverbrennung. Dissertation, Universität-GH-Siegen, 1987.

For Your Notes

Energy-Dissipation-Model for metallurgical multi-phase-systems

Konstantinos Th. Mavrommatis
Rheinisch-Westfälische Technische Hochschule Aachen
Institut für Eisenhüttenkunde
Intzestrasse 1, D-52072 Aachen

Abstract

Entropy production in real processes is directly associated with the dissipation of energy. Both are potential measures for the proceed of irreversible processes taking place in metallurgical systems. Many of these processes in multi-phase-systems could then be modelled on the basis of the energy-dissipation associated with. As this entity can often be estimated using very simple assumptions from first principles, the evolution of an overall measure of systems behaviour can be studied constructing an energy- dissipation-based modell of the system.

In this work a formulation of this concept, the Energy-Dissipation-Modell (EDM), for metallurgical multi-phase-systems is given. Special examples are studied to illustrate the concept, and benefits as well as the range of validity are shown. This concept might be understood as complement to usual CFD-modelling of complex systems on a more abstract level but reproducing essential attributes of complex metallurgical systems.

INTRODUCTION

Metallurgical systems consist usually of many phases and components and the processes taking place within metallurgical aggregates are usually located at high temperatures and far from equilibrium. Transport and interchange of mass, energy and momentum during metallurgical processing in large dimensions constitutes a special kind of complexity, making these systems to be theoretically tractable only with a combination of simplicity in the assumptions, for example thermodynamic equilibrium, with simultaneously high power in the computing methods, in order to scale-up from the small system under theoretical consideration to the real plant-scale system.

From the theory of thermodynamics of irreversible processes, which is the background for the theoretical treatment of real processes, it is known that three main assumptions are valid in order to apply this theory to real systems: The linear dependence of the fluxes, the validity of local equilibrium and the symmetry relations for the kinetic coefficients. These constitute the physical basis for linking the real processes with the powerful methods of thermodynamics.

As the entropy production in real processes is directly associated with the dissipation of energy, both are measures for the irreversible processes taking place in metallurgical systems. Many of these processes in multi-phase-systems can then be modelled on the basis of the energy-dissipation associated with. As this entity can often be estimated using very simple assumptions from first principles, and in agreement with the above three assumptions, the evolution of an overall measure of systems behaviour can be studied constructing an energy-dissipation-based model of the system.

In this work a formulation of this concept, the Energy-Dissipation-Modell (EDM), for metallurgical multi-phase-systems is given. Special examples are studied to illustrate the concept and benefits as well as the range of validity are shown. This concept might be understood as complement to usual CFD-modelling of complex systems on a more abstract level but reproducing essential attributes of complex metallurgical systems.

In many metallurgical systems the degree of complexity is due mainly to a large number of phases and of chemical components, which do not remain constant during the operation but are changed or created or destroyed. Convection, interface phenomena and the high temperatures of pyrometallurgical operations complicate full quantification of the behaviour of these systems. Use of the aggregates for recycling purposes introduces additional complexity because of the phases entering or created during the operation.

To find relevant measures for quantifying the proceed of the processes involved is essential for understanding, optimising and control the processes and the aggregates. The overall entropy production has been established as such a measure of proceed of irreversible processes. The procedure is as follows: First the system is defined, that is which parts belong to it and which are outside. The system is characterised to be open or closed for transport of mass or energy (heat). Then the application of the principles of thermodynamics allows to link between the system variables and parameters and to quantify their behaviour. The concept of entropy production is useful as a measure for irreversibility of the processes. But different processes are not always comparable regarding to this entropy-like numerical measure of their irreversibility /1,2/. Further, several underlying processes can contribute to the same value of entropy production, the contributions of which might not be separable. Thus, a further measure is needed, which is less abstract, easier tractable and physically measurable, and on the basis of which simple models to be used in optimisation and process control are possible. Here the energy dissipation is proposed, which fulfils the above requirements.

THE MODEL CONCEPT

Consider a metallurgical multi-phase system. For simplicity let assume that the system has the same number of phases and of components. To avoid very abstract treatment and in order to be more illustrative, restriction on three phases and components seems sufficient, gaseous (G), solid (S) and liquid (L). These are considered representatively for a wide variety of possible processes, to which later transfer would be possible. Different components could exist in each of this phases for short or for long time, but the model to be develop will focus on the kinetic interaction of the phases rather than on the chemical reactions between the phases. (The later is the object of fundamental and applied investigations in metallurgy since several decades.) In metallurgical systems usually permanent and transitory phase contact is given which means that in general one has to consider the possibility of entrainment of one phase by other phases. Thus, for each phase the changes of its energy from a thermodynamical point of view consists of performing mechanical work, surface work, chemical work and all other kinds of work which could be generally associated with, like electrical, magnetic a.o., and of heat transfer.

Dissipation means the distribution of energy from a few to many degrees of freedom. This takes place through a combination of bulk motion with intensive presence and action of shear forces. The essential assumption of the EDM is to allocate the dissipation according to the above concept to be taking place through the relative movement of the phases within the metallurgical aggregate, where locality of interaction is assumed, i.e. the transfer of energy down the size-scale to kinetic energy takes place immediately in the location of the different phases. The allocation of the dissipation to one of more possible mechanisms is equivalent to pseudo-thermostatical theories /3/, which allocate the irreversibility to some preferred mechanism, beeing often of high heuristic value.

The total energy of each of the phases

$$E = \iiint \varepsilon(\bar{r}, R, t) f(\bar{r}, R, t) d\bar{r} dR dt \quad (1)$$

must be integrated over the whole space the phase is extended, the size of the particles of the respective phase and the time. Here ε denotes the energy of the phase particle located in \bar{r} , having size R and to time t . The distribution of the phase particles among the different sizes is given by the density function f . The energy dissipation is the total time derivative of this expression. Respective conservation equations hold for mass (equations of continuity), momentum (equations of motion) and for the whole energy of the multi-phase system.

The main statement of the EDM is the splitting up of the total energy of each phase into a conservative and a dissipative part:

$$\varepsilon(\bar{r}, R, t) = \varepsilon^{con}(\bar{r}, R, t) + \varepsilon^{dis}(\bar{r}, R, t) \quad (2)$$

The dissipative part is associated with the motion of the phase, thus with its kinetic energy. It is evident that this is valid also for the multi-phase system. The interplay between the two parts of equation (2) in time can be modelled according to the specific constraints of the systems and the time evolution of the dissipating part enables monitoring the behaviour of the total energy of the system, thus of essential properties of the systems behaviour itself.

APPLICATIONS

The following table I summarises possible interactions of phases in metallurgical processes:

Table I: Different possible interactions between phases in metallurgy:

Interaction of phases	Mechanisms acting	Applications
L-L	transport of mass, chemical reactions	slag/metal reactions
S-L	surface/interface phenomena, mixing, separation	inclusions, alloying, deoxidation
G-L	transport of mass, energy, chemical reactions	degassing, purging, stirring

Successive dissipation of macroscopic energy inserted into melts with inert gas for purging, stirring, homogenisation and mixing purposes is first considered. A gas-liquid dispersion is created. Further introducing of solid particles of ferroalloys for deoxidation and alloying creates a gas- solid-liquid dispersion. In both cases, the link to monitor the different processes is the energy balance between the phases, where the energy dissipation is the main variable for monitoring the processes.

Gas-liquid dispersion

Before presenting the results of the work given, the main attributes, equations and assumptions of the energy-dissipation-model are summarised /4/. (Here W denotes energy and L, G, A, kin, respectively denote liquid phase (melt), gas, air (environment) and kinetic, further p is pressure, p_0 atmospheric pressure, z height of the melt from the bottom, H total height of the melt in ladle, M mass, V volume of the gas bubbles and α is the product from density of the melt and gravitational acceleration).

Energy interchange between gas bubbles and melt is given through a system of coupled ordinary differential equations:

$$dW_L = \alpha(H - z)dV - \alpha V(z)dz + dW_L^{kin} \quad (3)$$

$$dW_G = -p(z)dV + dW_G^{kin} \quad (4)$$

The system L+G is an open system, exchanging energy and mass with the environment (atmosphere) A. The amount of energy dissipating to the environment must be taken into account, as it is created as mechanical work by the system L+G:

$$dW_A = p_0 dV \quad (5)$$

The kinetic energies of the gas bubbles and of the melt are defined as usual in mechanics to depend on their mass and on the square of velocities respectively.

For the closed system (L + G + A) it follows:

$$dW_L^{kin} + dW_G^{kin} = \alpha V dz \quad (6)$$

From equations (3) to (6) the energy distribution can be computed.

The link from this conservative model to the dissipation of energy is given through the assumption that all kinetic energy of the melt is dissipating energy.

The specific energy dissipation rate is then:

$$\dot{\epsilon} = [p_0 + \alpha(H-z)] \frac{1}{M_L} \frac{dV}{dt} + \frac{1}{M_L} \frac{dW_G^{kin}}{dt} \quad (7)$$

The results are shown in figures (1) to (4). The energies of the liquid melt and of the environment, the kinetic energy of the liquid and the total energy are plotted as a function of time and of the bath height. The distribution of the energy among the different phases is shown, where the kinetic energy part of the liquid melt represents the successive energy dissipation. Further, the specific energy change in time for the different phases is plotted as a function of the gas flow rate.

Gas-solid-liquid dispersion

During deoxidation and alloying, small particles of solid ferroalloys (S) of heat capacity c and mass M_S are feeded into the melt. To quantify melting of the particles and dissolution in the steel melt, a three-phases open system must be considered (L+G+S), which is equivalent to the closed system (L+G+S+A):

$$dW_L = \alpha(H-z)dV - \alpha V(z)dz + dW_L^{kin} \quad (8)$$

$$dW_G = -p(z)dV + dW_G^{kin} \quad (9)$$

$$dW_S = cM_S dT \quad (10)$$

$$dW_A = p_0 dV \quad (11)$$

It is assumed that the melting of the particles consumes heat from the heat reservoir of the melt (infinite extent) without further effect on the above energy balance. Further, to compute the energy change during ferroalloy dissolution, the following assumption is made:

$$dW_L^{kin} = dW_L^{dissolution} + dW_L^{mixing} \quad (12)$$

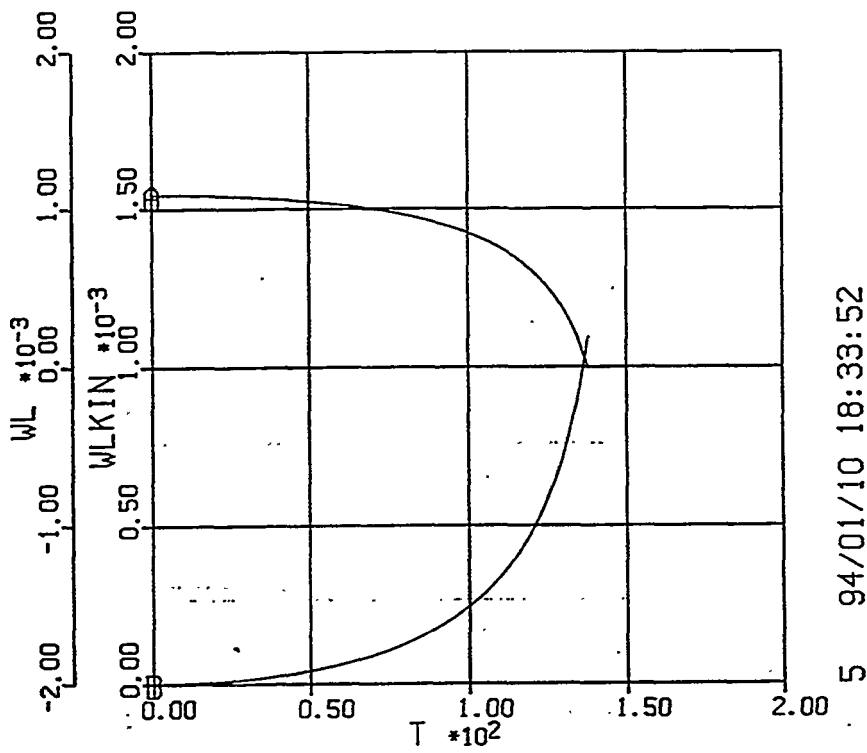
According to this model, the energy transport, as far described, is affected through the presence of the solid phase, the effect being here restricted to the alloying time of the steel melt. The results are shown in figures (5) to (6). The actual FeMn concentration in the melt, the optimum and the relative concentration are plotted for the system gas- solid-liquid, where the dissolution of the ferroalloy particles has been taken into account, with an instantaneous mechanism of swith-on of the diffusion process for mixing and homogenisation of the melt. The curves show that a competition between feeding and melting of FeMn is taking place, which is responsible for the specific form of the concentration curve with its peak (relative maximum) in the beginning of the alloying process.

References

1. G. N. Lewis, M. Randall, Thermodynamik, Verlag Julius Springer, Wien, 1927, X. Kapitel, p. 92-102
2. J. R. Waldram, The theory of thermodynamics, Cambridge University Press, 1985, p. 40-44
3. S. R. de Groot, Thermodynamik irreversibler Prozesse, Bibliographisches Institut Mannheim, 1960, p. 3-4.
4. K. Th. Mavrommatis, First-Principles-Modelling for Process Simulation and Control in Process Metallurgy, Proceedings of the 2nd Colloquium on Process Simulation, Helsinki University of Technology, 1995, ed. by A. Jokilaakso, p.259-272

Figure 1:

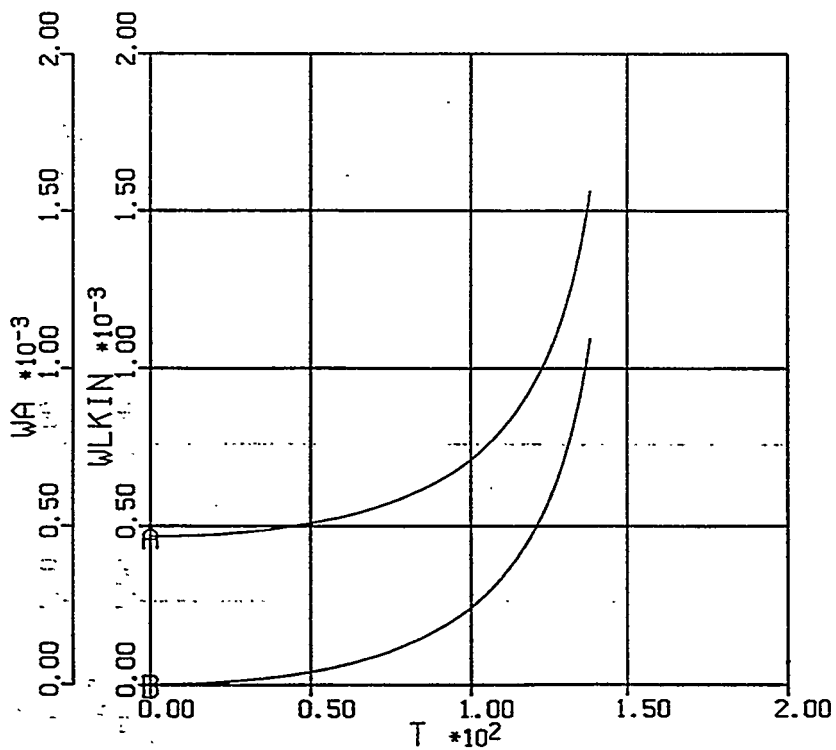
The total energy of the liquid melt WL (curve A) and the kinetic energy of the melt WLKIN (curve B), both in kJ/mole, are shown as a function of time (in s).



5 94/01/10 18:33:52

Figure 2:

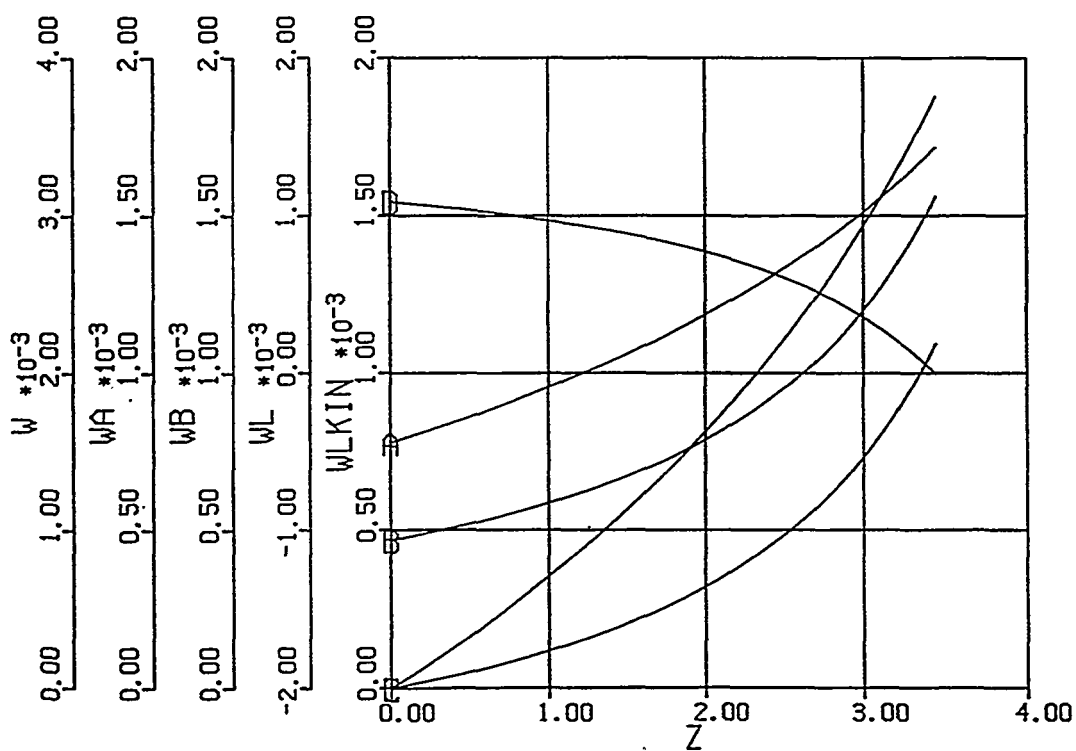
The energy dissipating to the environment WA (curve A) and the kinetic energy of the melt WLKIN (curve B), both in kJ/mole, are shown as a function of time (in s).



6 94/01/10 18:33:52

Figure 3:

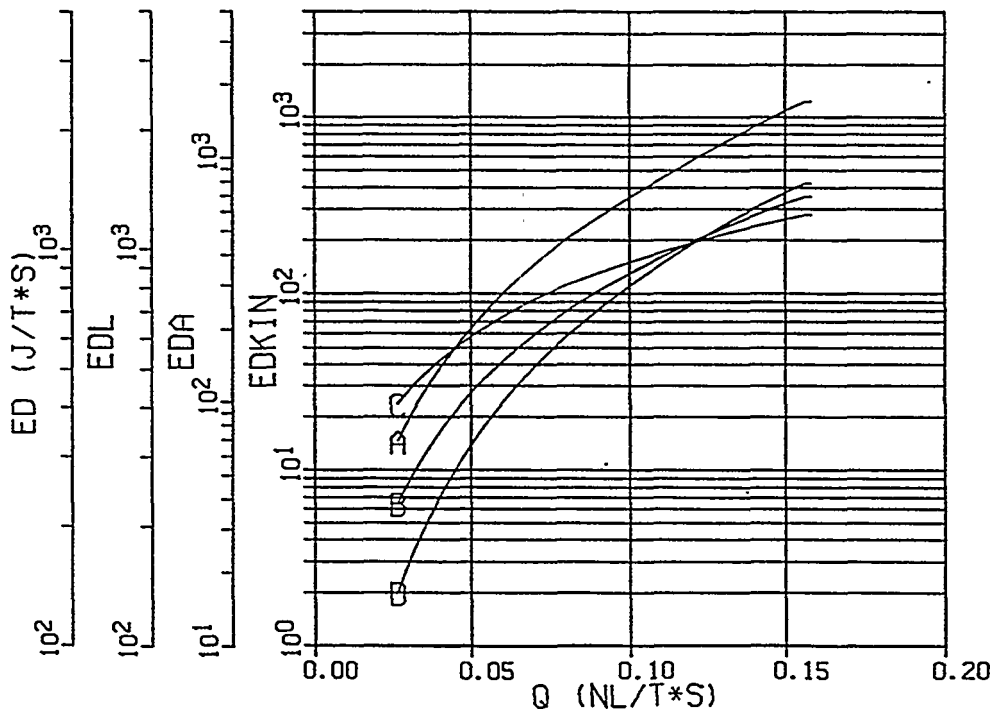
The total energy of the system WA (curve A), the energy dissipating to th environment WA (curve B), the energy of the gas bubbles WB (curve C), the energy of the liquid melt WL (curve D) and its kinetic energy WLKIN (curve E), all in J/mole, are shown as a function of the melt bath height z (in m).



8 94/01/10 18:33:52

Figure 4:

Specific total energy dissipation ED (curve A), energy dissipation of the liquid melt EDL (curve B), to the environment EDA (curve C) and as total kinetic energy EDKIN (curve D), all in J/ton s, are shown as a function of gas flow rate Q (in NL/ton s).



21 94/09/12 15:55:32

Figure 5: Concentration of Mn in the ladle as a function of time (s).

CMN: Mn concentration
CMNOP: Optimum concentration at the tangential point of the eddy induced through gas bubbling
CBEZ: Relative concentration, to be used for comparison

The following data have been used for computation:

Specific heat of FeMn (80% Mn) : 700 J/kgK
Feeding rate: 15kg/s
Feeding time: 20s
Melting time: 20s
Purging through one porous plug: Flow rate: 0.00876 Nl Ar/t s

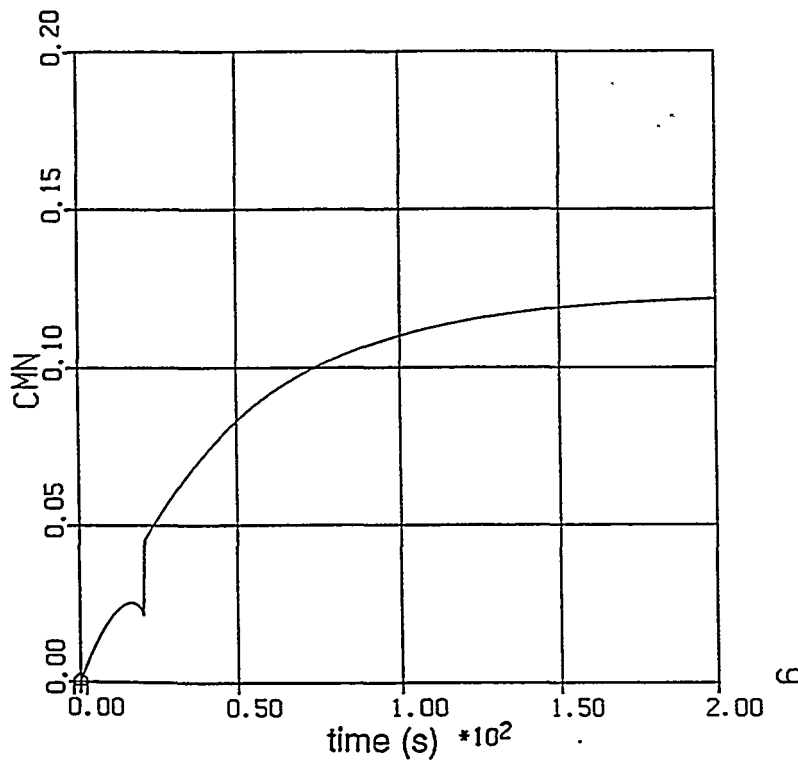
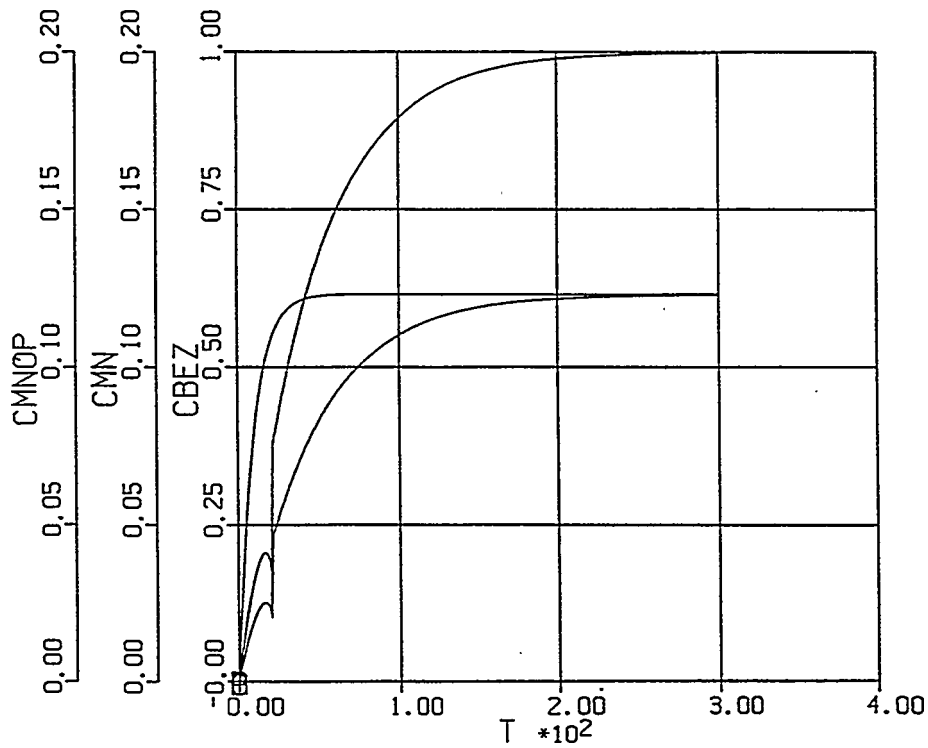


Figure 6: Concentration of Mn in the ladle as a function of time (s).

CMN: Mn concentration
 CMNOP: Optimum concentration at the tangential point of the eddy induced through gas bubbling
 CBEZ: Relative concentration, to be used for comparison

The following data have been used for computation:

Specific heat of FeMn (80%) Mn : 700 J/kgK
 Feeding rate: 15kg/s
 Feeding time: 20s
 Melting time: 20s
 Purging through one porous plug: Flow rate: 0.00876 NI Ar/t s



For Your Notes

MODELLING OF BAFFLED STIRRED TANKS

Hannu Ahlstedt and Mikko Lahtinen
Tampere University of Technology
Energy and Process Engineering
P.O.Box 589, FIN-33101 Tampere, Finland

Abstract

The three-dimensional flow field of a baffled stirred tank has been calculated using four different turbulence models. The tank is driven by a Rushton-type impeller. The boundary condition for the impeller region has been given as a source term or by calculating the impeller using the sliding mesh technique. Calculated values have been compared with measured data.

INTRODUCTION

Stirred tanks are widely used in process industries to carry out many different operations. In spite of the importance and variety of their applications the development of accurate turbulent mixing and scaleup models for stirred tanks has been limited by a lack of understanding of the three-dimensional turbulent velocity field in such vessels.

Although many rules of thumb and corrections of overall parameters have been developed to analyze and evaluate a mixing system, scaleup from a laboratory unit to full-size plant is still risky. Processes that are sensitive to nonhomogeneities in a mixture pose special problems because the correlations do not take the local effects into account.

Large-scale recirculating flows in stirred tanks have to be known when evaluating the results of mixing. The flow field has an important role in the design of an optimal mixing system. The impeller and vessel construction have to be chosen so that there is no so-called dead space inside the mixing tank. Also the power consumption must be as small as possible. The prediction of the turbulence field throughout the vessel is important because of its effects on the macro- and micro-mixing phenomena, reaction yields etc.

Most studies in the literature concerning the modelling of the flow field of stirred tanks have used measured data to add just a suitable source term to momentum equations to model the impeller [2,9]. Turbulence modelling is done usually by the standard $k - \epsilon$ model [6], but also anisotropic turbulence models have been used [1]. The earlier works used a two-dimensional grid. Full three-dimensional computations of the flow in a turbine stirred tank have been presented during the last ten years.

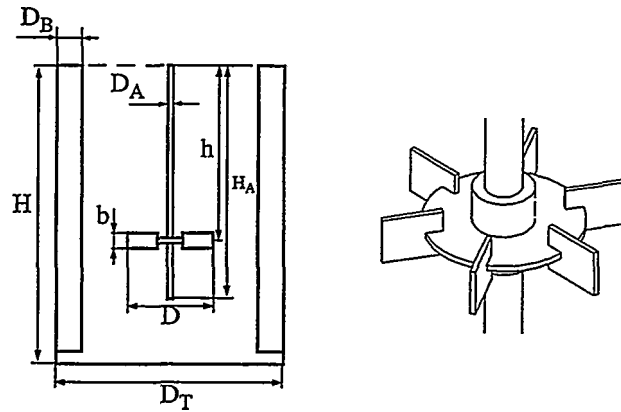
This paper deals with the modelling of the flow field of a baffled stirred tank with different turbulence models. The boundary condition for the impeller region is given on the basis of experimental data and then taking the impeller as a stationary boundary condition for the remaining computational domain. The other way used for giving this boundary condition is to explicitly calculate the impeller region and then to rotate this section of the grid relative to the rest of the domain. The geometry of the calculated tank is shown in Fig. 1. The mean and fluctuating velocity values have been measured by the laser-Doppler anemometer [10].

MODEL AND METHODS

Mean-flow equations

The continuity and momentum equations for an incompressible fluid in orthogonal tensor notation can be expressed as

$$\frac{\partial U_i}{\partial x_i} = 0 \quad (1)$$



D	0,2 m	b	0,04 m
D _T	0,7 m	h	0,35 m
D _B	0,07 m	H	0,7 m
D _A	0,03 m	H _A	0,58 m

Fig. 1 - Stirred tank and Rushton turbine.

$$\frac{\partial U_i}{\partial t} + U_j \frac{\partial U_i}{\partial x_j} = -\frac{1}{\rho} \frac{\partial p}{\partial x_i} + \frac{\partial}{\partial x_j} \left(\nu \frac{\partial U_i}{\partial x_j} - \overline{u_i u_j} \right) \quad (2)$$

where U_i is the velocity component in the x_i direction, p is the pressure, ν is the molecular viscosity, ρ is the density and $\overline{u_i u_j}$ Reynolds stress component. These equations are used in cylindrical coordinates in this case.

Turbulence models

Performance of the standard $k - \epsilon$ model, the RNG $k - \epsilon$ model, the algebraic Reynolds stress model (ASM) and the Reynolds stress model (RSM) to predict flow field in the mixing tank has been examined.

The two-equation turbulence models use Boussinesq's eddy-viscosity concept

$$-\overline{u_i u_j} = \nu_t \left(\frac{\partial U_i}{\partial x_j} + \frac{\partial U_j}{\partial x_i} \right) - \frac{2}{3} k \delta_{ij} \quad (3)$$

where ν_t is the turbulent viscosity, k is the turbulence kinetic energy and δ_{ij} the Kronecker delta. The turbulent viscosity can be calculated from expression

$$\nu_t = C_\mu \frac{k^2}{\epsilon} \quad (4)$$

where ε is the rate of dissipation. The transport equations for k and ε are

$$\frac{\partial k}{\partial t} + U_i \frac{\partial k}{\partial x_i} = \frac{\partial}{\partial x_i} \left(\frac{\nu_t}{\sigma_k} \frac{\partial k}{\partial x_i} \right) + P - \varepsilon \quad (5)$$

$$\frac{\partial \varepsilon}{\partial t} + U_i \frac{\partial \varepsilon}{\partial x_i} = \frac{\partial}{\partial x_i} \left(\frac{\nu_t}{\sigma_\varepsilon} \frac{\partial \varepsilon}{\partial x_i} \right) + C_1 \frac{\varepsilon}{k} P - C_2 \frac{\varepsilon^2}{k} \quad (6)$$

where P is the production of turbulence kinetic energy. The values of model constants were $C_\mu = 0.09$, $C_1 = 1.44$, $C_2 = 1.92$, $\sigma_k = 1.0$ and $\sigma_\varepsilon = 1.217$.

The difference between the RNG $k - \varepsilon$ model and the standard $k - \varepsilon$ model is in the values of model constants and the ε -equation has one new extra term. The dissipation equation is now

$$\frac{\partial \varepsilon}{\partial t} + U_i \frac{\partial \varepsilon}{\partial x_i} = \frac{\partial}{\partial x_i} \left(\frac{\nu_t}{\sigma_\varepsilon} \frac{\partial \varepsilon}{\partial x_i} \right) + C_1 \frac{\varepsilon}{k} P - C_2 \frac{\varepsilon^2}{k} - R \quad (7)$$

where extra term R can be calculated from equation

$$R = C_{1RNG} \frac{\varepsilon}{k} P \quad (8)$$

and C_{1RNG} is given through the equation

$$C_{1RNG} = \frac{\eta(1 - \eta/\eta_0)}{(1 + \beta\eta^3)} \quad (9)$$

where

$$\eta = \sqrt{\frac{P}{\nu}} \frac{k}{\varepsilon} \quad (10)$$

The values of model constants were $C_\mu = 0.085$, $C_1 = 1.42$, $C_2 = 1.68$, $\sigma_k = \sigma_\varepsilon = 0.7179$, $\beta = 0.015$ and $\eta_0 = 4.38$.

With the second-moment closures an exact transport equation for the individual Reynolds stresses can be used. These models are able to account for the effects of streamline curvature and swirl-induced body forces. The variant of RSM used in this work is the simplest in terms of the manner in which the redistribution and dissipation processes are modelled. This model proposed by Gibson and Launder [4] consists of the equations

$$\frac{\partial \overline{u_i u_j}}{\partial t} + \underbrace{U_l \frac{\partial \overline{u_i u_j}}{\partial x_l}}_{C_{ij}} = D_{ij} + P_{ij} + \Phi_{ij} - \underbrace{\frac{2}{3} \delta_{ij} \varepsilon}_{\varepsilon_{ij}} \quad (11)$$

in which

$$D_{ij} = \frac{\partial}{\partial x_k} \left(\frac{C_S}{\sigma_{DS}} \overline{u_k u_l} \frac{k}{\varepsilon} \frac{\partial \overline{u_i u_j}}{\partial x_l} \right) \quad (12)$$

models stress diffusion through a generalised tensorial diffusivity,

$$P_{ij} = -\overline{u_i u_l} \frac{\partial U_j}{\partial x_l} - \overline{u_j u_l} \frac{\partial U_i}{\partial x_l} \quad (13)$$

is the stress production and

$$\Phi_{ij} = \Phi_{ij,1} + \Phi_{ij,2} \quad (14)$$

represents pressure-strain interaction, where the first part is expressed

$$\Phi_{ij,1} = -C_{1S} \frac{\varepsilon}{k} (\overline{u_i u_j} - \frac{2}{3} \delta_{ij} k) \quad (15)$$

and the second part as

$$\Phi_{ij,2} = -C_{2S} (P_{ij} - \frac{2}{3} \delta_{ij} P) \quad (16)$$

In this model the dissipation rate ε is governed by

$$\frac{\partial \varepsilon}{\partial t} + U_i \frac{\partial \varepsilon}{\partial x_i} = \frac{\partial}{\partial x_i} \left(\frac{C_S}{\sigma_\varepsilon} \overline{u_i u_j} \frac{k}{\varepsilon} \frac{\partial \varepsilon}{\partial x_i} \right) + C_1 \frac{\varepsilon}{k} \frac{1}{2} P_{II} - C_2 \frac{\varepsilon^2}{k} \quad (17)$$

The values of constants appearing in the above model were $C_1 = 1.44$, $C_2 = 1.92$, $C_S = 0.22$, $C_{1S} = 1.8$, $C_{2S} = 0.6$, $\sigma_{DS} = 1.0$ and $\sigma_\varepsilon = 1.375$.

Rodi has proposed an approximation for the convection and diffusion terms of the transport equation (11) assuming that the transport of $\overline{u_i u_j}$ is proportional to the transport of k which is equal to $P - \varepsilon$ and that the proportionality factor is the ratio $\overline{u_i u_j} / k$ [8]

$$C_{ij} - D_{ij} = \frac{\overline{u_i u_j}}{k} (C_k - D_k) = \frac{\overline{u_i u_j}}{k} (P - \varepsilon) \quad (18)$$

With this approximation an algebraic relationship can be obtained for the components of the Reynolds stress tensor

$$\overline{u_i u_j} = \frac{2}{3} \delta_{ij} k + \frac{(1 - C_{2S})k(P_{ij} - \frac{2}{3} \delta_{ij} P)}{(C_{1S} - 1)\varepsilon + P} \quad (19)$$

where k is solved from the equation

$$\frac{\partial k}{\partial t} + U_i \frac{\partial k}{\partial x_i} = \frac{\partial}{\partial x_i} \left(\frac{C_S}{\sigma_k} \overline{u_i u_j} \frac{k}{\varepsilon} \frac{\partial k}{\partial x_i} \right) + P - \varepsilon \quad (20)$$

The values of constants were the same as were used with the RSM.

Boundary conditions

Impeller: Of prime importance in the modelling is the impeller treatment. The simultaneous calculation of the baffles and the rotating impeller blades requires special treatment. Two different boundary conditions for the impeller were used. One boundary condition alternative of the impeller region used in this study has been to take the impeller on the basis of experimental data as a stationary boundary condition for the remaining computational domain. The other way used was to explicitly calculate the impeller region and then to rotate this section of the grid relative to the rest of the domain.

In the source term model measured values of mean velocity components have been set throughout the volume swept by the impeller blades. All other variables are solved for within that volume as for any other part of the flow.

In the sliding mesh model one part of the calculation grid is at rest while the other part rotates with known angular velocity. The equation system now becomes time-dependent. Blades are modelled as thin, impermeable surfaces. When the calculation grid rotates, also surfaces describing blades rotate. This model does not need any experimental data for the impeller. The model of the impeller blades is shown in Fig. 2.

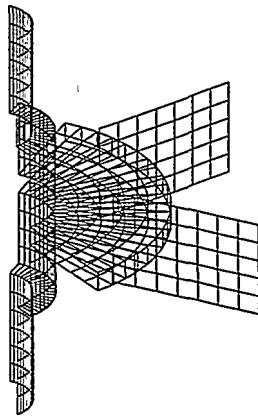


Fig. 2 - Impeller model.

Solid surfaces: No-slip boundary conditions are imposed on all solid surfaces. In order to eliminate the need for a fine mesh in the near-wall regions, the wall functions [7] were used based on a wall shear stress given by

$$\tau_w = \frac{\kappa C_\mu^{1/4} \rho U_p k_p^{1/2}}{\ln(EC_\mu^{1/4} k_p^{1/2} y_p / \nu)} \quad (21)$$

where U_p and k_p are values of U and k at the distance y_p from the wall, respectively, $\kappa = 0.4187$ and $E = 9.793$. Baffles were modelled as thin, impermeable surfaces.

Free surface: The free surface is assumed to be flat. The normal velocity, the tangential stress and the normal fluxes of k and ϵ fall to zero at the surface.

Calculation procedure

The set of governing equations was solved using the CFDS-Flow3d code, version 3.3 [3]. The code is based on the finite volume method and unstaggered grid. A hybrid differencing scheme and bounded modification of the QUICK scheme, the CCCT scheme, were used. In the sliding grid case only the hybrid scheme was available in the version of the calculation code used.

The grid refinement tests were made using a $37 \times 15 \times 28$, $37 \times 30 \times 28$ and $47 \times 36 \times 28$ (x-direction \times r-direction \times θ -direction) non-uniform grid system. The differences between the last two grids were so small that the calculations were made using grid $37 \times 30 \times 28$, shown in Fig. 3. With the sliding grid the total amount of points was the same, but the grid was $58 \times 28 \times 20$ in order to have a more denser grid around the impeller.

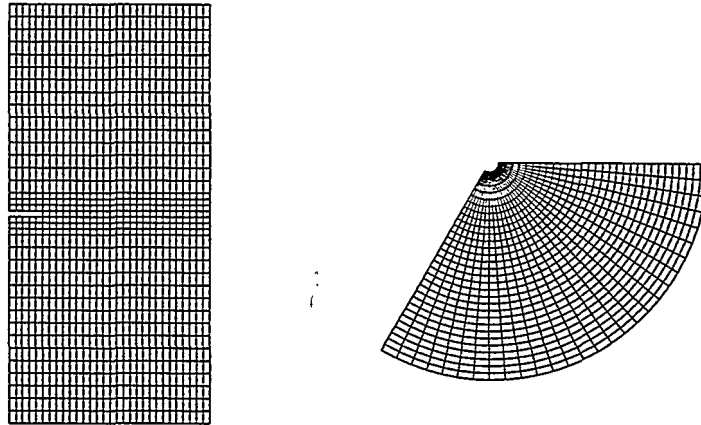


Fig. 3 - Calculation grid size $37 \times 30 \times 28$.

Table I gives a comparison of CPU time required for different models using a DEC 3000-700 AXP workstation. The number of iterations needed for a converged solution was between 8000 – 12000.

Table I CPU time used in calculations

Turbulence model	CPU time [s]/iteration	
	source model	sliding grid model
$k - \epsilon$	7.6	8.5
RNG $k - \epsilon$	7.9	8.7
RSM	59.3	-
ASM	11.4	33.7

RESULTS AND DISCUSSION

The Reynolds number of the measured case was $N_{Re} = (D^2 N / \nu) = 1.1 \cdot 10^5$ (D diameter of impeller, N angular velocity). The results are expressed using nondimensional values defined as

$$X^* = \frac{x}{0.7}, \quad R^* = \frac{r}{0.35}, \quad Z^* = \frac{\theta}{2/3\pi}, \quad U_i^* = \frac{U_i}{W_{tip}} \quad (22)$$

where $W_{tip} = 1.57$ m/s is the tangential velocity at the tip of the impeller. Measured cross-sections are shown in Fig. 4. The numerical results have been detailed by Lahtinen [5].

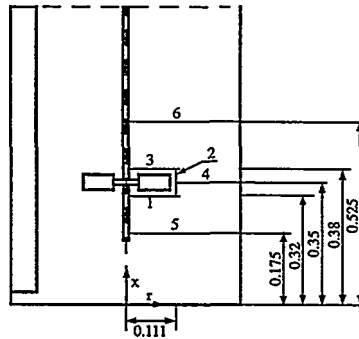


Fig. 4 - Measured cross-sections and their numbers.

Mean velocity profiles in axial, radial and tangential direction using different turbulence models and the source term model for the impeller are shown in Figs. 5-7. There are not very big differences between the results obtained by different turbulence models. But between the measured and calculated values there are some differences. Especially the radial velocity is not predicted very well near the impeller.

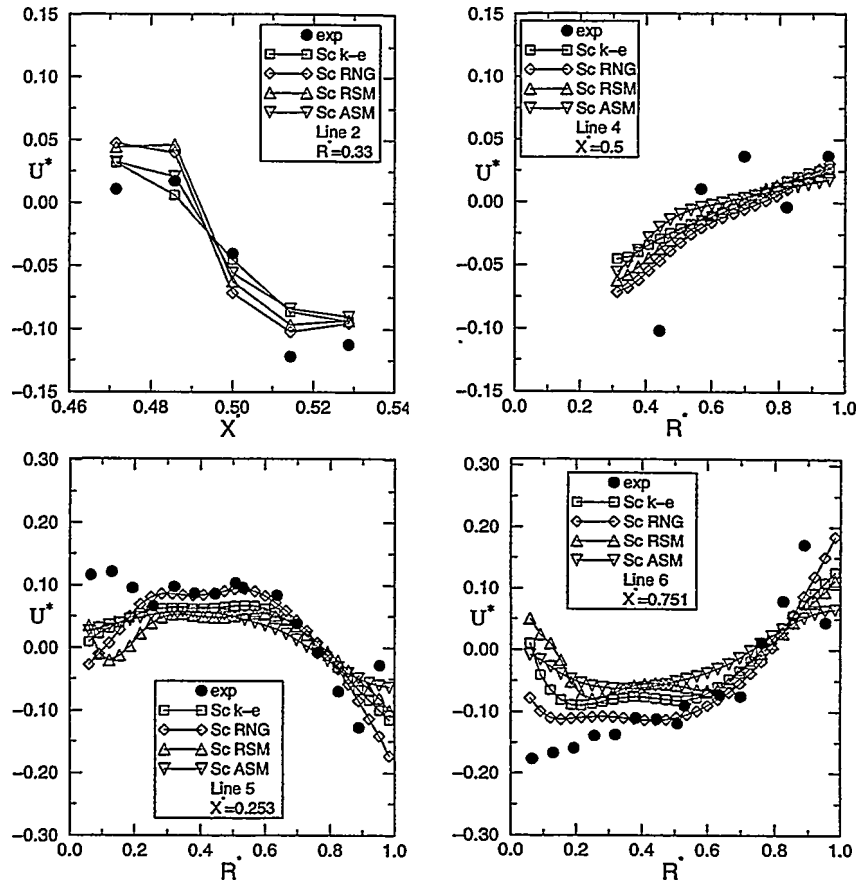


Fig. 5 - Axial velocities obtained by different turbulence models, source term model for impeller, • data [10].

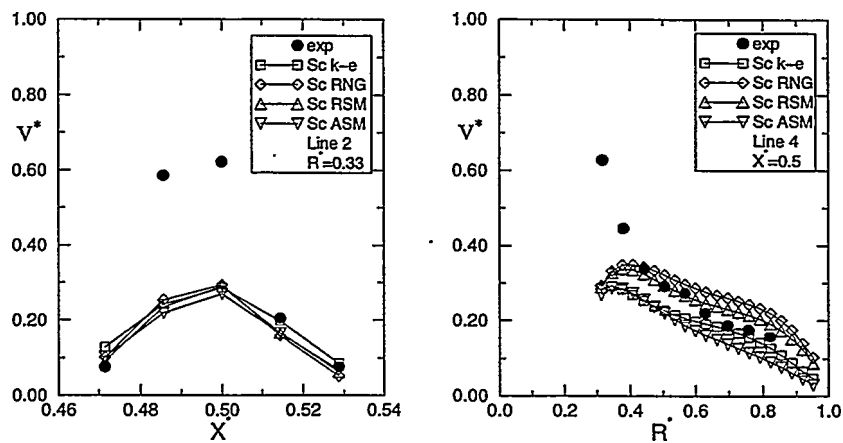


Fig. 6 - Radial velocities obtained by different turbulence models, source term model for impeller, • data [10].

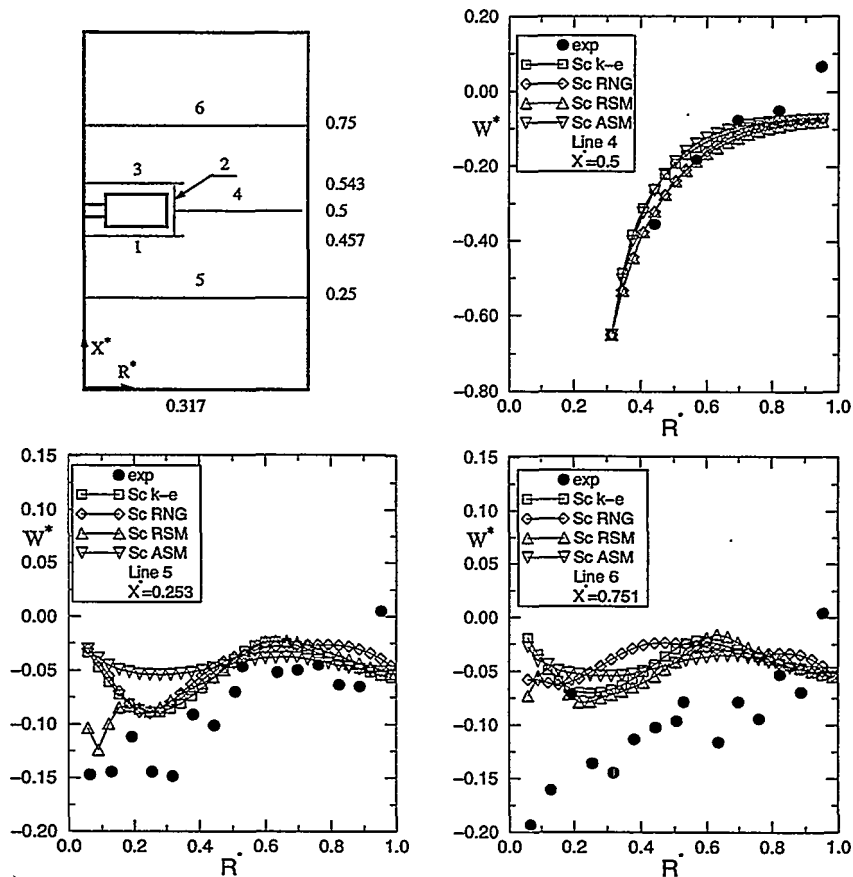


Fig. 7 - Tangential velocities obtained by different turbulence models, source term model for impeller, • data [10].

Mean velocity profiles in axial, radial and tangential direction using different turbulence models and the sliding grid model for the impeller are shown in Figs. 8-10. The RSM did not work with the sliding grid in the version of the calculation code used. There are again very slight differences between the results of the different turbulence models. Agreement with calculated and measured axial velocities is good. Calculated radial velocities are a little higher and tangential velocities a little lower than measured values. Generally the sliding grid model for the impeller can give velocity values near the impeller rather accurately without any measured initial data.

Comparison of velocity profiles obtained by source term (Sc) and sliding grid (Sl) model for the impeller is shown in Fig. 11. The greatest differences are in the values of the radial velocity.

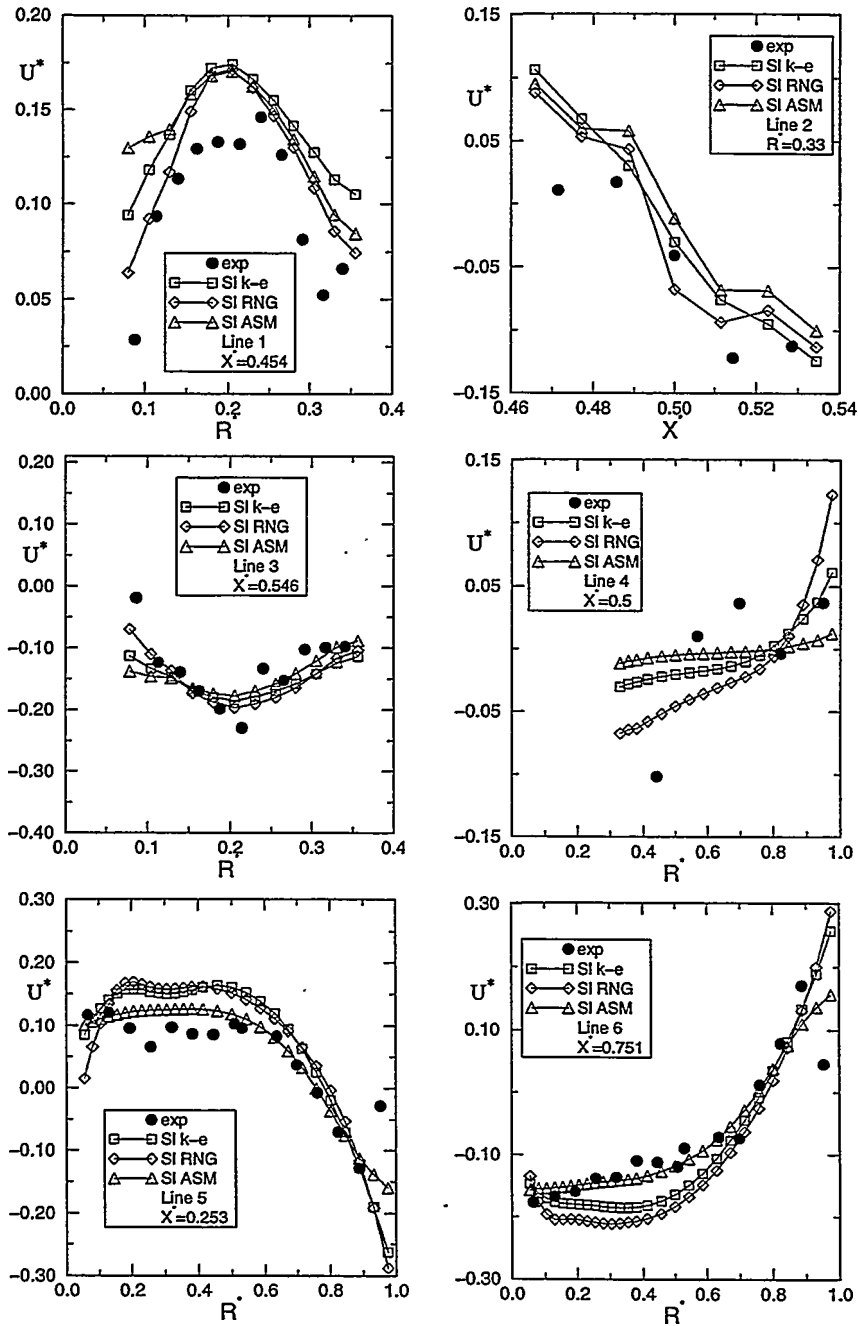


Fig. 8 - Axial velocities obtained by different turbulence models, sliding grid model for impeller, \bullet data [10].

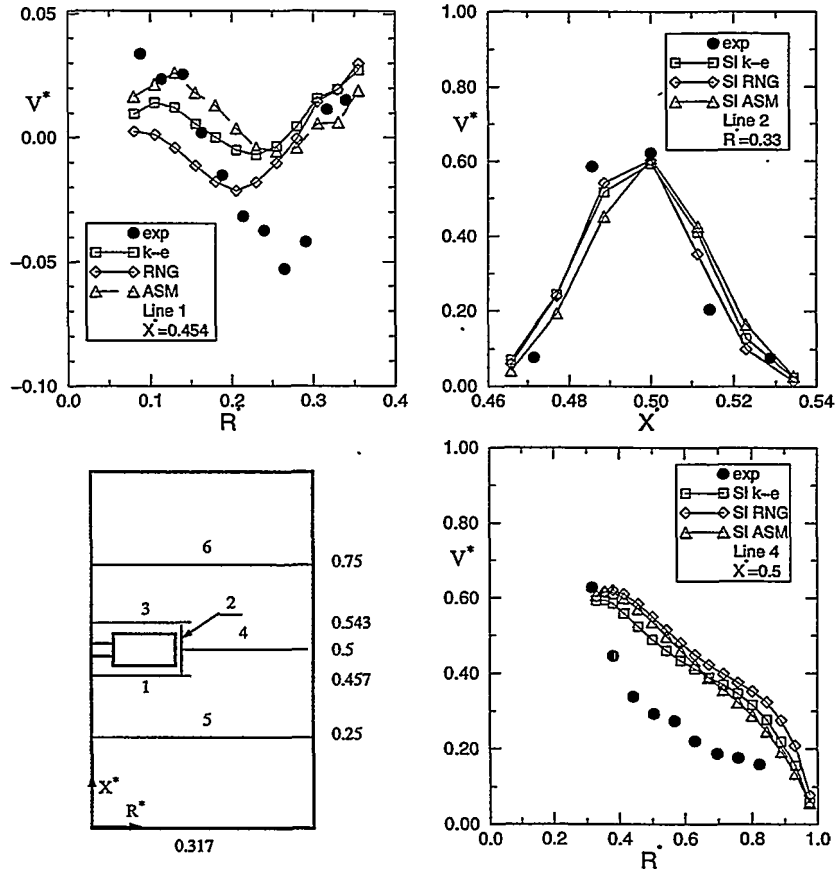


Fig. 9 - Radial velocities obtained by different turbulence models, sliding grid model for impeller, • data [10].

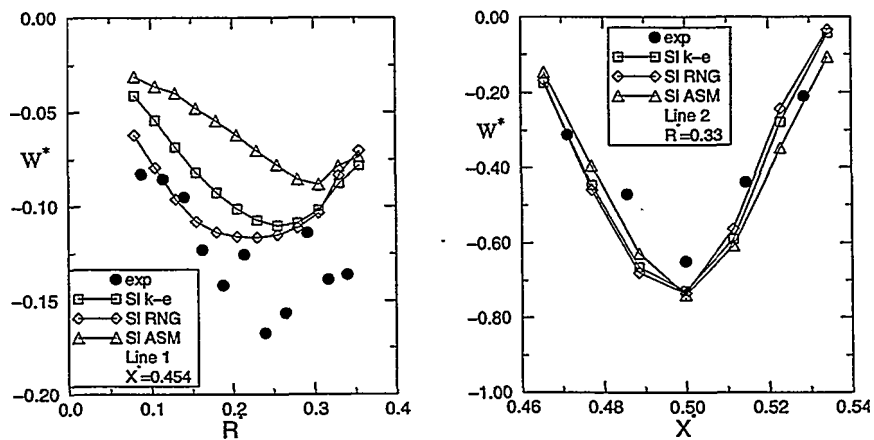


Fig. 10 - Tangential velocities obtained by different turbulence models, sliding grid model for impeller, • data [10].

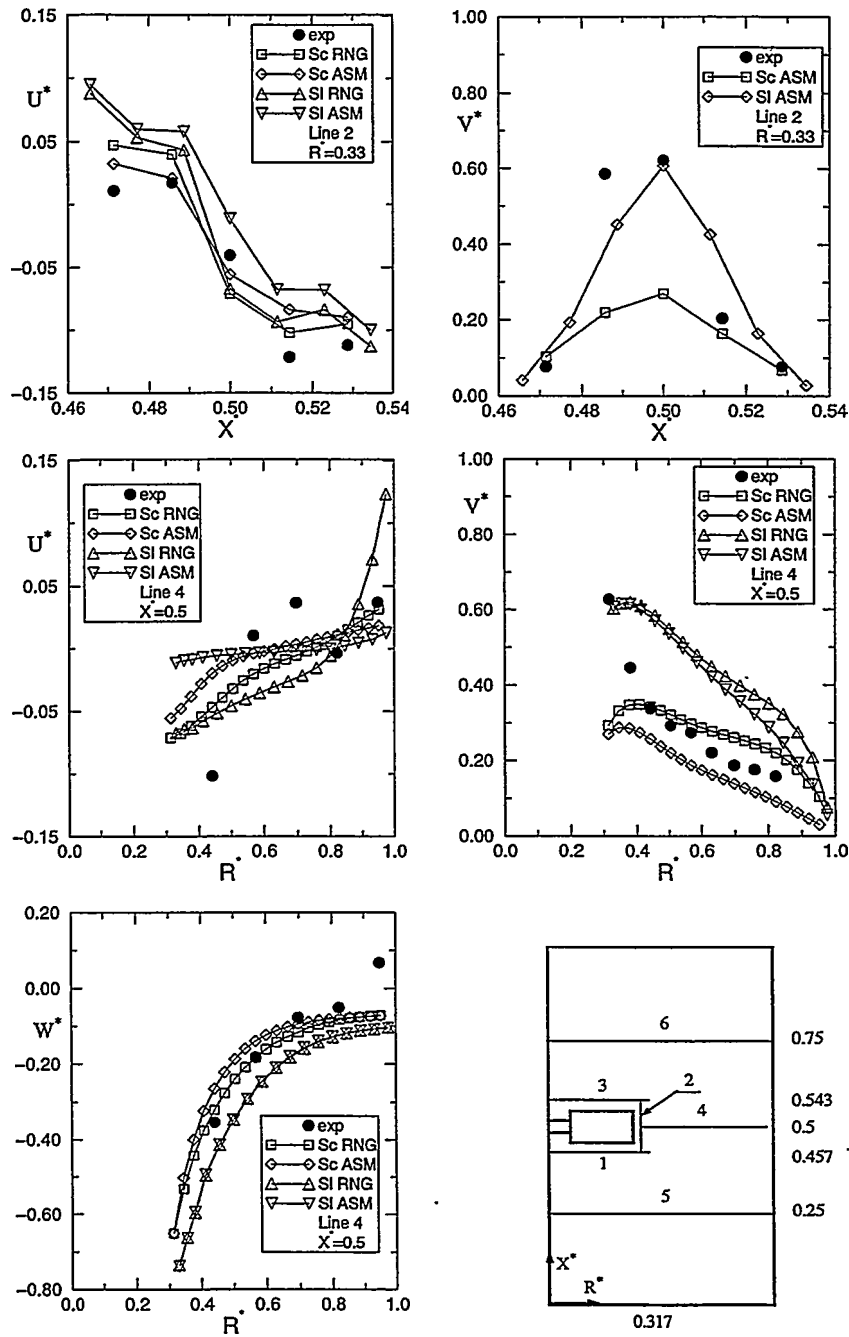


Fig. 11 - Velocity values at cross-sections 2 and 4 obtained by source term (Sc) and sliding grid (SI) model for impeller, • data [10].

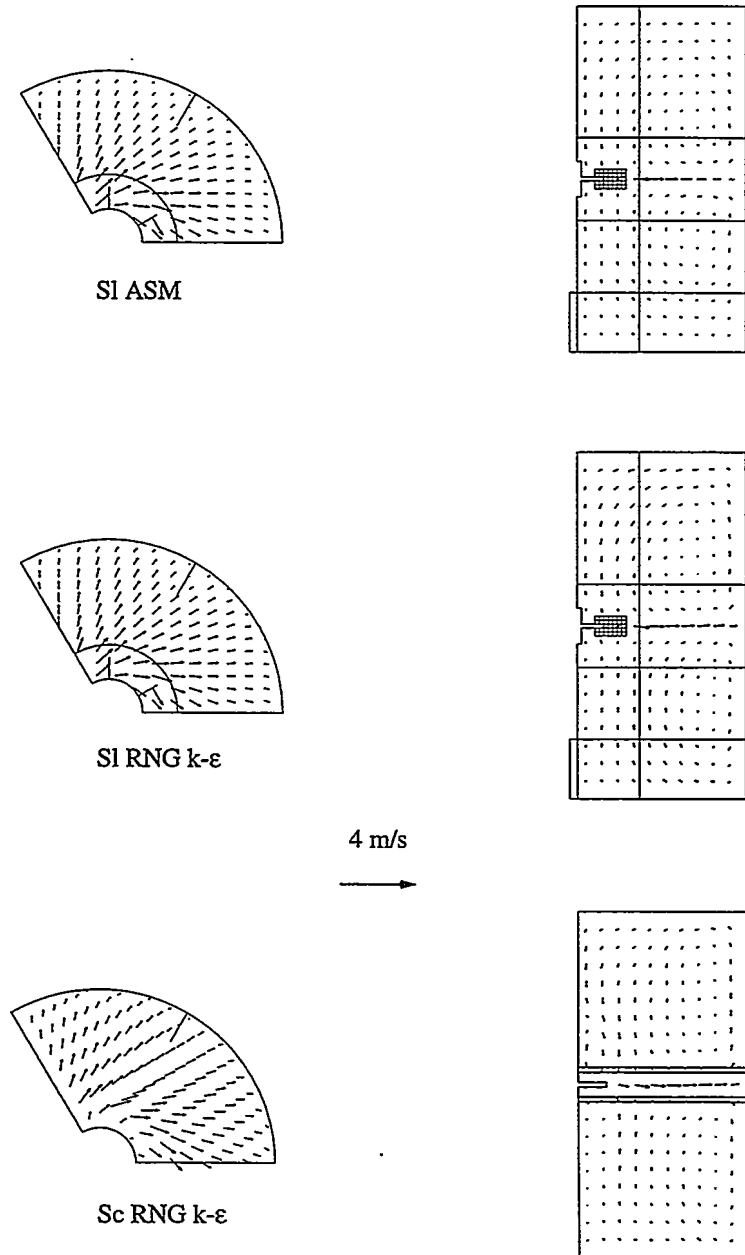


Fig. 12 - Flow pattern. Sliding grid model (SI): RNG $k-\epsilon$ and ASM, source term model (Sc): RNG $k-\epsilon$, planes $Z^* = 0.75$ and $X^* = 0.5$.

The flow pattern in the tank is shown in Fig. 12. The presented flow fields have been calculated using the source term model with the RNG $k - \varepsilon$ turbulence model and the sliding grid model with the RNG $k - \varepsilon$ model and ASM. In the plane $Z^* = 0.75$, 30° from the baffle, the size of the upper and lower ring vortices and the position of their centres can be seen changing according to the different models. In the plane $X^* = 0.5$ the flow fields look nearly the same.

With RSM and ASM calculated normal Reynolds stress components were compared to measured values. All these models produced lower values for normal stresses:

CONCLUSIONS

Numerical calculations of the complex fluid flow field in a baffled mechanically stirred tank were performed using the $k - \varepsilon$, RNG $k - \varepsilon$, ASM and RSM turbulence models. The six-blade Rushton turbine was modelled using source terms obtained from measured data or using the sliding grid technique.

The realistic description of the impeller region using the sliding grid model produced acceptable agreement with experimental data. The amount of available experimental data was too small for reliable comparison between the results of turbulence models used.

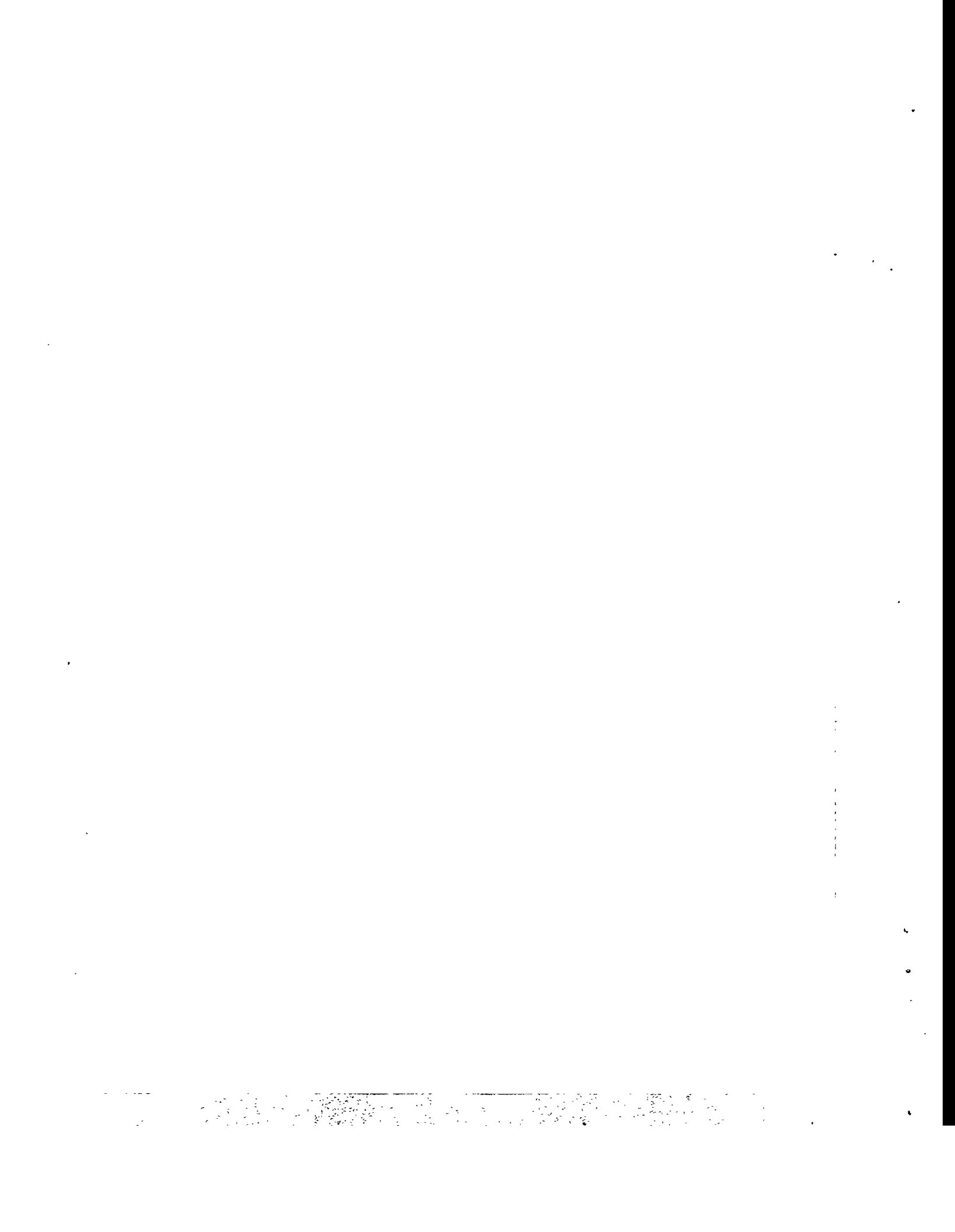
Acknowledgements - Financial support from TEKES Technology Development Centre is gratefully acknowledged.

REFERENCES

1. Bakker, A. and van der Akker, H. E. A., Single-phase flow in stirred reactors, *Trans IChemE*, 72 Part A (1994), 583-593.
2. Brucato, A., Ciofalo, M., Grisafi, F. and Rizzuti, L., Computer simulation of turbulent fluid flow in baffled and unbaffled tanks stirred by radial impellers, *Computer applications to batch processes*, Cengio, Italy, 1990.
3. Computational Fluid Dynamics Services, CFDS-Flow3d user guide, Harwell Laboratory, Oxfordshire OX11 0RA, United Kingdom, 1994.
4. Gibson, M. M. and Launder, B. E., Ground effects on pressure fluctuations in the atmospheric boundary layer, *J. Fluid Mech.*, 86 (1978), 491-511.
5. Lahtinen, M., Sekoittimen virtauskentän numeerinen laskenta (Numerical calculation of flow field of stirred tank), MSc thesis, Tampere University of Technology, 1996.

6. Launder, B. E. and Spalding, D. B., Mathematical models of turbulence, Academic Press, 1972.
7. Launder, B. E. and Spalding, D. B., The numerical computation of turbulent flows, *Computer Meth. in Appl. Mech. and Eng.*, 3 (1974), 269-289.
8. Rodi, W., A new algebraic relation for calculating the Reynolds stresses, *Z. Angew. Math. Mech.*, 56 (1976), 219-221.
9. Takeda, H., Narasaki, K., Kitajima, H., Sudoh, S., Onofusa, M. and Iguchi, S., Numerical simulation of mixing flows in agitated vessels with impellers and baffles, *Computers Fluids*, 22 (1993), 223-228.
10. Vienola, S., Sekoitinsäiliön virtauskentän mittaukset (Measurements of the flow field of stirred tank), Tampere University of Technology, Thermal Engineering, Internal Report, 1994.

For Your Notes



TURBULENT METHANE COMBUSTION IN A LABORATORY-SCALE FURNACE

Antti Oksanen, Erkki Mäki-Mantila
Tampere University of Technology
Energy and Process Engineering
P.O.Box 589, SF-33101 Tampere, Finland

Abstract

Methane combustion in the 400 rotational symmetric test chamber by *ENEL* was investigated. The prediction of the reaction rates of methane and carbon monoxide was based on the models which are taking into consideration the effect of turbulence on the oxidation phenomena namely the eddy dissipation concept model (*EDC*) (Gran et al. 1994, Lilleheie et al. 1991, Magnussen 1981, 1989) and the eddy dissipation model (*EDM*) (Magnussen et al. 1976, 1978). The experimental results of the distributions of the different species concentrations, temperature, velocities, turbulence quantities etc. were measured in the chamber cross-sections. The formation of nitric oxide was modelled using the thermal- and prompt-*NO* formation mechanisms and the formulation was based on the chemical kinetics and the probability density function (pdf) with the β - and δ -distributions. If more than one variable is taken into consideration in the use of pdf it is very difficult to find distribution for different variables and especially to solve them with the moderate amount of the computing time. Therefore, in this paper the amount of the pdf variables was limited as small as possible i.e. only one variable namely the mixture fraction f was used the variance of which was solved from the transport equation. The computational domain which was divided into about seven thousand cells includes areas where the mean values of the variables can be supposed to be known and where the distribution of the probability is very narrow. Because in every computational cell the probability distribution as accurate as possible is wanted the linearization of the integration was made. The effect of the local extinction on the reaction rates was also included in the paper. It was supposed the extinction is happening when the smallest time scale namely the so-called Kolmogorov time scale $\tau_k = \sqrt{\nu/\varepsilon}$ multiplied by the factor ξ less than unity is smaller than the time scale of chemistry τ_c . The factor ξ takes into consideration the proportion of the reacting fine structure. The time scale $\tau_c = \tau_c(T, \varphi)$ where φ is the equivalence ratio was calculated using the values and diagram proposed by Gran et al. (1994).
Keywords: Turbulent Reactions, Pdf, Low-NOx Burning, Methane, Modelling

INTRODUCTION

The combustion efficiency and the minimizing of the pollutant formation, especially nitrogen oxides, are the most important factors to be taken into account in the burner and furnace design about which the former one affects much the flame structure, the burning efficiency, the heat transfer distributions and naturally the formation of the different species concentrations, respectively. Therefore, the investigation of the burner design affects strongly the formation of emissions.

When the flow field is calculated the choice of the turbulence model plays an important role especially if the swirling flow is in question. There are several turbulence models to be able to use when turbulent reacting flows are calculated. However, in many practical combustion cases the standard two equation $k-\varepsilon$ model is one of the most often used to predict turbulence quantities because of its quite easy and successful use in the numerical modelling. However, certain limitations of the $k-\varepsilon$ model has to remember, namely it cannot take well enough into account the effect of the flow rotation and turbulence isotropy. In spite of these limitations the $k-\varepsilon$ model gives good possibilities to predict flow fields and the distributions of temperature and different species concentrations in many combustion applications.

The interaction between turbulence and chemical reactions is very important phenomena when turbulent reacting flows are calculated. In actual practice hydrocarbon flames include several intermediate reactions about which only a small part is able to take into consideration in the computations. Therefore, instead of the use of detailed chemistry in the modelling due to the required huge computing time it is argued to use in general the simplified reduced global reaction schemes. In this paper the two principal reactions i.e. the oxidation of methane and carbon monoxide are taken into account with the two-step reaction scheme.

In this paper the interaction between turbulence and chemical reactions is included applying the probability density function (pdf) into the nitric oxide formation. The reaction rates of methane and carbon monoxide were calculated using the eddy dissipation model and the eddy dissipation concept model, respectively. As it is known turbulence has the statistical structure and, therefore, it is natural to take more completely into consideration the effect of turbulence on the reactive flow modelling. The computations can be made using a wide range of the assumed forms of the pdf i.e. the β - and δ -functions and the distributions of both Gaussians and clipped Gaussians together with the experimental data for the conserved scalar field and for the mean composition. In this study the β - and δ -functions have been used in order to take into consideration the effect of turbulence fluctuation on the nitric oxide formation.

BASIC THEORY

In the steady state flow conditions the general form of the transport equation of the different variables to be solved can be written as follows

$$\frac{\partial}{\partial x_i} \left(\bar{\rho} \mu_i \tilde{\phi} - \Gamma_\phi \frac{\partial \tilde{\phi}}{\partial x_i} \right) = \bar{S}_\phi + \bar{S}_\phi^* \quad (1)$$

where Γ_ϕ is the effective diffusion coefficient and $\tilde{\phi}$ is the general transport variable, respectively. \bar{S}_ϕ and \bar{S}_ϕ^* are the source terms without and with the chemical reactions. Γ_ϕ can be predicted from the common used relation μ_{eff}/σ_ϕ . The effective dynamic viscosity μ_{eff} is the sum of laminar and turbulent viscosities

$$\mu_{eff} = \mu_l + \mu_t = \mu_l + C_\mu \bar{\rho} \left(\frac{\tilde{k}^2}{\tilde{\varepsilon}} \right) \quad (2)$$

where $\mu_l = \mu_l(\tilde{T}, \tilde{Y}_i)$ and $C_\mu = 0.09$. The density and the mean molecular weight of the gas mixture was calculated using the equations

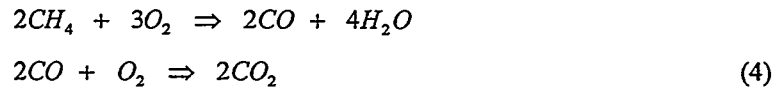
$$\bar{\rho} = \bar{p} \hat{M} / (R \tilde{T}); \quad \hat{M} = \left(\sum_i \tilde{Y}_i / M_i \right)^{-1} \quad (3)$$

where $R = 8.314 \text{ kJ}/(\text{kmolK})$. \bar{p} , \tilde{Y}_i and M_i stand for the cell pressure, the mass fractions and the molecular weights of the different species concentrations, respectively.

COMBUSTION MODELLING

Reaction Mechanism

A two-step reaction mechanism for methane combustion was used. It was based on the following two equations, namely



The reaction for methane oxidation is very fast compared with the corresponding of carbon monoxide in Eq. (4). Therefore, it is important to model the combustion of

methane at least by these two steps. Because turbulence is in actual practice the limiting factor in order to control the combustion intensity the reactions covered by chemical kinetics and turbulence have to be taken into consideration.

Reaction Rates in Kinetically Controlled Regimes

In the laminar reactive flow cases the combustion phenomena are mainly governed by chemical kinetics only. But also in the real turbulent reactive flows there are zones where chemical kinetics may be dominating. Therefore, it is also taken into consideration when the effective reaction rates are predicted. The following reaction rates for methane CH_4 and carbon monoxide CO are used (Flagan and Seinfeld, 1988)

$$\bar{R}_{CH_4} = 1.15 \times 10^9 e^{-24444K/\bar{T}} \bar{\rho} \bar{Y}_{CH_4}^{-0.3} \bar{Y}_{O_2}^{1.3} \quad (kg / s / m^3) \quad (R1)$$

$$\bar{R}_{CO} = 5.42 \times 10^9 e^{-15152K/\bar{T}} \bar{\rho}^{-1.75} \bar{Y}_{CO}^{0.25} \bar{Y}_{O_2}^{0.5} \bar{Y}_{H_2O}^{0.5} \quad (kg / s / m^3) \quad (R2)$$

Reaction Rates in Mixing Controlled Regimes

When the time scale of turbulence is larger than the corresponding value of the chemical kinetics the reaction rates were calculated by using the so-called eddy dissipation model (*EDM*) proposed by Magnussen and Hjertager (1976). They presented a modified expression for the fuel consumption rate, which is proportional to the average values to the species mass fractions and to the inverse value of the turbulent time scale as follows

$$\bar{R}_{EDM} = C_R \bar{\rho} \left(\frac{\bar{\varepsilon}}{\bar{k}} \right) \min \left\{ \bar{Y}_f, \frac{\bar{Y}_{O_2}}{i} \right\} \quad (R3)$$

where the coefficient C_R is equal to 4.0. The subscript f in Eq. (R3) stands both CH_4 and CO , respectively. The reaction rate (R3) is based much on the eddy breakup model first proposed by Spalding (1971). The another model which takes quite well into account the effect of turbulence on the reaction rates is the eddy dissipation concept model (*EDC*) proposed by Magnussen et al. (1978), Magnussen (1981, 1989) and Lilleheie et al. (1991). In this model the reaction space is divided into two different volumes namely into the perfectly stirred reactor called the reacting fine structure and into the surrounding, respectively. Thus, the reaction rate has the form

$$\bar{R}_{EDC} = \frac{\eta \chi \bar{\rho} \bar{m}^*}{1 - \chi \gamma^*} (Y_i^* - \bar{Y}_i) \quad (R4)$$

where the superscript * means conditions in the fine structure.

Local Extinction

The effect of the local extinction on the reaction rates was included in this paper together with the EDC model. If the Kolmogorov time scale $\tau_k = (\nu/\varepsilon)^{0.5}$ multiplied by a factor ξ is less than the time scale of chemical kinetics $\tau_c = \tau_c(T, \varphi)$ (Gran et al., 1994) the local extinction is happening. Thus, the reaction rate is equal to zero in Eq. (1). The coefficient ξ was equal to 0.4 or it was calculated from the equation $(1 - \chi\gamma^*)/\eta$. The reacting fine structure will consequently catch up reactants at a higher rate expressed by the factor η .

NITRIC OXIDE FORMATION

Thermal-NO

For the slow reactions such as for the oxidation of carbon monoxide and also for the formation of nitrogen oxides the fast reaction models are not applicable. Therefore, the extended Zeldovich mechanism based on the chemical kinetics can be applied in order to model the formation of nitric oxide *NO* from the molecular nitrogen N_2 in the combustion air



The global formation and reduction rates of the nitric oxide are (Flagan and Seinfeld 1988; Westbrook and Dryer, 1981)

$$\bar{R}_{NO,th}^+ = 1.35 \times 10^{16} \bar{T}^{-1} e^{-69160K/\bar{T}} \bar{\rho} \bar{Y}_{N_2} \bar{Y}_{O_2}^{0.5} \quad (kg/s/m^3) \quad (R5)$$

$$\bar{R}_{NO,th}^- = 7.45 \times 10^{14} \bar{T}^{-1} e^{-47355K/\bar{T}} \bar{\rho} \bar{Y}_{NO}^2 \bar{Y}_{O_2}^{-0.5} \quad (kg/s/m^3) \quad (R6)$$

Prompt-NO

The so-called prompt-*NO* formation mechanism proposed firstly by C.P. Fenimore (1971) describes the formation of nitric oxide in the near burner zones rich with hydrocarbons and the reaction mechanism has the form



Thus the global formation rate is, respectively, in the form (de Soete, 1974)

$$\bar{R}_{NO,pr}^+ = 2.2 \times 10^7 e^{-30200K/T} \bar{\rho} \bar{Y}_{N_2} \bar{Y}_{CH_4} \bar{Y}_{O_2}^b \quad (kg / s / m^3) \quad (R7)$$

where b is equal to 1 when \bar{Y}_{O_2} is less than 2500 ppm and it goes linearly to the value equal to zero when \bar{Y}_{O_2} reaches the value equal to 18000 ppm, respectively.

PDF MODELLING

The $k-\varepsilon$ turbulence model introduces the calculation only for velocity field and pressure. If it is wanted to take into account the turbulence effect on the reacting flow field more completely the problem becomes also more complex due to the continuous fluctuations of density, velocity, temperature, pressure and species concentrations. The covering equations take a very complicated unclosed form. Thus special formulation and closure methods are needed. During recent years the use of probability density function has become quite popular in the study of turbulent flames.

It can be described with the pdf such that the local value of the variable ϕ is between ϕ and $\phi+d\phi$ for a relative time $p(\phi)d\phi$. Thus the time mean value of the variable ϕ is

$$\bar{\phi} = \int_{-\infty}^{+\infty} \phi p(\phi) d\phi \quad (7)$$

Equation (7) is dependent on the place and the variable ϕ . The pdf can be formulated also by using the function based on the averaging of time or density, respectively.

When more than one variable is used in order to formulate with the pdf the mean value of the reaction rate the form of Eq. (8) has to be used

$$\bar{\omega}_i = \int_0^1 \int_0^1 \dots \int_0^\infty \omega_i p(\bar{\rho}, \bar{T}, \bar{Y}_1, \dots, \bar{Y}_N) d\rho dT dY_1 \dots dY_N \quad (8)$$

In the numerical calculations this kind of formula (8) is impossible to use in the practical applications because of the required huge computing time. Therefore, it is more reasonable and mostly accurate enough to use only one variable. When the chemical reactions are fast compared due to the time scale of the mixing the mean reaction rate of fuel and other reactive species are limited by the mixing, the process of which can be described simply by one equation: *fuel+burning air = product*. In this

case the reactive system can be modelled with the use of one parameter, namely with the mixture fraction f when the pdf depends only on f . It can be presented by the following equation (Bilger, 1980)

$$f = \frac{Z - Z_2}{Z_1 - Z_2}; \quad Z = \bar{Y}_f - \bar{Y}_{O_2} / i_f \quad (9)$$

The subscripts 1 and 2 refer to two feeds of Z which is a Shvab-Zeldovich function and it can be formed by using temperature or species concentrations, respectively. It can be seen that Z is equal to 1 in feed 1 and 0 in feed 2. When the mixture fraction f is used equation (8) can be written in the form

$$\bar{\omega}_i = \int_0^1 \omega_i(f) p(f) df \quad (10)$$

Probability Distribution

The probability distribution can be formed by using the Gaussian or β -distributions or the Joint function of these two ones. In this study the β -distribution is used and it's probability can be presented by equation (Abramowitz and Stegun, 1964)

$$p_\beta(f) = \frac{f^{a-1}(1-f)^{b-1}}{\int_0^1 f^{a-1}(1-f)^{b-1} df} \quad (11)$$

In the β -function there are two parameters a and b which depend on the flow situation and they are also functions of time and place and have a relation to the mean value \bar{f} and it's variance $\overline{f'^2}$ as follows

$$\bar{f} = \frac{a}{a+b}; \quad \overline{f'^2} = \frac{ab}{(a+b)^2(a+b+1)} \quad (12)$$

The parameters a and b can be defined from the equation (12) as follows

$$a = \bar{f} \left[\frac{\bar{f}(1-\bar{f})}{\overline{f'^2}} - 1 \right]; \quad b = (1-\bar{f}) \left[\frac{\bar{f}(1-\bar{f})}{\overline{f'^2}} - 1 \right] \quad (13)$$

In this paper pdf is applied to the formation of nitric oxide using the mixture fraction f as the probability parameter, the variance of the mixture fraction was solved and besides the β -distribution also the δ -distribution was used.

$$p_{\delta}(f) = \begin{cases} 1, & f = \bar{f} \\ 0, & f \neq \bar{f} \end{cases} \quad (14)$$

Thus when the probability distribution is very narrow the use of the δ -distribution makes it possible to model pdf without any integration and to save the computing time.

TEST CASES AND RESULTS

Test Furnace

The combustion measurements and calculations were made using the 400 kW rotational symmetric laboratory-scale test furnace (*ENEL*), Fig. 1. In this case the concentrations of nitric oxide, oxygen, methane, carbon monoxide, carbon dioxide, the velocity and turbulence values and the temperature distribution in five chamber cross-sections were measured. The full experimental data and computations are reported by Garretton and Simonin (1994).

Test Cases

In this paper the effect of three different kind of turbulence models (the standard k - ϵ , the renormalized k - ϵ and the multi-time-step k - ϵ models), two reaction rates based on the turbulent mixing, the local extinction and the probability density function on nitric oxide formation was calculated. In table I the test cases used in the computations are presented.

Table I. Explanation of test cases.

Case	Reaction Model	Turbulence Model	Extinction	PDF for NO Formation
[1]	EDM+Chem.Kin.	Stand. k - ϵ	Without	No
[2]	- " -	RNG k - ϵ	- " -	- " -
[3]	- " -	ChenKim k - ϵ	- " -	- " -
[4]	EDC+Chem.Kin.	Stand. k - ϵ	With	- " -
[5]	- " -	RNG k - ϵ	- " -	- " -
[6]	- " -	ChenKim k - ϵ	- " -	- " -
[7]	- " -	Stand. k - ϵ	- " -	Yes

Results of Computation

In figure 2 the nitric oxide and temperature distributions are presented when the comparison between the *EDM* and *EDC* models without and with the use of pdf and the local extinction, respectively. The calculated values in the cross-section $z/L = 0.28$ are quite the same with the experimental ones. Because the turbulence models have the great effect on the turbulent reaction rates the comparison between two model constant C_1 was made and the calculated values of nitric oxide, temperature and turbulence kinetic energy can be seen in figure 3. The corresponding comparison of the six cases 1-6 are presented in figure 4, respectively. It can be observed the *EDC* model gives better values than the *EDM* model especially in the near burner zones. In figures 1-4 it can also be seen the great effect of the local extinction on the distributions of temperature and nitric oxide. The distributions of the other species concentrations and the variables together with the results of twelve european teams are presented in the proceeding by Garreton and Simonin (1994). In figures 5 and 6 the effect of the local extinction on the distributions on temperature and nitric oxide can be seen when more accurate time scale of chemistry was used than in the case of figure 2, respectively. In figure 7 the comparison between three different pdf models was used. The Reynolds analogy was used at the first stage of the pdf computations and it can be noticed the values of nitric oxide are quite same than without any pdf and also near the experimental data. On the other hand, the conditions for the use of β - or δ -functions are presented in Fig. 8, respectively.

CONCLUSIONS

The principal aim of the study was to examine the effect of different reaction and turbulence models, the local extinction and the pdf with the β - and δ - functions on the formation of nitric oxide. The values of the nitric oxide concentrations in the cross-sections of the 400 kW test chamber were quite near the experimental data especially in the near burner zones. On the other hand, the use of the *EDC* model gave better results than *EDM*. The reaction rates based only on the mixing effect gave in the near burner zone ($z/L = 0.28$) temperature peaks because of the too high burning intensity. In that case the use of the local extinction gives much more better values than without it, respectively. It can be also observed very clearly the effect of different turbulence models on the distributions of temperature and nitric oxide. They have same kind effect also on the other species concentrations. The use of two different probability distributions (β - and δ -) gave results near the experimental data.

REFERENCES

1. Abramowitz, M.; Stegun, I.A. (1964). Handbook of Mathematical Functions, National Bureau of Standards, Applied Series 55.
2. Bilger, R.W. (1980). Turbulent Flows with Non-Premixed Reactants, Chap 3, pp. 65-114, Turbulent Reactive Flows, Ed. by P.A. Libby and F.A. Williams, Topics in Applied Physics, Springer-Verlag, New York.
3. Fenimore, C.P. (1971). *13th Symp. (Int.) on Combust.*, The Combustion Institute, pp. 373-380.
4. Flagan, R.C.; Seinfeld, J.H. (1988). Fundamentals of Air Pollution Engineering, Prentice-Hall Inc., New Jersey, USA, 542 p.
5. Garreton, D.; Simonin, O. (1994). *Final Results*. 1st ASCF Workshop, ERCOFTAC, Chatou, France.
6. Gran, I.R.; Melaaen, M.C.; Magnussen, B.F. (1994). Numerical Simulation of Local Extinction Effects in Turbulent Combustor Flows of Methane and Air. The 25th Int. Symp. on Combust. The Combustion Institute.
7. Lilleheie, N.I.; Bryggstøl, S.; Magnussen B.F.; Kilpinen, P.; Hupa, M.; Glarborg, P. (1991). *Nordic Gas Centre*. ISBN 87-89309-50-2.
8. Magnussen, B.F.; Hjertager, B.H. (1976). *16th Symp (Int.) on Combust.*, The Combustion Institute, pp. 719-729.
9. Magnussen, B.F.; Hjertager, B.H.; Olsen, J.G.; Bhaduri, D. (1978). *17th Symp. (Int.) on Combust.*, The Combustion Institute, pp. 1383-1391.
10. Magnussen, B.F. (1981). *AIAA 19th Aerospace Sci. Meeting*, Jan 12-15, 6 p.
11. Magnussen, B.F. (1989). *1st Topic Oriented Techn. Meeting (TOTeM)*, IFRF, 20 p.
12. de Soete, G.G. (1974). *15th Symp. (Int.) on Combust.*, The Combustion Institute, pp.1093-1102.
13. Spalding, D.B. (1971). *13th Symp. (Int.) on Combust.*, The Combustion Institute, pp.649-657.
14. Westbrook, C.K.; Dryer, F.L. (1981). *Comb. Sci. and Techn.*, Vol. 27, pp. 31-43.

NOMENCLATURE

a	parameter in β -distribution	v	radial velocity
b	parameter in β -distribution	w	tangential velocity
C	coefficient	x	axial coordinate
f	mixture fraction	Y	mass fraction
i	stoichiometric ratio	Γ	diffusion coefficient
k	turbulent kinetic energy	β	probability
M	molecular weight	δ	probability
p	pressure, pdf	ε	dissipation of k
r	radial coordinate, reaction rate	μ	dynamic viscosity
R	universal gas constant, reaction rate	ρ	density
S	source term	σ	Prandtl number
T	temperature	ϕ	general transport variable
u	axial velocity	τ	time scale

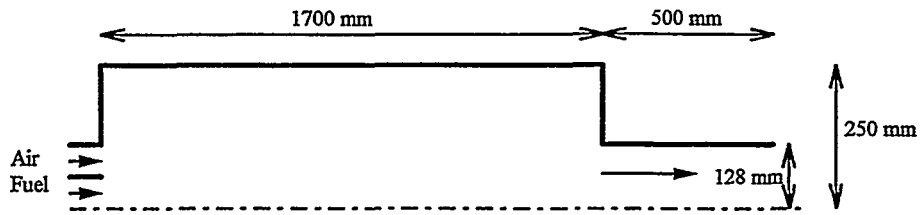


Fig. 1 – Scheme of 400 kW laboratory-scale test furnace (ENEL).

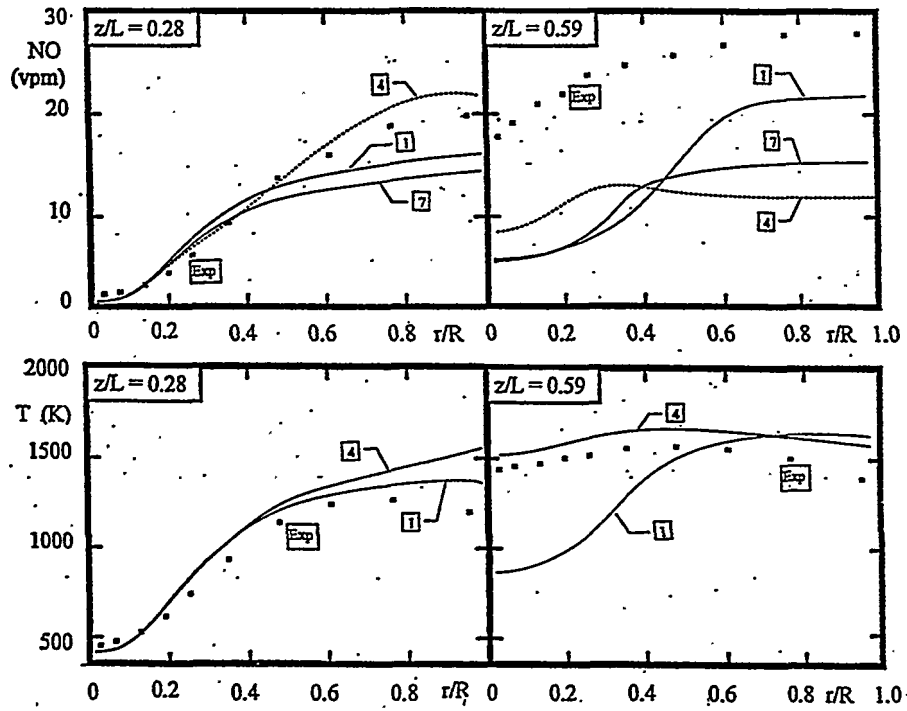


Fig. 2 – Nitric oxide and temperature distributions of three different cases in two cross-sections.

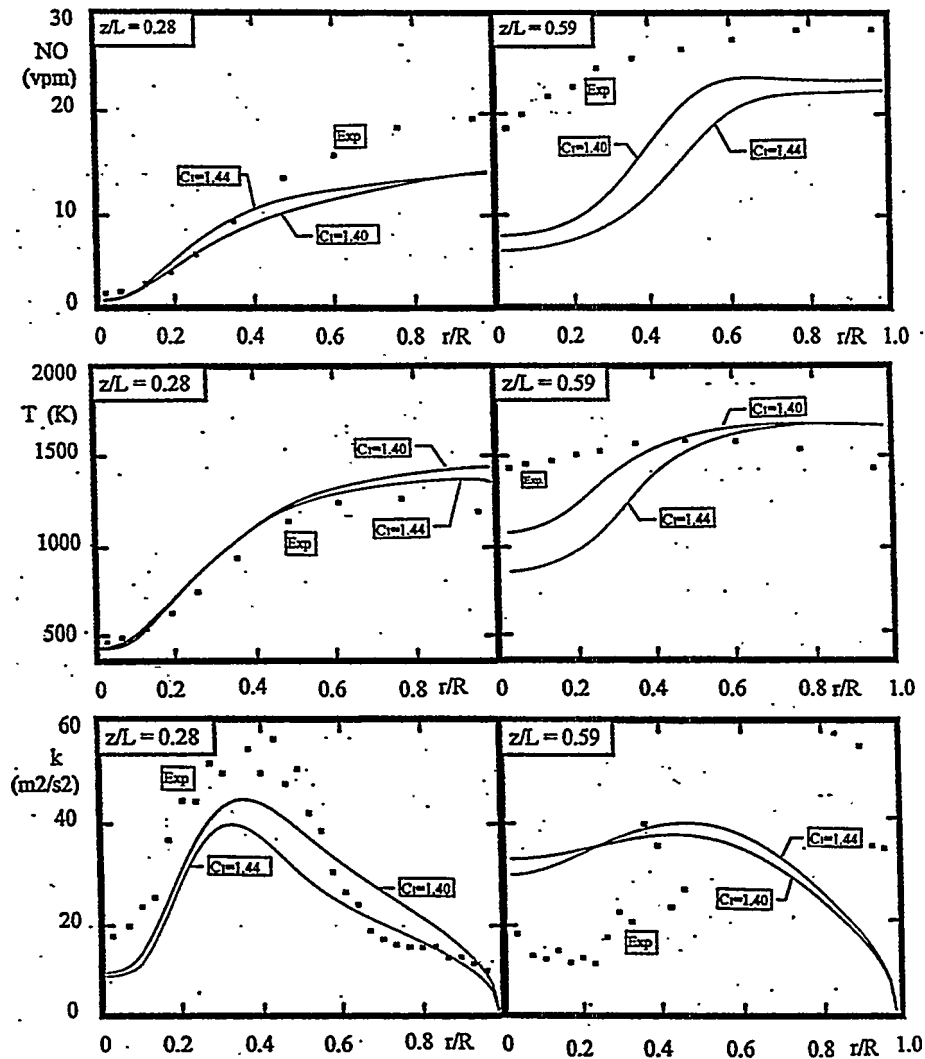


Fig. 3 – Distributions of nitric oxide, temperature and turbulence kinetic energy in two cross-sections when $k-\varepsilon$ turbulence model constant C_1 was changed.

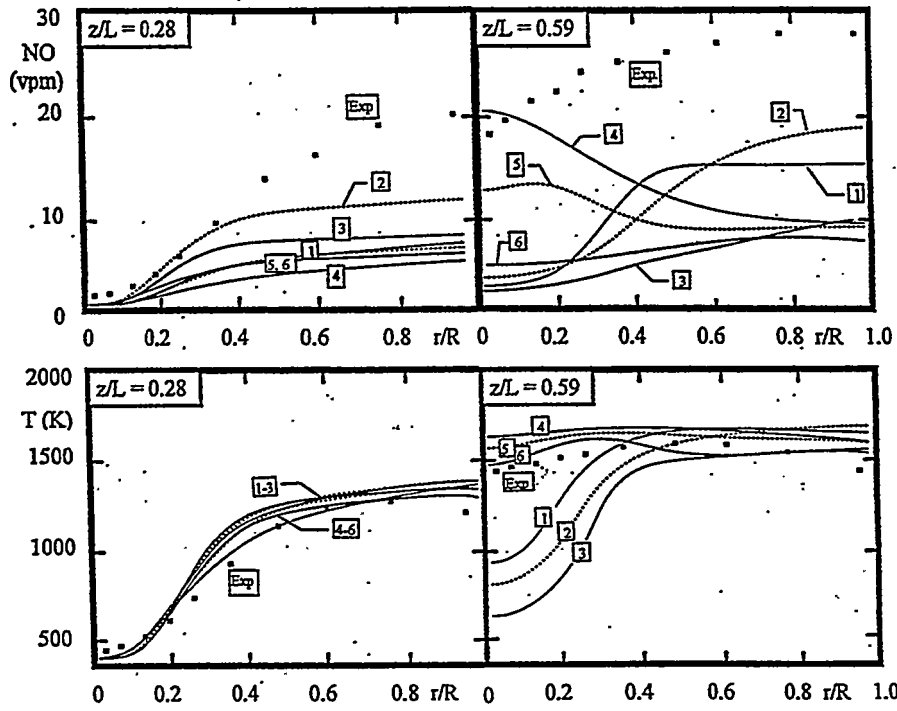


Fig. 4 – Nitric oxide and temperature distributions of six different cases in two cross-sections.

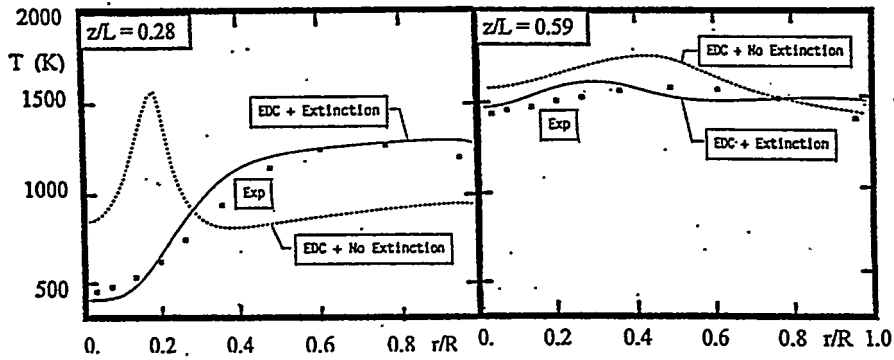


Fig. 5 – Temperature distributions in two cross-sections when *EDC* model was used with and without local extinction and with more accurate τ_c than in figure 2.

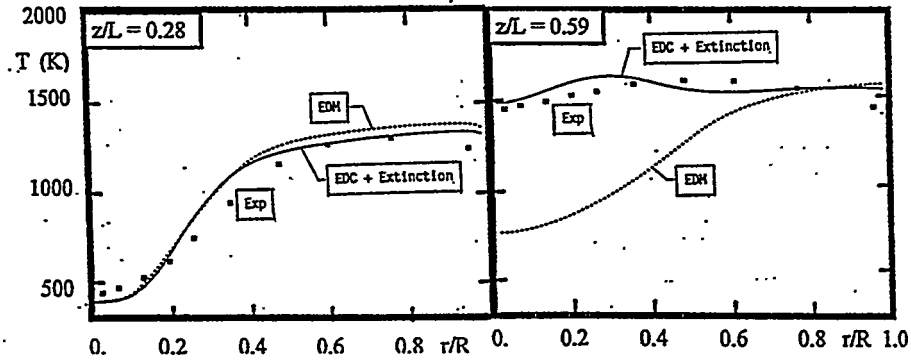


Fig. 6 – Temperature distributions in two cross-sections when *EDC* and *EDM* models were used with more accurate τ_c than in figure 2.

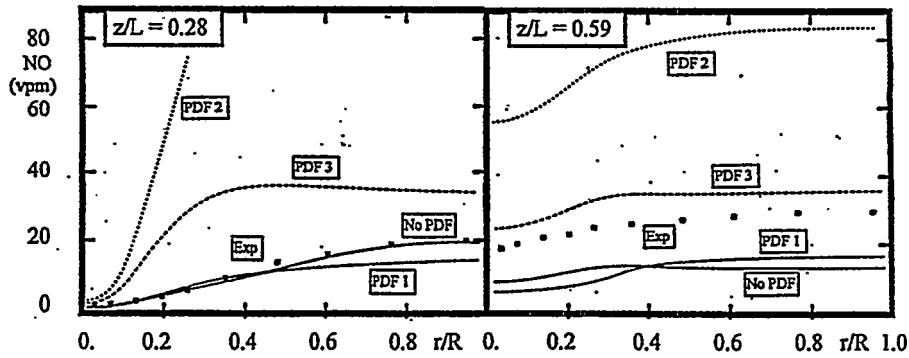


Fig. 7 – Distributions of nitric oxide in two cross-sections when three different kind of pdf models were used (*PDF 1* = Reynolds Analogy; *PDF 2* = $\overline{f'^2} + \beta$ -Distribution; *PDF 3* = $\overline{f'^2} + (\beta + \delta)$ -Distributions).

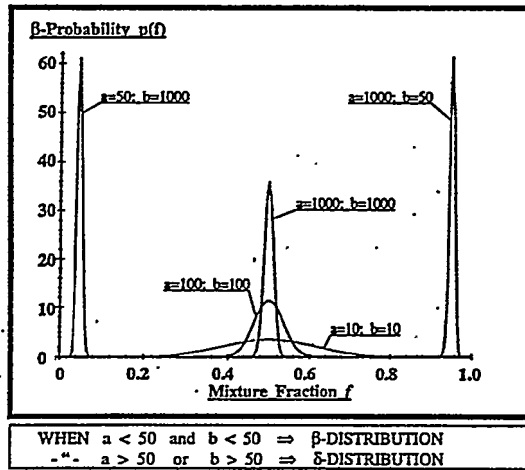


Fig. 8 – Conditions for use of β - and δ -distributions.

For Your Notes

Injection of Heavy Fuel Oil into the Blast Furnace

T. Paloposki*, J. Hakala*, P. Mannila**, J. Laukkanen**

* Helsinki University of Technology, FIN-02150 Espoo, Finland

** University of Oulu, FIN-90570 Oulu, Finland

Abstract

This study deals with the injection and combustion of heavy fuel oil in blast furnaces. The injection of the oil was studied experimentally in a small-scale test rig. The combustion of the oil was analyzed with a commercial computer program for flow and combustion simulations.

Results from computer simulations show that the combustion of the oil can be improved by decreasing the size of the oil drops and by enhancing the mixing between the oil drops and the hot blast. The devolatilization rate of the oil mainly depends on the size of the oil drops. The combustion rate of the volatiles mainly depends on the effectiveness of turbulent mixing with combustion air.

Methods to decrease the size of the oil drops were sought in the experimental part of the study. Experimental results show that the size of the oil drops increases with increasing mass flow rate of the oil and decreases with increasing velocity of the hot blast.

Methods to improve the mixing between the oil drops and the hot blast are suggested but have not yet been experimentally tested.

Introduction

The production of iron in a blast furnace requires a considerable amount of energy. Traditionally, the energy requirements have been met by the combustion of coke in the furnace and by the sensible heat of air (or a mixture of air and oxygen) which is preheated to a high temperature and blown into the furnace. However, it is often advantageous to use auxiliary fuels to replace part of the coke, both from the point of view of fuel prices and from the point of view of encouraging indirect reduction of iron oxides. Examples of auxiliary fuels include pulverized coal, heavy fuel oil and natural gas.

In Finland, the steel industry uses a significant amount of heavy fuel oil as an auxiliary fuel. Injection lances are used to feed the oil into the high-velocity stream of hot air which is blown into the furnace through tuyeres. As the oil jet is discharged from the tip of the injection lance and gets into contact with the hot blast, it immediately breaks up into drops. Earlier theoretical calculations have shown that the size distribution of the drops is a key factor in governing the devolatilization and subsequent combustion of the oil in the furnace. The drops should be small enough to ensure complete combustion of the oil. Complete combustion is important since soot and other products of incomplete combustion may cause operating problems in the furnace and in the gas cleaning equipment downstream from the furnace.

It has been anticipated that higher rates of oil injection will be employed in the future and that problems caused by incomplete combustion might therefore occur. Optimization of the oil injection process requires information on the drop size distribution in the oil spray at various operating conditions. Methods to decrease the sizes of the oil drops and other improvements of the oil injection process would be welcome.

Computations

The combustion of oil drops in the blowpipe-tuyere-raceway region of a blast furnace was analyzed at University of Oulu. The computations were carried out using CFDS-FLOW3D, which is a commercial program for the solving of fluid flow problems with simultaneous chemical reactions. The program was running at the Cypress mainframe computer of the Center for Scientific Computing in Espoo and was operated from Oulu using the FUNET network.

In the computations, the problem was set up to imitate the injection of heavy fuel oil at Blast Furnace #1 of Rautaruukki Raahel Steel. The oil mass flow rate was

chosen to be 8.7 kg/min, which corresponds to an injection rate of 90 kg oil per ton of hot metal.

The geometry of the blowpipe-tuyere-raceway region of the blast furnace is rather complex. In particular, the size and shape of the raceway are not known accurately. A simplified geometry which consisted of a gradually expanding straight pipe with a circular cross-section was therefore used. Cylindrical symmetry was also assumed.

The computational domain is shown in Figure 1. The grid had 24×28 cells, some of which were blocked out to produce the desired shape.

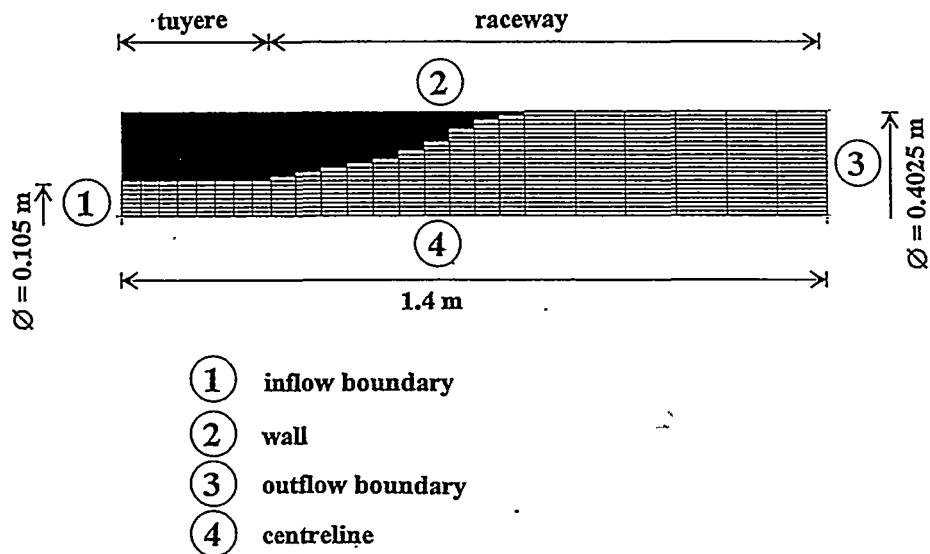


Figure 1. The computational domain.

A detailed description of the computations and of the initial and boundary conditions has been given by Laukkanen (1995). In this paper, we will discuss two particular questions:

- (1) What is the effect of drop size on the combustion of the oil?
- (2) What is the effect of mixing on the combustion of the oil?

To solve the first question, two different values were used for the initial drop size (50 μm and 100 μm). To solve the second question, two different values were used for the initial turbulence intensity in the hot blast (3.7 % and 11.5 %).

To analyze the results, we compare the distance needed for the devolatilization of the oil drops in each case. It can be assumed that rapid devolatilization and combustion of gaseous hydrocarbons is most important from the point of view of blast furnace operation. The formation of soot and other products of incomplete combustion cannot be avoided if unburned gaseous hydrocarbons escape the raceway.

The results are compiled in Table I. The results show that the combustion can be improved both by decreasing the size of the oil drops and by enhancing the mixing between the oil drops and the hot blast. The distance needed for the devolatilization of the oil drops mainly depends on the size of the drops. Although not shown in Table I, it was also found that the combustion rate of gaseous hydrocarbons depends on the effectiveness of turbulent mixing.

Table I Results of computations.

Case	Initial drop size [μm]	Initial turbulence intensity [%]	Distance needed for complete devolatilization [m]
(c)	50	3.7	0.34
(d)	50	11.5	0.28
(g)	100	3.7	1.06
(h)	100	11.5	0.87

Enhanced mixing (high turbulence intensity) could perhaps be achieved by using artificially created surface roughness and other turbulence generators in the blowpipe. These ideas have not been experimentally tested yet.

Experimental

The test rig is a small-scale model of the blowpipe-tuyere-raceway region of Blast Furnace #1 at Rautaruukki Raahé Steel. The test rig was designed and built at Helsinki University of Technology.

The size of the model is approximately 2/3 of the size of the actual equipment. The tuyere and the vertical walls of the raceway are made of transparent plastic; thus, visual observation of the oil injection process is possible. Air at atmospheric temperature and pressure is used to simulate the hot blast. Substitute liquids are used to simulate heavy fuel oil. So far, the substitute liquids have mostly been mixtures of water and glycerol. Some experiments have also been carried out with mixtures of water, glycerol and ethanol. The experiments reported in this paper were carried out with mixtures of water and glycerol.

Dimensional analysis was employed in the design of the test rig to achieve similarity between model experiments and the actual blast furnace. The selection of dimensionless variables and the design of the test rig have been described by Paloposki (1994) and by Hakala (1995). The operating conditions of the test rig and the actual blast furnace are illustrated in Table II. It can be seen that the test rig is much smaller and easier to handle than the actual blast furnace.

Table II Operating conditions of the test rig and the actual blast furnace.

	Test rig	Blast furnace
<i>Air flow:</i>		
Diameter of tuyere tip [mm]	77	115
Air flow rate [kg/s]	0.55	2.1
Air temperature [°C]	20	1090
Air pressure (abs.) [kPa]	100	360
Air velocity [m/s]	100	215
<i>Oil flow:</i>		
Diameter of lance tip [mm]	4.6	7
Oil flow rate [kg/min]	2.2	8.7
Oil temperature [°C]	20	190
Oil viscosity [cP]	16	41

The values of the characteristic dimensionless variables are given in Table III. Fairly good agreement between the values of the dimensionless variables in the model experiment and in the actual blast furnace was obtained. The only major problem was caused by the surface tension of the test liquid. To achieve a value of 0.102 for the Ohnesorge number, the surface tension of the test liquid should have been 4.6 mN/m (assuming that the other physical properties of the test liquid do not change). Such test liquids were not available and it was decided to carry out the experiments with a mixture of water and glycerol.

Table III The values of characteristic dimensionless variables in the test rig and in the actual blast furnace.

	Test rig	Blast furnace
<i>Air flow:</i>		
Reynolds number	509,000	430,000
Mach number	0.291	0.291
<i>Oil flow:</i>		
Reynolds number	634	643
Ohnesorge number	0.0264	0.102
<i>Air and oil flow:</i>		
Density ratio	987	1009
Viscosity ratio	889	774

All experiments were recorded on video tapes for studies of the visual appearance of the spray. The video material was edited to prepare video tapes in which the effect of changes in operating conditions on the spray was illustrated.

A Malvern Particle Sizer was used for the measurement of the drop size distributions in the spray. The Malvern Particle Sizer is an optical instrument based on the scattering of laser light by the drops. The drop size distributions were measured inside the raceway, at a distance of approximately 350 mm downstream from the tip of the injection lance. To make the measurements possible, two special windows were installed in the raceway. A stream of pressurized air was introduced near the windows to prevent the deposition of drops on window surfaces.

The effect of oil flow rate on the drop size distribution in the oil spray is shown in Figure 2. Three characteristic drop diameters are shown in the figure. They are $D[v, 0.1]$ which is the 10 % fractile of the cumulative volume distribution of the drops in the spray; $D[v, 0.5]$ which is the 50 % fractile of the cumulative volume distribution of the drops in the spray (volume median diameter); and $D[v, 0.9]$ which is the 90 % fractile of the cumulative volume distribution of the drops in the spray.

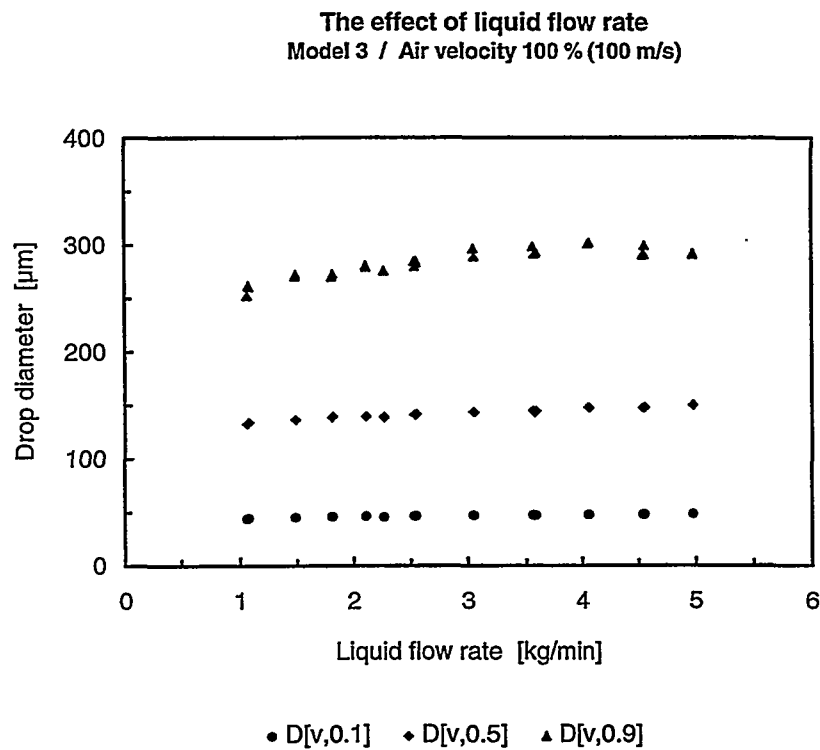


Figure 2. The effect of oil flow rate on the drop size distribution in the oil spray.

Figure 2 shows that the drop size distribution becomes coarser as the oil flow rate increases. Large drops and incomplete combustion of the oil may become a source of problems at higher injection rates.

The effect of air velocity on the drop size distribution in the oil spray is shown in Figure 3. Three characteristic drop diameters are shown in the figure. They are $D[v, 0.1]$ which is the 10 % fractile of the cumulative volume distribution of the drops in the spray; $D[v, 0.5]$ which is the 50 % fractile of the cumulative volume distribution of the drops in the spray (volume median diameter); and $D[v, 0.9]$ which is the 90 % fractile of the cumulative volume distribution of the drops in the spray.

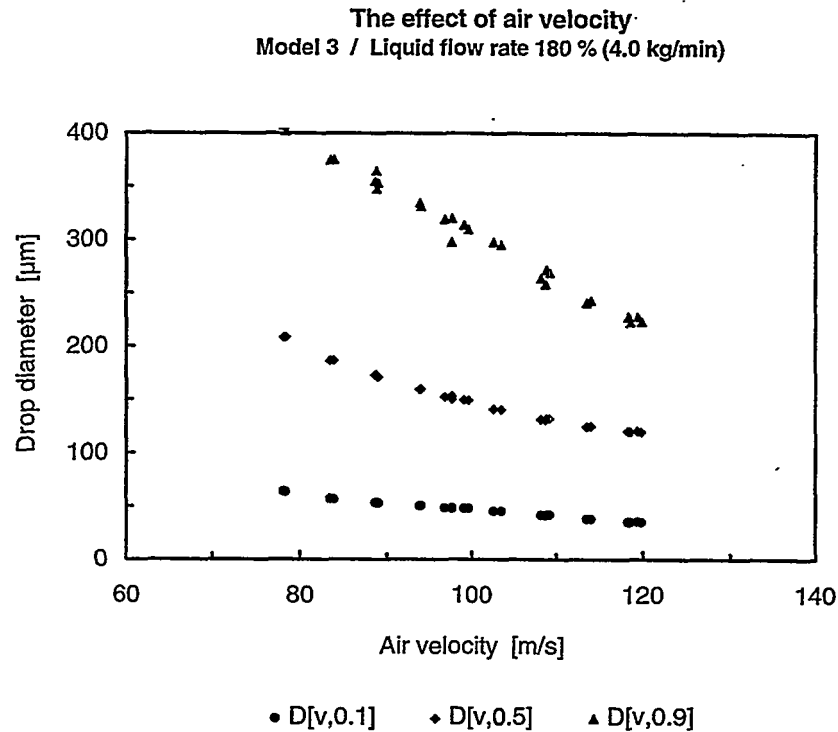


Figure 3. The effect of air velocity on the drop size distribution in the oil spray.

Figure 3 shows that the drop size distribution becomes finer as the air velocity increases. Large drops and incomplete combustion of the oil may occur in some locations inside the blast furnace if the air is unevenly distributed between the tuyeres.

The experimental results shown in Figures 2 and 3 can be expressed with the equation

$$D[v, 0.5] \propto \dot{m}_{oil}^{0.073} v_{air}^{-1.3}$$

where $D[v, 0.5]$ is the volume median diameter of the drops, \dot{m}_{oil} is the oil flow rate and v_{air} is the velocity of the blast.

Discussion

It is of interest to compare the results obtained in this study with the experiences gained in the injection and combustion of pulverized coal. Those experiences have recently been summarized by Hutny *et al.* (1991).

It was pointed out by Hutny *et al.* that the combustion rate of the coal increases as the particle size decreases. This is in agreement with our results. Hutny *et al.* noted, however, that the results of some experimental studies seem to indicate that the particle size of the coal has a stronger effect on the burnout of the residual char than on the devolatilization rate. Our results indicate that the drop size in the oil spray strongly affects the devolatilization rate of the oil.

Hutny *et al.* also emphasized the importance of the mixing between the fuel and the air. They suggested that in some cases the combustion rate of the coal may be determined by the rate of turbulent mixing rather than by the rate of devolatilization. Our results also indicate that improvements in mixing might increase the combustion rate of the oil.

Conclusions

The results of numerical computations showed that the drop size distribution in the oil spray is a key factor in governing the devolatilization rate of the oil in the blast furnace. Mixing between the fuel and the combustion air is a key factor in the combustion of the volatiles.

The experimental results show that the drop size distribution becomes coarser as the oil flow rate is increased. Incomplete combustion of the oil may therefore become a source of problems at high injection rates. The drop size distribution becomes finer as the velocity of the hot blast is increased. It is important to pay attention to the distribution of the air between the tuyeres.

Acknowledgements

This work was funded by Ministry of Trade and Industry, by Technology Development Centre, Finland and by Rautaruukki Raahе Steel and was a part of the National Energy Research Program SULA 2 in Finland.

References

- Hakala, J. (1995), Modelling oil injection into the blast furnace using small scale models with the object of increasing injection rate. M.Sc. Thesis, Helsinki University of Technology, Faculty of Mechanical Engineering (in Finnish).
- Hutny, W. P., Lee, G. K. & Price, J. T. (1991), Fundamentals of coal combustion during injection into a blast furnace. *Progress in Energy and Combustion Science* 17 pp. 373-395.
- Laukkanen, J. (1995), Numerical modelling of turbulent oil combustion in the race way of the blast furnace. M.Sc. Thesis, University of Oulu, Department of Process Engineering (in Finnish).
- Paloposki, T. (1994), Injection of heavy fuel oil into a blast furnace: feasibility of small-scale, cold-flow model experiments. Research report, Helsinki University of Technology, Laboratory of Energy Engineering and Environmental Protection.

**The Recovery Boiler Advisor — Combination of Practical Experience and
Advanced Thermodynamic Modelling**

R. Backman¹, G. Eriksson², and K. Sundström³

¹Åbo Akademi University, Finland

²LTH/RWTH, Germany

³Tampella Power Oy, Finland

Abstract

The Åbo Advisor is a computer based program intended to provide information about the high temperature ash and fluegas chemistry in pulping spent black liquor recovery boilers of kraft pulp mills. The program can be used for predictions of a variety of furnace and flue gas phenomena, such as fireside fouling of the heat exchanger surfaces caused by the flue gas particulate matter, emissions of SO₂(g), HCl(g) and NO_x(g) with the flue gas etc. The program determines the composition of the fluegas as well as the amount and composition of the two typical fly ash fractions found in recovery boiler fluegases, the condensed fly ash particles and the carry over particles. These data are used for calculating the melting behavior of the fly ash present at different locations in the boiler and this characteristic behavior is used for the fireside fouling predictions. The program may also be used for studying how different mill processes affecting the black liquor composition affects on the fireside chemistry of the recovery boiler.

As input data for the calculations only a few boiler operation parameters and the composition of the black liquor is required. The calculations are based on a one-dimensional, multi-stage chemistry model where both thermodynamic equilibrium calculations and stoichiometric material balances are used. The model calculates at first the chemistry in the lower furnace and smelt after which it moves to the upper furnace and the radiative parts of the fluegas channel. As the last block the program calculates the chemistry in the convective part, the electrostatic precipitator cath and stack. The results from each block are presented in tables, key numbers and melt curves representing the fluegas or fly ash fraction present at each location.

The program is a Windows application and it requires Windows 3.1x or Windows for Workgroups 3.11 and an Intel i386/486-compatible processor. Due to complex calculations a DX-33 or faster processor is highly recommended. The hard drive should have at least 5 MB free space.

For Your Notes

1948

New Applications with Time-Dependent Thermochemical Simulation

Koukkari, P.¹, Laukkanen I.², Penttilä K.³

¹VTT Chemical Technology, P.O. Box 1404, FIN-02044 VTT, FINLAND

²VTT Automation, P.O. Box 1301, FIN-02044 VTT, FINLAND

³Kemira Engineering Oy, P.O. Box 330, 01001 Helsinki, FINLAND

Abstract

A new method (RATEMIX[®]) to calculate multicomponent chemical reaction mixtures as a series of sequential thermochemical states was recently introduced. The procedure combines multicomponent thermodynamics with chemical kinetics and may be used to simulate the multicomponent reactors as a thermochemical natural process.

The method combines the desired reaction rates sequentially with constrained Gibbs energy minimization. The reactant concentrations are determined by the experimental (Arrhenius) rate laws. During the course of the given reaction the subsequent side reactions are supposed to occur reversibly. At every sequential stage of the given reaction the temperature and composition of the reaction mixture are calculated by a thermodynamic subroutine, which minimizes the Gibbs energy of the system and takes into account the heat transfer between the system and its surroundings. The extents of reaction are included as algorithmic constraints in the Gibbs energy minimization procedure. Initially, the reactants are introduced to the system as inert copies to match both the mass and energy balance of the reactive system. During the calculation the copies are sequentially interchanged to the actual reactants which allows one to simulate the time-dependent reaction route by using the thermochemical procedure. For each intermediate stage, the temperature and composition are calculated and as well numerical estimates of the thermodynamic functions are obtained.

The method is applicable in processes where the core thermodynamic and kinetic data of the system are known and the time-dependent heat transfer data can either be measured or estimated by calculation. The method has been used to simulate e.g. high temperature flame reactions, zinc vapour oxidation and a counter-current rotary drum with chemical reactions. The procedure has today been tested with SOLGASMIX, CHEMSAGE[®] and HSC[®] programs.

¹To whom the correspondence should be addressed. Fax: 358-0-456 6390, e-mail: pertti.koukkari@vtt.fi

1. Introduction

A thermochemical method (RATEMIX[®]) for the calculation of multicomponent chemical reaction mixtures as a series of sequential intermediate states by applying both reaction kinetics and multi-phase thermodynamics was recently introduced /1,2/. The procedure combines Gibbs energy minimization with the kinetic rate laws and can be used to simulate the multicomponent reactors as a thermochemical natural process. The model can be applied with systems for which the salient thermodynamic data is known and for which reaction kinetic data is also available. Time-dependent heat and mass transfer data can be incorporated with suitable models or by using experimental data.

The RATEMIX[®] procedure has been applied for high-temperature gas-condensed processes as well as for reaction mixtures in aqueous solutions. In what follows, the scope of the method is reviewed and results of the thermochemical simulation of a counter-current rotary drum with chemical reactions are described.

2. Thermochemical Algorithms for Process Calculation

The thermochemical computer programs can be used for process simulation in a variety of ways. The general advantage of the use of the non-stoichiometric multi-component thermodynamic approach with Gibbs energy minimization is that it provides the user with a systematic chemical method and results with more simple and yet comprehensive models without detailed stoichiometric analysis of the reacting system. In addition, the user is constantly dealing with the true energy and mass balances of the process. The simulation can thus be built on practical process units in terms of the feed and product rates, side streams, heating and cooling effects etc. When the multi-component thermodynamic description for the chemical system is used, it is not necessary to work with elaborate reaction stoichiometry and yet as the result of the calculation also the amounts of the minor constituents and side products are obtained.

The Gibbs energy minimization results with the equilibrium composition of the multicomponent system at given temperature and pressure. The processes which occur in practical chemical reactors are yet often controlled by time-dependent mass-transfer or reaction kinetic phenomena. The direction of the chemical change and the boundary conditions for the occurring reactions are set by the thermodynamic requirements and thus, at given temperature and pressure, the change proceeds towards the minimum of the Gibbs free energy and towards the 'final' equilibrium state. With advanced thermodynamic routines one may calculate sequential equilibrium stages by varying both T and P between stage steps /3/. Discretized mass and heat transfer effects can also be incorporated in the stepwise calculation. Conditions for metastable equilibria as well as systems controlled by well-defined reaction kinetic or mass transfer constraints can also be included in the multi-phase thermochemical simulation models /4,5/.

3. Use of Algorithmic Constraints for Reaction Rates

In this work, the extent of a chemical reaction has been applied as an additional, algorithmic constraint for the minimization calculation. Thus the reaction rate dependent phenomena can be taken into account in the Gibbs energy minimization [2]. The molar amount (n_i) of a reactive component (i), acting as reactant in the reaction (r) may be written

$$n_i = \sum_{\alpha} n_i^{\alpha} = z_i(0) + \nu_{ir} \xi_r \quad (1)$$

with $z_i(0)$ indicating the amount of the reactant (i) in the feed and summation goes over the phases (α) [6]. When the reaction proceeds, the $z_i(0)$ gets consumed in terms of the reaction rate and the advancement of the reaction may thus be used as a further restriction for the free energy calculation. Assuming that the rest of the system may equilibrate, while the chosen reaction is in process, one may 'freeze' the reaction at given values of $\xi_r = \xi'_r$, in which ξ'_r is a time-dependent function of the reaction rate. With well-defined reaction kinetics an algorithmic constraint is derived out of ξ'_r and applied together with the Gibbs energy minimization procedure [7]. Initially an inert thermophysical copy of the reactant (i) is written in the program input to replace $z_i(0)$. This copy then is transformed to actual n_i of equation (1) by finite differences and as the reaction proceeds, both the mass and energy balances of the thermochemical system remain fulfilled throughout the calculation. As a result, the time-dependent mass transfer or reaction kinetic sequence controls the thermochemical change taking place in the multi-component reaction mixture.

The calculation results with a series of intermediate states, for which also the characteristic thermochemical data will be calculated. The data is received as a function of the extent of the reaction (r) as is shown schematically in figure 1. Thus, if the algorithmic constraint (ξ_r) is given in terms of a reaction rate, a time-scale for this data derived out of the rate expression is received. The temperature of each intermediate state is either given by the user or can be calculated by an iterative target procedure from known heat transfer. The result of the calculation can be verified by experimental data from the process, or, e.g. by a reaction calorimetric experiment.

In the algorithmic model both the reaction rate and the driving force of the chemical change (decreasing Gibbs energy at constant T and P) are used. However, the reaction rate is not determined by the driving force, but for each sequence of calculation the direction of the chemical change and the energy changes accompanied to it are derived thereof.

The first applications of the method were developed in MS-DOS[®] environment [2] (see adjacent flowsheet in figure 2.). The MS-Windows[®] version of the program is being developed. In this version, four reaction rate equations can be incorporated and solved by an ode-solver such as e.g. STIFF3. The results are collected to an intermediate logbook file by subroutine IMRES. As the solution procedure is sequential, no particular requirements for the computer time are set other than those for ordinary free energy minimizers and ode-solvers.

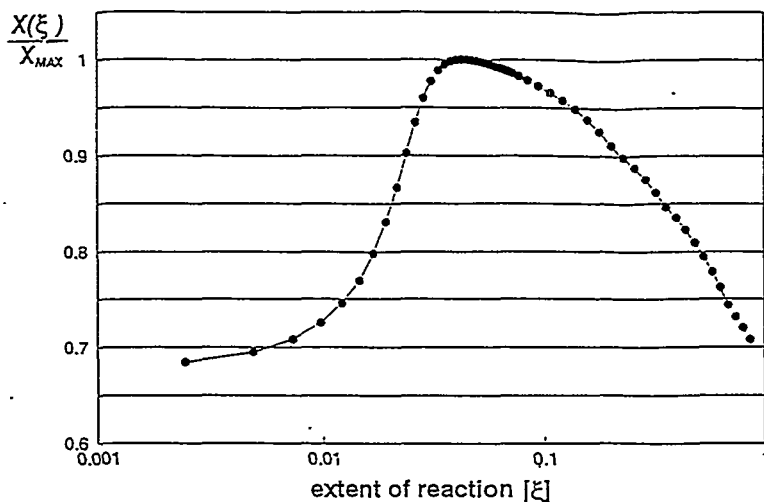


Figure 1. Calculated values for variable $X=X(\xi)$ of the reactor intermediate states.

4. Applications

The procedure can be applied to such multi-component reactors for which the thermodynamic and reaction rate data is known and for which the time-dependent heat transfer data can either be measured or estimated. The thermodynamic input data should be such as in SOLGASMIX or CHEMSAGE, with heat capacities given as functions of temperature. A possibility to use dormant species in the thermochemical input is an advantage. The reactions, for which the reaction kinetics is involved, should be between well-defined thermochemical substances so as to enable their inclusion in the thermodynamic description of the system.

The reactor simulations performed by Ratemix include /1,8/:

- high temperature aerosol reactors (e.g. $TiCl_4$ oxidation)
- zinc vapour oxidation during zinc condensation
- counter-current rotary drum with chemical reactions
- caustization of aqueous (impure) sodium carbonate solution with lime

The procedure is most straightforward to apply for systems, where one has one (or some) main reactants and a dominating overall reaction, which can be followed with the kinetic constraint. Then, the possible results of the side reactions are calculated by the thermodynamic routine in terms of the consumption of the reactants. However, more complicated kinetics can be incorporated by utilizing activation/deactivation of the dormant species and by defining time-dependent input/output streams into the system.

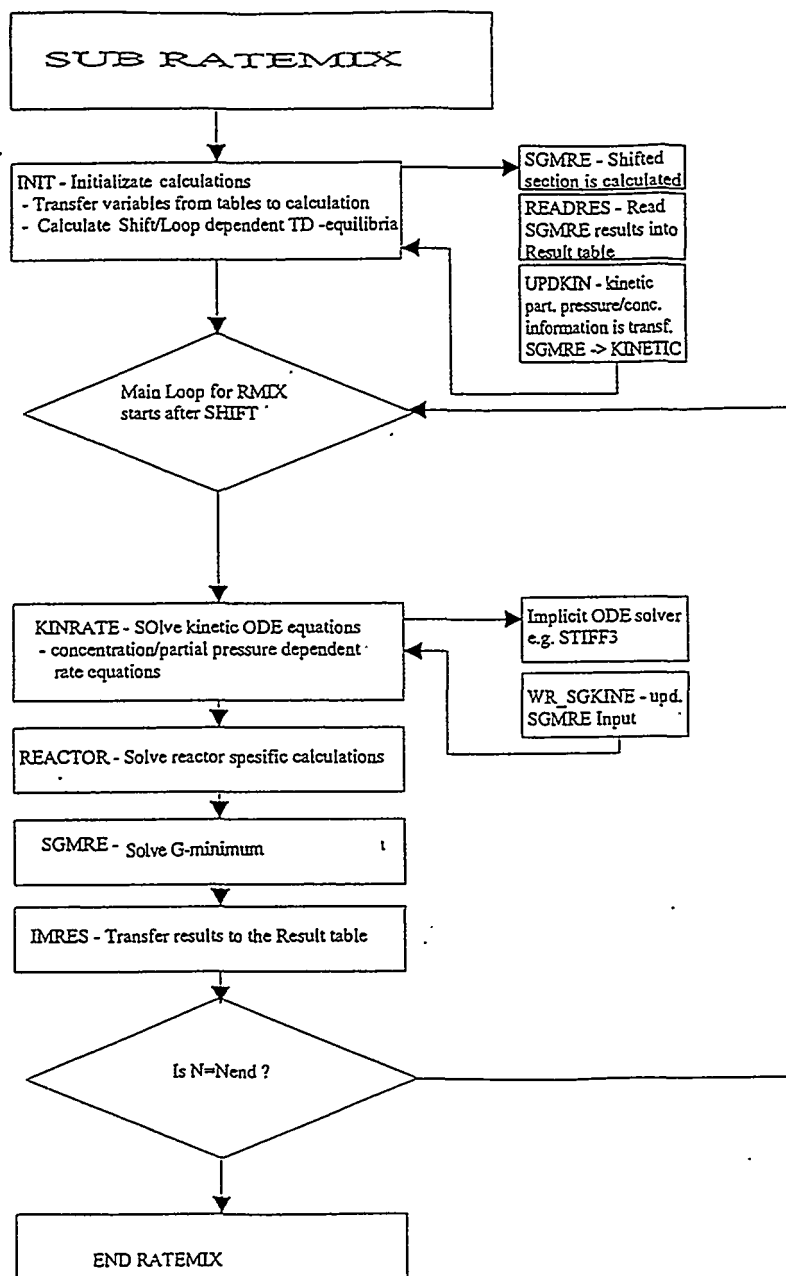


Figure 2. Flowsheet of the Ratemix routine.

Further, the combination of reaction kinetics with the Gibbs energy minimization calculation can be used as a tool to define the advancement of the chemical reactions in a system with known heat transfer. This approach requires that kinetic constraints have been used for the minimization algorithm and that the Gibbs energy of the system is written in terms of the specific heats (heat capacities) of the constituents of the system. Then the enthalpy change of the entire system may be calculated with respect to a chosen reference state at any given time of the chemical change. The calculated enthalpy or temperature change with a given reaction mechanism should then agree with measured results. The kinetically constrained Gibbs energy minimization algorithm can thus be used to adjust kinetic rate parameters with measured data from a reaction calorimeter [1,9].

5. The RATEMIX Model of the Rotary Drum Calciner

Pure white titanium dioxide (TiO_2) is a bulk commodity which is used as pigment for paints, plastics, paper and rubber. The most common raw material of TiO_2 is ilmenite, which is the natural ore of ferrous titanate (FeTiO_3). Alternatively, smelted slag in which the iron [FeO] content of the concentrate has been decreased to a level of 20-25 % can be used. In Europe, the pigment is most commonly produced by the well-established wet sulphuric acid process, in which the iron and other impurities of the raw material are leached by concentrated sulphuric acid and then removed by a number of repeated separation processes including vacuum crystallisation and filtering. After thermal hydrolysis of the purified reactant liquor, the titania is received as a slurry which contains hydrous titanium dioxide ($\text{TiO}_2 \cdot n\text{H}_2\text{O}$), anatase ($\text{TiO}_2(\text{A})$) and sulphuric acid.

The final stage of the manufacturing route is to calcine the hydrous slurry to the final titanium dioxide pigment, which is most often rutile, $\text{TiO}_2(\text{R})$. The phase transformation from anatase to rutile is an exothermic reaction ($\Delta_r H = -8,5 \text{ kJ/mol}$, $800 \text{ }^\circ\text{C}$) and rutile also is the more stable crystalline form. However, the phase transformation reaction has a high activation energy ($E_a = 300\text{-}400 \text{ kJ/mol}$) and occurs spontaneously only in temperatures which exceed $600 \text{ }^\circ\text{C}$. The desired rutile pigment is of $> 99. \%$ rutile and thus the final temperatures exceed $900 \text{ }^\circ\text{C}$ in the calcining reactor.

The calciner is a counter-current rotary kiln in which the hot gas coming from a propane burner provides the heat for the drying or the slurry and for the calcination processes. The wet slurry is introduced from the cool end of the reactor at ambient temperature. The kiln operates at close to atmospheric pressure (to prevent dust ejection) and the operation has two main purposes: (1) dry the slurry which is composed of the hydrous and non-hydrous anatase, water and sulphuric acid and (2) transform the titanium dioxide from anatase to rutile. The three operating zones of the kiln are, consequently the drying zone, heating zone and rutilization zone [10]. The zones with their adjacent chemical reactions are described in figure 3. In this figure, as well, a schematic of the temperature profiles of the TiO_2 -mass and gas are presented. The length of a typical kiln is 30-60 m and diameter 2-3 m.

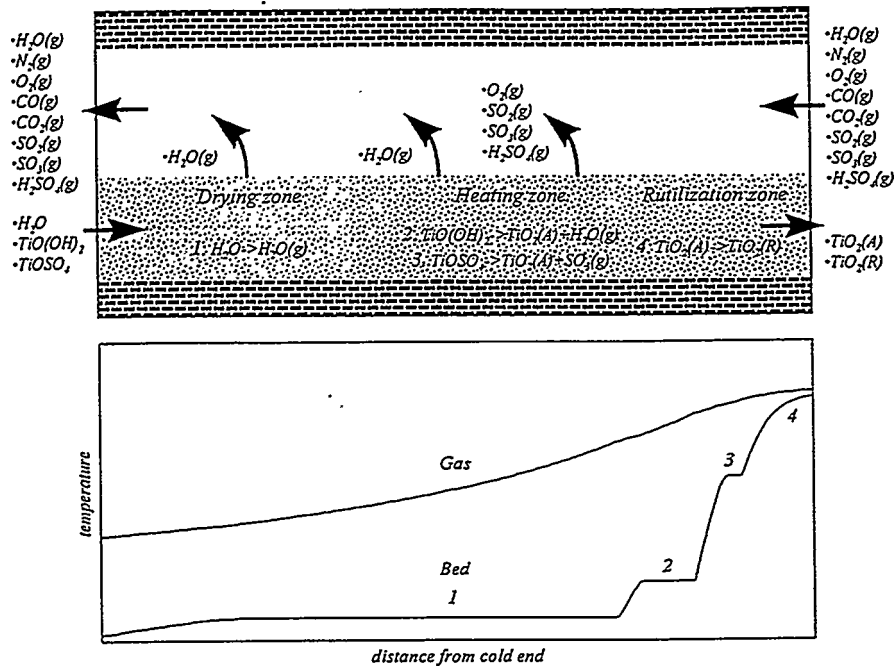


Figure 3. The calciner zones with chemical reactions.

As the partly circulated burner offgas encounters the solid mass, heat transfer occurs from the hot gas to the mass, from the gas to the walls of the kiln and from the hot walls again to the solid mass. A noticeable heat loss through the brick-lined walls takes place. Figure 4 shows a cross-section of the rotary kiln with heat transfer flows. The temperatures of the incoming and outgoing gas and solid mass are continuously measured, and the temperature of the outer wall of the kiln can easily be measured on-site e.g. by using a calibrated Infra-Red radiation pyrometer.

The simulation model was constructed to calculate the stationary temperature profiles of the rotary kiln. To achieve this the kiln was divided to 100-200 successive sections, in which the heat and mass transfer was assumed to occur in the radial direction (cf. figures 3 and 4). Axial heat transfer was neglected for the stationary operation. Further it was assumed that no axial mixing occurred in the reaction mass or in the gas. An axial plug flow model was used for both gas and the slurry. To take into account the effects of the physico-chemical transformations on the enthalpy balance of the reactor, the gas and the condensed mass were both described as thermodynamic systems. The main components of the gas phase are N_2 , O_2 , H_2O , CO_2 , CO , SO_2 , SO_3 and H_2SO_4 , and the condensed phase is respectively a mixture of water, sulphuric acid, hydrous titania [$TiO_2 \cdot nH_2O$], titanium sulphate, anatase and rutil. The gas was assumed to be ideal and the condensed species were introduced to the calculation as

stoichiometrically invariant substances. The non-ideal properties of the slurry were thus neglected. The standard thermodynamic data for most of the compounds could be found in the databases and standard tables, for some like $\text{TiO}_2 \cdot n\text{H}_2\text{O}$ with $n = 1,2$ estimates derived earlier /4/ were used. The heat transfer coefficients as well as the relevant radiation data were taken from literature /11/.

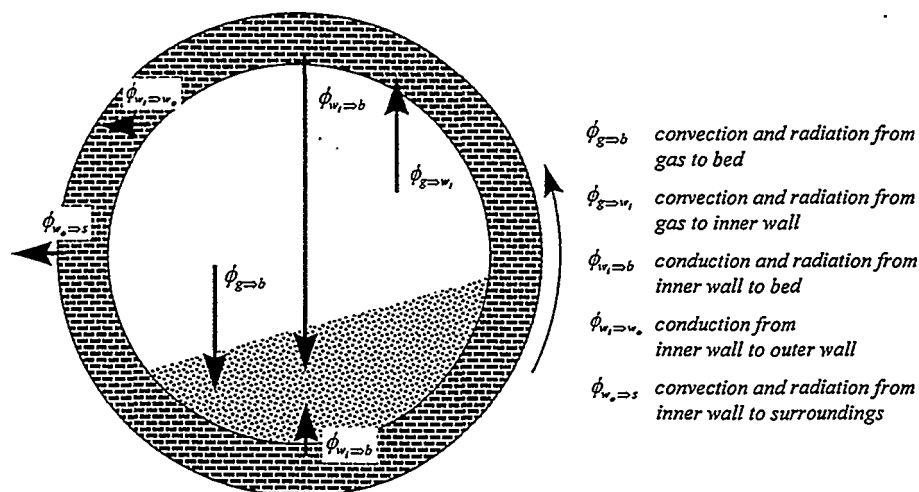


Figure 4. The cross section of the kiln with heat flows.

The stagewise simulation of the kiln was then performed by dividing both reactor streams to volume elements (respective to the reactor sections), which exchange heat and matter with each other. The streams encounter each other in a "zipper" iteration which converges according to the outgoing and incoming stream temperatures which are known by process measurement. To enable overall heat balance checking, propane (C_3H_8) was finally introduced to the thermodynamic description of the gas phase. As the heat losses from the propane burner were known, the incoming temperature of the hot gas could be calculated from the amount of fuel injection and the respective measured temperature could be used as a checking value. Reaction rate constraints were applied for the key reactions, while the vaporization and side reactions are controlled by the mass and heat transfer rates. The calculated temperature profiles of the reactor are shown in figure 5. The profiles show the estimated thermochemical zones of the reactor, in which the drying of the slurry as well as major chemical changes take place. The data is in accordance with previous literature /10/, though the result of RATEMIX[®] is more detailed, for example, in modelling of the phase transformations.

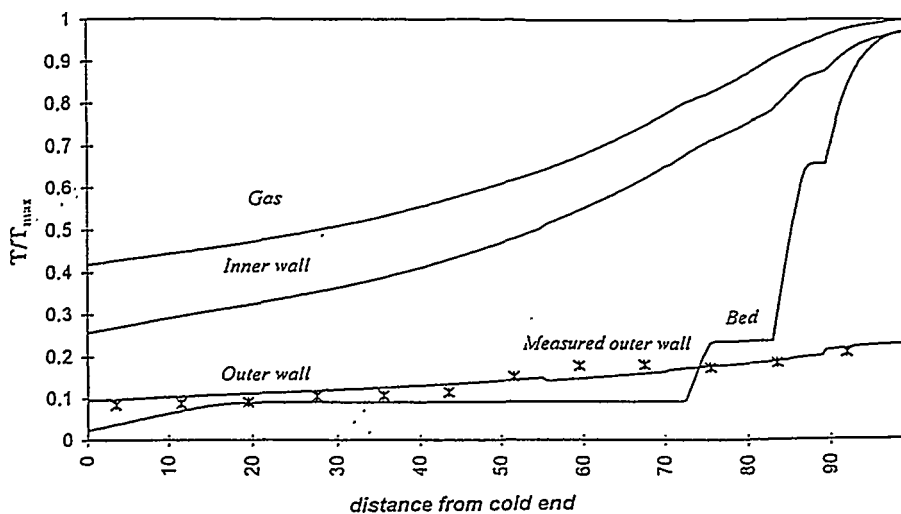


Figure 5. Characteristic temperature profiles of the calciner. Measured points are shown with asterisks. Distance in arbitrary units.

A measurement of the outer-wall temperatures of the kiln was performed by an IR-radiation pyrometer and the experimental points are also shown in figure 5. The agreement between model and measurement is appropriate. A customized model of the anatase-rutile transformation kinetics may be incorporated to achieve improved control of the salient operating factors which affect the pigment quality.

6. Conclusion

A novel method to incorporate time dependency of the chemical reactions or some other rate phenomena to a multi-component thermodynamic calculation has been developed. The RATEMIX procedure is currently being tested with different thermochemical processes by using both MS-DOS and Windows based programs. The method has been applied for various multi-component reactor systems to which the thermodynamic and reaction rate data is known and to which the time-dependent heat transfer data can either be measured or estimated. The major advantage of the method is the flexible adaptation of both the reaction kinetic and thermodynamic phenomena which occur during the chemical change.

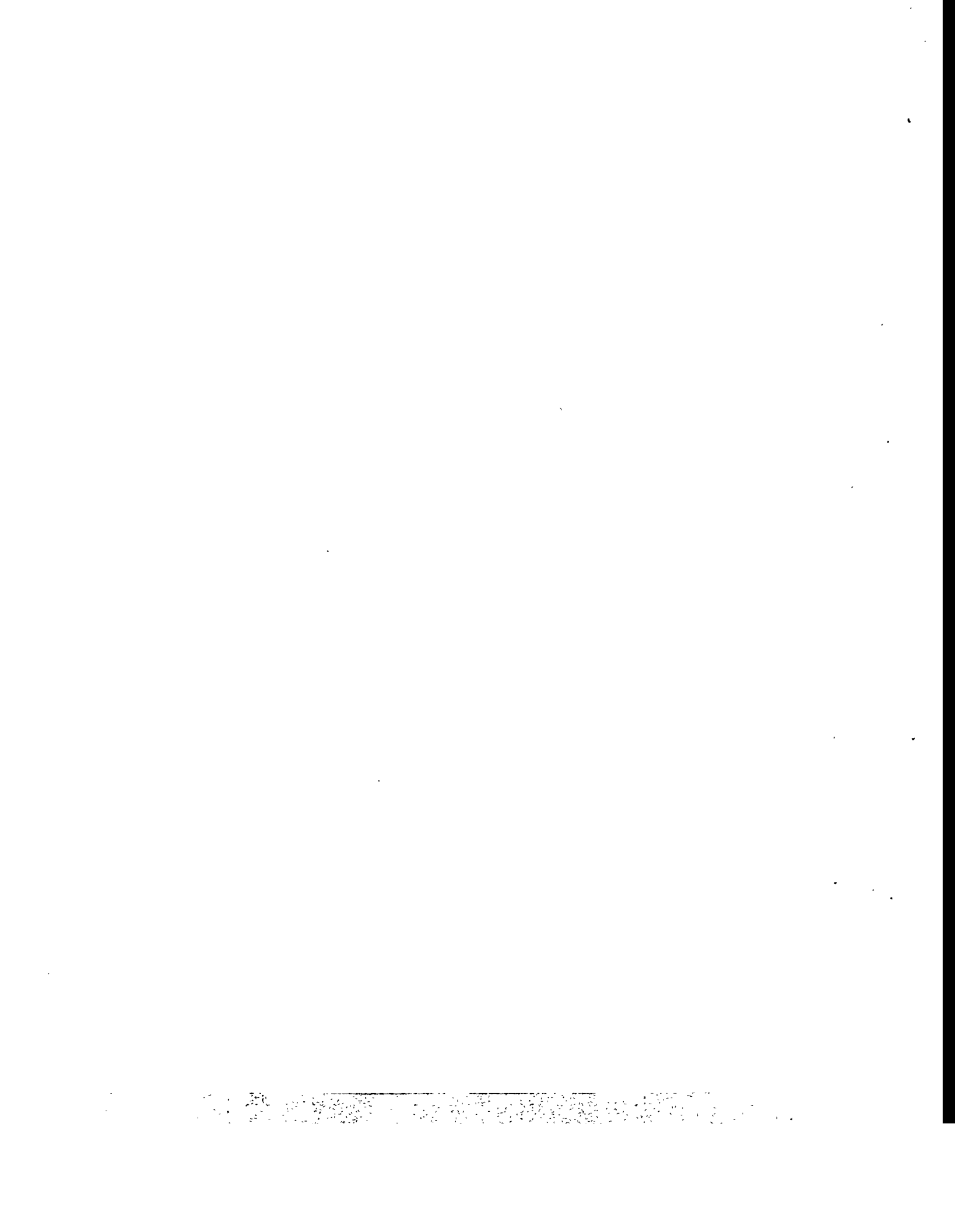
References:

1. Koukkari, P. and Laukkanen, I.: Calculation of Intermediate State Properties in a Multicomponent Chemical Reactor, 2nd Colloquium on Process Simulation, TKK-V-B104, 83-93, Helsinki University of Technology (1995).

2. Koukkari, P., A Physico-chemical Method to Calculate Time-Dependent Reaction Mixtures. *Computers Chem. Engng* 17 (1993), No 12, 1157-1165.
3. Eriksson G. and Spencer P.: Some Examples of the Use of a Thermodynamic Calculation Interface (TQ) with Chemsage, 1st Colloquium on Process Simulation, TKK-V-B99, 105-115, Helsinki University of Technology (1994).
4. Koukkari, P., Sippola, H., and Sundquist, A.: Multicomponent Equilibrium Calculations in Process Design: A Study of Some Acid Digester Reactors, *Hydrometallurgy 94*, Cambridge, England, 139-157, Chapman & Hall, (1994).
5. Robertson, D.G.C: The Computation of the Kinetics of Reactions between Multiple Phases, to be published in *Materials Transactions*, Japanese Institute of Metals, (1996).
6. Gupta, A. K., Raj Bishnoi, P. and Kalogerakis, N.: A Method for the Simultaneous Phase Equilibria and Stability Calculations for Multiphase Reacting and Non-Reacting Systems. *Fluid Phase Equilibria* 63 (1991), 65-69.
7. Koukkari P.: A Physico-Chemical Reactor Calculation by Successive Stationary States, *Acta Polytech.Scand.*, Chemical Technology Series 224, The Finnish Academy of Technology, Helsinki (1995).
8. Koukkari, P., Laukkanen I. and Liukkonen S.: Calculation of Multi-Component Reactors by Time-dependent Intermediate Thermodynamic States, to be published in 12th International Congress of Chemical and Process Engineering - CHISA '96, Praha, Czech Republic, 25.-30. August 1996.
9. Melhem, G.A.: An Advanced Method for the Estimation of Reaction Stoichiometry and Rate from Accelerated Rate Calorimeter Data, *Reaction Engineering V: Advanced Modelling and Measurement Techniques*, Engineering Foundation, St. Augustine, Florida, 8.-13. October 1995.
10. Dumont, G., Belanger, P.R.: Steady State Study of a Titanium Dioxide Rotary Kiln, *Ind.Eng.Chem. Process Des.Dev.*, 17, No2, 107-114, (1978).
11. Penttilä K.: TiO₂-kalsinointiuunin simulointimalli, M.Sc. thesis, to be published at Helsinki University of Technology, Faculty of Process Engineering and Materials Science, (1996).

The financial support of TEKES and Academy of Finland is gratefully acknowledged.

For Your Notes



**Mathematical Modeling and Numerical Simulation
of Czochralski Crystal Growth**

Jari Järvinen and Risto Nieminen
Center for Scientific Computing
P.O. Box 405, FIN-02101 Espoo, Finland .

Abstract

We have developed a detailed mathematical model and numerical simulation tools based on the SUPG Finite Element Method for the Czochralski crystal growth. In this paper we consider the mathematical modeling and numerical simulation of the melt flow and the temperature distribution in a rotationally symmetric crystal growth environment. The temperature distribution and the position of the free boundary between the solid and liquid phases are solved by using the Enthalpy method. Heat inside of the Czochralski furnace is transferred by radiation, conduction and convection. The melt flow is governed by the incompressible Navier-Stokes equations coupled with the enthalpy equation. We demonstrate numerically the melt flow and the temperature distribution in the whole Czochralski furnace.

1. Introduction

Worldwide the electronics industry is the largest and fastest growing manufacturing industry. In 1993 the investments of the electronics industry were estimated to be in the range of \$ 900 billion. The basis of the electronics industry is semiconductor processing whose investments alone were in the range of \$ 60-70 billion, [10].

The semiconductor industry can roughly be divided into two sections: a refining section which uses basic material, semiconductor wafers, to produce integrated circuits and a manufacturing section which produces semiconductor wafers, Figure 1.1.

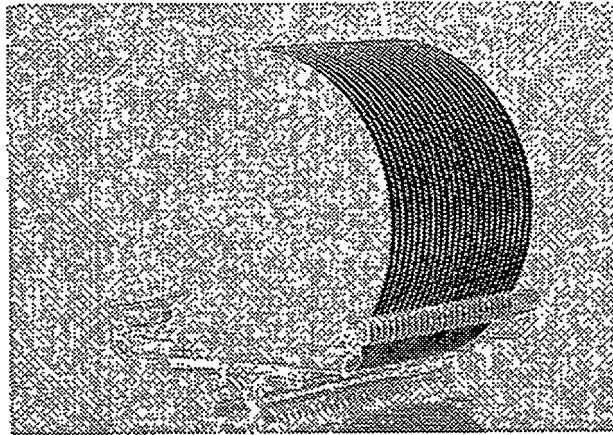


Figure 1.1 Semiconductor wafers

In the manufacturing section semiconductor wafers are produced from single crystals. Single crystals are grown from molten purified semiconductor materials and the result of crystal growth process has the form of a cylindrical crystal rod with the diameter of a few inches, Figure 1.2. Solid crystals are afterwards cut to form thin semiconductor wafers. Nowadays the Czochralski method, the float-zone pulling method and the Bridgman method are the most commonly used techniques to grow single crystals. The materials of crystals are mainly silicon, gallium-arsenide and germanium.

Typically the diameters of industrially produced single crystals have been in the range of 4-8 inches. The trend towards larger diameters is evident in the future. Some experiments have already been carried out with crystals whose diameter is even 12 inches. The demand for larger crystals arises from the desire to increase the profitability of manufacturing crystals and to improve the yield of integrated circuits fabricated from semiconductor wafers. The up-scaling of the existing equipments as well as the products of new technology, e.g., the continuous Czochralski

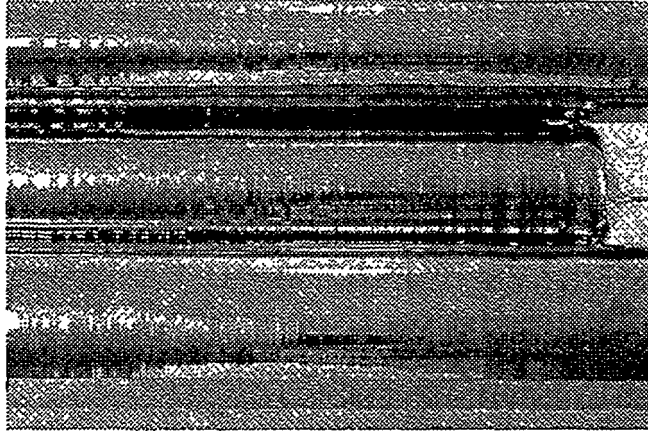


Figure 1.2 Silicon crystals

crystal growth (CCz) and the magnetic Czochralski crystal growth (MCz), set new challenges for scientists and engineers in the crystal growth field.

So far the development of the semiconductor technology has been mainly empirical. With rising industrial and economical importance and with new challenges in the product development scientists are now providing the knowledge required in this field. Several research projects, for instance in the field of mathematics, physics and chemistry, have already been carried out and the amount of research is undoubtedly going to grow in the future.

Our research is connected to mathematical modeling and numerical simulation of the Czochralski crystal growth, i.e., we restrict our research to concern the manufacturing section. Our special interests lie in the development of mathematical model and numerical simulation tools for the Czochralski method. With this method one can grow both one-component materials such as silicon and germanium and two-component materials such as gallium-arsenide. In the latter case the method is called the liquid encapsulated technique (LEC). In this work, however, we are interested in the Czochralski silicon crystal growth.

The Czochralski crystal growth technique requires high temperature environment and complicated growing furnaces (see Chapter 2). Experimental measurements, such as the measurements of the temperature and velocity field of the melt, offer invaluable information from the physical mechanisms. They are, however, very laborious to make and require possibly the construction of complicated experimental systems ([9], [16]) necessitating considerable economical investments.

At the same time computer hardwares and softwares have evolved to the point where very large and complex numerical simulations can be solved in a sufficiently short time frame. In this situation the development of mathematical model and numerical simulation tools for the Czochralski crystal growth can effectively support the Czochralski crystal growth process. The numerically solved mathematical model has an advantage of providing new insight into the physical phenomena.

They allow an easy way to study, for instance, new geometries of the Czochralski furnace or growth parameters.

In the literature numerical simulations of the Czochralski crystal growth have been carried out in the geometry where the diameters of crystals and crucibles are in the range of 2.32-8.25 cm and 7.2-25.4 cm, respectively. In this work the same values are 12.7 cm for crystals and 40.0 cm for crucibles. The diameters of industrially produced single crystals are typically more than 10.2 cm (4 inches) grown from crucibles with diameters exceeding 35.6 cm (14 inches). The main reasons for using small-scale crystal growth environments are the melt flow instabilities connected with the large scale crucibles. It is also noteworthy that the works discussed in the literature are based on either steady-state or quasi steady-state assumptions for the equations of the melt flow and temperature in the whole Czochralski geometry. The steady-state or the quasi steady-state assumption for the melt flow is however not valid, since in reality it is strongly time dependent. We stress that the key for the successful numerical simulation of the whole Czochralski crystal growth is the correct description of the melt flow which should be done with the time dependent analysis.

The melt flow, the temperature field in the whole Czochralski furnace and the free boundary position between the crystal and the melt are the quantities which we are most interested in. These quantities are governed by the time dependent and coupled enthalpy and Navier-Stokes equations with appropriate boundary conditions (Chapter 3).

The Czochralski crystal growth is a very challenging task from the mathematical modeling and numerical simulation point of view. First, the modeling of the pure melt flow demands the coupling of the heat and Navier-Stokes equations. On the other hand, if we consider the crystal-melt system, we have to handle the coupled heat and Navier-Stokes equations in the varying geometry so that the free boundary between the crystal and the melt is considered as a part of the solution. The modeling of the whole Czochralski crystal growth itself requires in addition the presence of all other geometrical objects and the description of global heat transfer. A significant part of heat is transferred by radiation between various surfaces in the Czochralski configuration. This mechanism can be described by the diffuse-gray radiation.

The formulation of the diffuse-gray radiation presented in this work differs from previously published crystal growth articles on which radiative heat transfer is considered. Instead of treating a radiative surface as a finite union of simple surface elements ([1], [11]) we introduce a non-local boundary condition on the radiating part of the surface.

If we then take a closer look at the free boundary problem in the crystal-melt system, there are in fact three different kinds of free boundaries. Namely, the free boundaries between crystal and melt, crystal and gas and melt and gas. In this work only the crystal-melt interface is considered as a free boundary. The radius of the crystal is assumed to be constant and the shape of the melt-gas interface is based on the analytical representation of the shape of the meniscus presented by Hurle, [5].

In the mathematical modeling of the free boundary problem we shall consider enthalpy as a primary unknown instead of temperature. This leads to a use of the enthalpy method which offers a way to treat the free boundary problem in a two phase system ([3], [4], [17]). It is, however, non-trivial to apply the method in such systems where more than two different materials appear. A standard definition of enthalpy leads to a case where enthalpy is discontinuous at the melt-silica crucible interface. In order to guarantee the continuity of enthalpy at this interface some modifications in the definition of enthalpy are required.

The enthalpy method is a typical fixed grid method. The use of this method offers a significant benefit especially in the entire Czochralski geometry compared to research based on the front-tracking methods. The application of the diffuse-gray radiation demands the calculation of view factors which are dependent on the geometry. Since our finite element mesh remains unchanged, the view factors have to be calculated only once, at the beginning of the simulations.

Our numerical simulation tools are based on the finite element method since it has proved its capability to handle complex geometries and problems in many circumstances. Since the melt flow is highly convection dominated the streamline upwinding/Petrov-Galerkin finite element method is applied.

2. Czochralski Crystal Growth Technique

The Czochralski method, the float-zone pulling method and the Bridgman method are the most important techniques to grow single crystals. More than 90% of all semiconductor crystals are produced by the Czochralski method and the rest mainly by the float-zone pulling method. The Bridgman method is used only for the production of crystals with a small diameter.

The principle of the pulling of the single silicon crystal from the silicon melt by the conventional Czochralski method is depicted in Figures 2.1-2.4, [12], [18]. The Czochralski configuration is shown semantically in three dimensional case in Figure 2.1 while in Figures 2.2-2.4 the cross sections of the Czochralski configuration are presented. In Figure 2.2 the initial state of the pulling process is presented. In Figures 2.3 and 2.4 the process is in the advanced and final state, respectively.

The main components of the furnace are shown in Figure 2.2. A seed holder supports the crystal which consists of a seed, a crystal neck, a crystal shoulder and a single crystal silicon rod. The single crystal silicon rod is withdrawn vertically from the silicon melt which is inside of the silica (SiO_2) crucible. The surrounding parts of the silica crucible are a graphite susceptor, a crucible shaft, a graphite resistance heater and thermal shields. The silica crucible is kept in the stabilizing susceptor rotating axially (counter to the crystal rotation) to provide axisymmetric heating conditions.

At the beginning of the process pieces of silicon (polycrystalline silicon) are melted in the crucible under an inert gas atmosphere. After the pieces of silicon are completely melted, temperature of the silicon melt rises for a short time. This is because during the melting a higher temperature difference between the heater and the whole crucible is needed than during the pulling process, since the heat

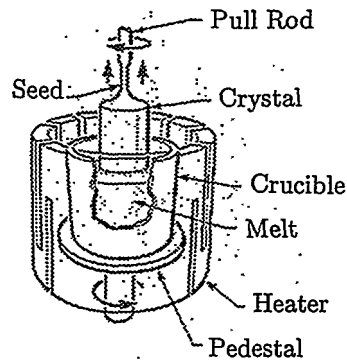


Figure 2.1 Three dimensional Czochralski crystal growth

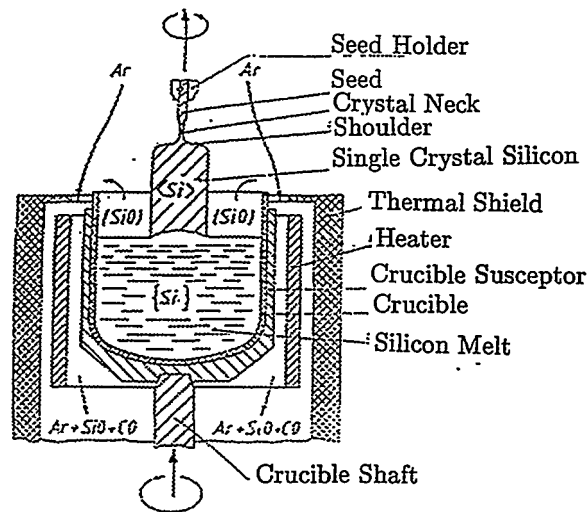


Figure 2.2 Initial state of pulling process

of fusion should be transmitted in the shortest possible time. During the crystal growth this heat is then released, but over a much longer period of time. In order to avoid the loss of energy after silicon is completely melted, the heating power is reduced to a level which maintains the melt as a liquid.

During the Czochralski process the silica crucible is eroded by the hot silicon melt and oxygen dissolves to the melt. Oxygen is transported in the silicon melt by the convection processes. Most of oxygen evaporates through the melt-gas surface and therefore the inert gas (argon) has to flow continuously downwards through the pulling chamber to remove these byproducts. However, a certain amount of oxygen, around 10^{17} atoms/cm³, [10], drifts in the silicon melt to the crystal

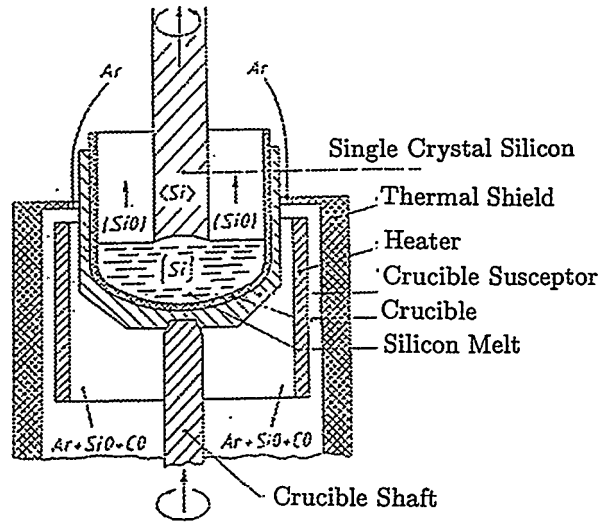


Figure 2.3 Advanced state of pulling process

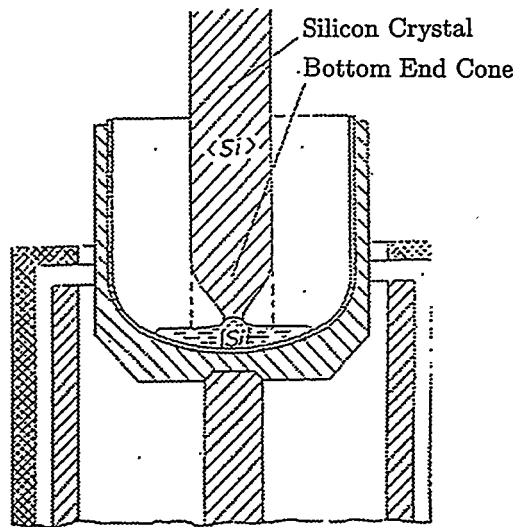


Figure 2.4 Final state of pulling process

growth interface and incorporates to the silicon crystal. Oxygen has a positive and a negative influence on the quality of the silicon crystal. A certain amount of oxygen is required in the silicon crystal since oxygen hardens the silicon lattice giving silicon wafers the desired mechanical strength. On the other hand, if too

much oxygen incorporates to the crystal, oxygen precipitates during the cooling and this forms crystallographic defects, such as dislocations, [18].

Before the pulling process can be started, temperature in the whole furnace should be stabilized. After reaching required starting temperature the seed crystal is dipped into the melt until it begins to melt itself. The melt should not, however, be so hot that the seed melts too much losing its contact to the melt. The seed is then withdrawn from the silicon melt so that it begins to grow but there is no increase in its diameter.

It is very important for present-day applications that single silicon crystals are dislocation-free, [18]. For this reason the so called Dash technique is applied for the crystal pulling: The crystal diameter is gradually reduced to about 2-4 mm and the growth velocity is raised. With a suitable combination of these two factors the silicon crystal becomes dislocation-free after a few centimeters. After receiving the dislocation-free state the diameter of the crystal can be enlarged by reducing the pulling velocity until the diameter of the crystal reaches the desired value.

Shortly before the desired value of the diameter is reached the pulling velocity is raised to the specific value at which the silicon crystal grows with the required diameter. In general the pulling velocity is not kept constant but is reduced towards the bottom of the silicon crystal. This is mainly caused by increasing heat radiation from the crucible walls as the melt level sinks.

To avoid dislocations at the bottom of the silicon crystal the silicon diameter has to be reduced gradually to a small size. While the pulling velocity is increased the diameter of the silicon crystal decreases and an end-cone begins to develop, Figure 2.4. If the diameter is small enough the dislocation-free silicon crystal can be separated from the rest of the silicon melt.

3. Mathematical Model of Czochralski Crystal Growth

In this chapter a mathematical model for the Czochralski crystal growth is constructed in the axisymmetric geometry, Figure 3.1. The model includes equations for global heat transfer and melt flow in the crucible. Global heat transfer includes transient equations for enthalpy (including the definition of the phase change interface) and heat exchange between various surfaces inside of the Czochralski configuration by radiation. The external temperature of the Czochralski furnace and the temperature of the low temperature enclosure are assumed to be known. The melt flow is governed by the transient and cylindrically symmetric Navier-Stokes equations.

We characterize the axisymmetric domains by using the following notations: Crystal - Ω_c , melt - Ω_m , silica crucible - Ω_s , graphite susceptor - Ω_g , graphite resistance heater - Ω_h , crucible shaft Ω_a and thermal shields - Ω_t . Every domain is characterized by different thermophysical properties. In reality these properties, such as the densities, heat capacities and heat conductivities, are temperature dependent. In this work, however, we assume that they are constant in each material.

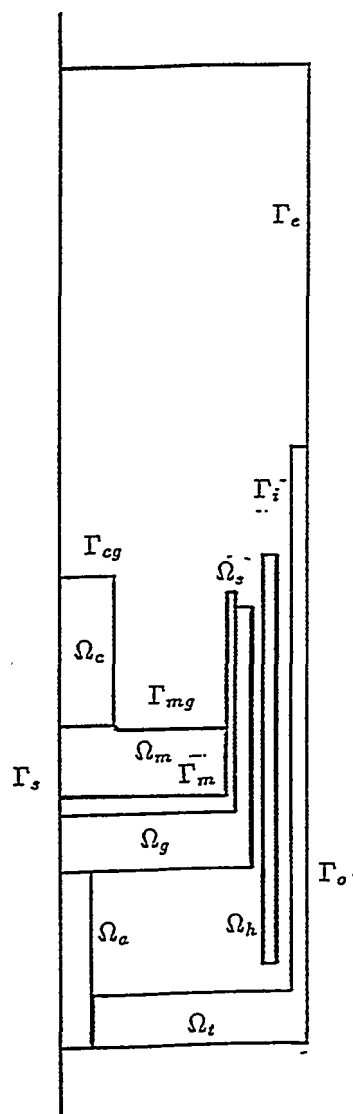


Figure 3.1 Axisymmetric Czochralski crystal growth geometry

The following notations for the boundaries in the system are applied: The crystal-gas interface is denoted by Γ_{cg} , the melt-gas interface by Γ_{mg} and the other interfaces connected to the gas by Γ_i . The melt-silica crucible interface is denoted by Γ_m and the low temperature enclosure by Γ_e . Finally the outer interface is denoted by Γ_o . The cylindrical co-ordinate system (r, z, θ) is centered at the bottom

of the crucible shaft. We emphasize that Γ_e is only a one dimensional object on which temperature is known.

Let us begin with the modeling of radiation. The following discussion is based on the references [6], [13], [14] and [15]. We make the following assumptions: The argon gas within the enclosure is non-participating and an opaque, diffuse and gray behavior from the surfaces is expected.

Consider a set $\Gamma = \Gamma_{cg} \cup \Gamma_{mg} \cup \Gamma_i \cup \Gamma_e$. On Γ heat balance reads as

$$q + J - R = 0, \quad (3.1)$$

where q is heat flux caused by conduction to the surface, J irradiation and R the radiosity on the surface. The radiosity can be expressed as a sum of surface emissive power and reflected irradiation, i.e.,

$$R = E + \rho J, \quad (3.2)$$

where ρ is the reflectivity. If the surface emissive power E is proportional to the corresponding value of a black body, and the Stefan-Boltzmann law and the assumption of the opaque, diffuse and gray surface are used, then

$$R = \sigma \epsilon T^4 + (1 - \epsilon)J. \quad (3.3)$$

Here σ is the Stefan-Boltzmann constant and ϵ the emissivity of the surface.

Irradiation on Γ is proportional to radiation emitted by the different parts of Γ itself due to the equation

$$J(s) = \int_{\Gamma} \omega(s, z) \Xi(s, z) R(z) dz \quad (3.4)$$

for any $s \in \Gamma$. $\omega(s, z)$ is called a view factor and it has a form

$$\omega(s, z) = \frac{n_z \cdot (s - z) n_s \cdot (z - s)}{\pi |s - z|^4}, \quad (3.5)$$

where n_s and n_z are the surface normals directed to the vacuum. In (3.4) $\Xi(s, z)$ is a visibility factor and it has a value 1, if the points s and z see each others otherwise it has a value 0.

If we define an operator

$$K\lambda(s) = \int_{\Gamma} \omega(s, z) \Xi(s, z) \lambda(z) dz \quad \forall s \in \Gamma,$$

we can write $J = KR$ and from (3.3) we get

$$R = \sigma \epsilon T^4 + (1 - \epsilon)KR$$

or

$$R = (I - (1 - \epsilon)K)^{-1} \sigma \epsilon T^4. \quad (3.6)$$

By substituting the definition of R in (3.6) into the equation of the heat balance (3.1) we arrive at

$$q = G(\sigma T^4), \tag{3.7}$$

where

$$G = (I - K)(I - (1 - \epsilon)K)^{-1}\epsilon. \tag{3.8}$$

G can be also written in the form

$$G = (I - \epsilon K(I - (1 - \epsilon)K)^{-1})\epsilon, \tag{3.9}$$

which is an infinite dimensional equivalent of so called Gebhart factors.

Let us consider then global heat transfer induced by conduction and convection containing the phase change between the crystal and melt. Outside of the crystal and melt, heat transfer is described by the heat equation

$$\rho_i c_{p_i} \frac{\partial T_i}{\partial t} - \frac{1}{r} \frac{\partial}{\partial r} \left(r \frac{\partial}{\partial r} k_i T_i \right) - \frac{\partial}{\partial z} \left(\frac{\partial}{\partial z} k_i T_i \right) = \rho_i h_i, \tag{3.10}$$

where the subscript i is associated with separate domains characterized by the density ρ_i , the heat capacity c_{p_i} and the heat conductivity k_i . The heat source h_i is nonzero only in the heater.

On the other hand, we have the enthalpy equation (including a definition of phase change)

$$\frac{\partial}{\partial t} H + \vec{u} \cdot \nabla H - \frac{1}{r} \frac{\partial}{\partial r} \left(r \frac{\partial}{\partial r} k T(H) \right) - \frac{\partial}{\partial z} \left(\frac{\partial}{\partial z} k T(H) \right) = 0 \tag{3.11}$$

in the crystal-melt system, where the functions H and $T(H)$ are defined in a standard way:

$$H(T) = \begin{cases} \rho_c c_{p_c} T, & T < T_f \\ [\rho_c c_{p_c} T_f, \rho_c c_{p_c} T_f + \rho_c L], & T = T_f \\ \rho_m c_{p_m} (T - T_f) + \rho_c c_{p_c} T_f + \rho_c L, & T > T_f, \end{cases} \tag{3.12}$$

$$T(H) = \begin{cases} \frac{1}{\rho_c c_{p_c}} H, & H < \rho_c c_{p_c} T_f \\ T_f, & H \in [\rho_c c_{p_c} T_f, \rho_c c_{p_c} T_f + \rho_c L] \\ \frac{H - \rho_c L - \rho_c c_{p_c} T_f}{\rho_m c_{p_m}} + T_f, & H > \rho_c c_{p_c} T_f + \rho_c L, \end{cases} \tag{3.13}$$

where the subscripts c and m correspond the crystal and the melt, respectively, L is the latent heat and T_f the melting temperature. Thus in the whole system we have two separate equations (3.10) and (3.11) describing heat transfer with appropriate boundary conditions.

Remark 3.1 The enthalpy equation (3.11) offers a way to treat the free boundary problem in the crystal-melt system. If we now make a definition $H = \rho_i c_{p_i} T_i$ in

the heat equation (3.10) we get an equation of the type (3.11) for enthalpy in the whole domain. The equation is, however, not meaningful since enthalpy is discontinuous at the interface between two different materials (for instance at the melt-silica crucible interface).

We proceed by modifying the definition of the enthalpy (equation (3.12)) so that it equals to temperature in the melt region. The definition can be rewritten in the form

$$H(T) = \begin{cases} \rho_c c_{p_c} T - \rho_c L + T_f (\rho_m c_{p_m} - \rho_c c_{p_c}), & T < T_f \\ [\rho_m c_{p_m} T_f - \rho_c L, \rho_m c_{p_m} T_f], & T = T_f \\ \rho_m c_{p_m} T, & T > T_f. \end{cases} \quad (3.14)$$

If we now define a function $\tilde{H} := H/\rho_m c_{p_m}$ we come to an expression (the density and heat capacity of the melt are constant)

$$\tilde{H}(T) = \begin{cases} \frac{\rho_c c_{p_c} T - \rho_c L + T_f (\rho_m c_{p_m} - \rho_c c_{p_c})}{\rho_m c_{p_m}}, & T < T_f \\ [T_f - \frac{\rho_c L}{\rho_m c_{p_m}}, T_f], & T = T_f \\ T, & T > T_f. \end{cases} \quad (3.15)$$

Temperature as a function of \tilde{H} is correspondingly

$$T(\tilde{H}) = \begin{cases} \frac{\rho_m c_{p_m} \tilde{H} + \rho_c L - T_f (\rho_m c_{p_m} - \rho_c c_{p_c})}{\rho_c c_{p_c}}, & \tilde{H} < T_f - \frac{\rho_c L}{\rho_m c_{p_m}} \\ T_f, & \tilde{H} \in [T_f - \frac{\rho_c L}{\rho_m c_{p_m}}, T_f] \\ \tilde{H}, & \tilde{H} > T_f. \end{cases} \quad (3.16)$$

If we now divide the equation (3.10) by $\rho_i c_{p_i}$ and define $\tilde{H} = T$ we come to

$$\frac{\partial}{\partial t} \tilde{H} + \vec{u} \cdot \nabla \tilde{H} - \frac{1}{r} \frac{\partial}{\partial r} \left(r \frac{\partial}{\partial r} \hat{k} T(\tilde{H}) \right) - \frac{\partial}{\partial z} \left(\frac{\partial}{\partial z} \hat{k} T(\tilde{H}) \right) = \hat{f}. \quad (3.17)$$

This equation has exactly the same form as in (3.11) and thus the enthalpy equation of the type (3.17) governs heat transfer in the whole system. The enthalpy \tilde{H} is now continuous at the melt-silica crucible interface since in the crystal and melt it is defined as in (3.15) and in the other parts as $\tilde{H} = T$. In the crystal and melt $\hat{f} = 0$ and $\hat{k} = k/\rho_m c_{p_m}$, where k depends on enthalpy. In the other parts $\hat{k} = k_i/\rho_i c_{p_i}$ and $\hat{f} = h_i/c_{p_i}$.

A mathematical model for the Czochralski crystal growth now reads: Find the velocity vector $\vec{u} = (u_r, u_z, u_\theta)$ and the pressure p in $\Omega_m \times (0, t_0)$ and the enthalpy

\tilde{H} in $\Omega \times (0, t_0)$, where $\Omega = \Omega_m \cup \Omega_c \cup \Omega_s \cup \Omega_g \cup \Omega_h \cup \Omega_a \cup \Omega_t$, such that

$$\left\{ \begin{aligned} \rho_m \frac{\partial u_r}{\partial t} - \frac{\partial \sigma_{zr}}{\partial z} - \frac{1}{r} \frac{\partial}{\partial r} (r \sigma_{rr}) + \frac{1}{r} \sigma_{\theta\theta} + \rho_m \left(u_r \frac{\partial u_r}{\partial r} + u_z \frac{\partial u_r}{\partial z} - \frac{u_\theta^2}{r} \right) &= 0 \\ \rho_m \frac{\partial u_z}{\partial t} - \frac{\partial \sigma_{zz}}{\partial z} - \frac{1}{r} \frac{\partial}{\partial r} (r \sigma_{zr}) + \rho_m \left(u_r \frac{\partial u_z}{\partial r} + u_z \frac{\partial u_z}{\partial z} \right) &= \rho_m g \beta (T - T_0) \\ \rho_m \frac{\partial u_\theta}{\partial t} - \frac{1}{r^2} \frac{\partial}{\partial r} (r^2 \sigma_{r\theta}) - \frac{\partial \sigma_{\theta z}}{\partial z} + \rho_m \left(u_r \frac{\partial u_\theta}{\partial r} + u_z \frac{\partial u_\theta}{\partial z} + \frac{u_r u_\theta}{r} \right) &= 0 \\ \frac{1}{r} \frac{\partial}{\partial r} (r u_r) + \frac{\partial u_z}{\partial z} &= 0 \end{aligned} \right.$$

in $\Omega_m \times (0, t_0)$,

$$\frac{\partial}{\partial t} \tilde{H} + \vec{u} \cdot \nabla \tilde{H} - \frac{1}{r} \frac{\partial}{\partial r} \left(r \frac{\partial}{\partial r} \hat{k} T(\tilde{H}) \right) - \frac{\partial}{\partial z} \left(\frac{\partial}{\partial z} \hat{k} T(\tilde{H}) \right) = \hat{f}$$

in $\Omega \times (0, t_0)$ with the initial and boundary conditions

$$\left\{ \begin{aligned} \vec{u}(r, z, 0) &= \vec{u}^0(r, z) \text{ in } \Omega_m \cup \Omega_c \\ \tilde{H}(r, z, 0) &= \tilde{H}^0(r, z) \text{ in } \Omega \\ u_r = 0, \frac{\partial u_z}{\partial r} = 0, u_\theta = 0 &\text{ on } (\Gamma_s \cap \Omega_m) \times (0, t_0) \\ \frac{\partial T(\tilde{H})}{\partial r} &= 0 \text{ on } (\Gamma_s \cap \Omega) \times (0, t_0) \\ u_r = 0, u_z = 0, u_\theta = \omega_m r &\text{ on } \Gamma_m \times (0, t_0) \\ \vec{u} \cdot \vec{n} = 0, \sigma_n = \frac{\gamma_0}{R} - p_a, \sigma_\tau = \frac{\partial \gamma}{\partial \tau} &\text{ on } \Gamma_{mg} \times (0, t_0) \\ u_r = 0, u_z = 0, u_\theta = \omega_c r &\text{ on } \Sigma \times (0, t_0), \\ \rho_m \vec{u}_m \cdot \vec{n}_\Sigma - \rho_c \vec{u}_c \cdot \vec{n}_\Sigma &= (\rho_m - \rho_c) \vec{u}_\Sigma \cdot \vec{n}_\Sigma \text{ on } \Sigma \times (0, t_0) \\ -\hat{k} \frac{\partial T(\tilde{H})}{\partial n} &= G(\hat{\sigma}(T(\tilde{H}))^4) \text{ on } (\Gamma_{mg} \cup \Gamma_{cg} \cup \Gamma_i) \times (0, t_0) \\ -\hat{k} \frac{\partial T(\tilde{H})}{\partial n} &= \hat{\alpha}(T(\tilde{H}) - T_{ext}) \text{ on } \Gamma_o \times (0, t_0) \\ \tilde{H} &= \tilde{H}_e \text{ on } \Gamma_e \times (0, t_0). \end{aligned} \right.$$

Remark 3.2 A division of the heat equation (3.10) by $\rho_i c_{p_i}$ leads to a scaling of the boundary conditions for $T(\tilde{H})$. We denote the scaled heat transfer coefficient and the Stefan-Boltzmann coefficient by $\hat{\alpha} = \alpha / \rho_i c_{p_i}$ and $\hat{\sigma} = \sigma / \rho_i c_{p_i}$, respectively, where ρ_i and c_{p_i} are characterized by each material.

Remark 3.3 In the mathematical model presented above we assumed that the Boussinesq approximation is valid in the melt. This means that the density of the

in $(\Omega_m \cup \Omega_c) \times (0, t_0)$,

$$\frac{\partial}{\partial t} \bar{H} + \bar{u} \cdot \nabla \bar{H} - \frac{1}{r} \frac{\partial}{\partial r} \left(r \frac{\partial}{\partial r} \hat{k} T(\bar{H}) \right) - \frac{\partial}{\partial z} \left(\frac{\partial}{\partial z} \hat{k} T(\bar{H}) \right) = \hat{f}$$

in $\Omega \times (0, t_0)$ with the initial and boundary conditions

$$\begin{cases} \bar{u}(r, z, 0) = \bar{u}^0(r, z) & \text{in } \Omega_m \cup \Omega_c \\ \bar{H}(r, z, 0) = \bar{H}^0(r, z) & \text{in } \Omega \end{cases}$$

$$\left\{ \begin{array}{l} u_r = 0, \quad \frac{\partial u_z}{\partial r} = 0, \quad u_\theta = 0, \quad \text{on } (\Gamma_s \cap (\Omega_m \cup \Omega_c)) \times (0, t_0) \\ \frac{\partial T(\bar{H})}{\partial r} = 0 \quad \text{on } \Gamma_s \times (0, t_0) \\ u_r = 0, \quad u_z = 0, \quad u_\theta = \omega_m r \quad \text{on } \Gamma_m \times (0, t_0) \\ \bar{u} \cdot \bar{n} = 0, \quad \sigma_n = \frac{\gamma_0}{R} - p_a, \quad \sigma_\tau = -\vartheta \gamma_0 \frac{\partial T(\bar{H})}{\partial \tau} \quad \text{on } \Gamma_{mg} \times (0, t_0) \\ u_r = 0, \quad u_z = 0, \quad u_\theta = \omega_c r \quad \text{on } \Gamma_{cg} \times (0, t_0) \\ -\hat{k} \frac{\partial T(\bar{H})}{\partial n} = G(\hat{\sigma}(T(\bar{H})))^4 \quad \text{on } (\Gamma_{mg} \cup \Gamma_{cg} \cup \Gamma_i) \times (0, t_0) \\ -\hat{k} \frac{\partial T(\bar{H})}{\partial n} = \hat{\alpha}(T(\bar{H}) - T_{ext}) \quad \text{on } \Gamma_o \times (0, t_0) \\ \bar{H} = \bar{H}_e \quad \text{on } \Gamma_e \times (0, t_0) \end{array} \right.$$

+ transmission conditions $\hat{k}_i \frac{\partial T_i(\bar{H})}{\partial n} = \hat{k}_j \frac{\partial T_j(\bar{H})}{\partial n}$, $i \neq j$, on the common boundaries of two different materials.

The finite element analysis contains the variational formulation of the Navier-Stokes and enthalpy equations. They are derived in [7] and we refer from these parts therein. We emphasize that the shape of the melt-gas interface is based on the analytical representation of the shape of the meniscus presented by Hurle. Therefore we can neglect the boundary condition $\sigma_n = \frac{\gamma_0}{R} - p_a$ on Γ_{mg} .

4.1 Computation of the View Factors

On the internal boundary $\Gamma_{mg} \cup \Gamma_{cg} \cup \Gamma_i$ the boundary condition for enthalpy contains an infinite dimensional Gebhart factor G . In the finite element analysis a finite dimensional equivalent of the Gebhart factor is achieved by introducing a view factor

$$F_{ij} = \frac{1}{A_i} \int_{A_i} \int_{A_j} \frac{\bar{n}_i \cdot (\bar{x}_j - \bar{x}_i) \bar{n}_j \cdot (\bar{x}_i - \bar{x}_j)}{\pi |\bar{x}_i - \bar{x}_j|^4} \Xi(\bar{x}_i, \bar{x}_j) dA_i dA_j, \quad (4.1)$$

and replacing the integral operator K in the equation (3.9) with this factor. In (4.1) A_i and A_j represent the element surface areas, $\bar{x}_i \in A_i$, $\bar{x}_j \in A_j$ and \bar{n}_i and \bar{n}_j are the corresponding outward unit normals. $\Xi(\bar{x}_i, \bar{x}_j)$ is the visibility factor.

The view factor F_{ij} represents the fraction of energy leaving a surface i which reaches a surface j . In axisymmetric geometry surfaces are cutted cones (in certain cases also cylinders or planes) which are generated by rotating two dimensional element boundaries around the symmetry axis. By taking into account the rotational symmetry we get

$$\begin{aligned}
 F_{ij} &= \frac{1}{A_i} \int_{A_i} \int_{A_j} \frac{\vec{n}_i \cdot (\vec{x}_j - \vec{x}_i) \vec{n}_j \cdot (\vec{x}_i - \vec{x}_j)}{\pi |\vec{x}_i - \vec{x}_j|^4} \Xi(\vec{x}_i, \vec{x}_j) dA_i dA_j \\
 &= \frac{2}{A_i} \int_{\Gamma_i} r_i \int_{A_j} \frac{\vec{n}_i(\theta_i) \cdot (\vec{x}_j - \vec{x}_i) \vec{n}_j \cdot (\vec{x}_i - \vec{x}_j)}{|\vec{x}_i - \vec{x}_j|^4} \Xi(\vec{x}_i, \vec{x}_j) dA_j d\Gamma_i \\
 &= \frac{2}{A_i} \int_{\Gamma_i} r_i \int_{\Gamma_j} r_j \int_0^{2\pi} \frac{\vec{n}_i(\theta_i) \cdot (\vec{x}_j - \vec{x}_i) \vec{n}_j(\theta_j) \cdot (\vec{x}_i - \vec{x}_j)}{|\vec{x}_i - \vec{x}_j|^4} \Xi(\vec{x}_i, \vec{x}_j) d\theta_j d\Gamma_j d\Gamma_i.
 \end{aligned} \tag{4.2}$$

Here Γ_i is the cross section of A_i on the r - z -plane. For simplicity we can assume that $\theta_i = 0$. The computer program which computes the view factors was developed at the Center for Scientific Computing by Mr. J. Katajamäki. The implementation includes the determination of the visibility factor in the axisymmetric Czochralski geometry and the numerical integration of the view factors. The integration is based on the Stokes theorem and the integrals are evaluated numerically by using the Gaussian integration points. For further details we refer to [8].

4.2 Numerical Simulation

The finite element discretization of the Navier-Stokes and enthalpy equations produces the matrix equations [7]

$$\begin{aligned}
 M^u \frac{\partial u_r}{\partial t} + A_{rr} u_r + A_{rz} u_z + A_{r\theta} u_\theta &= -G_r^u + D_r^u \\
 M^u \frac{\partial u_z}{\partial t} + A_{zr} u_r + A_{zz} u_z &= F^u - G_z^u + D_z^u, \\
 M^u \frac{\partial u_\theta}{\partial t} + A_{\theta r} u_r + A_{\theta z} u_z + A_{\theta\theta} u_\theta &= D_\theta^u, \\
 M^H \frac{\partial \bar{H}}{\partial t} + C^H \bar{H} + K^H T(\bar{H}) + G^H T^4(\bar{H}) + B T(\bar{H}) &= F_1^H + F_2^H.
 \end{aligned}$$

Here the matrices D_r^u , D_z^u and D_θ^u contain the Dirichlet data.

The matrix equations for the velocity components are applied in the crystal and melt whereas the matrix equation for the enthalpy is applied in the entire geometry. We emphasize that the velocity field is computed by using the variable viscosity method. The discretized Navier-Stokes equations are nonlinear and the nonlinearity caused by convection is treated by the Newton's linearization technique. The pressure is eliminated from the Navier-Stokes equations by the penalty method. The velocity field depends on temperature. At each time step we uncouple the computation of velocity and enthalpy, and the temperature field is computed afterwards from the values of enthalpy.

We discretize the Navier-Stokes equations by the backward Euler method in time. The time discretization of the enthalpy equation is handled explicitly so that the radiation part is taken from the previous time step.

Quantity	Value
Density of crystal	2490.0 kg/m^3
Density of melt	2490.0 kg/m^3
Density of silica crucible	2200.0 kg/m^3
Density of graphite	1600.0 kg/m^3
Density of felt	100.0 kg/m^3
Heat capacity of crystal	900.0 J/kgK
Heat capacity of melt	1000.0 J/kgK
Heat capacity of silica crucible	1300.0 J/kgK
Heat capacity of graphite	2100.0 J/kgK
Heat capacity of felt	1010.0 J/kgK
Heat conductivity of crystal	22.0 W/mK
Heat conductivity of melt	64.0 W/mK
Heat conductivity of silica crucible	6.0 W/mK
Heat conductivity of graphite	60.0 W/mK
Heat conductivity of felt	0.4 W/mK
Emissivity of crystal	0.7
Emissivity of melt	0.3
Emissivity of silica crucible	0.35
Emissivity of graphite	0.8
Emissivity of felt	1.0
Emissivity of low temperature enclosure	1.0
Heating power	70 kW/kg
External temperature of the Cz-furnace	500.0 K
Heat transfer coefficient	40.0 W/m^2K
Temperature of low temperature enclosure	900.0 K
Melting temperature	1685.0 K
Latent heat	1800.0 kJ/kg
Stefan-Boltzmann constant	$5.67 \cdot 10^{-8} W/m^2 K^4$
Viscosity of melt	0.00075 kg/ms
Surface tension coefficient	0.72 N/m
Temperature coefficient of surface tension	0.00013881/ K
Heat expansion coefficient	0.00014 $1/K$
Reference temperature	1685.0 K
Gravity	9.82 m/s^2

Table 4.1 Material parameters in Czochralski silicon crystal growth

Component	Material	Height	Radius/Thickn.
Crystal	Silicon	20.0 cm	6.35 cm
Melt	Silicon	12.0 cm	20.0 cm
Crucible bottom	Silica	1.0 cm	21.0 cm
Crucible side	Silica	27.5 cm	1.0 cm
Susceptor bottom	Graphite	6.6 cm	23.0 cm
Susceptor side	Graphite	30.4 cm	2.0 cm
Heater	Graphite	54.8 cm	1.5 cm
Crucible shaft	Graphite	23.5 cm	3.6 cm
Thermal shields bottom	Graphite, felt	9.0 cm	27.5 cm
Thermal shields side	Graphite, felt	79.9 cm	2.0 cm

Table 4.2 Czochralski construction

In the submatrices containing the convection terms the modified basis functions proposed by Brooks and Hughes are used. The linearization of the discretized Navier-Stokes equations and the uncoupling with temperature produces a linear matrix equation for the velocity which is solved by the Gaussian elimination. For the enthalpy the SOR method is used. The SOR iteration at each time step is terminated when the relative error is less than 10^{-3} . The limit 10^{-2} for the relative error of velocity causes the termination of the Navier-Stokes iteration. The penalty parameter in the Navier-Stokes equation is chosen to be 10^{-7} . At each time step the uncoupled problem is solved only once.

In the Czochralski silicon crystal growth every material is characterized by the different thermophysical properties which are listed in Table 4.1. In Table 4.2 the details of the Czochralski construction used in this work are explained.

The finite element mesh which is used throughout the simulations is depicted in Figure 4.1. The mesh consists of 3632 quadrilateral elements and 3849 nodes. The number of surface elements required in the view factor computation is 315.

The temperature and velocity fields and the position of the crystal-melt interface are the quantities which we are most interested in. We visualize the numerical results of the computations in the following manner. The temperature distribution in the whole geometry is presented with 50 temperature contours between the minimum and maximum temperature values. In the melt region the temperature and velocity fields and the position of the crystal-melt interface are additionally shown. The temperature field consists of 10 contours between the melting point temperature T_f and $T_f + 30$.

In the following we simulate heat transfer in the whole geometry and the melt flow induced by all convection mechanisms (Grashof and Marangoni convections, rotation of crystal -5 rpm and rotation of crucible 5 rpm). An initial guess for the flow field is obtained by taking into account only the Grashof and Marangoni convections and rotation of the crystal. The simulation is carried out 12 seconds. The time step is 0.05 seconds in order to guarantee the convergence of the Navier-Stokes iteration.

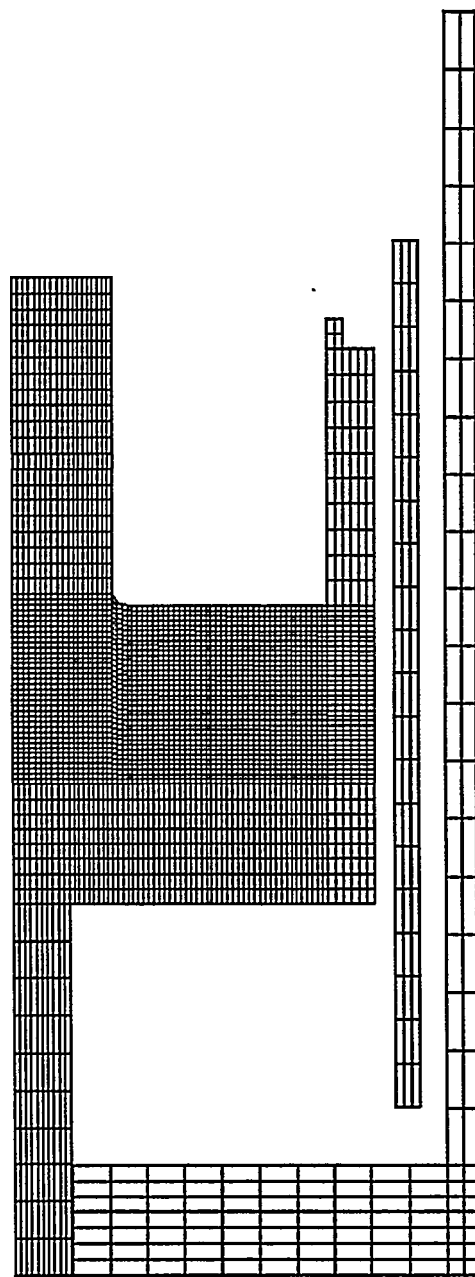


Figure 4.1 Finite element mesh in Czochralski crystal growth

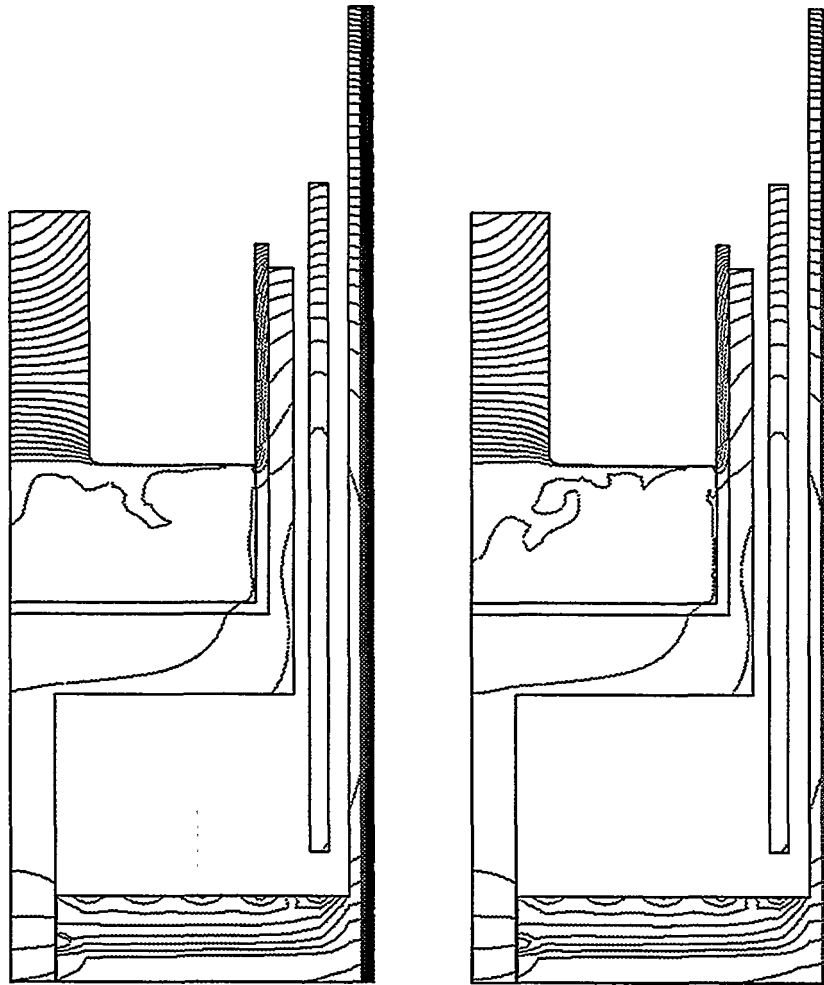


Figure 4.2 Temperature fields at $t = 3$ s (left), $t = 6$ s (right), Grashof and Marangoni convections, rotation of crystal and crucible (-5 and 5 rpm)

At the beginning of the simulation the melt flow behaves relatively well, but oscillations occur when the simulations have proceeded for a while. The time frame is short compared to the real crystal growth occurrence. This is because we have great difficulties in maintaining the convergence in the Navier-Stokes iterations. In fact in the simulation we lose the convergence. On the other hand this is not surprising and strengthens our impression of the three dimensional character of the melt flow. Our own experiences show that the main reason for the loss of convergence is the effect of the Grashof convection and the rotations of the crystal and crucible.

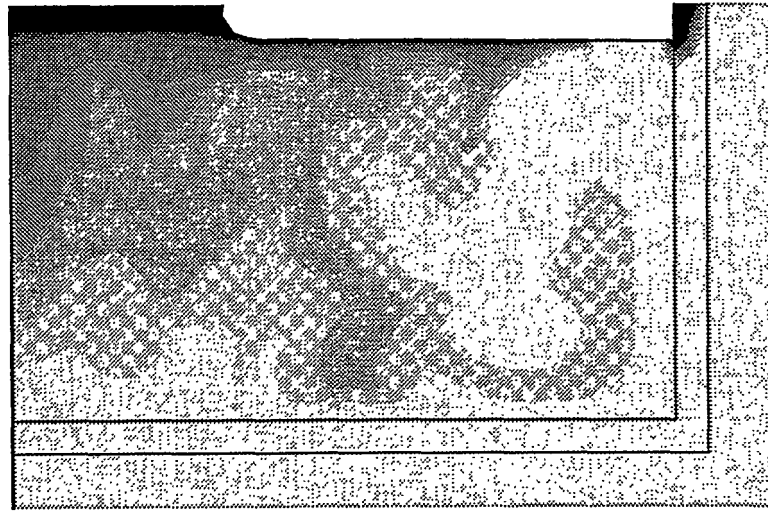


Figure 4.3a Temperature field in melt induced by Grashof and Marangoni convection and rotation of crystal and crucible (-5 and 5 rpm) at $t = 3$ s

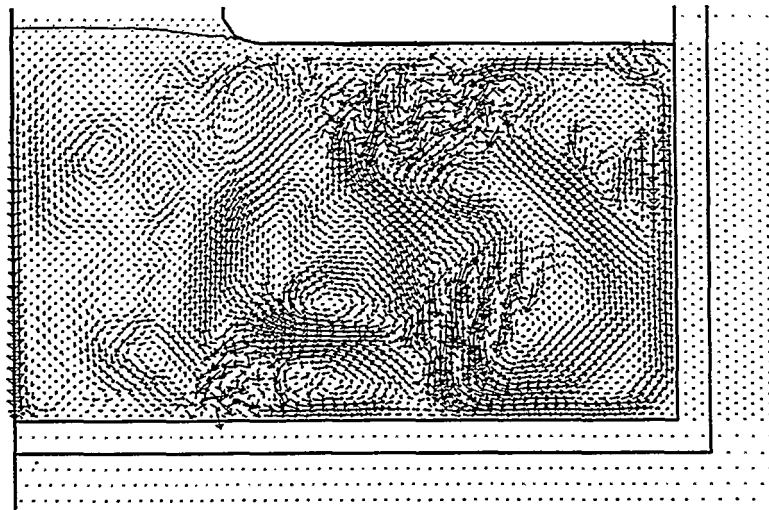


Figure 4.3b Velocity field in melt induced by Grashof and Marangoni convection and rotation of crystal and crucible (-5 and 5 rpm) at $t = 3$ s

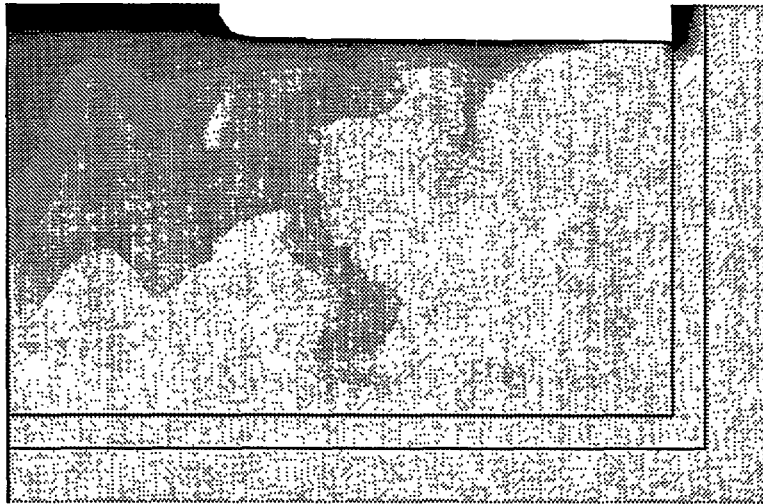


Figure 4.4a Temperature field in melt induced by Grashof and Marangoni convection and rotation of crystal and crucible (-5 and 5 rpm) at $t = 6$ s

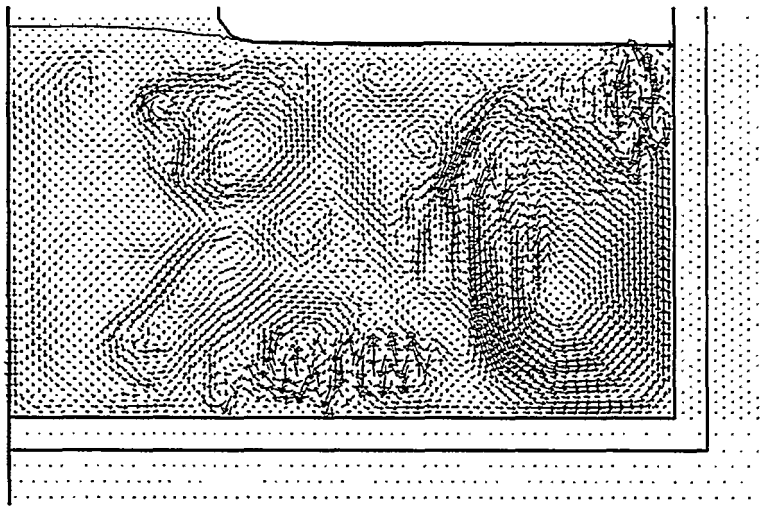


Figure 4.4b Velocity field in melt induced by Grashof and Marangoni convection and rotation of crystal and crucible (-5 and 5 rpm) at $t = 6$ s

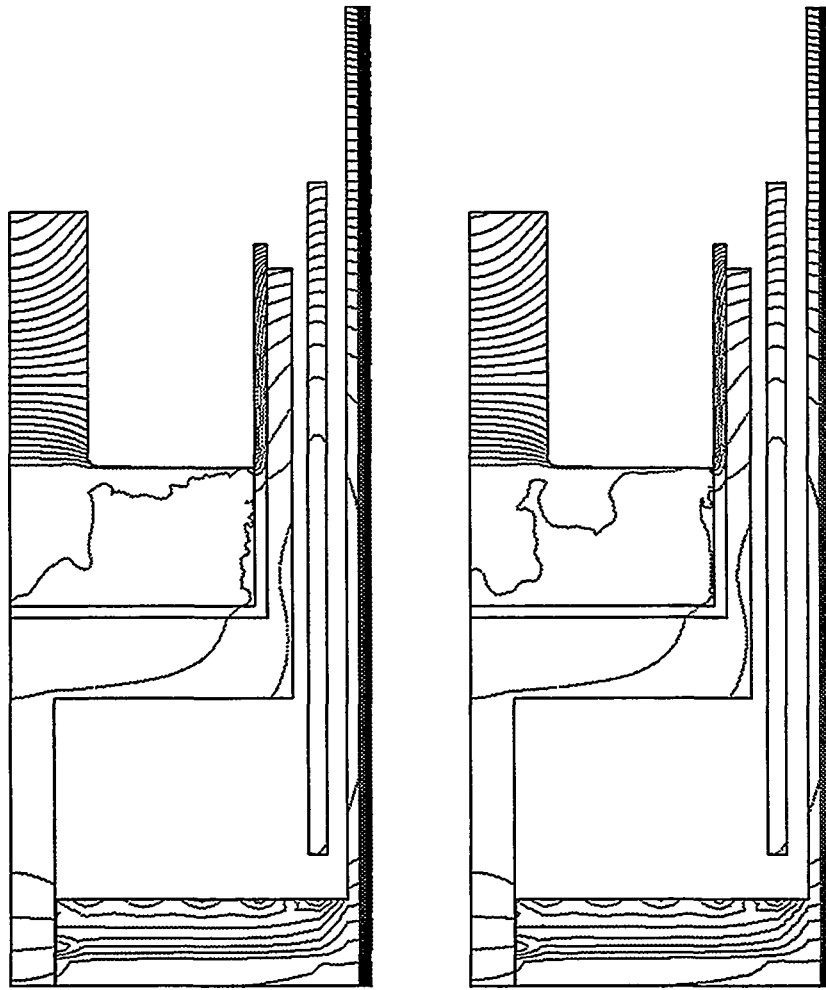


Figure 4.5 Temperature fields at $t = 9$ s (left), $t = 12$ s (right), Grashof and Marangoni convections, rotation of crystal and crucible (-5 and 5 rpm)

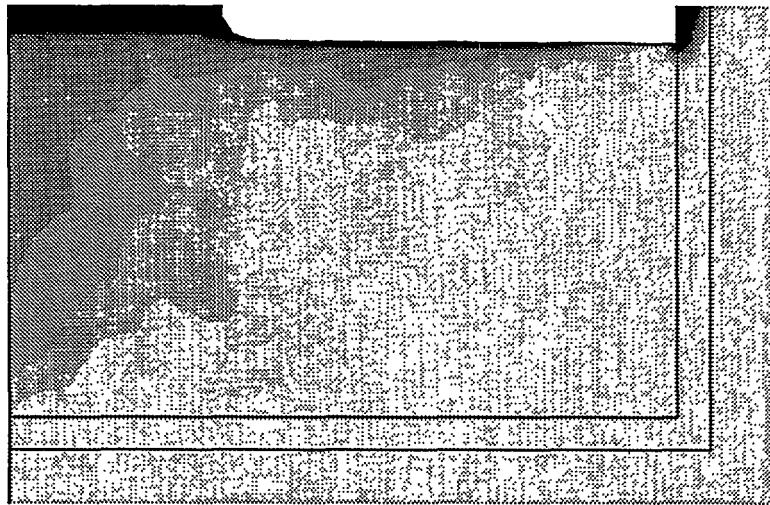


Figure 4.6a Temperature field in melt induced by Grashof and Marangoni convection and rotation of crystal and crucible (-5 and 5 rpm) at $t = 9$ s

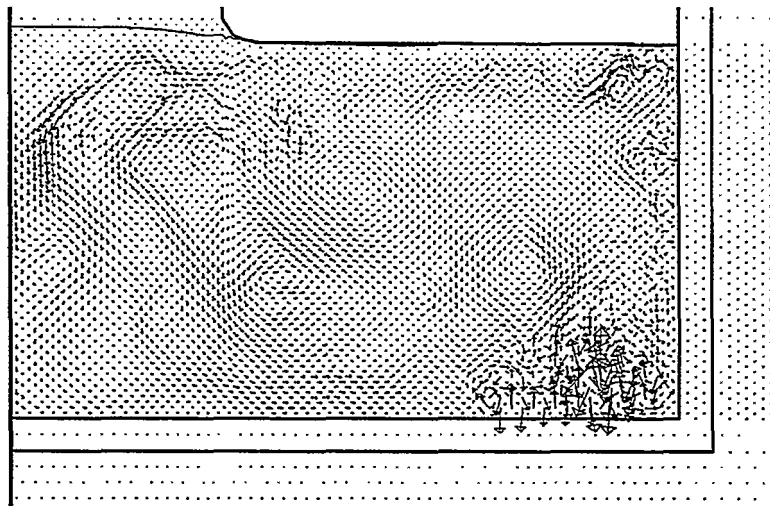


Figure 4.6b Velocity field in melt induced by Grashof and Marangoni convection and rotation of crystal and crucible (-5 and 5 rpm) at $t = 9$ s

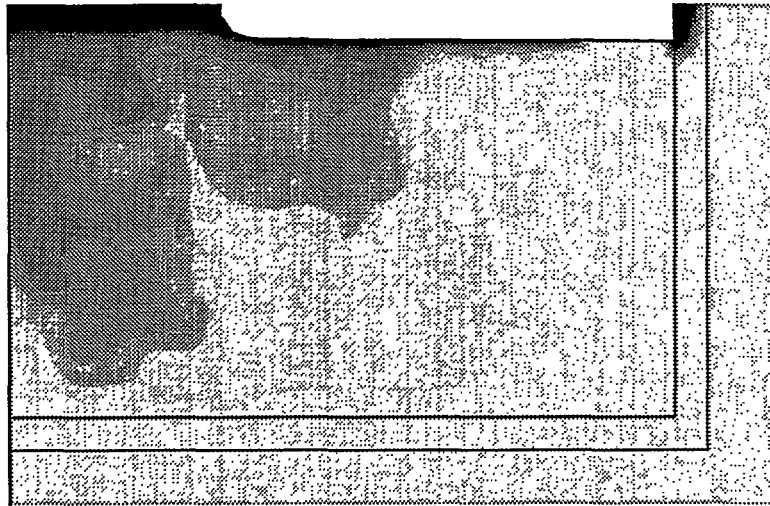


Figure 4.7a Temperature field in melt induced by Grashof and Marangoni convection and rotation of crystal and crucible (-5 and 5 rpm) at $t = 12$ s

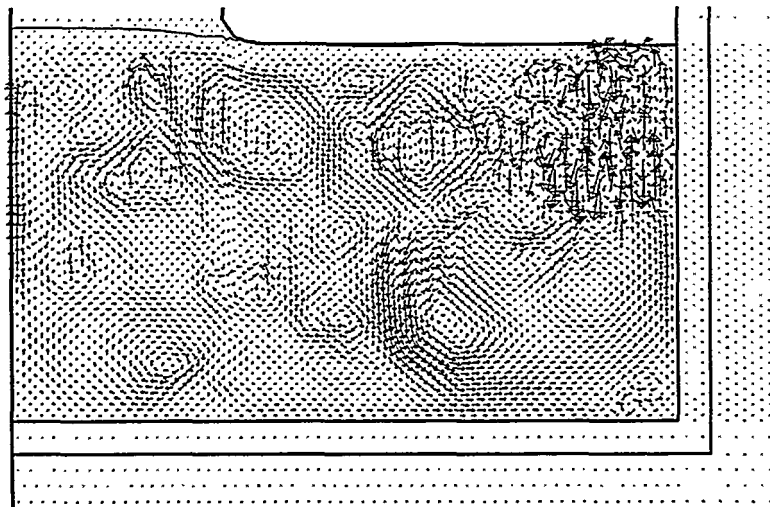


Figure 4.7b Velocity field in melt induced by Grashof and Marangoni convection and rotation of crystal and crucible (-5 and 5 rpm) at $t = 12$ s

5. References

- " [1]" L.J. Atherton, J.J. Derby, R.A. Brown, *Radiative Heat Exchange in Czochralski Crystal Growth*, Journal of Crystal Growth 84 (1987), pp. 57-78.
- " [2]" C. Cuvelier, J.M. Driessen, *Thermocapillary Free Boundaries in Crystal Growth*, J. Fluid Mech. (1986), vol. 169, pp. 1-26.
- " [3]" A.J. Dalhuijsen, A. Segal, *Comparison of Finite Element Techniques for Solidification Problems*, International Journal for Numerical Methods in Engineering, Vol. 23, pp. 1807-1829 (1986).
- " [4]" C.M. Elliot, J.R. Ockendon, *Weak and Variational Methods for Moving Boundary Problems*, Research Notes in Mathematics, Res. Notes Math., Pitman, 1982.
- " [5]" D.T.J. Hurle, G. Müller, R. Nitsche, *Crystal Growth from the Melt*, Fluid Sciences and Material Science in Space, H.U. Walter (editor), pp. 313-354, Springer-Verlag, 1987.
- " [6]" F.P. Incropera, D.P. De Witt, *Fundamentals of Heat and Mass Transfer*, Second Edition, John Wiley and Sons, 1985.
- " [7]" J.Järvinen, *Mathematical Modeling and Numerical Simulation of Czochralski Silicon Crystal Growth*, Ph.D. Thesis, To be published at the Department of Mathematics, University of Jyväskylä, 1996.
- " [8]" J. Katajamäki, *Microcomputer Implementation of a Silicon Crystal Growth Simulation Program (in finnish)*, M.Sc. Thesis, Technical University of Helsinki, Department of Technical Physics, 1993.
- " [9]" T.A. Kinney, D.E. Bornside, R.A. Brown, *Quantitative Assessment of an Integrated Hydrodynamic Thermal-capillary Model for Large-diameter Czochralski Growth of Silicon: Comparison of Predicted Temperature Field with Experiment*, Journal of Crystal Growth 126 (1993), pp. 413-434.
- " [10]" G. Müller, *Numerical Simulation of Crystal Growth Process*, Symposium Technisch-Wissenschaftliches Hochleistungsrechnen, München, Juli, 1993.
- " [11]" P.A. Ramachandran, M.P. Duduković, *Simulation of Temperature Distribution in Crystals Grown by Czochralski Method*, Journal of Crystal Growth 71 (1985), pp. 399-408.
- " [12]" P.A. Sackinger, R.A. Brown, *A Finite Element Method for Analysis of Fluid Flow, Heat Transfer and Free Interfaces in Czochralski Growth*, International Journal for Numerical Methods in Fluids, Vol. 9, pp. 453-492 (1989).
- " [13]" E.M. Sparrow, R.D. Cess, *Radiation Heat Transfer*, Hemisphere Publishing Company, 1978.
- " [14]" T. Tiihonen, *Stefan-Boltzmann Radiation on Non-convex Surfaces*, Preprint 172, University of Jyväskylä, Department of Mathematics, September 1994.
- " [15]" T. Tiihonen, *Stefan Problem with Non-local Radiation Condition*, to be published.
- " [16]" M. Watanabe, M. Eguchi, K. Kakimoto, T. Hibiya, *Double-beam X-ray*

Radiography System for Three-dimensional Flow Visualization of Molten Silicon Convection, Journal of Crystal Growth 133 (1993), pp. 23-28.

" [17]" R.E. White, *An Enthalpy Formulation of the Stefan Problem*, SIAM J. Numer. Anal. Vol.19, No. 6, December 1982.

" [18]" W. Zulehner, D. Huber, *Czochralski-Grown Silicon*, Crystals, vol. 8, pp. 1-144, Springer-Verlag, 1982.

For Your Notes

1950

Analysis of a waste-heat boiler by CFD simulation

Yongxiang Yang, Ari Jokilaakso*
Helsinki University of Technology
Vuorimiehentie 2 K
FIN-02150 Espoo, Finland
*Academy of Finland

Abstract

Waste-heat boilers play important roles in the continuous operation of a smelter and in the conservation of energy. However, the fluid flow and heat transfer behaviour has not been well studied, concerning the boiler performance and design. This paper describes simulated gas flow and heat transfer of a waste-heat boiler in the Outokumpu copper flash smelting process. The governing transport equations for the conservation of mass, momentum and enthalpy were solved with a commercial CFD-code PHOENICS. The standard k- ϵ turbulence model and a composite-flux radiation model were used in the computations. The computational results show that the flow is strongly recirculating and distinctly three-dimensional in most part of the boiler, particularly in the radiation section. The predicted flow pattern and temperature distribution were in a good agreement with laboratory models and industrial measurements. The results provide detailed information of flow pattern, the temperature distribution and gas cooling efficiency. The CFD proved to be a useful tool in analysing the boiler operation.

INTRODUCTION

The Outokumpu flash smelting process [1] is widely used for production of primary copper and nickel as an energy efficient and environmentally clean technology. In this process, horizontal waste-heat boilers are normally used for cleaning and cooling the gases from both flash smelting furnaces and converters.

The waste-heat boiler consists of two consecutive parts: radiation and convection sections, as can be seen in Fig. 1. The high temperature flue gas with fine molten or semi-molten dust from the smelting furnace cools, while the molten dust is solidified and partly separated from the gas phase. In the radiation section, the oxide dust is partly sulphated in SO_2 atmosphere before entering the convection section. The radiation section is normally equipped with a number of radiation screens to increase the heat transfer surfaces. In the upper part of the convection section, a number of tube-banks are implemented in order to efficiently extract the heat by convection. On the bottom of both sections, there are several dust hoppers to collect captured dust. The boiler walls and the plates or tube-banks are cooled by circulating high-pressure water-steam mixture.

In industrial operation, sometimes, part of the cooled off-gas is recirculated to the radiation section from the electrostatic precipitator in order to more efficiently cool the dust-laden off-gas, to assist dust sulphating reactions, and to decrease the thermal load, hot corrosion, and erosion on the top wall of the radiation section. Additionally, cold air leakage into the boiler always occurs in practice, which may affect the local flow pattern and heat transfer.

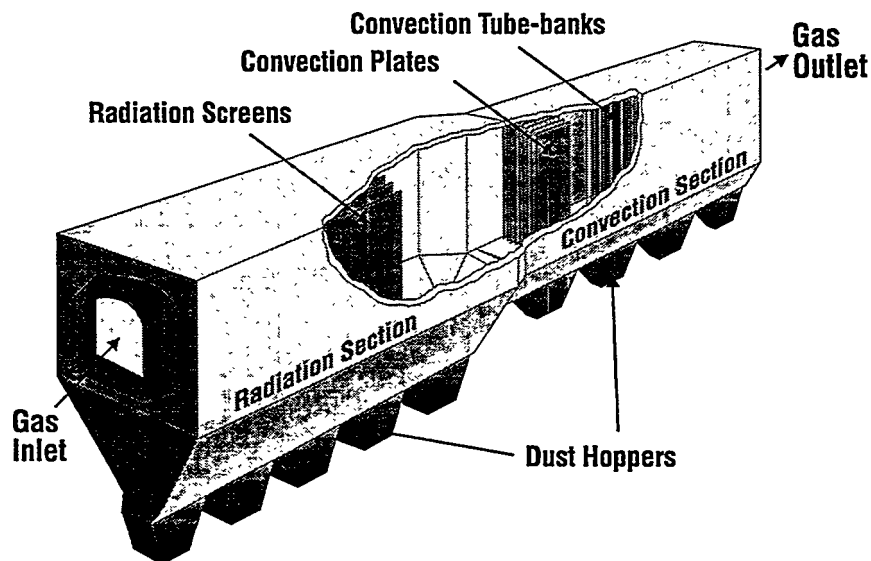


Fig. 1 – A schematic presentation of the waste-heat boiler.

Continuous and smooth operation of the waste-heat boilers plays an important role in maintaining the continuity of the whole smelting process. Nowadays, the boiler is regarded as an integrated part of the metallurgical process, not as a separate apparatus just used for gas cooling [2]. Dust build-ups and tube leaks are two challenging problems to overcome for most of the boiler operations. These two major problems are closely related to the gas flow pattern and heat transfer features of the boiler. The aerodynamic study is important in boiler design and modification for optimal performance.

Physical modelling work on the waste-heat boiler on a laboratory scale has continuously been carried out by Outokumpu Research Oy, Pori, Finland, for more than two decades [3-4]. In contrast, only a limited number of publications have been found concerning the flow and temperature distribution or temperature measurements in the waste-heat boilers [5-6]. It is difficult to simulate high temperature processes in laboratory physical models, and thus a different modelling approach with heat transfer is required. Computational Fluid Dynamics (CFD) provides a convenient tool to fulfil this need, combined with validations from experimental or industrial measurements and laboratory scale physical model results.

In the present study, computer modelling with commercial software was chosen to simulate the fluid flow, heat and mass transfer processes in the waste-heat boiler. This paper presents the results of the flow and heat transfer in a commercial waste-heat boiler of the Outokumpu copper flash smelting process. The simulation results are expected to give more information about the flow pattern and thermal performance of the boiler. This is essential for analysing the operation and eventually improving the energy efficiency and dust separation by helping to modify the design and dimensions of the boiler.

COMPUTATIONS

Transport processes of gas flow, heat and mass transfer in waste-heat boilers are governed by a set of partial differential equations (PDEs). The transport equations are solved numerically with a general purpose CFD-code PHOENICS [7]. The standard $k-\epsilon$ two-equation model was chosen to estimate gas turbulence and a composite-flux model was used for the computation of the radiation fluxes and the enthalpy source for heat transfer in the present study.

The waste-heat boiler operated in Outokumpu Harjavalta Metals Oy at Harjavalta, Finland before May 1995 for copper production was simulated with a Cartesian grid for the radiation section. This grid consists of 25,350 cells, and it was used to study both the symmetric and asymmetric circulation of cooler off-gases from the electrostatic precipitator. A few Body-Fitted Co-ordinate (BFC) grids were also used to simulate the full boiler domain. The following conditions were assumed for the needs of the computation.

- Only gas-phase was considered in the flow and heat transfer simulation. The heat release from dust sulphating reactions and SO₃ formation was thermodynamically estimated and included in the heat transfer computation as macroscopic enthalpy sources.
- Ambient air was assumed to leak into the boiler through 5 rectangular narrow slots in the bottom of the dust hoppers in the radiation section.
- In the full boiler models, the convection tube-banks were simplified to groups of thin blockages with similar total surface area to the reality.

The volume flow rate and inlet temperatures of different gases [8] are summarised in Table I. The logarithmic wall functions were applied to the solid surfaces, and the fixed wall temperatures at different values were defined.

Table I General boundary conditions in the boiler simulation.

Item	Property	Values
Process	Temperature (°C)	1350
Gas	Vol. flow rate (Nm ³ /h)	19,100
Circulated	Temperature (°C)	200
Off-gas	Vol. flow rate (Nm ³ /h)	7,000
Leakage	Temperature (°C)	25
Air	Vol. flow rate (Nm ³ /h)	1,560 (total)

The off-gas from the flash smelting furnace is composed mainly of SO₂ and N₂ with small amounts of CO₂, H₂O and O₂. In the flow and heat transfer simulation, the thermophysical properties were defined as temperature dependent functions at the specified composition. The radiation properties were estimated according to the three absorbing-emitting components SO₂, CO₂ and H₂O. The emissivity of the different components was calculated from Hottel's chart [9] except SO₂ which was from the chart of Chan and Tien [10]. The mixture absorption coefficient was calculated from the boiler characteristic length (L) in relation to the total emissivity of the gas mixture [11]:

$$K_a = -\ln(1-\epsilon) / L \quad (1),$$

where L is the mean beam length estimated with the volume of the boiler domain (V) and the total surface area experiencing the radiation heat transfer (A): $L=3.6V/A$. The emissivity values of the gas components were averaged at temperatures of 800 - 1200°C. The scattering is significant only for the dust particles, and its contribution was averaged with the dust loading of 150 - 220 g/Nm³ and 10 - 50 µm particle size.

RESULTS AND DISCUSSION

Gas flow and mixing

General Flow Pattern. The flow in the waste-heat boiler was found to be clearly three-dimensional which is not shown by two-dimensional models. The flow is obviously recirculating, especially in the radiation section. The velocity near the boiler ceiling is high and forward. The flow inside the upper convection section is generally horizontal and rather uniform. The side-wise flow cross the tube-banks cannot be accurately predicted due to the simplification of the tube-banks. Fig. 2 illustrates the general flow pattern near the centreline of the boiler for the radiation section and the full boiler.

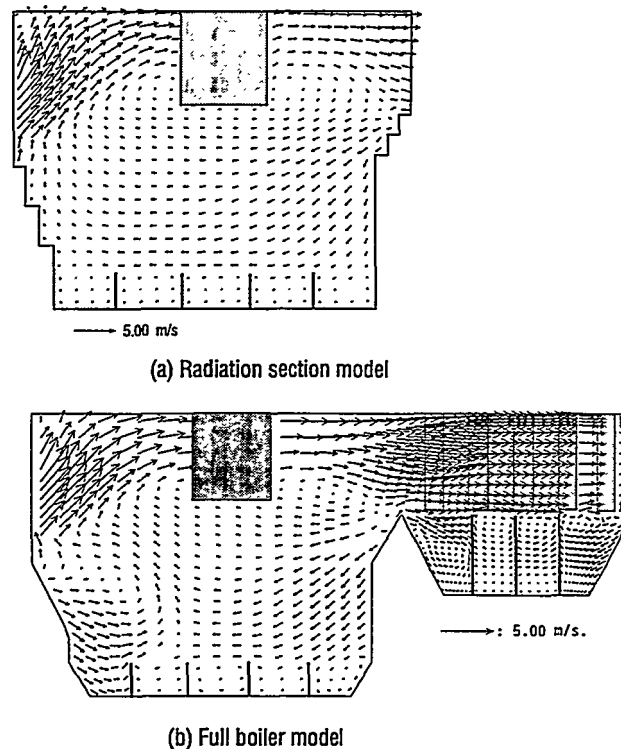


Fig. 2 – Gas flow pattern near the centreline of the boiler: (a) radiation section (Cartesian grid), (b) full boiler (BFC grid).

Symmetric Off-gas Circulation. The symmetric circulation of the cooler off-gas was estimated mainly in the Cartesian grid of the radiation section. The incoming velocity of the circulation off-gas is 12.44 m/s. The effect of the circulated off-gas on the original flow pattern is very significant. The recirculating back flow near the centreline in the lower part of the radiation section somehow changes to down and forward flow, and the influence is spread to a broader extent in the width direction. The velocity vectors at some planes are shown in Fig. 3. At the front-view planes, it can be seen that two mir-

rored swirls are generated in the upper part of the radiation section. The swirls are significant in the whole section. However, the existence of the radiation screens depresses the swirls. In this model, leakage air was also included.

Asymmetric Off-gas Circulation. Asymmetric circulation of the cooler off-gas complicates the flow pattern significantly. The flow field is non-uniform in both front-view cross-sections and in side-view cross-sections. The downward fast stream from the left side of the radiation section roof generates a single strong counter clockwise swirl, and this swirl extends to the outlet of the radiation section. The flow pattern is illustrated in Fig. 4. The back recirculation swirl near the centreline changes more clearly from clockwise to anti-clockwise than in the case with symmetric off-gas circulation.

The simulation results indicate that the cold air leaked from the boiler bottom does not disturb the main flow pattern, but it follows the main swirl. In the cases with off-gas circulation (either symmetric or asymmetric), most of the leakage air travels more directly to the outlet (except the air leaked from the first dust hopper), due to the main anti-clockwise swirl in the lower part of the radiation section. When the circulation off-gas is absent, the main circulation swirl is clockwise, and the leakage air is all swept back to the near inlet region.

Heat Transfer

Basic Features. The heat transfer simulation showed that the hot stream of process gas cools down rapidly from 1350°C to about 1000°C, immediately after entering the radiation section. The heat flux to the top-wall near the inlet of the radiation section is high, because of the strong upward hot stream. In contrast, the temperature distribution in the lower part of the radiation section is more uniform. In the basic case without off-gas circulation and air leakage, the computed outlet temperature in the radiation section is around 930°C, which is much higher than in practice with the circulated off-gas.

Symmetric Off-gas Circulation. Under the symmetric circulation conditions, the flow field and temperature contours are more evenly distributed in the two half regions in the side-wise direction, and the mirrored results are obtained. Fig. 5 shows the temperature contours at a few essential planes of the radiation section. It is obvious that the cooling effect from the off-gas circulation in the radiation section is significant. According to the averaged outlet temperatures, the symmetric off-gas circulation results in about 130°C further cooling in the radiation section outlet, compared to the case without off-gas circulation. Further gas cooling due to the leakage air is about 25°C under the condition of the symmetric off-gas circulation.

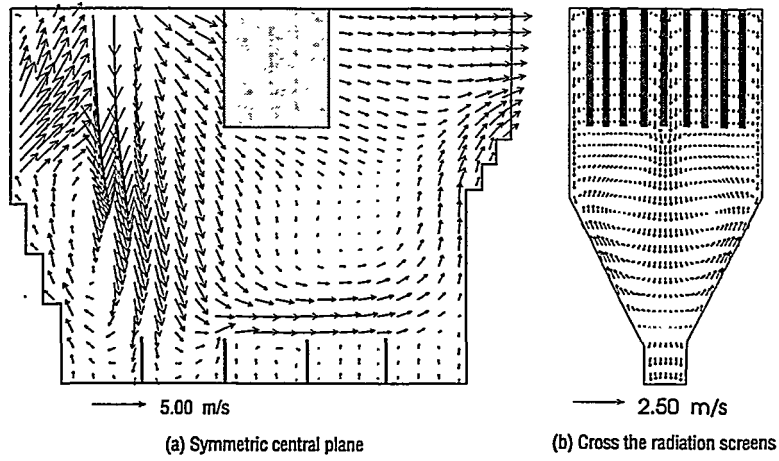


Fig. 3 – Effect of the symmetric off-gas circulation and air leakage on the flow pattern in the radiation section.

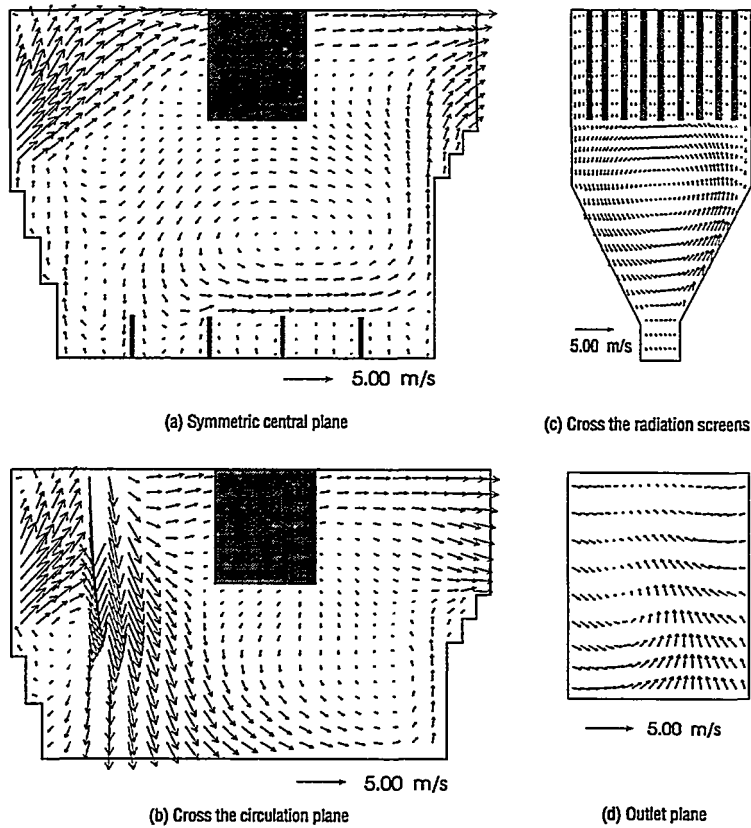


Fig. 4 – Effect of the asymmetric off-gas circulation and air leakage on the flow pattern in the radiation section.

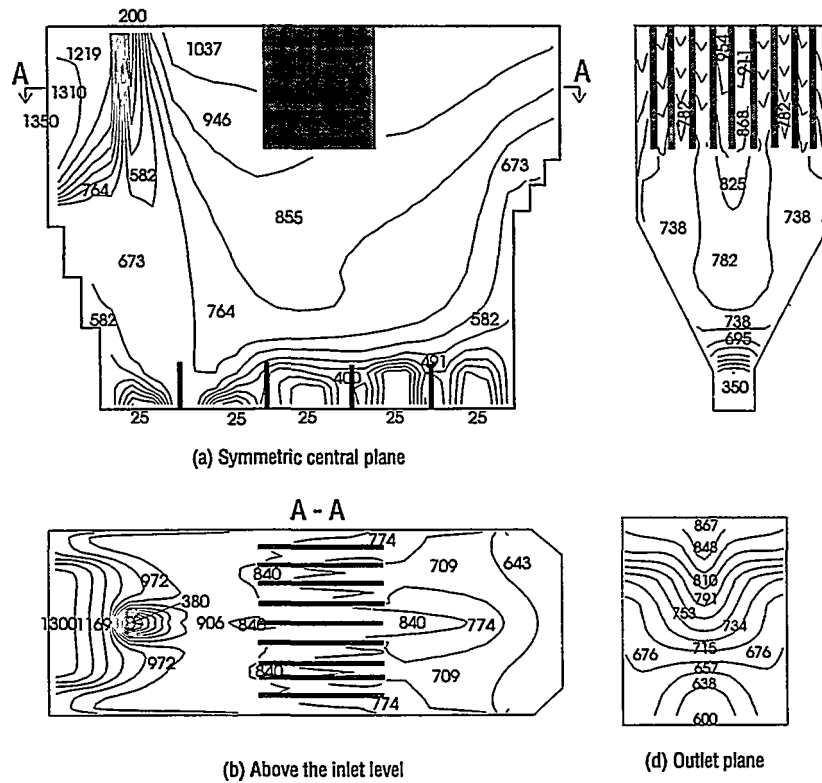


Fig. 5 – Temperature contours ($^{\circ}\text{C}$) at a few characteristic planes with symmetric off-gas circulation.

Asymmetric Off-gas Circulation. When the off-gas is circulated to the radiation section via an asymmetrically located opening as was discussed previously, the temperature distribution changes significantly, mainly due to the dramatic flow pattern change. From the sectional front-view, it can be seen that the high velocity stream generates strong uneven cooling of the gas in the radiation section, shown in Fig. 6. The anti-clockwise stream squeezes the hot process gas flow closer to the side-wall on the side of the circulation location. The cooler part of the gas circulates to the other side-wall direction and upwards, so that the temperature on the other side can even be about 100°C lower than in the off-gas circulation side. This uneven temperature distribution extends to the outlet of the radiation section. At the outlet, the temperature near the lower right corner is around 630°C , while it increases towards the upper left corner to about 850°C . The uneven temperature distribution is manifested in side-view and top-view cross-sections, too. Asymmetric flow and temperature distributions cause an uneven thermal load to the boiler walls, and may lead to unwanted consequences for boiler operation. For instance, molten or semi-molten dust droplets may more probably hit the side wall due to the gas stream carriage. Therefore, a boiler wall fouling problem may result. This effect will be transported to the convection section but it is buffed by the tube-banks.

Energy Distribution and Boiler Efficiency. Fig. 7 shows the overall energy balance and the boiler efficiencies in the radiation section from the computations under three different operating conditions. It is clear that heat release from the dust sulphating and SO₂ oxidation is an important part of the incoming energies, accounting for 16-18% of the total. The circulated off-gas and leakage air contribute about 8-9% of the total energy. Concerning the boiler efficiency, it can be seen that the basic case without off-gas circulation and air leakage has the highest value of 41%. When the air leakage is included, the efficiency is about 37%. With symmetric off-gas circulation, the efficiency is lowered to 29%, and for asymmetric off-gas circulation the efficiency is only 25%.

The computational results indicate that radiation is the major heat transfer mode in the radiation section of the boiler. Radiation accounts for about 80 - 90% of the total heat transferred through all boiler walls in the radiation section, depending on the operating conditions.

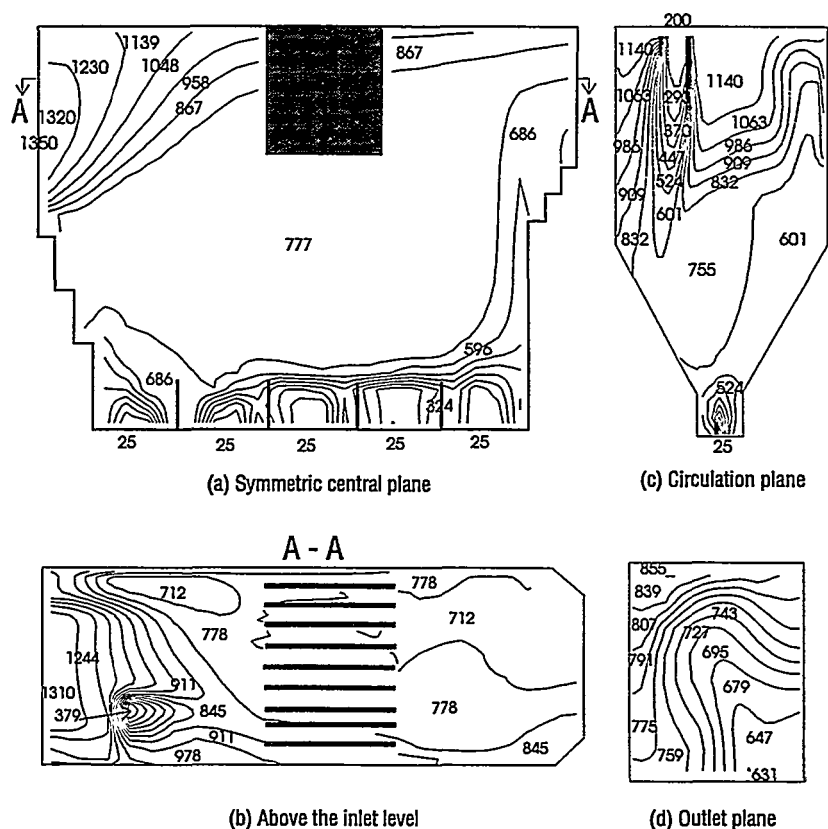


Fig. 6 – Temperature contours (°C) at a few characteristic planes with asymmetric off-gas circulation.

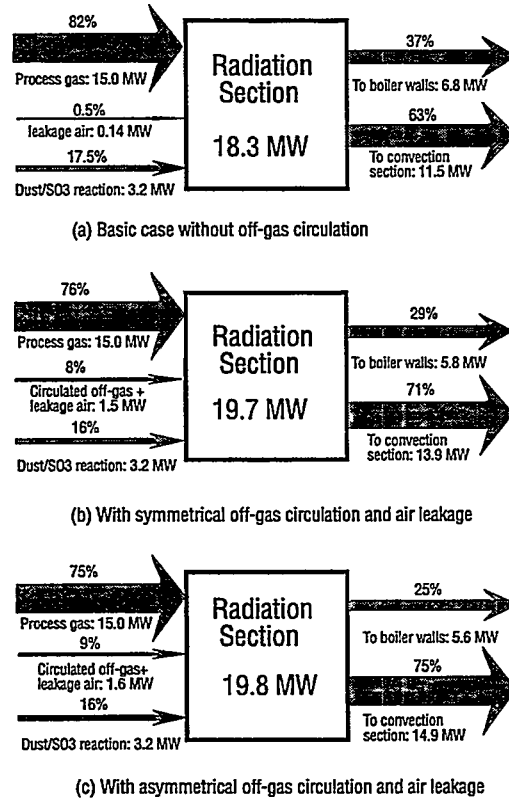


Fig. 7 – Computed energy distribution in the radiation section of the waste-heat boiler under different operating conditions.

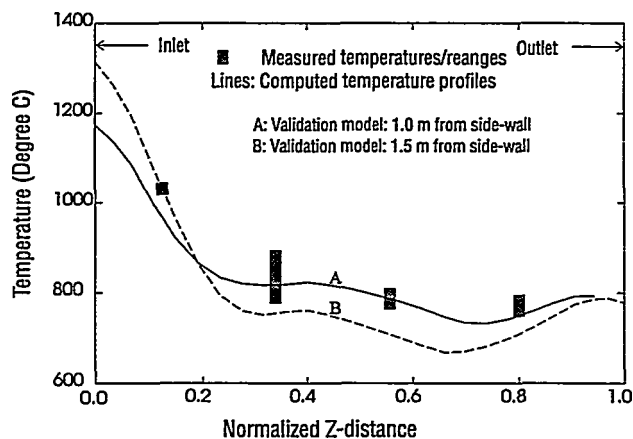
Comparison with Laboratory Models and Industrial Measurements

Fluid Flow. The computational results of the full-scale industrial boiler were compared with a physical two-dimensional water model and a three-dimensional gas/smoke model conducted by Outokumpu Research Oy on a laboratory scale [12]. Videotaped physical gas model was also used for comparison. The large recirculation swirl was predicted in the radiation section by both methods. Both cases reflect a fast stream just below the ceiling. The flow behaviour was found to be in good agreement with both the water and gas models.

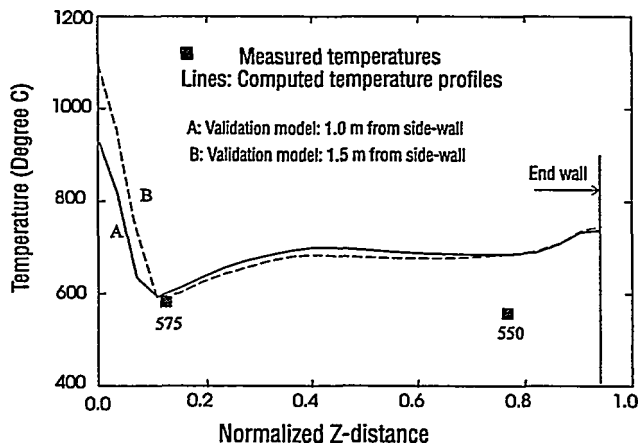
Heat Transfer. Some temperature measurements for the waste-heat boiler at the copper flash smelting line of Outokumpu Harjavalta Metals Oy are available [5]. The data provide important validation information for the heat transfer simulation. During the measurements, the gas volume flow rate was between 10,000 and 20,000 Nm³/h, without off-gas circulation. Fig. 8 shows the computed temperature profiles close to the measuring plane in the validating model of the radiation section. The measured temperature values or ranges are also marked in the same figure. The measuring distance away from the side wall was between 1.0 m and 1.5 m. It is obvious that the temperature of

the off-gas dropped rapidly from about 1350°C to about 1000°C after entering the radiation section. Near the outlet to the convection section, temperatures from 750 to 800°C remained.

The calculated temperature distribution agrees very well with the measured data in the upper part of the radiation section, but the measured value in the lower part near the convection section is about 100 to 150°C lower than the calculated one. Generally speaking, the difference between the predicted and measured temperatures is below 100°C. In the high temperature area of the first two points near the inlet, the agreement is even better, and the difference is within 50°C. It is noteworthy that the trend of the temperature distribution is fully predicted by the simulation. The predicted rapid cooling near the boiler inlet by thermal radiation is confirmed well by the measurements.



(a) Upper four measurement points



(b) Lower two measurement points

Fig. 8 – Comparison of the calculated temperature profiles in the validation model with the measured data.

SUMMARY

Both gas flow and heat transfer phenomena occurring in an industrial scale waste-heat boiler of the Outokumpu flash smelting process have been simulated with CFD-software PHOENICS. The flow was computed for a single gas phase with the standard $k-\epsilon$ turbulence model, and the radiation heat transfer was simulated with the composite-flux model. At this stage, no chemical reactions, such as dust oxidation or sulphating, were taken into account, but the heat release from the sulphating reactions and SO_3 formation was included to the heat transfer simulation.

The flow inside the boiler was found to be distinctly three-dimensional. An obvious recirculating flow is present in the main part of the radiation section. A fast forward flow exists in the upper part of the radiation section below the top wall. In the convection section, the flow is more uniform in the upper part, and the fast horizontal flow dominates.

General success was obtained by applying the radiation model in the radiation section of the boiler. A reasonable temperature distribution was achieved in the simulation, compared with the industrial measurements. Radiation is the main heat transfer mode in the radiation section, and the share of radiation is in the range of 80 to 90% under various operating conditions. The boiler efficiency of the radiation section is between 25% and 40%.

Circulating part of the cooler off-gas from the electrostatic precipitator to the radiation section of the boiler changes the flow pattern to a large extent, mainly in the radiation section. Asymmetric off-gas circulation makes the flow strongly uneven, and a larger circulating swirl was formed in the side-wise direction. The cooling effect from the circulated off-gas is significant in the radiation section, and the average further cooling to the process gas is about 130°C . However, the circulated off-gas lowers the boiler efficiency.

Air leakage in the radiation section does not influence the main flow pattern, but brings about some cooling effect near the bottom region. With or without circulated off-gas, the leakage air flows to the different direction, and this brings slightly different cooling ($20 - 25^\circ\text{C}$) to the off-gases.

ACKNOWLEDGEMENTS

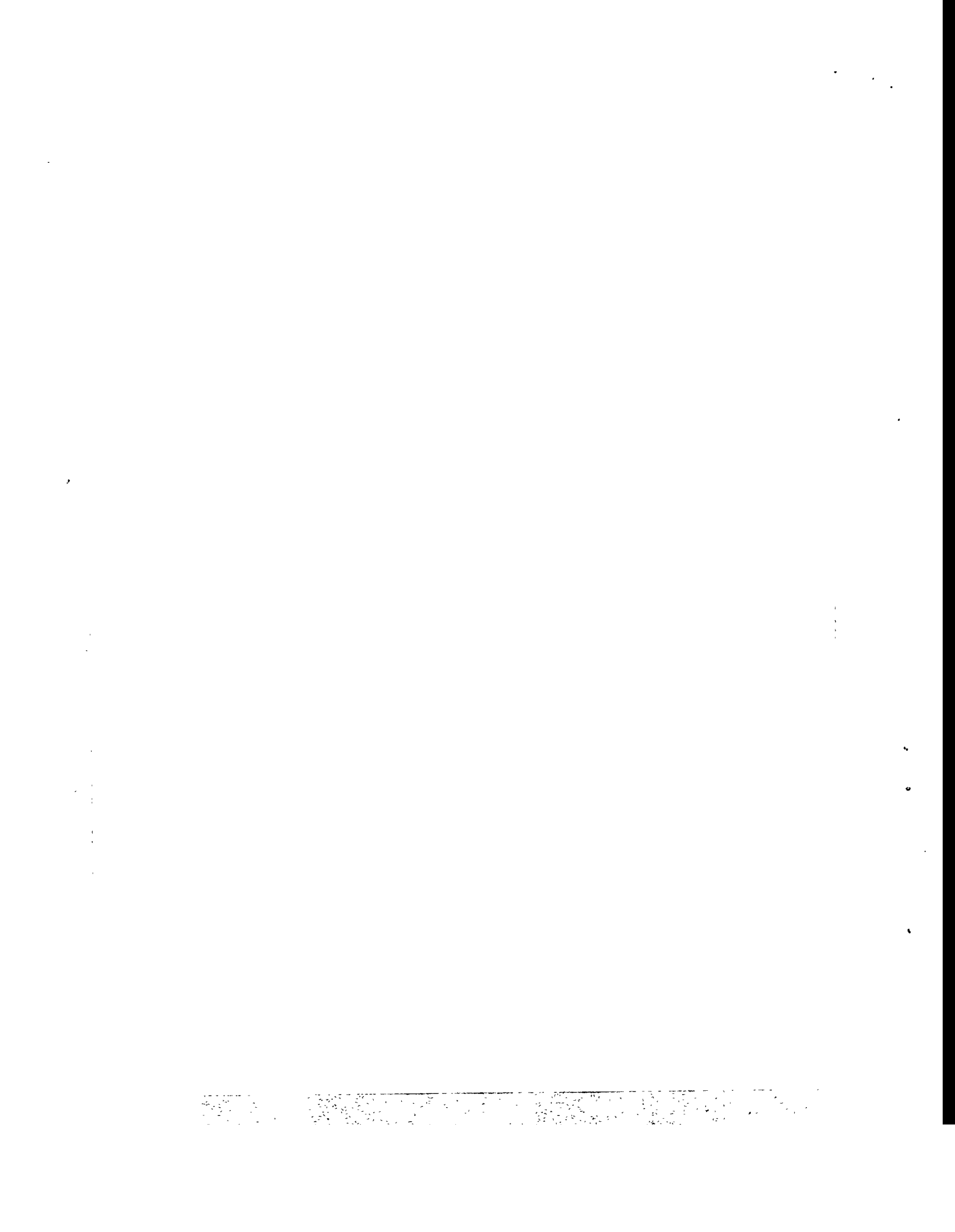
The authors wish to thank the Ministry of Trade and Industry and the Technology Development Center (Tekes), Finland, for financing the work and Outokumpu Research Oy for permission to publish this paper. The authors are also indebted to Mr. Markku Kytö, Vice President of Outokumpu Engineering Oy, and Docent Pekka Taskinen, Pyrometallurgy Research Director of Outokumpu Research Oy, for their interest in this work and for their valuable advice.

REFERENCES

1. T. Mäntymäki, "Development of flash smelting to become the leading smelting method for copper and nickel concentrates", *Vuoriteollisuus-Bergshanteringen*, 43(1) (1985), 29-33 (in Finnish).
2. P. Hanniala and I. Kojo, "Utilization of Outokumpu flash technology to meet environmental requirements", *Proceedings of COPPER 95 International Conference, Vol. II - Mineral Processing and Environment*. Eds. A. Casali et al. (The Metallurgical Society of CIM, 1995), 305-318.
3. K. Kaasila and E. Löytymäki, "Heat recovery in metallurgical processes and applications within Outokumpu Company", *Advances in extractive metallurgy and refining*, ed. M. J. Jones (London, UK: IMM, 1972), 591-603.
4. L. Lilja and K. Rajainmäki, "On the experimental and computational modeling at Outokumpu Research Oy", *The 2nd Colloquium on process simulation*, ed. A. Jokilaakso, 6-8 June 1995, Espoo, Finland. 217-230.
5. R. Backman, H. Hupa and J.K. Mäkinen, "Formation and corrosion effects of sulfur trioxide in copper smelting processes", (*Metallurgical Society of AIME, TMS Technical Paper*, 1986), Paper No. A86-56.
6. T. Inami, et al., "Modification of concentrate burner for a copper flash smelting furnace", *Pyrometallurgy of Copper, Proceedings of the Copper 91 International Symposium - Volume IV*, eds. C. Diaz, C. Landolt, A. Luraschi and C.J. Newman, Aug. 18-21, 1991, Ottawa, Ontario, Canada, 49-63.
7. D.B. Spalding, *The PHOENICS Beginner's Guide*, CHAM TR/100, CHAM Limited, (London, 1990).
8. M. Kytö, P. Taskinen and L. Lilja, Private communication Outokumpu Research Oy, Pori, Finland, 1993.
9. H.C. Hottel and A.F. Sarofim, *Radiative Transfer*, (McGraw-Hill Book Company, 1967), 411.
10. S.H. Chan and C.L. Tien., "Infrared radiation properties of sulfur dioxide", *J. Heat Transfer (Trans. ASME)*, May (1971), 172-178.
11. R. Siegel and J.R. Howell, *Thermal Radiation Heat Transfer*, 2nd Edition, (Hemisphere Publishing Corp., Washington, 1981), 617.
12. Outokumpu Internal Report, Outokumpu Research Oy, Pori, Finland, 1993.

For Your Notes

1950



AUTHOR INDEX

A		M	
Ablitzer, D.	225, 251	Majander, E.O.J.	7
Ahlstedt, H.	309	Mannila, P.	345
Ahokainen, T.	167	Manninen, M.T.	7
B		Mavrommatis, K.	295
Backman, R.	357	Mäki-Mantila, E.	327
Brink, A.	151	N	
E		Nieminen, R.	373
Eriksson, G.	357	O	
F		Oksanen, A.	327
Fang, G.	127	P	
G		Paloposki, T.	345
Green, R.K.	127	Patisson, F.	251
H		Penttilä, K.	361
Hakala, J.	345	Pérez-Tello, M.	189
Houzelot, J.L.	251	Petitnicolas, L.	225
Hupa, M.	133, 151	R	
Hurme, M.	113	Riihilahti, K.M.	189
Hyppänen, T.	277	Robertson, D.G.C.	221
J		Rodrigues Jr., R.	27
Jardy, A.	225	Rusanov, A.V.	69
Jokilaakso, A.	167, 403	S	
Jourde, J.	251	Smith, A.G.	43
Järvinen, J.	373	Sohn, H.Y.	189
Jääskeläinen, K.	151	Solodov, V.G.	89
K		Spalding, D. B.	3
Kilpinen, P.	133, 151	Sundström, K.	357
Kjaldman, L.	151	Y	
Koukkari, P.	361	Yanagihara, J.I.	27
L		Yang, Y.	403
Lahtinen, M.	309	Yershov, S.V.	69
Laine, J.	113		
Laukkanen, I.	361		
Laukkanen, J.	345		
Luoma, M.	43		